

N O T I C E

THIS DOCUMENT HAS BEEN REPRODUCED FROM
MICROFICHE. ALTHOUGH IT IS RECOGNIZED THAT
CERTAIN PORTIONS ARE ILLEGIBLE, IT IS BEING RELEASED
IN THE INTEREST OF MAKING AVAILABLE AS MUCH
INFORMATION AS POSSIBLE

DOE/NASA/0167-80/1
NASA CR-165175
AIRESEARCH No 31-3725

1/81
2-16-81
4-17-81
JUL 9 '81
10/26/81
1/15/82

ADVANCED GAS TURBINE (AGT) POWERTRAIN SYSTEM DEVELOPMENT FOR AUTOMOTIVE APPLICATIONS

PROGRESS REPORT NUMBER 1 (OCTOBER 1979 - JUNE 1980)

Engineering Staff of
AiResearch Manufacturing Company of Arizona
A Division of the Garrett Corporation

November 1980

Prepared for

NATIONAL AERONAUTICS AND SPACE ADMINISTRATION
Lewis Research Center
Cleveland, Ohio 44135
Under Contract DEN3-167

(NASA-CR-165 75) ADVANCED GAS TURBINE (AGT)
POWERTRAIN SYSTEM DEVELOPMENT FOR AUTOMOTIVE
APPLICATIONS Progress Report, Oct. 1979 -
Jun. 1980 (AiResearch Mfg. Co., Phoenix,
Ariz.) 431 p HC A19/MF A01

N82-16937

for

Unclas
CSCI 13F G3/85 05554

U.S. DEPARTMENT OF ENERGY
Office of Transportation Programs
Division of Automotive Technology Development
Washington D.C. 20585



DOE/NASA/0167—80/1
NASA CR— 165175
AIRESEARCH No 31-3725

**ADVANCED GAS TURBINE (AGT)
POWERTRAIN SYSTEM DEVELOPMENT
FOR AUTOMOTIVE APPLICATIONS**

PROGRESS REPORT NUMBER 1 (OCTOBER 1979 - JUNE 1980)

Engineering Staff of
AiResearch Manufacturing Company of Arizona
A Division of the Garrett Corporation

November 1980

Prepared for
NATIONAL AERONAUTICS AND SPACE ADMINISTRATION
Lewis Research Center
Cleveland, Ohio 44135
Under Contract DEN3—167

for
U.S. DEPARTMENT OF ENERGY
Office of Transportation Programs
Division of Automotive Technology Development
Washington D.C. 20585

PRECEDING PAGE BLANK NOT FILMED

TABLE OF CONTENTS

	<u>Page</u>
1.0 SUMMARY	1
2.0 INTRODUCTION	9
3.0 POWERTRAIN DEVELOPMENT	17
3.1 Reference Powertrain Design (RPD)	19
3.2 Performance	24
3.3 Vehicle Integration	32
4.0 COMPONENT/SUBSYSTEM DEVELOPMENT	35
4.1 Compressor Development	37
4.2 Turbine Development	80
4.3 Combustion System	151
4.4 Regenerator	169
4.5 Gearbox/Transmission	197
4.6 Structures	211
4.7 Ceramic Component Development	241
4.8 Foil Gas Bearing	284
4.9 Bearings and Seals	292
4.10 Rotor Dynamics Development	298
4.11 Controls and Accessories	304
APPENDIX I FORD MOTOR COMPANY ADVANCED GAS TURBINE (AGT) POWERTRAIN PROGRAM FIRST SEMI-ANNUAL TECHNICAL PROGRESS REPORT	321
APPENDIX II AIRESEARCH CASTING COMPANY (ACC) ADVANCED GAS TURBINE (AGT) POWERTRAIN PROGRAM FIRST SEMI-ANNUAL TECHNICAL PROGRESS REPORT	375
APPENDIX III CARBORUNDUM COMPANY ADVANCED GAS TURBINE (AGT) POWERTRAIN PROGRAM FIRST SEMI-ANNUAL TECHNICAL PROGRESS REPORT, COMMON WORK	397
APPENDIX IV CARBORUNDUM COMPANY ADVANCED GAS TURBINE (AGT) POWERTRAIN PROGRAM FIRST SEMI-ANNUAL TECHNICAL PROGRESS REPORT, UNIQUE WORK	403
APPENDIX V PURE CARBON COMPANY ADVANCED GAS TURBINE (AGT) POWERTRAIN PROGRAM FIRST SEMI-ANNUAL TECHNICAL PROGRESS REPORT	423
REFERENCES	427

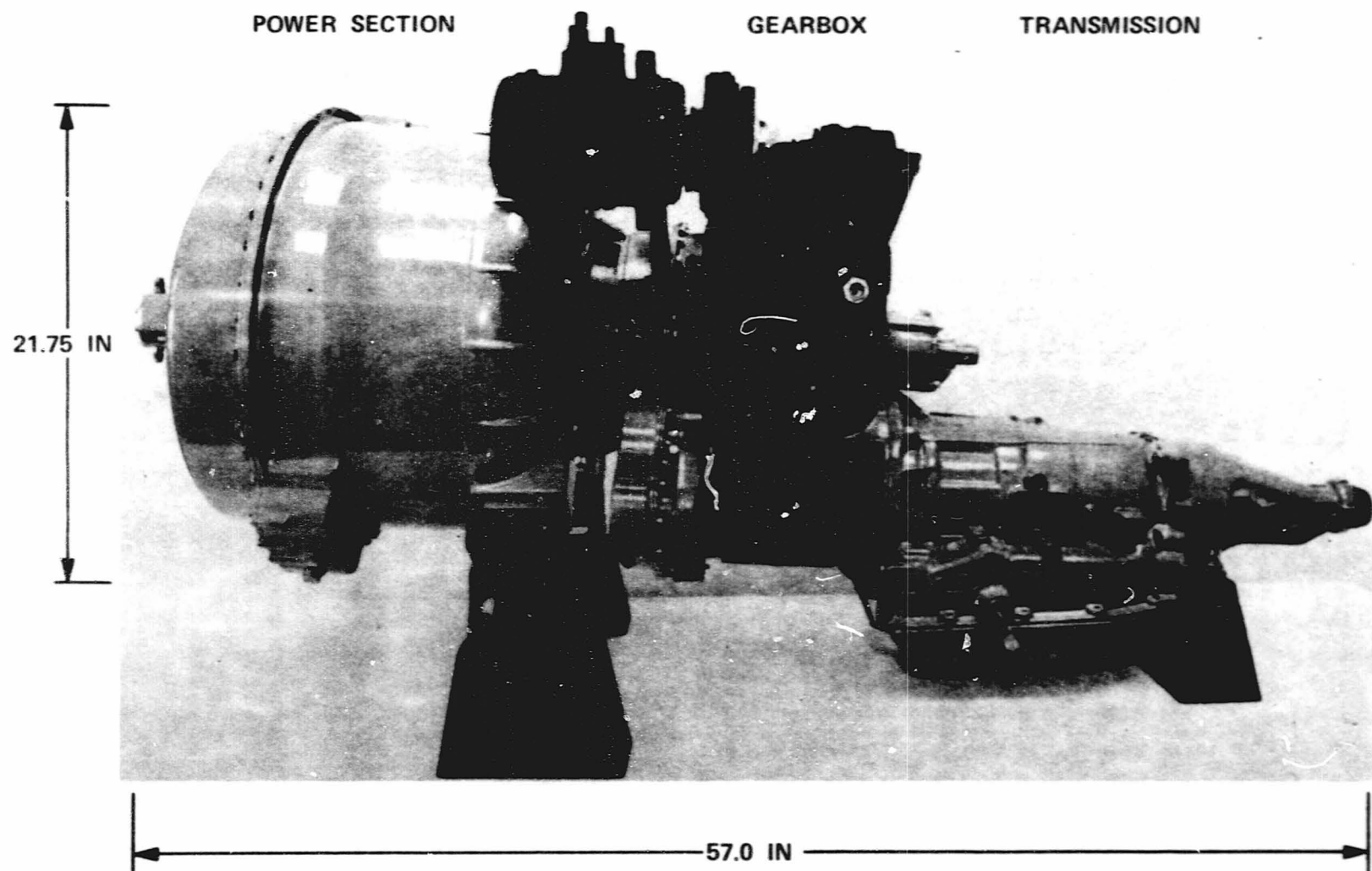
1.0 SUMMARY

The AGT101 Powertrain, pictorially shown in Figure 1, consists of a regenerated single shaft gas turbine engine (flat-rated at 100 horsepower), a split differential gearbox and a Ford Automatic Overdrive (AOD) production transmission. The powertrain is controlled by an electronic digital microprocessor and associated actuators, instrumentation, and sensors. Standard automotive accessories are driven by engine power provided by an accessory pad on the gearbox.

The AGT101 power section, Figure 2 is characterized by a single-stage 5:1 backward swept centrifugal compressor and single-stage ceramic radial inflow turbine mounted on a common shaft. This rotating group is supported at the output pinion gear by an angular contact ball bearing and an air lubricated foil bearing located between the compressor and turbine. Maximum rotor speed of the AGT101 is 100,000 rpm. Ceramic combustor and hot section structural components are utilized in conjunction with the ceramic radial turbine rotor. This allows engine operation at turbine inlet temperatures (TIT) of 2500°F (maximum power) and 2150°F (idle) to maintain maximum thermodynamic efficiency over the operating range. Variable geometry has been utilized in the compressor and combustion sections to vary engine airflow and control combustion primary zone temperatures to approximately 3000°F. Table 1 summarizes the power section salient features.

The gearbox, Figure 3, is a split-path differential design accepting power directly from the output pinion gear. Power is split in the differential planetary gears with a portion taken through an output gear on the planetary carrier directly to the AOD transmission. The remaining power continues via the same differential planetary to a rotating ring gear and associated gear train to the variable stator torque converter (VSTC). The VSTC provides a variable speed ratio output that is fed back to the planetary carrier and combines with the power delivered to the transmission.

AGT101 powertrain development was initiated in October 1979 through detail design activities based on prior studies conducted and reported in References 1 and 2. Design efforts on the Reference Powertrain Design were approved in January 1980 by NASA. Evolutionary progress toward the realization of the RPD continued with design approval in April 1980 of the Mod I, powertrain concept. As shown in Figure 4, the AGT101 evolution begins with the Mod I, Build 1 all metallic (except regenerator) version of the engine. As ceramic hot section structural components are qualified in dedicated test rigs, the Mod I, Build 1 is selectively upgraded to the Mod I concept (2100°F TIT, metal rotor, ceramic structures). This stepwise evolutionary process enables early verification of component technology development, controls interface and validation of computer programs used to predict engine performance. In addition, based on "systems



ORIGIN PAGE
BLACK AND WHITE PHOTOGRAPH

Figure 1. AGT101 Powertrain Configuration.

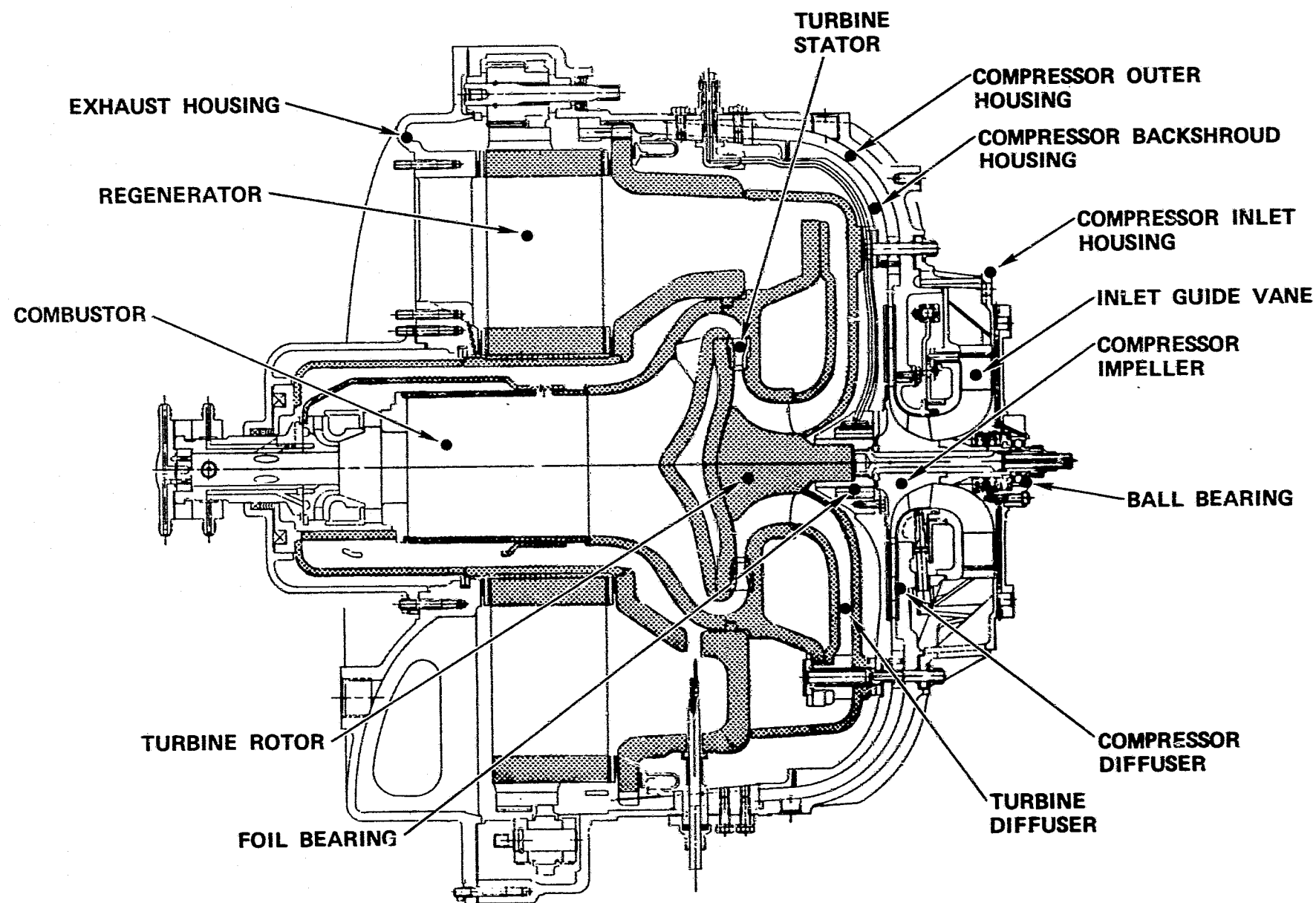


Figure 2. AGT101 Power Section Layout.

TABLE 1. AGT101 DESIGN SUMMARY (MAXIMUM POWER)

COMPRESSOR - CENTRIFUGAL

Material	Aluminum
Design flow, lbs/sec	0.85
Number of blades	12/12
Backward curvature, degrees	50
VIGV type, number of vanes	Articulated, 17
Diffuser type	2D vane island cascade deswirl
Predicted stage efficiency, percent	80.5

TURBINE - RADIAL INFLOW

Material	SiC or Si_3N_4
Maximum inlet temperature, °F	2500
Maximum tip speed, fps	2300
Number of blades	13
Stator type, number of vanes	Radial, 19
Diffuser type	Radial
Predicted stage efficiency, percent	90.1

REGENERATOR - ROTARY

Material, fabrication process	AS or MAS, extruded
Active matrix diameter, in	18.2
Matrix thickness, in	3.3
Hydraulic diameter, in	0.020
Support type, drive	Rim, rim drive
Predicted effectiveness, percent	92.9
Predicted seal leakage, percent	3.6

COMBUSTOR - PILOTED, VARIABLE GEOMETRY

Material	Ceramic
Outlet temperature, °F	2150 to 2500
Maximum primary zone temperature, °F	3000

BALL BEARING - SPLIT INNER RACE, ANGULAR CONTACT

Material	52100
Size, mm	15
Maximum load - radial/axial, lbs	9/255

FOIL BEARING

Number of foils	7
Diameter, in	1.35
Length, in	1.075
Maximum load - steady state, lbs	3
Maximum load - shock, g's	X6

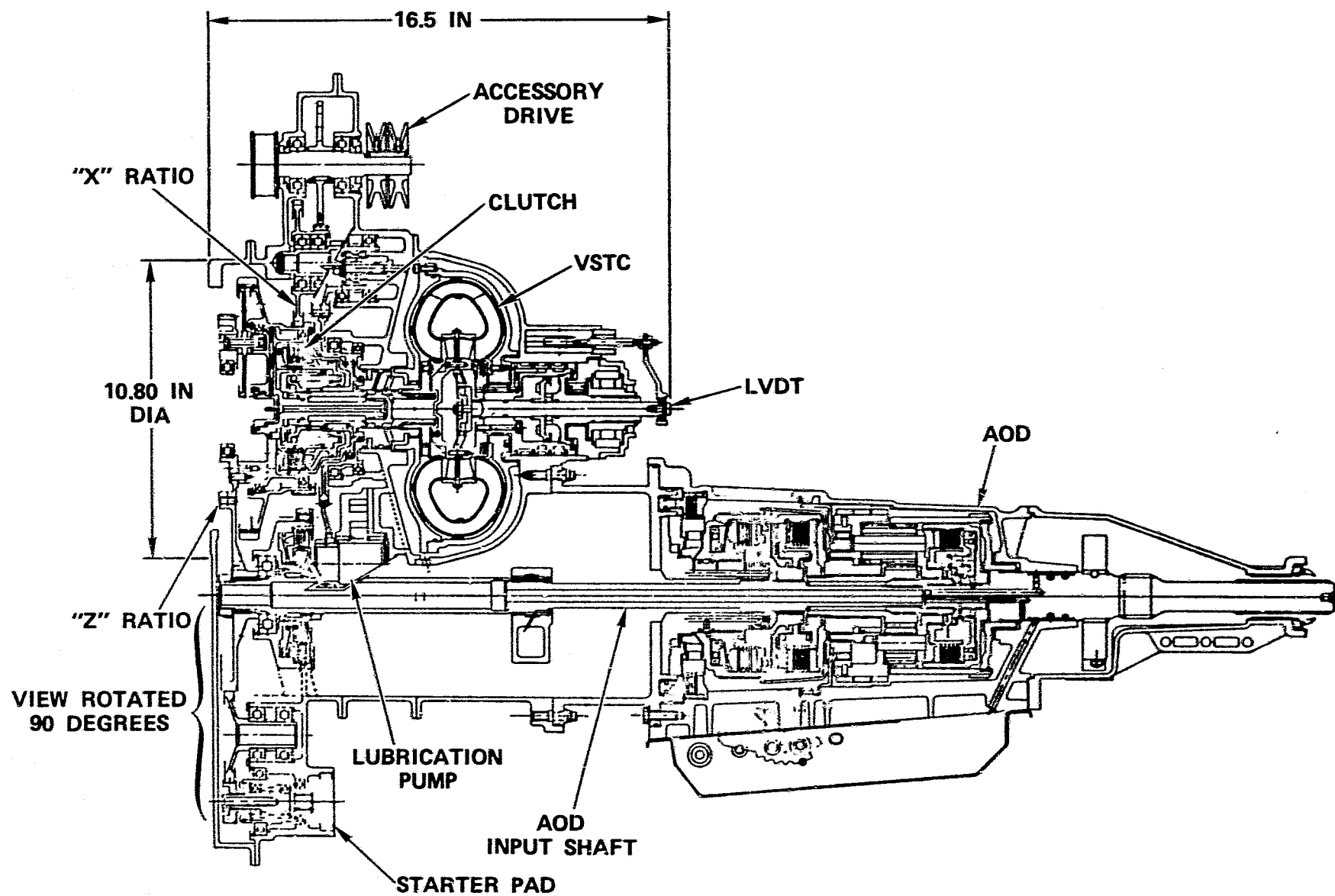


Figure 3. AGT101 Gearbox and Transmission Layout.

ORIGINAL PAGE IS
OF POOR QUALITY

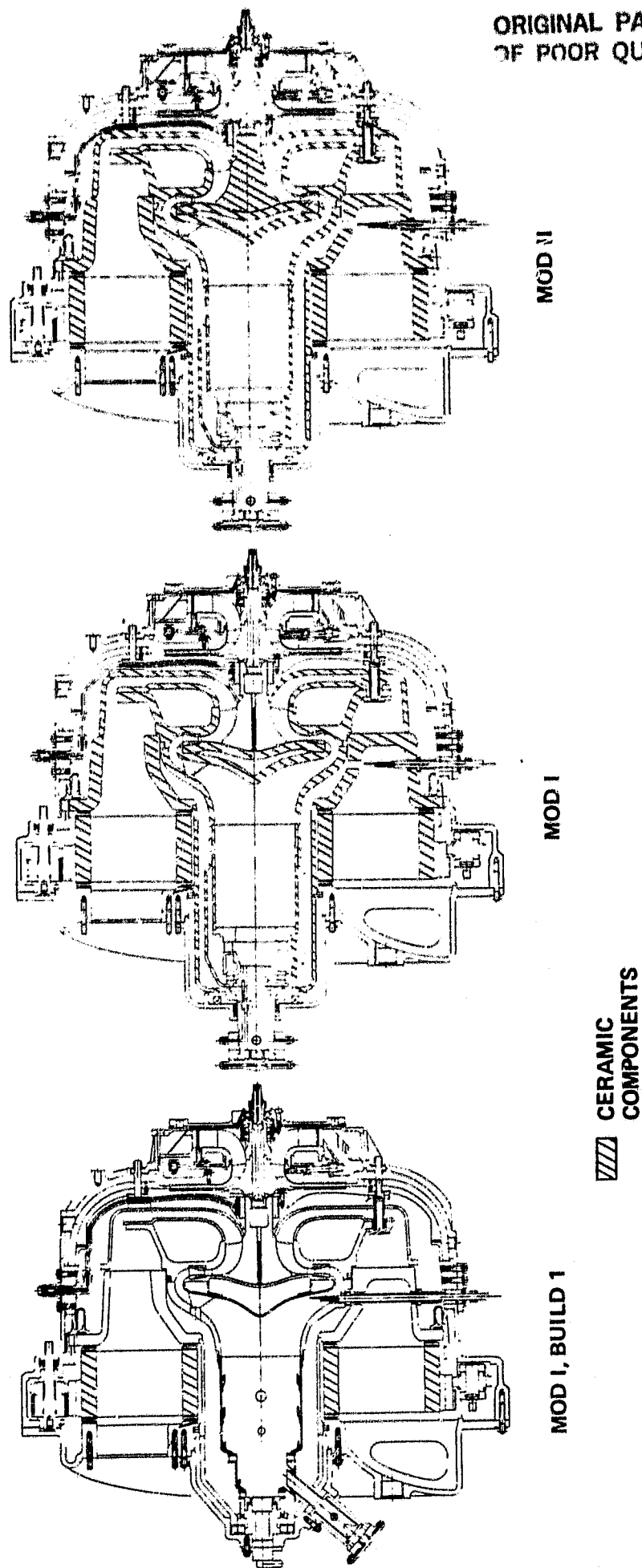


Figure 4. AGT101 Ceramic Evolution.

design" philosophy wherein distinct recognition is given to the AGT101 operating range over the CFDC, an interactive component/engine design feedback loop is established to further optimize program goals (i.e., fuel economy, driveability, emissions, etc.). The evolutionary process continues with the introduction of the ceramic radial turbine rotor into the Mod I powertrain. This configuration has been entitled Mod II and is equivalent to the RPD at this time. Incorporation of the ceramic rotor will allow TIT to be increased to 2500°F. Mod I equipped vehicles will be delivered to EPA prior to May 1984 for evaluation and demonstration of progress toward the program goals. Mod II equipped vehicles will be delivered prior to May 1985 for final evaluation. Table 2 shows the AGT101 powertrain performance summary and salient component configuration.

As noted herein, AGT101 project analytical and empirical results through June 1980 indicate that all contract goals, objectives, and milestones, can be achieved.

TABLE 2. AGT101 POWERTRAIN SUMMARY

	Mod I Build 1	Mod I	Mod II	RPD
Reference Fuel	Gasoline	Gasoline	DF-2	Gasoline
Ambient Conditions (CFDC)	85°F, 500 ft	85°F, 500 ft	59°F, SL	85°F, 500 ft
CFDC (mpg) (3163 lb Vehicle)	N/A	30	41.4	36
Cruise sfc	0.503	0.309	0.329	0.329
Maximum rpm	100,000	100,000	100,000	100,000
Maximum Power (hp net)	50	93.6	100	130
Turbine Inlet Temp (°F)	1600	2100	2500	2500
Regenerator Maximum Temperature (°F)	1441	1936	2000	2000
Powersection Configuration				
Compressor	2219 T6	PM Alum	PM Alum	PM Alum
Combustor	Diff Flame	Var Geom	Var Geom	Var Geom
Turbine	Metal	Metal	Ceramic	Ceramic
Regenerator	NGK-Thick	Corning Thin	Extruded	Extruded
Structures	Metal	Ceramic	Ceramic	Ceramic
Controls Configuration	Analog	Digital	Digital	Digital

2.0 INTRODUCTION

This report is the first of a series of Semi-Annual Technical Summary reports for the Advanced Gas Turbine (AGT) Powertrain System Development Project, authorized under NASA Contract DEN3-167, and sponsored by The Department of Energy. This report has been prepared by the AiResearch Manufacturing Company of Arizona, a Division of The Garrett Corporation, and includes information provided by Ford Motor Company, The Carborundum Company, AiResearch Casting Company and The Pure Carbon Company. The project is administered by Mr. Roger Palmer, Project Manager, NASA-Lewis Research Center, Cleveland, Ohio. This report presents plans and progress from contract start (October 1979) through June 1980.

Project effort conducted under this contract is part of the DOE Gas Turbine Highway Vehicle System Program. This program is oriented at providing the United States automotive industry the technology base necessary to produce gas turbine powertrains for automobiles that will have reduced fuel consumption and reduced environmental impact. It is intended that technology resulting from this program be capable of reaching the marketplace by the early 1990's.

The goal of this project is to develop and demonstrate, by May 1985, an advanced automotive gas turbine powertrain system which, when installed in a 1985 production vehicle of the Ford Fairmont class (3125 pound inertia weight), meets the following objectives:

- o A combined federal driving cycle (CFDC) fuel economy of 36 miles per gallon based on Environmental Protection Agency (EPA) test procedures and gasoline fuel. The AGT powered vehicle will substantially provide the same overall vehicle driveability and performance as a comparable 1985 production vehicle powered by a conventional spark ignition powertrain system

- o Gaseous emissions and particulate levels less than the following:

$\text{NO}_x = 0.4 \text{ gm/mile}$

$\text{HC} = 0.41 \text{ gm/mile}$

$\text{CO} = 3.4 \text{ gm/mile}$

and a total particulate of 0.2 gm/mile, using the same fuel as used for fuel economy measurements

- o Ability to use a variety of alternate fuels

Progress toward achieving these objectives will be demonstrated in dynamometer and vehicle testing of AGT powertrains at several points during the project. In addition to the objectives to be demonstrated, the following are system design objectives:

- o Reliability and life equal to or better than powertrains currently on the market
- o A competitive initial cost and a life cycle cost no greater than that of a comparable conventionally-powered automotive vehicle
- o Acceleration suitable for safety and consumer considerations
- o Noise and safety characteristics that meet the currently legislated and the Federal Standards and those projected for 1984

The following are major contract milestones:

- o Complete initial Reference Powertrain Design (RPD) and Mod I powertrain preliminary design review
- o Complete dynamometer characterization and assessment of first build of Mod I powertrain by May 31, 1982
- o Complete dynamometer characterization and assessment of Mod I powertrain by May 31, 1983
- o Complete vehicle testing of fuel economy and emissions using the Mod I powertrain system by May 31, 1984. Testing to be performed by the EPA on two vehicles
- o Complete dynamometer characterization and assessment of Mod II powertrain prior to May 31, 1984
- o Complete vehicle testing of fuel economy and emissions using the Mod II powertrain system by May 31, 1985. Testing to be performed by the EPA on two vehicles

The advanced Automotive Gas Turbine Powertrain System has been designated the "AGT101" and is shown installed in a 1980 Ford Fairmont in Figure 5. The AGT101 represents a significant advancement in gas turbine state-of-the-art. A significant quantity of ceramic parts are employed to enhance high temperature operation and provide low cost manufacturing potential for automotive application.

The AGT101 project team is depicted in Figure 6. AiResearch Manufacturing Company of Arizona, A Division of The Garrett Corpora-

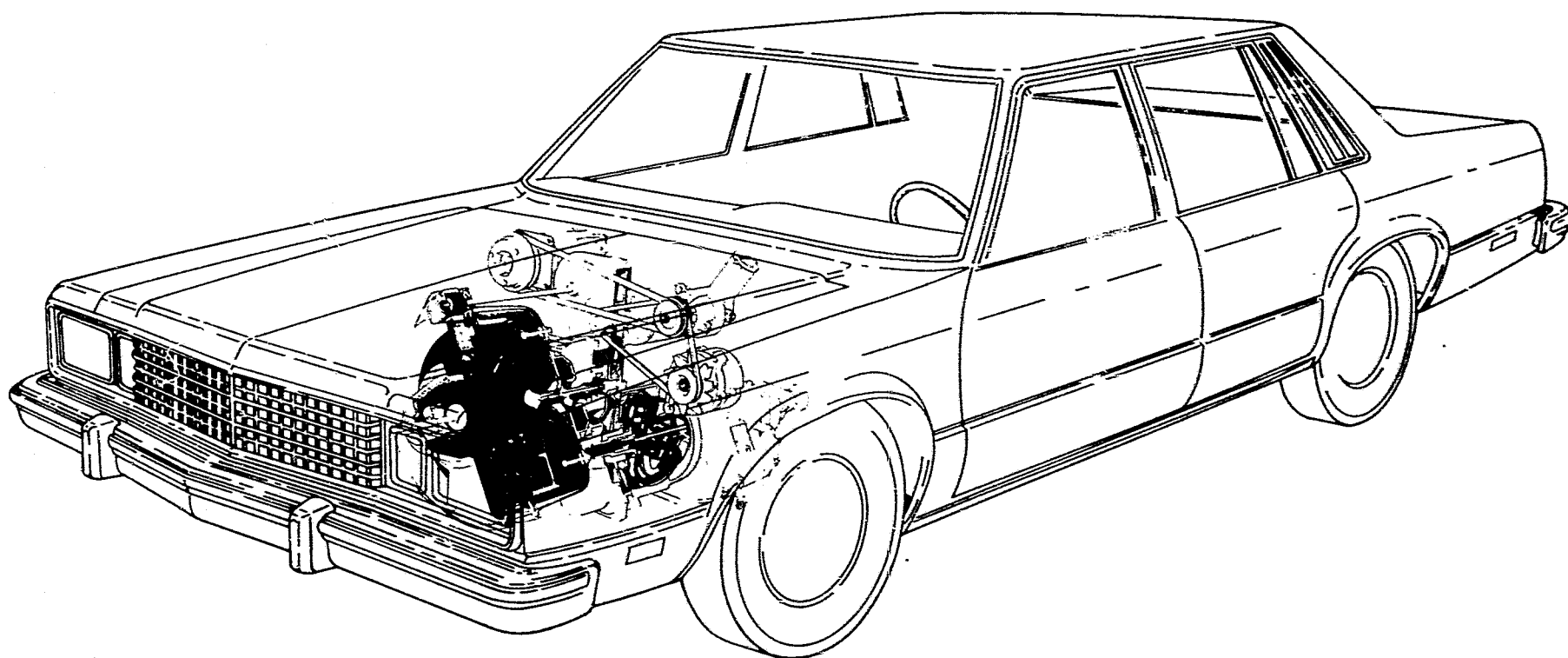


Figure 5. AGT Powertrain Installed in 1980 Ford Fairmont Vehicle.

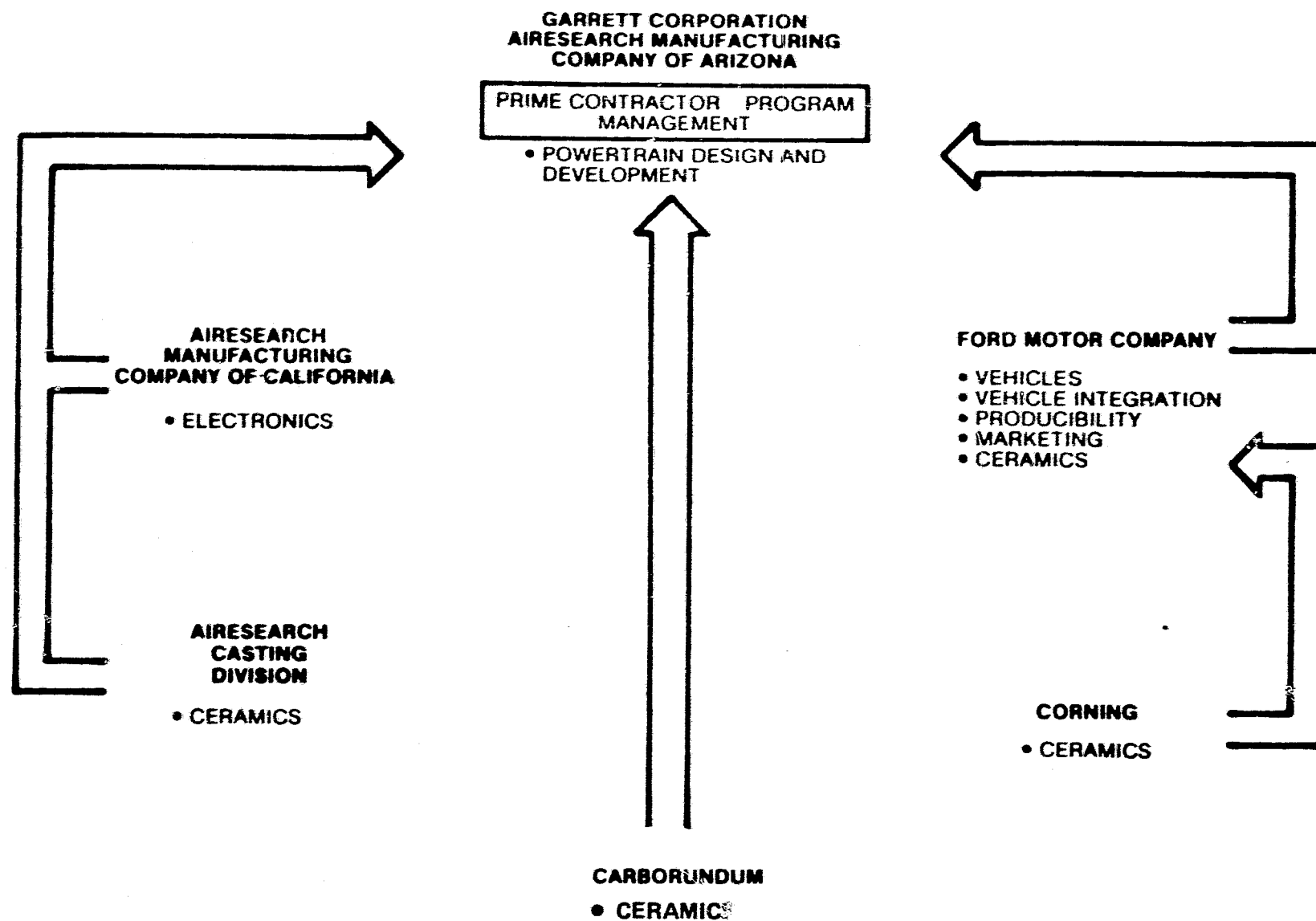


Figure 6. AGT101 Project Team.

tion, hereafter referred to as AiResearch Phoenix is the prime contractor responsible for overall powertrain design and development, and project management. Ford Motor Company as a major subcontractor, is responsible for providing the vehicle-related tasks (i.e., production manufacturing and marketing studies), regenerator technology, and major ceramics development efforts. The Corning Company, located in Corning, New York, is providing ceramic regenerator cores and one of the major ceramic structural components, under subcontract to Ford Motor Company. As shown in Figure 6, there are three other major subcontractors:

- o The Carborundum Company, a Division of Kennecott, located in Niagara Falls, New York, developing and providing ceramic components
- o AiResearch Casting Company, located in Torrance, California also developing and providing ceramic components
- o AiResearch Manufacturing Company of California, located in Torrance, California, developing and providing the electronic control system

The Garrett/Ford AGT101 project team organization is shown on Figure 7. The AiResearch Phoenix organization falls under the Power Systems Product Line in Phoenix, while the Ford organization is located in the Research Department at Dearborn, Michigan. Both companies provide upper management visibility via an executive review team which meets on a quarterly basis to review progress. The team is comprised of three executives of various disciplines from each organization providing guidance to help assure the success of the AGT101 Project. In addition, a Ceramic Advisory Committee, comprised of members of both organizations, meets on a periodic basis to review ceramic development progress.

The AGT101 project schedule, shown in Figure 8, includes the eight project tasks and six major contract milestones. The project duration is 68 months and is comprised of Phase I (45 months) and Phase II (23 months). At the conclusion of Phase I, DOE and NASA will evaluate progress of the AGT project prior to preceeding to Phase II.

The RPD design (Task 1, Figure 8) reflects the ultimate powertrain configuration to be achieved at the end of this project. Ford may utilize the RPD as a baseline to proceed into automotive preproduction and production phases which is the overall goal of the DOE Gas Turbine Highway Vehicle Systems Program. Mod I and Mod II are sequential development versions of the ultimate RPD powertrain. The Mod I engine initially begins with an all metallic power section. As Mod I development progresses, ceramic structural parts will be integrated into the Mod I power section until, at the end of Phase I, all hot section components will be ceramic except for the turbine rotor.

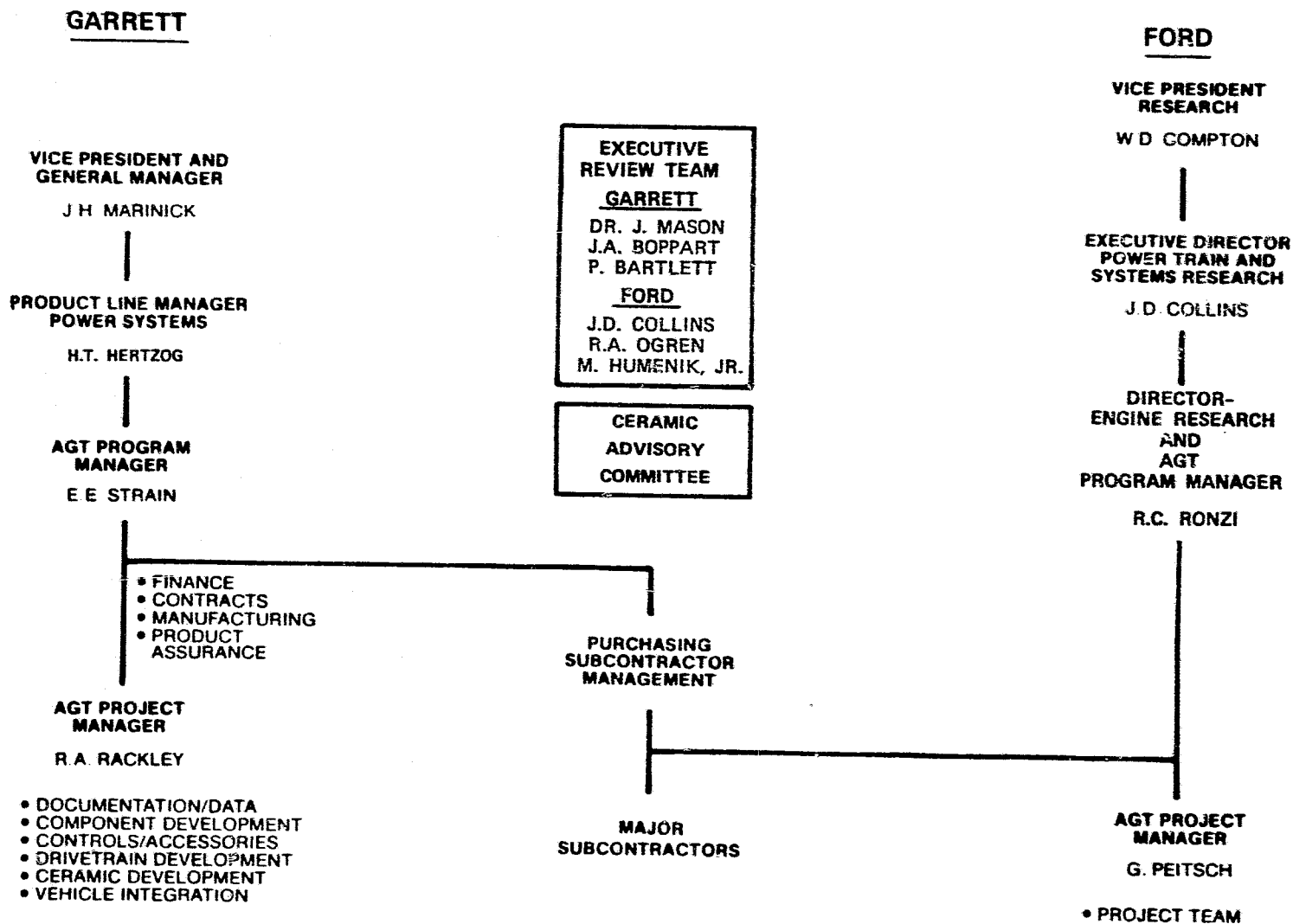


Figure 7. Garrett/Ford AGT101 Project Organization.

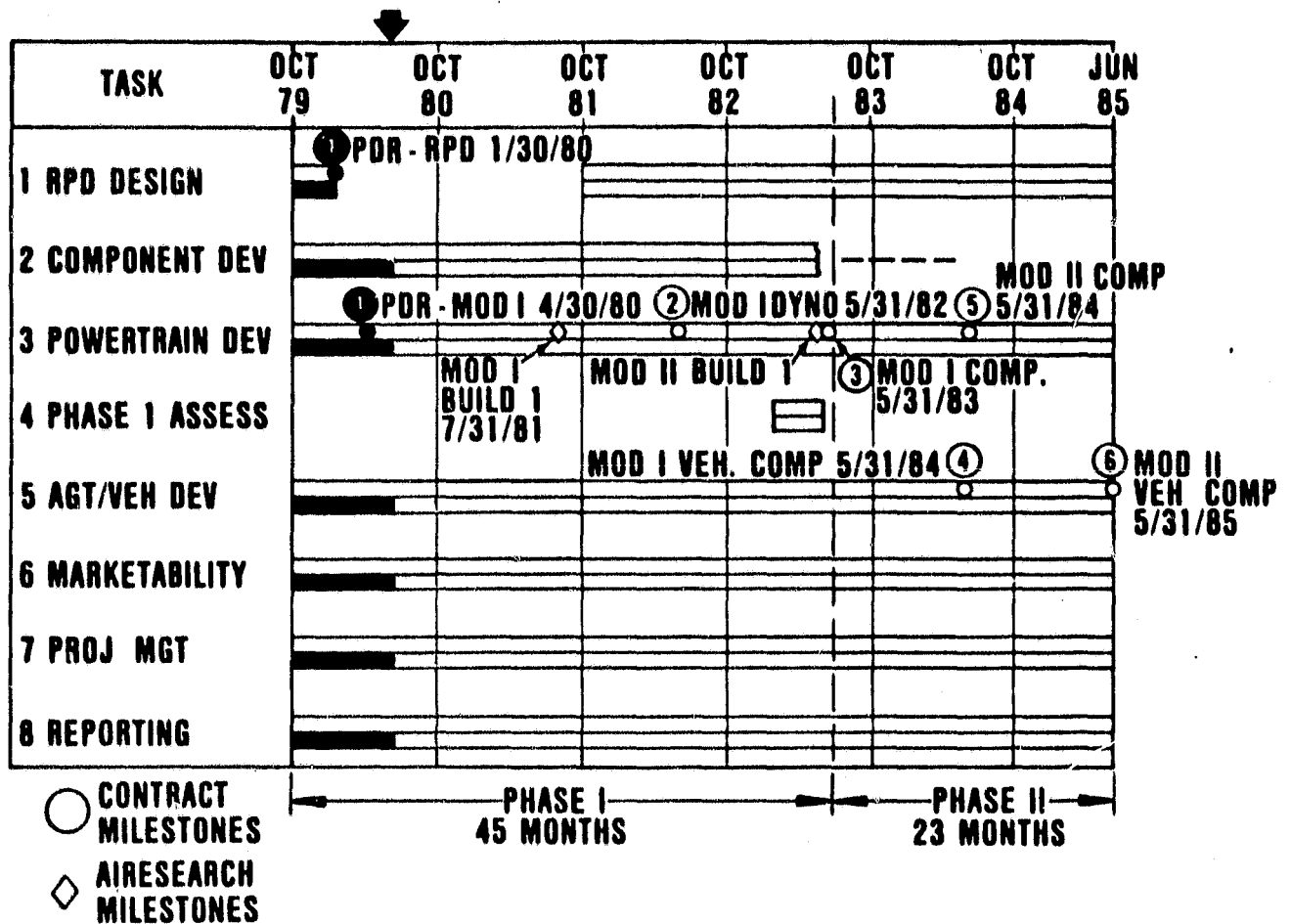


Figure 8. AGT101 Project Schedule.

Mod II development initiates with the inclusion of the ceramic turbine rotor into the final Mod I and continues through development to the end of Phase II.

Extensive component development is planned throughout the project (Task 2, Figure 8) and is discussed in detail in Section 4 of this report. Powertrain development (Task 3) includes engine, gearbox and transmission testing and is discussed in Section 3 herein. Vehicle development (Task 5) incorporates powertrains from Task 3 into production-styled vehicles, and provides for testing by AiResearch and Ford, and ultimately by EPA. This task is also discussed in Section 3 herein.

As depicted in Figure 8, the AGT101 team has successfully completed the first major contract milestone; The Preliminary Design Review for the RPD and Mod I powertrains. These were respectively completed on January 30, 1980, and April 30, 1980. The majority of component designs have been completed for the planned first design iteration, and hardware procurement and fabrication of the component test rigs has been initiated. Early testing has been initiated on the regenerator cold flow test rigs and the foil bearing test rig. It currently is planned that the first build of the Mod I power section will begin testing by July 31, 1981.

As of the end of this reporting period (June 30, 1980) all activities relative to meeting the project contractual milestones are on schedule.

3.0 POWERTRAIN DEVELOPMENT

Figure 9 depicts the planned evolution of the AGT101. As noted earlier, the Mod II power section is comprised of ceramic hot end components including the radial turbine rotor. Since the ceramic technologies to be demonstrated for this program (in particular, the ceramic turbine rotor) represent the highest risk and longest lead items, initial development will begin with an all-metallic Mod I, Build 1 engine (except regenerator). AGT101 development then progresses through stepwise evolutionary changes incorporating ceramic components from the component/subsystem development activities to the Mod I configuration (ceramic hot end components less ceramic rotor) and culminates with the Mod II all-ceramic hot end power section.

This evolutionary development permits component/subsystem technologies to be fully tested in dedicated test rigs and later in the Mod I, Build 1 engines to verify aerodynamic, thermodynamic, and mechanical designs. Activities are time-phased to allow design interaction based on test rig evaluation and engine development. This interactive rig/engine development program thus provides adequate time for the more difficult ceramic structural components (required for Mod I and Mod II engines to be developed in parallel with the component/subsystems Mod I, Build 1 development. As ceramic structural hardware is "qualified" in appropriate test rigs, selective introduction into the Mod I powertrain is made. Time also is available for ceramic structures design iterations that now may result from engine operation at the 2100°F TIT for Mod I.

In concert with Mod I development, the most difficult component development task (ceramic turbine rotor) progresses in parallel. The ceramic turbine rotor undergoes thorough component development to assure that Mod II design requirements are satisfied. Thus the most difficult development task is permitted maximum development time without impacting other activities. Introduction of the turbine rotor initiates final powertrain testing; Mod II development. Time-phased design iterations also are planned during Mod II development due to operation at 2500°F TIT.

Upon satisfactory completion of powertrain testing, the powertrains will be installed in the 3125-pound inertia weight class Ford Fairmont production vehicle. Ford will provide vehicle installation modifications and initial checkout. AiResearch Phoenix, in conjunction with Ford, will provide contractor testing to validate the vehicle operation and performance requirements previously stated. Following contractor testing, two vehicles will be equipped with AGT powertrains for EPA fuel economy and emissions testing. As noted earlier, Mod I vehicles will be delivered to EPA prior to May 1984, and Mod II vehicles prior to May 1985.

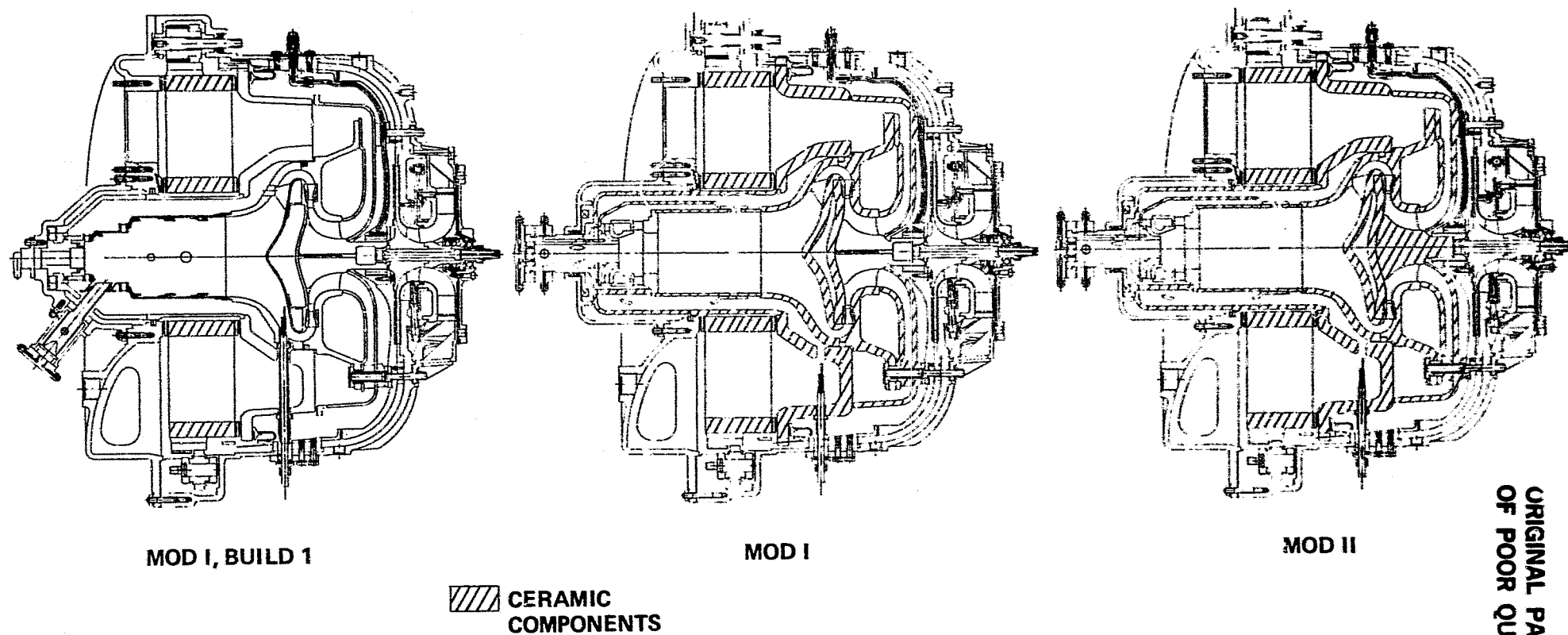


Figure 9. AGT101 Ceramic Parts.

ORIGINAL PAGE IS
OF POOR QUALITY

3.1 Reference Powertrain Design (RPD)

The RPD consists of three major elements, the advanced gas turbine engine, gearbox, and transmission, as shown in Figure 10, and the powertrain controls. Projected fuel economy of the AGT powered baseline vehicle is 36 mpg (gasoline) or 41 mpg (DF2). Zero to 60 mph acceleration time is 11.6 seconds with a 4-second acceleration distance of 68.9 feet which provides the AGT vehicle with driveability equal to or better than the baseline spark ignition (SI) vehicle.

3.1.1 Powertrain Description

The RPD has been established through an iterative design process using a total "systems design" philosophy. The philosophy of "systems design" incorporates a distinct recognition of the duty cycle of a passenger vehicle over the CFDC and, in particular, the amount of time that is expended at low power levels. Therefore, in the "systems design" approach, optimization of the components is being made at the intermediate power levels and not at maximum power which is typical of normal gas turbine design techniques.

Based on the "systems design" philosophy, the RPD is a single-shaft regenerated gas turbine engine utilizing ceramic hot end components, coupled to a split differential powertrain with an available VSTC and an available Ford AOD.

The controls feature microprocessor digital technology integrating all powertrain control functions into one master control system, stressing driveability and integrated performance as related to consumer acceptance. The drivetrain package has the flexibility of either providing front or rear wheel drive.

As shown in Figure 11, ambient air, after passing through an inlet barrier filter, is routed through the variable inlet guide vanes (VIGV) to the compressor. The twelve full/twelve splitter bladed centrifugal impeller compresses the inlet air to a pressure ratio of 5 atmospheres at maximum shaft speed (100,000 rpm) and radially diffuses the air through a three-stage radial vane diffuser to maximum static pressure recovery. Pressurized air then is ducted through the high pressure side of the rotating ceramic regenerator, collected in a toroidal plenum and routed to the low emissions variable geometry combustion system. Fuel is introduced along with the heated pressurized air in the burner premix/prevaporizing section and then is efficiently burned in the primary zone of the ceramic variable geometry combustor. The 2500°F vitiated air then is accelerated through the turbine transition duct to the nineteen-vane nonparallel walled ceramic stator. The stator accepts the 2500°F vitiated air, and routes it to the thirteen-bladed ceramic radial turbine rotor. The air is expanded across the turbine rotor, radially diffused to a collector plenum and exhausted through the low pressure side of the rotating regenerator.

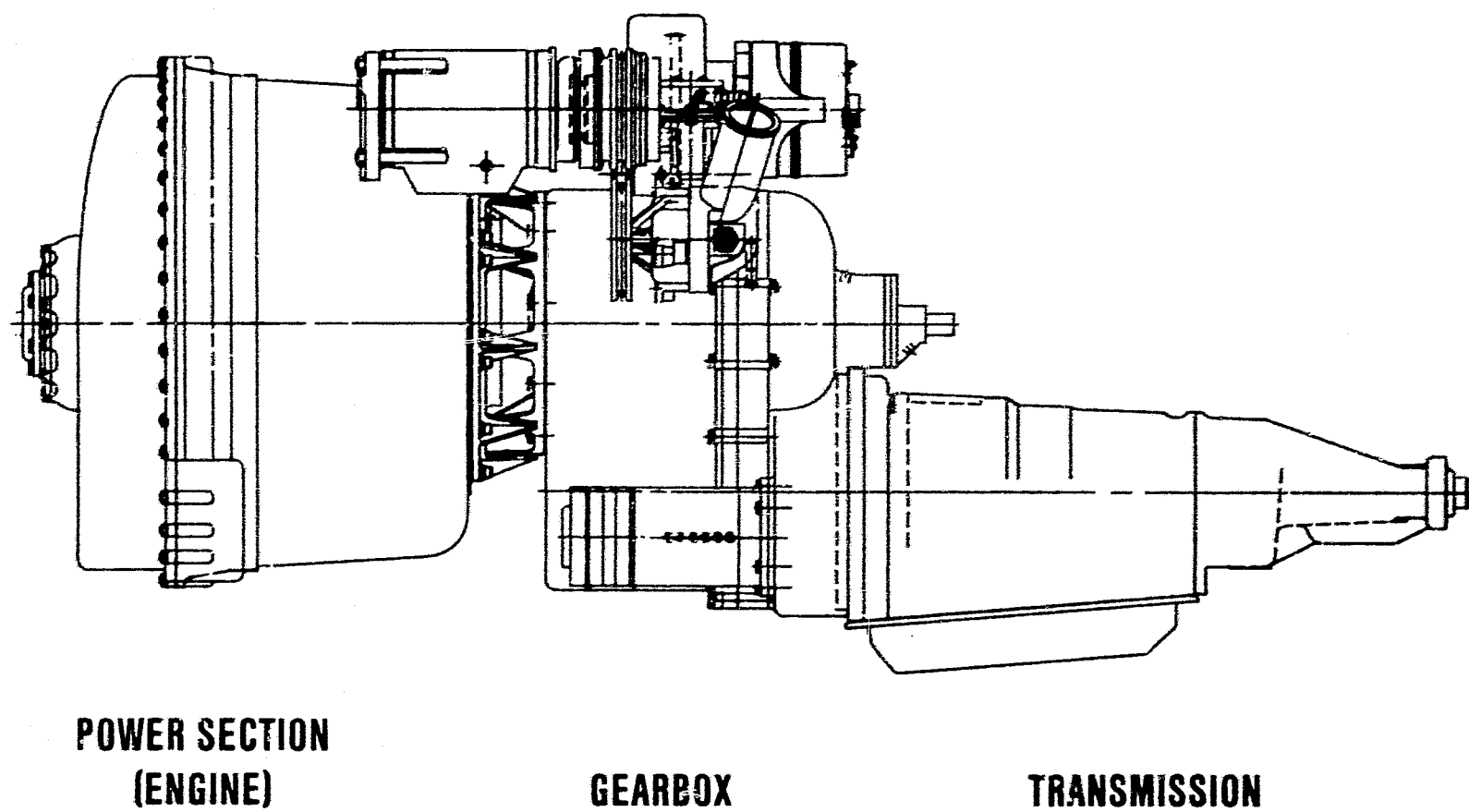


Figure 10. AGT101 Reference Powertrain Design.

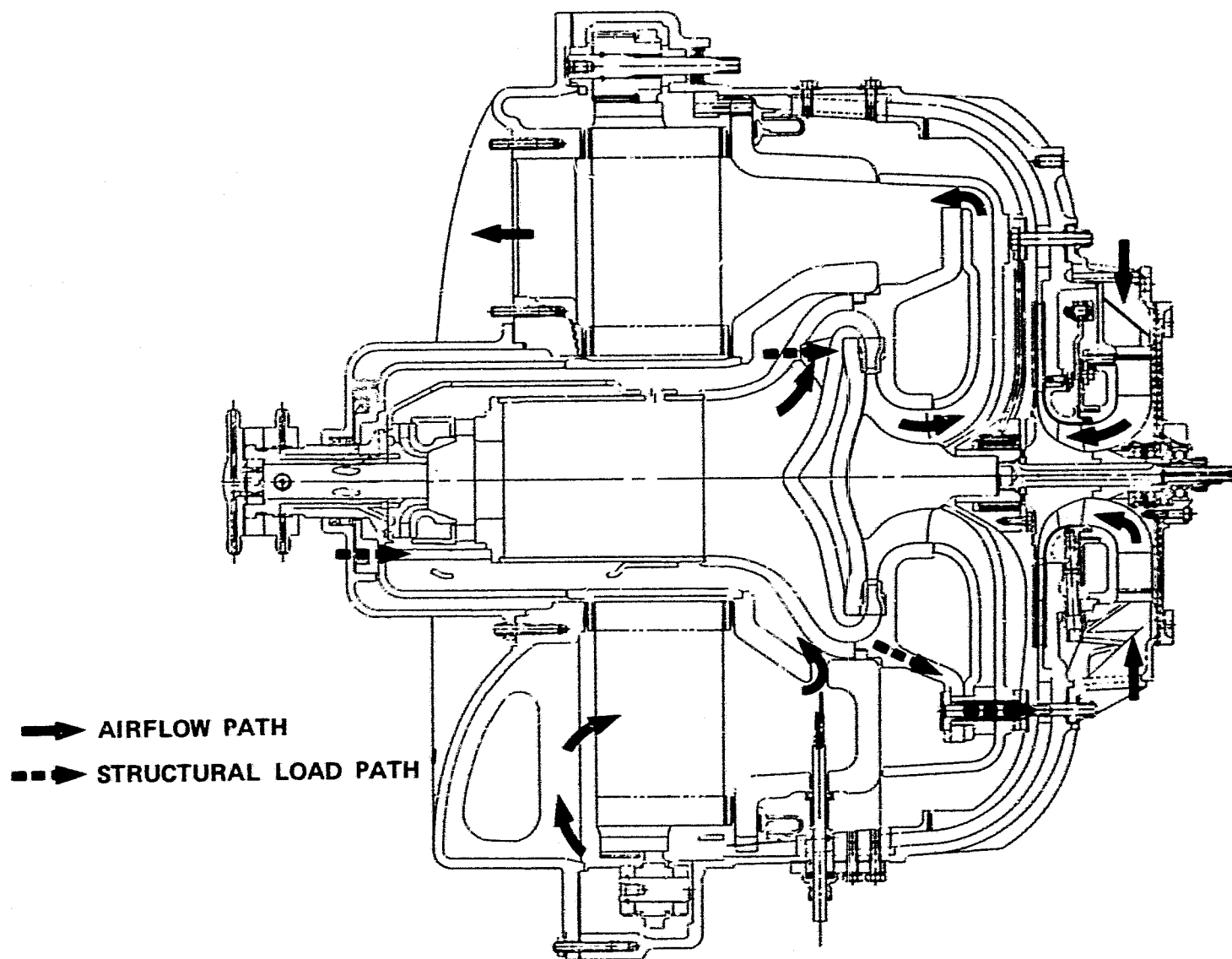


Figure 11. AGT101 Aerodynamic Flow Path.

As shown in Figure 11, the centrifugal compressor and radial turbine are coupled using proven curvic coupling technology, loaded through an axially-stretched tiebolt. The rotating group is supported on the compressor end by a hydraulically mounted angular contact 15mm ball bearing (202 series) and between the turbine and compressor by a gas lubricated foil bearing (1.35 inch diameter). The thickness of each of the seven foil leaves is 0.005 inch including coating. At maximum power, load on the foil bearing is approximately 2 psi, and bearing power loss is estimated at 150 watts. The ball bearing accepts the total thrust load of the rotating group (255 pounds at maximum shaft speed).

AGT critical speed analyses are complete. The first, second and third critical speeds, using 4000 lb/in stiffness and 25,000 lb/in stiffness for the foil bearing and ball bearing, respectively, have been calculated to occur at 5850, 38,260, and 135,200 rpm. The first and second critical speeds are predominately rigid body modes and AiResearch Phoenix experience shows that with hydraulically mounted bearings these modes are sufficiently damped to allow transient operation through the first and second critical speeds with acceptable shaft excursions. The third critical is 35.2 percent above the maximum operating speed and consistent with Garrett/Ford experience.

Structural design of the AGT101 is characterized by simple symmetrical ceramic structures (except the flow separator housing) and flow path arranged to keep the lowest temperature gas outermost to minimize heat loss. The structural load path, as depicted in Figure 11, originates at the combustor dome. A mechanical spring load of approximately 150 pounds is applied to the combustor dome to hold the structural components in position when the engine is not operating. This spring load combined with the aerodynamic loads across the individual components is transmitted through the combustor inner liner to the combustor transition duct, across the three struts, through the combustor baffle and turbine backshroud to the turbine stator, across the stator vane leading edge section to the turbine shroud conical webs and through the duct spacer and axial/radial piloting keys to the compressor outer housing.

The aerodynamic load on the regenerator is reacted by the exhaust housing and the flow separator housing. The exhaust housing transmits load directly into the compressor outer housing. The flow separator housing portion of the regenerator load, combined with aerodynamic loads, is reacted by the flow separator support ring which transmits the load to the compressor outer housing.

Output power from the gas turbine is delivered to the vehicle via a variable high speed single-stage differential planetary gearbox in conjunction with a modified four-speed Ford AOD transmission. This combination results in a continuously variable speed transmission required for the optimization of a single-shaft gas turbine vehicle system.

The planetary gearbox (schematically shown in Figure 12) incorporates a differential in which power is split into two paths. Gas turbine power is input at the planetary sun gear and extracted from the planetary carrier. One power path extends directly to the carrier while the second path passes through the planetary ring gear to a VSTC utilized as a speed changing device. The variable output speed of the VSTC is connected to the carrier via a clutch that is open during vehicle idle and closed during normal driving modes. Speed ratio modulation across the VSTC results in a variable output speed of the planetary carrier which in turn is geared directly to the AOD transmission. Step ratio changes in the AOD are phased with off-setting speed ratio changes in the variable speed gearbox. This produces a continuously variable drive line system which allows the engine to operate at optimum speeds to deliver high efficiency cruise power, acceleration power, or engine braking power.

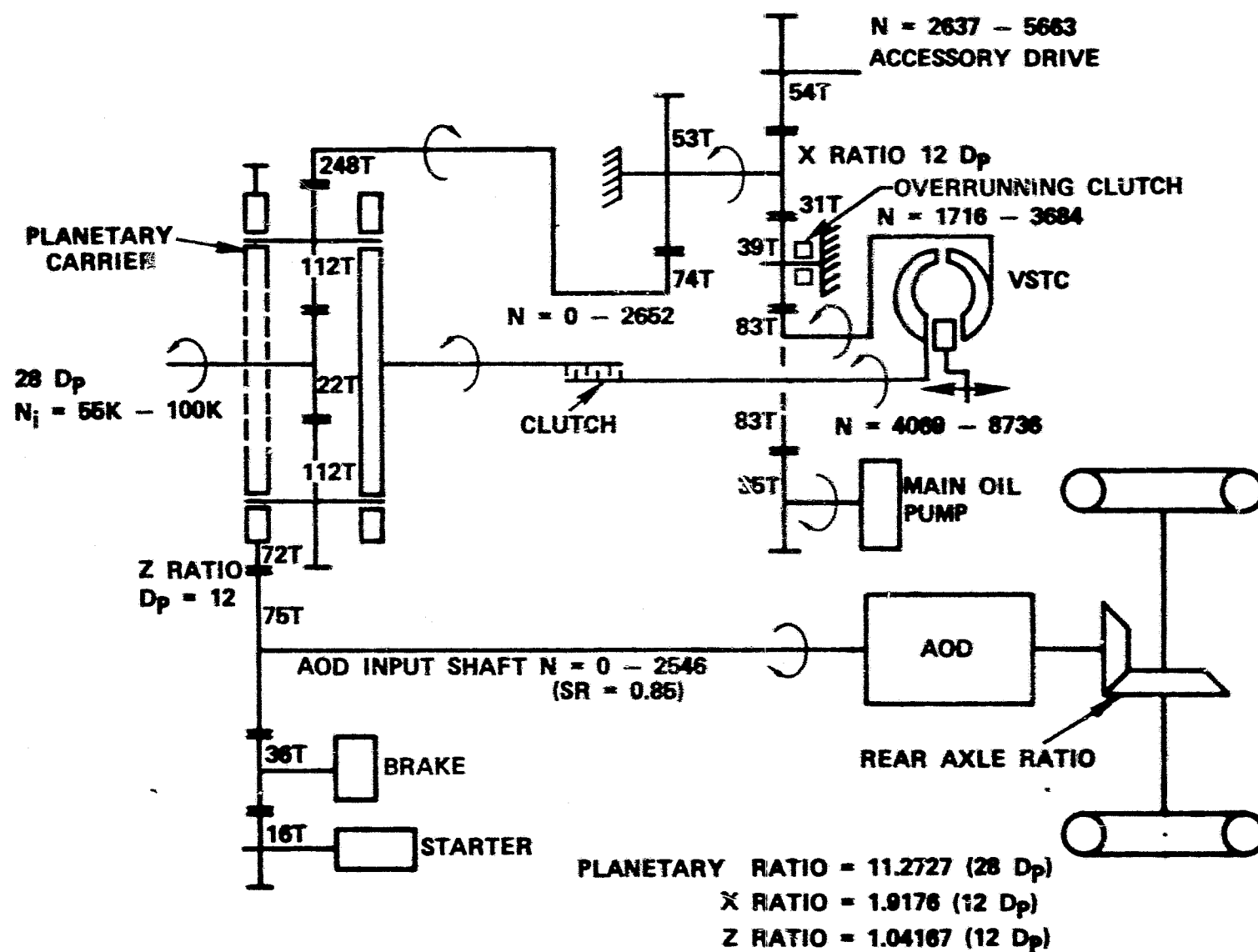


Figure 12. AGT101 Drive System Schematic.

3.2 Performance

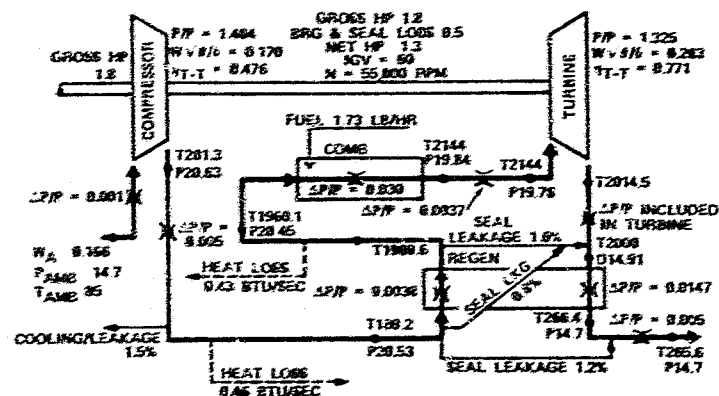
The vehicle performance model presently in use is a rigorously distributed inertia analysis of the engine, gearbox, driveline and vehicle. Included in these analyses are the latest performance models for each of the components.

Changes in the predicted RPD and Mod II performance from January 1980 to present are the cumulative effect of:

- o Engine performance model refinement
 - o Updated and more accurate turbine map
 - o Refined heat rejection model
 - o Refined internal heat transfer model
 - o Regenerator map replaced with off-design analytical model
 - o Off-design regenerator seal leakage model added
- o Vehicle dynamics model refinement
 - o Improved dynamic model of the split path gearbox
 - o Redefined power split between engine and vehicle acceleration
 - o Incorporation of VSTC map based on recent test data
- o Changes in engine design requirements and rating point
 - o Cooling flow reduced and internal bleed path redefined
 - o Ambient conditions for rating changed to 59°F, sea level
 - o Reference fuel changed to diesel No. 2
 - o Cruise condition redefined to approximate 55 mph steady state
 - o Engine flat rated at 100 shp net

Figure 13 summarizes the engine performance presented at the RPD Preliminary Design Review (January 1980). Current engine performance for the Mod II engine is presented in Figure 14. Note that the ambient temperature value, fuel lower heating value, and idle speed have been changed when SFC comparisons are made between schematics.

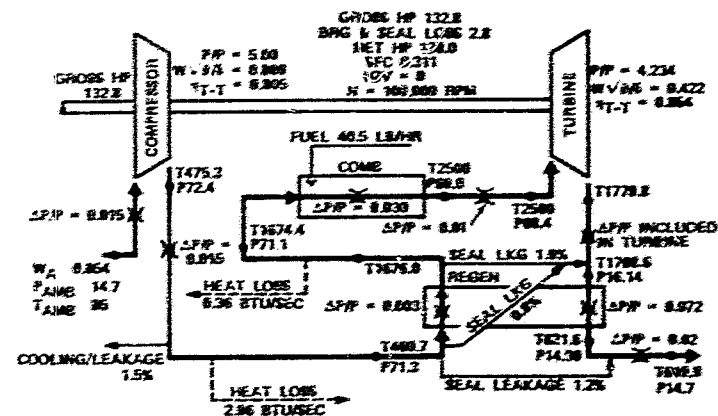
IDLE OPERATION



T = °F
P = PSIA
W = LB/SEC
LHV = 18,860 BTU/LB

(a)

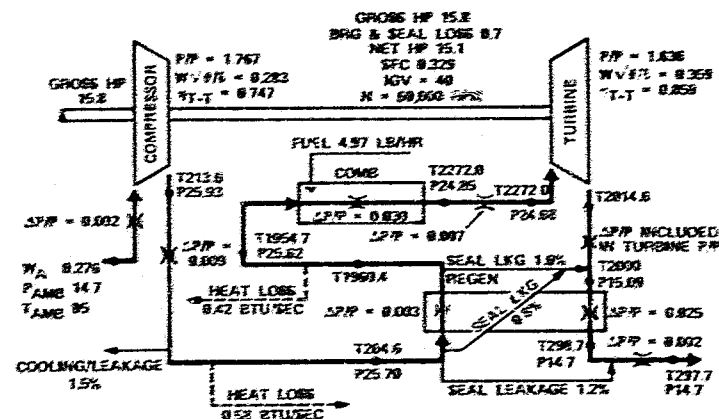
MAXIMUM POWER



T = °F
P = PSIA
W = LB/SEC
LHV = 18,860 BTU/LB

(b)

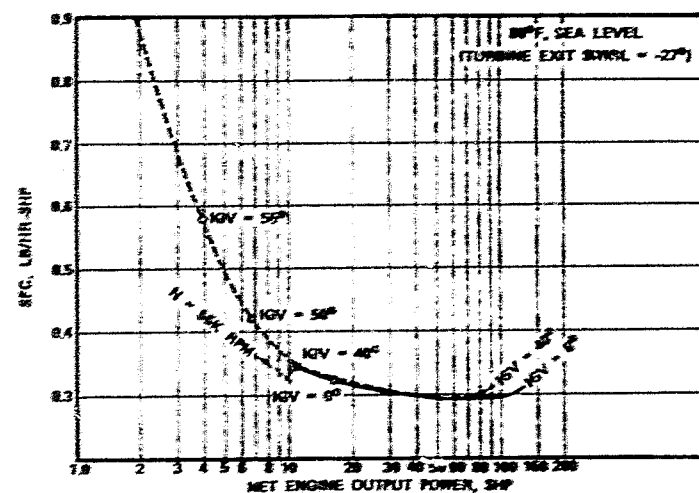
CRUISE



T = °F
P = PSIA
W = LB/SEC
LHV = 18,860 BTU/LB

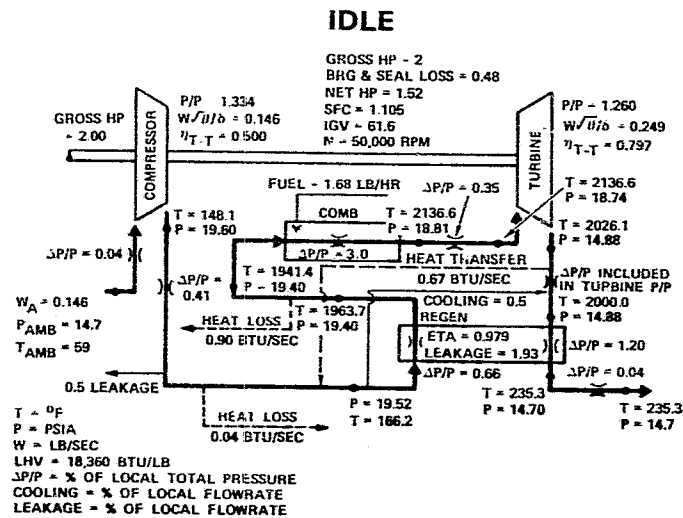
(c)

SFC CHARACTERISTICS

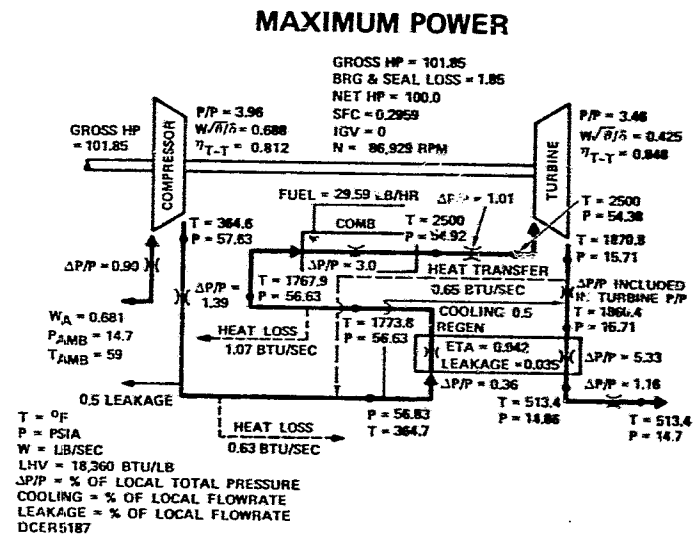


(d)

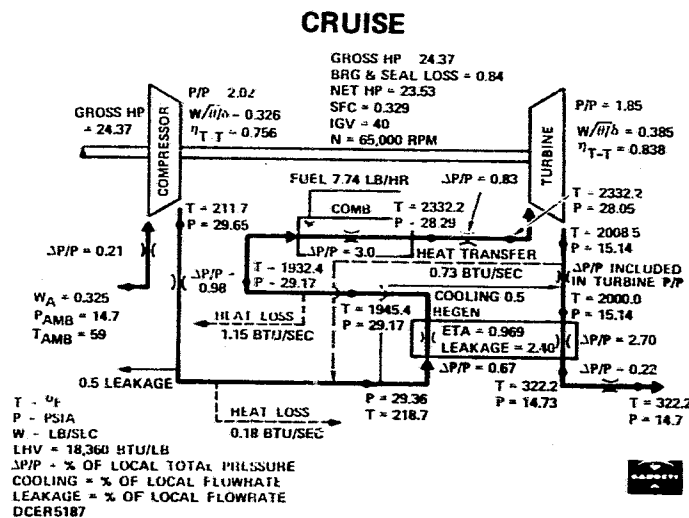
Figure 13. AGT101 RPD Performance (85°F, Sea Level, Gasoline).



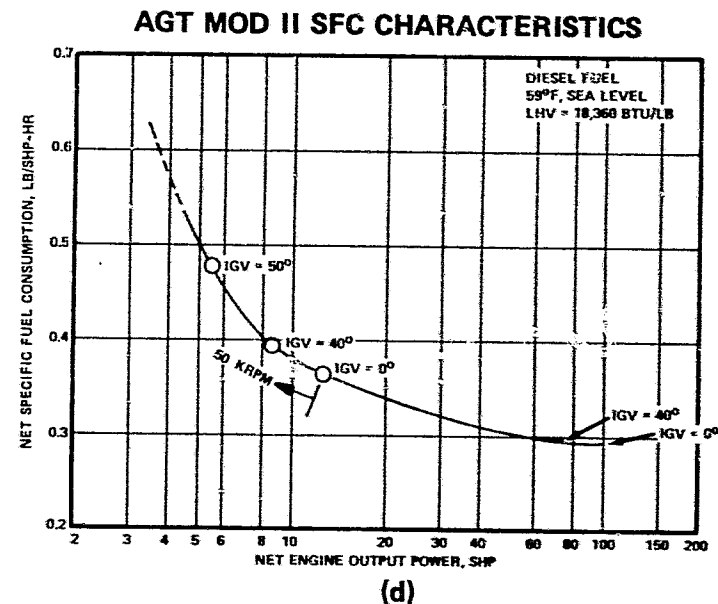
(a)



(b)



(c)



(d)

Figure 14. AGT101 Mod II Performance (59°F, Sea Level, Diesel Fuel No. 2).

ORIGINAL PAGE IS
OF POOR QUALITY

Since the inception of the RPD which had a 4-second acceleration requirement of 69 feet, the definition of "driveability" has been modified to incorporate Ford effort to define consumer acceptance on a 1985 vehicle with a conventional SI engine. Ford is conducting tests with a simulation vehicle, to determine minimum time/distance relationships that will apply to the AGT101 powered vehicle. Preliminary requirements from this testing are:

- 1 second - 1 foot
- 2 seconds - 8 feet
- 3 seconds - 23 feet
- 4 seconds - 50 feet

A procedure to maximize fuel economy and meet the above preliminary time/distance requirements has been developed using the optimum combination of engine idle speed and gearbox clutch engagement speed. Figure 15 shows the composite relationship between engine idle speed and clutch engagement speed required to achieve the time-distance criteria. Note that the 1- and 2-second criteria determine the selection, whereas the 3- and 4-second criteria do not influence the selection. A point at approximately 53,700 rpm idle (57,750 rpm clutch engagement) meets all criteria. A point at 52,000 rpm idle (64,500 rpm clutch engagement) meets the 2- through 4-second criteria while sacrificing only a few inches in 1-second distance. This figure will be updated to determine the appropriate idle speed for 59°F ambient conditions.

The CFDC mileage estimate for the AGT101 Mod II currently is 41.39 mpg with diesel fuel (3149 Btu/mile) compared to 36 mpg with gasoline (3185 Btu/mile) for the RPD system. Note that due to the large difference in fuel density and lower heating value used in each case, only Btu/mile values should be used for comparison.

Performance predictions for the Mod I are shown in Figure 16. Turbine inlet temperature to maximize life of the metal turbine rotor has been limited to effect a 1930°F turbine blade relative temperature. Figure 17 characterizes the relationship between engine idle speed, 4-second distance, and CFDC mileage estimates for the Mod I powertrain.

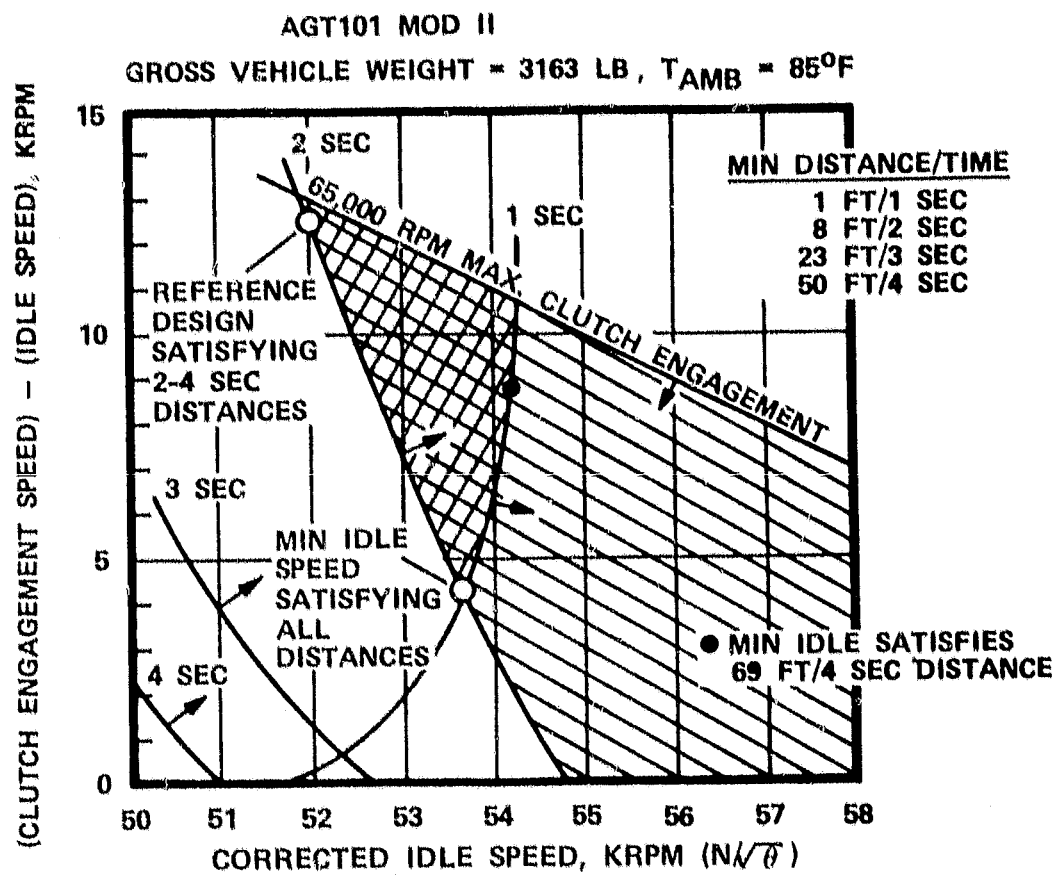
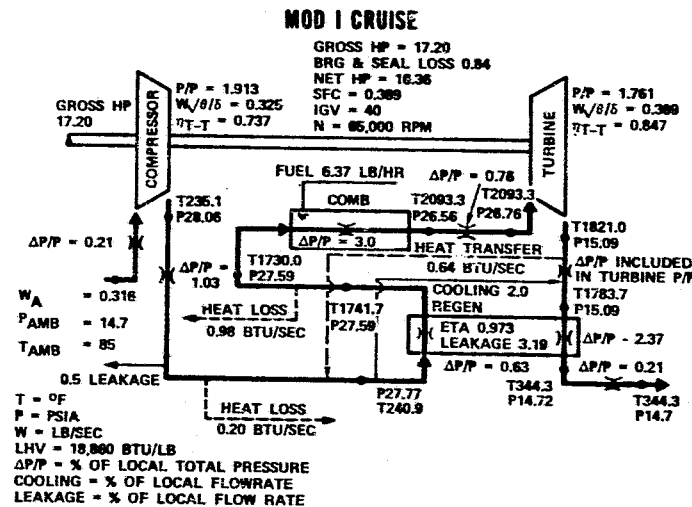
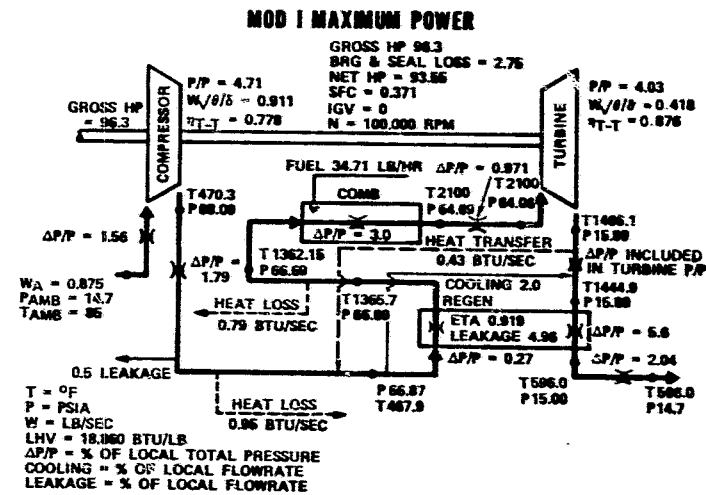
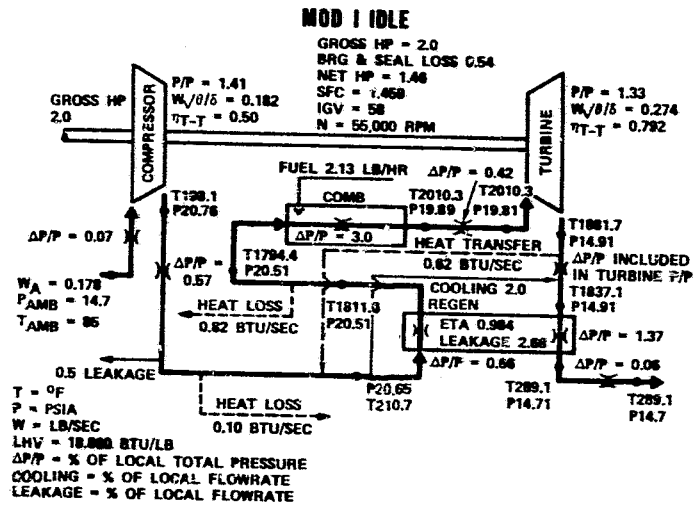


Figure 15. Determination of Idle and Clutch Engagement Speeds.



SFC CHARACTERISTICS MOD I

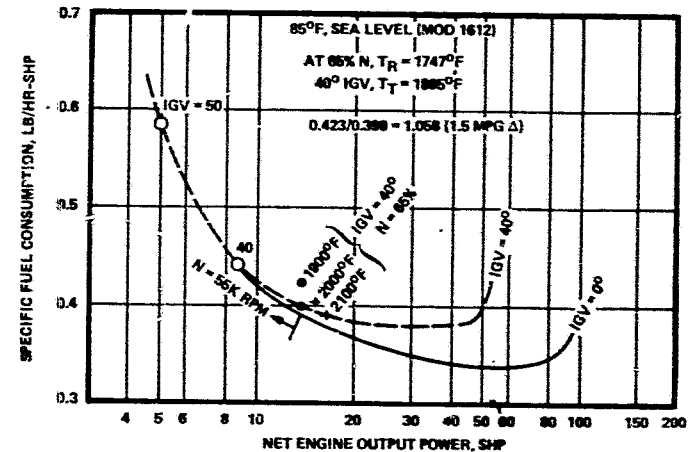


Figure 16. AGT101 Mod I Performance (85°F, Sea Level, Gasoline).

ORIGINAL PAGE IS
OF POOR QUALITY

MOD I COMPLETE

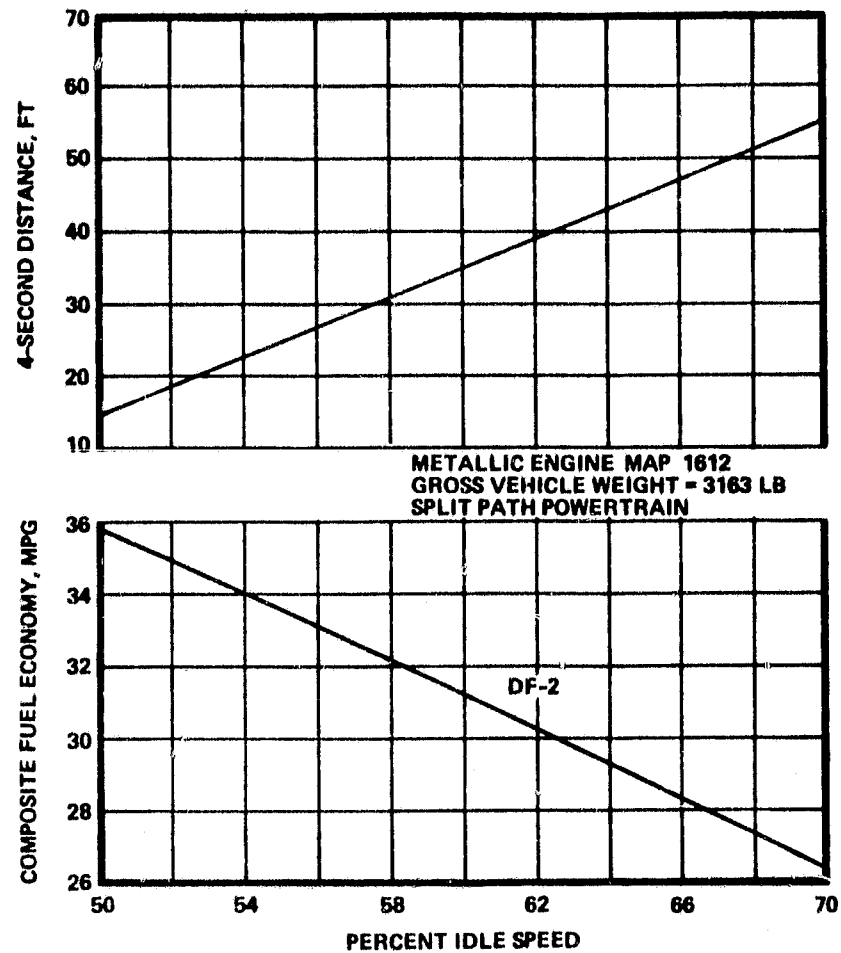


Figure 17. Effect of Idle Speed on Performance and Fuel Economy.

3.3 Vehicle Integration

Preliminary packaging studies have been completed for incorporating the RPD in Ford rear-wheel and front-wheel drive configurations. The rear-wheel drive configuration is the reference powertrain design (Figures 18 and 19) and can be installed in a Fairmont without modifications to the engine compartment structure. The same configuration with a modified gearbox and transmission was repackaged and shown to fit a front-wheel drive vehicle.

A preliminary design study has been initiated and preliminary results indicate that the AGT engine, with a suitable gearbox and transmission arrangement also could be installed in a front-wheel drive Ford Escort for demonstration purposes. Thus it appears that the AGT101 powertrain is capable of being incorporated in a wide range of Ford vehicles.

The passenger heating system for the Ford Fairmont was investigated using AGT engine exhaust gas as the heat source. Calculations indicate insufficient exhaust temperature and flow to give desired passenger compartment heating on a 0°F day. Other heating concepts are being investigated with the most promising being the use of engine/transmission oil as the heat source. If the oil temperature proves to be insufficient, the heater can be supplemented by heated air from a separate fuel-fired burner. Selection of the heater system will be reported in subsequent reports.

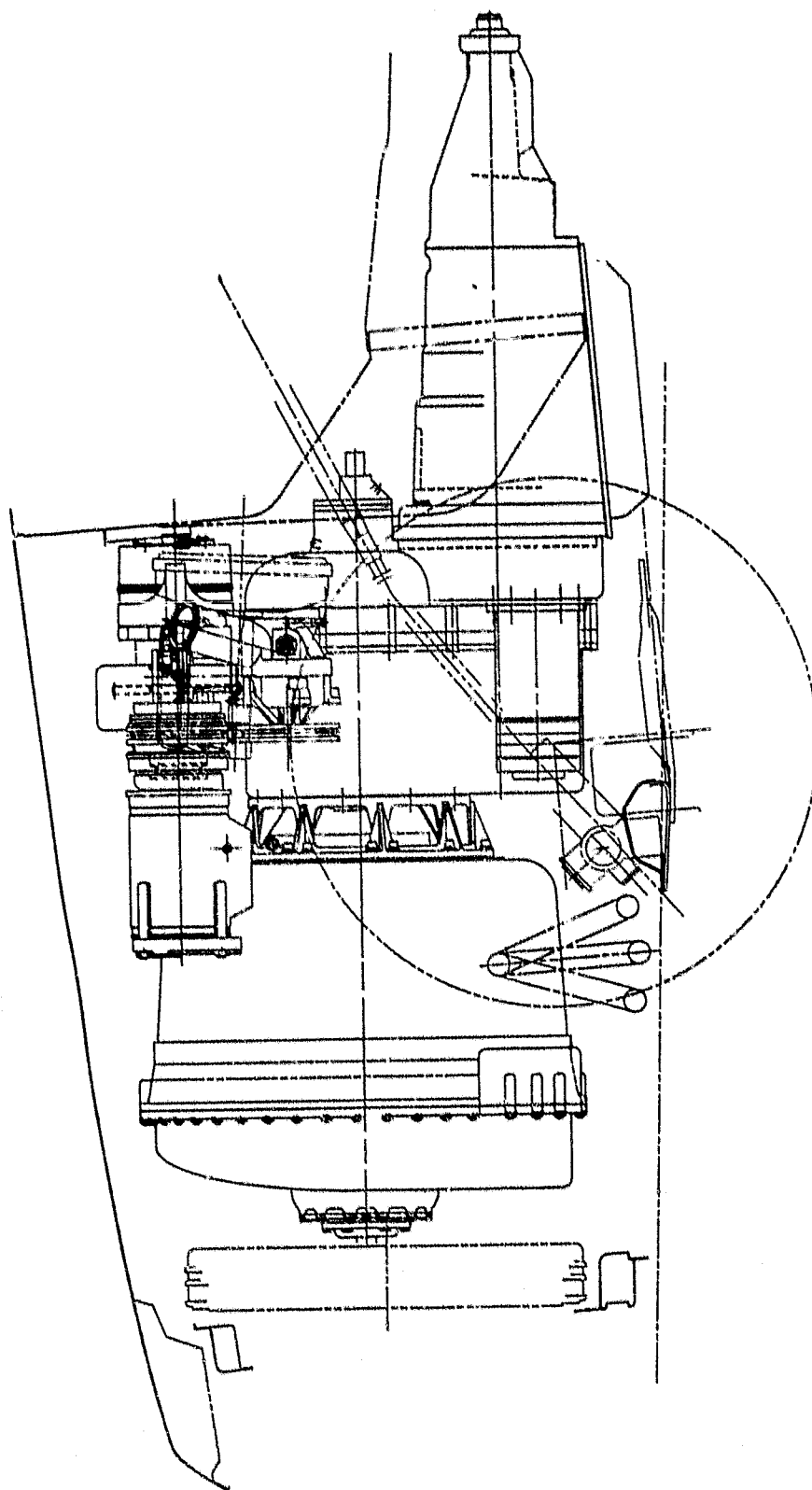


Figure 18. AGT101 Installation - Side View.

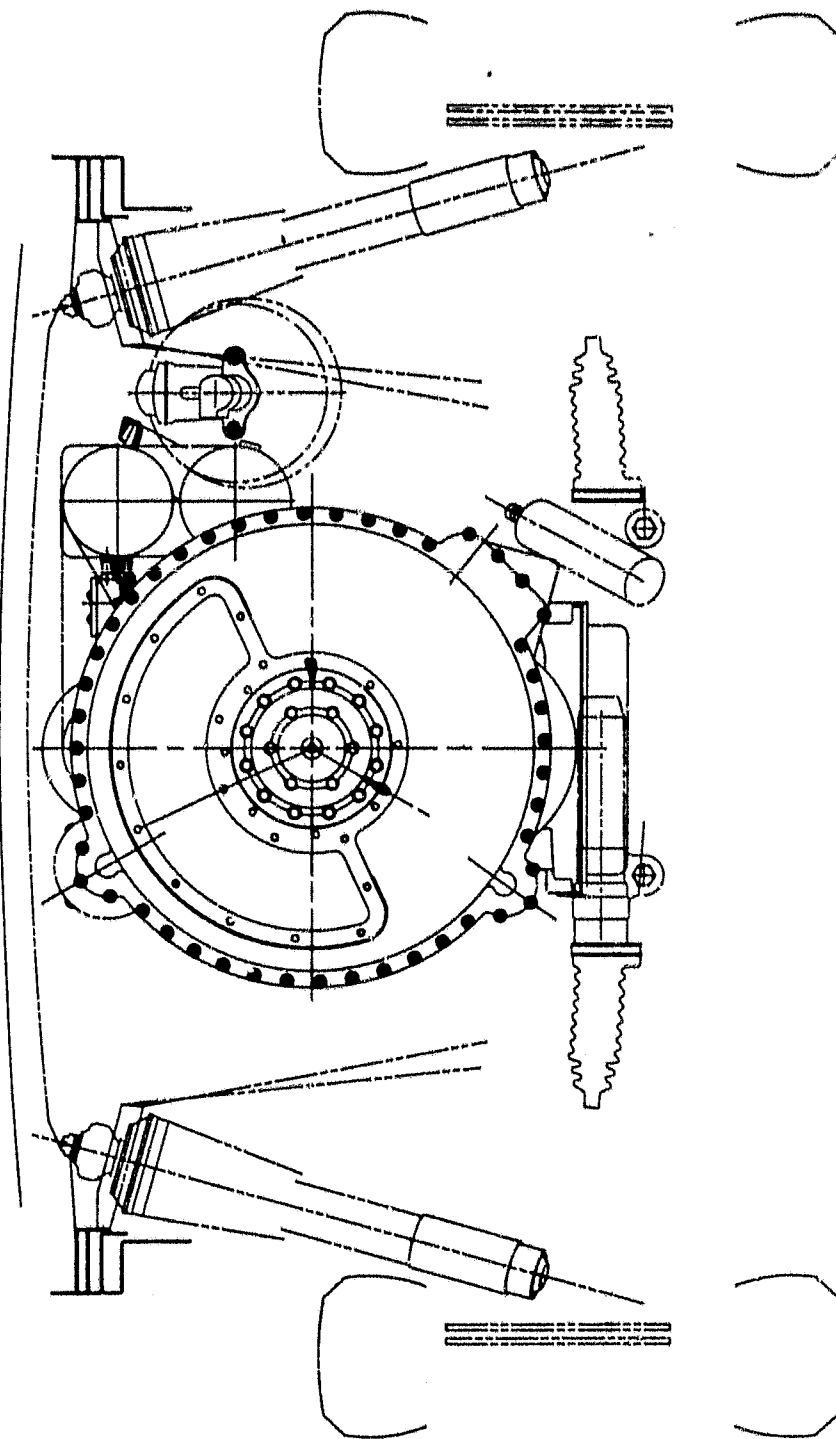


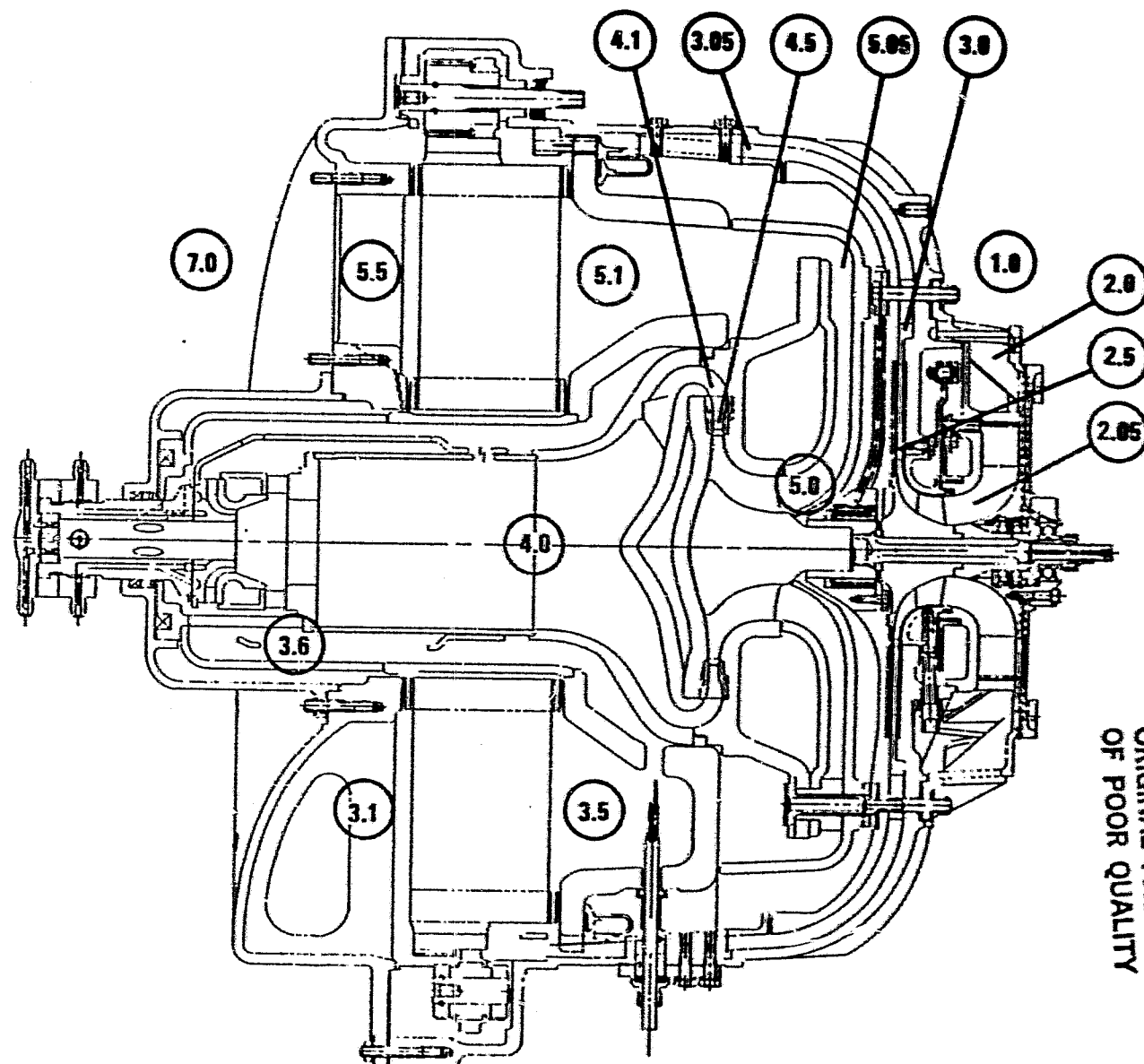
Figure 19. AGT101 Installation-Front View.

4.0 COMPONENT/SUBSYSTEM DEVELOPMENT

Task 2, Component Subsystem Development, activities comprise the design, test and developmental efforts for each major component and/or subsystem. Development of each component will be undertaken using dedicated test rigs specifically designed to fully evaluate the component both for performance and mechanical integrity. Performance rating stations are defined as shown in Figure 20. Three distinct design iterations have been planned for each component/subsystem, such that, as information from Task 2 - Testing and Task 3 - Powertrain Development becomes available, an interactive rig/engine feedback loop is realized. This allows further optimization of the "systems design" philosophy as related to program goals (i.e., fuel economy, manufacturing compromises, marketability, packaging, etc.)

This section discusses the efforts to date on each major component/subsystem.

- 1.0 AMBIENT
- 2.0 COMPRESSOR INLET (IGV)
- 2.05 IMPELLER INLET
- 2.5 DIFFUSER INLET
- 3.0 DIFFUSER DISCHARGE
- 3.05 DUCT COMMON INSTRUMENTATION PLANE (RIGS)
- 3.1 REGENERATOR H P INLET
- 3.5 REGENERATOR H P EXIT
- 3.6 COMBUSTOR INLET
- 4.0 COMBUSTOR EXIT, TURBINE INLET
- 4.1 STATOR INLET
- 4.5 STATOR DISCHARGE
- 5.0 TURBINE ROTOR EXIT
- 5.05 DIFFUSER EXIT (RIGS)
- 5.1 REGENERATOR L P INLET
- 5.5 REGENERATOR L P EXIT
- 7.0 POWER SECTION EXHAUST



ORIGINAL PAGE IS
OF POOR QUALITY

Figure 20. Performance Rating Stations.

4.1 Compressor Development

The AGT101 Compressor System is comprised of a single-stage backward swept aluminum centrifugal impeller having 12 full blades and 12 splitter blades, a three stage radial diffuser with one stage of diffusion vanes and two stages of deswirl vanes, and an upstream set of seventeen variable inlet guide vanes (VIGV). Current performance predictions of this compressor system at maximum power operating condition are as follows:

o	Mass Flow (85°F, sea level)	0.8542 lb/sec
o	Stage Pressure Ratio	5
o	Stage Efficiency, Total-to-Total	0.805
o	Rotational Speed	100,000 rpm

These performance goals are quoted at maximum power; however, as previously stated, the AGT101 is being designed using a "systems design" philosophy with a distinct recognition of CFDC duty cycle. Therefore, since a significant portion of operation is at low power levels, during the course of development, maximum power performance goals most likely will be sacrificed for more important program goals, i.e., fuel economy over the duty cycle. The design point ultimately chosen will be the result of further cycle studies based on detailed compressor system tests and related aero/thermodynamic component and engine testing to arrive at the optimum system.

4.1.1 Aerodynamic Design

Compressor system aerodynamic design continued, as a result of the Reference 1 and 2 studies. Final blade geometry, loading, and vector diagrams have been completed. Optimization of the radial diffuser system has been accomplished and reported herein. The predicted compressor map without VIGVs is shown in Figure 21.

4.1.1.1 Impeller Design

The aerodynamic and geometric impeller design summary is shown in Tables 3 and 4. The final impeller flowpath is shown in Figure 22.

Aerodynamic boundary conditions used in the detailed blade shape design are shown in Figures 23 and 24. These conditions include impeller exit crosspassage distributions of the entropy function, which relates total pressure to total temperature and blade deviation angle. The entropy function (Q) and aerodynamic blockage (A_{eff}/A_{geo}) were distributed linearly through the impeller along each streamline from the leading to trailing edge. Deviation was distributed parabolically from the point of inception to the exit according to an established method.³

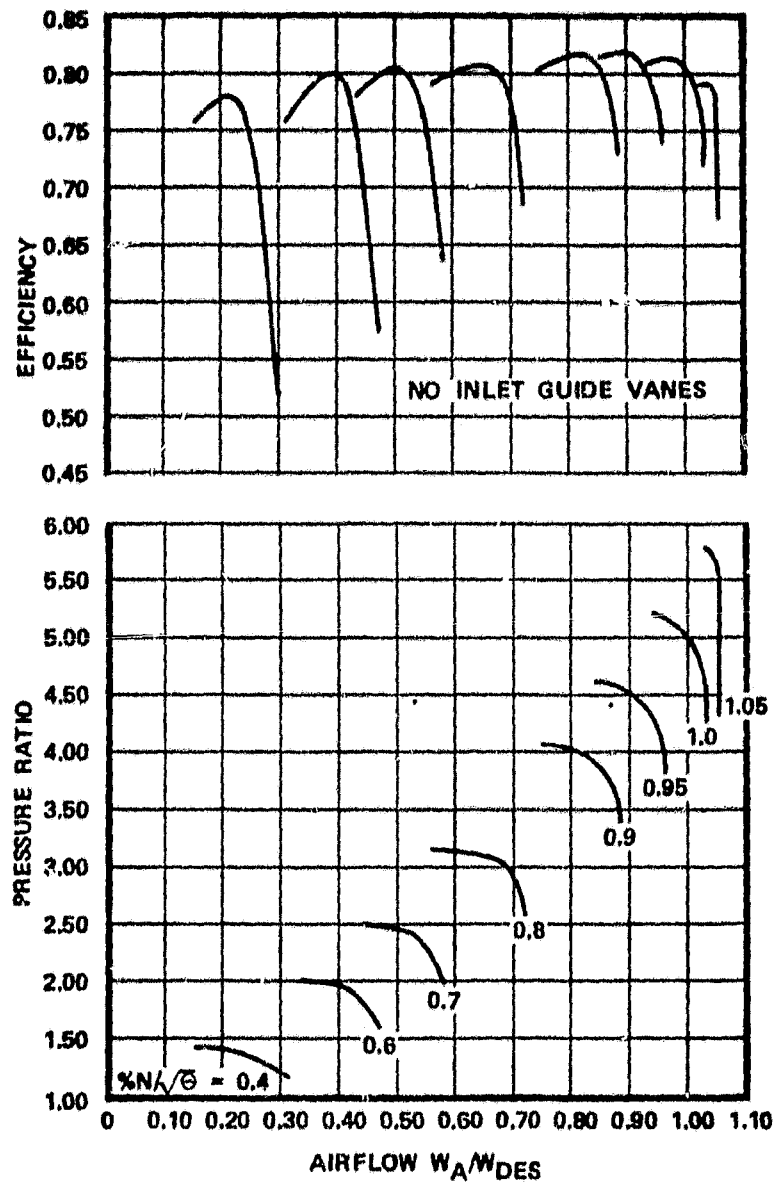


Figure 21. AGT101 Compressor Map.

TABLE 3. AGT101 IMPELLER DESIGN AERODYNAMIC DESIGN SUMMARY.

INLET TOTAL TEMPERATURE	544.7°R
INLET TOTAL PRESSURE	14.431 PSIA
SPEED	100,000 RPM
FLOW RATE	0.8542 LB/SEC
TIP SPEED	1872 FPS
IMPELLER EFFICIENCY, TOTAL/TOTAL, NO DUMP LOSS	89.67 PERCENT
SPECIFIC SPEED	57.2
SHROUD INLET RELATIVE MACH NUMBER	1.125
SHROUD RELATIVE VELOCITY RATIO (PD ANALYSIS)	0.600 (0.529 CAPS)
SHROUD/MEAN MERIDIONAL VELOCITY RATIO (PD ANALYSIS)	1.25 (1.194 CAPS)
AVERAGE EXIT BLADE DEVIATION	3.27
INLET AERODYNAMIC BLOCKAGE	0.98
EXIT AERODYNAMIC BLOCKAGE	0.90
AVERAGE SLIP FACTOR	0.9488

TABLE 4. AGT101 IMPELLER DESIGN GEOMETRIC DESIGN SUMMARY.

INLET HUB/TIP RATIO	0.464
INLET HUB RADIUS	0.600 IN
INLET SWEEP ANGLE (MERIDIONAL PROJECTION)	7.47
EXIT RADIUS	2.146 IN
EXIT B-WIDTH	0.154 IN
BLADE NUMBER	12/24
AVERAGE EXIT BLADE ANGLE	49
EXIT RAKE ANGLE	0
AXIAL & RADIAL CLEARANCE	0.003 IN
INLET SHROUD NORMAL THICKNESS	0.015 IN
INLET HUB NORMAL THICKNESS	0.025 IN
EXIT SHROUD NORMAL THICKNESS	0.015 IN
EXIT HUB NORMAL THICKNESS	0.052 IN

ALL ANGLES IN DEGREES

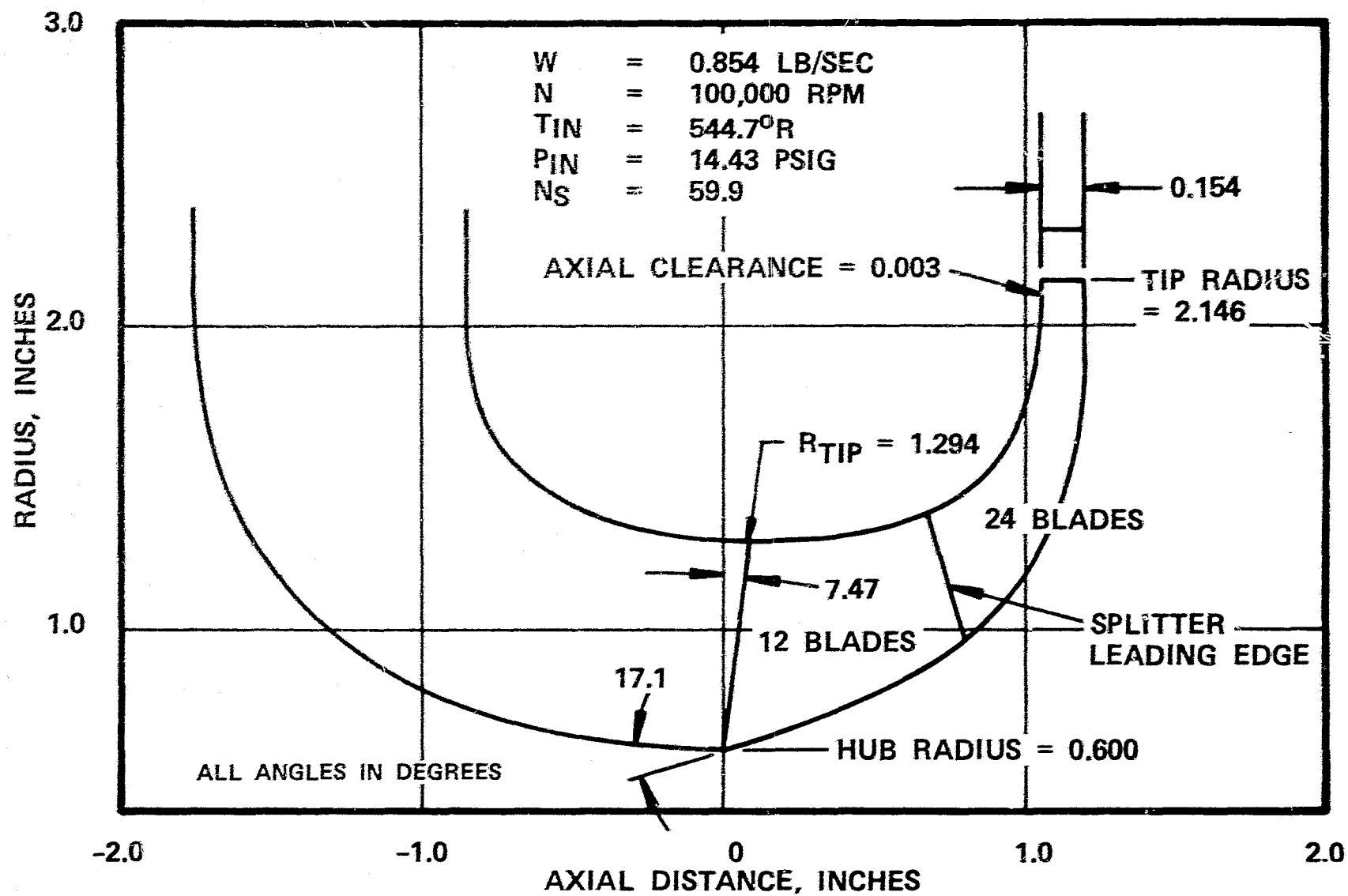


Figure 22. AGT101 Impeller Flow Path.

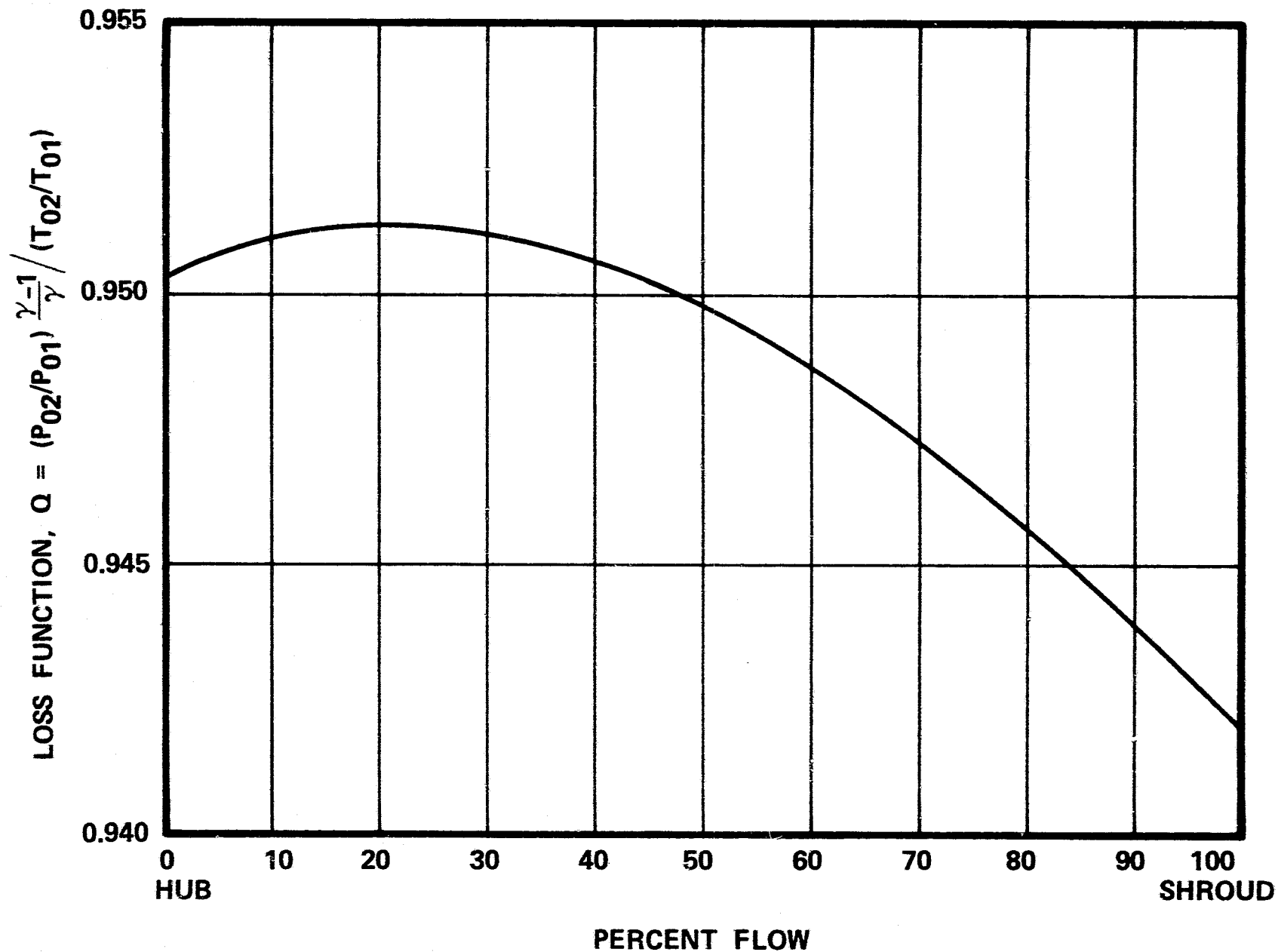


Figure 23. AGT101 Impeller Design Exit Loss Function Distribution.

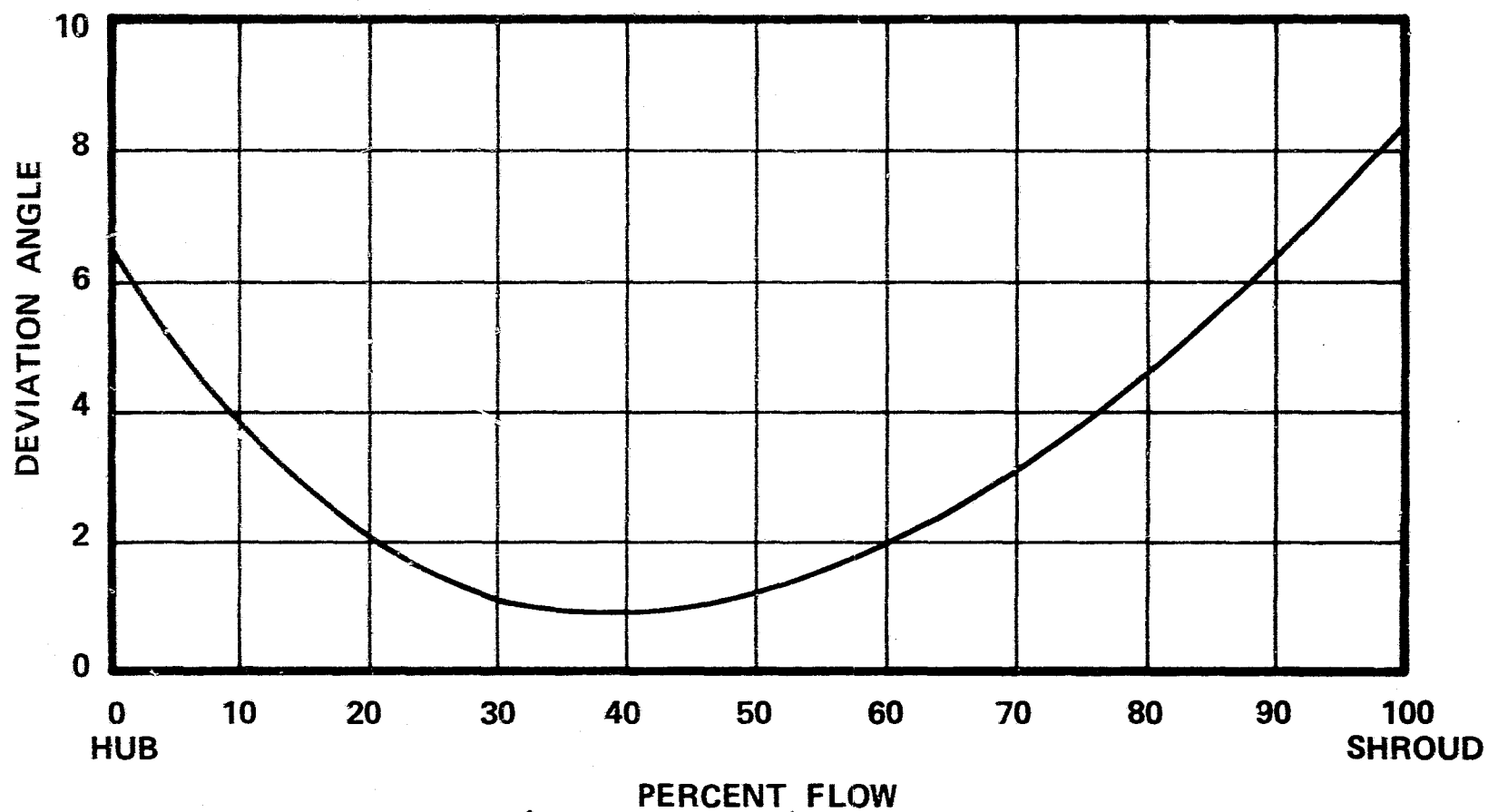


Figure 24. AGT101 Impeller Design Exit Deviation Angle.

The blade/air angle relationship at the inducer leading edge is shown in Figure 25. For completely subsonic flow conditions, the impact-free incidence relationship⁴, corrected for compressibility, the normally is used. However, proceeding outward to the inducer tip, Mach number exceeds 1. For this region, blade incidence was modified (from impact free) according to transonic axial compressor blade design rules (toward 0-degree meanline incidence). Higher blade angles resulting from this correction will be advantageous for part-speed operation.

Final air/blade angle distributions are shown for shroud, mean, and hub streamlines in Figure 26. Resulting blade suction and pressure surface velocities are shown in Figures 27 through 29 for the shroud, mean (50-percent flow), and hub streamlines. These velocity distributions compare favorably with previously designed, successful compressors of similar pressure ratios.

To assure adequate impeller flow area at design point conditions, a check of available inducer throat area was made using a ratio of local geometric (blade-to-blade) area to the area required for sonic flow conditions at leading edge stagnation conditions. A minimum value curve of this parameter across the inducer is shown in Figure 30. Current design procedure requires that the local value not be less than 1.04, a condition met for all streamlines.

The final main blade normal thickness distribution is shown in Figure 31. This distribution was required to satisfy blade stress and vibration criteria.

Impeller vector diagrams are shown in Figure 32.

Impeller splitter aerodynamic and stress analyses were successfully completed. To reduce a locally high splitter leading edge stress, the hub leading edge was moved axially forward from the original position to make the edge more radial (Figure 33). The circumferential position of the splitter leading edge then was shifted to match the 50-percent mass flow streamline across the entire blade height. This meanline shift was accomplished as shown in Figure 34 for each streamline calculation. The repositioning was performed to eliminate a potential loss penalty associated with a non-uniform flow split which might result if the splitter blades were left in the mean tangential position between main blades. This technique has been successfully used on previous AiResearch Phoenix high pressure ratio compressor designs.

4.1.1.2 Diffuser Design

Based on the reference study and subsequent design analyses, the final radial diffuser design consists of three vane rows. The first row is a standard 2-D vane island diffuser with a converging end wall

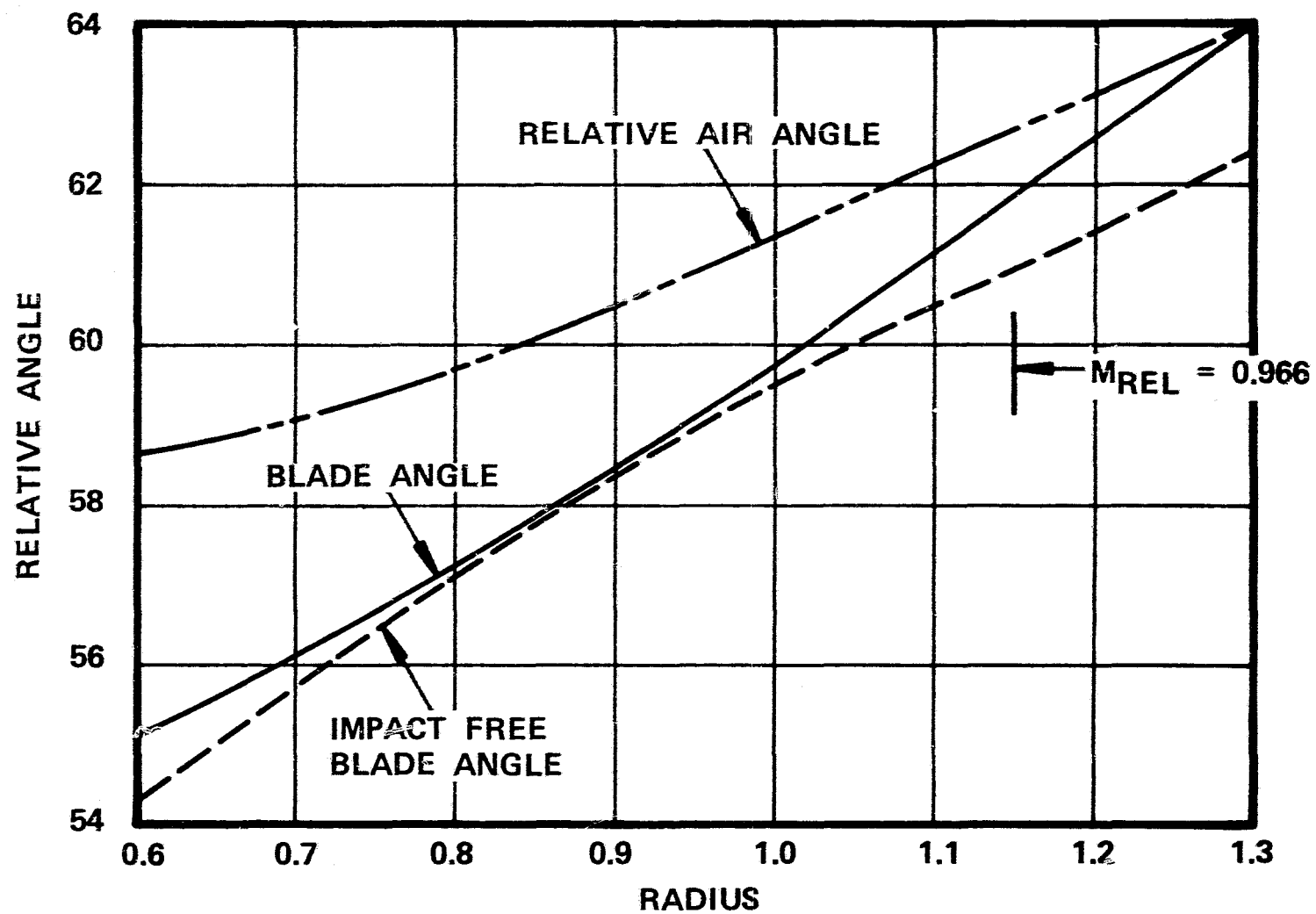


Figure 25. Compressor Inducer Leading Edge Blade, Air Angle Distributions.

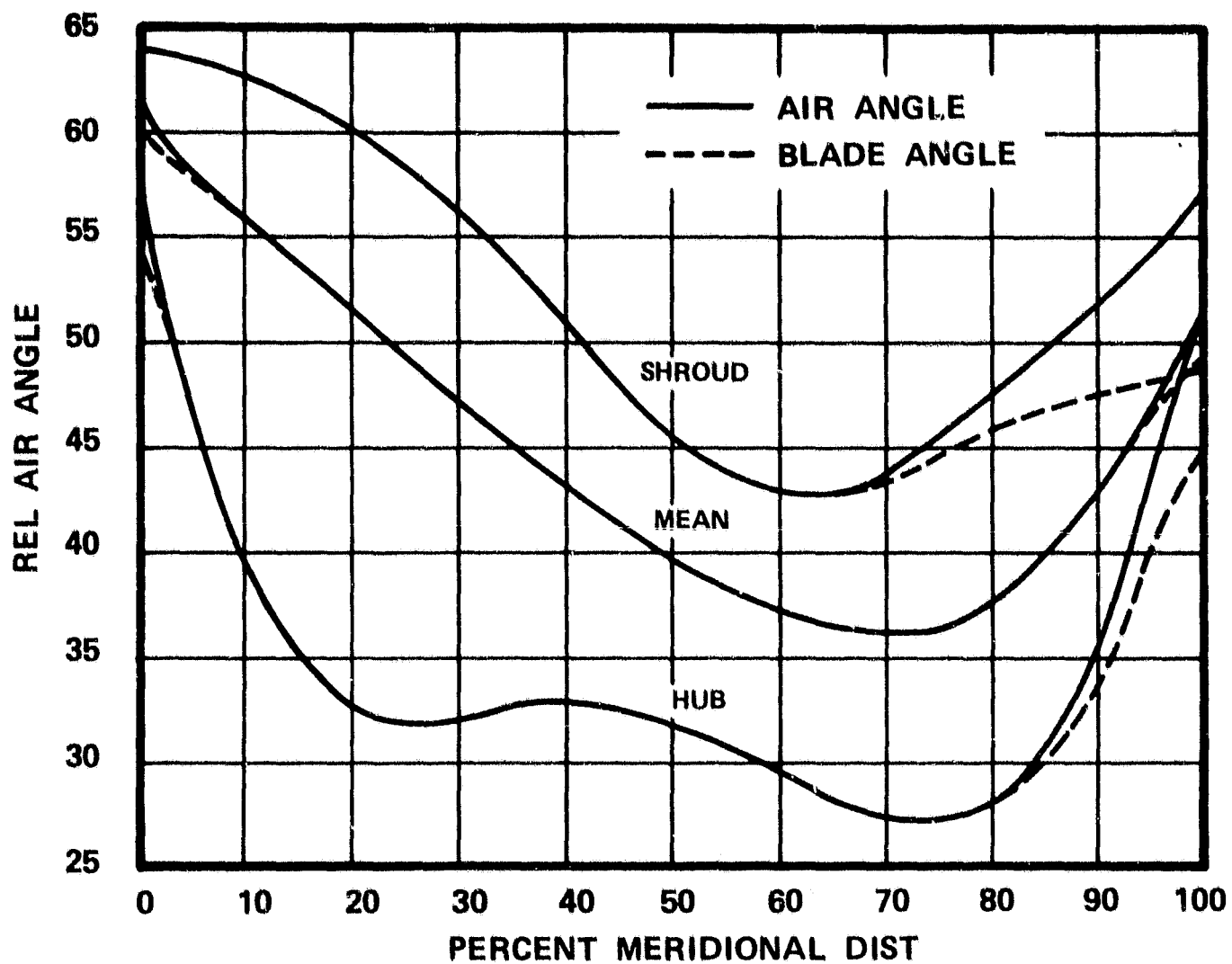


Figure 26. Compressor Impeller Relative Air Angle Distribution.

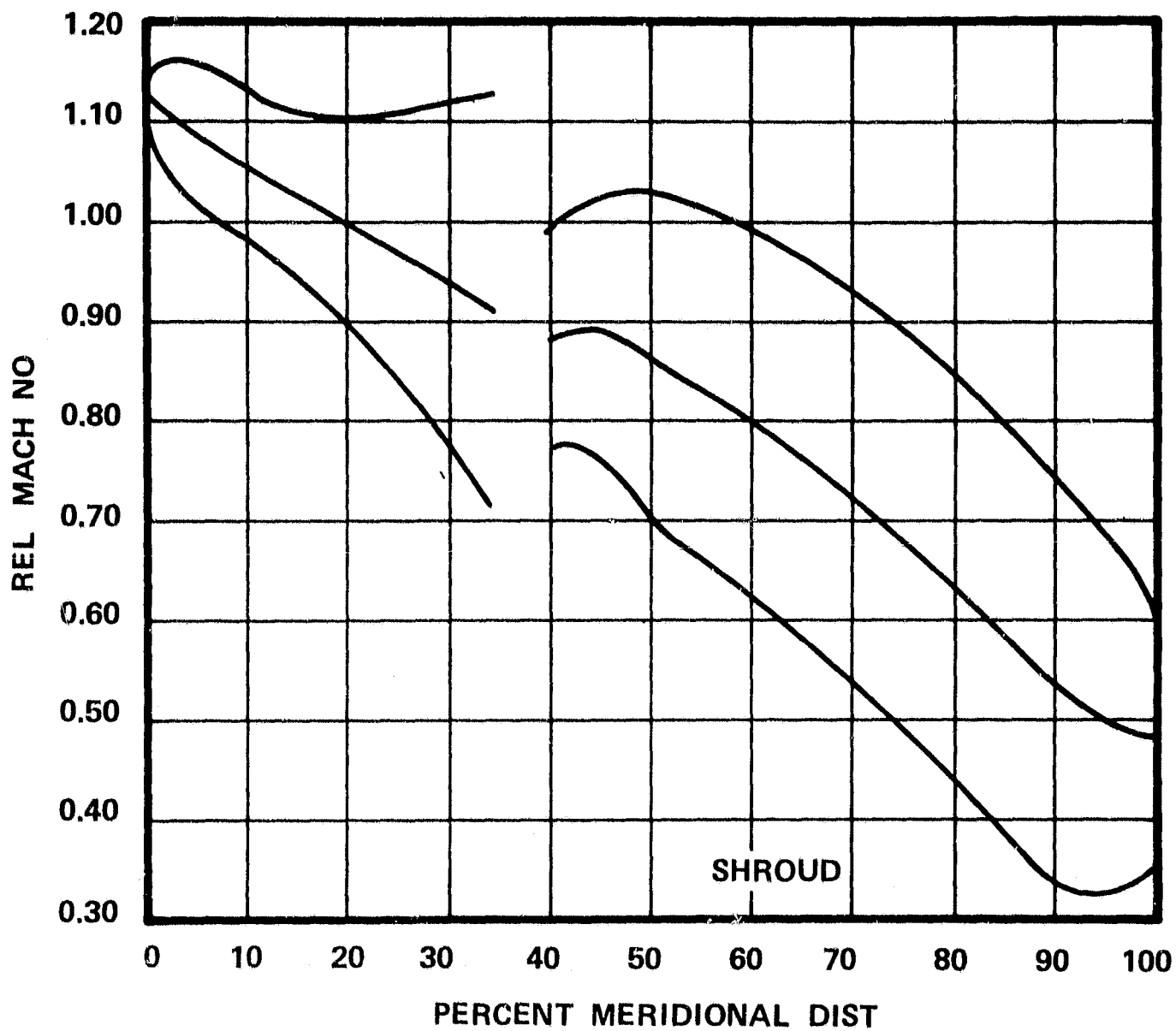


Figure 27. Compressor Impeller Blade Surface Mach No Distribution.

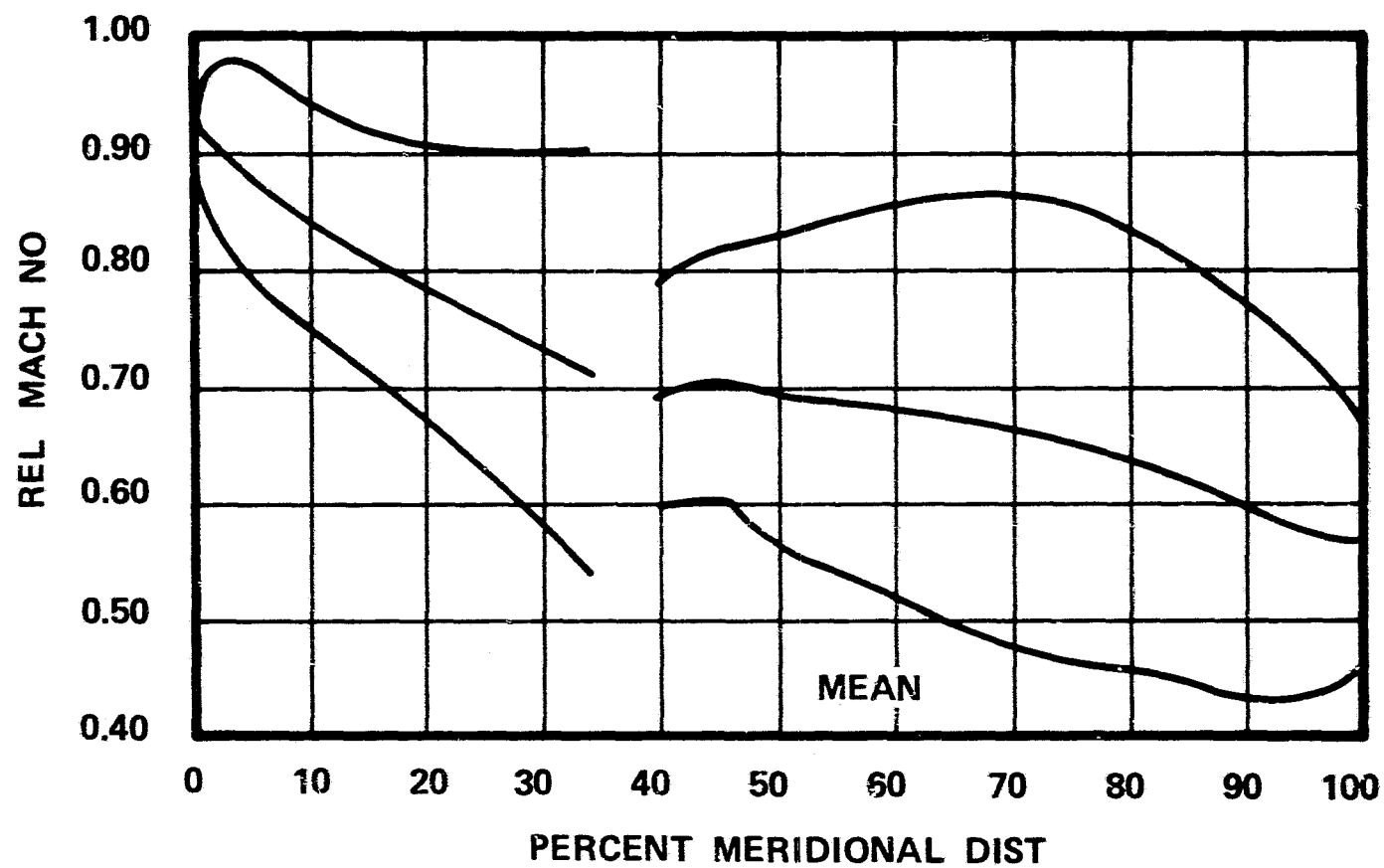


Figure 28. Compressor Impeller Blade Surface Mach No Distribution.

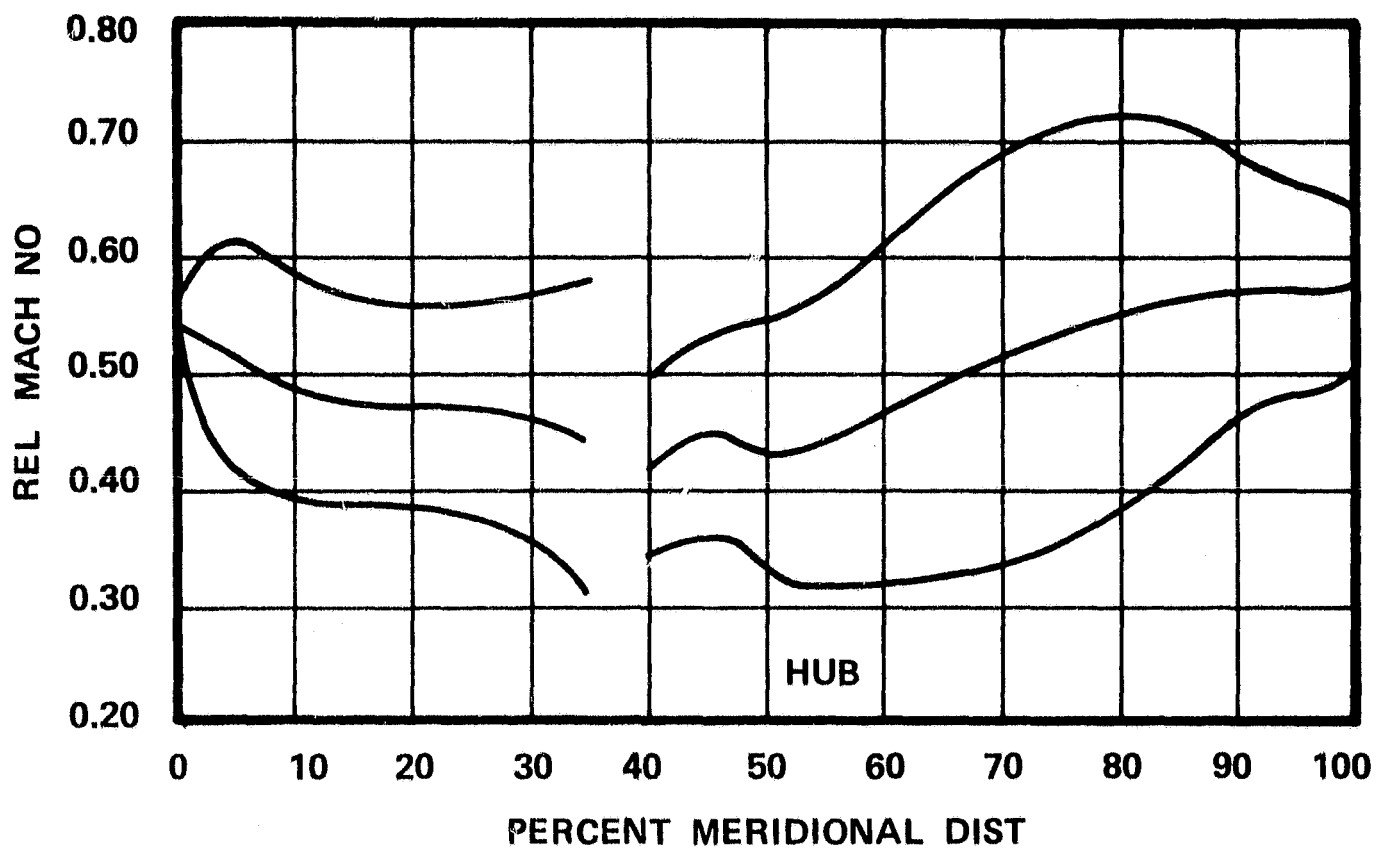


Figure 29. Compressor Impeller Blade Surface Mach No Distribution.

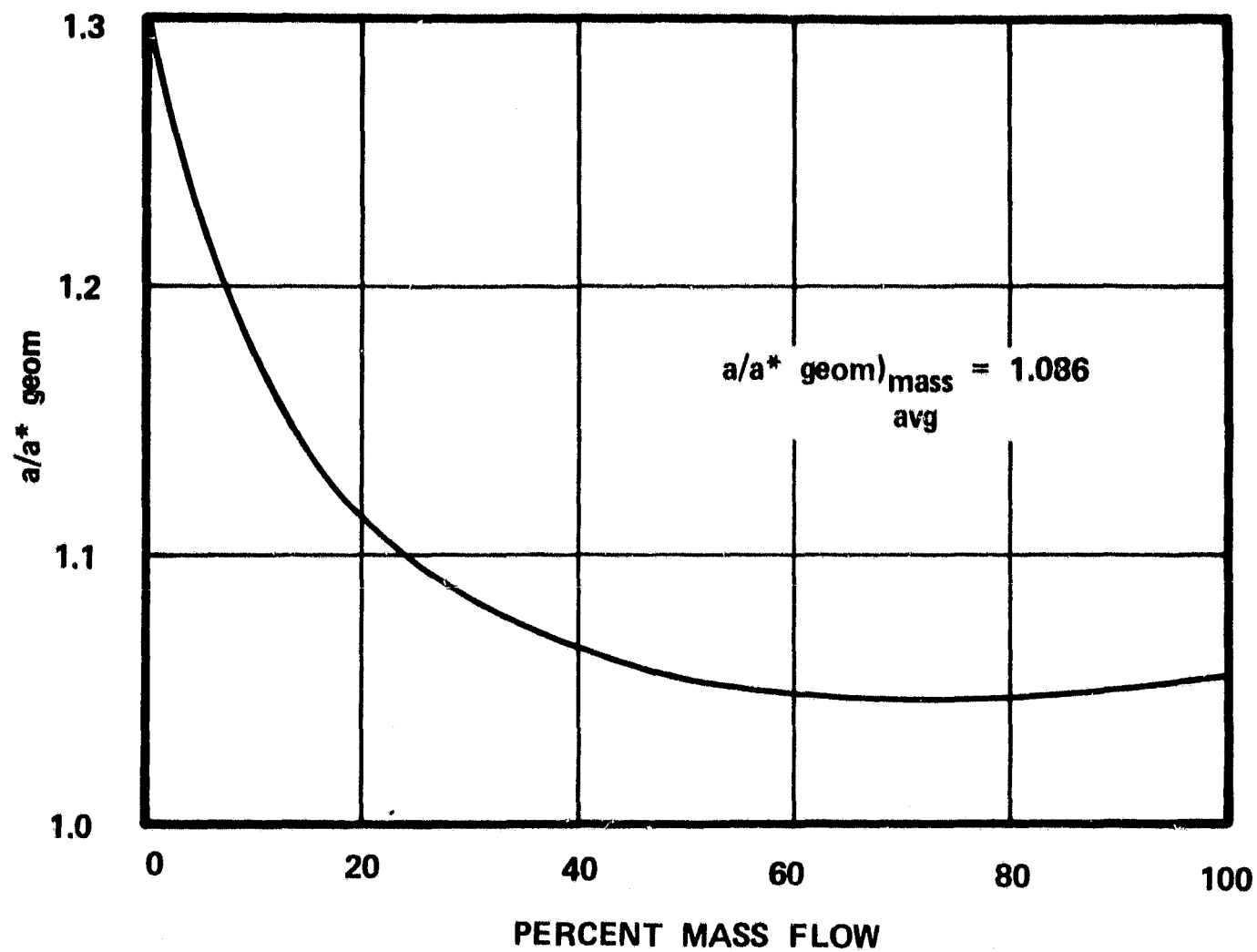


Figure 30. AGT101 Impeller Design Minimum a/a^*_{geom} .

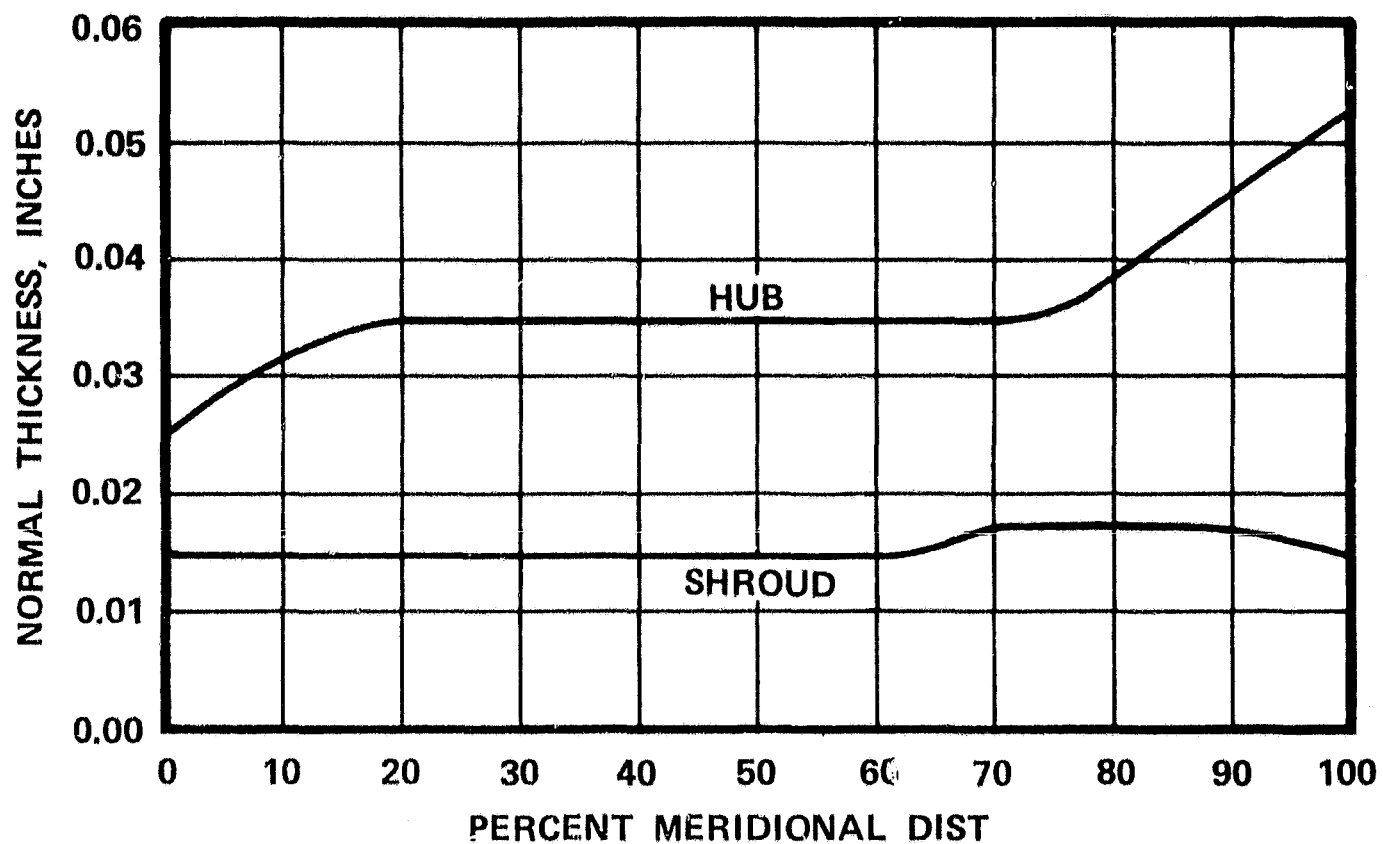


Figure 31. Impeller Normal Thickness Distribution.

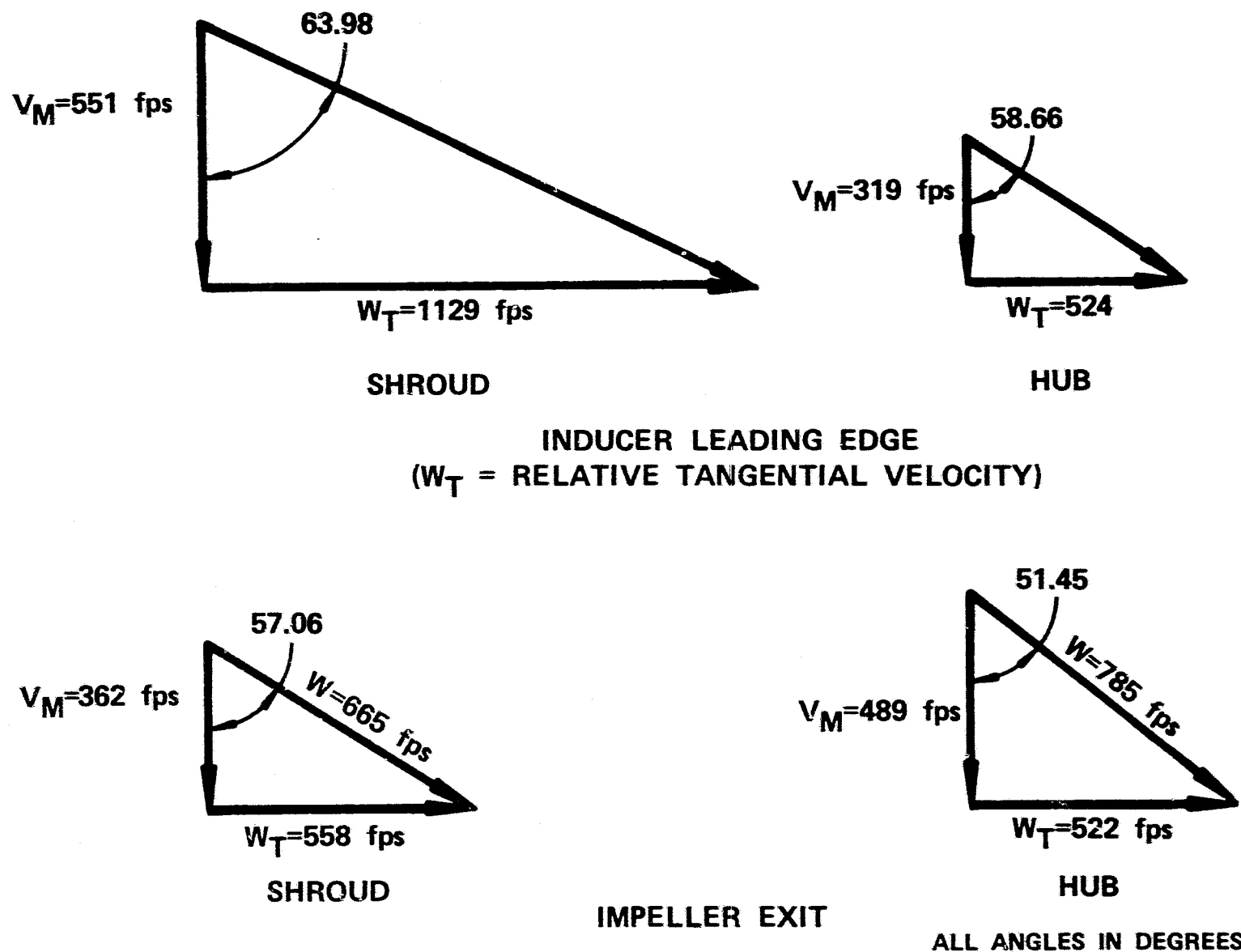


Figure 32. AGT101 Impeller Design Vector Diagrams.

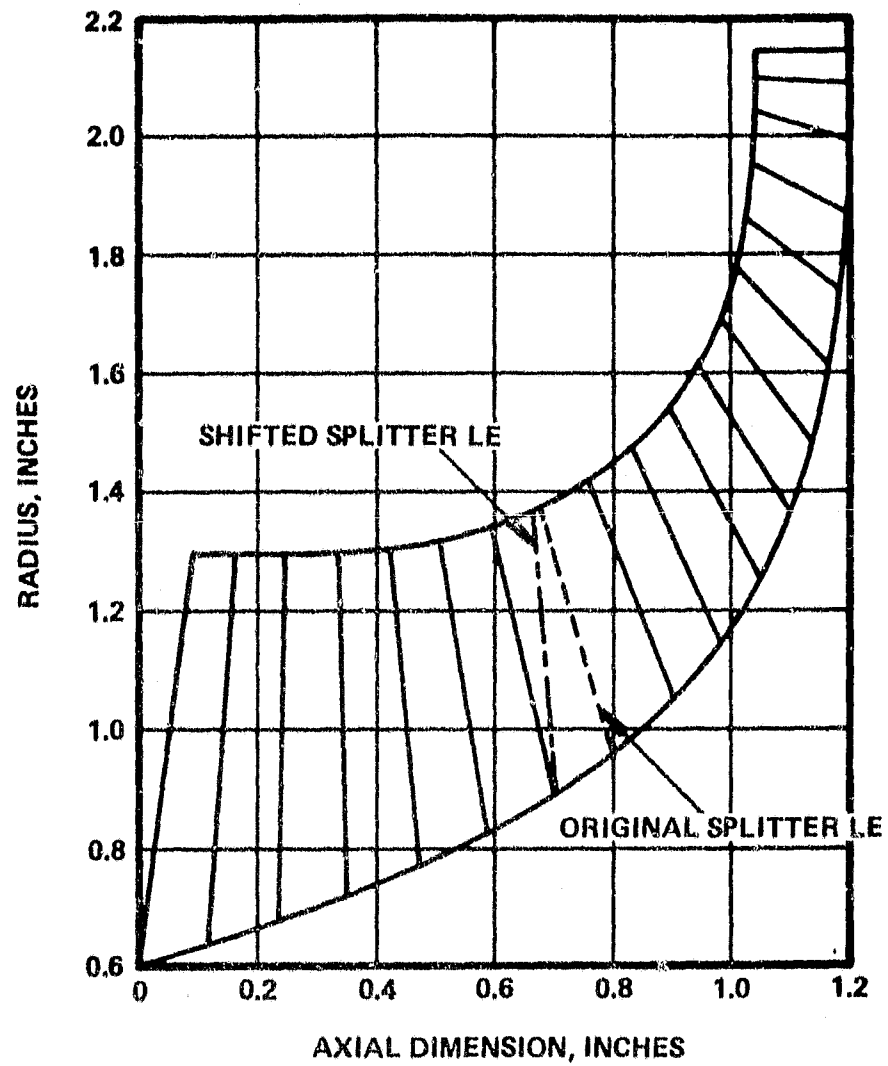


Figure 33. Splitter Blade Hub Leading Edge Movement.

[illegible]

followed by a cascade of two deswirl vane rows. During the analysis, a tradeoff was made between the first stage (vane island) diffuser area ratio and the tandem deswirl vane diffusion factors. The effect of varying the first deswirl vane exit angle on the diffusion factor of each row is shown in Figure 35. The first deswirl vane row inlet Mach Number was 0.225, a value providing the vane island diffuser with an area ratio of 2.59 which is consistent with AiResearch Phoenix experience.

Further design iterations resulted in a diffusion system having a convergence over the radial vane island of 0.020 inch from the leading to trailing edge, trailing edge thickness of the vane island of 0.070 inch and 34 vanes. An axial projection of the diffuser-system is shown in Figure 36 and meridional flowpath in Figure 37. Diffuser vector diagrams are shown in Figure 38.

4.1.1.3 Variable Inlet Guide Vane Design

The VIGV is an articulated design (fixed leading edge, movable trailing edge) using a NASA 63-0012 series thickness distribution modified to a maximum thickness of 13.5 percent of chord for the articulated portion of the vane. The fixed leading edge uses 26 percent of a NASA 63-0010 modified for a maximum thickness of 13 percent of chord. This design (Figure 39) is based on a similar articulated guide vane successfully being used on several engine compressors under development at AiResearch Phoenix. Results of tests conducted on these similar designs have been used in the off-design compressor performance for AGT101 cycle calculations.

4.1.2 Mechanical Design

4.1.2.1 Impeller Mechanical Design

Impeller material for the compressor test rig and early development engine tests will be forged 2219 T6 AL. This material was selected because of forging availability, good fatigue resistance, and high temperature strength. Current analysis and life estimates will be based on 2219 T6 properties. A change to a powder metal alloy will be accomplished when this material becomes available. Impeller properties are provided in Table 5.

Elastic three-dimensional stress and frequency analysis was performed on the final blade configuration. The blade was optimized to provide good aerodynamic performance while maintaining stress levels necessary to assure mechanical integrity. Blade vibrations primarily are confined to the inducer region of low specific speed impellers. The exducer short blade height makes this blade region insensitive to aerodynamic excitations. To assure an inducer region vibratory margin, stress levels were limited to 20 ksi, thereby permitting vibratory stress levels of 5 ksi with 2219 T6 AL. Plots showing stress

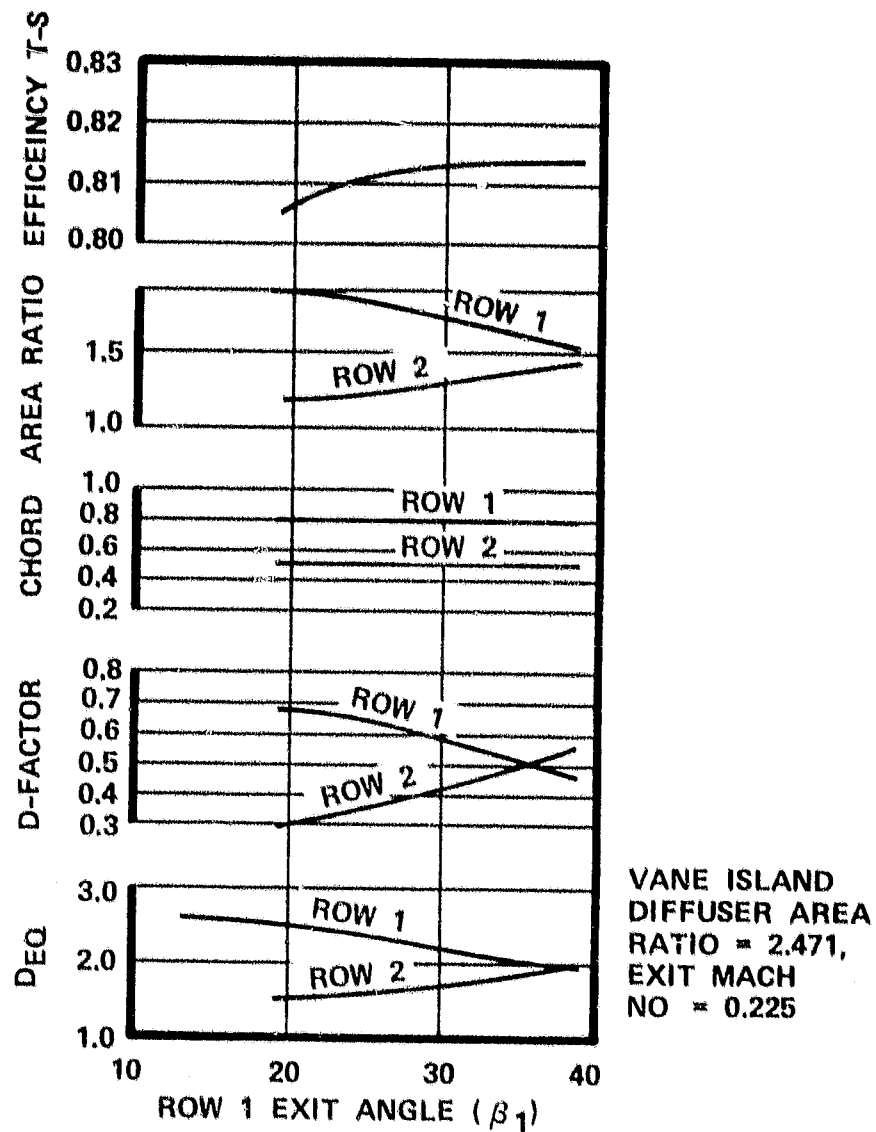


Figure 35. Diffuser Deswirl Vane Analysis.

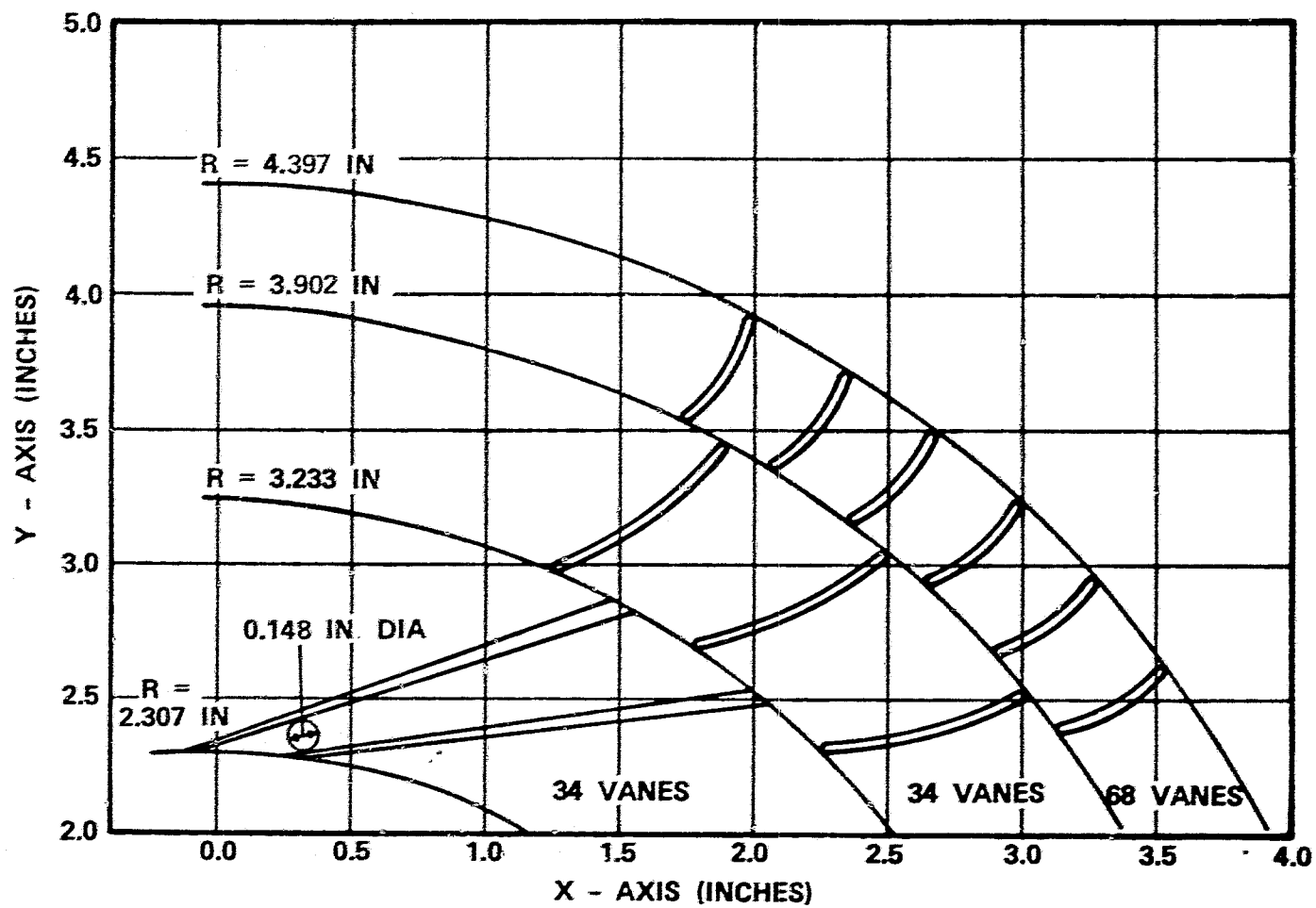


Figure 36. AGT101 Diffuser and Deswirl Vane Assembly Axial View.

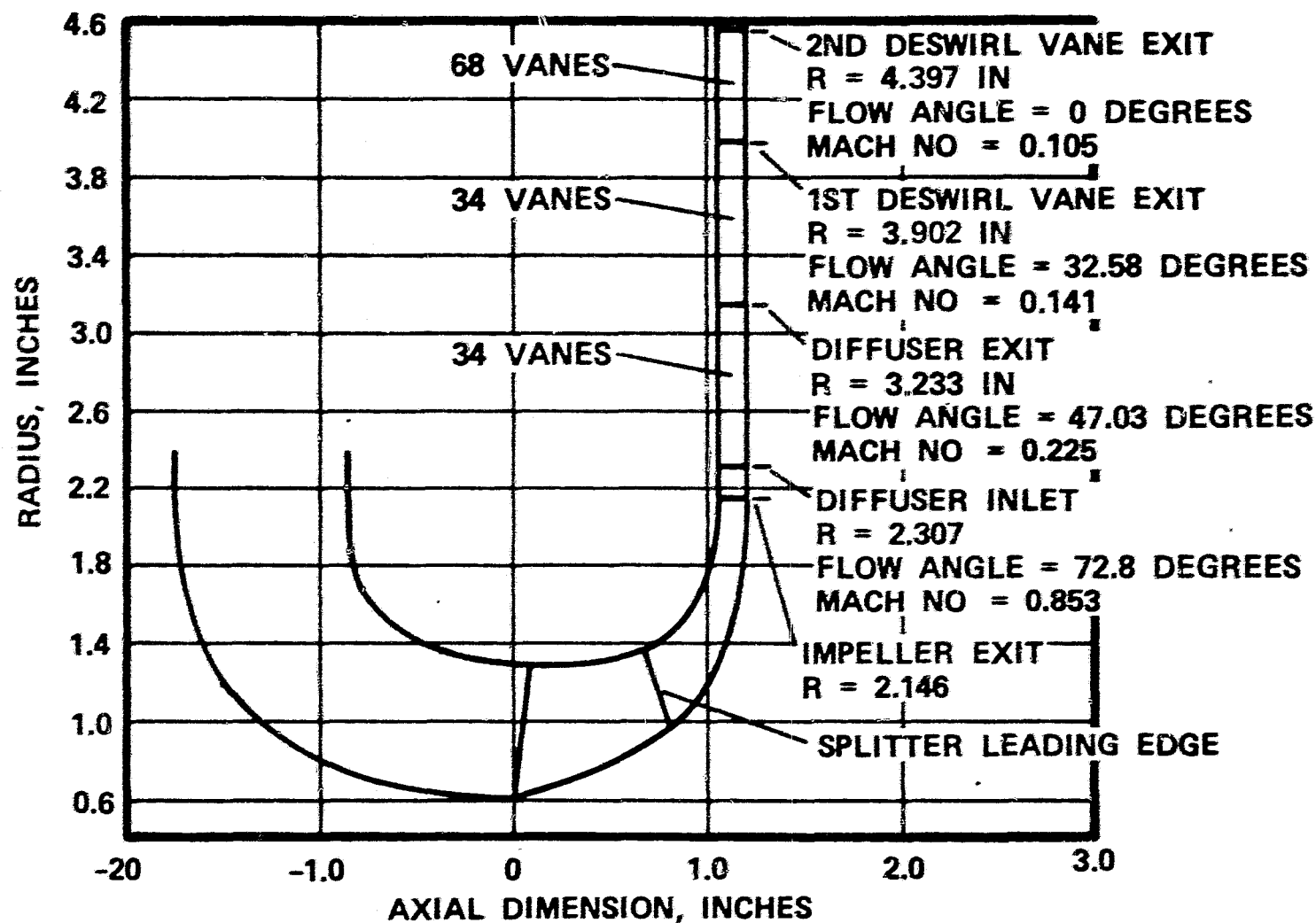
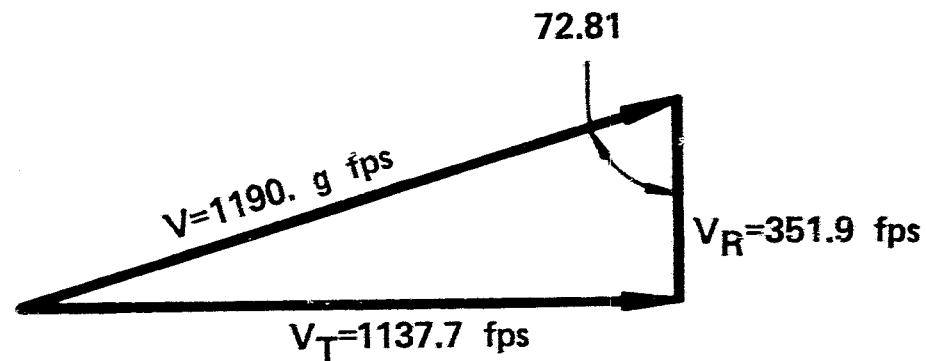
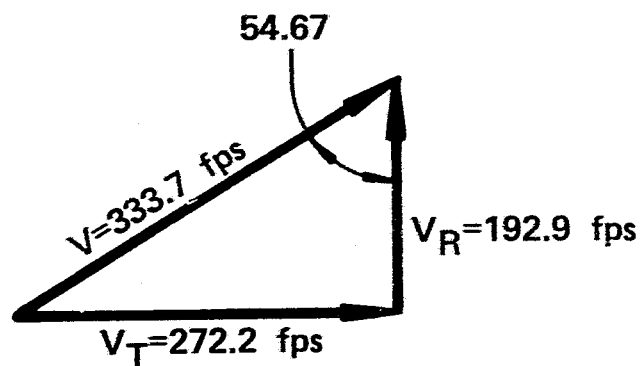


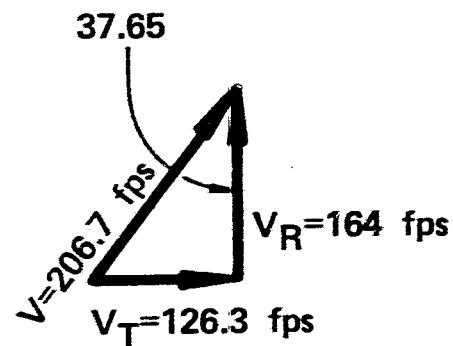
Figure 37. AGT101 Diffuser Meridional Flowpath.



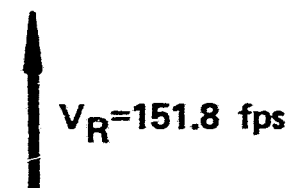
DIFFUSER LEADING EDGE (VANE ISLAND)



1st DESWIRL VANE
LEADING EDGE



2nd DESWIRL VANE
LEADING EDGE



2nd DESWIRL
VANE EXIT

Figure 38. AGT101 Diffuser Vector Diagrams.

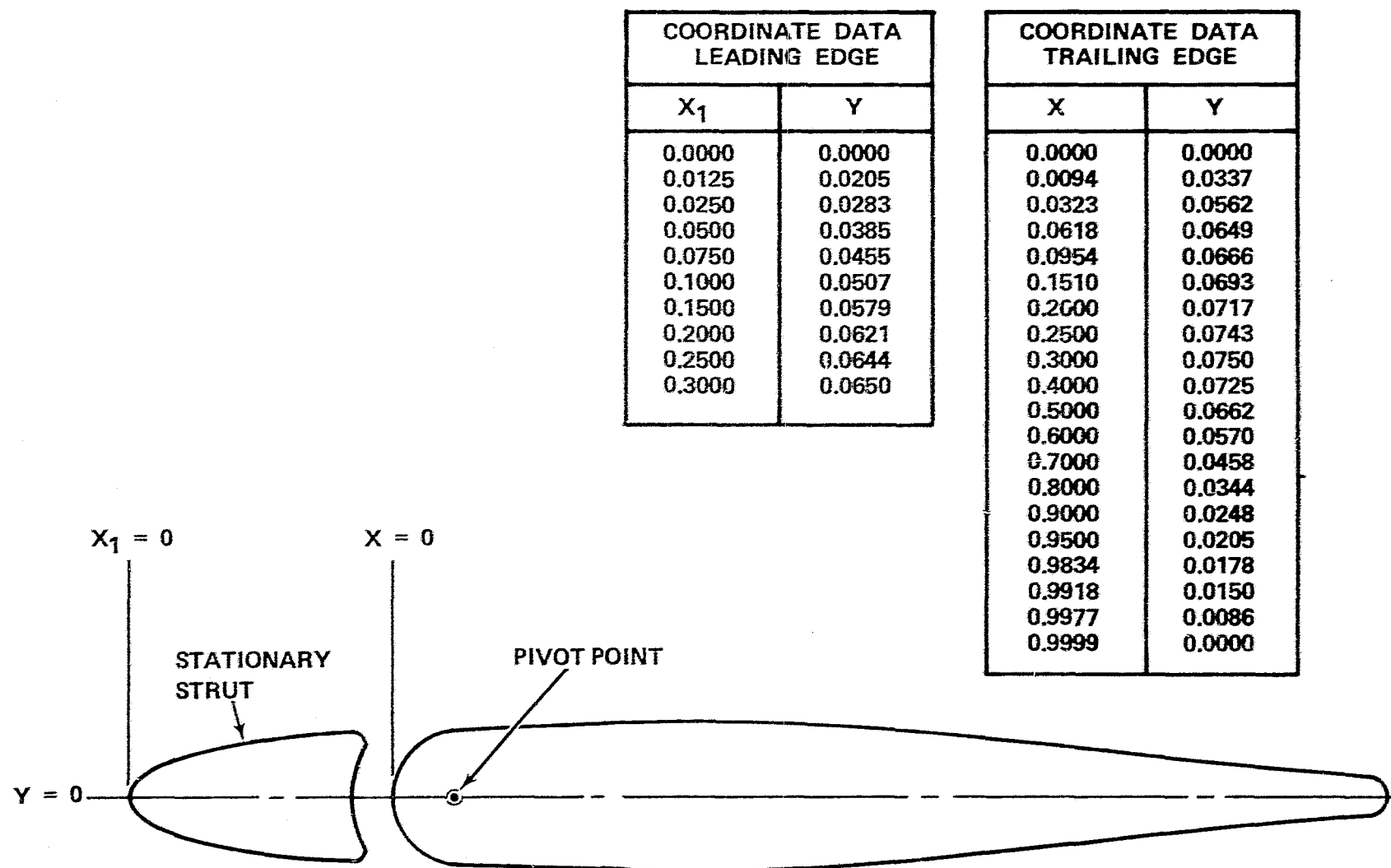


Figure 39. AGT101 Inlet Guide Vane.

TABLE 5. IMPELLER PROPERTIES

Total Weight (lbs)	0.549
Blade Weight (lbs)	0.034
I_p (lb-in-sec ²)	0.0014
I_d (lb-in-sec ²)	0.001
Hub Area (in ²)	1.185
CG (in) (Forward of Blade Root Exit)	0.277
Kinetic Energy (in-lb)	78700
Density (lb-in ³)	0.101

results from a three-dimensional finite element analysis are presented in Figure 40. This analysis was performed with zero displacement boundary conditions at the blade/hub interface. Calculated blade frequencies are shown in Figure 41 and the first four mode shapes in Figure 42. The first vibratory mode is at 3.5E at 100-percent speed. Experience has shown that impeller blades are relatively insensitive to distortion related excitations when the first mode frequency is above 3E. The first three blade modes will not have interferences with 17E IGV wakes in the operating range. With the relatively long flow space between the IGVs and blades, higher mode excitation is not expected.

Exducer region stress levels have to be controlled to provide adequate rupture life. The combination of 1872 feet/second tip speed and 50-degree backward curvature results in a maximum elastic stress at the exit of 31 ksi and an adiabatic wall temperature of 374°F.

A three-dimensional elastic stress and vibration analysis was performed on the final splitter configuration. Results are provided in Figures 43 and 44. The splitter stress levels are similar to the levels in the main blade. Frequency analysis of the impeller splitter blades shows potential interferences of the first and second vibratory modes with the IGV excitation. This analysis also shows physical location on the airfoil where the maximum vibratory strain would occur for each of these modes. Since these modes occur at part speed, the blade steady-stress level and metal temperatures will be significantly lower than the levels that exist at the 100-percent speed mechanical design point. Using the stress and temperature values that exist at the peak vibratory strain location for the predicted speeds of the interferences, the analysis shows that the allowable vibratory stresses of the first and second modes respectively are 7.5 and 10 ksi. This allowable vibratory stress should provide adequate fatigue margin, particularly since the vane to rotor spacing is more than 1.5 times the chord length of the IGVs.

Elastic stress analysis was completed for the impeller hub. Results of this analysis are shown on Figures 45 and 46 along with the isotherms for the 85°F day design point. These stress levels are consistent with AiResearch Phoenix experience on similar aluminum impeller designs. A preliminary life summary is presented in Table 6. These results show adequate burst margin and LCF life for the rig and early development impellers.

The axial and radial displacements of the blade, taking into account maximum temperature 100-percent operating speed and centrifugal stiffening is shown in Figure 47.

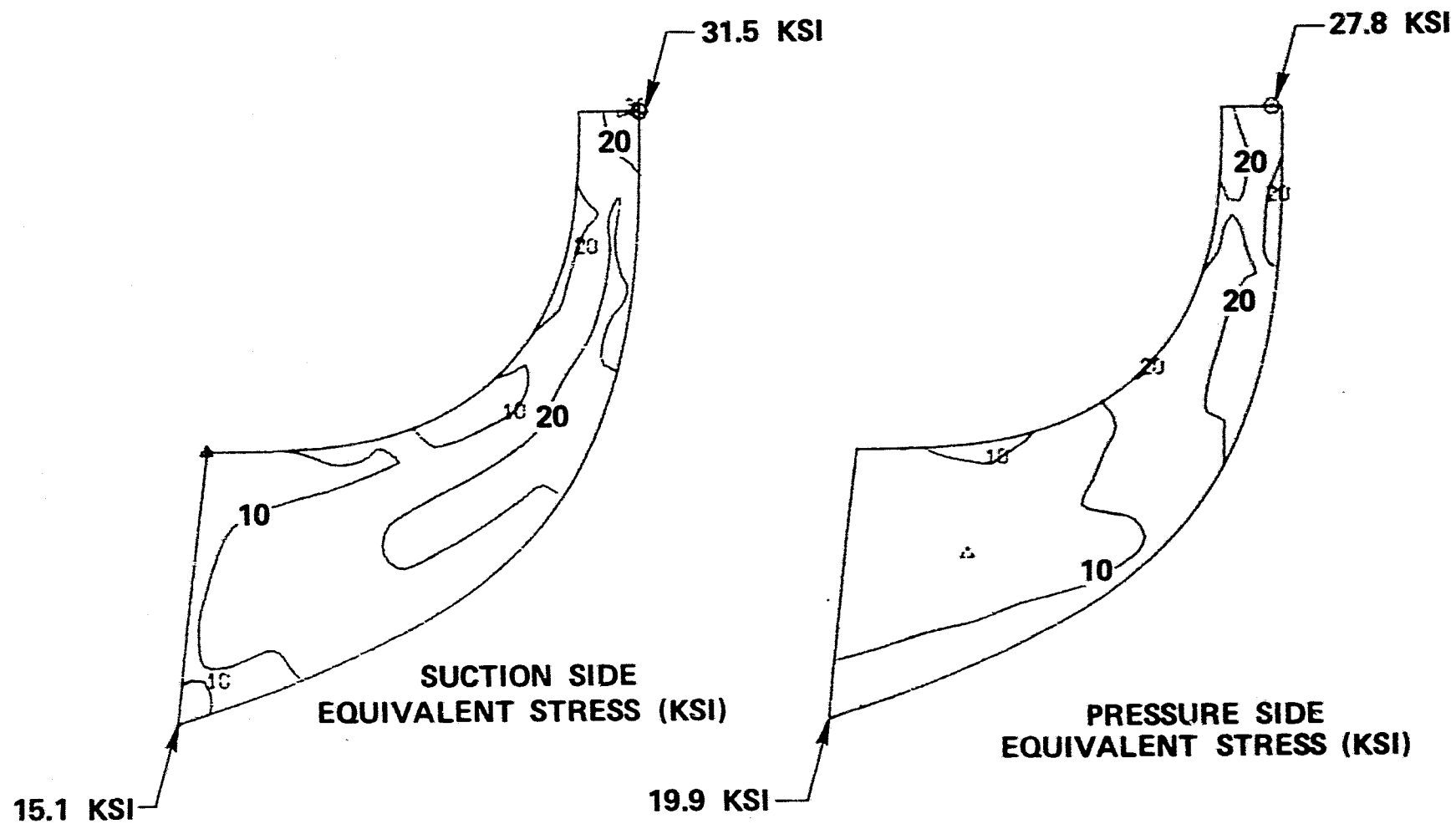


Figure 40. AGT101 3-D Airfoil Elastic Stress at 100,000 rpm.

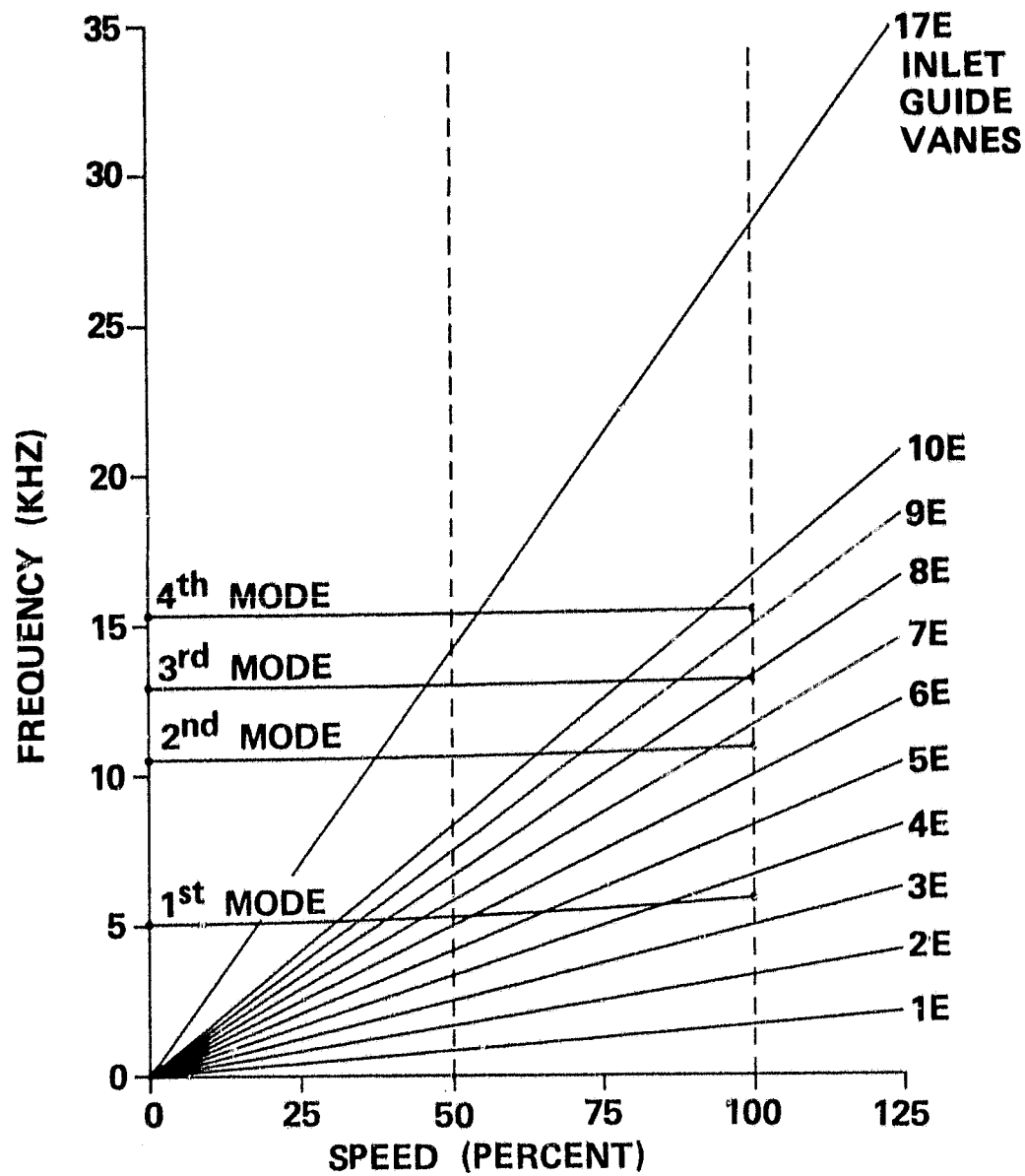
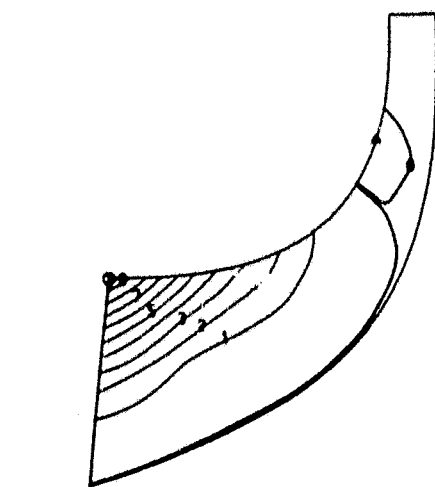
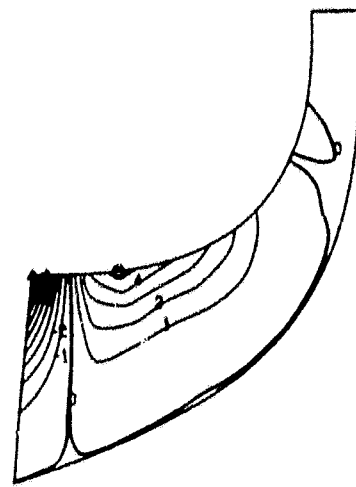


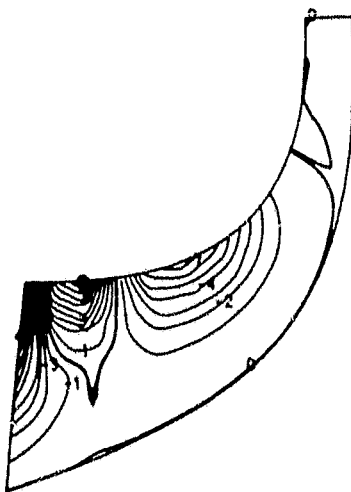
Figure 41. AGT101 Impeller Airfoil Campbell Diagram.



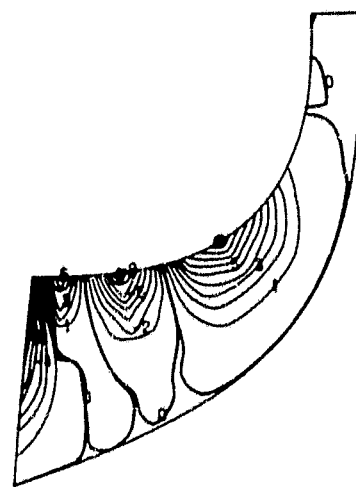
NORMAL MODE SHAPE
MODE 1 FREQ(HZ)=5063



NORMAL MODE SHAPE
MODE 2 FREQ(HZ)=10531



NORMAL MODE SHAPE
MODE 3 FREQ(HZ)=12930



NORMAL MODE SHAPE
MODE 4 FREQ(HZ)=15341

Figure 42. AGT101 Impeller Blade Vibratory Modes.

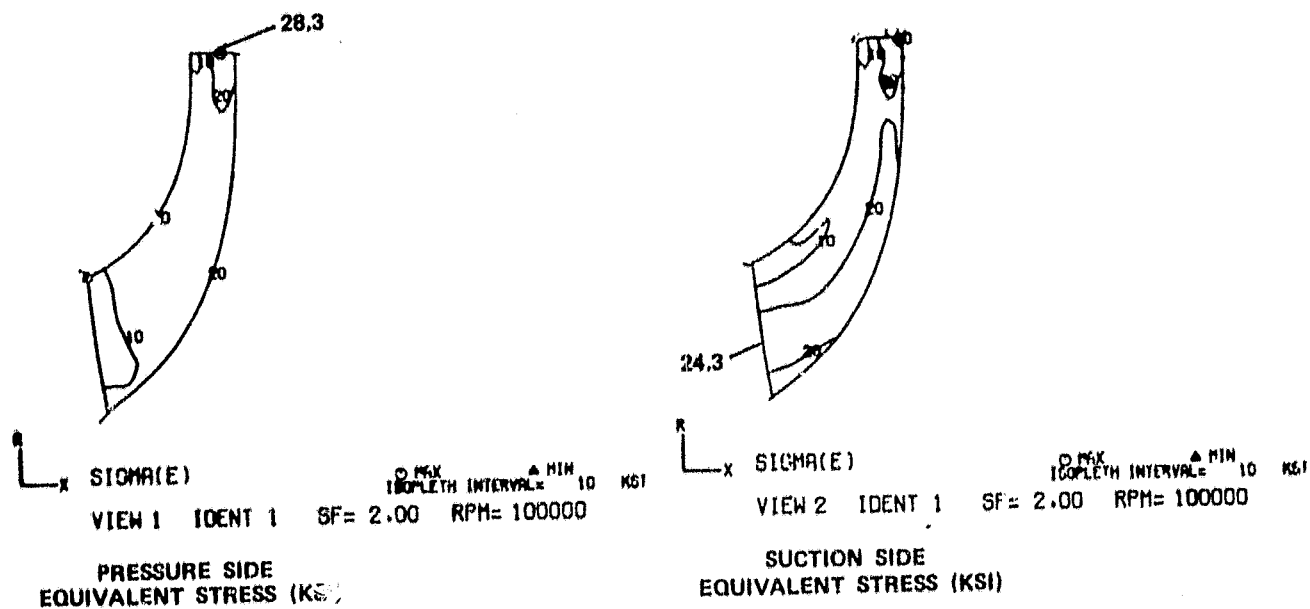


Figure 43. AGT101 3-D Splitter Elastic Stress at 100,000 rpm.

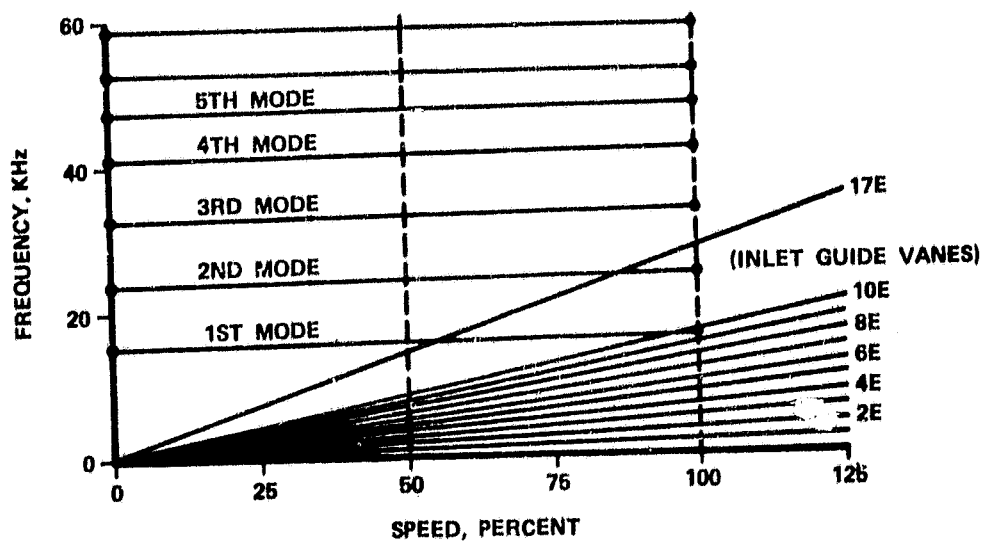
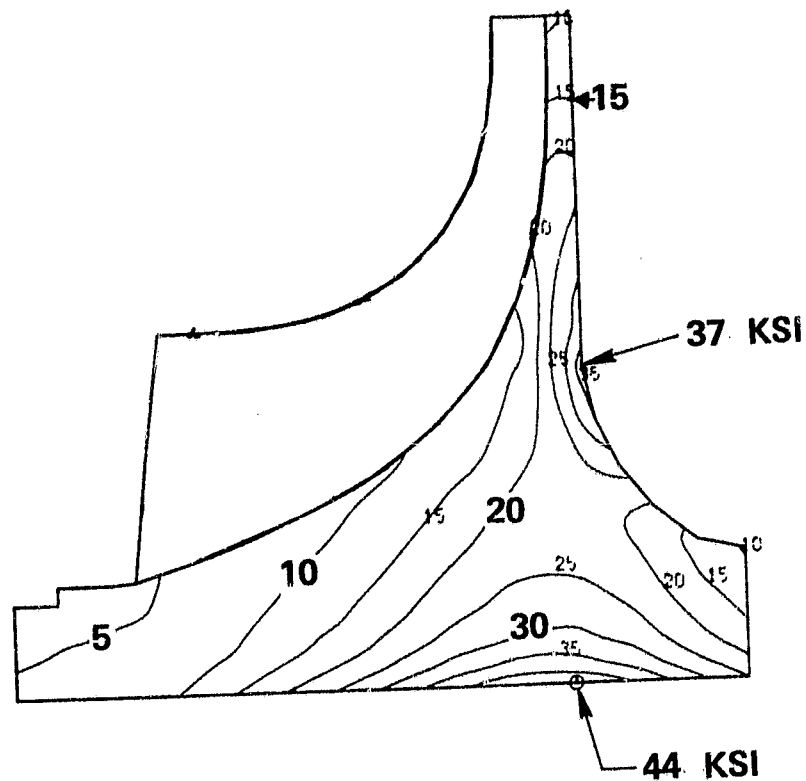


Figure 44. AGT101 Impeller Splitter Campbell Diagram.



EFFECTIVE STRESS

Figure 45. AGT101 Impeller Stress at 100 Percent Speed.

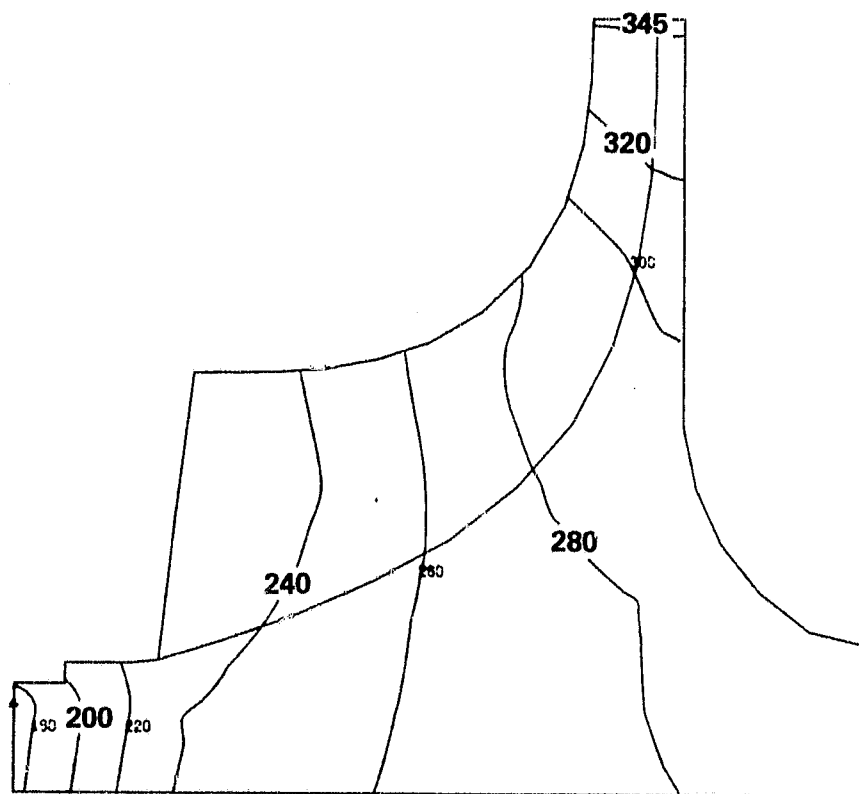


Figure 46. AGT101 Impeller Isotherms - 85°F Inlet Temperature.

TABLE 6. AGT101 IMPELLER PRELIMINARY LIFE SUMMARY (-3 MATERIAL PROPERTIES)

- **MATERIAL - 2219T6 AL DEVELOPMENT IMPELLERS**

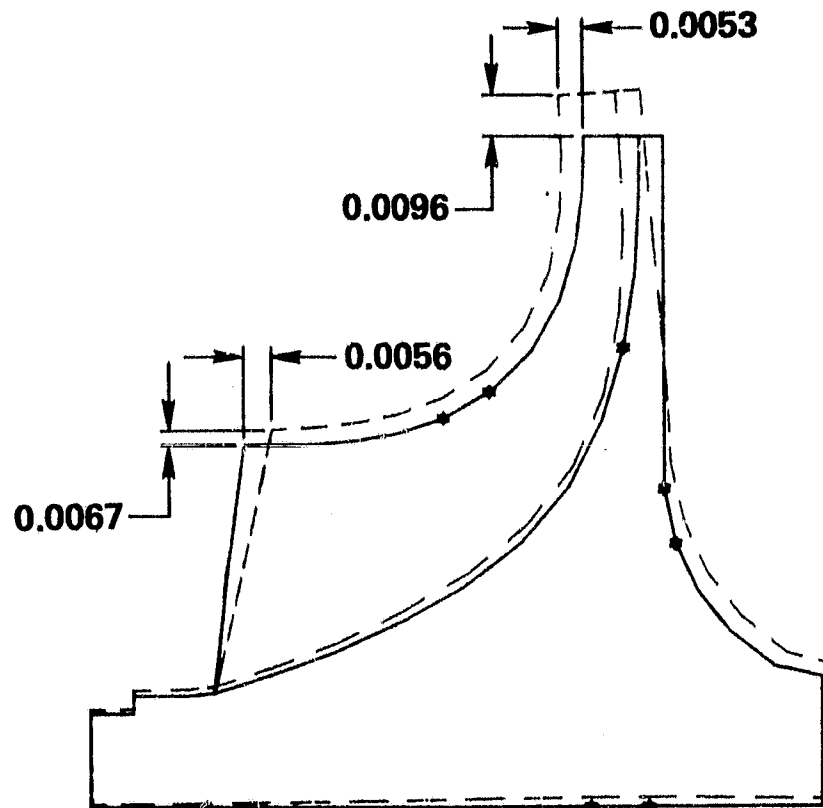
- **BURST RATIO** **1.50**

$$BR = \sqrt{\frac{0.85 (UTS-3\sigma)}{\sigma_{AVE TAN}}}$$

- **BORE LCF LIFE** **>10,000 CYCLES**
[STARTS TO 100% SPEED
W/O TRANSIENT THERMAL STRESS]

- **STRESS RUPTURE LIFE** **>100 HOURS**
BASED ON ESTIMATES FROM ELASTIC
STRESS LEVELS (3D CREEP ANALYSIS
HAS BEEN INITIATED)

- **AIRFOIL ALLOWABLE VIBRATORY STRESS** **5 KSI**
(INDUCER REGION)



DEFORMATION

Figure 47. AGT101 Impeller Deformation at 100 Percent Speed.

4.1.2.2 Powder Metal

Initial thermal analysis indicated that the aluminum compressor impeller would need to withstand temperatures in excess of 400°F. However, currently available materials lose strength during extended exposures at these temperatures. Therefore a more temperature resistant material is required for long term production concepts. Several new alloys relying on oxide, carbide dispersions, or stable phases formed by alloy additions of low diffusibility elements show promise for better temperature resistance. Advancements in aluminum alloys include two primary approaches; mechanically alloyed oxide dispersion-strengthened alloys (INCO), and insoluble alloy additions, using powder metallurgy fabrication (ALCOA). Both alloys exhibited properties (Figure 48) in the laboratory that indicated potential as possible longterm production candidates.

These candidate aluminum alloy systems are dependent on secondary phase dispersions, which are stable at use temperatures, for improved high-temperature strength. The ALCOA Al-Fe-Ce alloy, developed under Contract F33615-77-C-5086, is strengthened by FeAl_6 and $\text{Al}_3\text{Fe}_4\text{Ce}$ intermetallic phases. The IN9081 alloy, being developed by Novamet (a Division of INCO) under Contract F33615-76-C-5227, primarily is strengthened by oxide and carbide dispersions.

The scope of the ALCOA program has been narrowed to an Al-7.4%Fe-3.4%Ce alloy and currently is in the material characterization phase. Material is produced in alloyed powder form, hot compressed, and then forged to a pancake shape.

Thus far, data from this program (Figure 48) indicates that forged Al-Fe-Ce alloy shows better strength versus temperature capability than other alloy systems considered. Initial stress-rupture data also is very promising for this alloy.

The Novamet (INCO) program is focused on the Al-1.2Ni-0.7-Fe alloyed (named IN9081) with a minimum of 3-percent dispersed oxide and 1.5-percent carbide phases. The powder is prepared by the mechanical alloying process and then is hot-compacted and forged. IN9081 properties also are shown in Figure 48.

Both Novamet and AiResearch Phoenix have obtained mechanical property data for IN9081 alloy extrusions (Figure 49). This data indicates that an adequate understanding of thermal-mechanical processing characteristics of the alloy is necessary. Similar considerations are expected to apply to the ALCOA Al-Fe-Ce alloy.

As a consequence of the IN9081 alloy deformation rate sensitivity, AiResearch has focused on characterizing the mechanical properties of these alloys in high-deformation rate pancake forgings of sufficient size to yield impellers. Data from these tests currently are being analyzed.

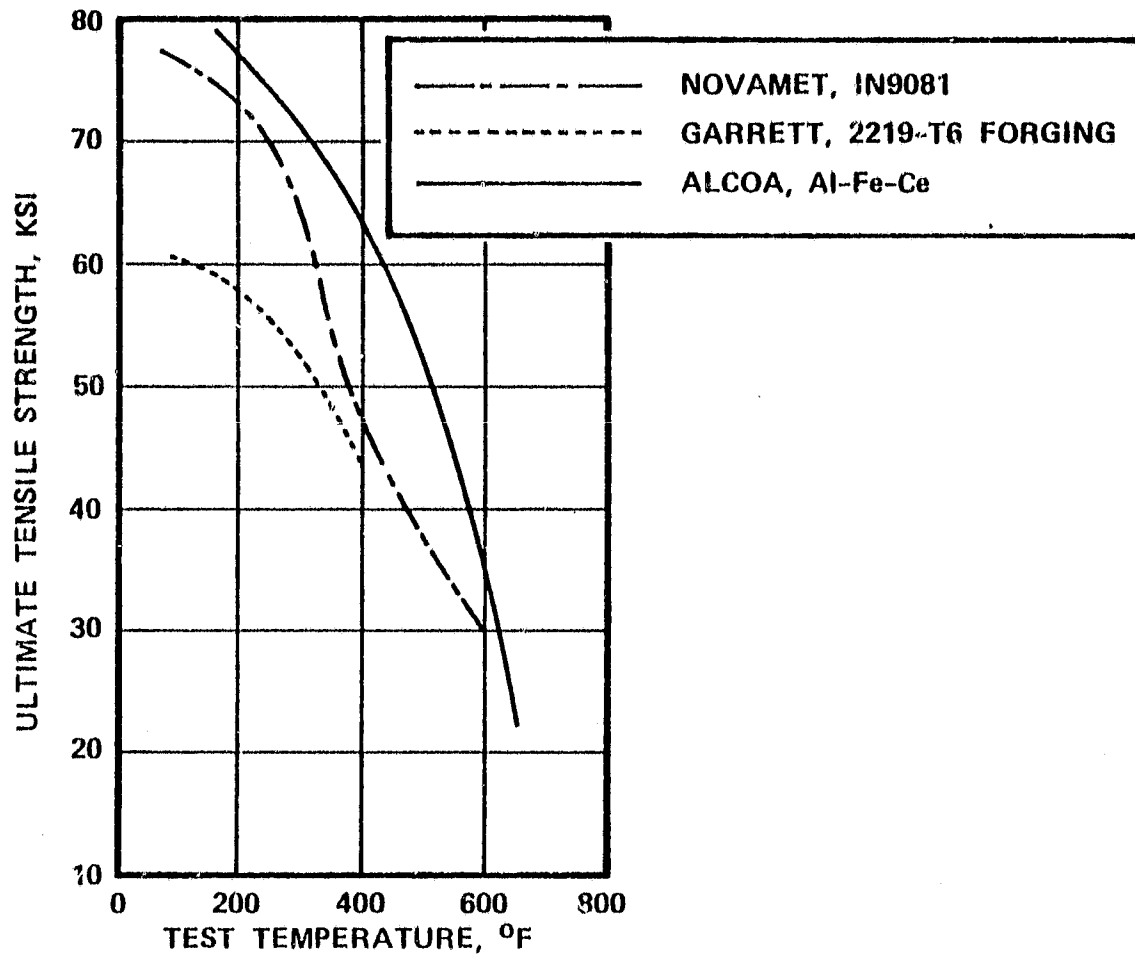


Figure 48. Mechanical Property Comparison of Novamet IN9081 and ALCOA Al-Fe-Ce Alloys with Respect to Conventional Aluminum Alloys (2219-T6 and 201-T7).

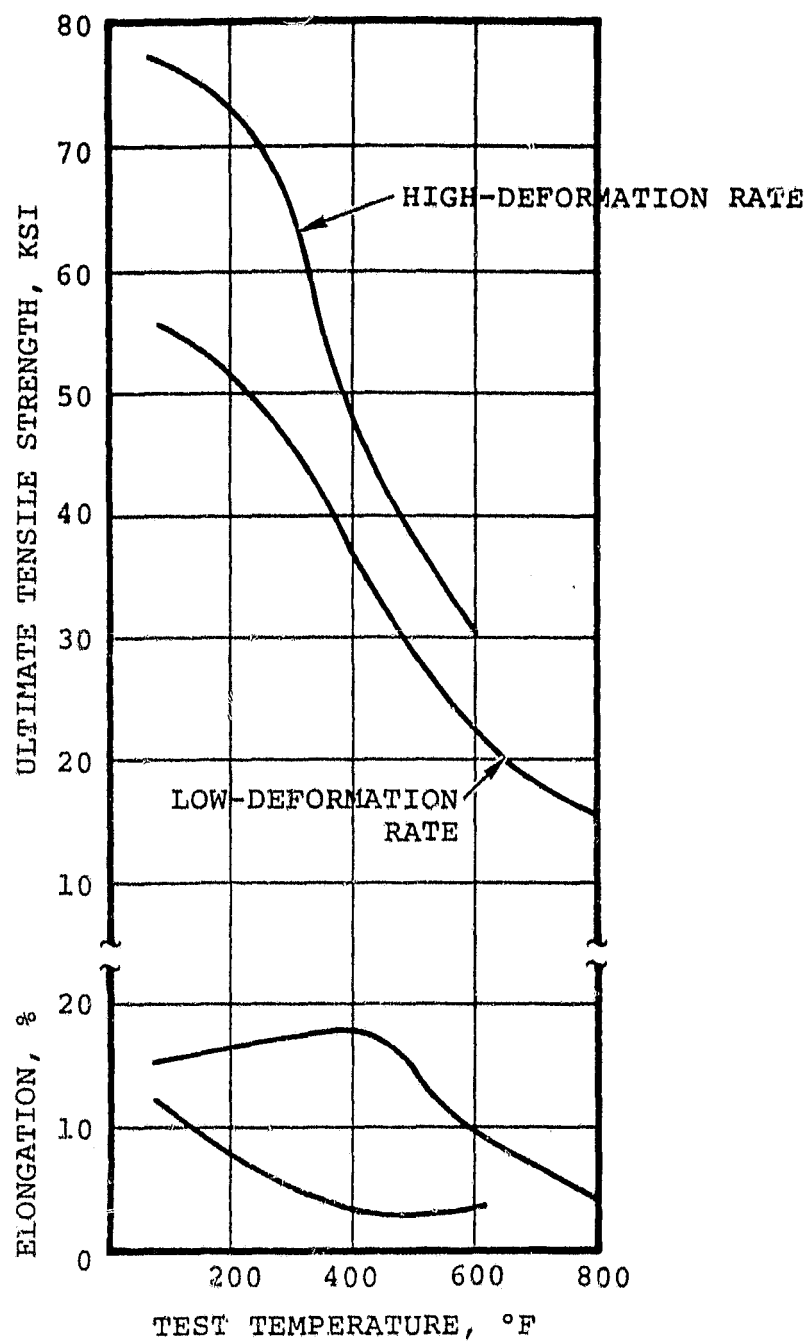


Figure 49. Effect of Deformation Rate During Extrusion on IN9081 Mechanical Properties.

4.1.3 Test Rigs

Compressor development testing will be conducted on a test rig suitable to aerodynamically and mechanically evaluate the impeller, diffuser, VIGVs, inlet plenum and compressor discharge airflow path.

4.1.3.1 Compressor Test Rig

The compressor test rig, is a straddle-mounted bearing configuration utilizing the AGT101 engine ball bearings. Power is derived from a drive turbine system composed primarily of the Garrett Model TV81 turbocharger hot flowpath components. Actual AGT compressor stage hardware (VIGVs, impeller and diffuser) is utilized in the rig to permit detailed compressor design performance mapping. As shown in Figure 50, power section ducting has been incorporated to establish any flow phenomena effects resulting from transitioning compressor discharge flow to regenerator high pressure inlet. In addition, the inlet air filter and associated ducting (not shown) can be accommodated to verify aerodynamic design intent and again establish any detrimental flow effects resulting from the installation.

The rig incorporates the capability for controlling and evaluating critical compressor impeller running clearance based on capacitance probe measurements at selected stations along the impeller meridional flowpath. The clearance control mechanism is based on a design concept successfully demonstrated on other AiResearch Phoenix programs. This mechanism features an Acme thread, used to axially adjust the position of the impeller under dynamic operation. This is accomplished by fixing the internal thread and turning the external thread, thus forcing the externally threaded members (impeller shafting) to move axially. Clearance control capability allows thermal stabilization of the test rig and dynamic stabilization of the impeller prior to recording data such that desired clearances can be evaluated. In addition, this mechanism will allow performance evaluation of larger than desired clearances and/or duplication of engine conditions for performance comparisons.

As shown in Figure 51, compressor test rig instrumentation has been identified such that detailed evaluation of individual and system compressor components can be achieved. Instrumentation is of a size consistent with the small stage dimensions and of sufficient number and spacing to provide realistic average values for all parameters measured.

4.1.3.2 VIGV Rig

In an effort to further quantify the losses and associated velocity profiled, a secondary test rig has been designed and is shown in

ORIGINAL PAGE IS
OF POOR QUALITY

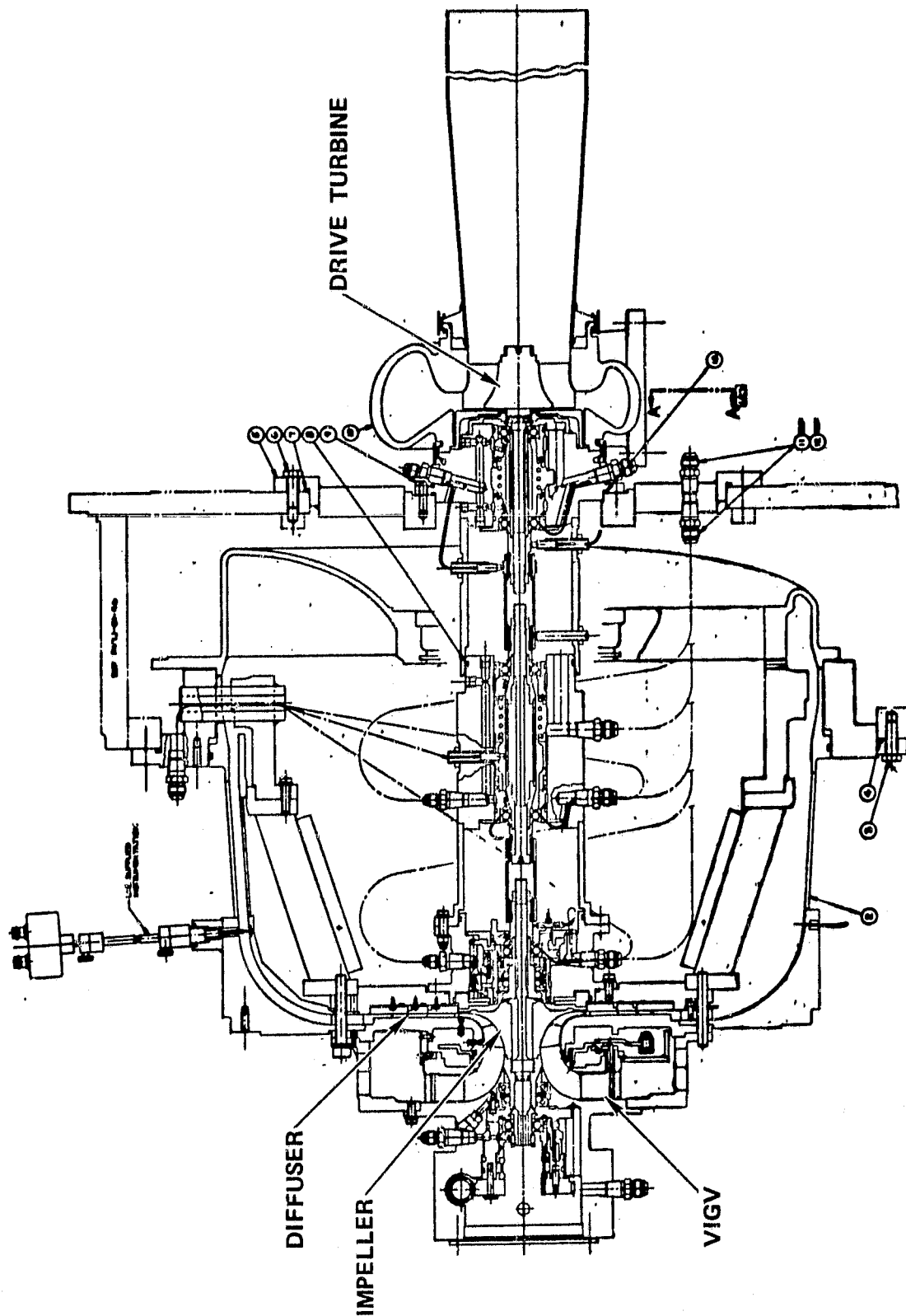


Figure 50. Compressor Rig.

ORIGINAL PAGE IS
OF POOR QUALITY

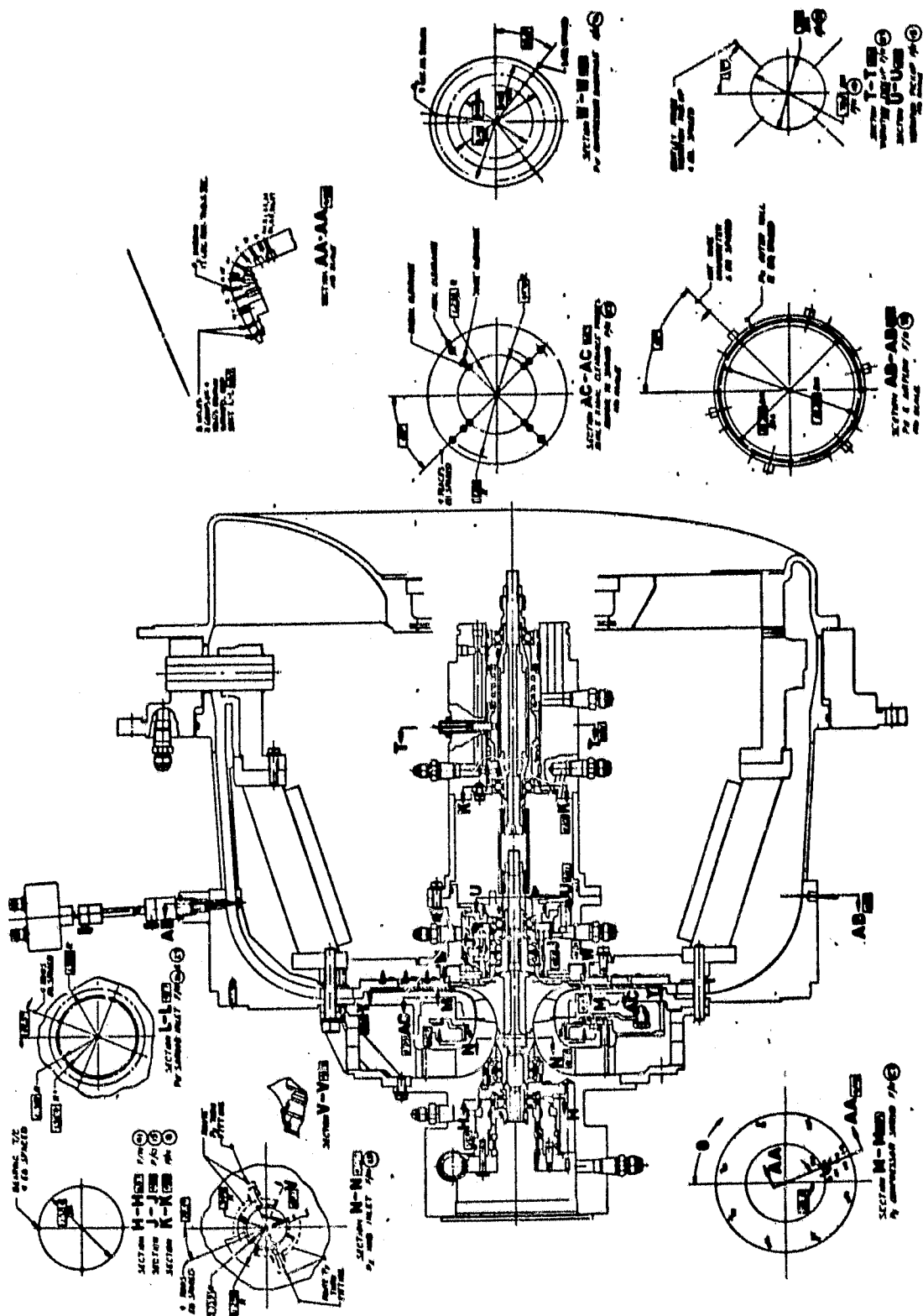


Figure 51. Compressor Rig Instrumentation.

Figure 52. The rig is patterned after an existing IGV rig currently on test. Vane trailing edge and rotor leading edge surveys have been accommodated in addition to static and total pressure instrumentation. A simplified indexing mechanism will allow cross passage survey via vane rotation relative to the probe. IGV setting angles will be accomplished using accurate vane angle tooling. The rig will allow evaluation of IGV settings from -20 to 80 degrees. Data generated from these tests will be incorporated into compressor design methodology, in conjunction with detailed compressor mapping on the compressor test rig.

ORIGINAL PAGE IS
OF POOR QUALITY

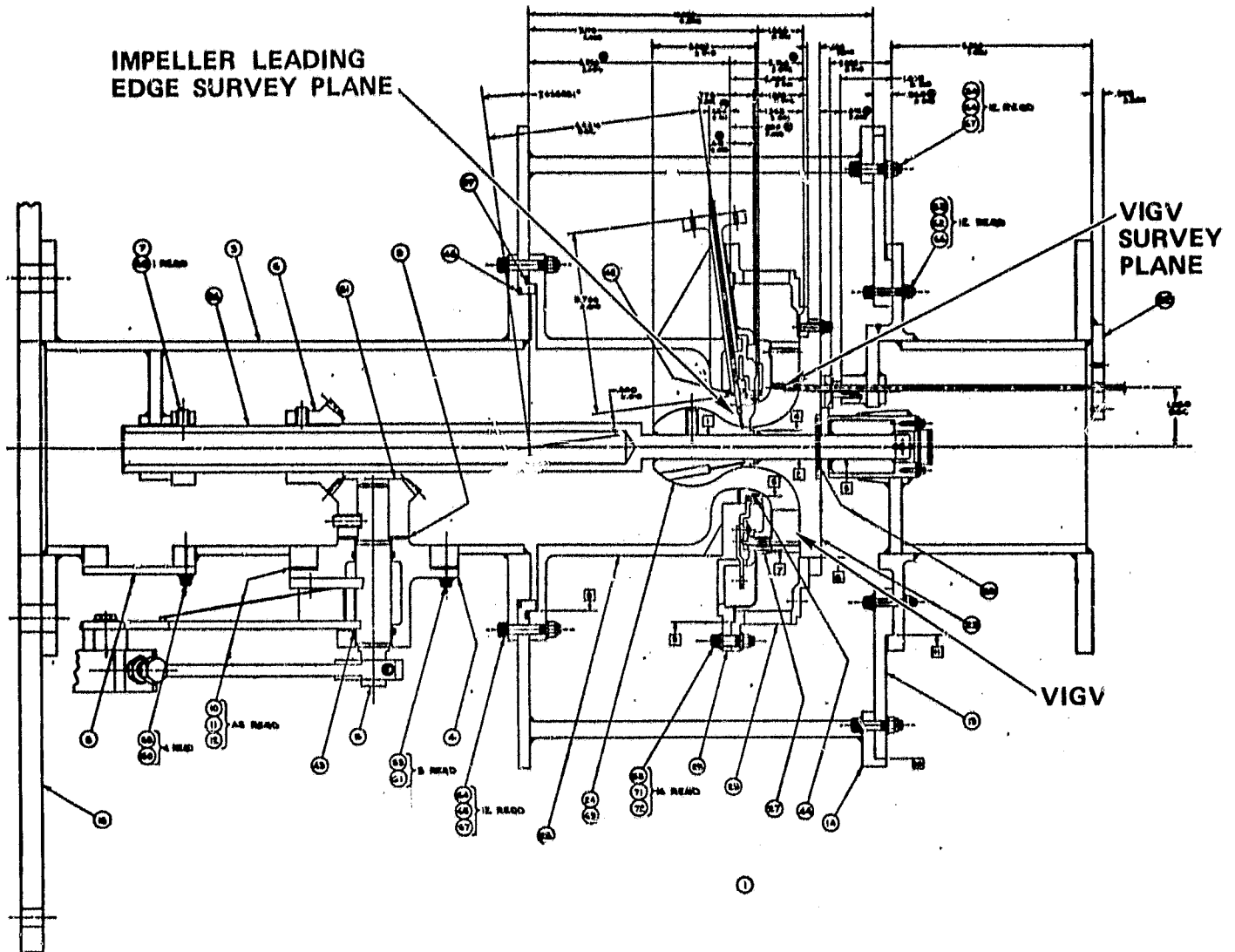


Figure 52. Variable Inlet Guide Vane Test Rig.

4.2 Turbine Development

Three maximum power design point vector diagrams were evaluated with the engine driving cycle. The three turbine designs were identified as -9.8 (low), -27 (high) and -37 degree (maximum) rotor exit swirl designs. As shown in Figure 53, examination of the original optimized -9.8 degree case showed significant performance decrement at engine idle, and since "system design" objectives are to maximize engine performance at low power while maintaining acceptable vehicle acceleration capabilities, the -27 degree exit swirl design has been selected for the baseline ceramic turbine. Vector diagrams for maximum power and idle are presented in Figure 54 for the -27 degree exit swirl design. Also shown is the maximum power vector diagram for the Mod I complete metallic rotor configuration.

The maximum power design point cycle conditions for the selected -27 degree rotor exit swirl design are presented in Table 7. The predicted 1979 and 1985 turbine efficiency summaries are presented in Table 8 and Figure 55. The turbine system station designations are shown in Figure 56. Turbine off-design performance maps are presented in Figures 57 and 58. Note that the predicted characteristics are based on a constant design point Reynolds Number ($Re = 1.06 \times 10^5$). In the cycle analysis, the effect of Reynolds Number relative to the design point value are accounted for with a correlation of NASA and AiResearch Phoenix in-house data.

4.2.1 Aerodynamic Design

4.2.1.1 Stator Inlet Flowpath

The turbine inlet duct design has been completed as shown in Figure 59. Three modified NACA 16-021 airfoil design struts have been selected to reduce strut tip blockage and thus decrease tip loading (Figure 60). The resulting inlet duct velocity distribution is shown in Figure 61. A 2-D boundary layer analysis, which verifies that flow through the inlet duct is stable was performed.

4.2.1.2 Stator

The stator vane profile design objective was to maximize stator inlet loading (which is then relieved with end-wall contouring) and minimize exit loading from the throat region to the trailing edge. This approach minimizes total vane loading and; therefore, secondary flow losses. Nineteen vanes have been selected based on turbine rotor blade vibration analyses.

Two stator vane profile designs have been completed. The baseline design is based on a trailing edge thickness (normal) of 0.020 inch and a fillet radius of 0.030 inch. The design is consistent with previous turbine designs used for the specific speed correlation

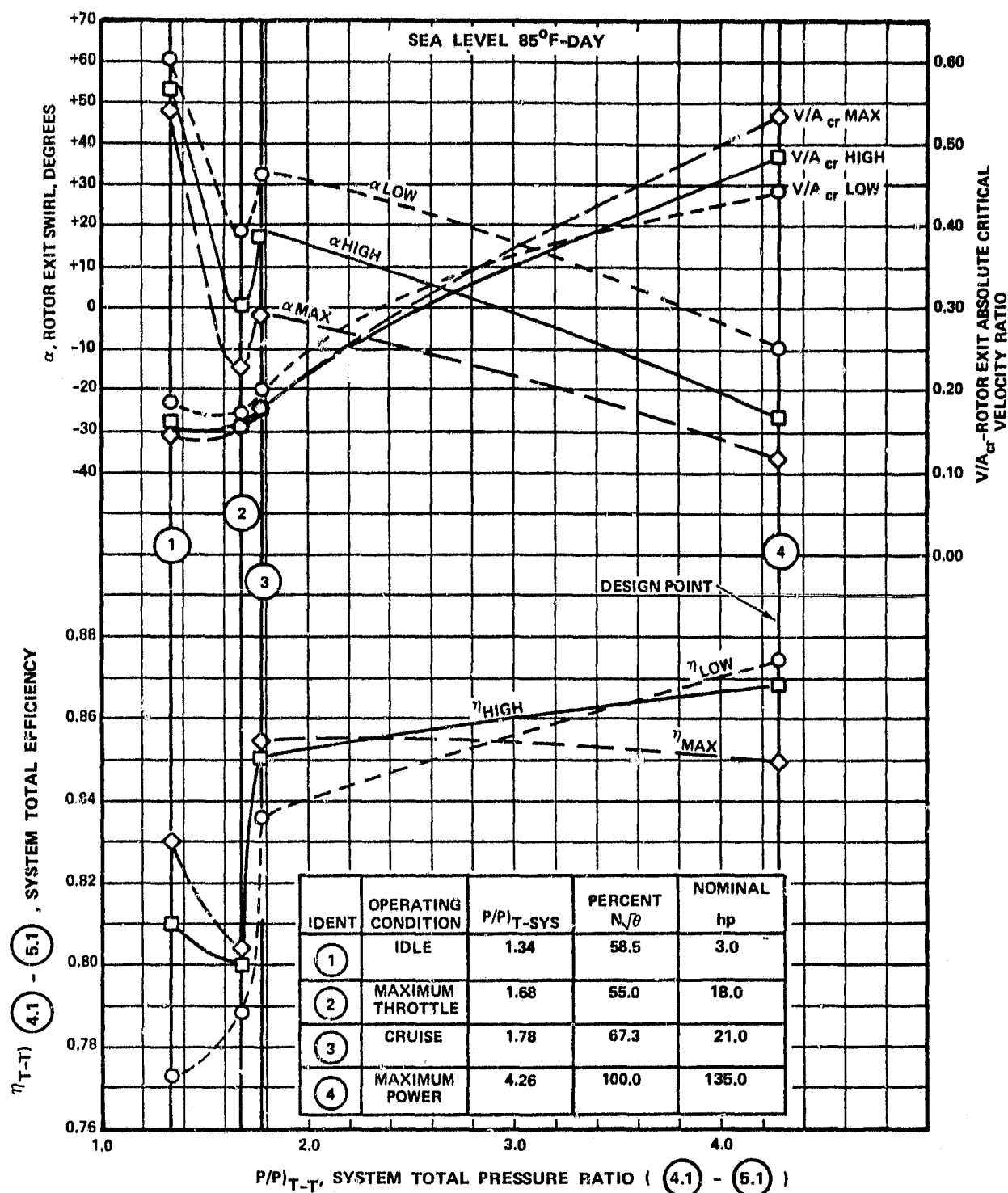
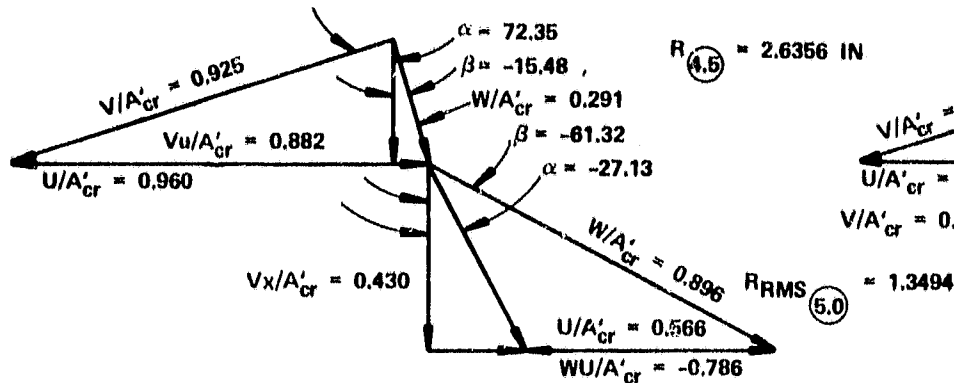


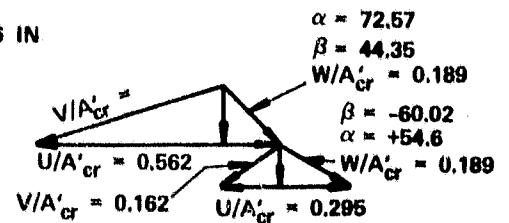
Figure 53. Off-Design Performance Characteristics as a Function of Design-Point Exit Swirl for NASA-DOE Advanced Gas Turbine Powertrain System Development Program.

(A) 1985 MAXIMUM POWER CONDITION



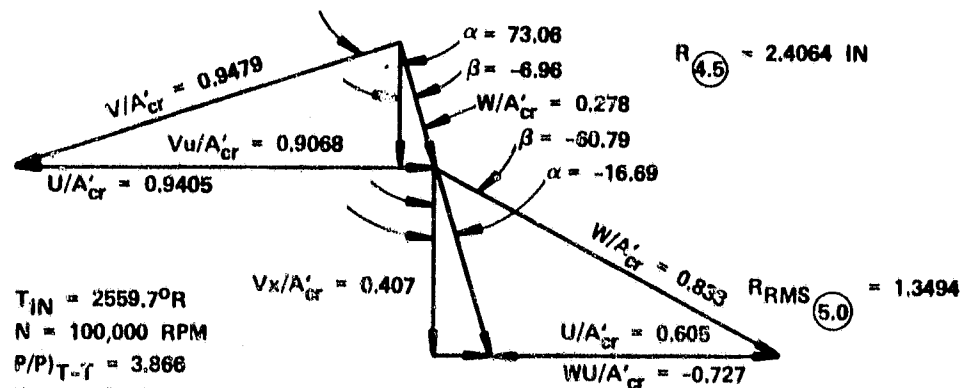
$T_{IN} = 2959.7^{\circ}R$
 $N = 100,000 \text{ RPM}$
 $P/P)_{T-SYS} = 4.25$
 $\eta_{T-SYS} = 0.868$
 $\frac{W_g \sqrt{\theta}}{\delta} = 0.421$

(B) 1985 IDLE CONDITION



$T_{IN} = 2604.0^{\circ}R$
 $N = 55,000 \text{ RPM}$
 $P/P)_{T-SYS} = 1.325$
 $\eta_{T-SYS} = 0.810$
 $\frac{W_g \sqrt{\theta}}{\delta} = 0.263$

(C) 1983 METALLIC TURBINE (MOD I COMPLETE) MAXIMUM POWER CONDITION



$T_{IN} = 2559.7^{\circ}R$
 $N = 100,000 \text{ RPM}$
 $P/P)_{T-T} = 3.866$
 $\eta_{T-T} = 0.878$
 $\frac{W_g \sqrt{\theta}}{\delta} = 0.417$

ALL ANGLES IN DEGREES

Figure 54. Turbine One-Dimensional Vector Diagrams.

TABLE 7. TURBINE DESIGN POINT CYCLE CONDITIONS
SEA LEVEL, 85°F DAY, MAXIMUM POWER

	MAY 1985 CERAMIC	MAY 1983 (MOD I) COMPLETE METALLIC
T_{IN} , TURBINE INLET TOTAL TEMPERATURE, °R	= 2959.7	2559.7
P/P_{T-T} , STAGE TOTAL-TO-TOTAL PRESSURE RATIO	= 4.000	3.866
$W_g\sqrt{\theta/\delta}$, STAGE INLET CORRECTED FLOW, LBM/SEC	= 0.421	0.417
W_g , MASS FLOW, LBM/SEC	= 0.8231	0.8325
ΔH , STAGE SPECIFIC WORK, BTU/LBM	= 216.68	180.96
$\Delta H/\theta$ STAGE CORRECTED WORK, BTU/LBM	= 37.970	36.669
P_{T-IN} , STAGE INLET TOTAL PRESSURE, PSIA	= 68.637	65.177
η_{t-t} , STAGE TOTAL-TO-TOTAL EFFICIENCY	= 0.901	0.892
N , ROTATIONAL SPEED, RPM	= 100,000	100,000
$N/\sqrt{\theta}$, CORRECTED SPEED, RPM	= 41863.3	45015.6
U_t , ROTOR INDUCER TIP SPEED, FT/SEC	= 2300.0	2100.0
$\Delta P_{T/P_{T-EXHAUST}}$ TOTAL PRESSURE LOSS FROM ROTOR EXIT-TO-REGENERATOR INLET	= 0.0607	0.0312
$\Delta P_{T/P_{T-INLET}}$ TOTAL PRESSURE LOSS FROM TURBINE DUCT INLET-TO- STATOR INLET	= 0.010	0.010
α_{EXIT} , EXIT SWIRL, DEGREE	= -27.0	-16.7

TABLE 8. 1979 TURBINE DESIGN POINT EFFICIENCY SUMMARY

	CERAMIC TURBINE $U_t = 2300$ FT/SEC, $N = 100,000$ RPM $N_b = 13$ BLADES MAXIMUM POWER		METALLIC TURBINE (MOD I) $U_t = 2100$ FT/SEC $N = 100,000$ RPM $N_b = 13$ BLADES MAXIMUM POWER	
	η_{T-T}	$\Delta\eta_{T-T}$	η_{T-T}	$\Delta\eta_{T-T}$
BASE EFFICIENCY FROM SPECIFIC SPEED CORRELATION AT $R_e = 3.0 \times 10^5$	0.948		0.946	
REYNOLDS NUMBER EFFECTS FROM $R_e = 3.0 \times 10^5$ - to - $R_e = 1.06$ AND 1.21×10^5	0.937	-1.15 PTS	0.937	-0.96 PTS
ROTOR INDUCER INCIDENCE EFFECTS	0.934	-0.30 PTS	0.932	-0.45 PTS
ROTOR SHROUD CLEARANCE EFFECTS AT 0.010 INCH CLEARANCE	0.911	-2.35 PTS	0.910	-2.21 PTS
ROTOR BACKFACE CLEARANCE EFFECTS AT 0.030 INCH CLEARANCE	0.889	-2.14 PTS	0.894	-1.59 PTS
ROTOR BLADE NUMBER EFFECTS $N_B = 13.0$	0.884	-0.60 PTS	0.888	-0.60 PTS
ROTOR BACKFACE DISK FRICTION	0.877	-0.68 PTS	0.882	-0.56 PTS
REACTION EFFECTS, (ROTOR BLADE SURFACE DIFFUSIONS)	0.877	0.0 PTS	0.882	0.0 PTS
ROTOR TRAILING EDGE BLOCKAGE EFFECTS (MIXING LOSS)	0.873	-0.40 PTS	0.878	-0.40 PTS
1979 PREDICTED TOTAL-TO-TOTAL STAGE EFFICIENCY, $\eta_{T-T_{1979}}$	0.873		0.878	
$\Delta P_T/P_T$ EXHAUST, TOTAL PRESSURE LOSS FROM ROTOR EXIT-TO-REGENERATOR INLET	0.0607		0.0312	
η_{T-SYS} , STATOR INLET TOTAL-TO-REGENERATOR INLET TOTAL	0.841		0.864	

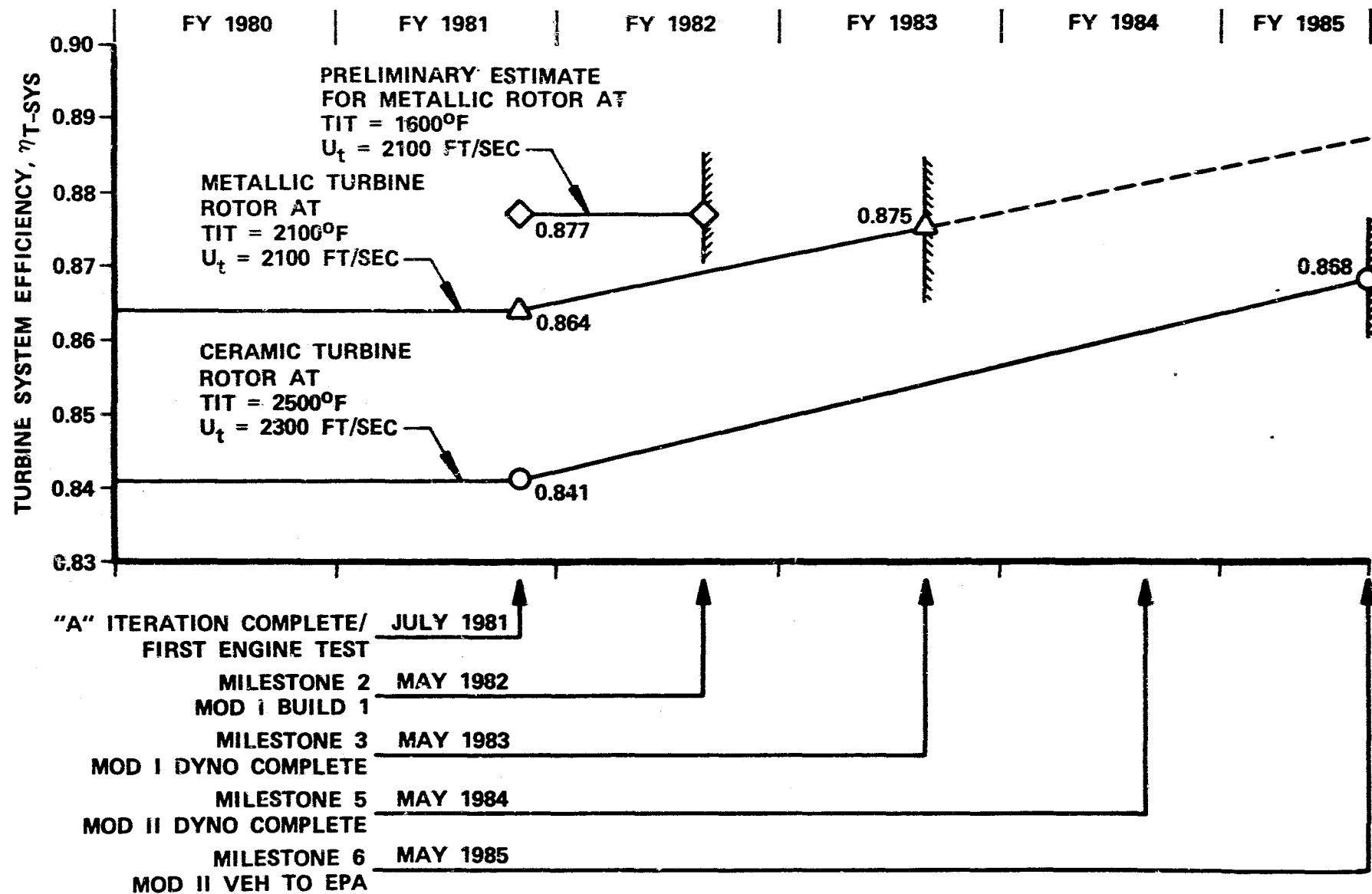
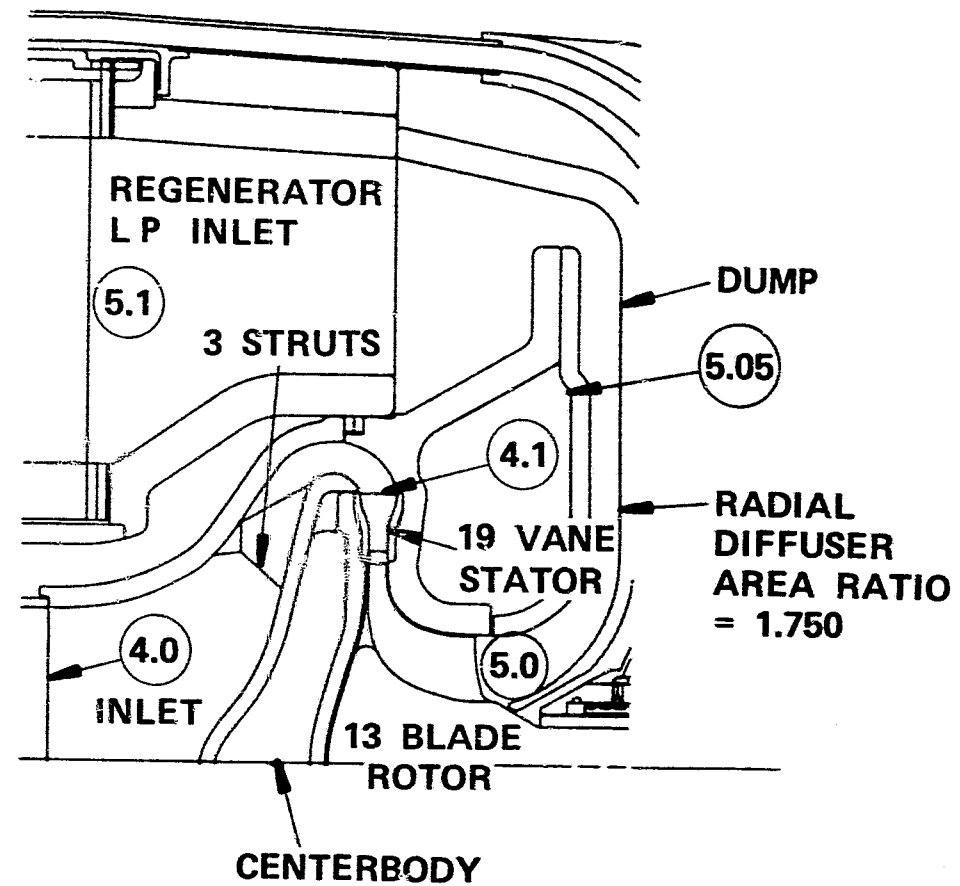


Figure 55. Ceramic and Metallic Turbine Performance Milestones.

1985 PERFORMANCE GOALS WITH PREDICTED IMPROVEMENTS

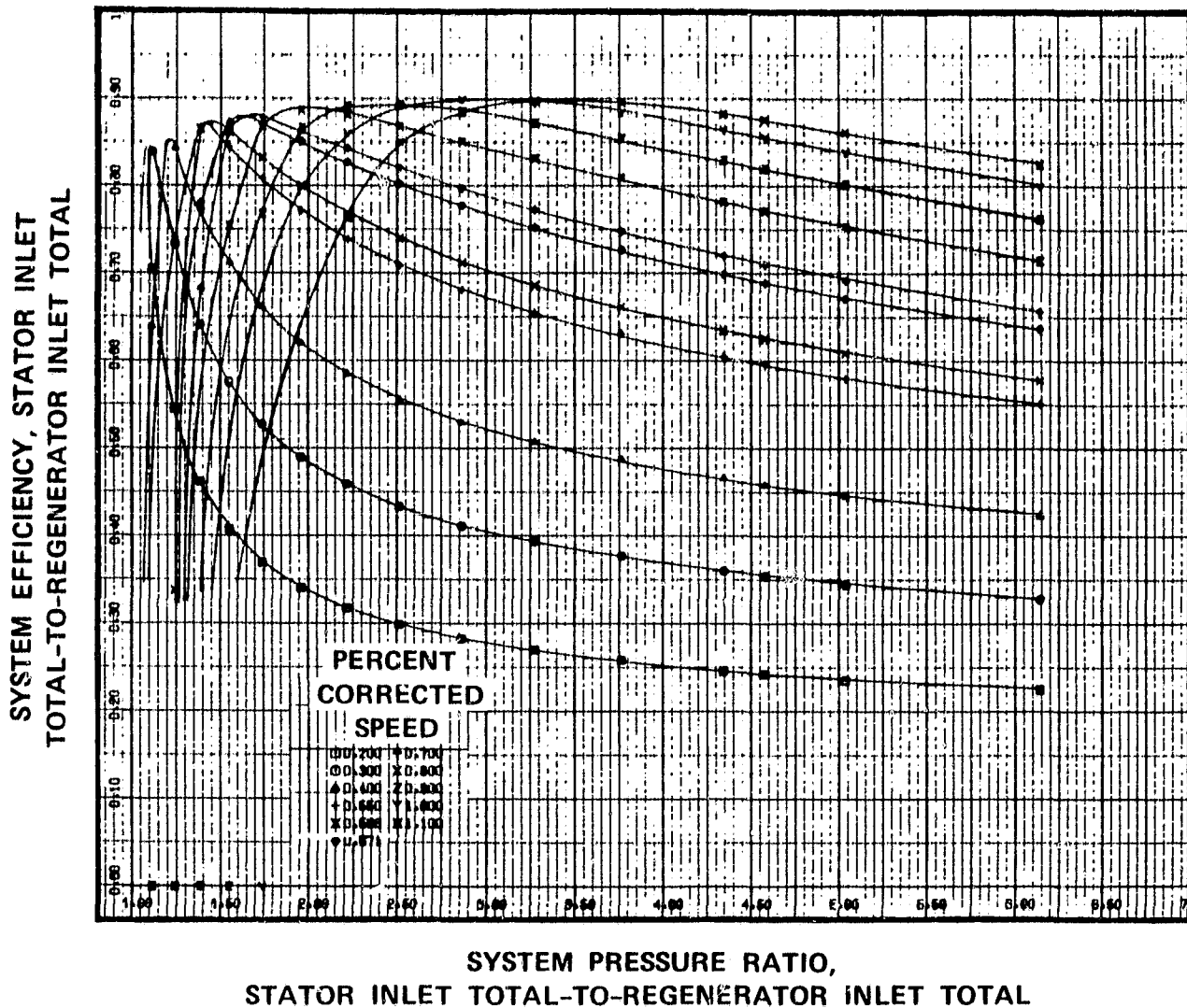
- STAGE TOTAL EFFICIENCY,
 $\eta_{T-T} = 0.901$
- SYSTEM TOTAL EFFICIENCY,
 $\eta_{T-SYS} = (4.1) - (5.1) = 0.868$



TURBINE SYSTEM CONFIGURATION

Figure 56. Turbine Design Summary.

ORIGINAL PAGE IS
OF POOR QUALITY



ORIGINAL PAGE IS
OF POOR QUALITY

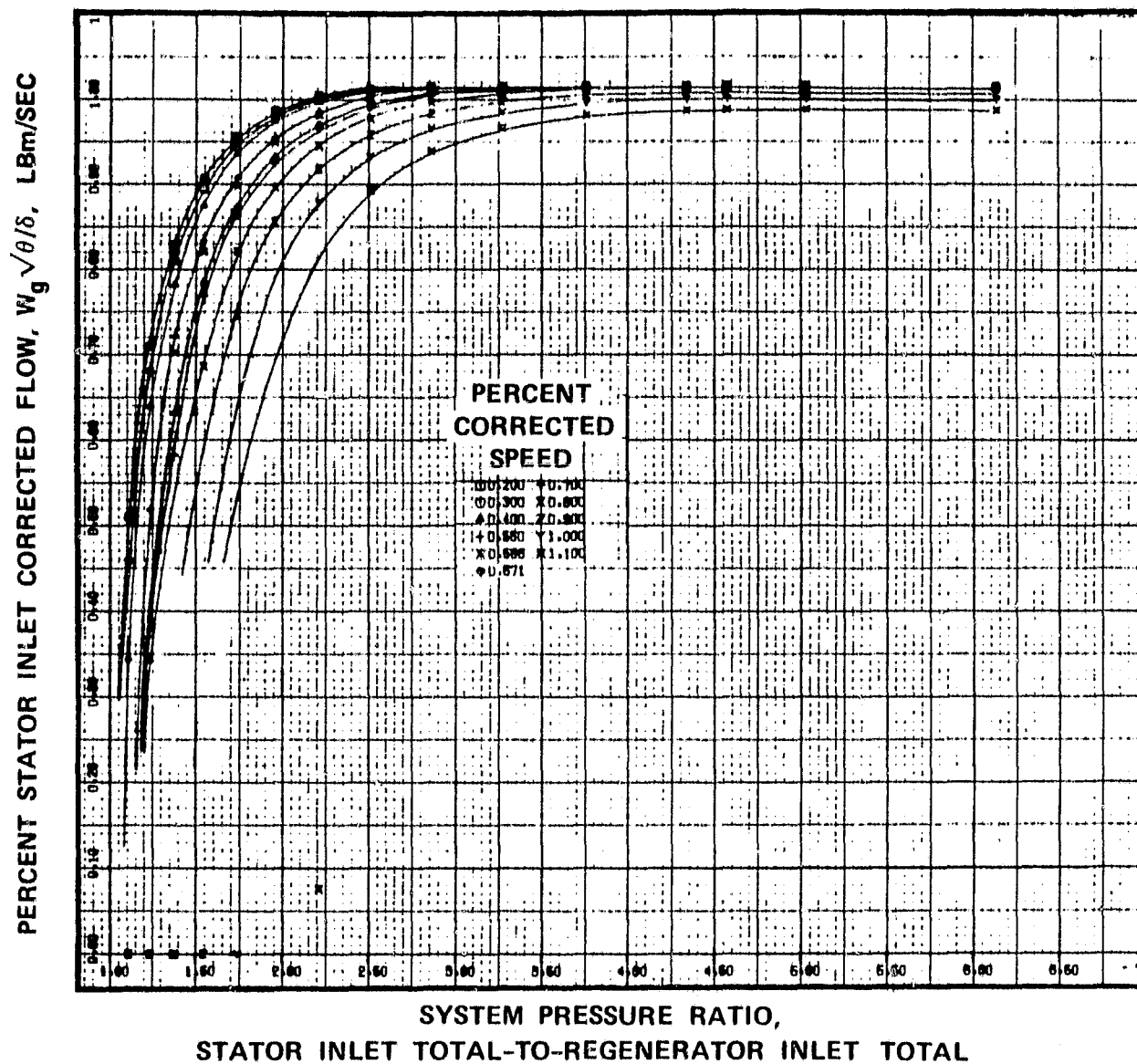


Figure 58. Ceramic Turbine Predicted Off-Design Performance (Corrected Flow Characteristics).

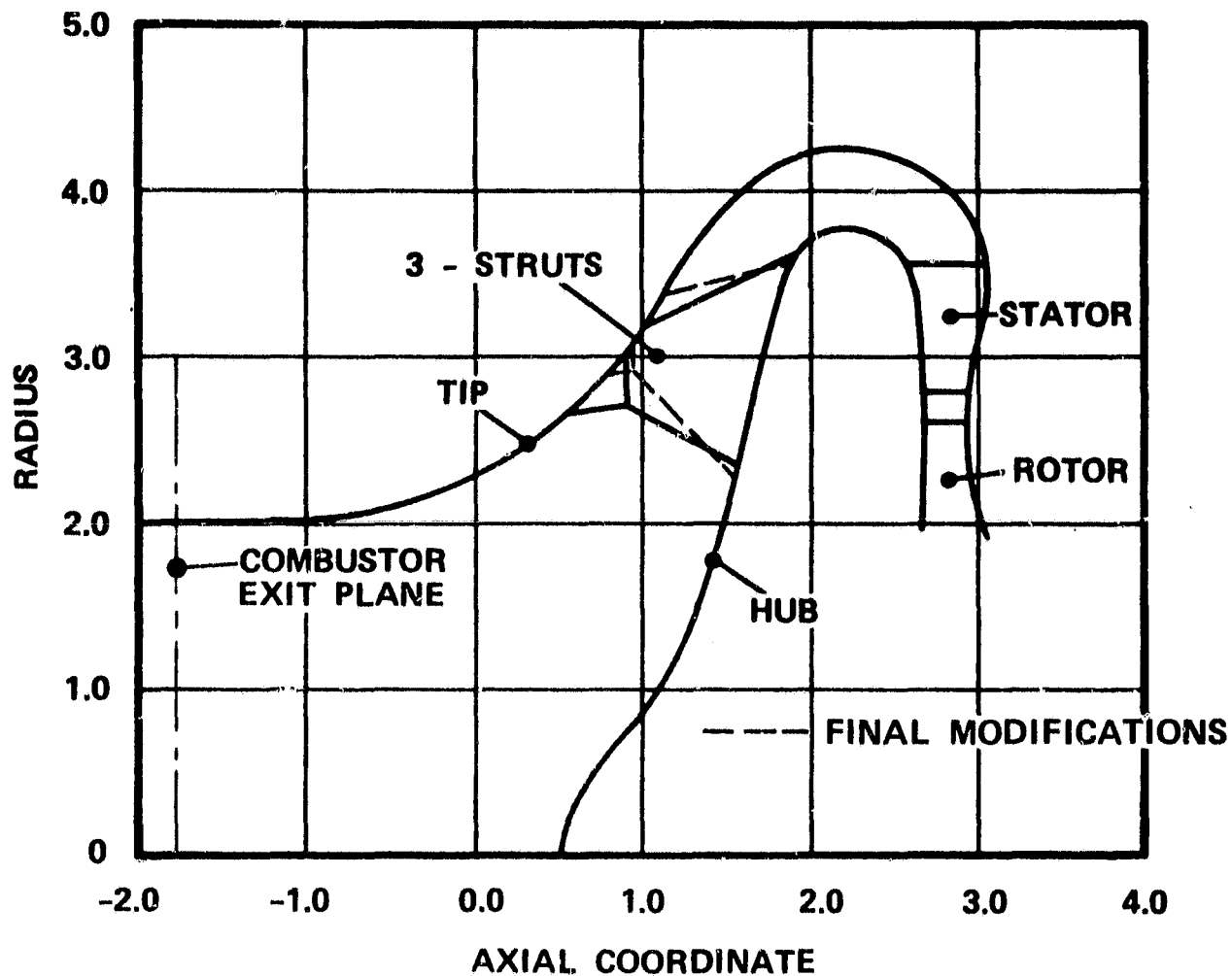


Figure 59. Baseline Turbine Inlet Duct Configuration.

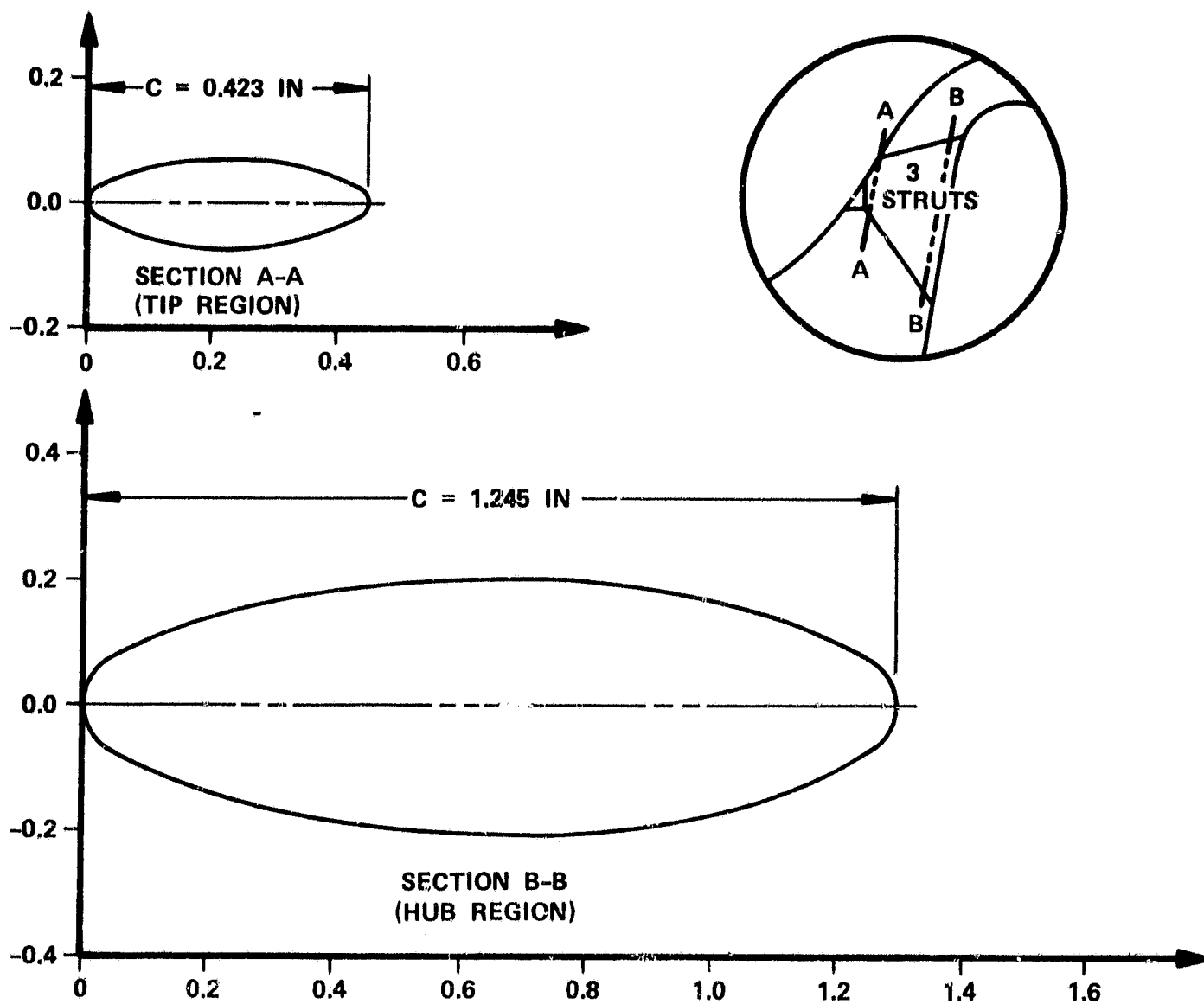


Figure 60. Turbine Inlet Strut Sections
[Modified NACA 16-201 ($t/c = 0.30$)].

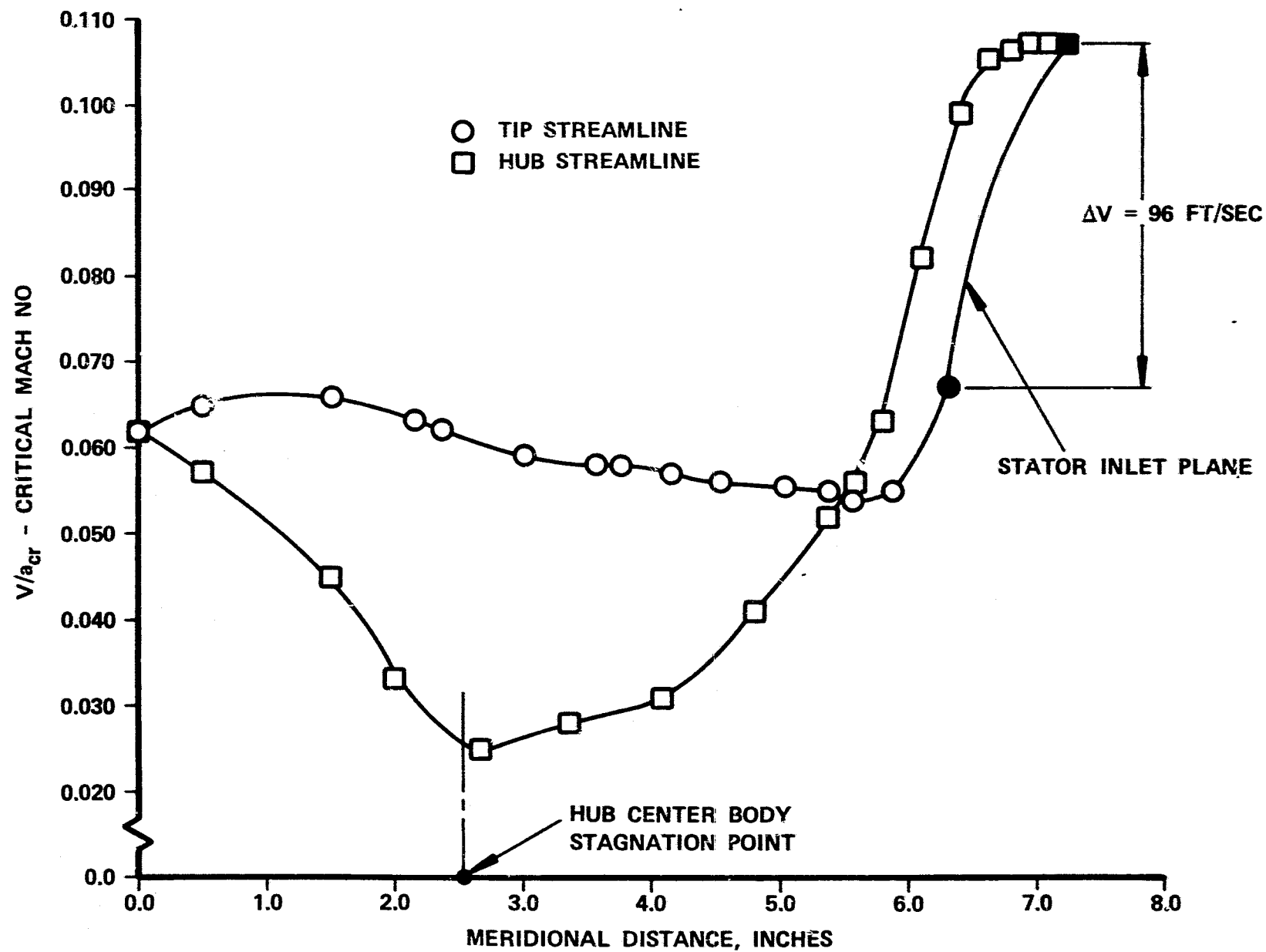


Figure 61. Turbine Inlet Duct Velocity Distribution for Baseline Configuration.

(i.e., no additional aerodynamic performance penalty is required). This profile, presented in Figure 62, is based on the selected vane number of 19. Vane suction and pressure surface velocity distribution is presented in Figure 63 with the end-wall contour established from the inlet duct optimization. The second vane profile is designed to facilitate tooling for an integral vane ring. Trailing edge thickness has been increased to 0.030 inch and the fillet to 0.050 inch. In addition, the entire pressure surface and a portion of the suction surface have been modified to straight lines. Profile modifications are shown in Figure 64. The effect of a linear pressure surface on the vane velocity distribution is presented in Figure 65.

4.2.1.3 Rotor

Figure 66 shows the meridional view of the ceramic and metallic rotor design. Since the metallic rotor blading geometry is identical to the ceramic, the metallic rotor is achieved by a simple tip cutback to reduce stresses in the rotor.

The turbine rotor blade angle distribution for the hub, mean, and shroud streamlines are shown in Figure 67. Calculated radial rotor loss distribution as a function of blade height is shown in Figure 68. These calculations are consistent with past design and AiResearch Phoenix empirical experience wherein rotor exit survey data shows that the radial loss characteristics for radial turbines are similar. That is, in the hub region the losses are low (due to lower loading) and progressively increase to about 80-percent blade height, and then are fairly uniform to the tip. Velocity distributions for the rotor are shown in Figure 69. The velocity distribution for the ceramic and metallic rotors are similar at shroud, mean, and hub streamlines except in the inducer area where the higher inducer loading of the metallic rotor is evident.

4.2.1.4 Exhaust Diffuser

For the exhaust diffuser, additional calculation stations were added to the rotor flow solution, since the velocity distribution into the exhaust diffuser is strongly dependent on the rotor exit radial swirl and associated loss distribution, both uniform and non-uniform inlet conditions are being evaluated. The current configuration is shown in Figure 70 for an area ratio of 1.75.

4.2.2 Ceramic Turbine Rotor Mechanical Analyses

The 13-bladed ceramic radial turbine rotor stress and thermal analyses are complete. Evaluation of the rotor included steady-state, normal start, normal shutdown, worst-case start and worst-case shutdown using finite element three-dimensional analysis techniques (Figure 71). The rotor also was analyzed for cumulative probability of success (CPS), using Weibull analysis, accounting for fast fracture

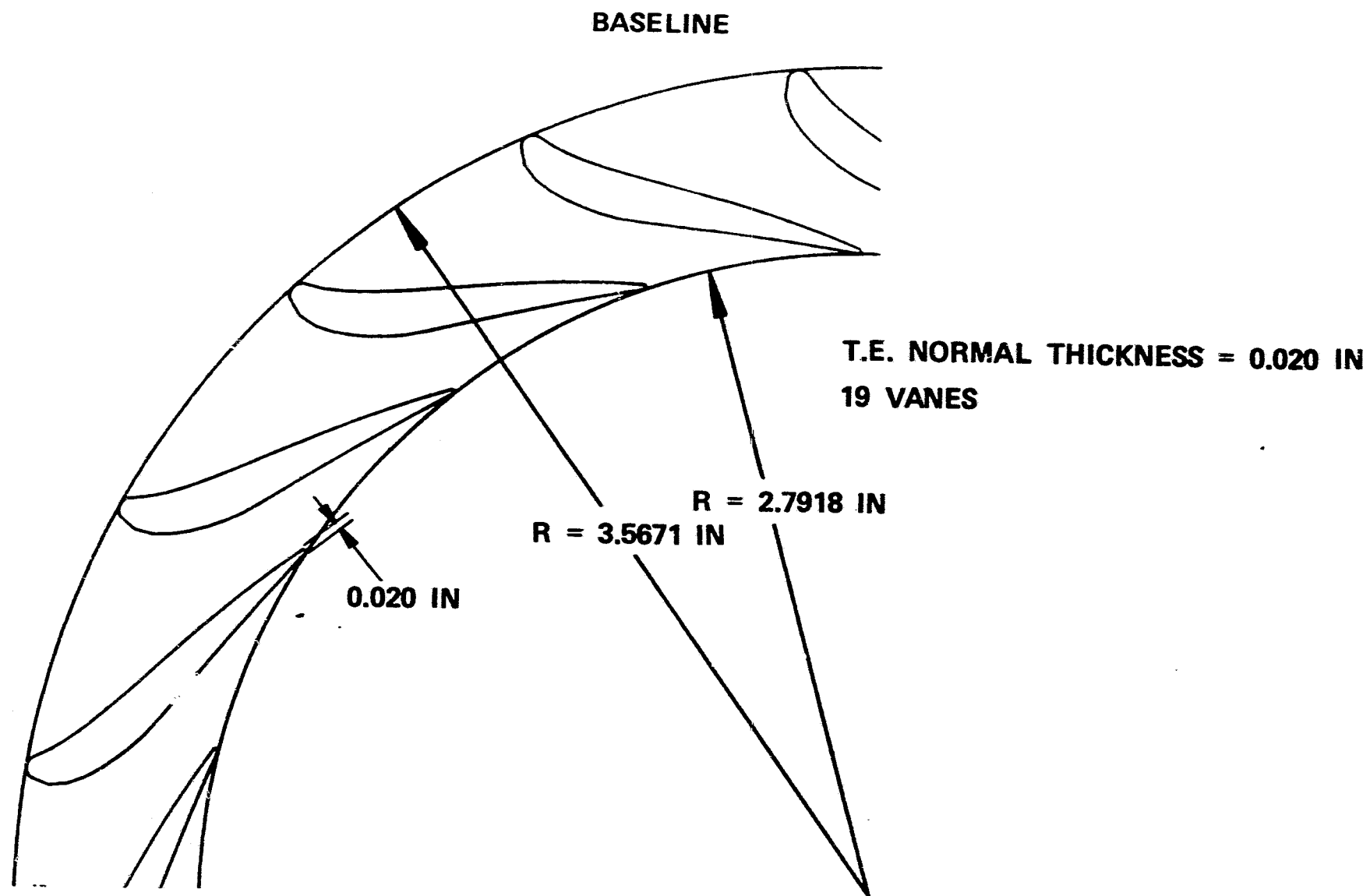


Figure 62. Ceramic Turbine Stator Profile Design.

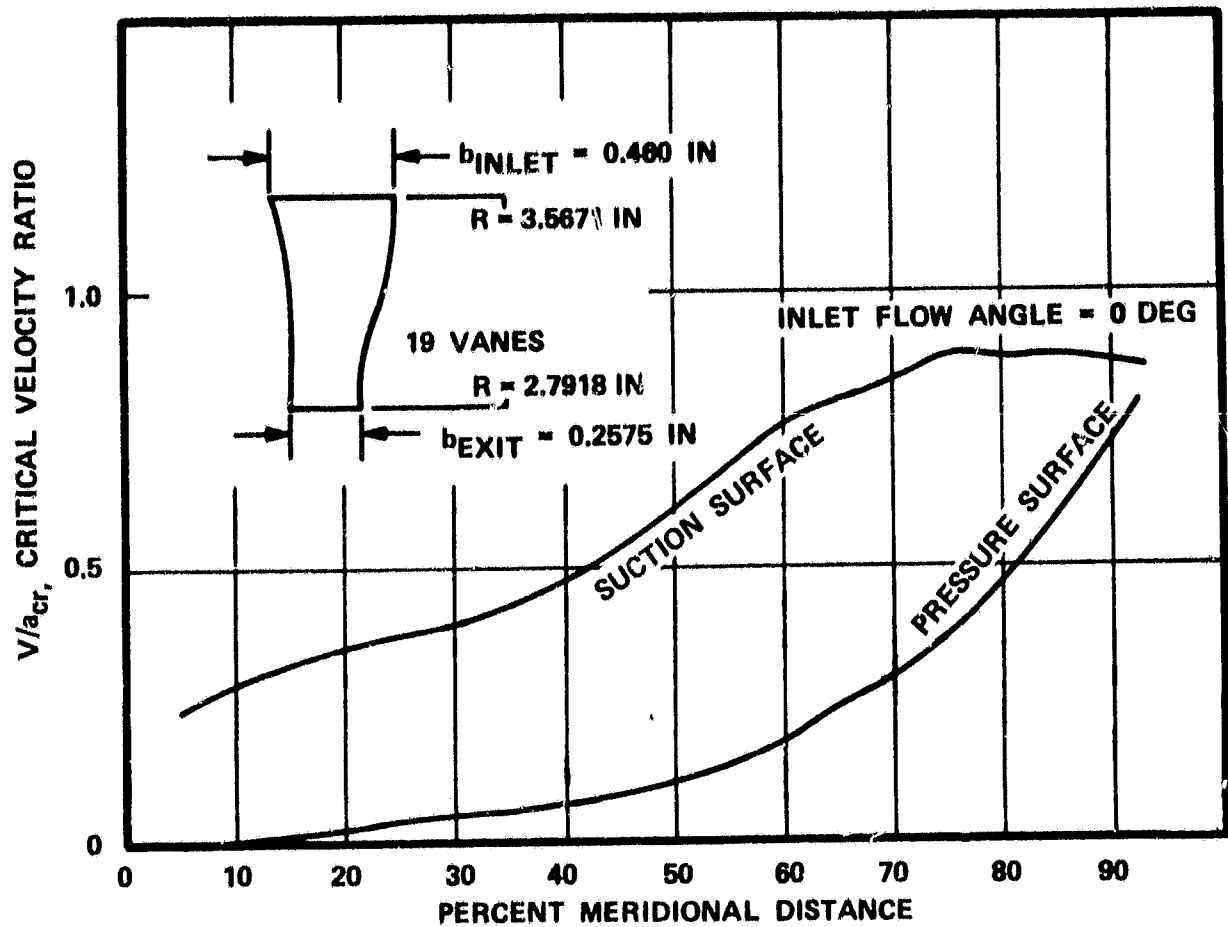


Figure 63. Ceramic Turbine Stator Velocity Distribution
Baseline 19 Vanes.

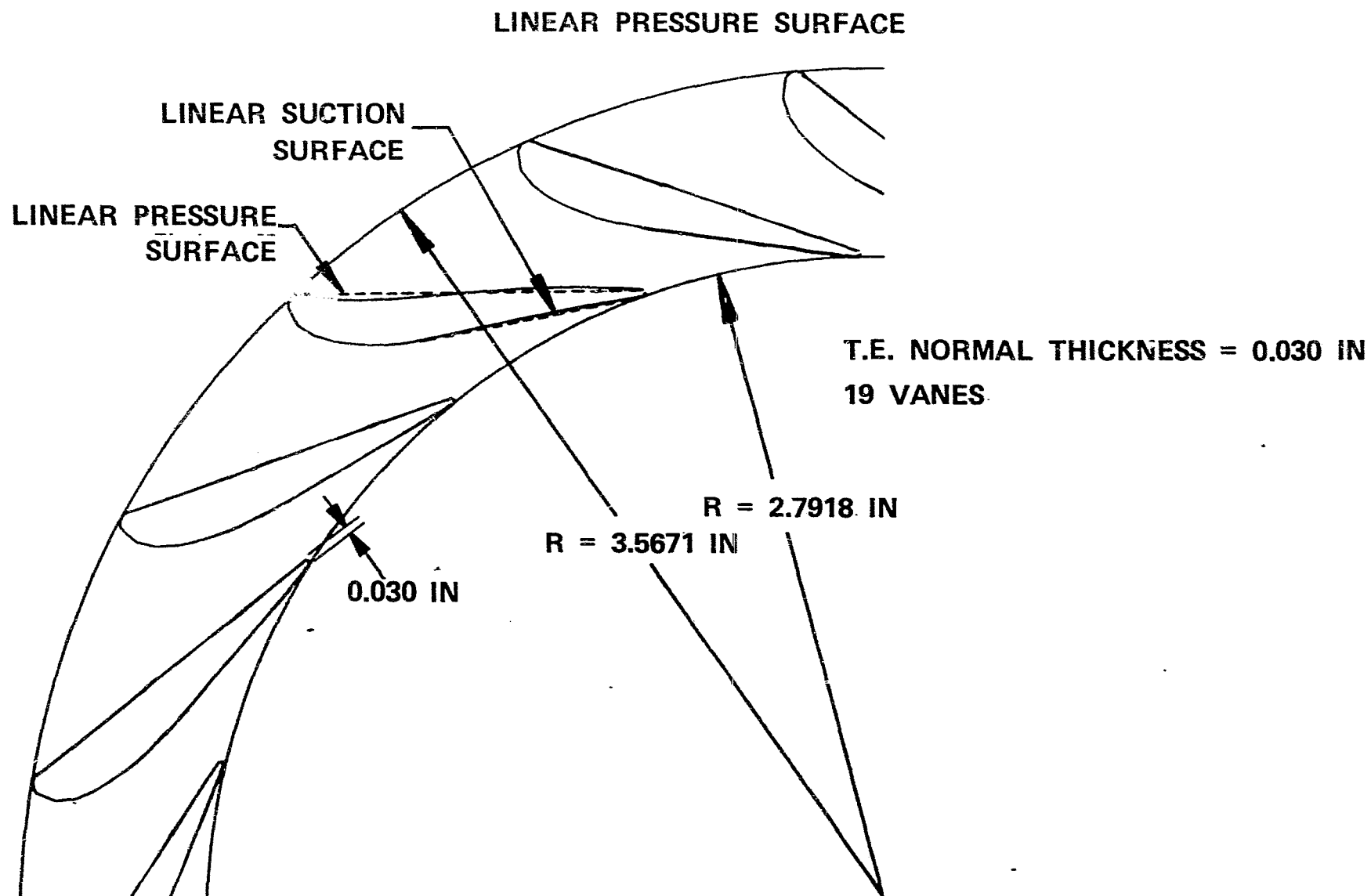


Figure 64. Ceramic Turbine Stator Profile Design.

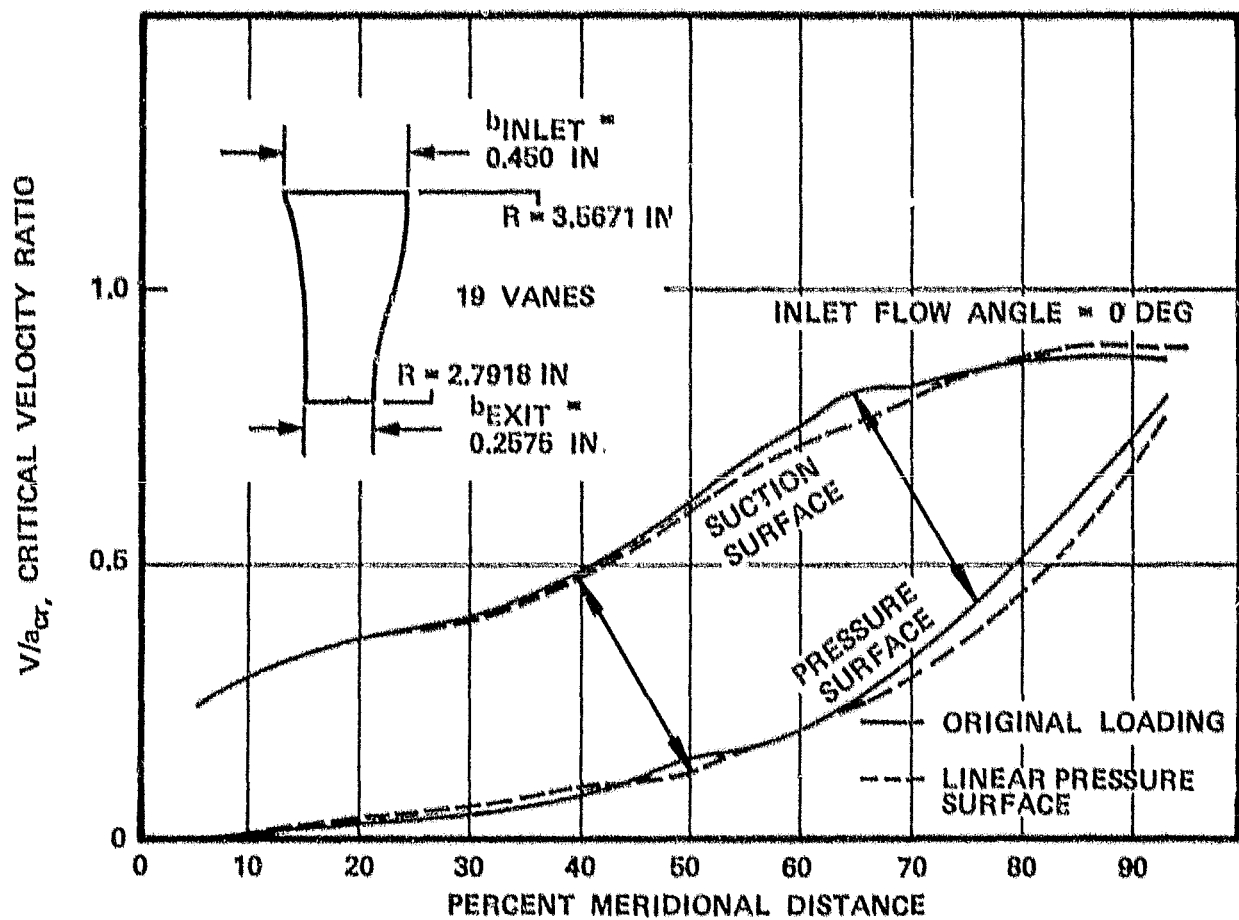


Figure 65. Ceramic Turbine Stator Velocity Distribution Linear Pressure Surface 19 Vanes.

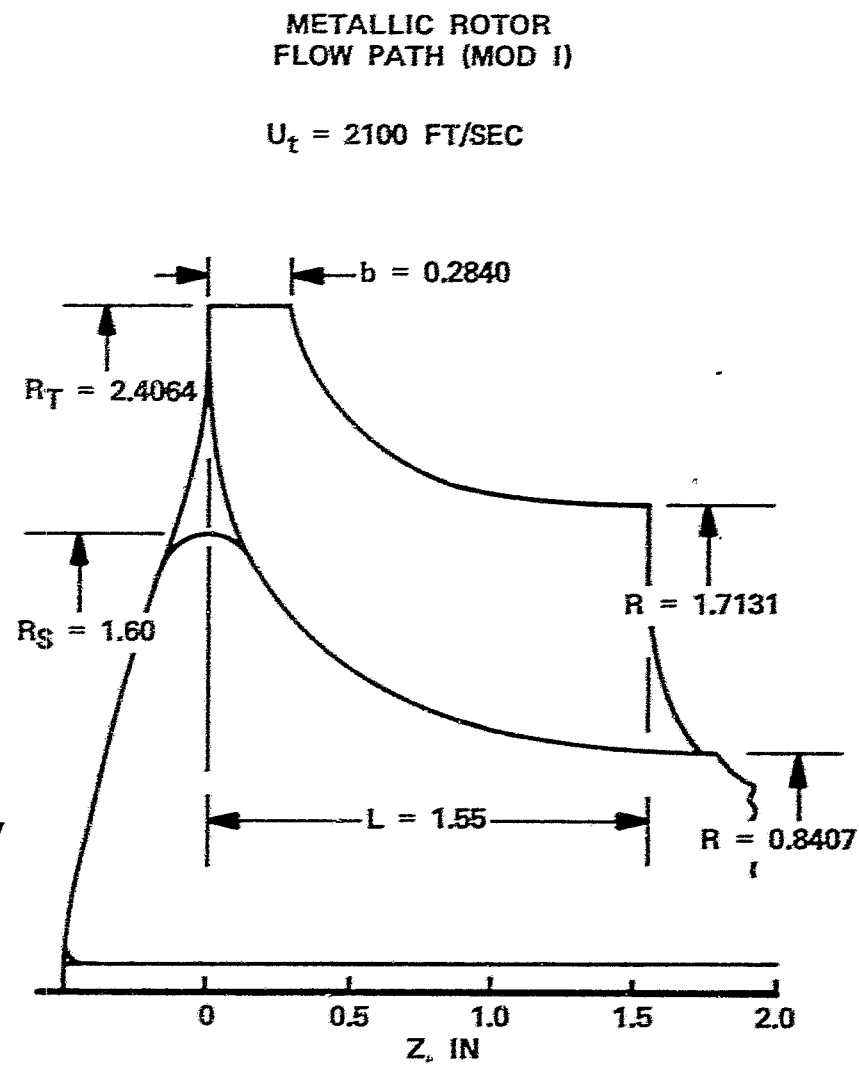
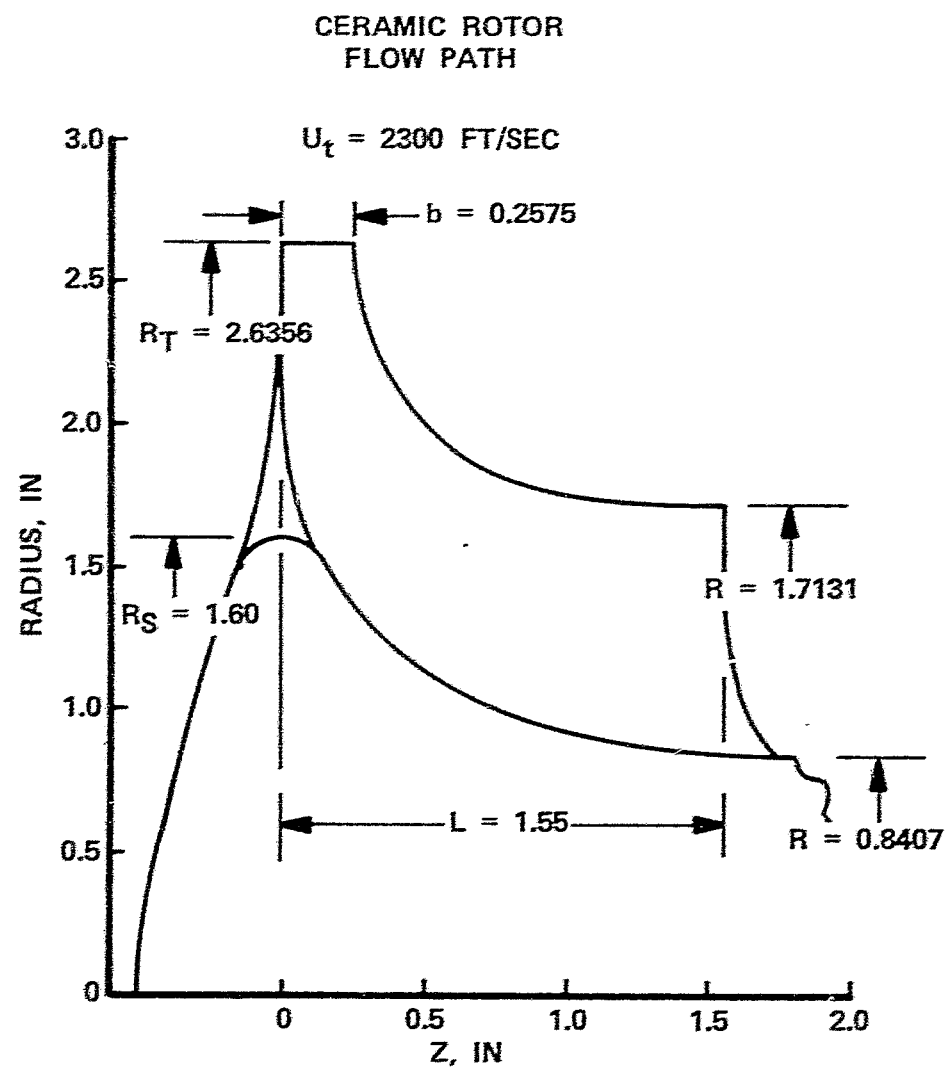


Figure 66. Ceramic and Metal Turbine Flow Paths.

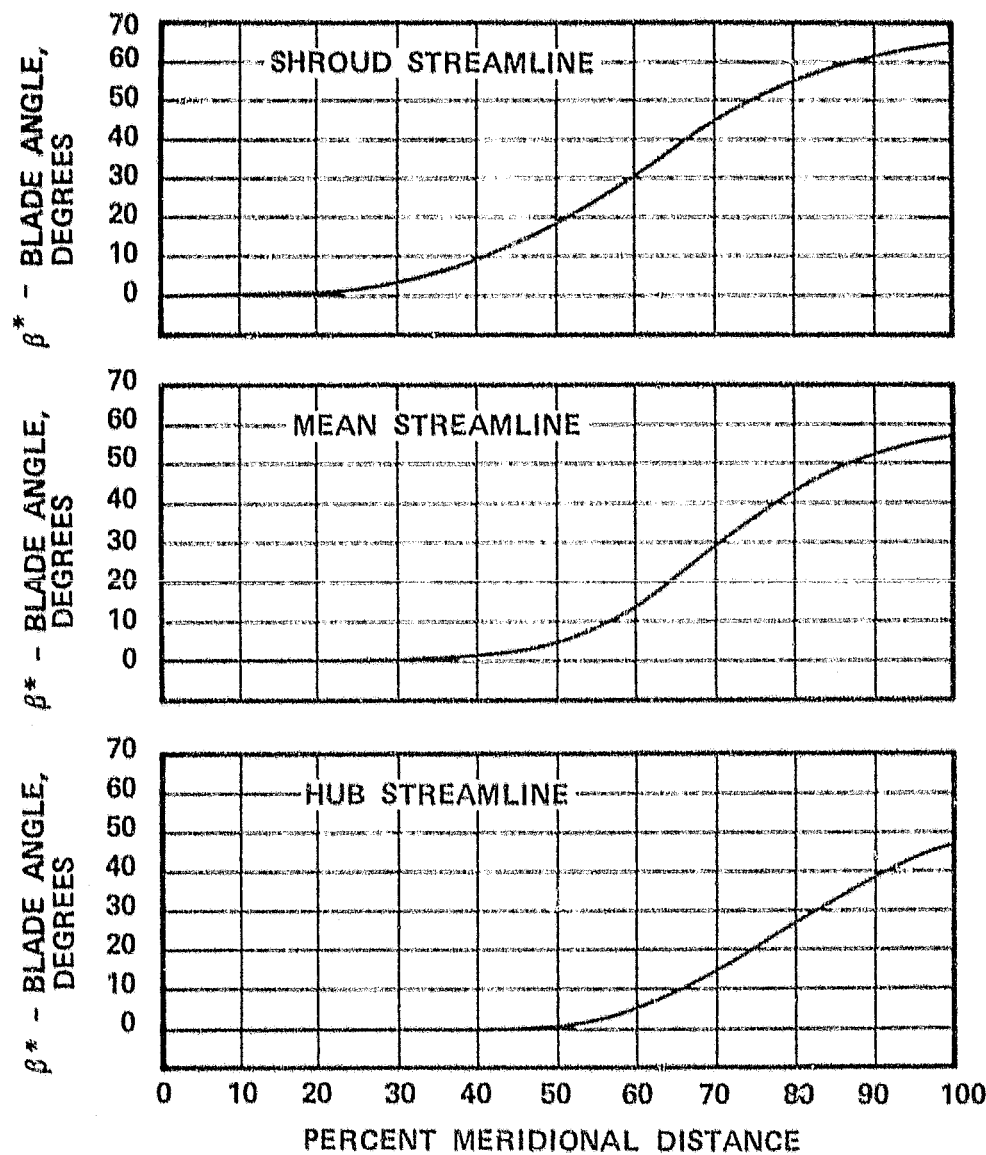


Figure 67. Turbine Rotor Blade Angle Distribution.

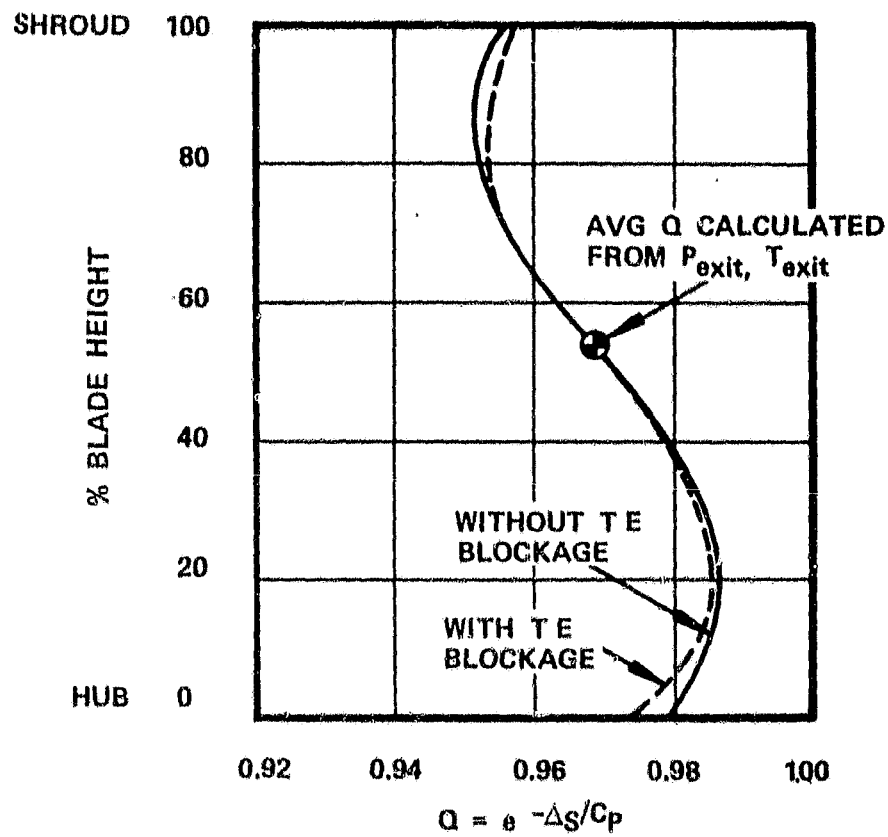


Figure 68. AGT101 Rotor Radial Loss Distribution.

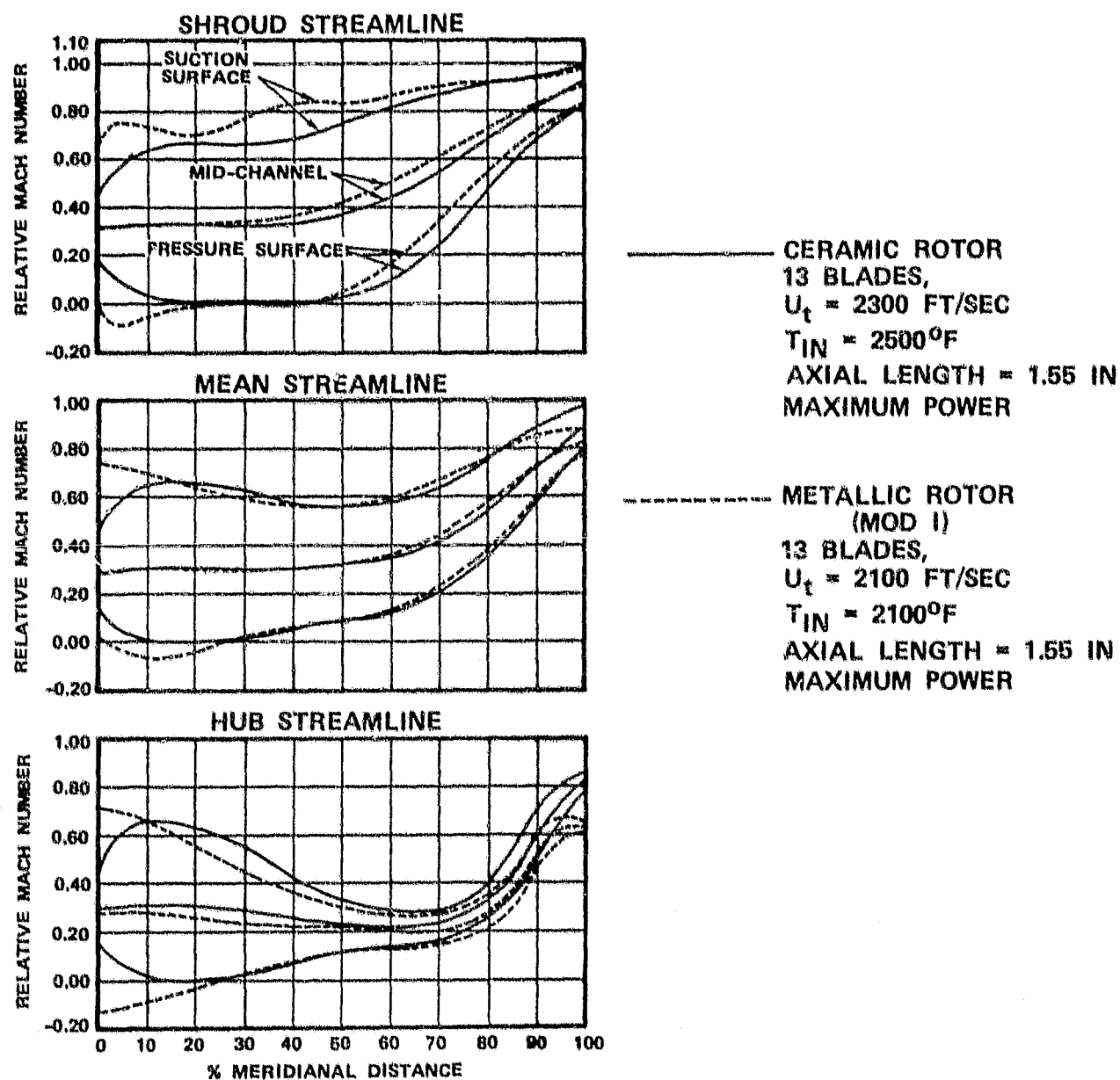


Figure 69. Turbine Rotor Velocity Distribution.

MAXIMUM POWER CONDITION

$$(A_e/A_i = 1.75, L/\Delta R = 5.31)$$

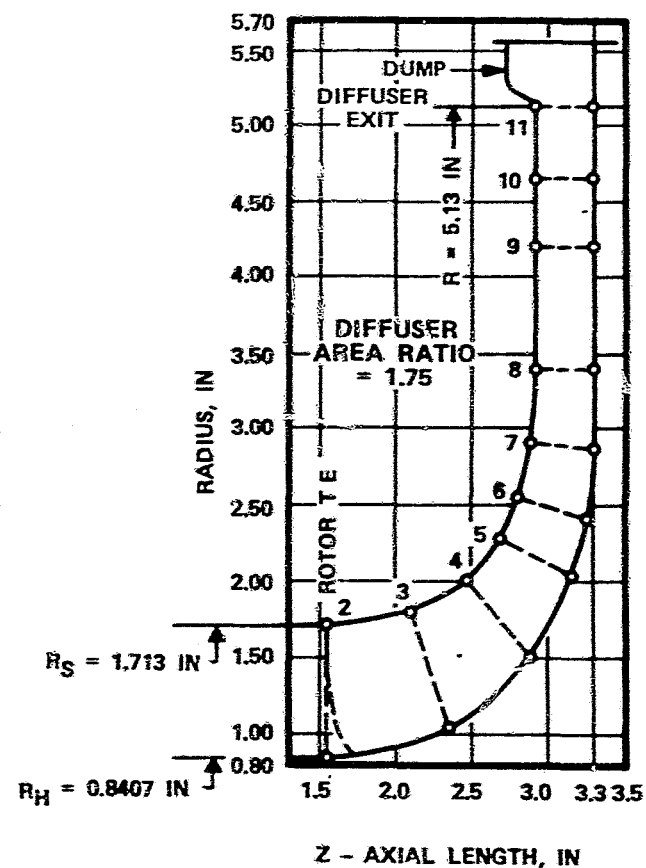
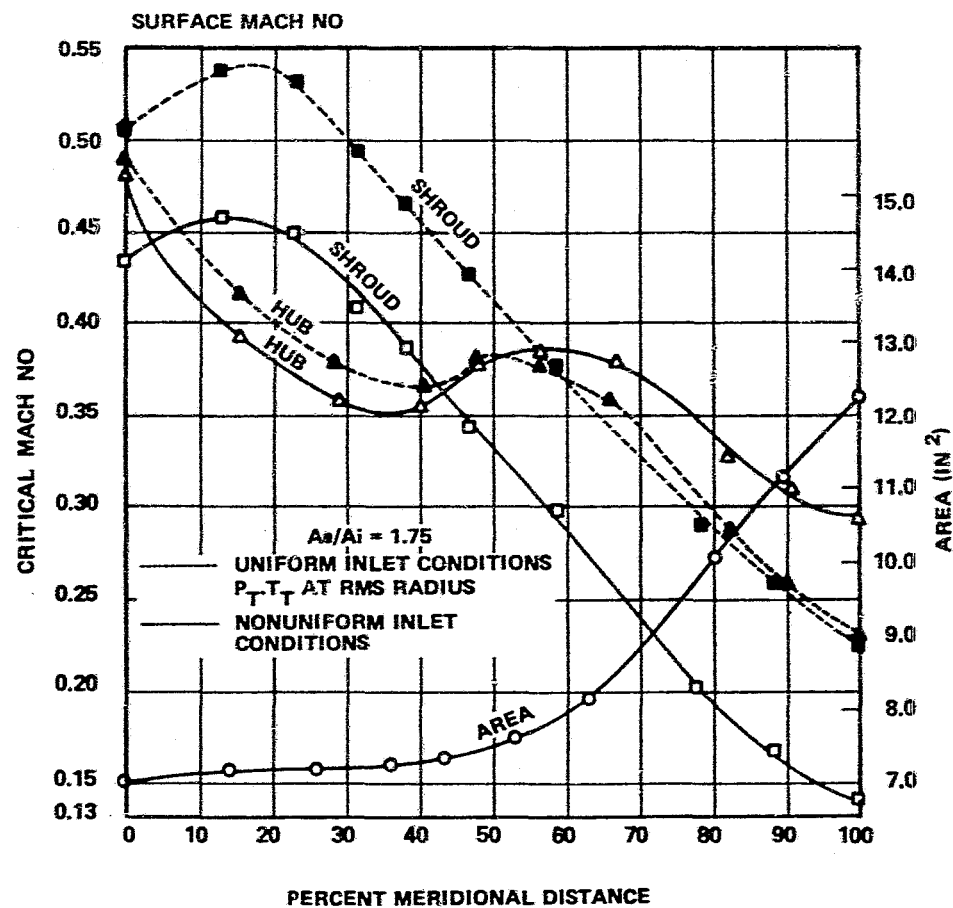


Figure 70. Exhaust Diffuser Velocity Distribution.

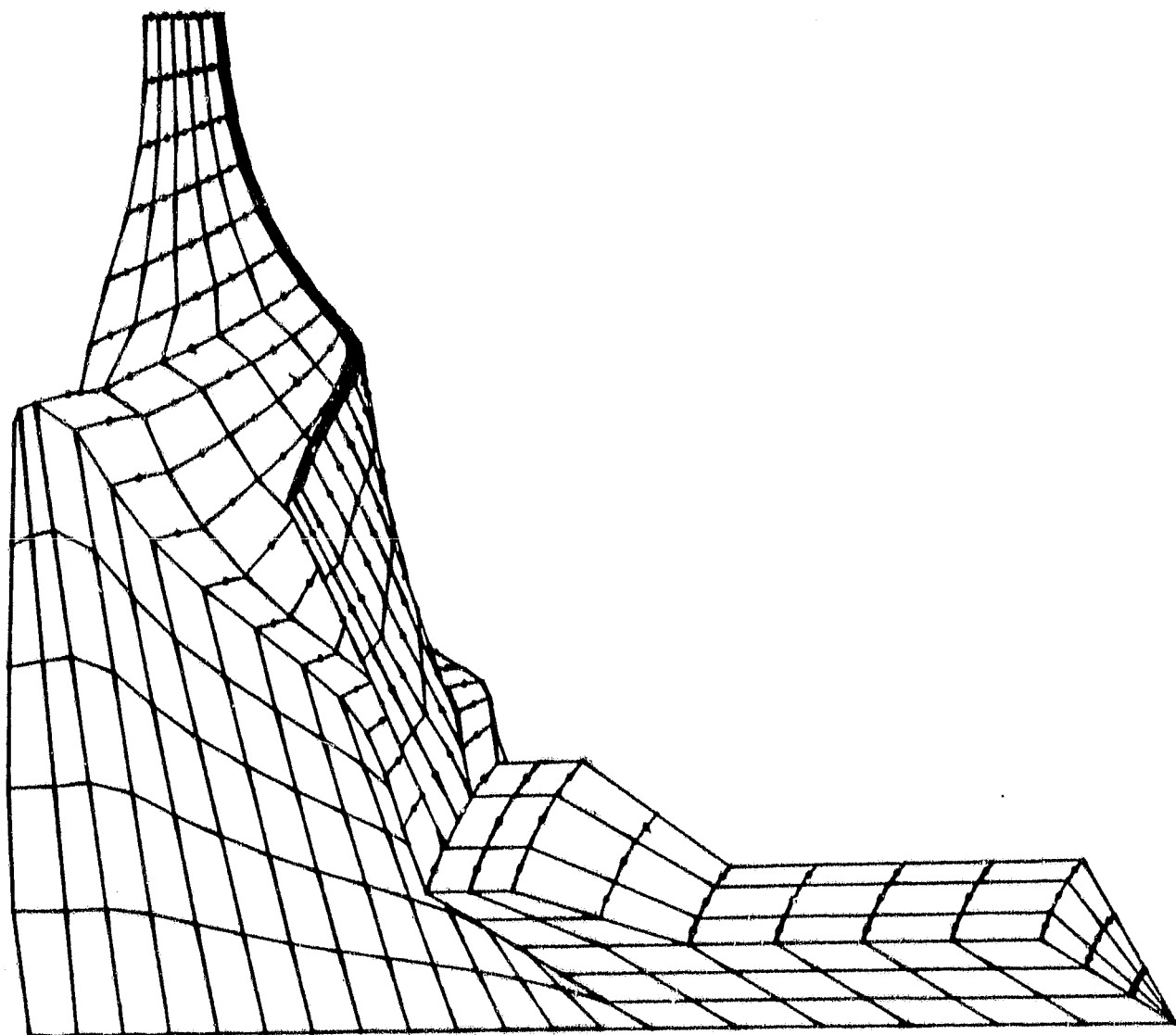


Figure 71. AGT101 Ceramic Turbine Rotor Thermal and Stress Model.

mode of failure. Two candidate materials are being considered for the turbine rotor, silicon carbide (SiC) and silicon nitride (Si₃N₄). Since these materials are not fully developed, only projected strength property values were used as depicted in Figure 72 and Table 9. In addition, turbine blade vibration characteristics were evaluated.

The following paragraphs discuss transient operating characteristics, analytical model and results or analyses.

4.2.2.1 Operating Conditions

The analyses were conducted for engine operating conditions outlined below:

- o Maximum power - steady-state
 - o Turbine Inlet Temperature (TIT) = 2500°F
 - o Engine Speed = 100,000 rpm
 - o Engine Mass Flow = 0.885 lbm/sec
 - o Engine Pressure Ratio = 5:1
- o Idle - steady-state
 - o TIT = 2144°F
 - o Engine Speed = 55,000 rpm
 - o Engine Mass Flow = 0.1581 lbm/sec
 - o Engine Pressure Ratio = 1.325:1
- o Worst Case Start-Up Transient (Figure 73)
 - o Cold Start to Maximum Power
 - o TIT from ambient to 2500°F in 4 seconds as speed increases to 75,000 rpm in 10 seconds
 - o Following delay of 150 seconds, engine speed increased to 100,000 rpm
- o Worst-case Roll Down Transient (Figure 74)
 - o Flame out at maximum power
 - o TIT reduced from 2500 to 1800°F immediately, and continuously reduced to 600°F after 40 seconds

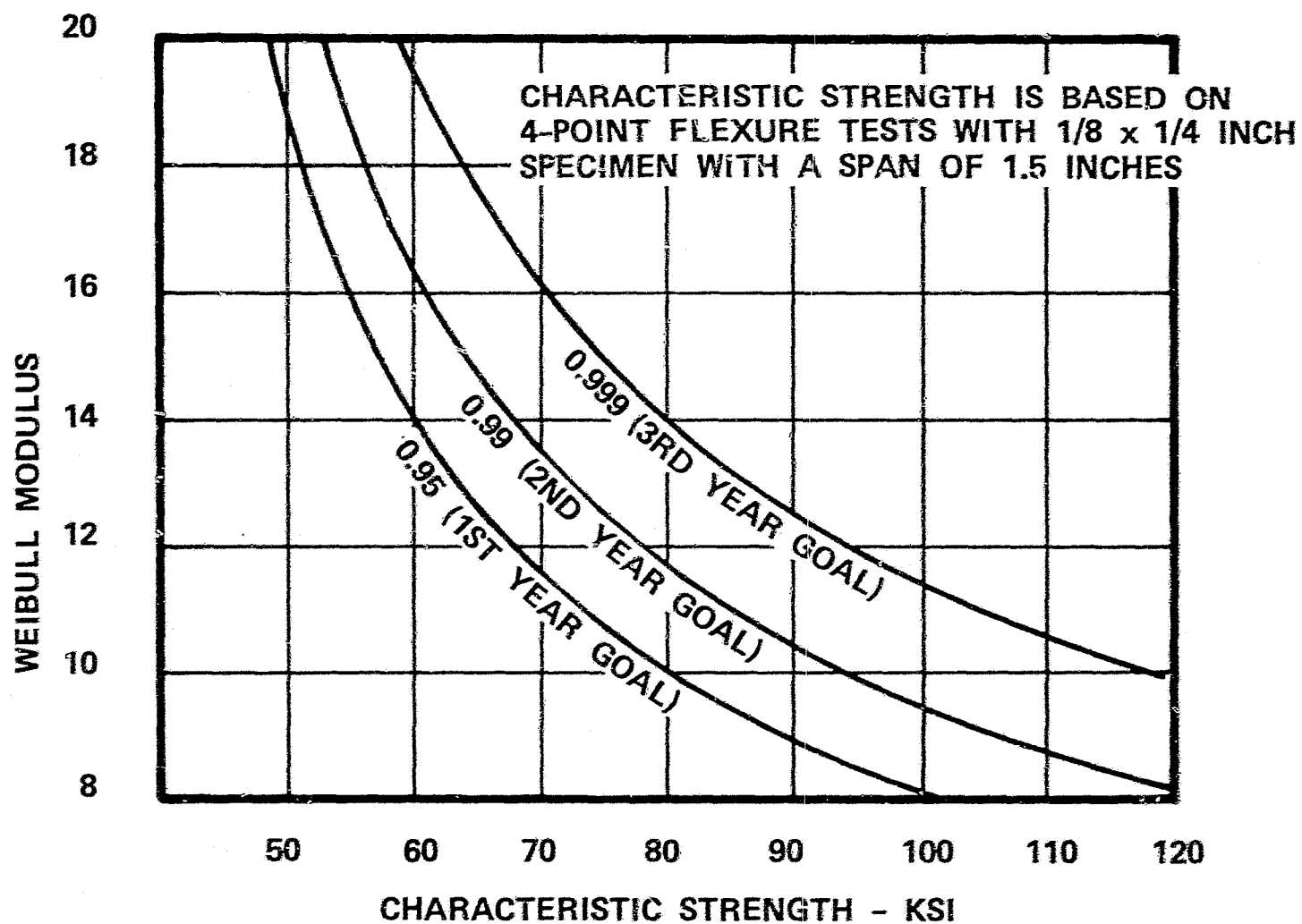


Figure 72. Objectives for AGT101 Turbine Rotor Material.

TABLE 9. CERAMIC TURBINE WHEEL PROPERTIES

	Sintered Silicon Nitride	Sintered Silicon Carbide
Inlet Temperature, (°F)	2500	2500
Number of Blades	13	13
Density, (lb/in ³)	0.118	0.114
Modulus, (lb/in ²)	45×10^6	59×10^6
Poisson's Ratio	0.22	0.14
Weight (lb)	1.36	1.32
I_p (lb-in-sec ²)	0.0033	0.0033

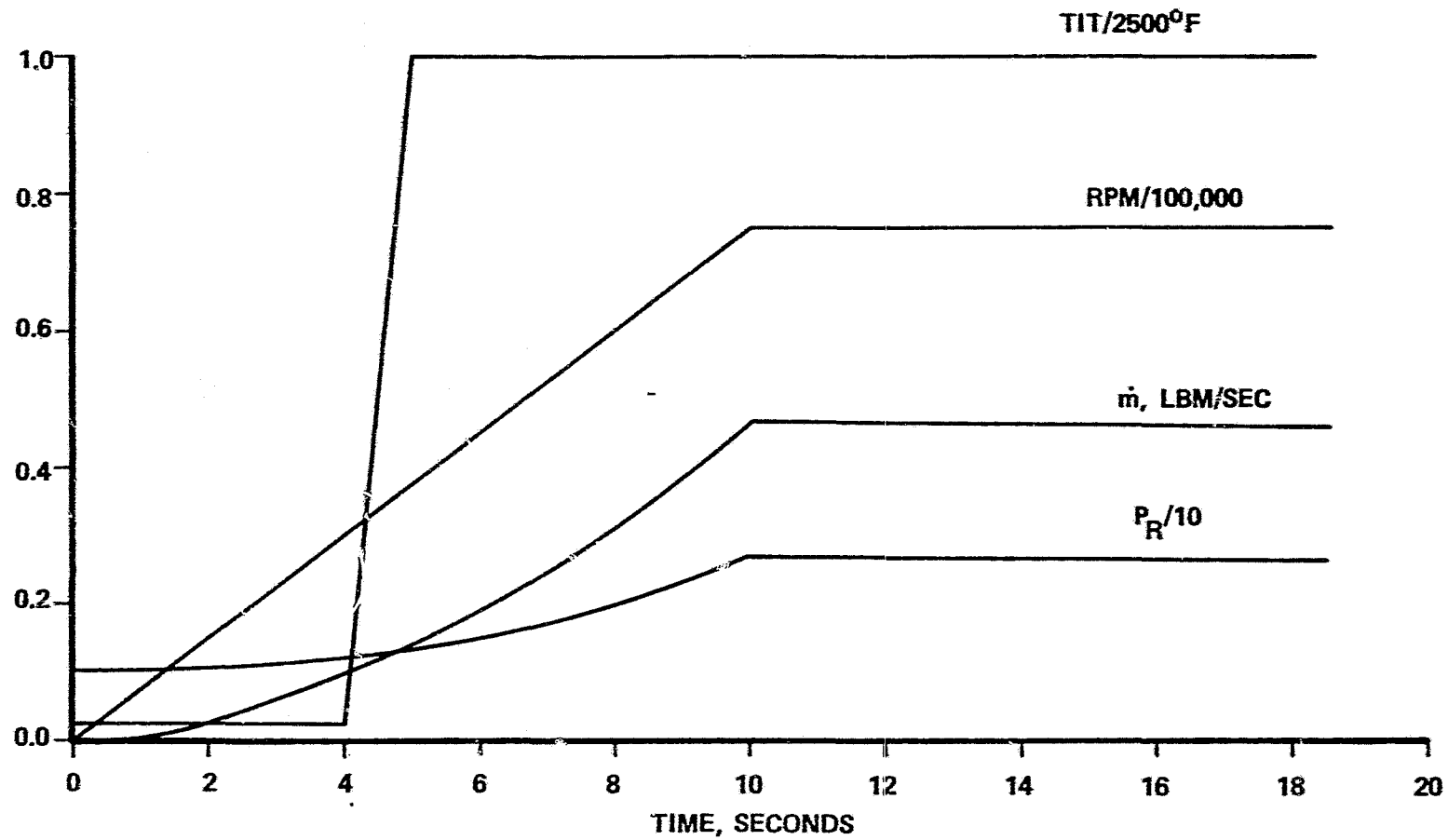


Figure 73. Worst Cast Start Up Transient AGT101 Ceramic Turbine.

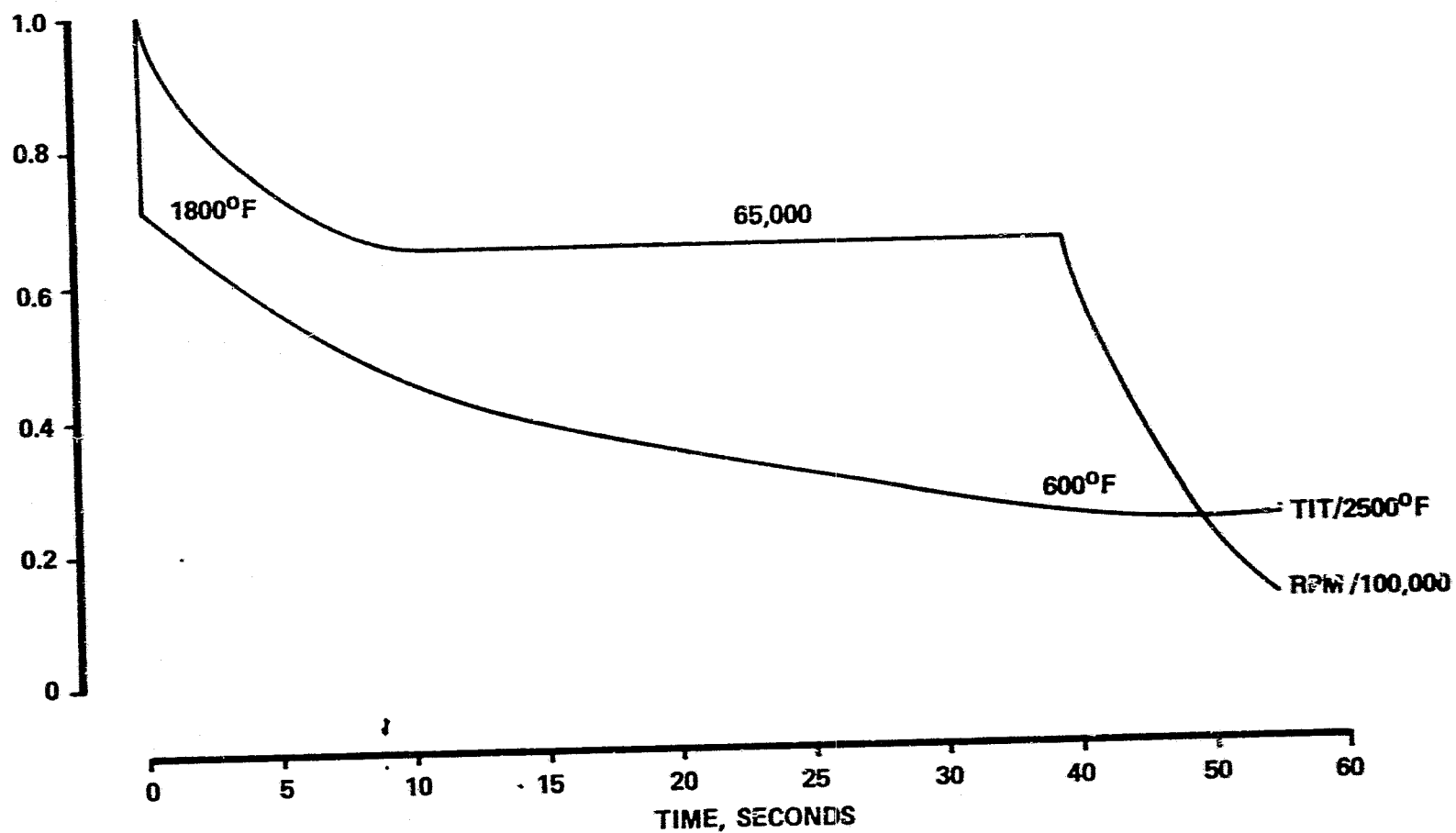


Figure 74. Worst Case Roll Down Transient AGT101 Ceramic Turbine Wheel.

ORIGINAL PAGE IS
OF POOR QUALITY

- o Engine speed decreased to 65,000 rpm in 10 seconds, held for 30 seconds, then reduced to zero
- o Normal Start (Figure 75)
 - o Cold start to idle conditions
 - o Start engine, ignite pilot, raising TIT to 1500°F increasing to 2225°F in 5 seconds
 - o Engine speed increased to 65,000 rpm within 10 seconds.
- o Normal Shutdown (Figure 76)
 - o Idle conditions to rest
 - o TIT reduced from 2160 to 1960°F immediately, gradually reduced to 700°F in 25 seconds
 - o Engine speed reduced from 60,000 rpm to 55,000 rpm immediately, held for 19 seconds, rolldown to zero within 25 seconds from initiation of shutdown

4.2.2.2 Analytical Modeling

Three-dimensional finite element models were constructed for the thermal and stress analyses. Fast fracture was considered as the primary mode of failure, although other failure modes could be present.

Thermal boundary conditions were determined based on two-dimensional boundary layer analysis, using prescribed velocity distributions, along seven pressure and suction surface streamlines. Transient boundary conditions were calculated as functions of transient turbine speed, TIT, mass flow rate, and pressure ratio.

Rotor backface and shaft thermal boundary conditions were imposed based on available empirical correlations. These later conditions have only a second order effect on computed cumulative probability of success (CPS).

For shutdown transients, analyses were carried to a time at which engine rpm reached zero. Thermal conditions subsequent to this time are not included in the current analysis. Work continues in this area.

4.2.2.3 Cumulative Probability of Success (CPS)

CPS values were calculated based on the computed multi-axial stress field utilizing material predicted characteristic strength and

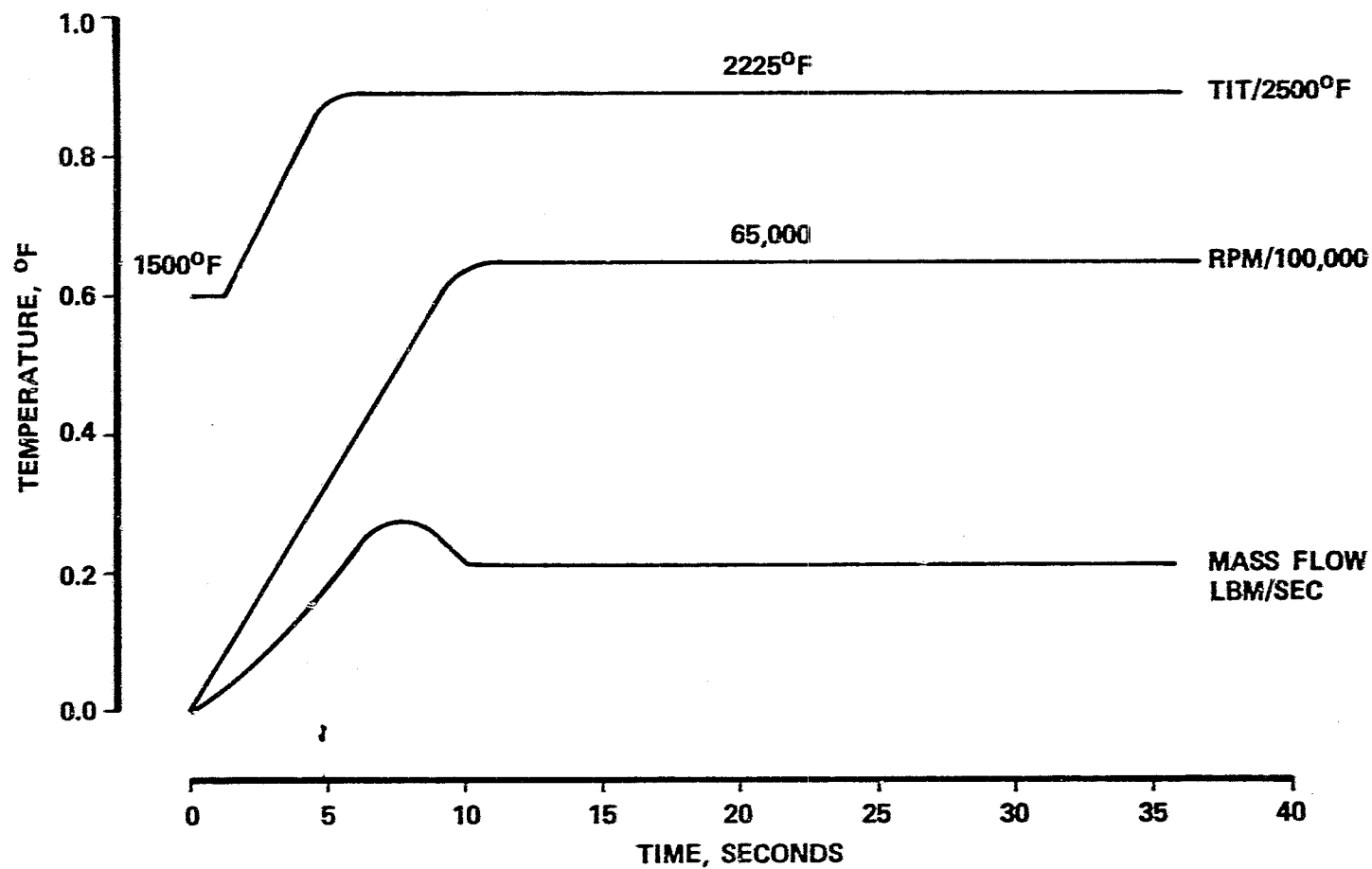


Figure 75. Normal Start Up Transient AGT101 Ceramic Turbine Wheel.

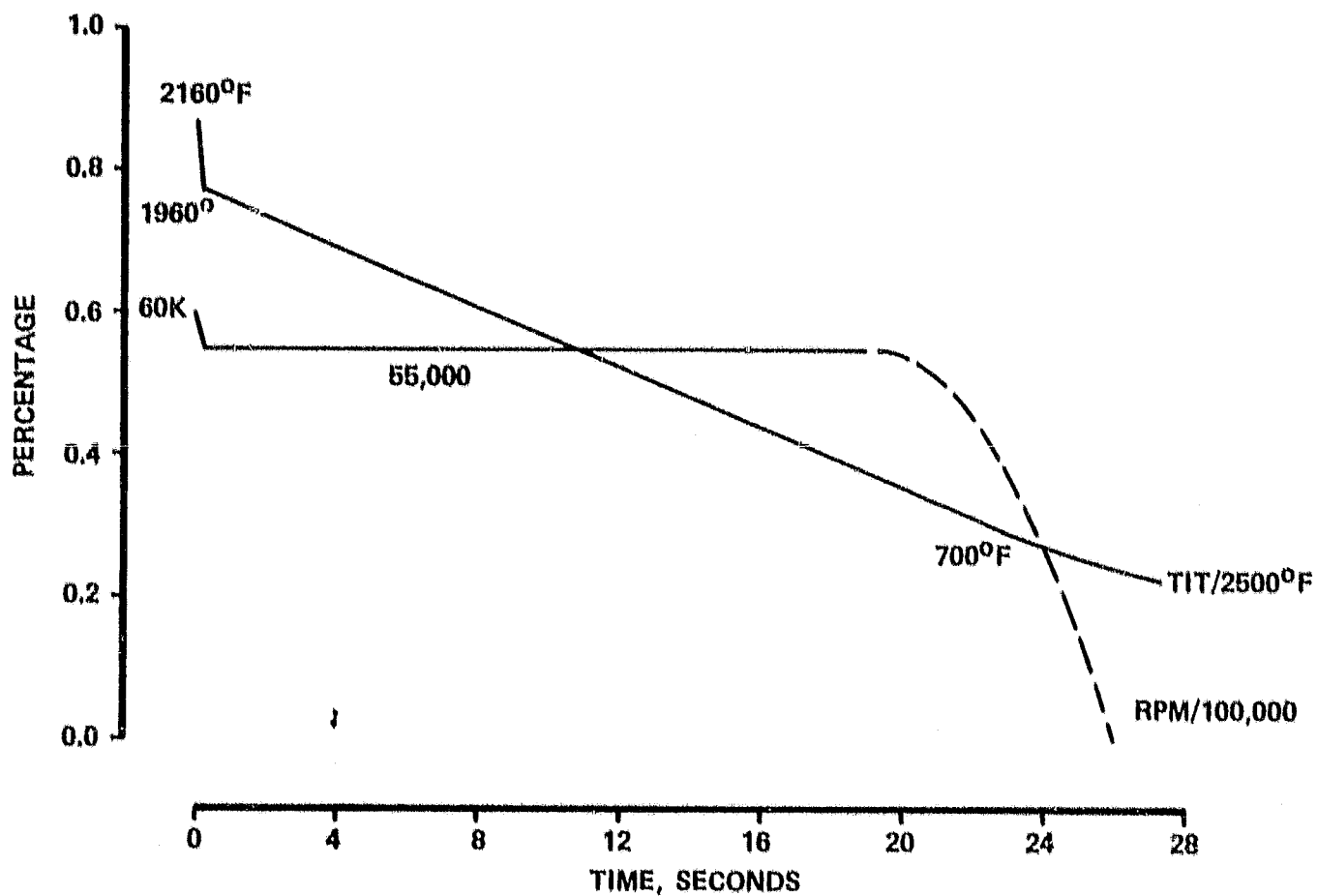


Figure 76. Normal Shutdown Transient AGT101 Ceramic Turbine.

Weibull slope, which were assumed constant with respect to temperature and service life.

4.2.2.4 Results

The transient and steady-state thermal and stress results are presented in Figures 77 through 86.

Table 10 summarizes the computed CPS values for the engine operating conditions analyzed for the third-year properties. Minimum computed CPS values are 99.54 percent for worst case transients, and 99.97 percent for normal transient operation. Using first-year properties, minimum values obtained were 80 percent and 98.57 percent for worst case and normal transients, respectively. An overspeed screening test at 115 percent cold speed raises the CPS values during worst case start from 83 to 94.2 percent but has no appreciable effect on other transient CPS values. As shown in Table 10, comparative differences are small in CPS values for Si_3N_4 and SiC for third-year projected property values.

Blade vibration analysis results are shown in Figure 87. Since the stator (19E) is expected to be the primary source of blade excitation, no vibration problems are anticipated. Although the rotor passes through two resonant frequencies during start, acceleration through the excitation is rather rapid. Superimposed steady-state blade stresses at these low rpm levels are negligible. Figure 88 depicts the mode shapes for the two natural frequencies excited during start.

4.2.3 Metallic Dual Alloy Mechanical Analyses

Thermal and stress analyses were conducted for the Mod I dual-alloy turbine rotor at maximum power (100,000 rpm) and idle power (55,000 rpm). Turbine inlet temperature is limited to 1930°F relative blade temperature to maximize life during the Mod I development. The rotor is comprised of a Mar-M 247 cast blade ring and a powder metal astroloy hub HIP bonded as shown in Figure 89. The rotor is bore cooled using one percent of total mass flow.

The predicted temperature distributions for maximum power and idle are shown in Figures 90 and 91, respectively. Maximum power equivalent stress distribution is shown in Figure 92. Blade vibration analysis results are shown in Figure 93 and 94. No significant problems are anticipated. Table 11 summarizes the dual alloy rotor mechanical properties.

4.2.4 Test Rigs

Turbine performance mapping will be conducted on a cold turbine test rig capable of mapping the turbine stage components at corrected

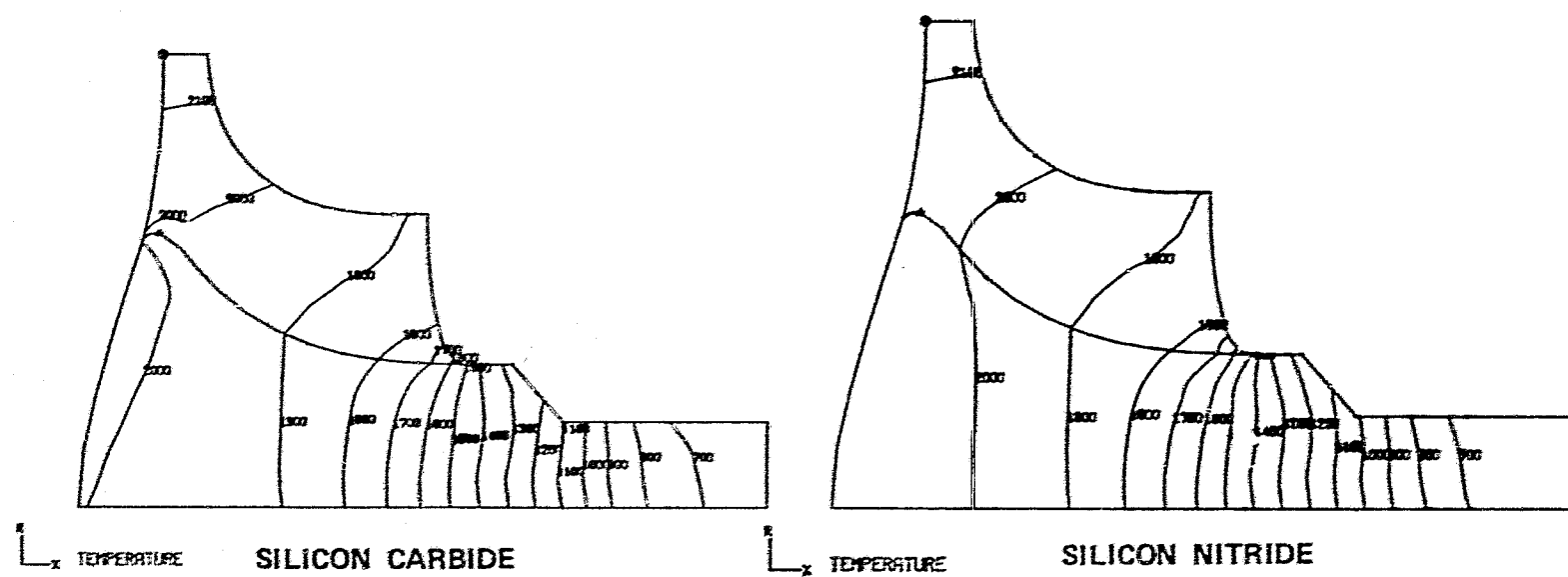


Figure 77. Steady State Maximum Power (TIT = 2500°F, RPM = 100,000).

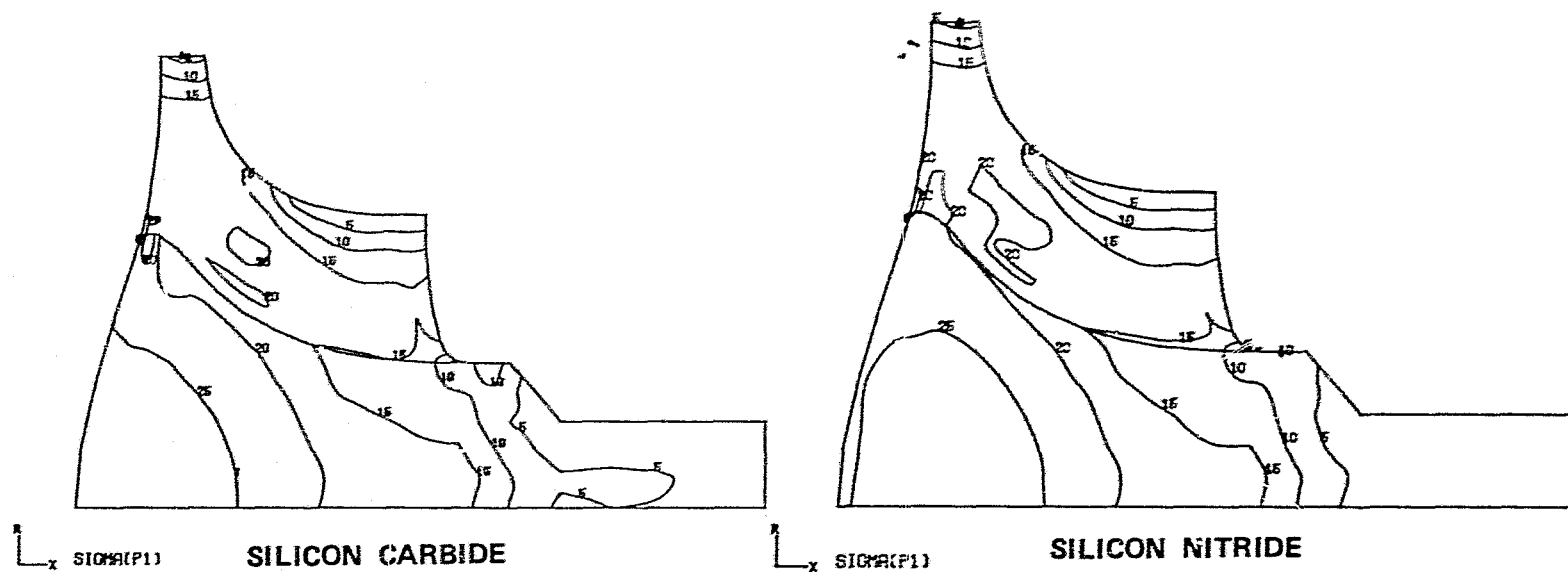


Figure 78. Steady State Maximum Power (RPM = 120,000, TIT = 2500°F).

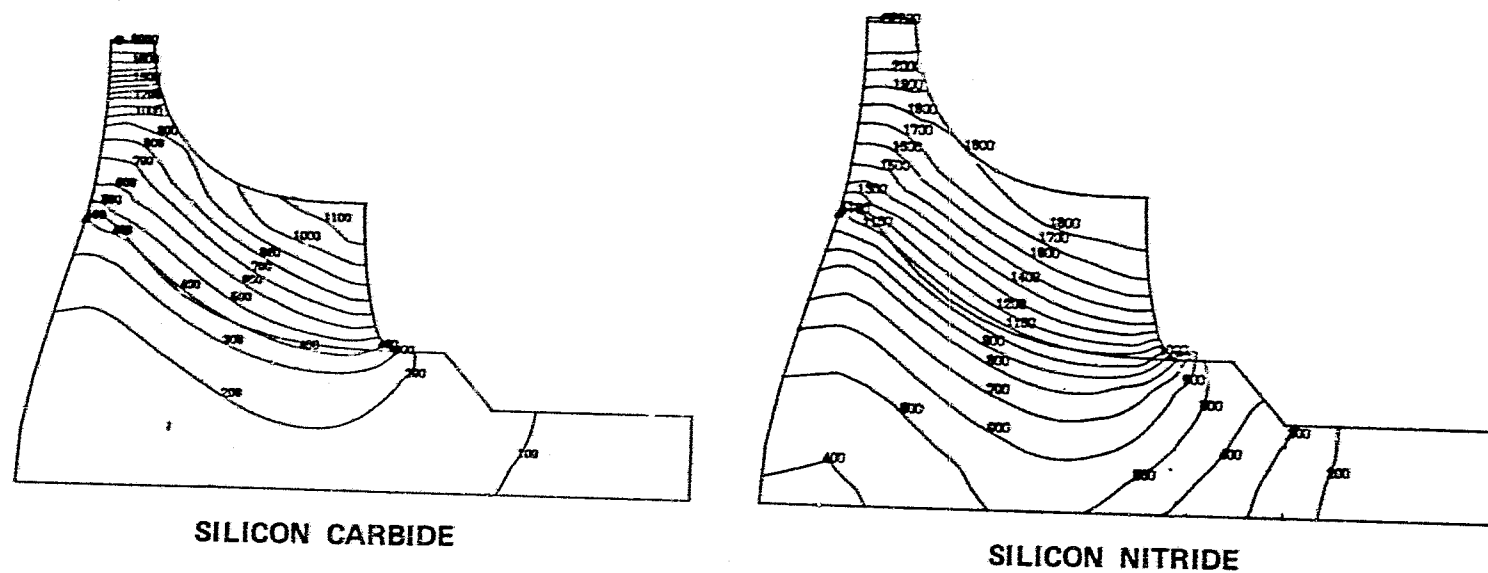
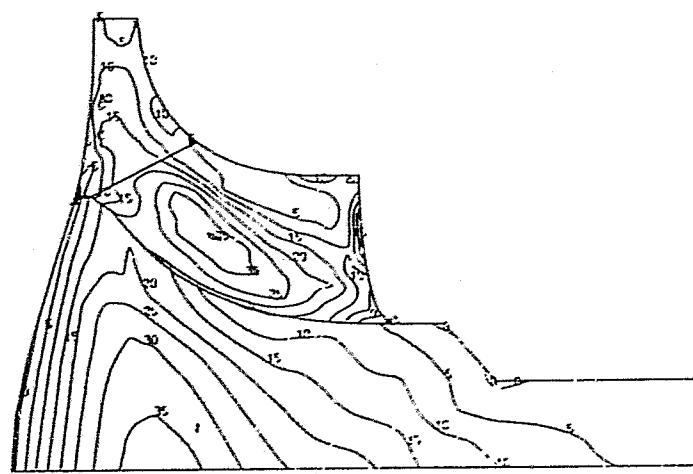
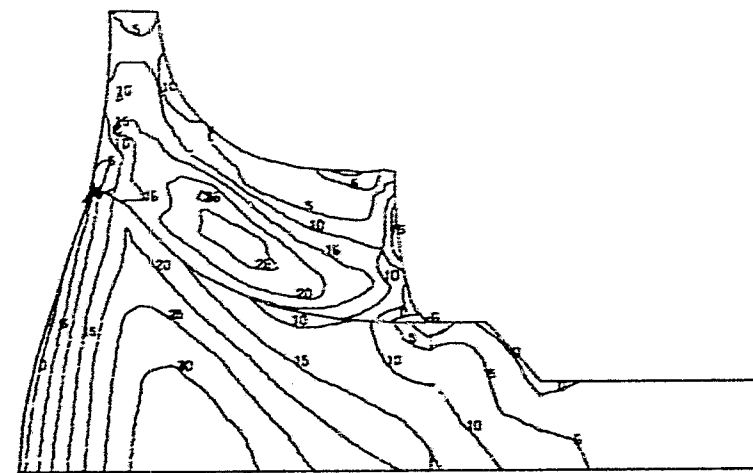


Figure 79. Worst Case Start Up Transient Time = 10 Seconds.



SILICON CARBIDE



L_x SIGMA(P1)

SILICON NITRIDE

Figure 80. Worst Case Start Up Transient Time = 30 Seconds.

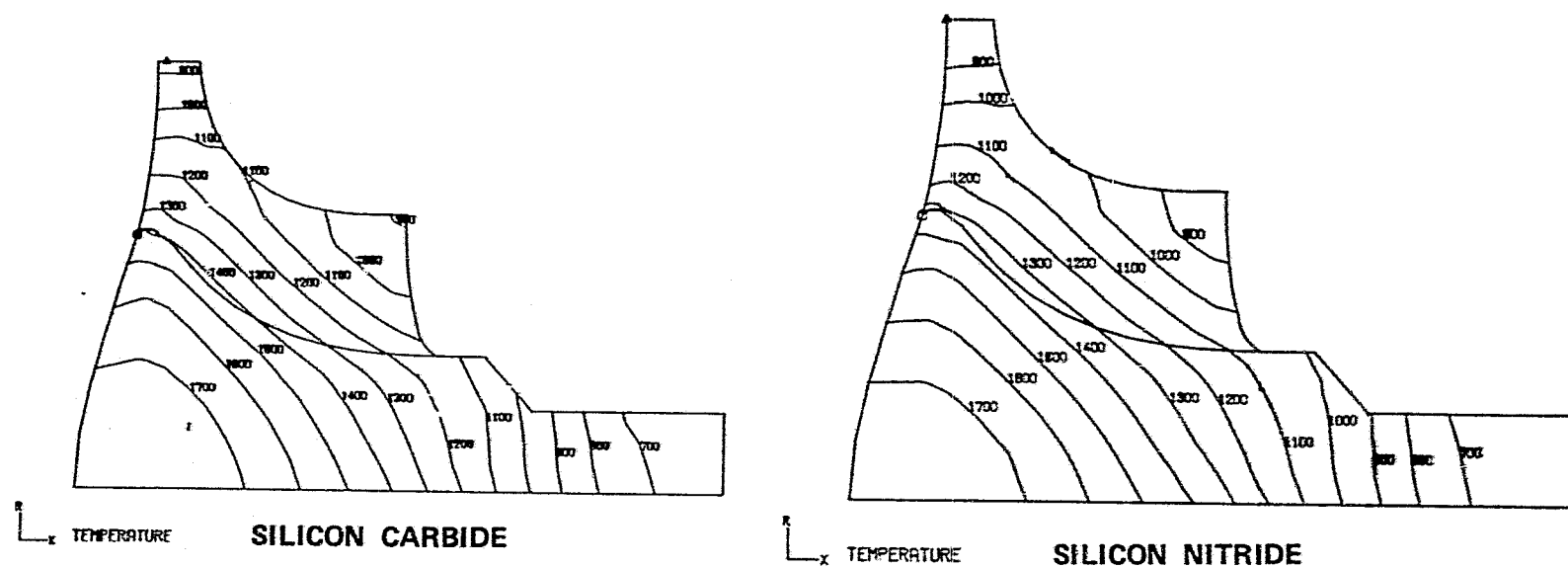


Figure 81. Worst Case Roll Down Transient Time = 40 Seconds.

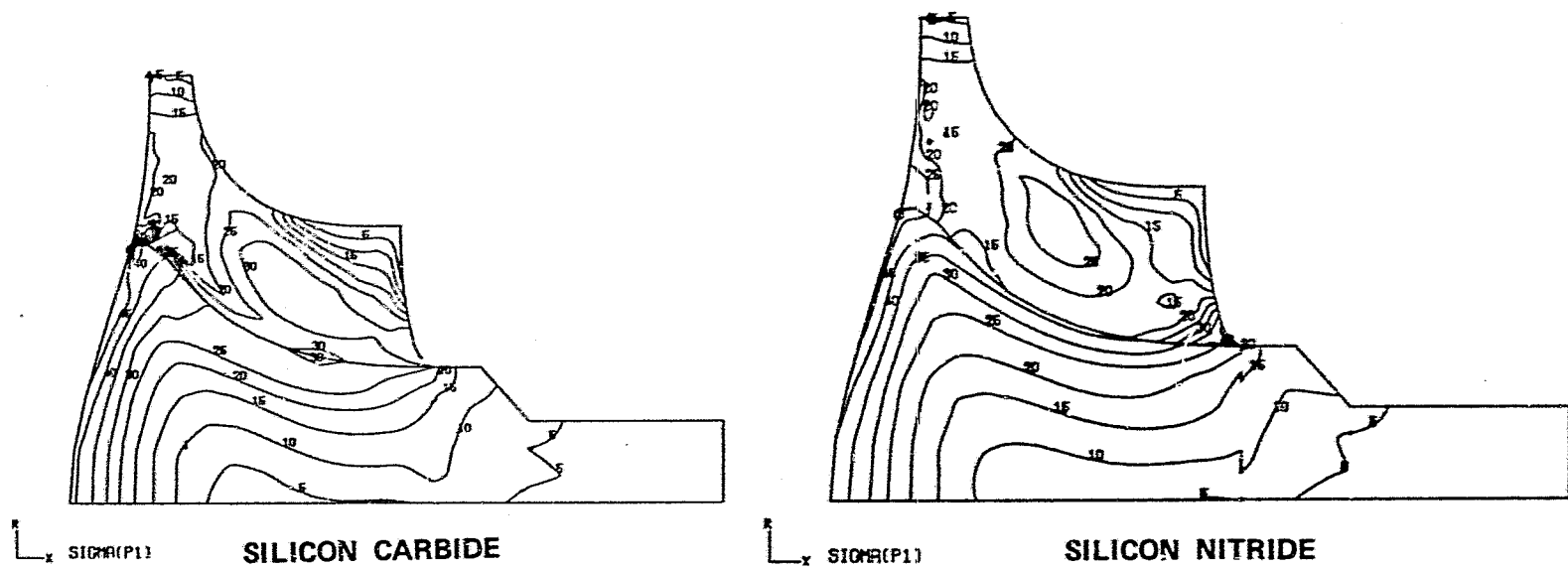


Figure 82. Worst Case Roll Down Transient Time = 40 Seconds.

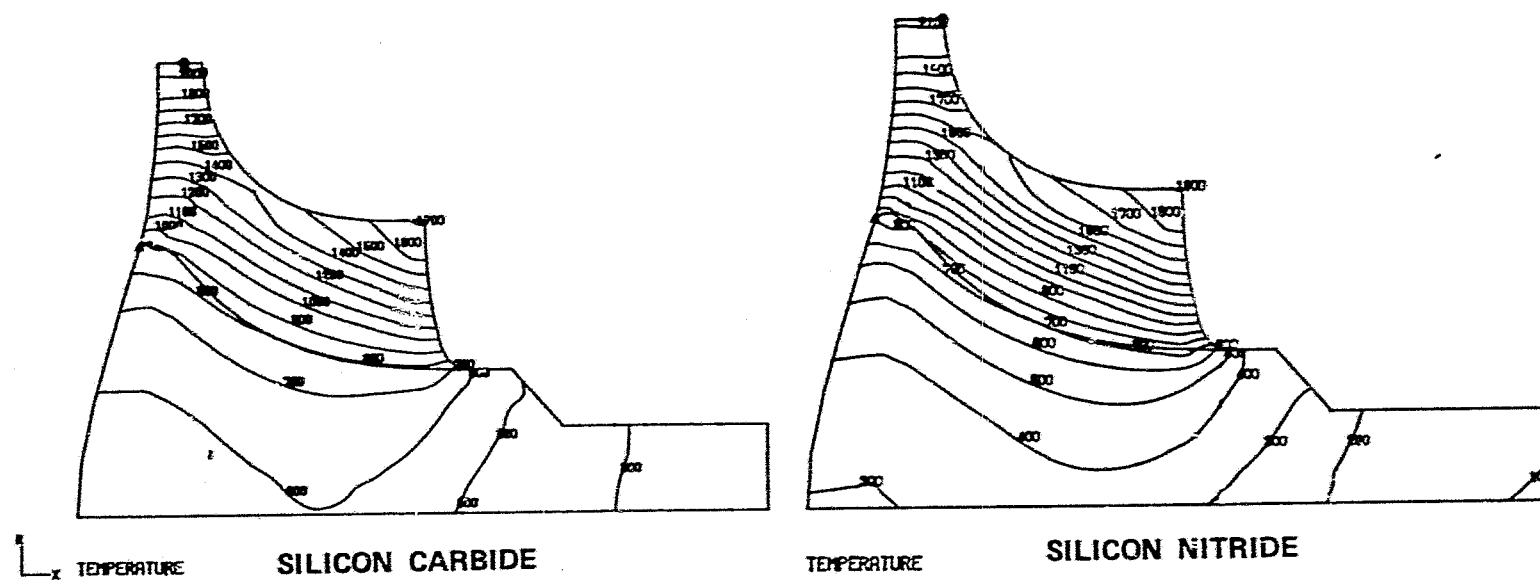


Figure 83. Normal Start Up Transient Time = 30 Seconds.

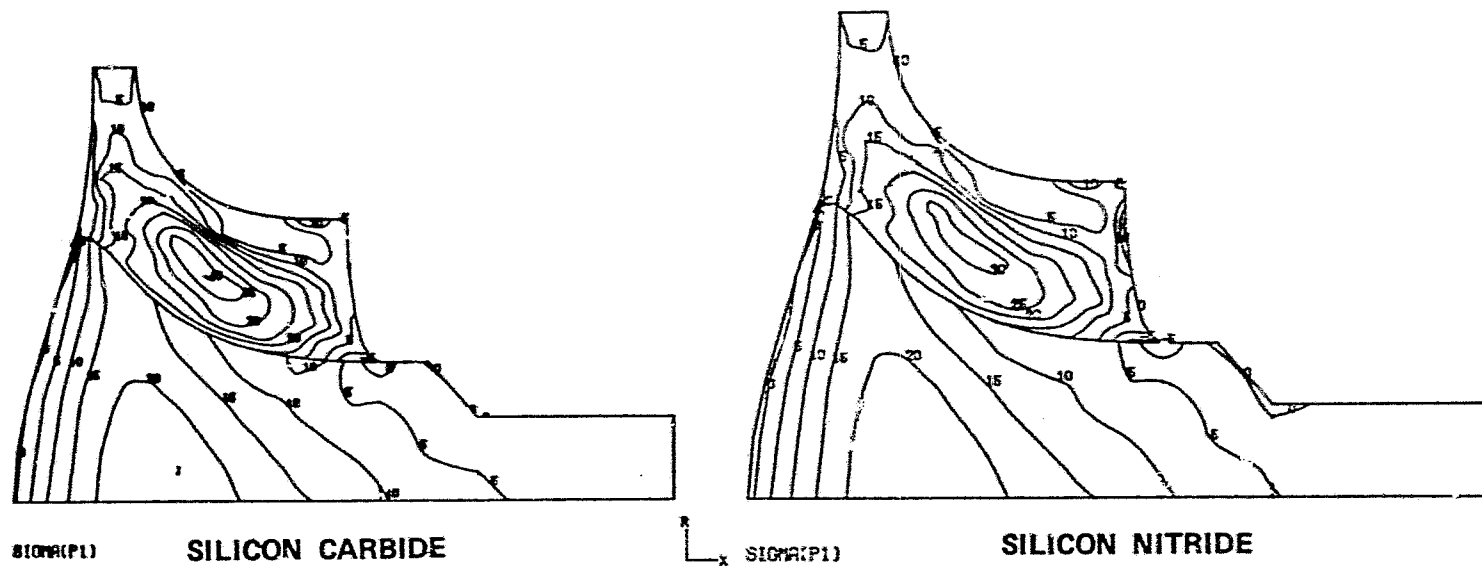


Figure 84. Normal Start Up Transient Time = 30 Seconds.

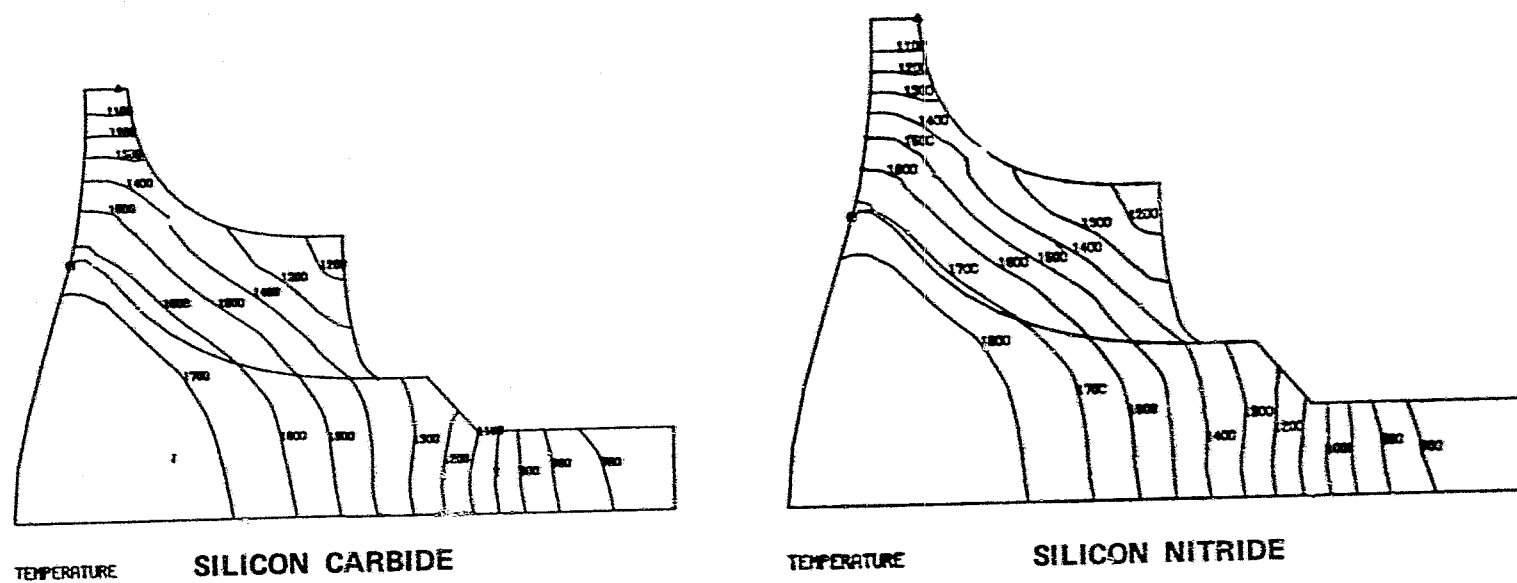


Figure 85. Normal Shutdown Transient Time = 20 Seconds.

ROT CERAMIC TURBINE SILICON NITRIDE SHUT DOWN TRANS JUNE 80

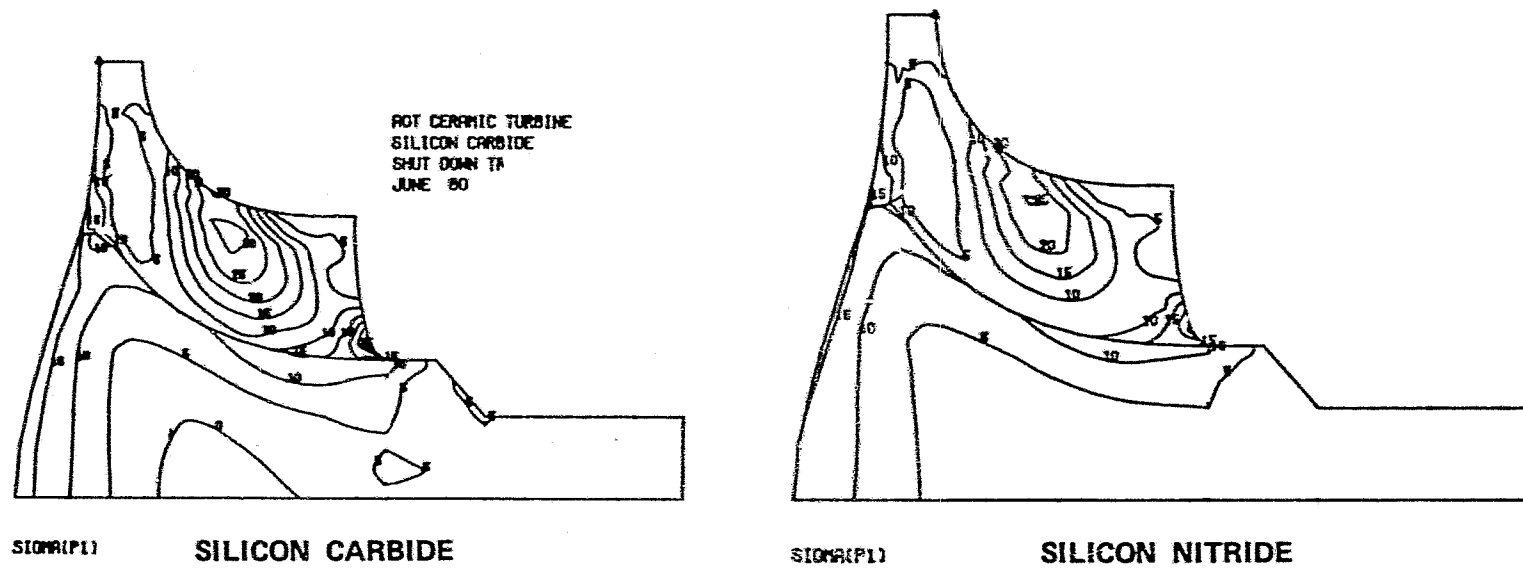


Figure 86. Normal Shutdown Transient Time = 20 Seconds.

TABLE 10. AGT101 CERAMIC TURBINE CUMULATIVE PROBABILITY OF SUCCESS

NO.	TURBINE OPERATING CONDITION	CUMULATIVE PROBABILITY OF SUCCESS (CPS), PERCENT			
		FIRST YEAR PROPERTIES		THIRD YEAR PROPERTIES	
		SiC	Si ₃ N ₄	SiC	Si ₃ N ₄
1.	ROTATION ONLY RPM = 100,000	97.53	96.90	99.95	99.94
2.	ROTATION ONLY RPM = 115,000 (SCREENING TEST)	51.15	32.75	98.63	97.73
3.	STEADY STATE, MAX POWER TIT = 2500°F, RPM = 100,000	96.00	96.4	99.92	99.92
4.	WORST CASE START-UP TRANSIENT TO 75,000 RPM IN 10 SECONDS. TIT TO 2500°F IN 4 SECONDS.	83.00	85.00	99.62	99.57
5.	CASE 4 WITH SCREENING TEST AT 115,000 RPM	94.20	99.88	99.80	99.99
6.	WORST CASE ROLL DOWN TRANSIENT FROM FULL POWER (NO SIGNIFICANT IMPROVEMENT BY PROOF TEST AT 115,000 RPM)	80.0	95.10	99.54	99.90
7.	NORMAL START-UP TRANSIENT TO 65,000 RPM IN 10 SECONDS. TIT TO 2225°F IN 5 SECONDS	98.70	99.80	99.97	99.99
8.	NORMAL SHUTDOWN FROM 65,000 RPM AND 2160°F TIT IN 25 SECONDS	99.87	99.99	99.99	99.99
9.	NORMAL START-UP AND SHUT DOWN	98.57	99.80	99.97	99.99

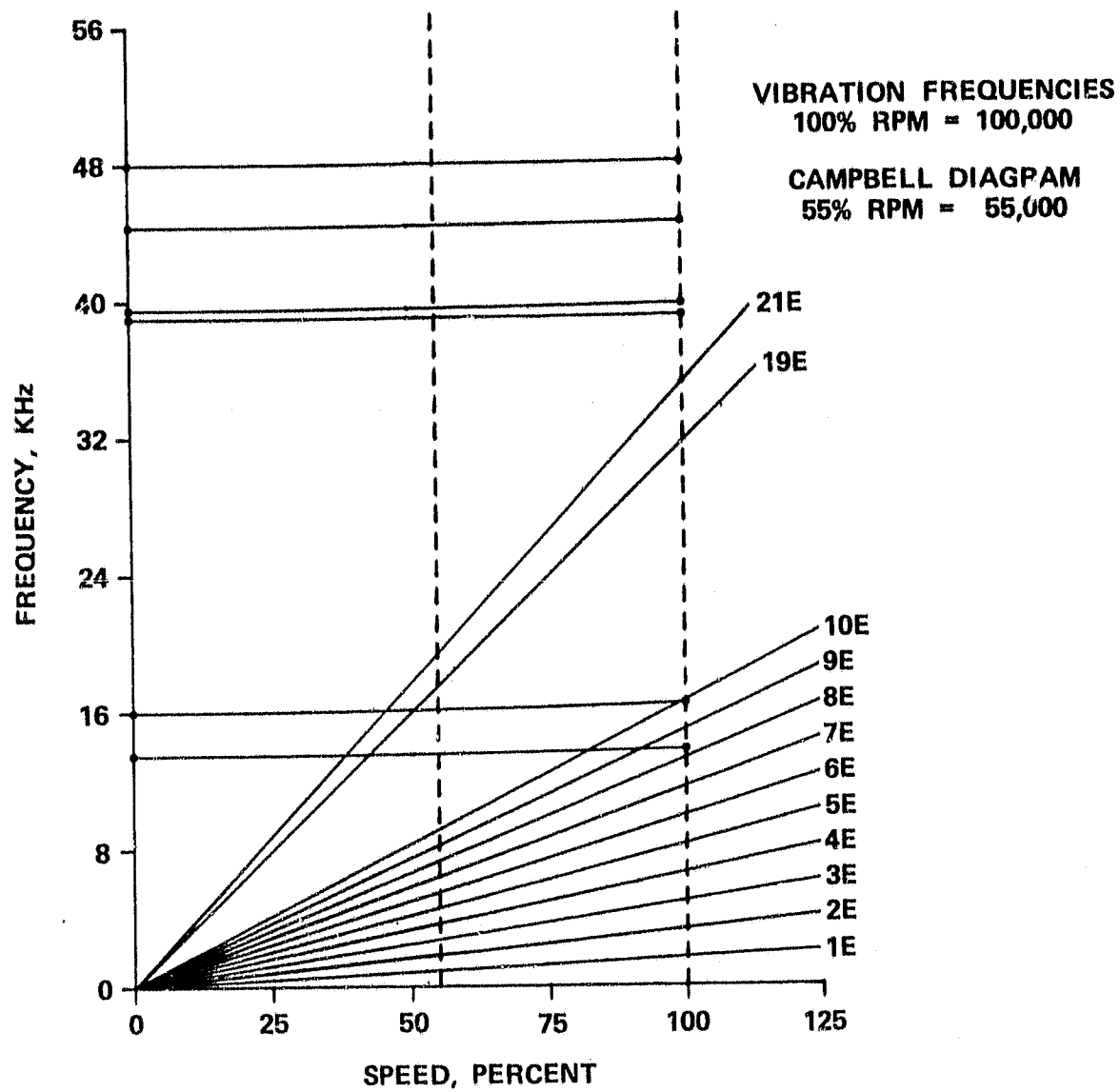


Figure 87. AGT101 Ceramic Blade.

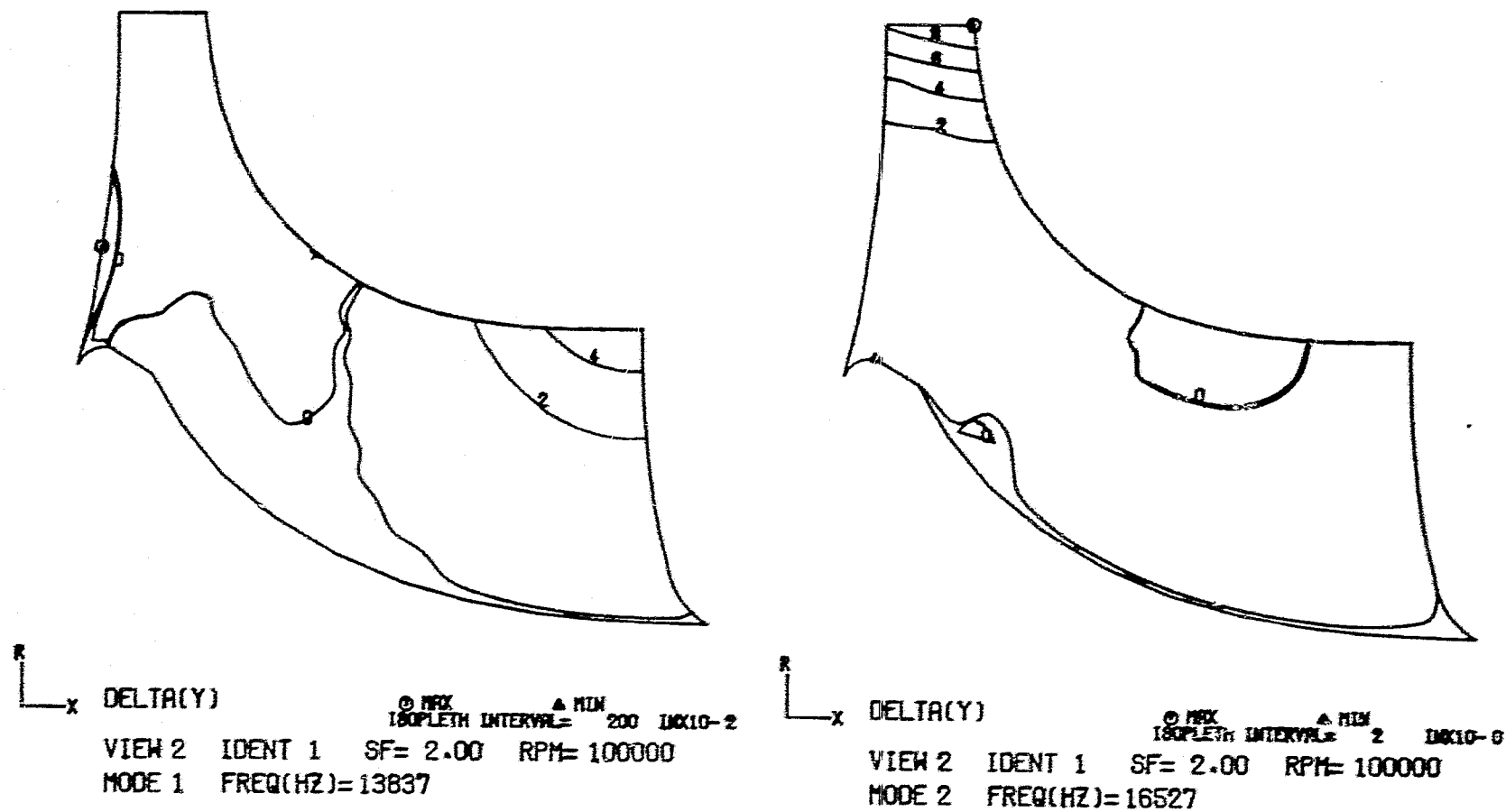
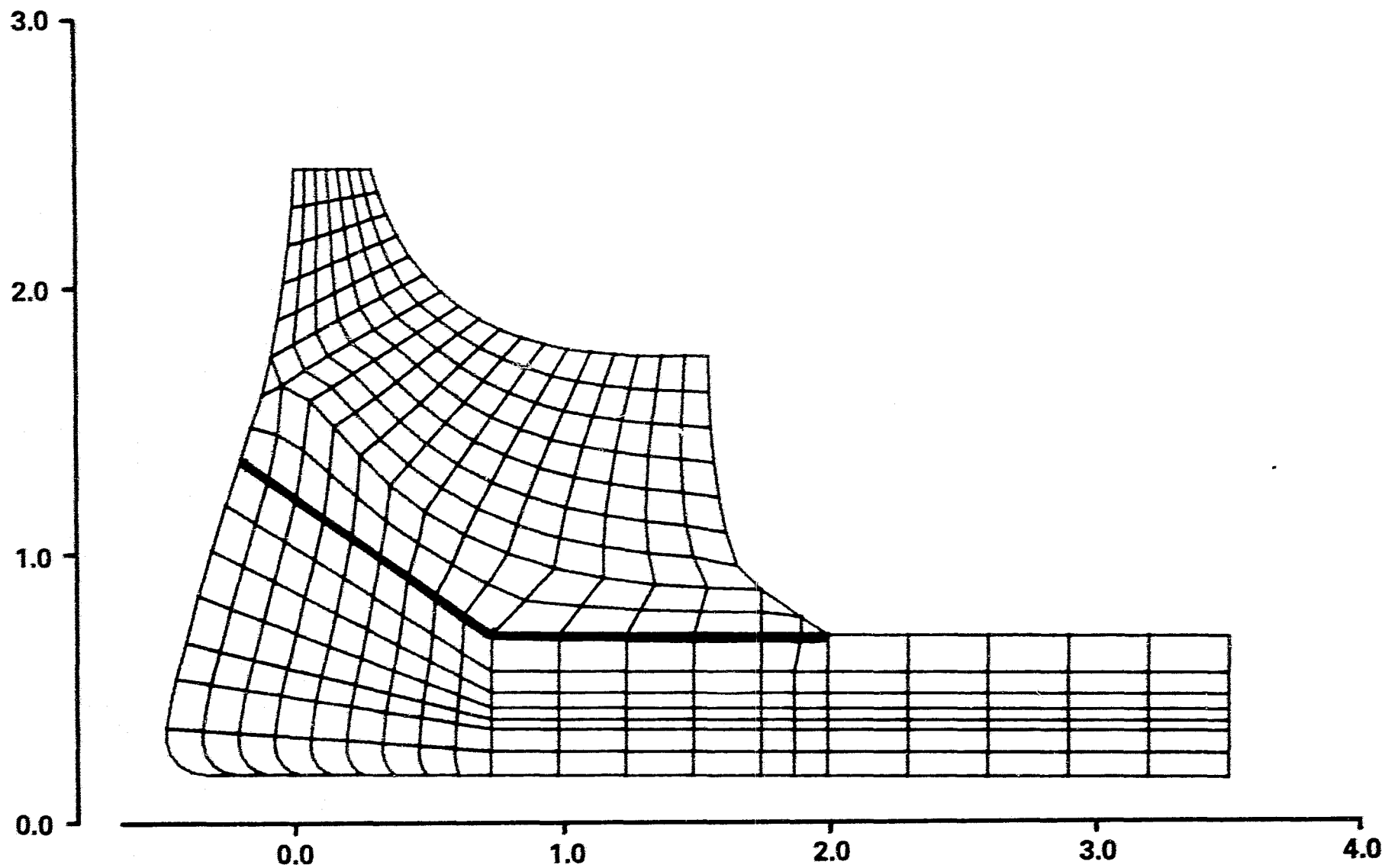


Figure 88. AGT101 Ceramic Blade Mode Shapes.



GRID

Figure 89. AGT101 Metal Dual Alloy Wheel 13 Blades Conical Astroloy Hub.

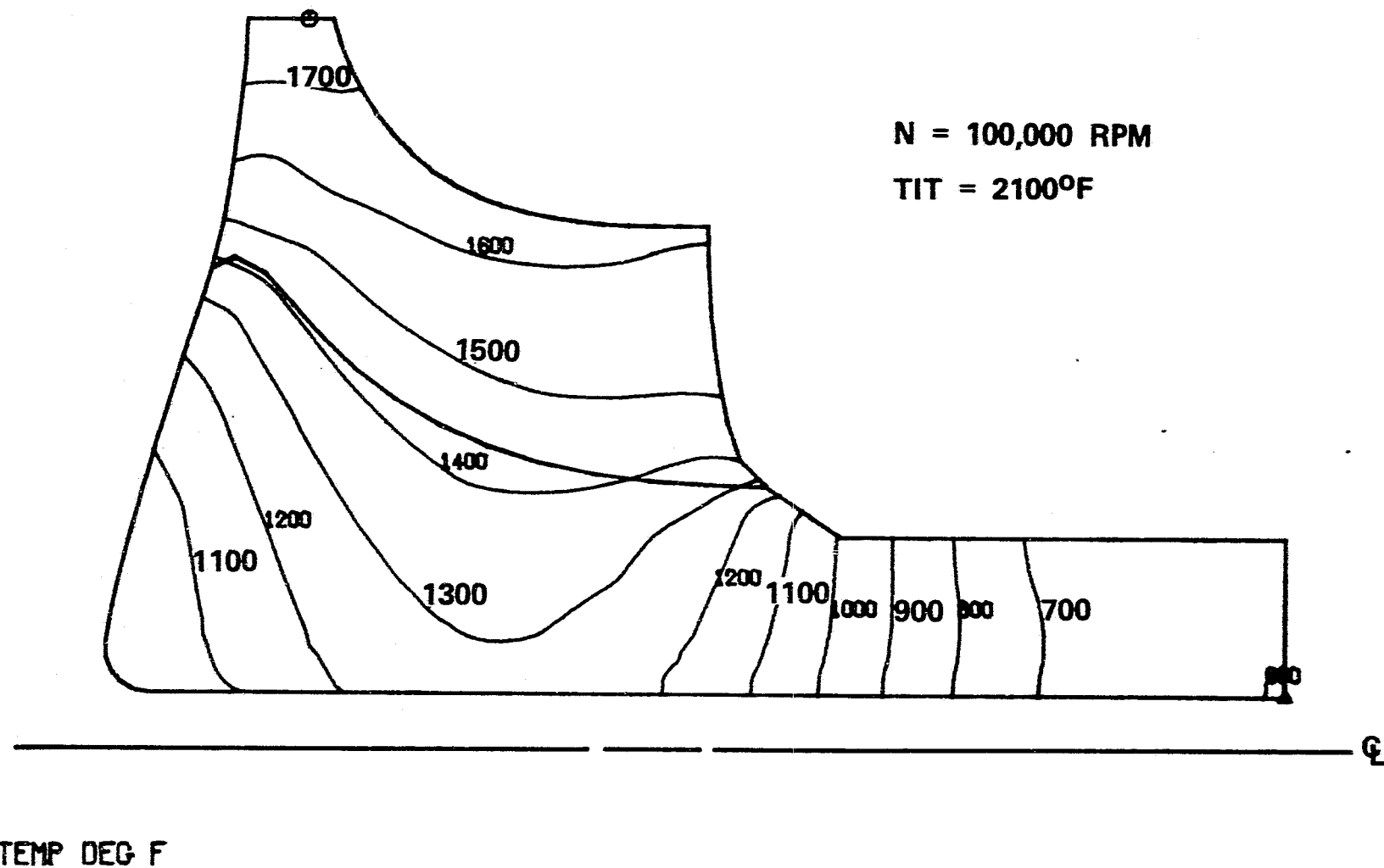


Figure 90. AGT101 Dual Alloy Steady-State Temperature Distribution - $^{\circ}\text{F}$.

IDLE CONDITION

- $N = 55,000$ RPM
- $TIT = 1993^{\circ}F$
- $COOLING\ FLOW\ RATE = 1\% \times W_A$

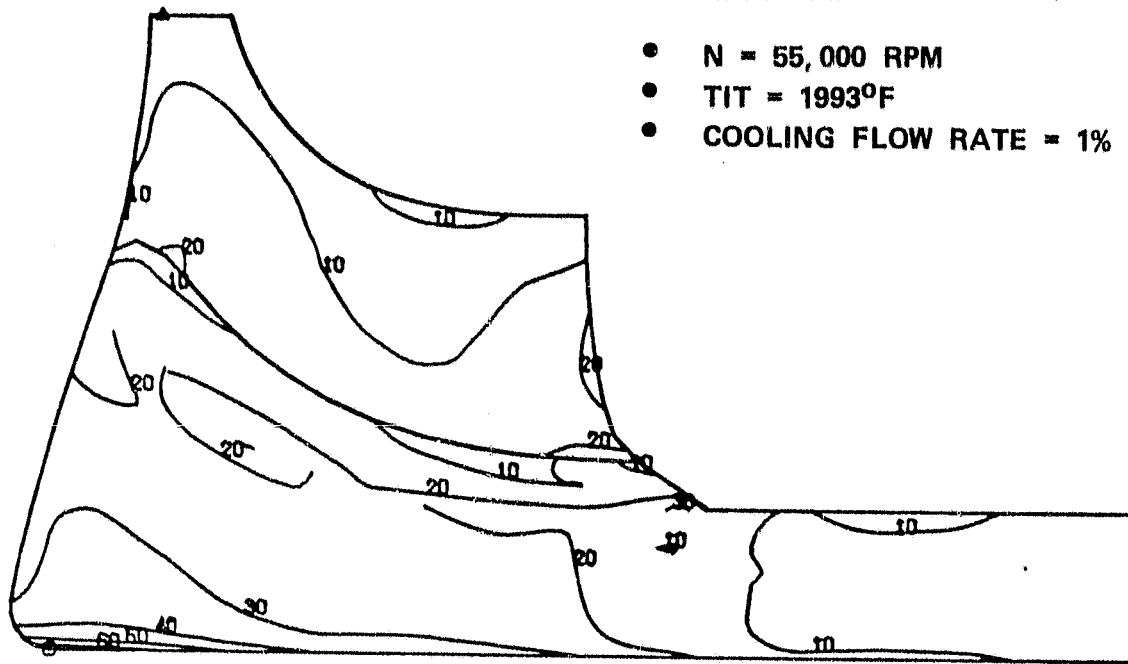


Figure 91. Stress Distribution for Dual Alloy Turbine Wheel.

ORIGINAL PAGE IS
OF POOR QUALITY

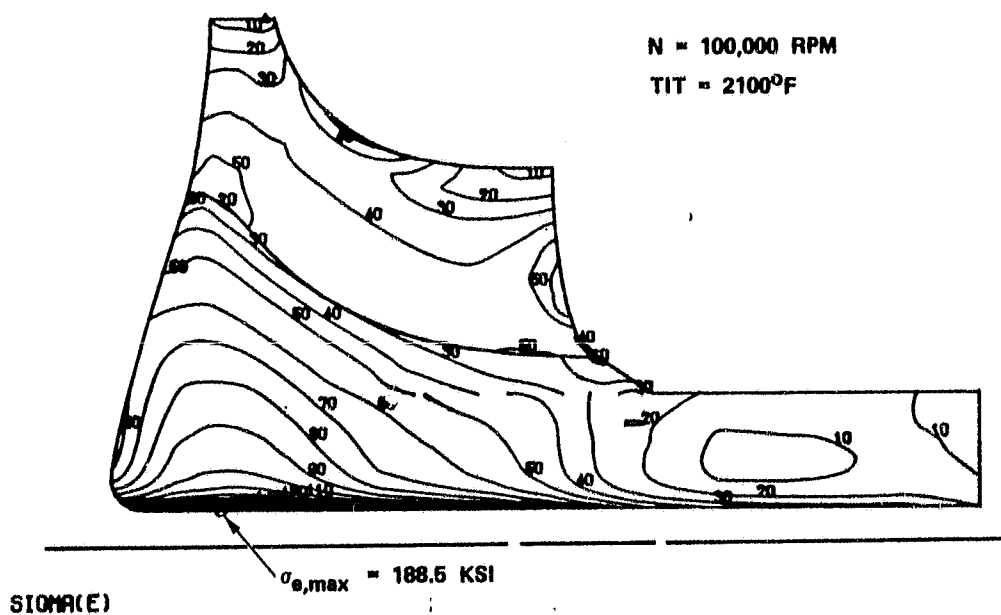


Figure 92. AGT101 Dual Alloy Steady-State Equivalent Stresses - KSI.

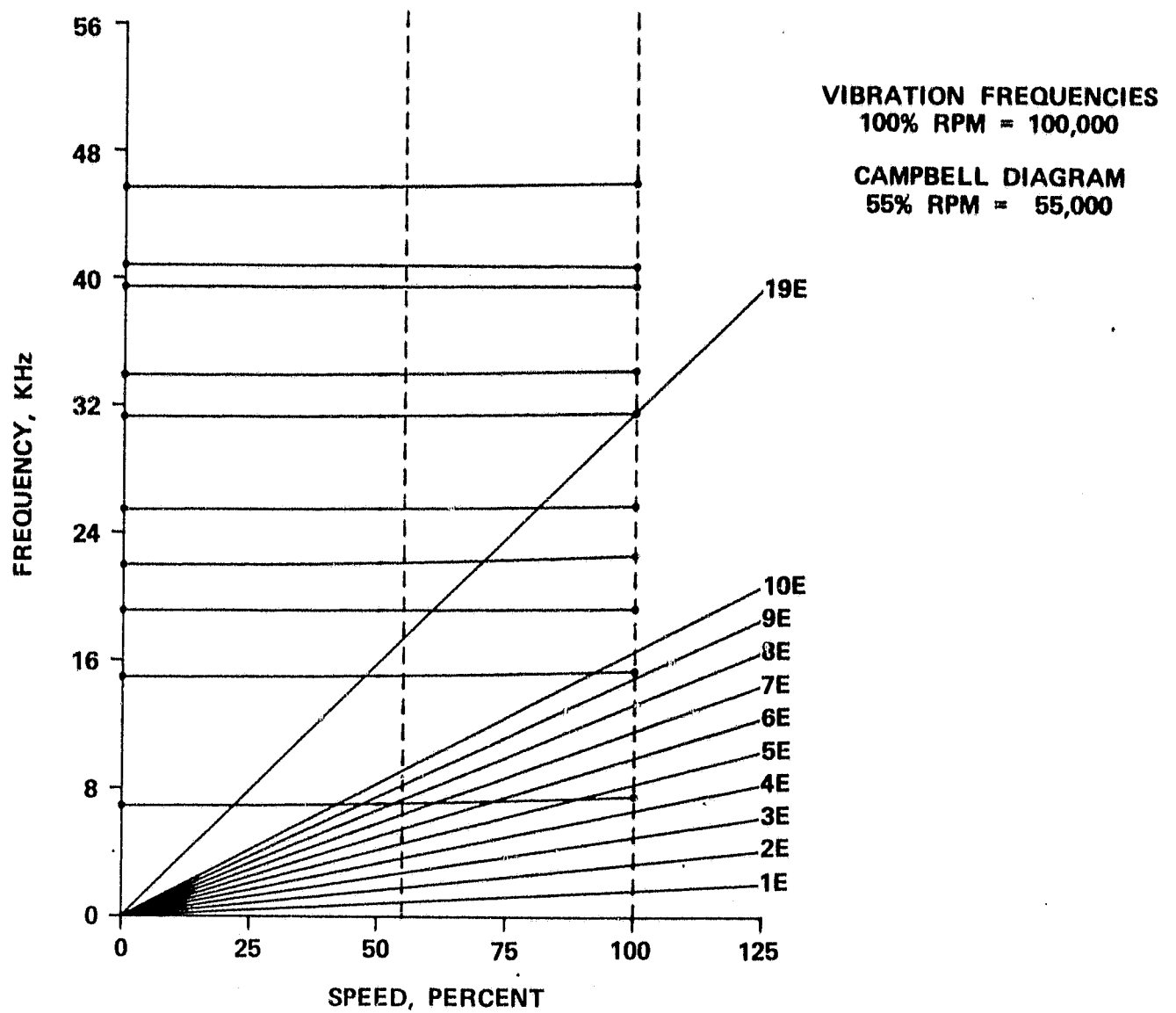


Figure 93. AGT101 Metal Dual Alloy Wheel.

ORIGINAL PAGE IS
OF POOR QUALITY

VIEW 2 IDENT 1 SF= 2.00 RPM= 100000
MODE 1 FREQ(HZ)=7670

VIEW 2 IDENT 1 SF= 2.00 RPM= 100000
MODE 2 FREQ(HZ)=16468

VIEW 2 IDENT 1 SF= 2.00 RPM= 100000
MODE 3 FREQ(HZ)=18384

VIEW 2 IDENT 1 SF= 2.00 RPM= 100000
MODE 4 FREQ(HZ)=22709

VIEW 2 IDENT 1 SF= 2.00 RPM= 100000
MODE 5 FREQ(HZ)=26818

VIEW 2 IDENT 1 SF= 2.00 RPM= 100000
MODE 6 FREQ(HZ)=31860

130

TABLE 11. DUAL ALLOY TURBINE WHEEL

Metal Turbine Wheel Properties

Inlet Temperature (°F)	2100
Number of Blades	13
Material	Mar-M 247 (DS)/Astroloy
Weight (lb)	3.82
I_p (lb-in-sec ²)	0.0092

Properties at Max Power (100,000 Rpm)

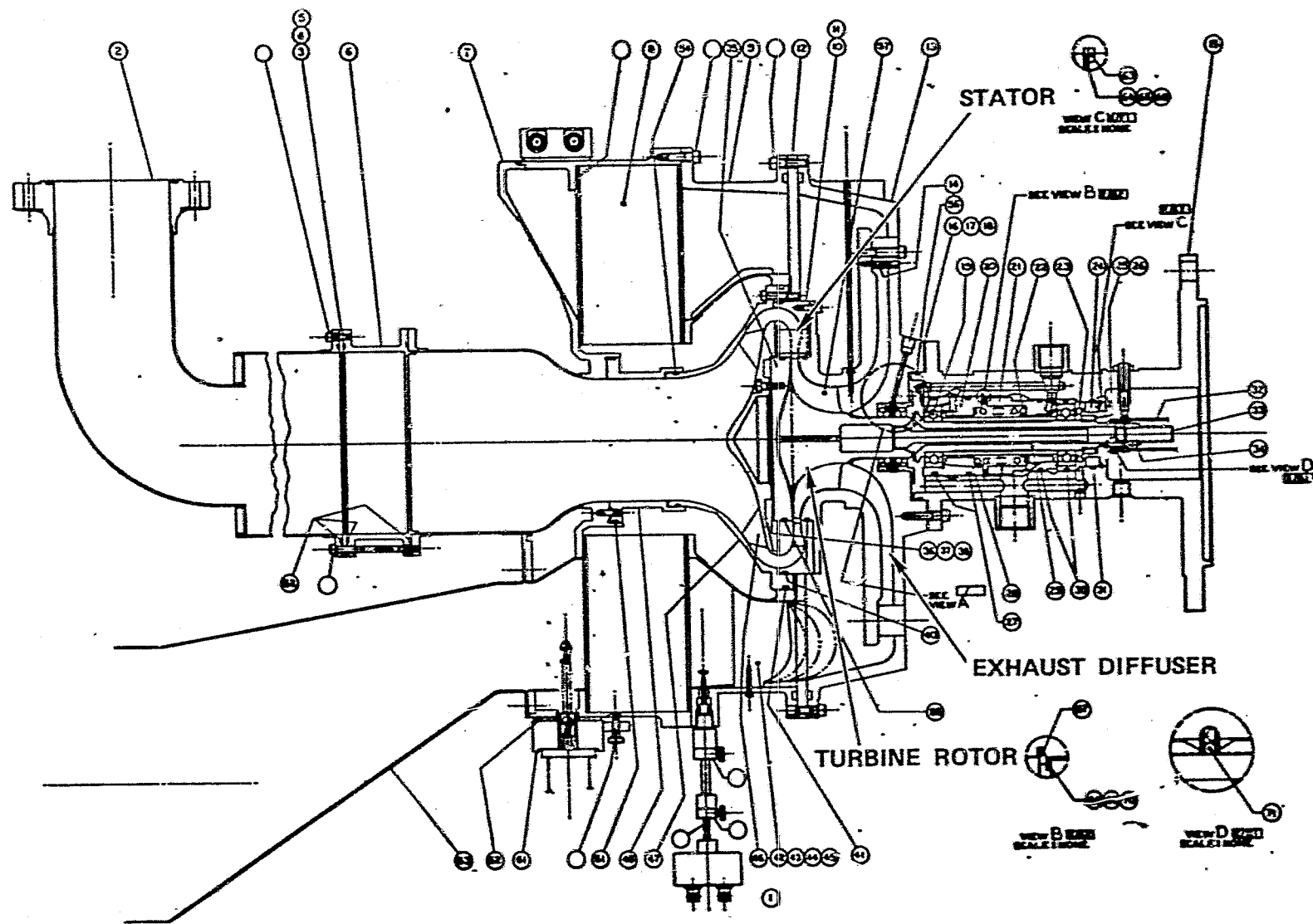
Tip Speed (ft/sec)	2100
Ave. Tangential Stress (ksi)	64
Burst Margin	1.49
Energy (lb-in)	503,400
S-R Life (Hrs) at $R = 1.96$ in	103

operating conditions. In addition, a hot turbine rig will be utilized to develop the ceramic turbine rotor at speeds and temperatures duplicating engine operating conditions. The following paragraphs describe these test rigs.

4.2.4.1 Cold Turbine Test Rig

Cold turbine testing will be conducted using the test rig shown in Figure 95. This rig is a double overhung assembly supported by two angular contact ball bearings. During the turbine and rig design effort, an investigation was conducted concerning off-design performance mapping, particularly accurate performance measurement at the idle-cruise regime of the CFDC. A summary of the investigation and subsequent impact on the cold turbine test rig design is outlined below.

- o The aerodynamic analysis has shown cold turbine rig horsepower requirements at maximum power of 26 to 27 hp with a temperature differential across the rig of 208-224°F. The horsepower level drops to 0.75-3.2 at idle-cruise and the temperature differential decreases to 37-67°F for these conditions. The hp/rpm ratio varies from 5×10^{-4} at maximum power to a low of 3×10^{-5} at the idle condition (see Table 12)
- o Preliminary results of the heat transfer analysis of the cold turbine test rig indicates heat transfer losses could introduce significant errors. Revisions have been introduced to the test rig design to provide insulation both internal and external to the rig, and to introduce conduction heat transfer barriers where possible
- o The survey of the industry for precision instrumentation confirmed the availability of platinum resistant temperature sensors and direct-coupled, high speed electronic torque meters with the desired accuracy
 - o The high speed, direct-coupled, torque meter represents the instrumentation with accuracy both for high and low power mapping (MFG, Torque Meters Ltd., Northampton, England)
 - o The platinum resistive temperature sensors provide secondary or backup measurement of performance and provide an important reference for the temperature surveys at various points in the turbine system
- o The combination of direct coupled torque meter and platinum resistive temperature sensors as backup provides the most desirable performance measurement system to assure design



ORIGINAL PAGE IS
OF POOR QUALITY

Figure 95. Cold Turbine Test Rig.

TABLE 12. AGT101 COLD TURBINE RIG OPERATING CONDITIONS

Parameter	Maximum Power	Cruise No 1	Cruise No 2	Maximum Throttle	Idle
$P/P_{T\text{-System}}$	4.263	1.787	1.639	1.676	1.341
$T_{IN}, ^\circ F$	304.3	159.5	146.5	145.5	117.4
$T_{OUT}, ^\circ F$ (Assumed)	80.0	80.0	80.0	80.0	80.0
N, rpm	52,000	30,804	28,379	24,870	25,849
$N/\sqrt{\theta}, \text{rpm}$	41,863	28,194	26,251	23,025	24,507
$W\sqrt{\theta}/\delta$, Corrected Flow, lb/sec	0.423	0.377	0.362	0.376	0.259
W , Physical Flow, lb/sec	0.35141	0.11556	0.10120	0.0983	0.0588
Reynolds Number, $R_e = W/R_t \mu$	1.0×10^5	38,128	34,130	33,150	20,600
$P_{T_{IN}}, \text{psia}$	14.816	4.92	4.44	4.15	3.52
$P_{T_{EXIT}}, \text{psia}$	3.50	2.75	2.71	2.476	2.625
hp	26.76	3.119	2.28	2.186	0.7468
hp/rpm	0.0005	0.00010	0.000081	0.00009	0.00003

NOTE: Gamma effects not included will alter results by few percent

goals and CFDC mileage estimates are properly assessed during the cold turbine mapping program

A layout of the turbine test rig with the direct-coupled torque meter is shown in Figure 96. Instrumentation stations and types are shown in Figure 97.

4.2.4.2 Hot Turbine Test Rig

As the ceramic turbine analysis progressed it appeared that the test objectives for the hot turbine rig could be altered to simplify this expensive test rig. The turbine analysis supports the fact that hub stresses can be induced in a room temperature overspeed test and defective parts screened out by this process. This allows the test objective for the hot turbine rig to be altered to impose maximum thermal stresses in the rotor blades. The maximum thermal stress in the blade occurs during the start transient. Therefore, the hot turbine rig is to test the rotor blade thermal stress integrity by impinging hot gas (up to 2500°F) on the ceramic rotor during startup. Therefore, the hot turbine rig design concept can change from a complicated rig utilizing engine structural parts to a simple blow torch on a pin wheel approach.

Conceptually the hot turbine rig would include the test rotor/shaft assembly mounted on a bearing assembly driving a small power absorption device. Two or more ceramic ducts carrying hot gas from a lab combustor would direct flow onto the rotor at the desired entrance angle. A firebrick-lined casing could be utilized to enclose the assembly and direct the exiting hot gas away from the rig. Conceptual layouts of this rig will be developed in October/November 1980.

4.2.5 Ceramic Turbine Shaft Attachment

The selected means of attachment for the ceramic turbine rotor to metallic shaft is a thermal shrink fit. While analysis of this attachment method is in progress, results to date are discussed below.

Referring to Figure 98, IN903 is selected as the metal sleeve material due to its high strength at temperature and low thermal coefficient of expansion (see Figure 99). At this time, both SiC and Si₃N₄ are the ceramic rotor material candidates. Figure 100 illustrates attachment temperature distribution at steady-state maximum power operating conditions for the respective ceramic materials.

At this time, two major concerns with the shrink fit attachment are the possibility of thermal ratcheting and locally high axial stresses (end effects). To assess these concerns, a finite element analytical approach has been developed. Axial and radial force ratios (F_z/F_R) at each nodal point along the interface of the two contacting surfaces are evaluated. These values are compared to the static

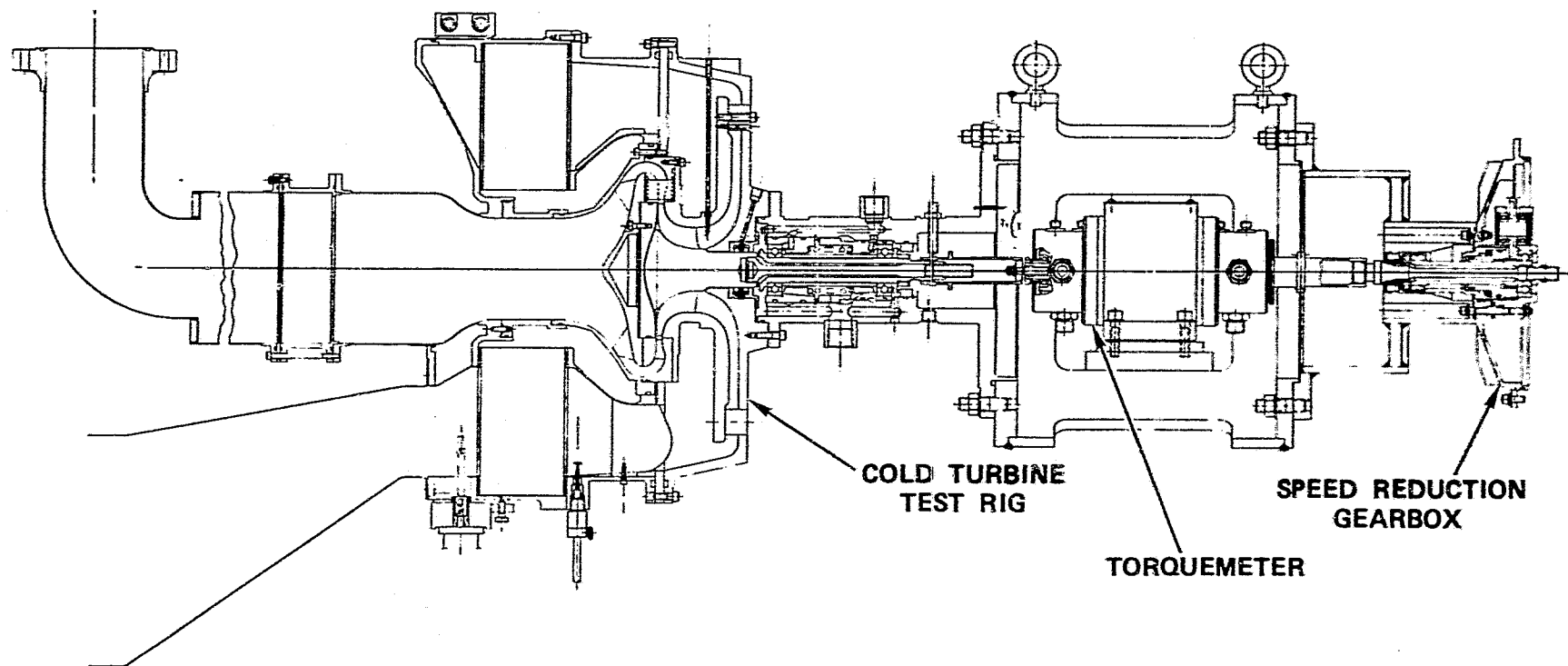


Figure 96. Test Rig with Direct Coupled Torque Meter.

ORIGINAL PAGE IS
OF POOR QUALITY

ORIGINAL PAGE IS
OF POOR QUALITY

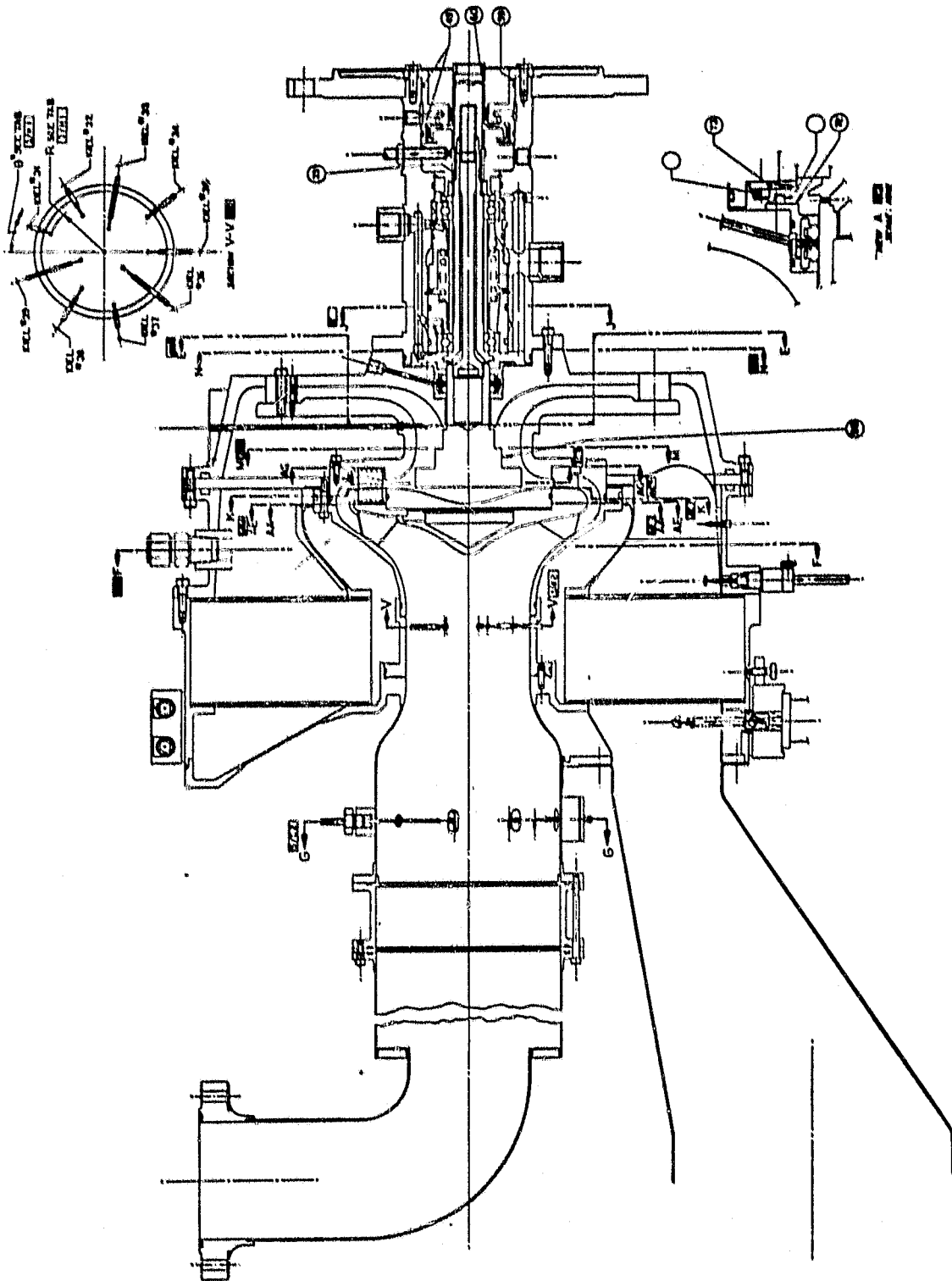


Figure 97. Test Rig Instrumentation Stations.

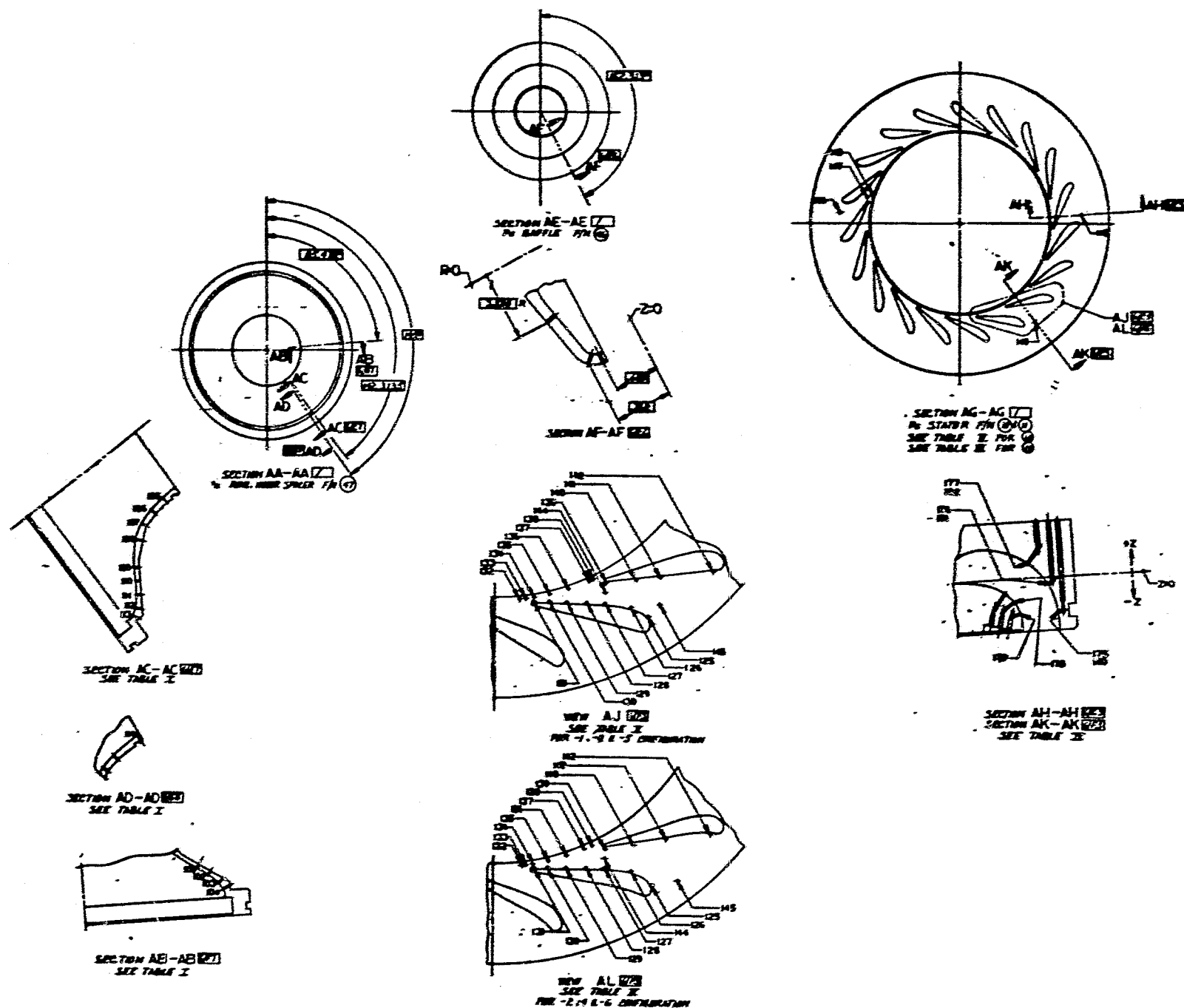
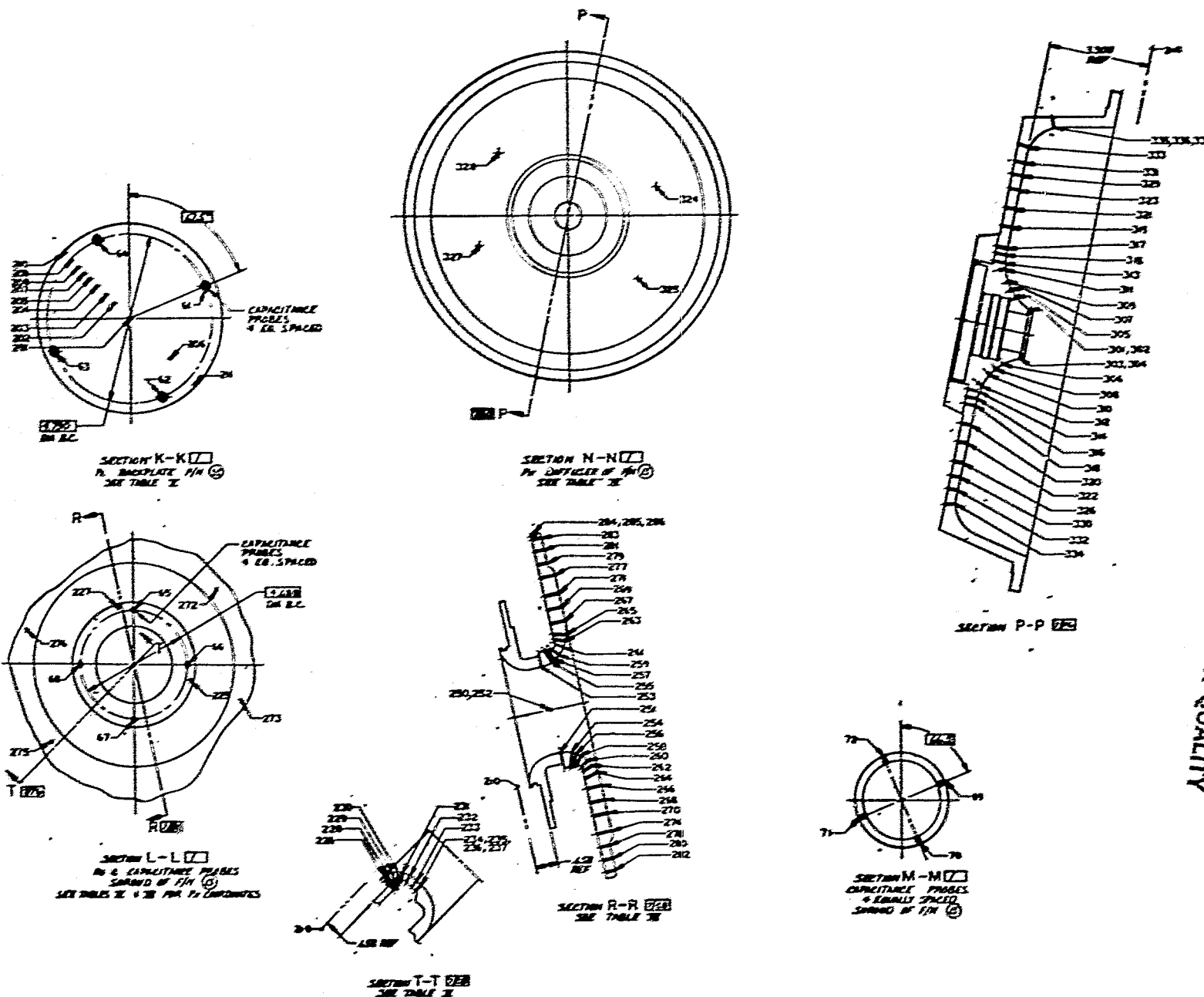


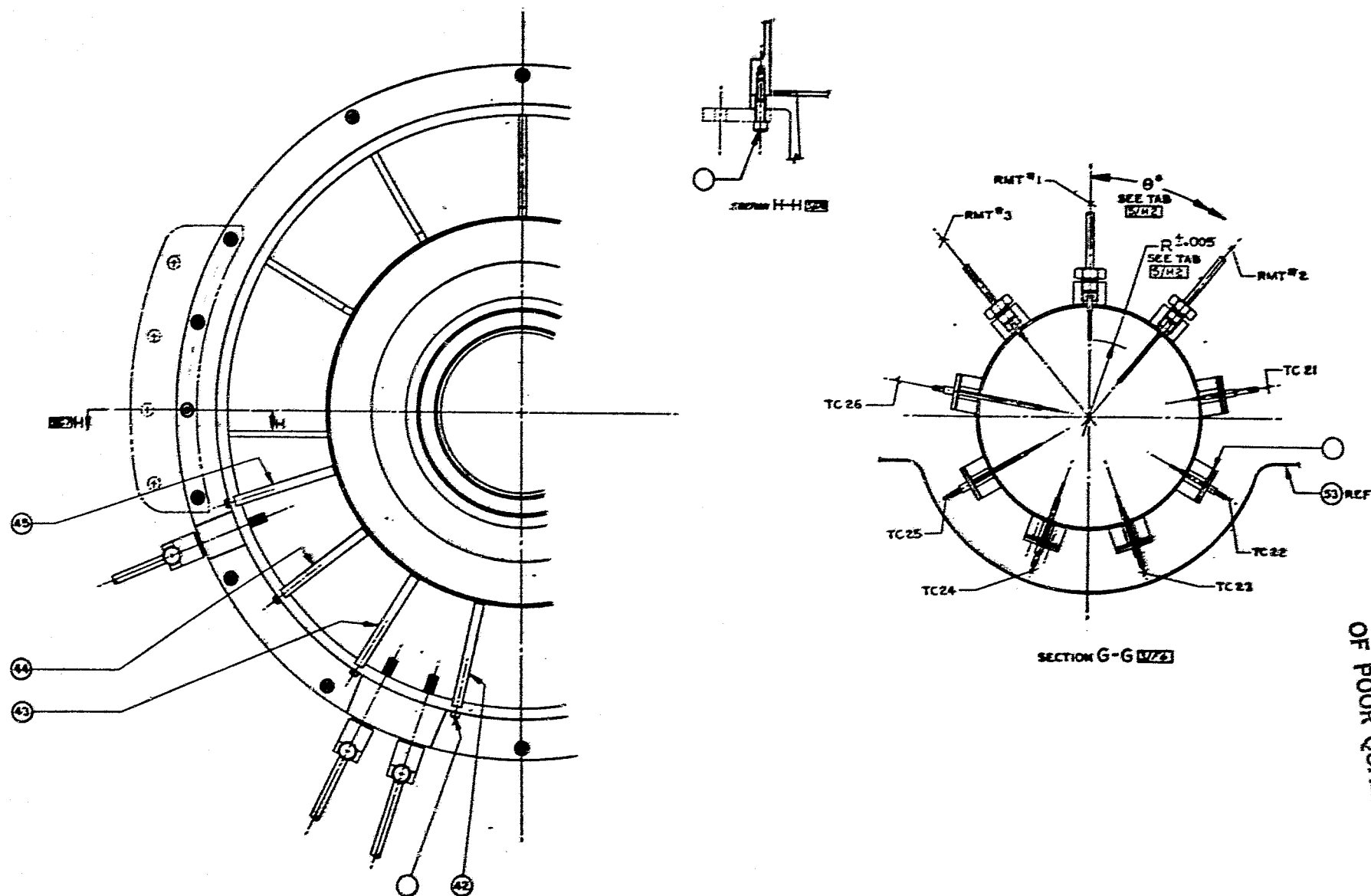
Figure 97. Test Rig Instrumentation Stations (Contd).

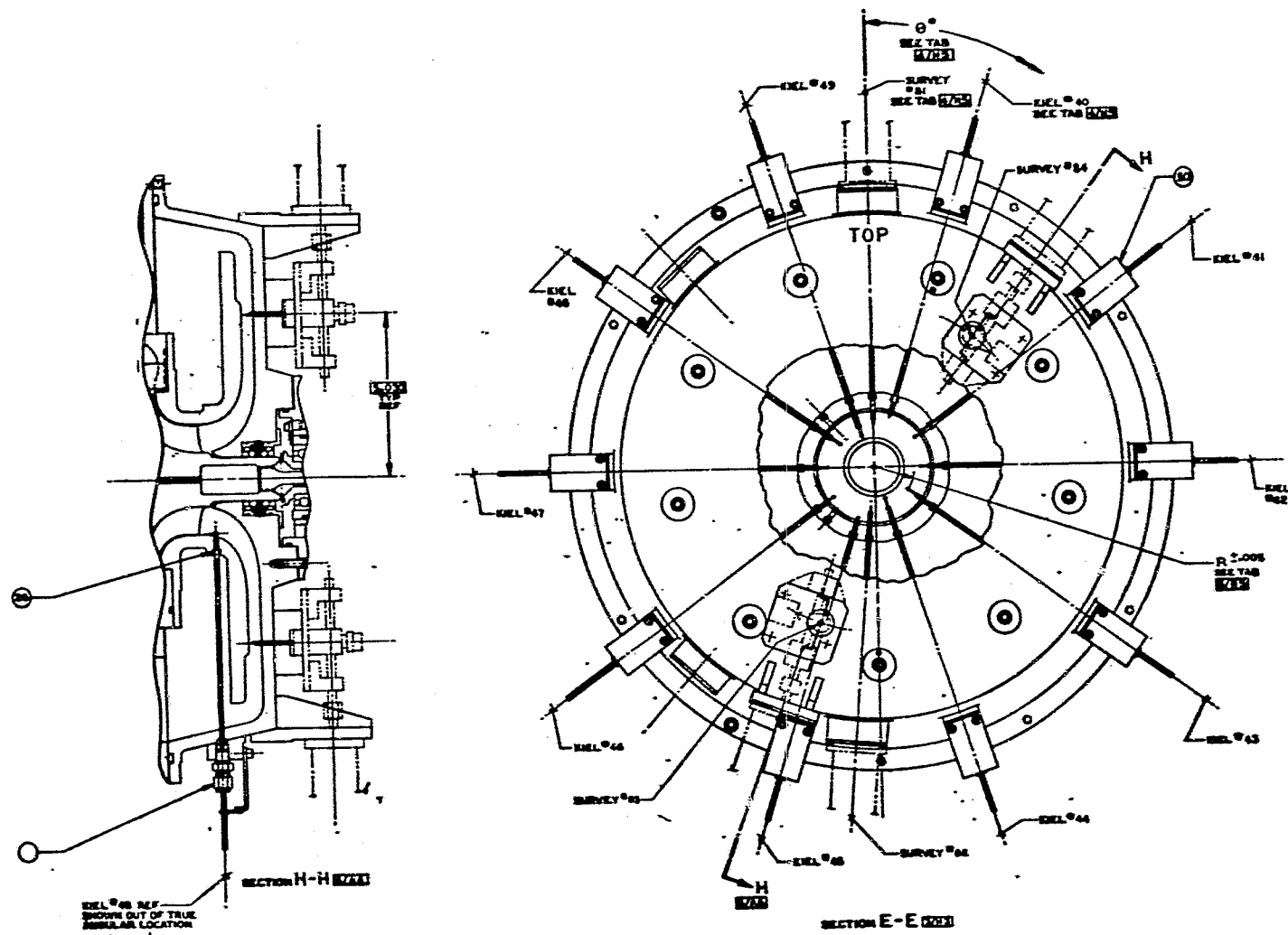
ORIGINAL PAGE IS
OF POOR QUALITY



ORIGINAL PAGE IS
OF POOR QUALITY

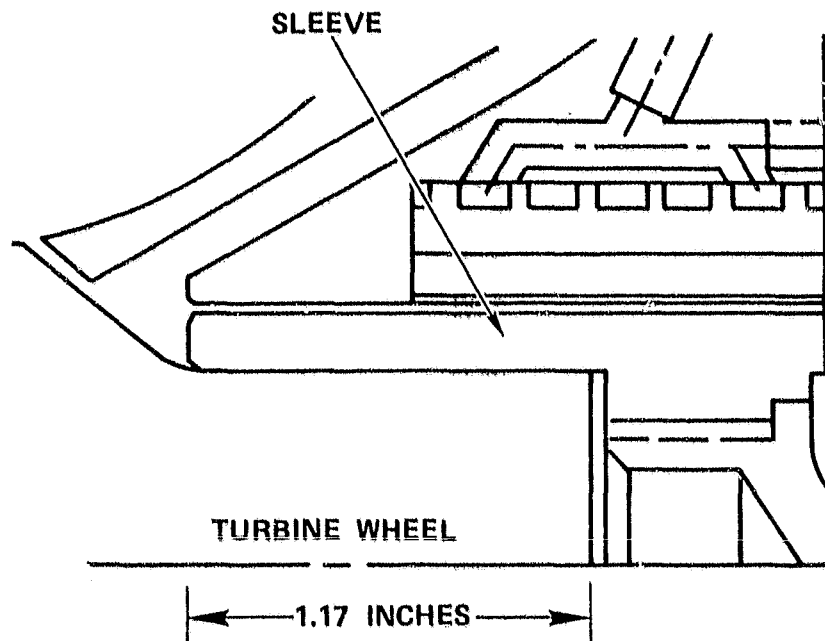
Figure 97. Test Rig Instrumentation Stations (Contd.).





ORIGINAL PAGE IS
OF POOR QUALITY

Figure 97. Test Rig Instrumentation Stations (Contd).



NOMINAL DIMENSIONS

SLEEVE OD = 1.35 INCHES

ID = 0.946 INCH

INTERFERENCE FIT = 0.0038 INCH

Figure 98. Turbine Wheel Sleeve Attachment.

$$\rho = 0.294 \text{ LB/IN}^3$$

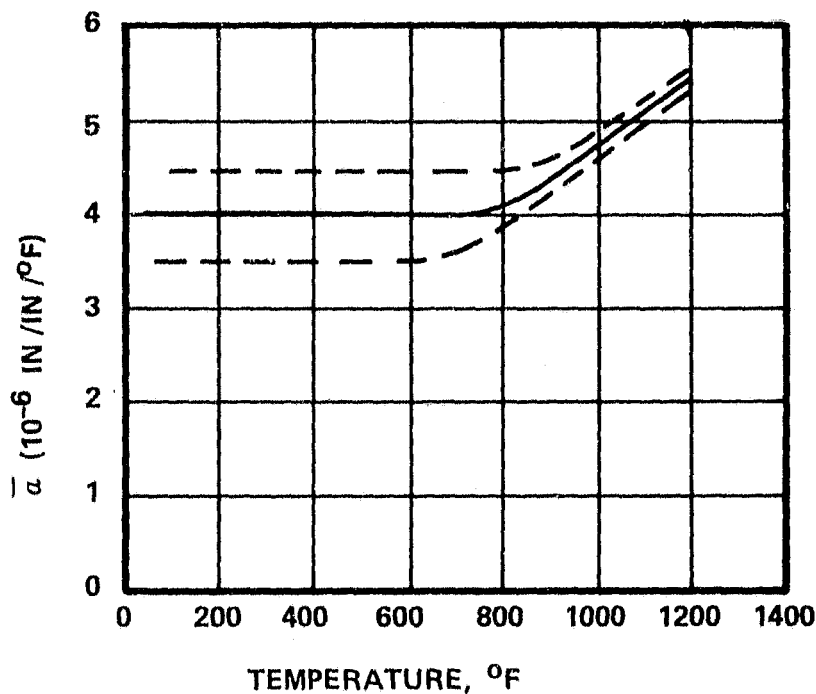
$$\nu = 0.24$$

$$21.29 \times 10^6 < E < 22.34 \times 10^6$$

$$-320^\circ\text{F} \longrightarrow 1200^\circ\text{F}$$

TENSILE PROPERTIES (TYPICAL)

TEMP ($^\circ\text{F}$)	σ_{YP} (PSI)	σ_{ULT} (PSI)	R A (%)
70	160,000	190,000	40
1200	130,000	145,000	55



TYPICAL LOCAL a

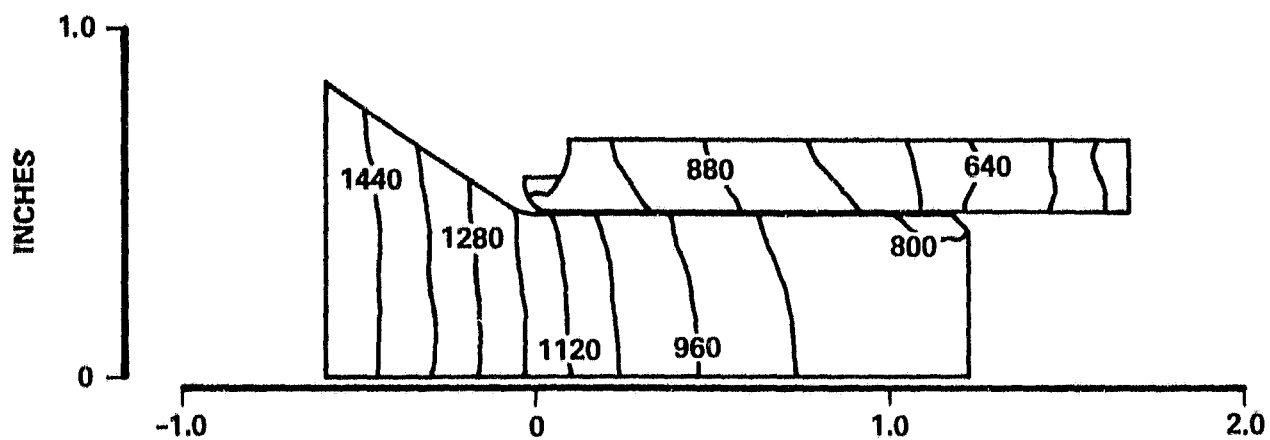
$$a(T) \approx a_0 + a_1 (T-800)$$

$$a_0 = 4 \times 10^{-6}$$

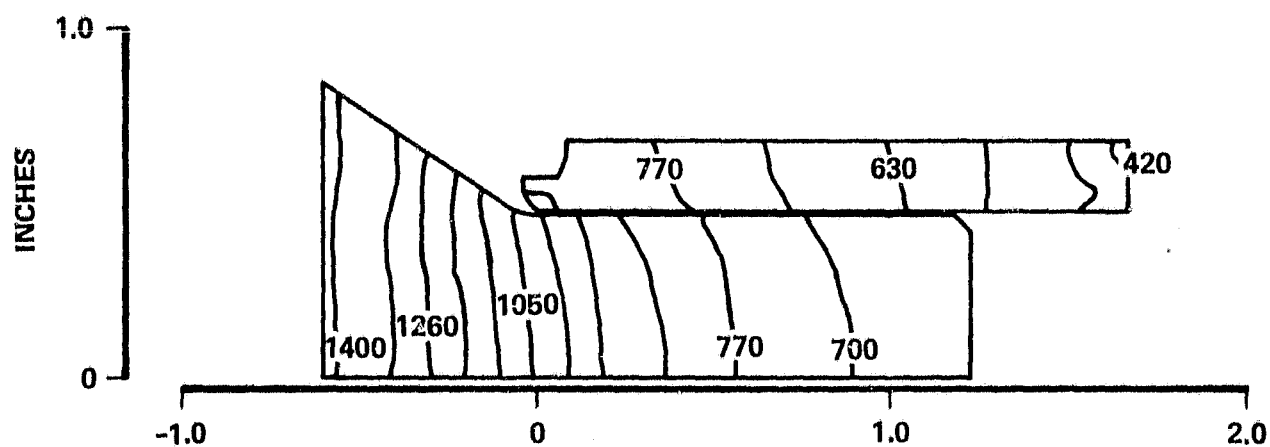
$$a_1 \approx 0.024 \times 10^{-6}$$

REF: HUNTINGTON ALLOYS

Figure 99. IN903 Physical Properties (Ref: Huntington Alloys).



IN903/SASC



IN903/SSN

Figure 100. Steady State Temperature at 100,000 RPM.

(Coulomb) friction coefficient (μ). If $(F_z/F_R) \geq \mu$, an equivalent μF_R force is applied to each surface, and relative slippage is allowed. If $(F_z/F_R) < \mu$, no-slip results. The solution is iterative in nature. Sample results are shown in Figure 101 for a 0.0034 inch shrink-fit. Corresponding differential displacements are shown in Figure 102.

Figure 103 shows differential displacements when temperature and speed effects are imposed from assembly to maximum power for two initial interferences.

Utilization of either SiC or Si₃N₄ as the turbine rotor material has essentially the same effect on the net stress patterns at the interference. Si₃N₄ has a lower coefficient of thermal expansion than SiC, but as shown in Figure 100, Si₃N₄ temperature levels at maximum power are somewhat lower than SiC. These two factors tend to offset each other with respect to resulting contact stresses.

Although the stress patterns are quite similar, differential displacements from assembly to operating conditions vary for the two material considerations, as shown in Figure 104.

Results of the analyses indicate that experimental determination of the friction coefficient versus interference fit is essential to successful application of the selected joining method. A comprehensive test program is being formulated to resolve this parameter. In addition, alternate methods of turbine/compressor/tiebolt shaft loading are being examined. Figure 105 illustrates an alternative.

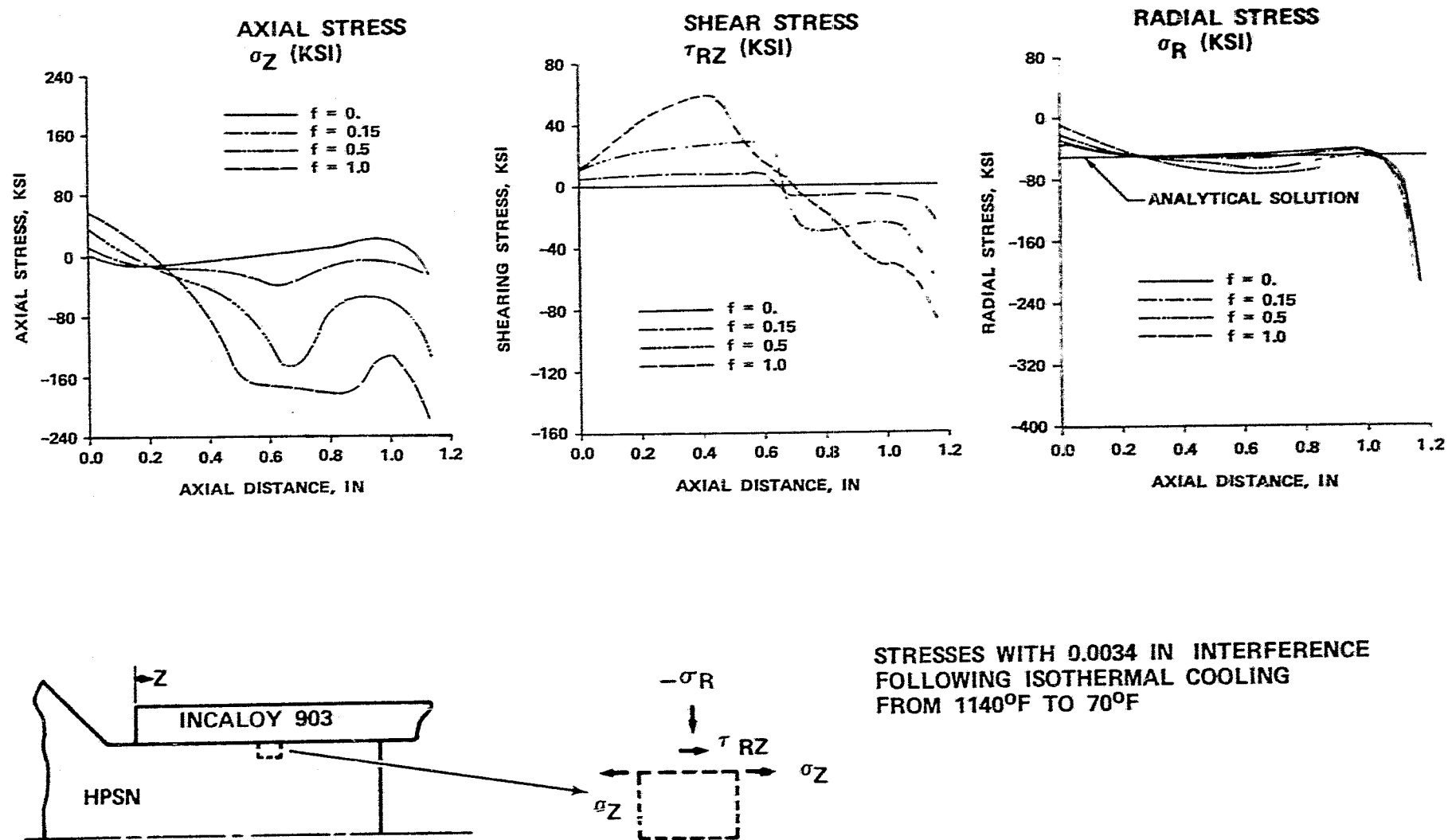
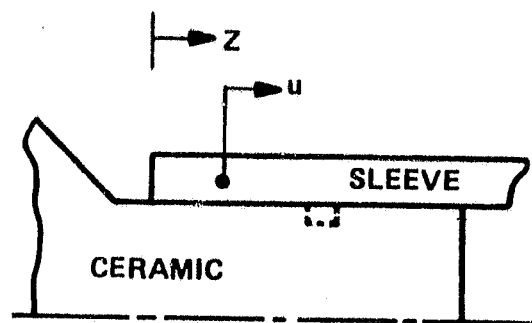
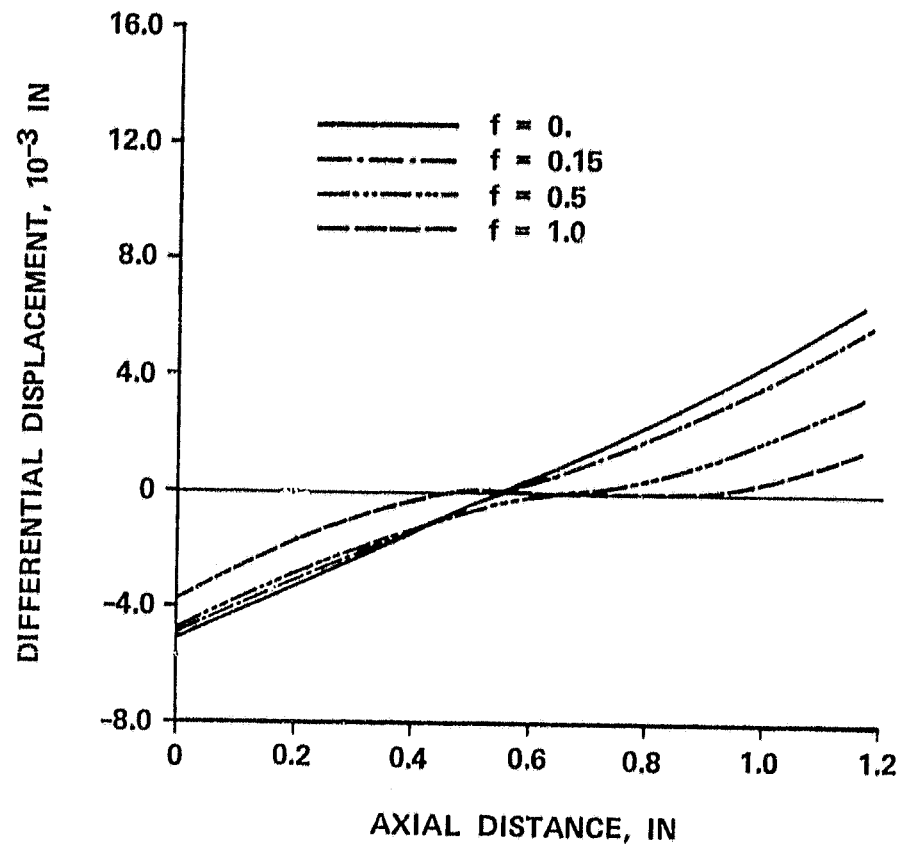


Figure 101. Effects of Friction Coefficients on the Axial Stress (σ_Z) at the Interface (Room State).



Δu = DISPLACEMENT OF CERAMIC
MINUS THAT OF SLEEVE

Figure 102. Effects of Friction Coefficients on the Differential Displacements at the Interface (Room State).

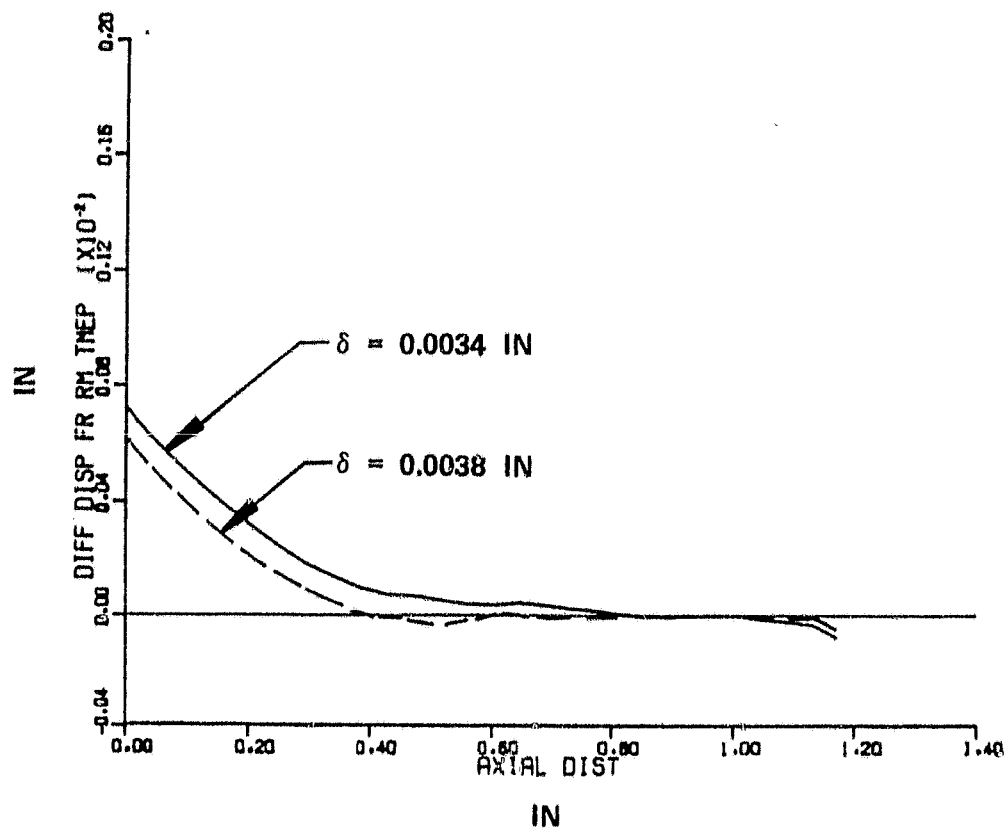


Figure 103. Differential Displacements at the Interface (Room State to Operating State).

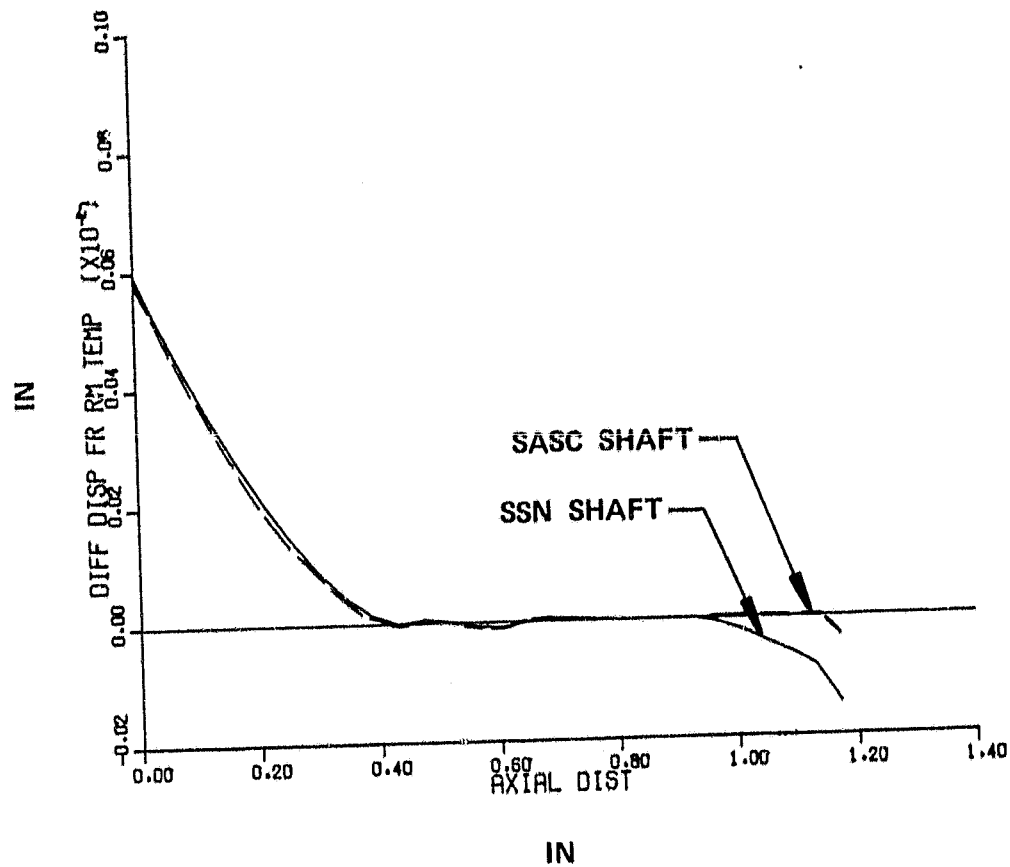


Figure 104. Differential Displacements at the Interface, Room State to Operating State (SSN Shaft - IN903 Sleeve).

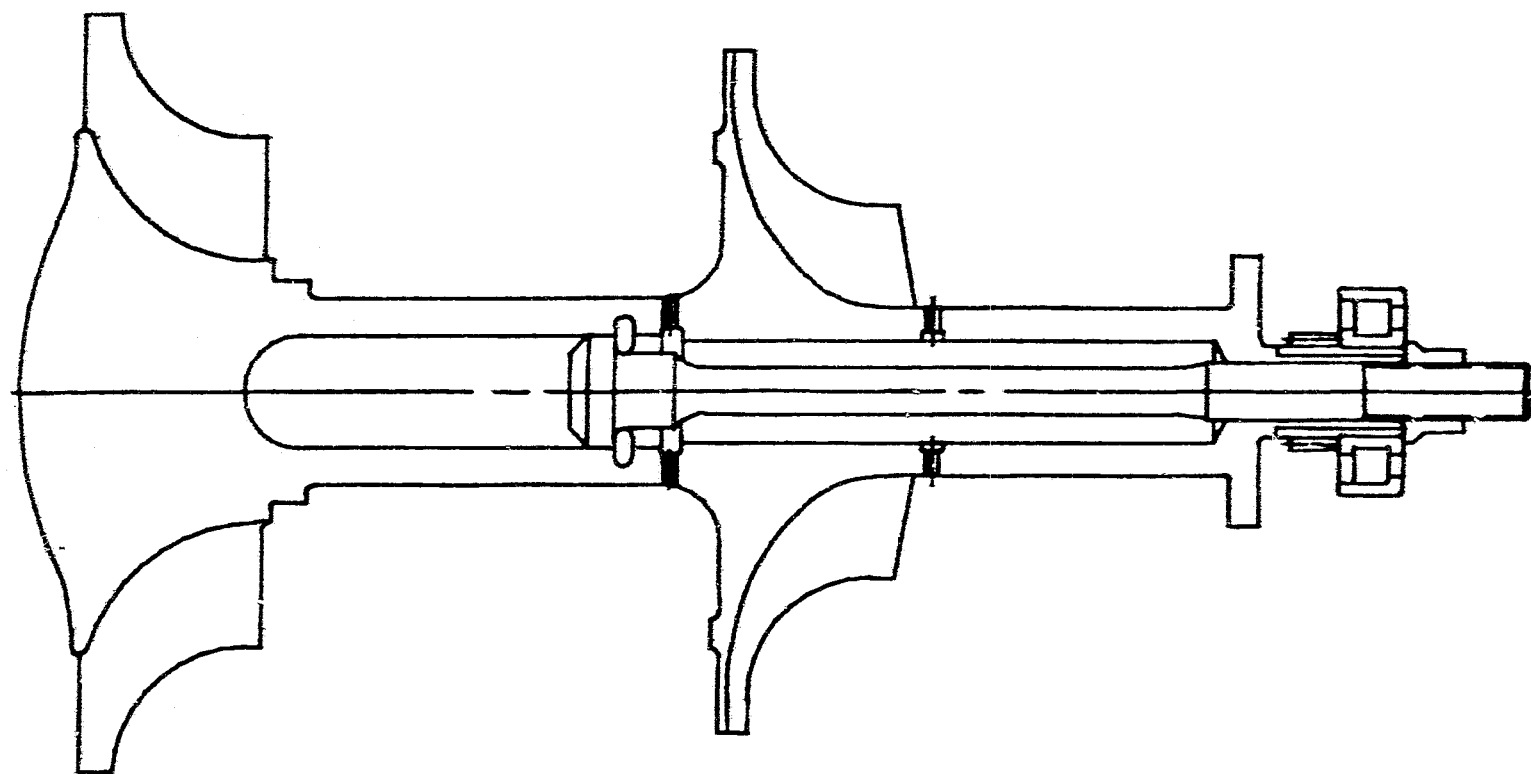


Figure 105. Ceramic Turbine Curvic Attachment.

4.3 Combustion System

4.3.1 Variable Geometry Combustor Design

The variable geometry combustor is shown in Figure 106 and the attendant air flow splits and effective areas as a function of fuel flow are shown in Figure 107. As shown in Figure 108, streamline and isotherms are plotted as a function of axial and radial location for the idle power point. The cross-hatched section represents blockage due to the change in diameter from the vaporizer to the main combustor. The streamline plot shows the large recirculation zone represented by the area under the zero streamline. The large central recirculation zone at idle is created by the swirling flow from the nozzle and should provide a stable combustion region for lean fuel-air ratio idle conditions. The isotherm plot shows that the maximum temperature in the recirculation zone is 1700°K. Similar plots are shown for a maximum power case in Figure 109. The increased flow through the vaporizer has eliminated the central recirculation zone and the reverse flow region is adjacent to step change in cross-sectional area created by the sudden area expansion. The isotherm plot shows that there is a potential problem with early ignition in the vaporizer experimental work on the auto ignition and element test rigs will assist in evaluating this potential problem.

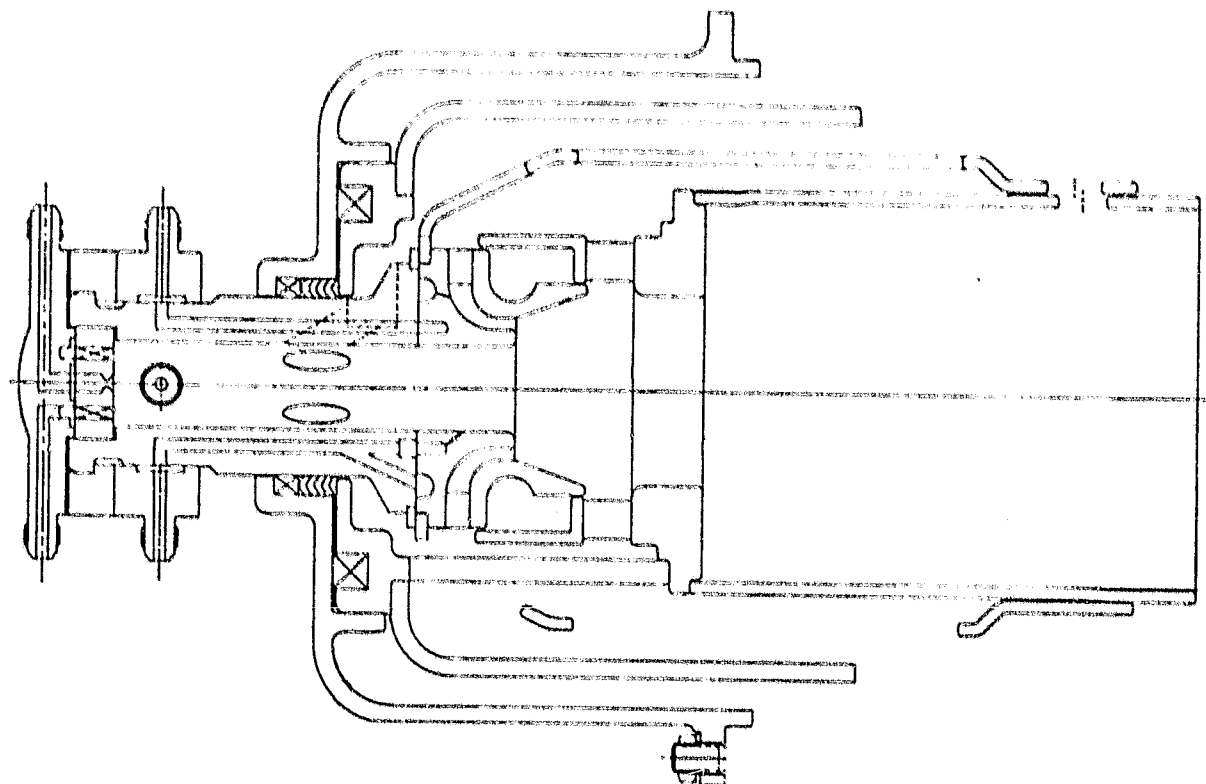
4.3.1.1 Pilot Combustor

To assist in cold starting, a pilot combustor has been designed axially in-line with main combustor. During a start, approximately 20 percent of engine fuel flow is fed to the pilot combustor, a small amount of air is bled from compressor discharge, boosted 1 to 2 psia by an external pump and fed into the dome of the pilot combustor for fuel atomization and combustion. Dilution air for the pilot combustor is supplied from the the main combustor inlet air, while the remainder of the air passes through the main combustor dilution orifices.

The pilot combustor configuration, boost pump airflow, fuel flow split, pilot discharge temperature, and combustor inlet temperature are shown in Figure 110. Based on preliminary performance estimates, the pilot will operate for the first 23 seconds of the start, at which time regenerator discharge temperature is high enough to adequately vaporize fuel in the main nozzle.

4.3.1.2 Variable Geometry Thermal Analysis

A preliminary thermal analysis of the combustor has been completed. The thermal model consisted of analyzing two separate combustor cross sections. One section was the radial plane which includes the webbed section of the sliding outer shell. The second section was the plane which does not intersect the shell.



	<u>MAX POWER</u>	<u>IDLE</u>
PM/PV LENGTH, IN.	0.44 - 2.0	0.14 - 0.68
REFERENCE VELOCITY, FPS	250	56.5
PM/PV RESIDENCE TIME, MS	0.15 - 0.7	0.2 - 1.0
PM/PV AIR, % W_a	59.1	17.1
NOZZLE A/F	20.0	35.4
PM/PV F/A	0.0234	0.0183
PRIMARY ZONE τ , MS	1.33	5.9
LOADING PARAMETER, PPS/FT ³ ATM	0.0197	0.0062

Figure 106. Piloted Premixed/Prevaporizing Variable Geometry Combustor.

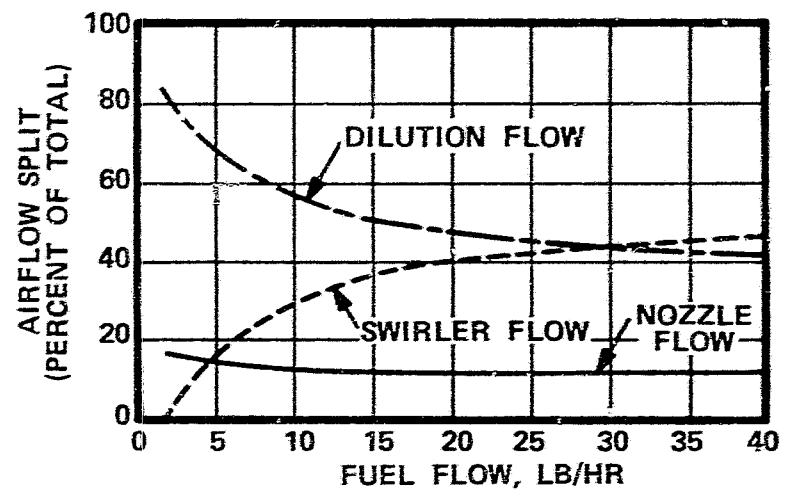
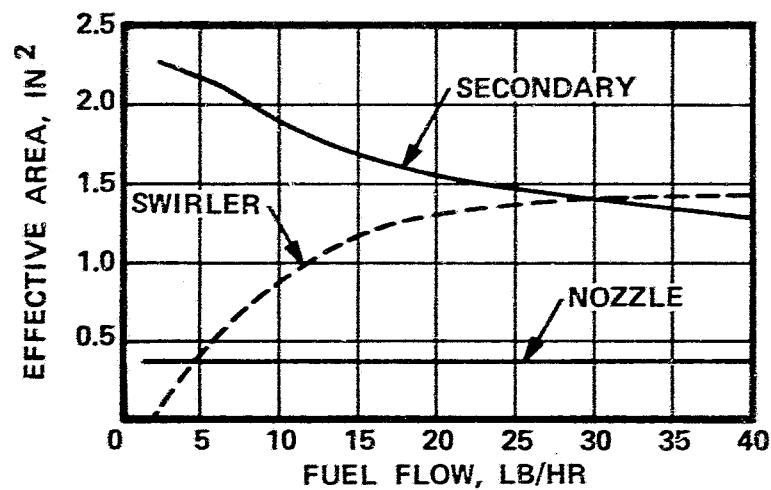


Figure 107. Ideal Effective Areas and Airflow Splits.

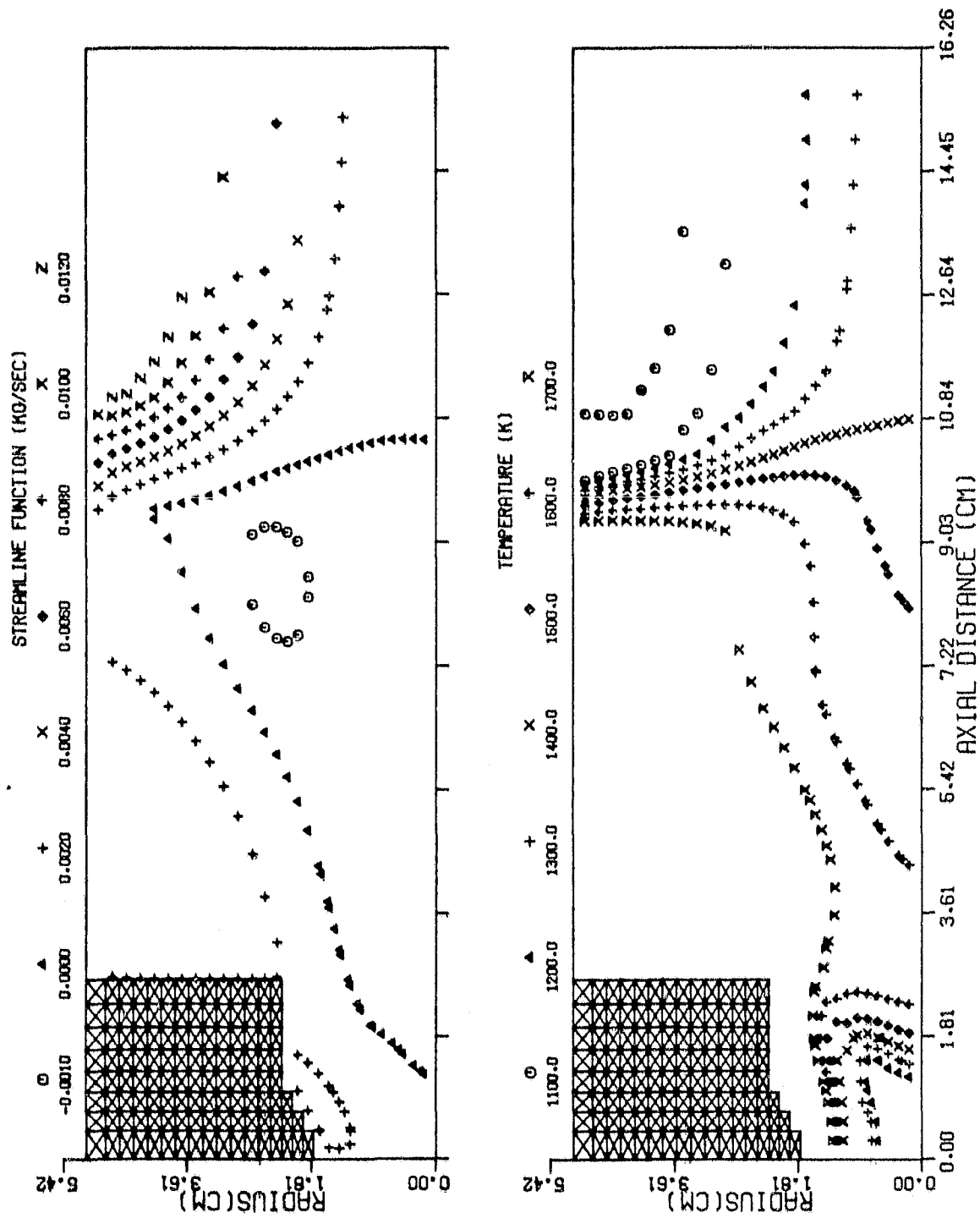
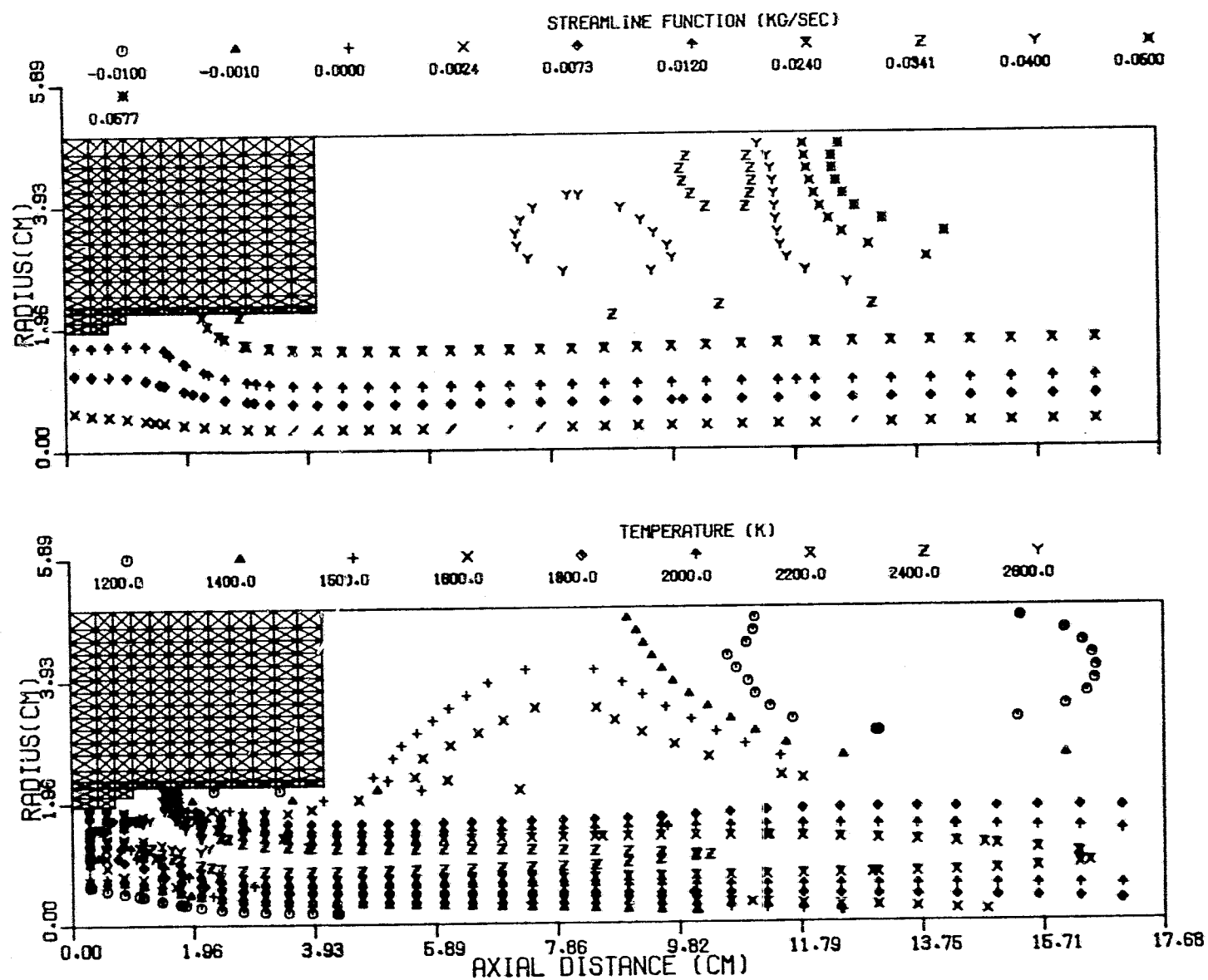


Figure 108. Predicted Profiles at Idle Point.



ORIGINAL PAGE IS
OF POOR QUALITY

Figure 109. Predicted Profiles at Maximum Power Point.

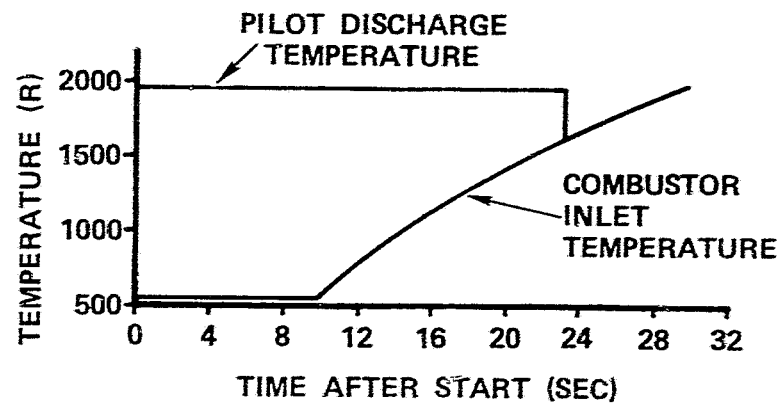
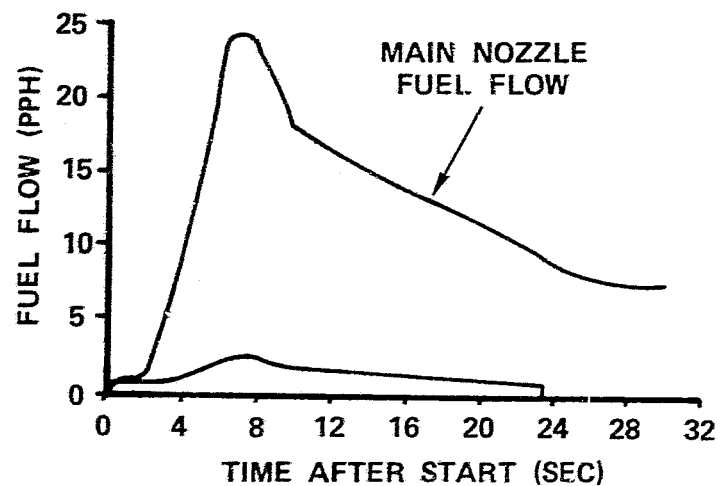
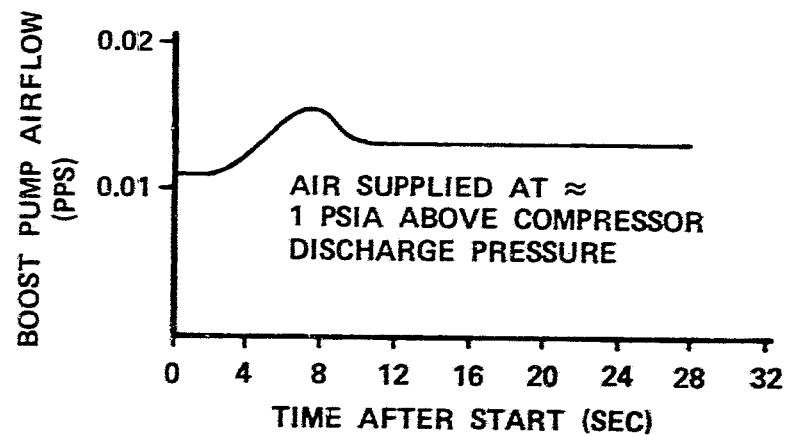
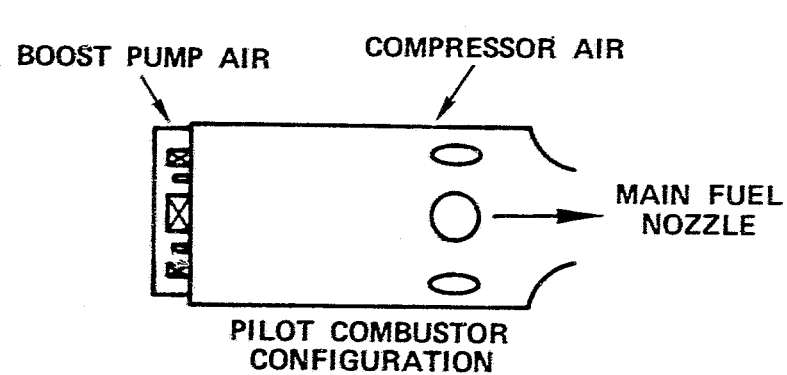


Figure 110. Pilot Combustor.

Figures 111 through 113 show the results of this analysis for the idle power condition (worst case) for three ceramic materials; sintered silicon nitride, sintered silicon carbide, and REFEL silicon carbide.

4.3.2 Diffusion Flame Combustor

To assist in early development (Mod I, Build 1) a scaled version of the Garrett GT601 truck engine combustor design has been completed (Figure 114). The system incorporates the same pilot combustor designed for the variable geometry combustor except that the discharge diameter has been enlarged to decrease the gas velocity into the main burner.

The system is designed to operate with a pressure drop (cold) at maximum power of 3.76 percent while allowing a 2.34-percent pressure drop at idle to provide adequate air blast fuel nozzle operation. Maximum combustor air inlet and discharge temperatures for this system respectively are 1862 and 2059°R. Hastelloy material will be used for fabrication with conventional film cooling used to protect the liner surfaces. Total combustor volume is approximately 0.042 ft³, which results in an overall reference velocity of approximately 84 ft/sec and a loading parameter of 0.103 lb/sec/atm ft³. The overall residence time is 0.0057 second at maximum power, which should result in good combustion efficiency values with minimum CO, HC, and NO_x emissions. Operating parameters of Mod I, Build I, Mod I and GT601 are tabulated in Table 13.

4.3.3 Fuel Nozzles

Work currently is underway on the design and fabrication of fuel nozzles for the AGT101 program. The Delavan Corporation will supply aerated and airblast type fuel nozzles in simplex and duplex designs for the variable geometry combustor. In parallel with this work, Delavan also is developing nozzles for the diffusion flame combustor and the pilot combustor.

All nozzles for use in the variable geometry combustor will incorporate means for fuel cooling and will be configured such that the air swirlers can be changed to optimize atomization and mixing.

4.3.4 Combustion Test Rigs

The following paragraphs describe the test rigs that will be used for AGT combustion system development. The rig description includes rig function and purpose along with the type and placement of instrumentation.

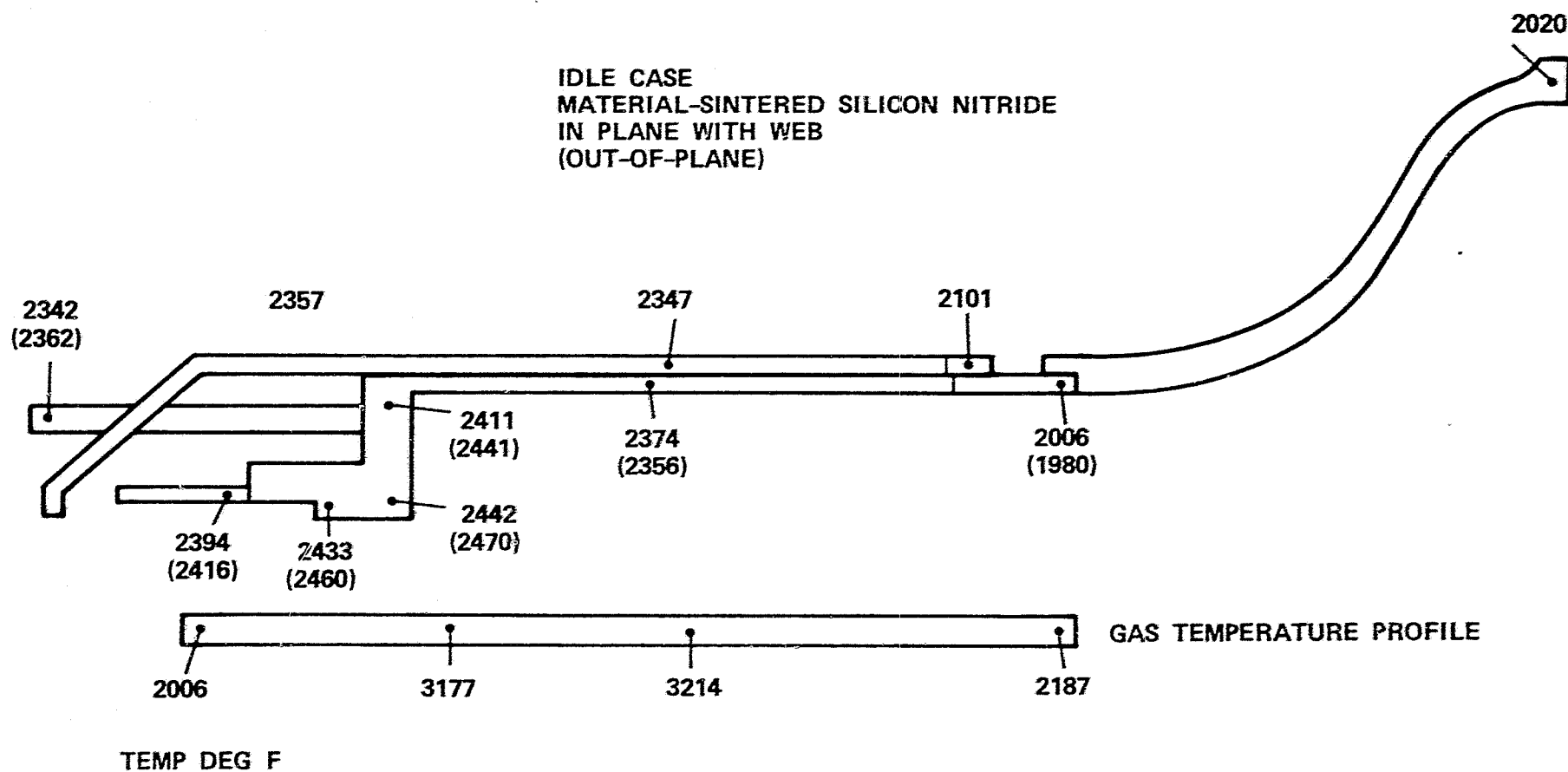


Figure 111. AGT101 Combustor Thermal Analysis.

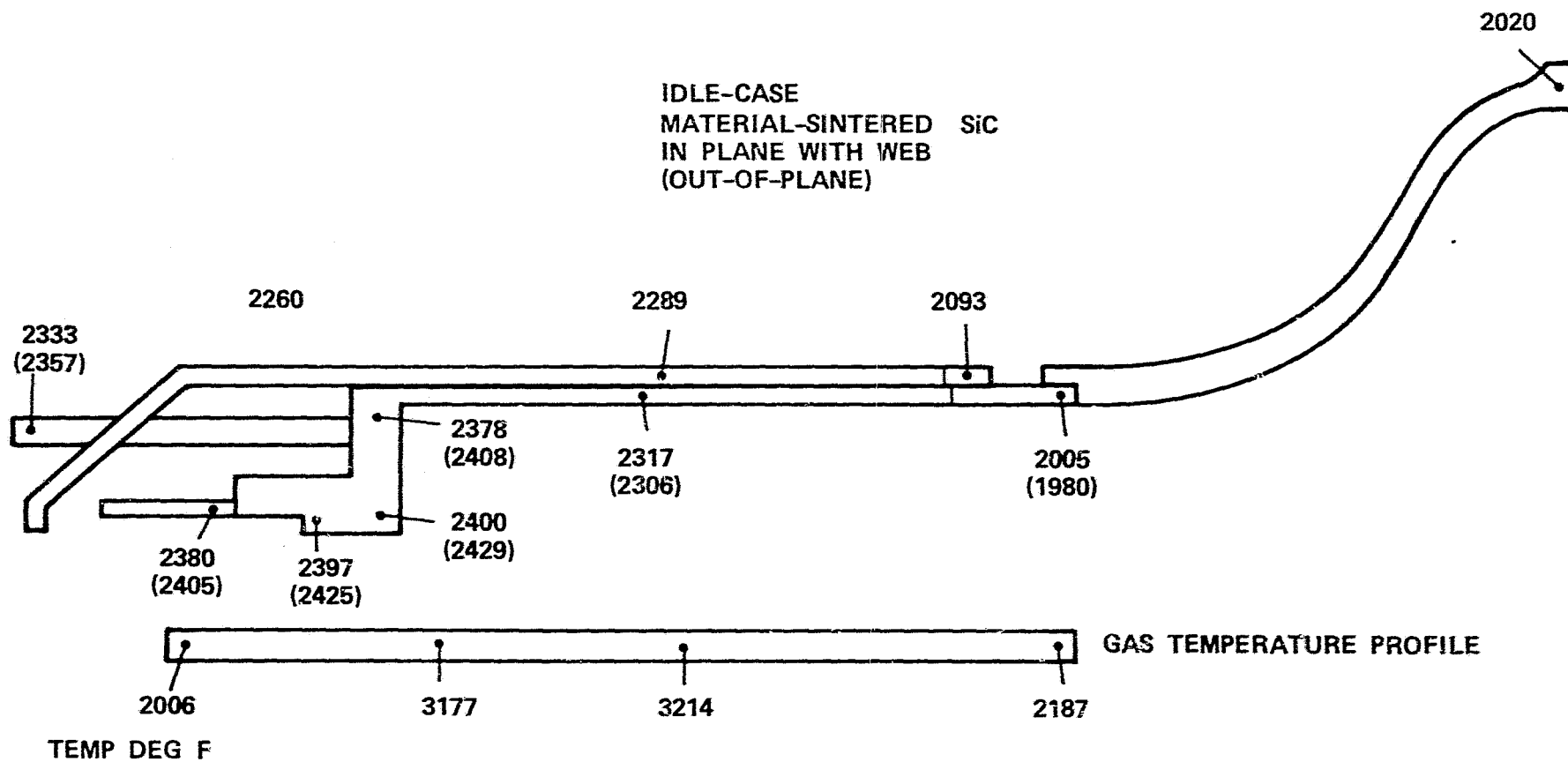


Figure 112. AGT101 Combustor Thermal Analysis.

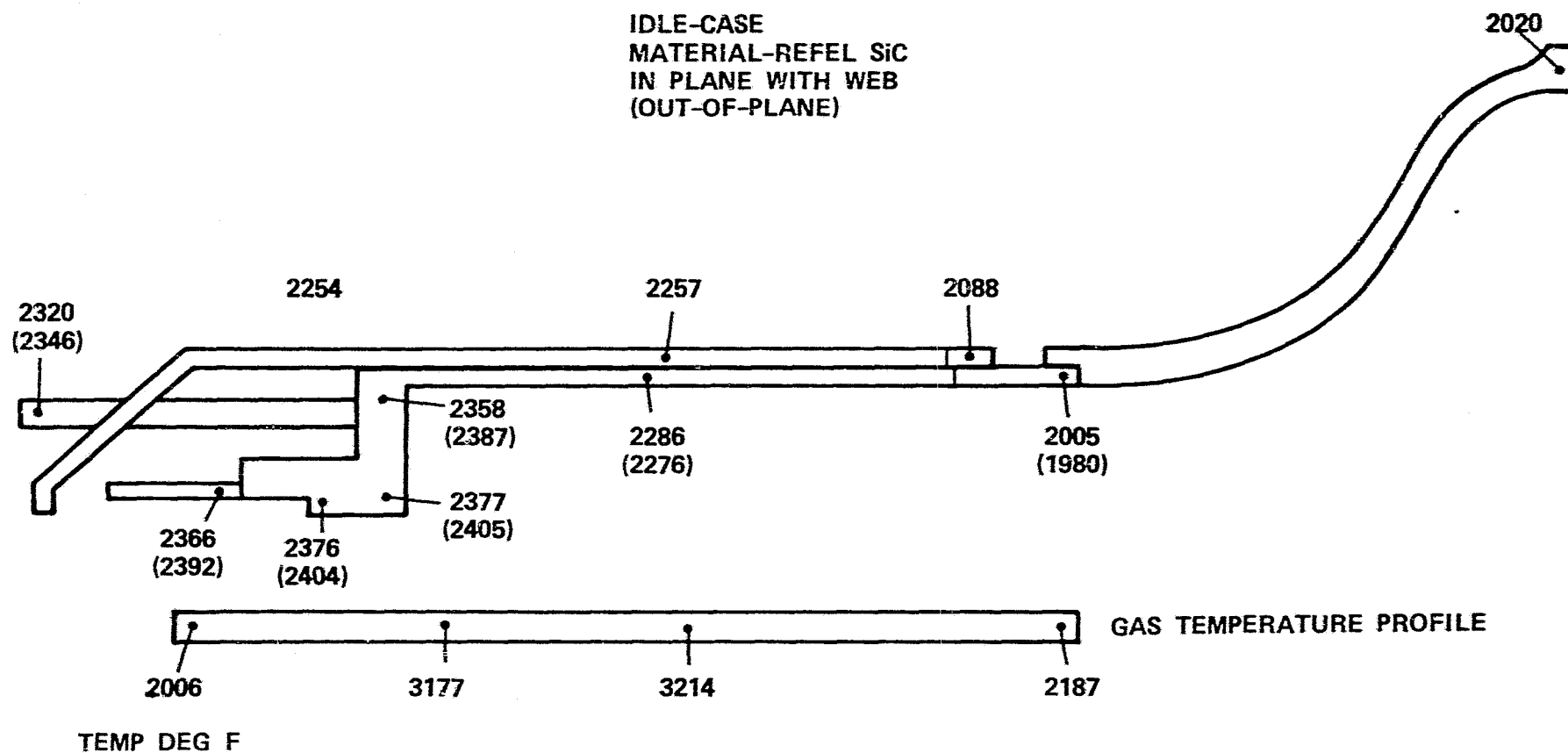
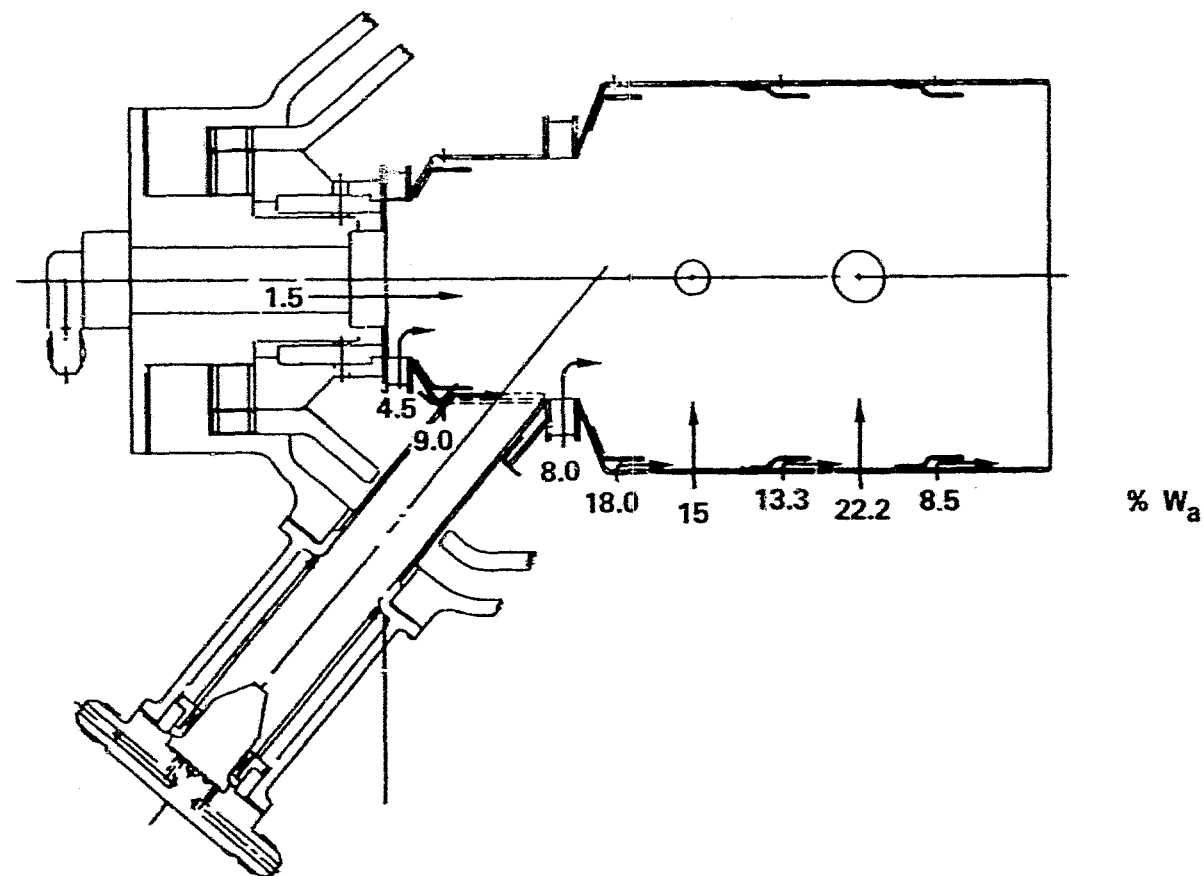


Figure 113. AGT101 Combustor Thermal Analysis.



	MAXIMUM POWER		
	GT601	AGT MOD I BUILD 1	MOD I
REFERENCE VELOCITY	134 FT/SEC	83 FT/SEC	96.5 FT/SEC
LOADING PARAMETER	0.06 LB/SEC/ATM FT ³	0.103 LB/SEC/ATM FT ³	0.045 LB/SEC/ATM FT ³
COMBUSTOR VOLUME	0.176 FT ³	0.042 FT ³	0.042 FT ³
RESIDENCE TIME	0.00645 SEC	0.0057 SEC	0.0049 SEC

Figure 114. Mod I Build 1 Combustion System Preliminary Design.

TABLE 13. DIFFUSION-FLAME COMBUSTOR FLOW CONDITIONS

MAXIMUM POWER	MOD I BUILD 1	MOD I ENGINE	GT601
COMBUSTOR INLET TEMPERATURE, T_{IN} (°F)	1200	1573	1220
INLET PRESSURE, P_{IN} (PSIA)	63.1	67.8	94.3
AIRFLOW RATE, W_a (PPS)	0.841	0.836	4.633
BURNER FUEL/AIR RATIO, F/A	0.0089	0.0113	0.0139
DISCHARGE TEMPERATURE, T_{OUT} (°F)	1786	2287	2092
IDLE POINT			
T_{IN} (°F)	1589	2071	1020
P_{IN} (PSIA)	21.8	20.2	25.8
W_a (PPS)	0.204	0.162	1.39
F/A	0.0031	0.0035	0.0041
T_{OUT} (°F)	1786	2287	1286

4.3.4.1 Autoignition Rig

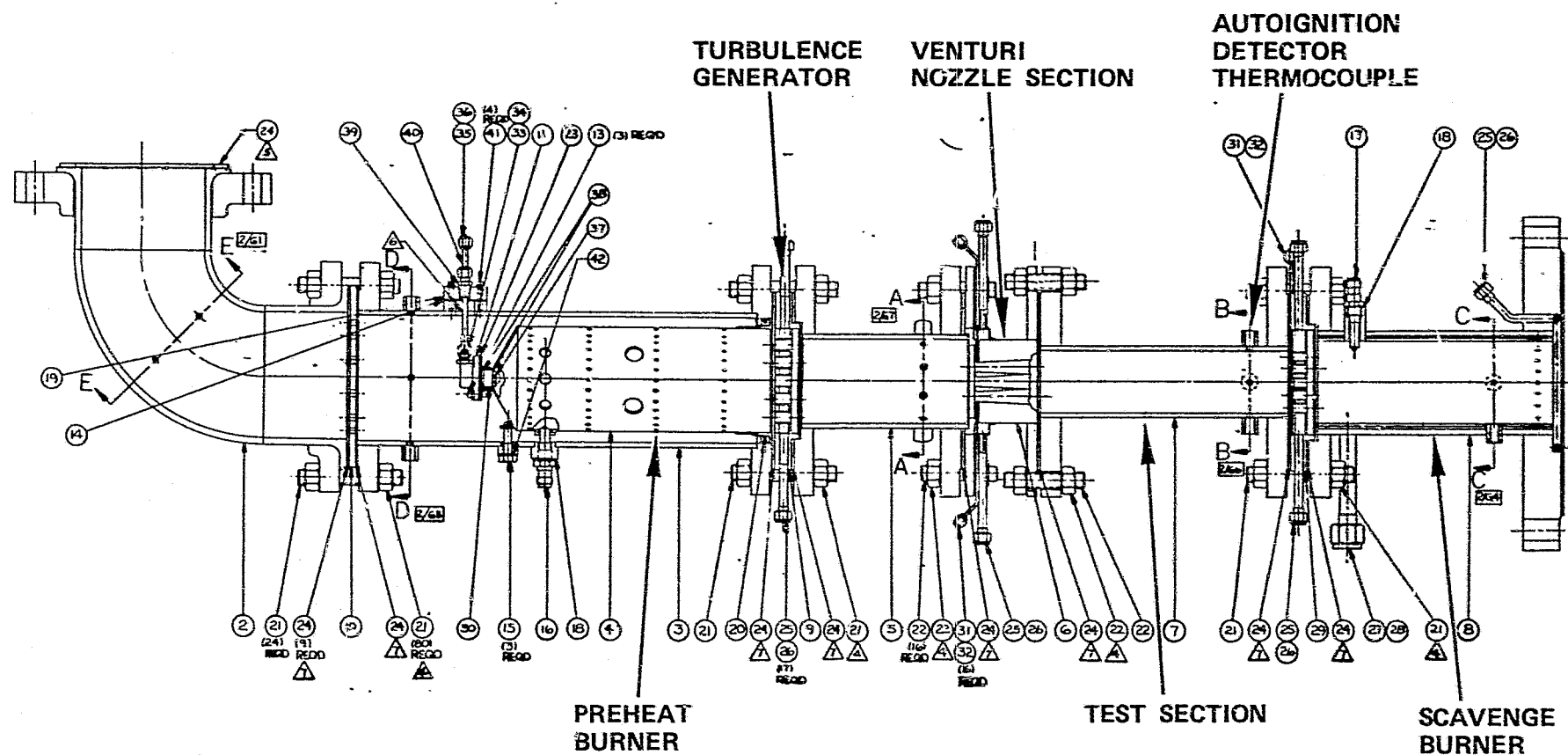
The purpose of the autoignition rig will be to obtain ignition delay data at inlet temperatures and pressures similar to those expected in the AGT combustion system. The data will be used for optimization of the fuel injection-vaporizer design for the AGT variable geometry combustors and further, for comparison with analytical model predictions and evaluations of appropriate reaction rate constants.

A schematic of the autoignition rig is shown in Figure 115. Facility air is supplied to the rig inlet elbow. Before entering the preheat combustor, the air passes through a screen to create a uniform flow distribution to the preheat combustor. The preheat combustor elevates the air temperature to the required level at the fuel injector inlet. Upon leaving the preheat combustor, the air passes through the turbulence generator, simulating different mixing intensities and reducing any temperature or velocity distortion exiting the preheat combustor. Air then is routed to the fuel injection station. The injector, similar to the NASA conical injector, is made of a number of venturis followed by a gradually expanding cone. Fuel is injected into the venturi throat and atomized by the high velocity air. Static pressure and total temperature instrumentation is located just upstream of the fuel injection to verify inlet conditions. In addition to the conical injector the simplex and duplex injectors will be evaluated.

Downstream of the fuel injector are two 6-inch test sections. The test section length can be reduced by one-half by removing one section and placing it between the preheat combustor discharge and the turbulence generator. Changing the test section length will allow investigation of a wider range of residence times. Autoignition is detected by a temperature rise measured by a thermocouple located upstream of the water-cooled flame holder. A scavenge combustor is located downstream to burn fuel when autoignition does not occur.

In summary the testing will cover the following configurations under the listed test conditions:

- o Fuel Injectors: Conical, Simplex and Duplex Airblast
- o Test Section: 6 and 12 inches
- o Pressure Range: 15 to 100 psia
- o Temperature Range: 1000 to 2000°F
- o Equivalence Ratio Range: 0 to 0.7
- o Reference Velocity Range: 50 to 450 fps



ORIGINAL PAGE IS
OF POOR QUALITY

Figure 115. Autoignition Rig Layout.

The above parametric study will result in residence times of 0.5 to 20 milliseconds for conditions similar to the AGT combustor inlet conditions. Residence times less than 0.5 millisecond will not be measured due to approaching sonic conditions in the throat of the venturi fuel injector.

4.3.4.2 Element Test Rig

The element test rig is similar to the autoignition rig. The major purpose of the element test rig is to define the optimum nozzle type and location at idle, and the best flow rate at maximum power. As shown in Figure 116, the fuel injector and test section of the autoignition rig is replaced with a new test section. The new test section simulates the actual fuel injector-vaporizer combination for the variable area combustor and/or diffusion flame combustors. The fuel injector can be positioned at various axial locations. Emissions from the combustion process are taken via a rotating water-cooled probe and the gas concentration levels measured by the following equipment:

o	Hydrocarbons	Beckman Flame Ionization Detector
o	Carbon monoxide	Beckman Model 315B Analyzer
o	Carbon Dioxide	Beckman Model 315B Analyzer
o	Oxides of nitrogen	Thermo Electron Chemiluminescent

All tests requiring emission measurement on any rig will use the above equipment for gas composition.

The element test rig also is fitted with a cooled quartz window for observing flame location, shape, and type. For any portion of testing when the sampling probe and the view port are not being used the thermocouple upstream of the water-cooled flame holder will be used to detect autoignition.

Element rig test results, will determine the optimum fuel nozzle axial location in the vaporizer idle and the correct amount of airflow through the vaporizer air swirler at maximum power. These conditions will be determined by visually observing the flame as well as emission sampling.

4.3.4.3 Combustor Test Rig

A preliminary schematic of the initial full scale combustor rig configuration is shown in Figure 117. This rig will duplicate the flow from the regenerator discharge to the combustor discharge. A

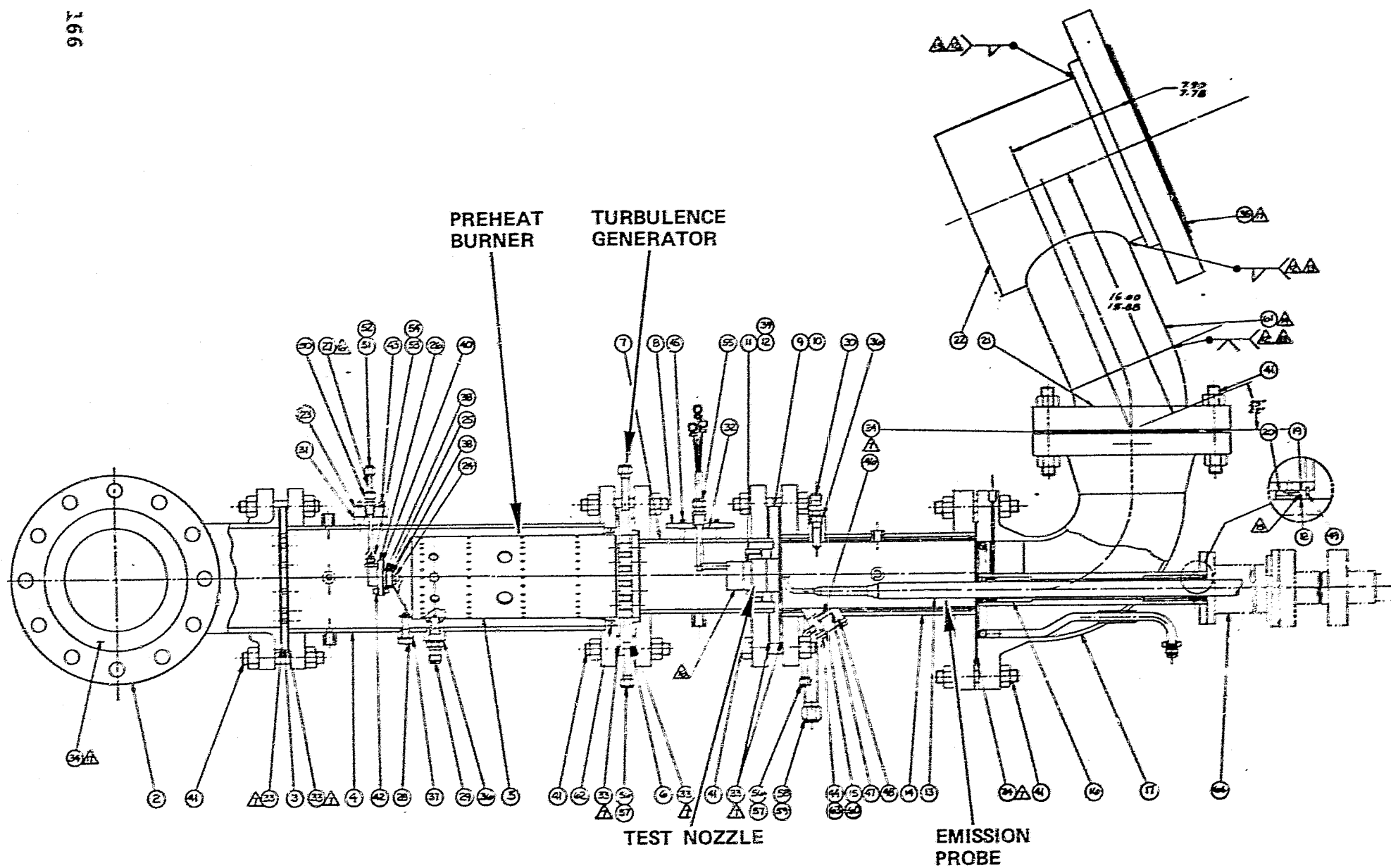


Figure 116. Element Rig Layout.

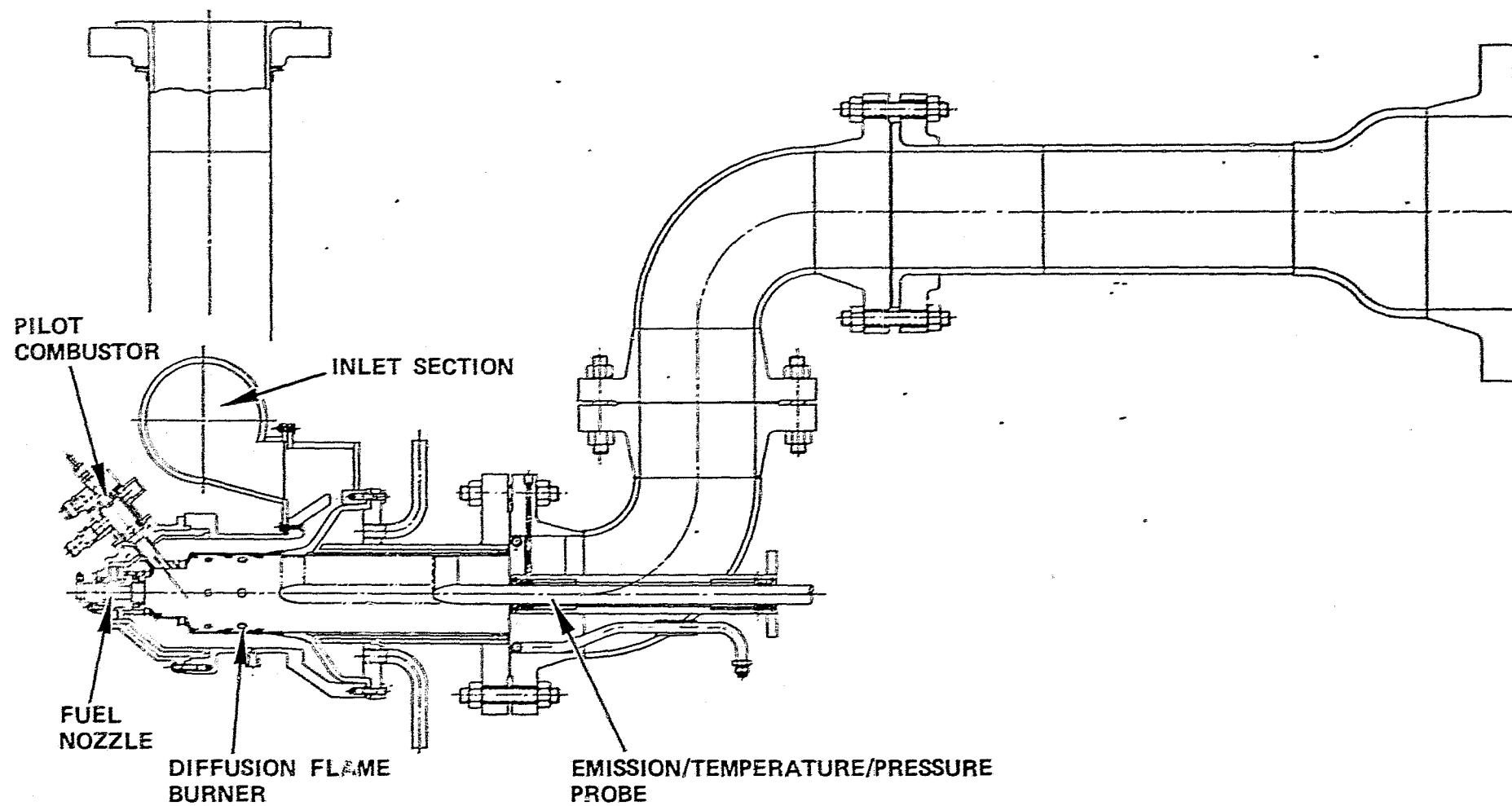


Figure 117. Preliminary Combustor Rig.

screen in the inlet plenum approximates the flow characteristics exiting the regenerator. Thermocouples, kiel probes, and flush pressure taps respectively, will measure combustor inlet temperature and total pressure measurements taken at various axial and circumferential positions. Combustor discharge temperature, pressure and emission levels will be measured by an axially traversing rotating rake. This will allow temperatures and pressures to be recorded at a location corresponding to the inlet of the turbine transition duct, forward limit of the rake. The rearward limit of the rake is a volumetric plane downstream of combustor discharge replicating the flow volume from combustor exit to radial turbine nozzle inlet.

A second version of the combustor test rig, currently in design, fully replicates the engine flow path; in particular, the combustor baffle, transition liner and radial turbine nozzle inlet flow path. Testing with this revised configuration will allow determination of detrimental effects created by the turbine flow path. The stepwise testing facilitates combustion system testing by allowing initial combustor geometry development activities to proceed on a timely basis.

4.4 Regenerator

4.4.1 Ford Regenerator System

The regenerator "system" design, during the last six months, has focused on the following areas:

- o Regenerator Matrix Performance
- o Core Durability
- o Elastomer
- o Mount and Drive
- o Seal Coatings
- o Seal Configuration
- o Seal Stress
- o Regenerator "Pocket"

4.4.1.1 Regenerator Matrix Performance

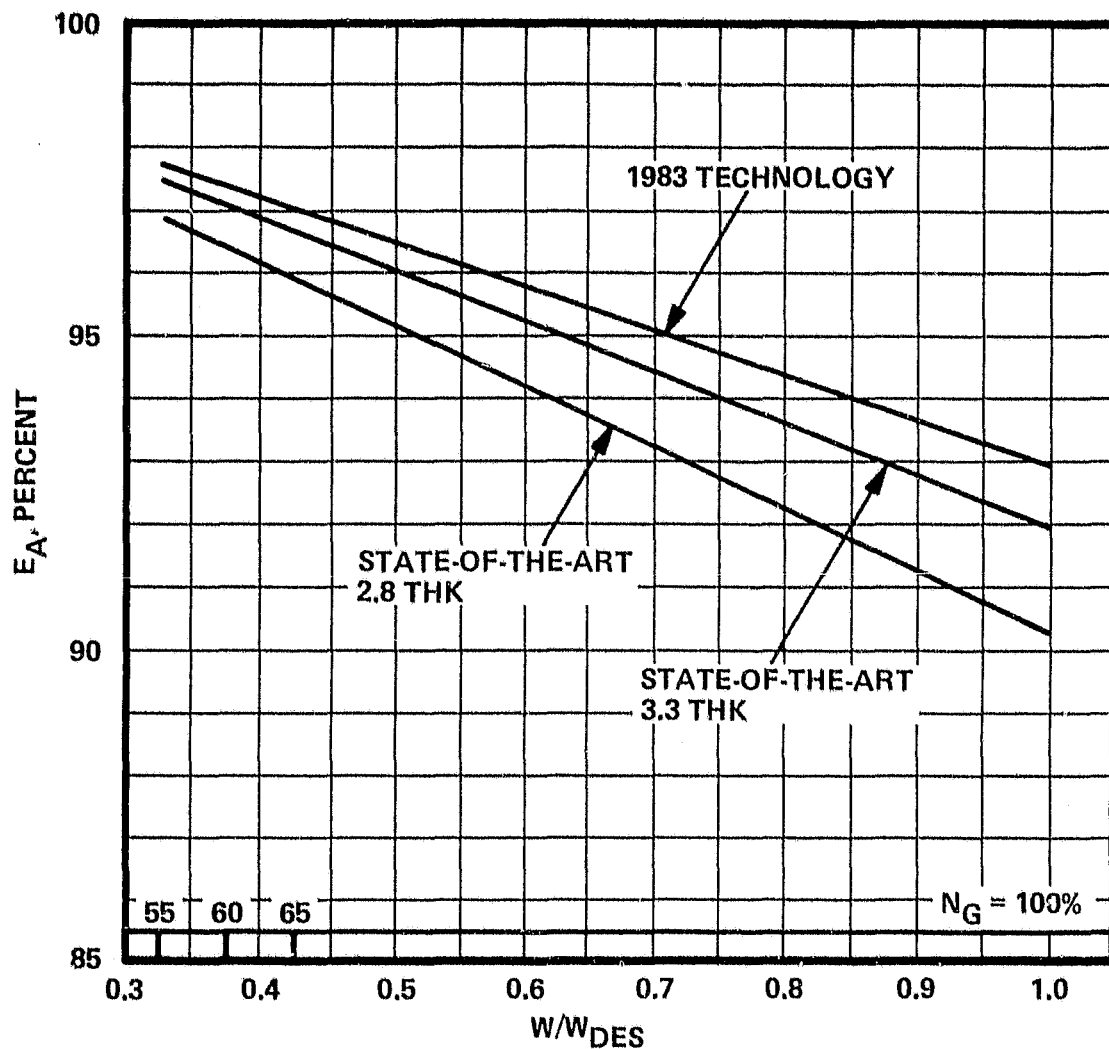
Figure 118 indicates the matrix performance goals established for the AGT program by 1983. Ford shuttle rig tests, used to determine matrix performance, show that to achieve these design goal levels, the regenerator matrix configuration must evolve as follows (Figures 119 and 120):

- o Matrix fin thickness reduced from 0.005 to 0.0025 inch
- o Matrix geometry - extruded rectangular or isosceles triangular
- o Core thickness increase from 2.8 to 3.3 inches for AGT package size

Significant matrix performance improvements over the baseline sinusoidal triangular (2 sheet thin wall) matrix are shown in Figure 119.

4.4.1.2 Core Durability

Regenerator core durability testing under the Ford/DOE/NASA Contract DEN3-8 concludes that Corning's AS and NGK's MAS will meet the 2000°F program objective for a minimum of 3500 hours on the CFDC. Typical durability records for AS and MAS cores as of September 1978



W_{DES} = DESIGN FLOW RATE
 N_G = GAS GENERATOR SPEED

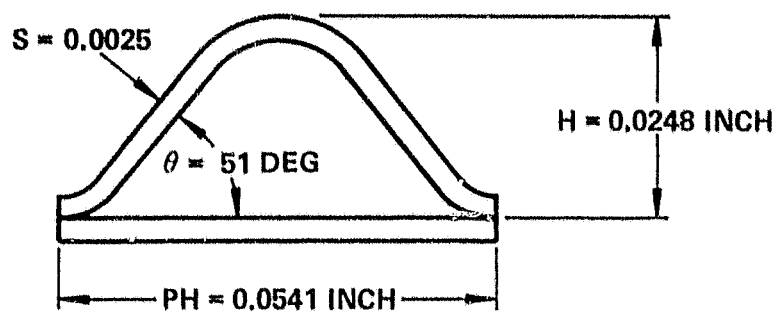
	CURRENT TECHNOLOGY	PROJECTED FOR AGT
EFFECTIVENESS	90.1	92.9
TEMPERATURE	1832°F	2000°F
LEAKAGE	7.2 PERCENT	3.6 PERCENT

Figure 118. Program Goals (at Maximum Power).

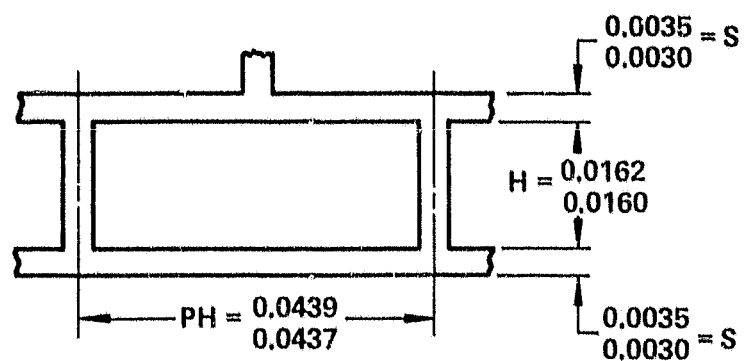
	Effectiveness (Percent)	Pressure Loss (Percent)	Gain on Hot Metro Hwy (Percent)	Gain on CFDC (Percent)
Corning Thin Wall - 2.8 in Thick	90.2	6.3	Base	Base
Corning Thin Wall - 3.3 in Thick	91.9	7.3	+2-2/3	+2-1/4
Extruded Thin Wall - 2.8 in Thick	92.9	7.8	+3-3/4	+3-1/2
Extruded Thin Wall -* 3.3 in Thick	92.9	7.3	+4	+3-1/2
Corning Thick Wall - Las-2.8 in Thick	87.1	6.1	-4-3/4	-4-3/4
NGK Current Fin - 2.8 in Thick	88	5.2	-2-1/4	-1-3/4
NGK Current Fin - 3.3 in Thick	89.9	6	0	+1/2
NR Grace Current Fin -	87.8	8.3	-6.0	-5-1/2

*Selected AGT Geometry

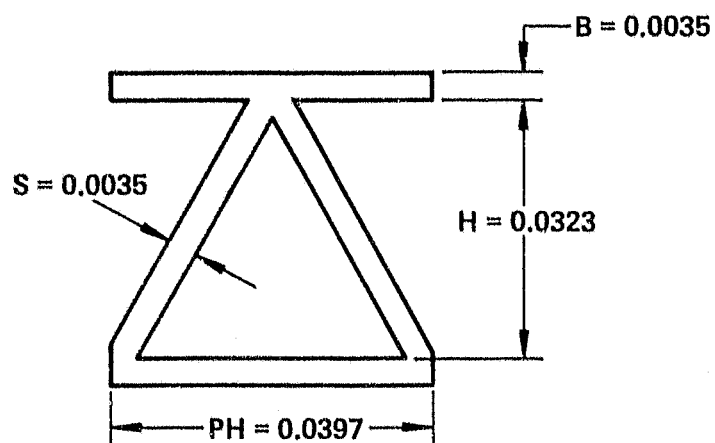
Figure 119. Regenerator Matrix Configuration Comparison.



CORNING THIN WALL WRAPPED



THIN WALL EXTRUSION (CORNING)



THIN WALL EXTRUSION (NGK)

Figure 120. Matrix Fin Configurations.

are shown in Figures 121 and 122. Subsequent data from that program now is being prepared for a final report to be published later.

4.4.1.3 Elastomer

There are two key areas involved in the elastomer bonded ring gear to regenerator matrix design for the AGT application that fall within Ford Regenerator "System" experience. These are: elastomer operating temperature and compliancy.

Figure 123 compares AGT analytically predicted elastomer temperatures with those of the Ford 707 engine. Experience indicates this elastomer will have no difficulty meeting AGT cycle conditions. From the standpoint of compliance, several candidate configurations again have been selected from prior Ford experience. Figure 124 shows the selected configurations in order of increasing compliance. 3-D finite element stress analysis of the AS regenerator outer rim indicates the lower radial MOR of this material in compression requires the higher compliance elastomer design. All three configurations have been successfully tested in the Ford 707 engine on both AS and the higher strength MAS material cores.

4.4.1.4 Mount and Drive

The regenerator mounting and drive system is a derivative of the 707 engine support system. Support roller locations have been optimized as shown in Figure 125 based on the interacting forces of the system as well as ring gear flexure. This optimum configuration minimizes the load concentrated on the pinion and support rollers (Figure 126) and provides a durable system consistent with prior Ford engine experience. A comparison of the AGT mount and drive systems is shown in Figure 127.

4.4.1.5 Seal Coatings

An extensive evaluation of seal substrate temperatures was performed on a 707 engine system in which projections were made for seals at 2000°F gas side core temperatures. This test provided temperature data for all critical seal locations (Figure 128) and was the basis for the seal coating selections of Table 14. Further evaluation of the I-112 coating at 2000°F is scheduled for the hot seal wear rig during the first quarter of FY81. This is the only coating to be used on the AGT that does not have documented durability at the required operating temperature although the material has demonstrated stability at temperatures in excess of 2000°F.

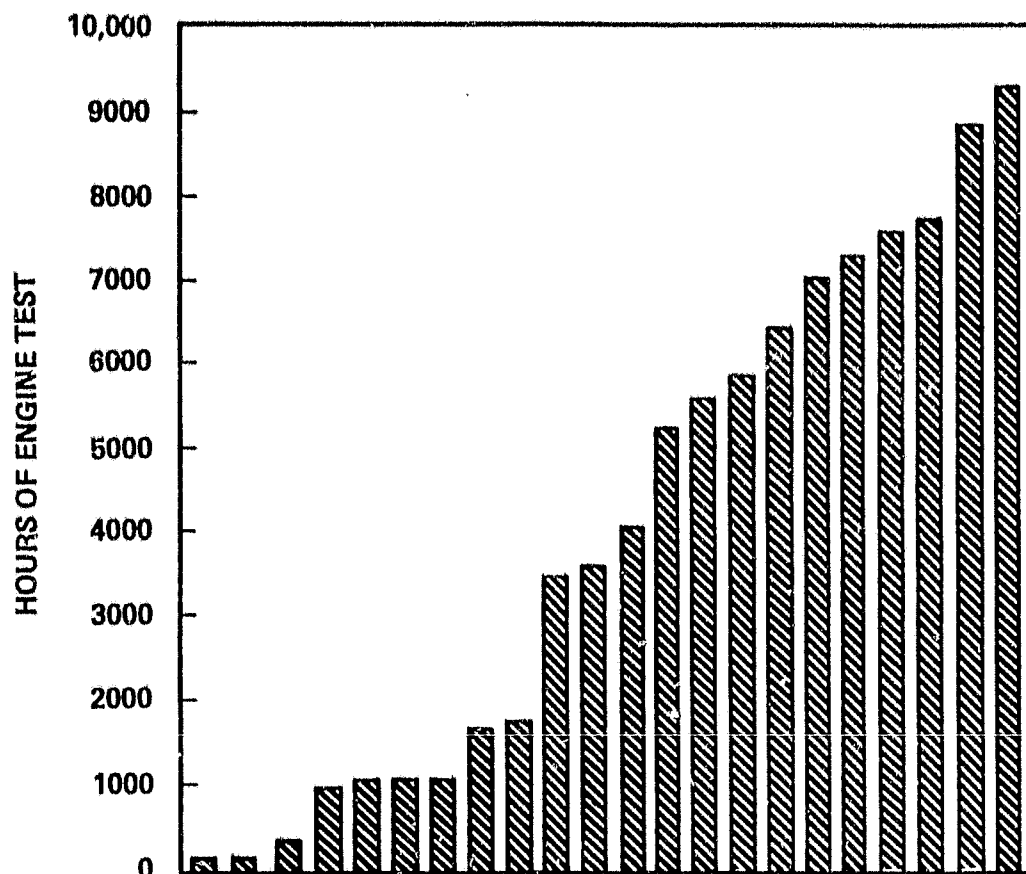


Figure 121. Durability Record of All AS Regenerators Tested in the Ford 707 Turbine Engine.

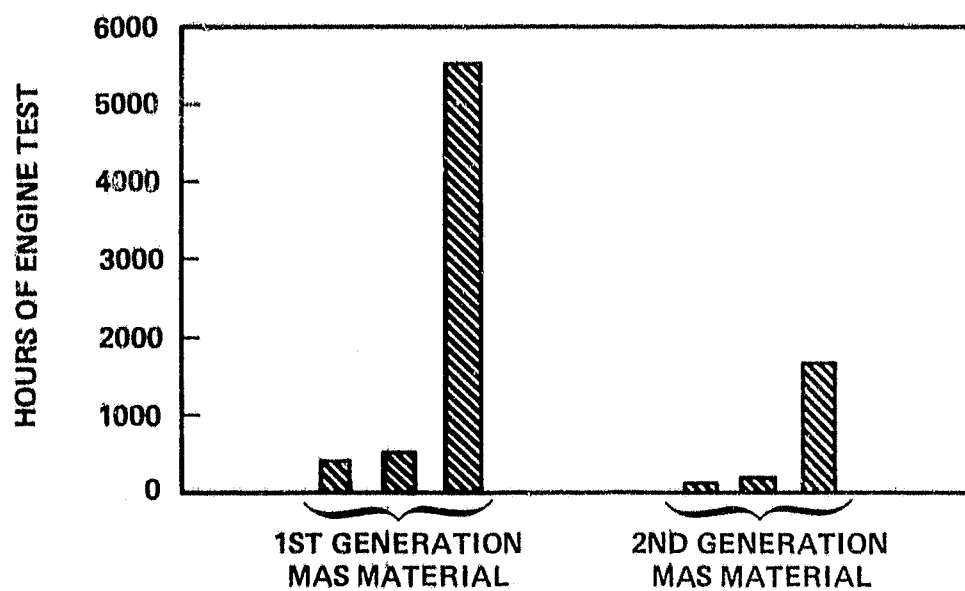


Figure 122. Durability Record of First and Second Generation MAS Regenerators.

CALCULATED ELASTOMER TEMPERATURES

<u>Configuration</u>	<u>Temp (°F)</u>
Ford 707 Standard	550
Ford 707 Undercut Experimental	650
AGT as Metro/Hwy	369
AGT as Wide Open Throttle (WOT)	576
AGT MAS - Metro/Hwy	448
AGT MAS - WOT	651

Figure 123. Calculated Elastomer Temperatures.

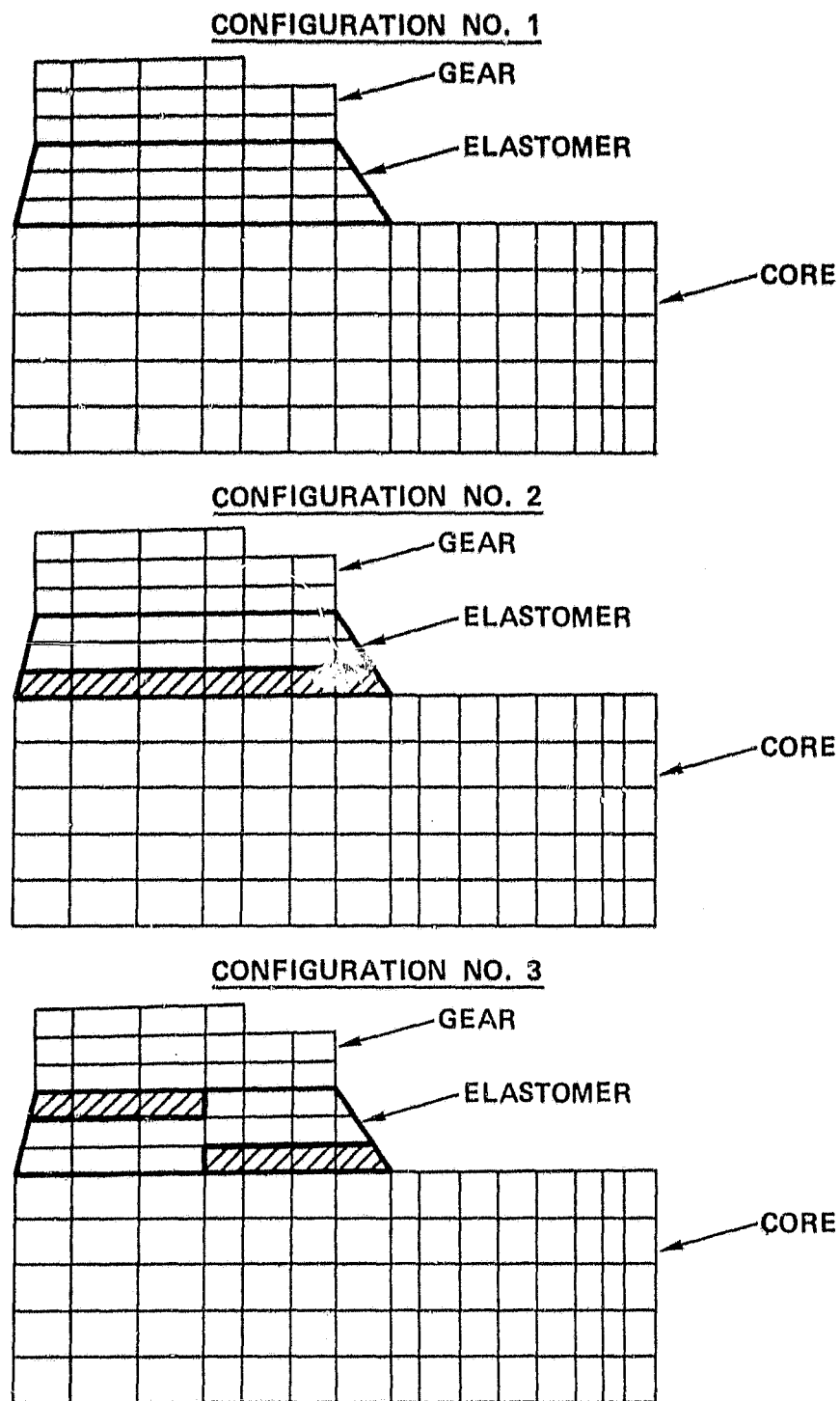
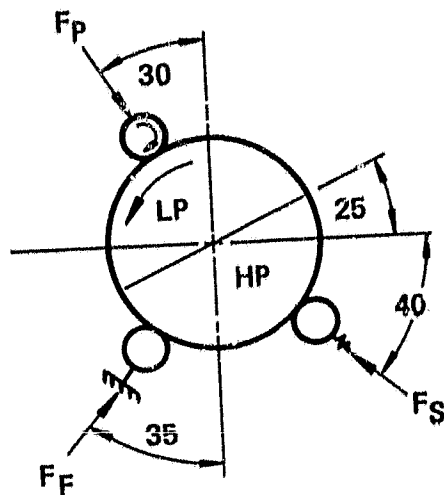
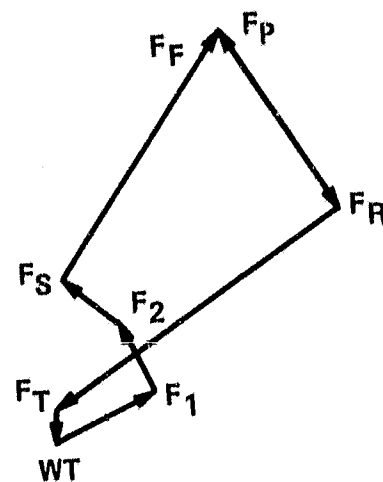


Figure 124. Elastomer-Bonded Ring Gear Configurations.



ALL ANGLES IN DEGREES



(NO FRICTION)

TORQUE = 200 FT-LB

WT = 20 LB

F_R = GEAR SEPARATING FORCE = 86 LB

F_T = GEAR DRIVING FORCE = 239 LB

F_1 = PERIPHERAL SEAL REACTION FORCE = 80 LB

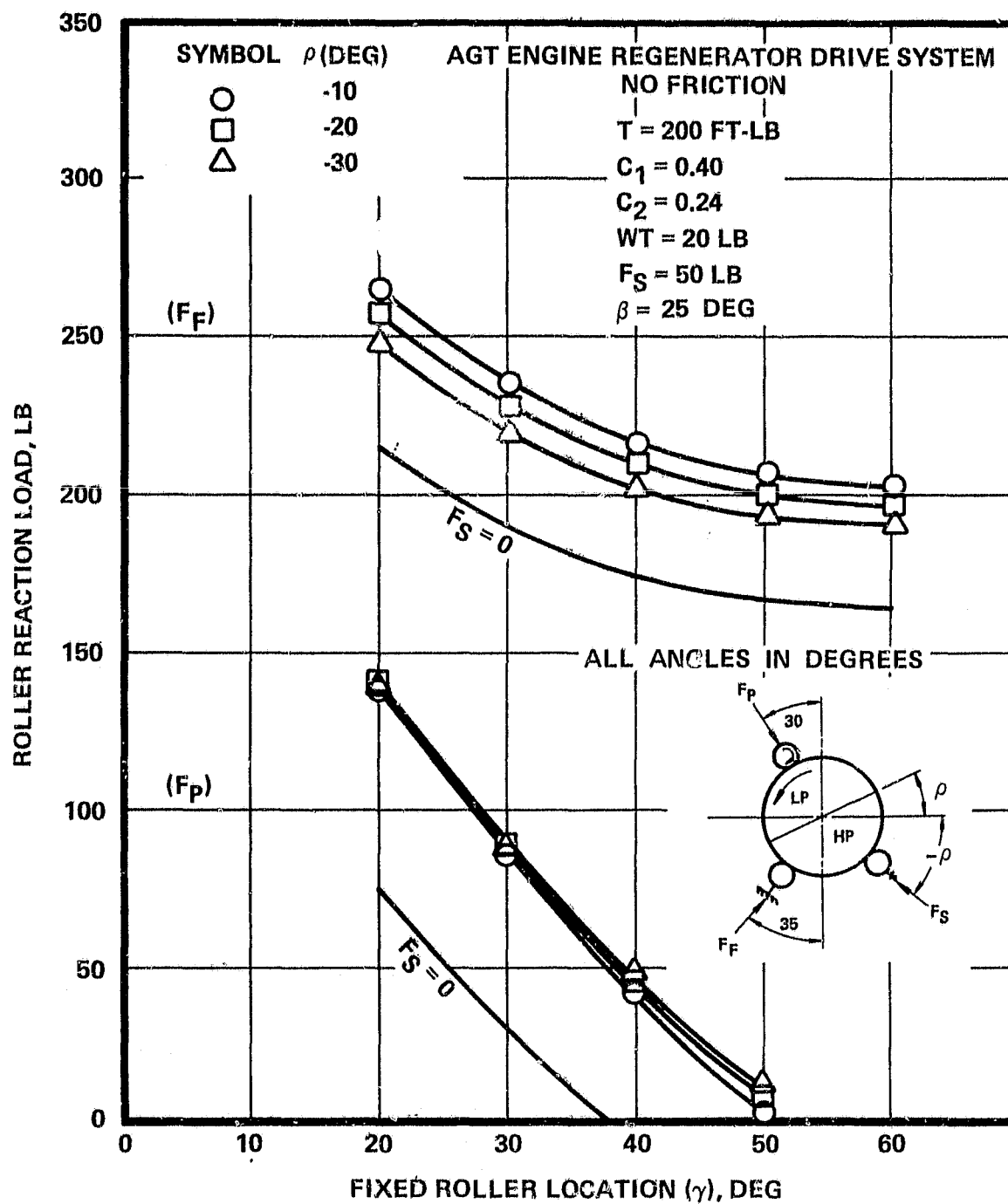
F_2 = CROSSARM SEAL REACTION FORCE = 48 LB

F_S = SPRING ROLLER FORCE = 50 LB

F_F = FIXED ROLLER FORCE = 200 LB

F_P = PINION ROLLER FORCE = 64 LB

Figure 125. Regenerator Support Roller Locations.



ρ = SPRING ROLLER LOCATION

Figure 126. Regenerator Support Loads.

	FORD 707	AGT
DRIVE TORQUE	550 FT LB	200 FT LB
CORE ROTATIONAL SPEED	15	25
CORE RIM SPEED	112 FT/MIN	117 FT/MIN
DRIVE HP	1.57	0.95
SPRING ROLLER LOAD	50 LB	50 LB
PINION LOAD	185 LB	110 LB
FIXED ROLLER LOAD	360 LB	245 LB
NO OF TEETH	42 X 417	30 X 349
D.P. & PRESSURE ANGLE	14 and 20 DEG	18 and 22.5 DEG
GEAR BENDING STRESS	12,139 PSI	10,052 PSI
GEAR COMPRESSIVE STRESS	72,794 PSI	69,012 PSI
GEAR TIP PV FACTOR	14,401	11,625

Figure 127. Drive and Mounting System Comparison.

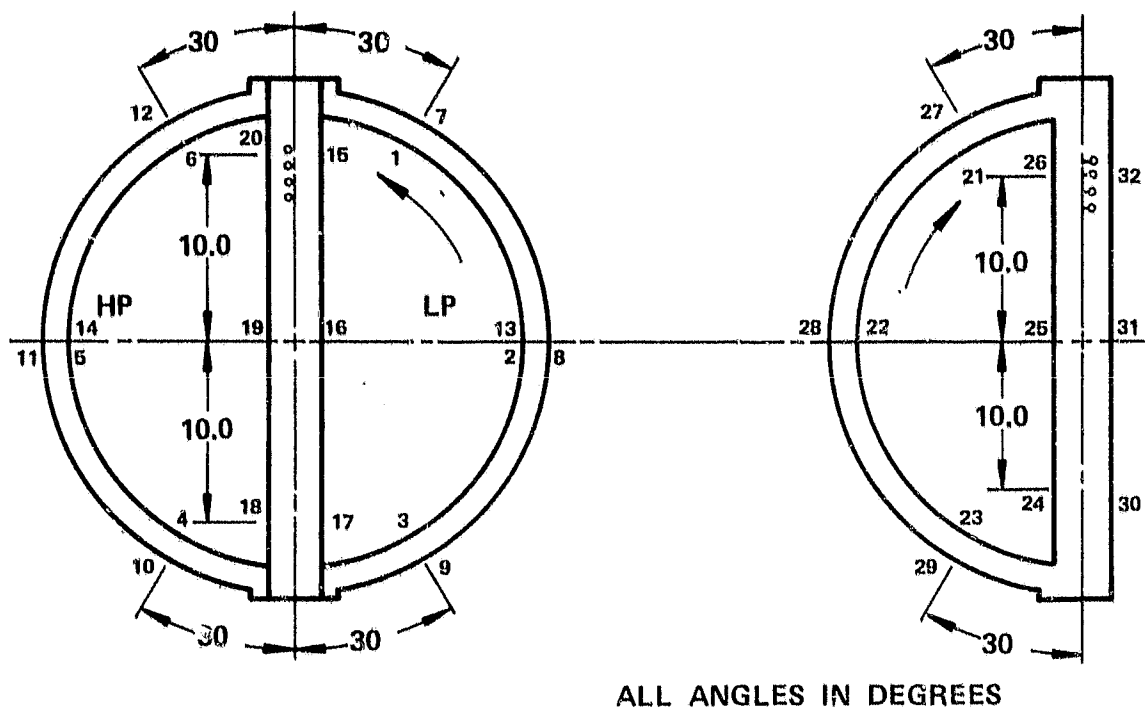


Figure 128. Ford 707 Seal Temperatures.

TABLE 14. AGT101 SEAL COATINGS

Seal Component	Current Ford Coating	AGT Coatings	Method of Application
1. INNER SEAL			
A. High Pressure "C" Show	I-85	I-112 or I-151	Plasma Spray
B. Low Pressure "C" Show	I-85	I-112 or I-151	Plasma Spray
C. Cross-Arm			
1. HP Carry-Over	I-112	I-112	Plasma Spray
2. LP Carry-Over	I-112	I-112	Plasma Spray
2. OUTER SEAL			
A. Periphery	II-26	I-85	II-26 Temperature and Pressure Bonded I-85 Plasma Sprayed
B. Cross-Arm			
1. HP Carry-Over	II-26	I-85	Plasma Spray
2. LP Carry-Over	I-85	I-112 or I-151	Plasma Spray

4.4.1.6 Seal Configuration

Several inner seal configurations were analyzed for AGT usage as shown in Figure 129. The analysis looked at a variation in flow split from the HP to LP sides and concluded that although a slight gain in effectiveness might be achieved at high power factor operation (i.e., WOT), the added seal complexity and cost could not be justified. Configuration 1 with an equal flow split therefore has been selected for AGT application.

4.4.1.7 Seal Stress

Regenerator seal shoe stress has been calculated for the X-arm location where the combination of temperature and pressure differential create a high stress picture. Figure 130 shows the stress level variation in the inner seal X-arm as a function of temperature and pressure - the LP carry over position having the highest temperature.

The seal diaphragm design has been based on Ford experience. The major consideration in this regard has been with the design of an air cooled inner seal X-arm (LP carry over) configuration (Figure 131) that incorporates a third diaphragm to form a cooling air passage. Cooling air requirements have been analytically predicted (Figure 132) to be approximately 0.1 percent of engine flow. This will be confirmed on the hot regenerator rig during FY81. Diaphragm stress levels are significantly reduced by cooling in this region and are not expected to hinder seal life.

4.4.1.8 Ford Regenerator System Summary

Performance

- o Extruded matrix meets effectiveness objective
- o Leakage rig indicates objective can be met

Core Durability

- o Cornings AS and NGKs MAS meet 2000°F objective

Elastomer

- o Will exceed 5000 hours at 2000°F and 1000 hours at WOT

Mount and Drive

- o Will exceed 5000 hours at 2000°F and 1000 hours at WOT

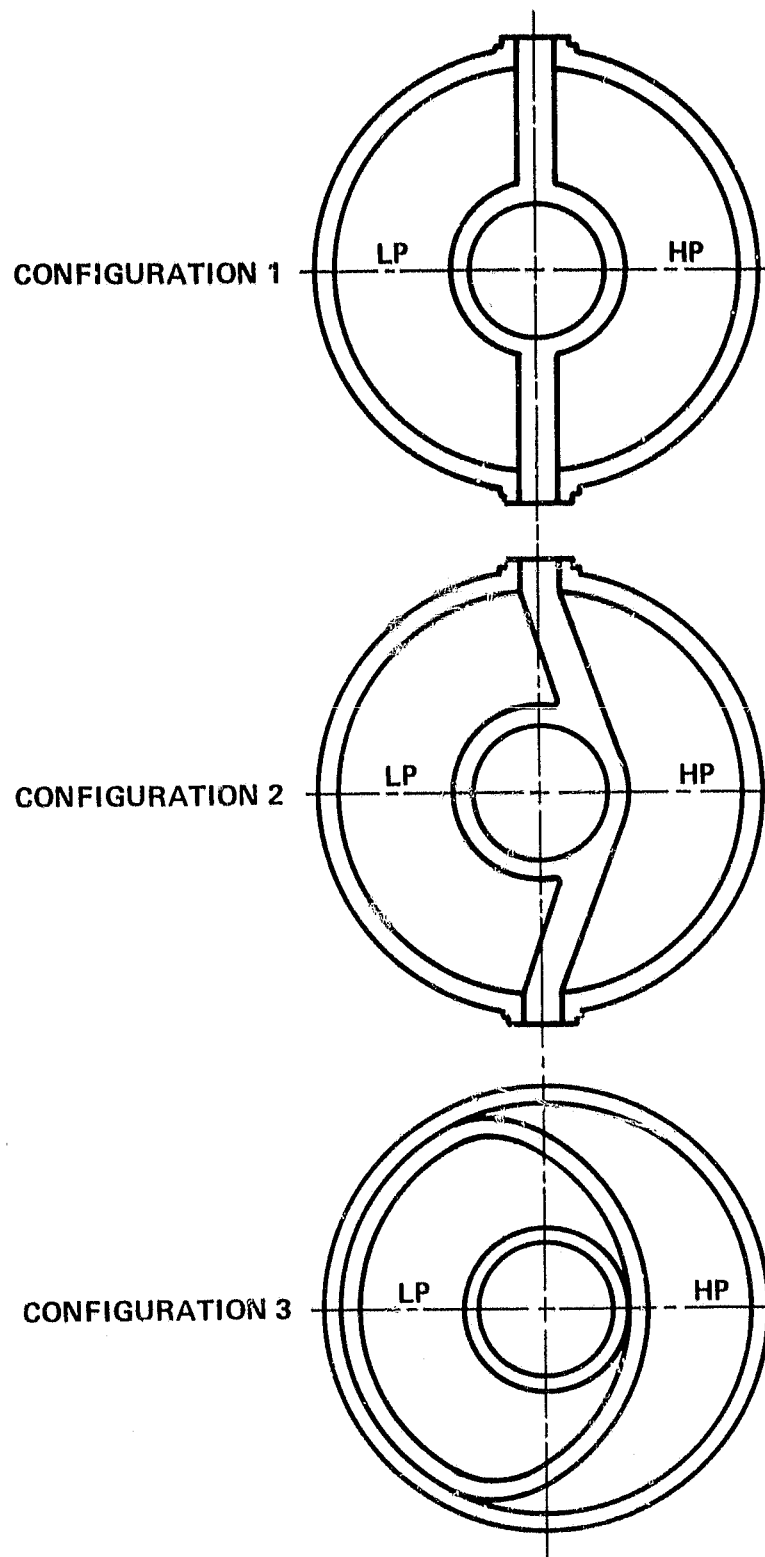


Figure 129. AGT101 Inner Seal Configuration Study.

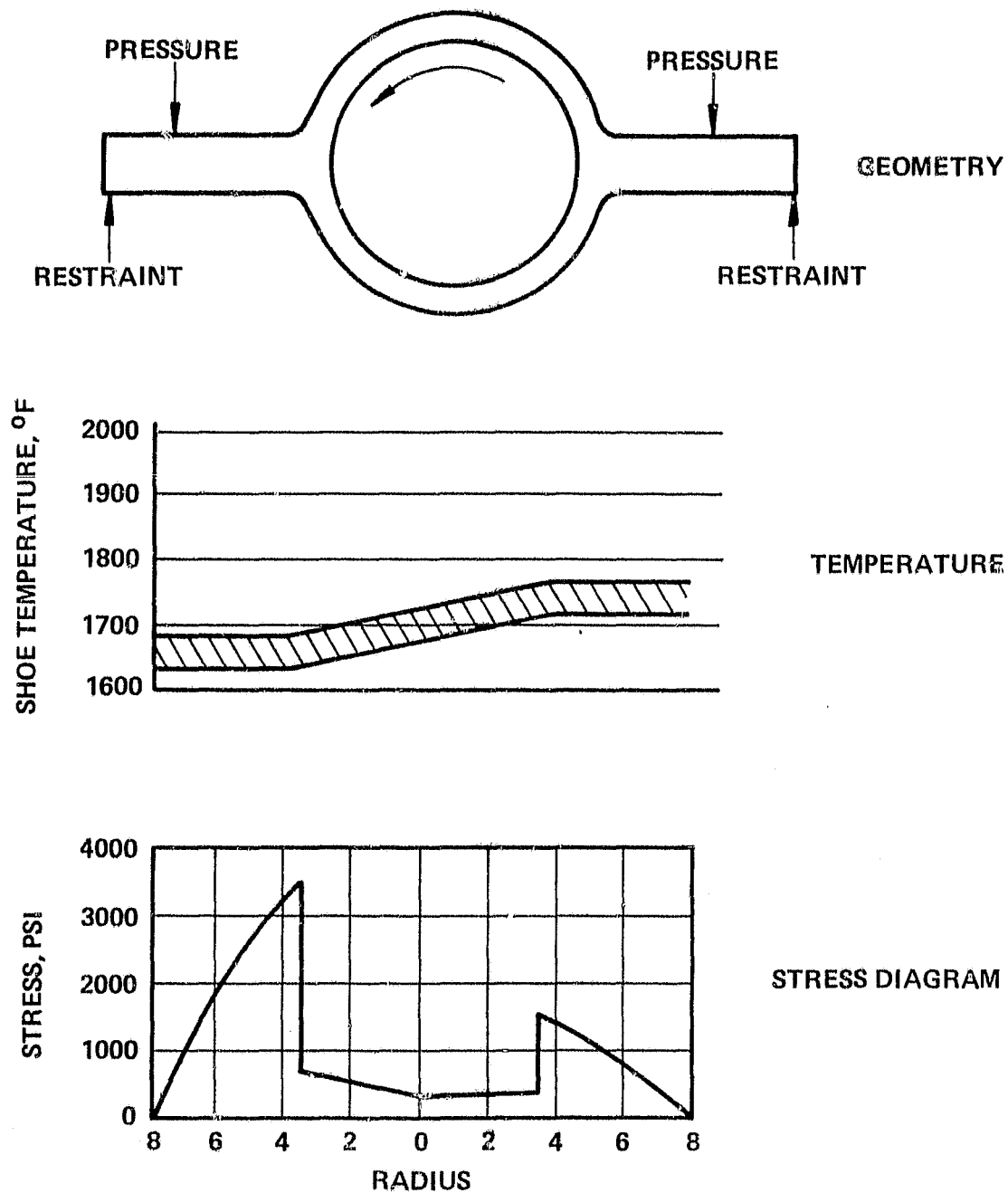


Figure 130. AGT101 Regenerator Seal Shoe Stress at WOT.

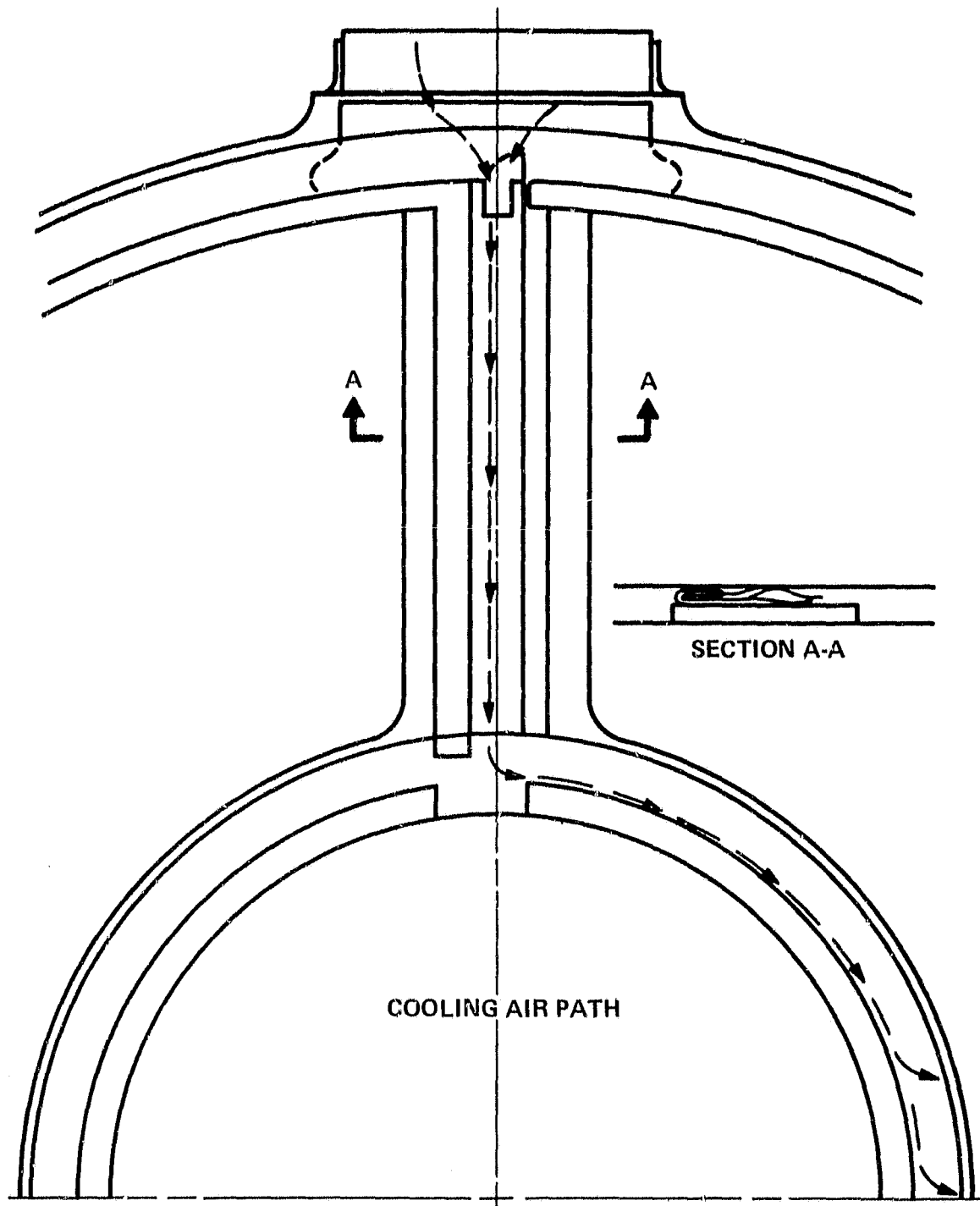


Figure 131. AGT101 Seal Diaphragm Cooling Air Paths.

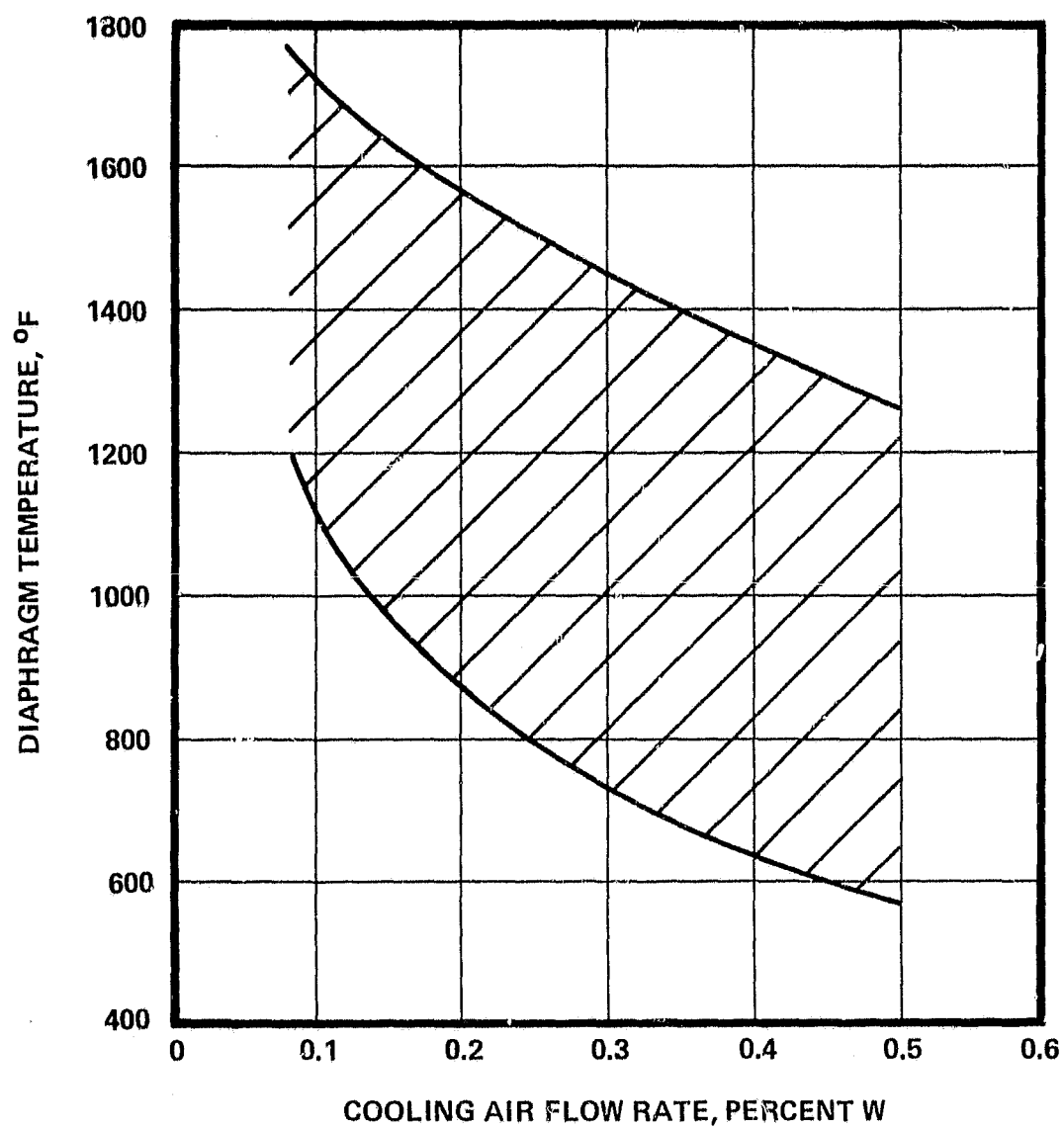


Figure 132. AGT101 Cooling Air Requirements.

Seal Coatings

- o All satisfactory at 2000°F
- o Rig test "X" arm needed to confirm 2000°F

Seal Configuration

- o Similar to 707 and Stirling
- o ~0.1 percent cooling required

Seal Stress

- o Shoe exceeds 5000 hours at 2000°F and 1000 hours at WOT
- o "X"-arm diaphragm exceeds 4000 hours at 2000°F and 1000 hours at WOT
- o "C" diaphragm exceeds 10,000 hours at 2000°F and 1000 hours at WOT

4.4.2 AiResearch Phoenix Test Rigs

4.4.2.1 Regenerator Low Pressure (LP) Cold Rig

The LP regenerator cold rig design concept, Figure 133, is based on Engine/Model similarity in areas of flow path geometry, regenerator matrix frontal area and pressure drop, and engine corrected mass flow in the turbine discharge plane. Rig objectives include baseline turbine diffuser performance mapping and regenerator flow pattern mapping. Instrumentation requirements for the diffuser performance are shown in Figure 133. Special instrumentation (hot wire anemometry) is required for accurate low level velocity measurements in the regenerator core mapping test.

The hot wire technical capability required for testing was developed in a specially designed calibration tunnel (Figure 134). The calibration tunnel was utilized to calibrate a total of eight, 2-D and two, 3-D hot wire probes for use in the core survey test. Additionally, an in-house hot wire probe repair capability was developed to support the test.

Analytically predicted turbine discharge conditions had to be duplicated for the diffuser testing. Specifically, turbine exit swirl, radial pressure profile, and corrected flow rates were duplicated for the idle, cruise, and maximum power engine conditions. Hardware configurations to meet these requirements are shown in Figure 135. Preswirl assemblies for idle (+55 degrees), cruise (0 degrees), and maximum power (-27 degrees), were fabricated along with various percent open area screens to generate the analytically predicted 5-percent radial pressure gradient.

ORIGINAL PAGE IS
OF POOR QUALITY

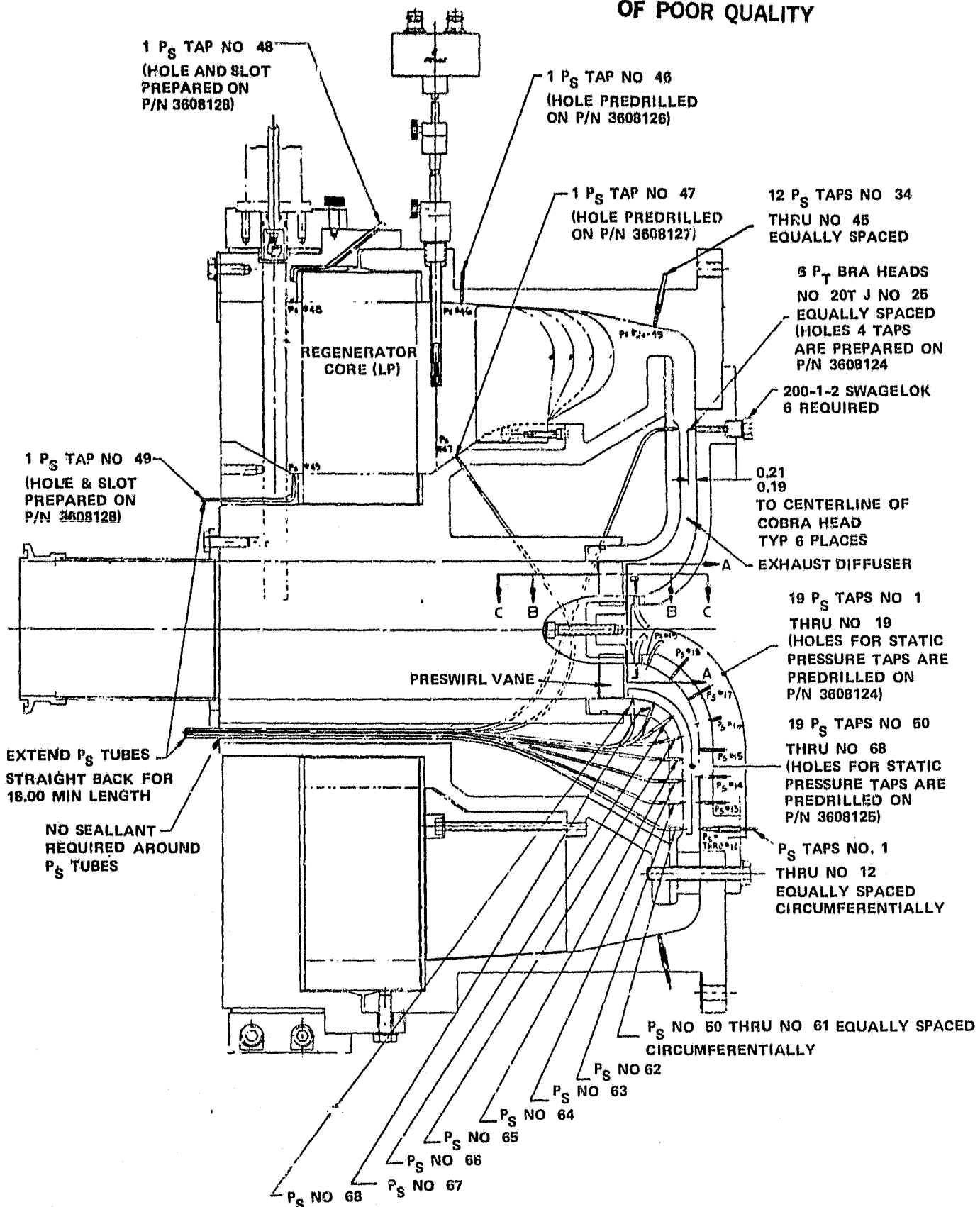


Figure 133. Regenerator LP Cold Rig.

ORIGINAL PAGE
BLACK AND WHITE PHOTOGRAPH

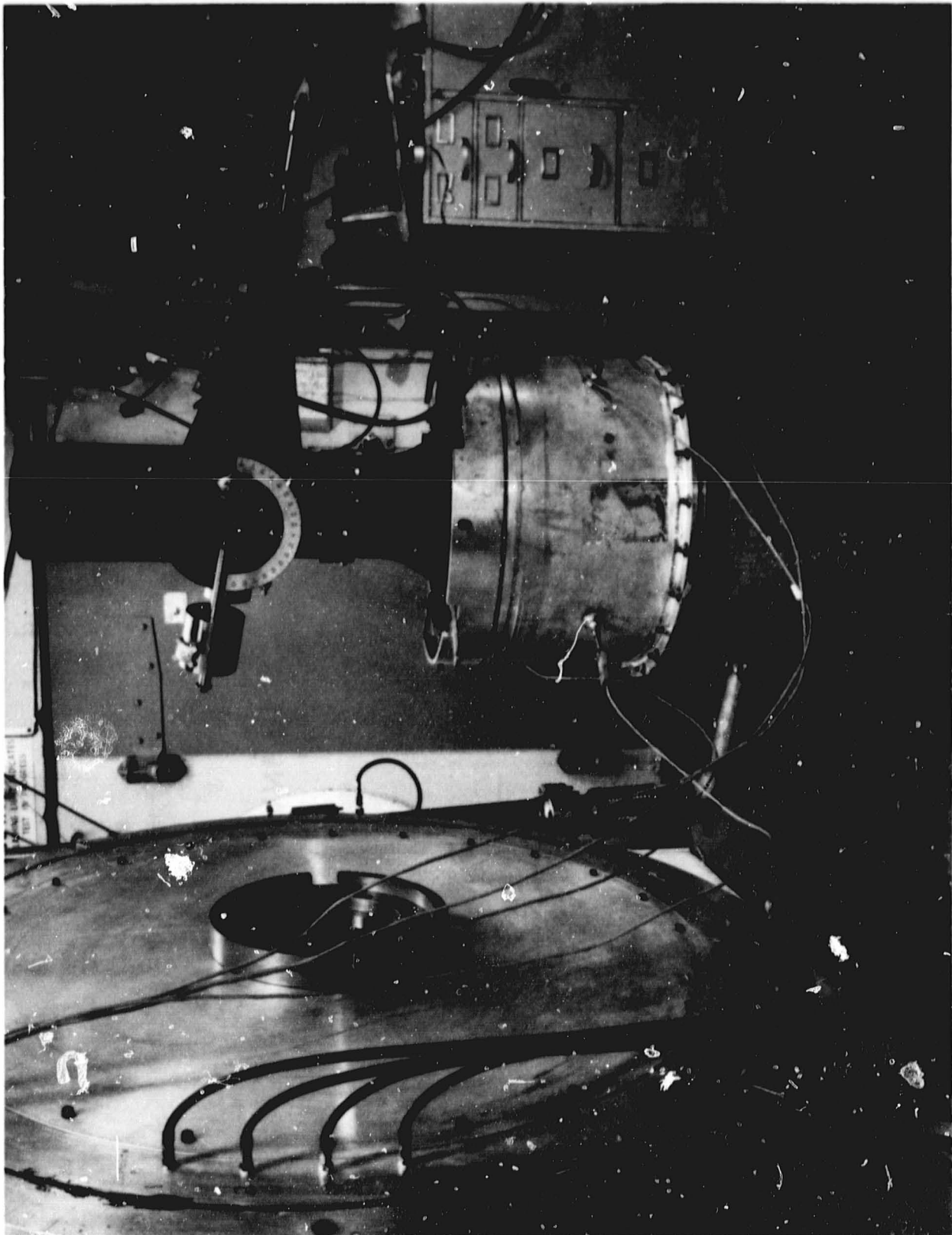
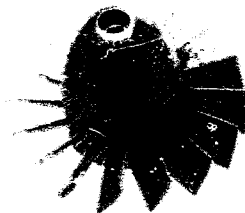
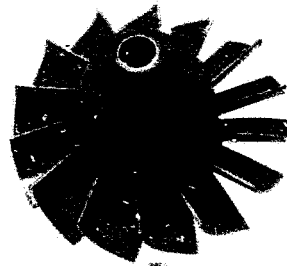


Figure 134. 3-D Hot Wire Calibration Tunnel.

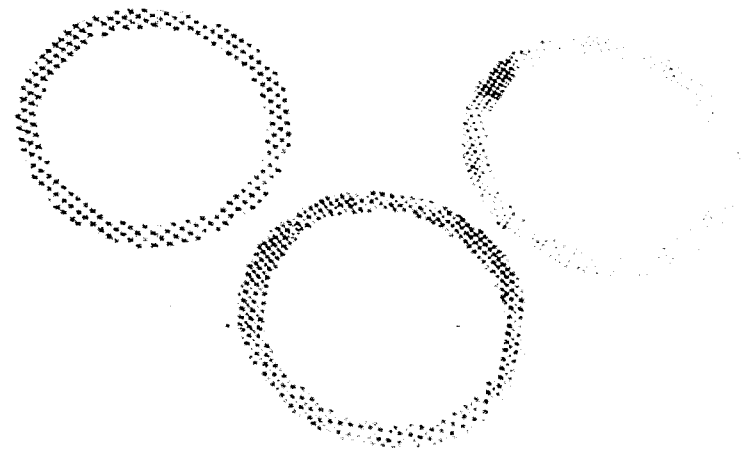


**8 PRESWIRL VANE ASSY
MAX POWER**

**10 FLOW CONDITIONER
PLATE**



**9 PRESWIRL VANE ASSY
IDLE**



ORIGINAL PAGE
BLACK AND WHITE PHOTOGRAPH

Figure 135. Regenerator LP Cold Rig Preswirl and Screen Assemblies.

The regenerator survey test (baseline velocity profile data) will be conducted to determine the effects of the diffuser exit swirl condition, mass flow rate, and core delta P on the flow profiles upstream of the core. A computer program to calculate gas side effectiveness, based on the cold rig flow distortion data, currently is being modified. The 3-D hot wire anemometer will be used to measure the downstream velocity enabling calculation of the upstream pressure profile, and therefore the flow and temperature distribution in the core.

4.4.2.2 Regenerator High Pressure (HP) Test Rig

The HP side regenerator cold rig (Figure 136) has the same criteria for engine similarity as the LP side of the cold rig. The objectives of this rig are to match the flow patterns of the LP side such that the maximum heat transfer conductance is consistently realized. Flow control techniques for this purpose include various hole patterns and radial web stiffeners in the exhaust housing and possible internal recontouring of the housing. Here again, a 3-D hot wire probe is installed immediately downstream of the core for direct low level velocity measurement. Additional instrumentation is included for the determination of the combustor annulus inlet velocity profile such that an optimum shape can be determined for the regenerator exit/combustor inlet guide vane. A uniform circumferential flow profile is desired at the combustor inlet to assure the best flame control and secondary mixing in the combustor. Effects of this guide vane selection on the regenerator flow profile also will be determined and corrected as required.

4.4.2.3 Regenerator System Structures

Results of the 3-D finite element temperature and pressure distortion analysis on the regenerator system structures indicated a large thermal growth differential between the engine outer case and flow separator housing support. This excessive growth differential was manifested by large regenerator "pocket" dimensional changes. These large "pocket" dimensional changes, Table 15, created the need for regenerator seal systems capable of absorbing seal gap closures as high as 0.091 inch from maximum power cold to hot idle condition. Seal platform distortion of this magnitude would make the 3.5-percent seal leakage prediction a difficult goal to achieve. A further complication of the internally supported flow separator housing is in the cold stack tolerances of the components that make up the regenerator pocket. Selective assembly would have been required to achieve the cold pocket dimension, adding complexity and cost to the power section. The solution to this problem of excessive regenerator pocket dimensional change was to shorten the load path to the inner pocket platform by supporting the flow separator housing to the outer case, thereby eliminating the number of components involved in the stack. This solution isolates the outer case pressure distortion, thus maintaining the seal platforms in a flat and parallel configuration throughout the operating cycle.

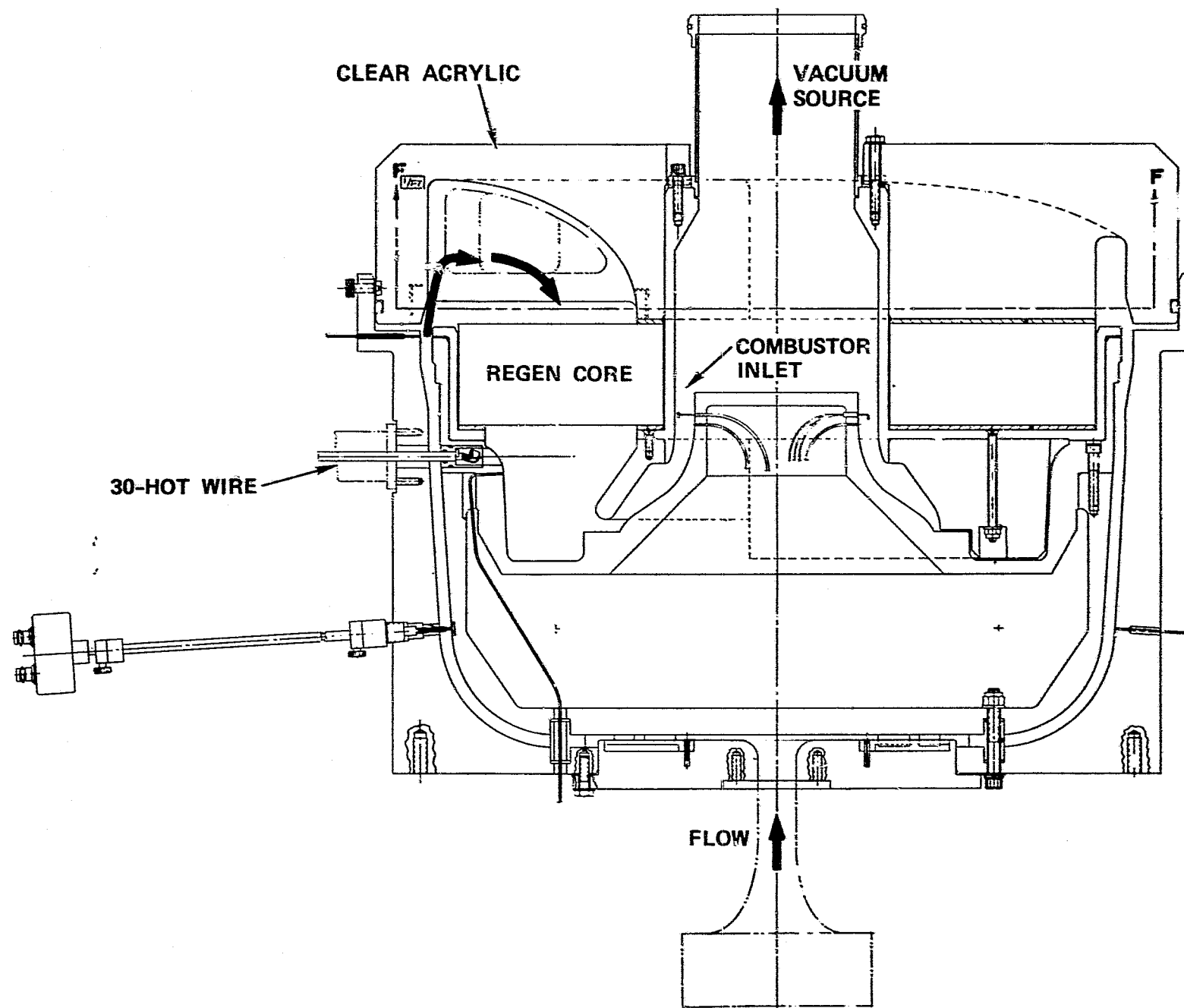


Figure 136. Regenerator HP Cold Rig.

TABLE 15. CHANGE IN POCKET DIMENSION (AT OD OF CROSSARM)

		FLOW DIVIDER SUPPORTED BY TURBINE SHROUD (INCHES)		FLOW DIVIDER SUPPORTED BY OUTER CASING (INCHES)	
		COLD	HOT	COLD	HOT
MOD I BUILD I (METAL STRUCTURE)	IDLE	0.001 CLOSED	0.073 CLOSED	0.001 OPEN	0.019 OPEN
	MAX POWER	0.003 CLOSED	0.036 CLOSED	0.003 OPEN	0.002 CLOSED
MOD I COMPLETE AND MODE II (CERAMIC STRUCTURE)	IDLE	0.001 CLOSED	0.002 CLOSED	0.001 OPEN	0.013 CLOSED
	MAX POWER	0.003 CLOSED	0.016 OPEN	0.003 OPEN	0.004 CLOSED

4.4.2.4 Exhaust Housing (Header) Design

The design criteria for the exhaust housing primarily is related to the requirement for axial stability of the outer seal platform. The blowoff loads imposed on the housing (HP side) have a tendency to rotate the center of the cover forward, translating the outer seals inner periphery out of the desired seal plane. A 3-D finite element analysis again was utilized to determine the magnitude of this translation and the extent of the radial stiffening required to limit the axial movement to 0.005 inch or less. The model used for this analysis is shown in Figure 137. Web stiffeners also were analyzed with various hole geometries to accommodate the circumferential flow from the LP side of the housing. These geometries will be tested to determine an optimum hole configuration for the desired flow match with the LP rig. Figure 138 shows the HP rig exhaust housing constructed of clear acrylic for 3-D flow visualization purposes.

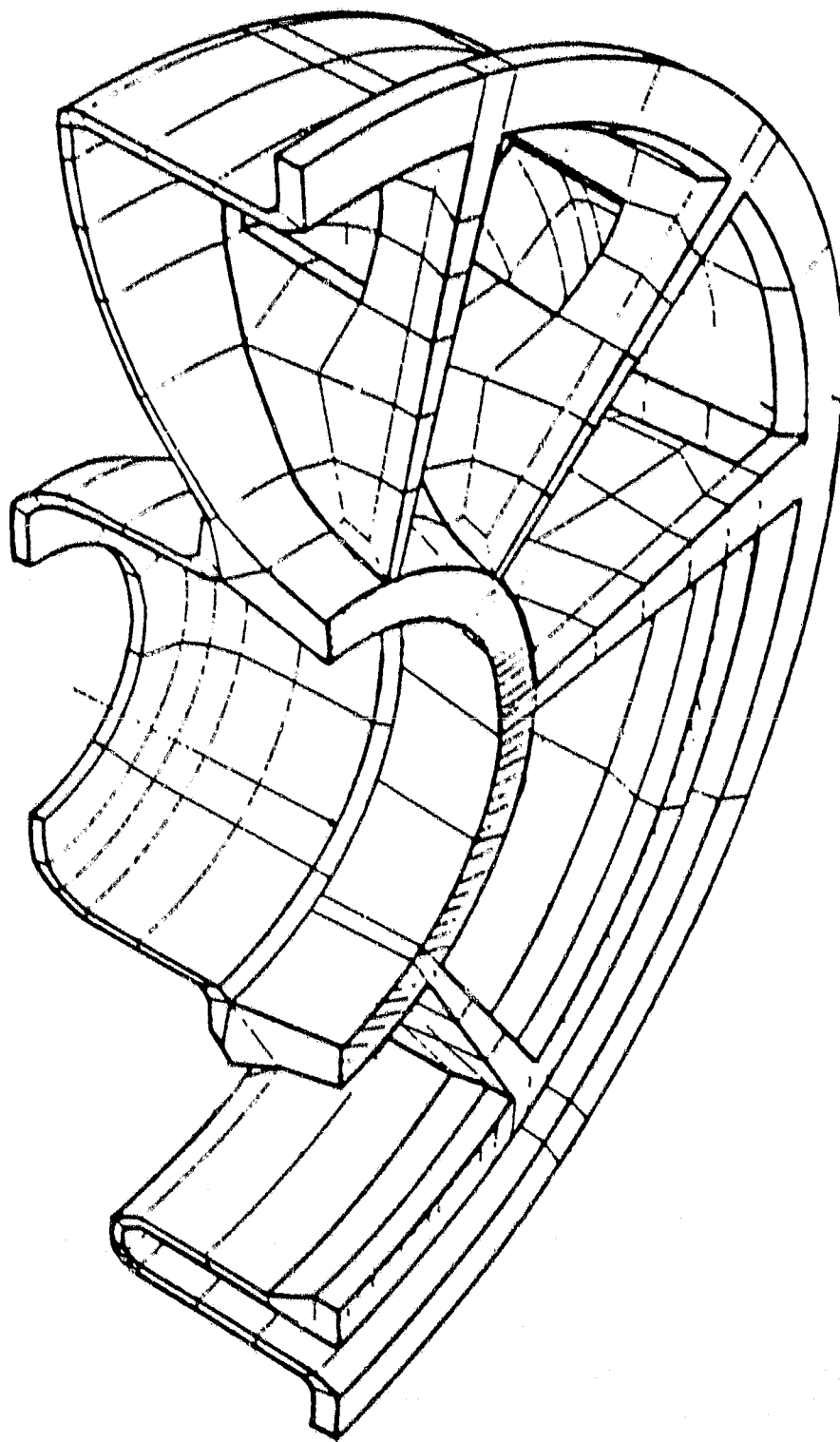


Figure 137. Exhaust Housing 3-D Finite Element Model.

ORIGINAL PAGE
BLACK AND WHITE PHOTOGRAPH

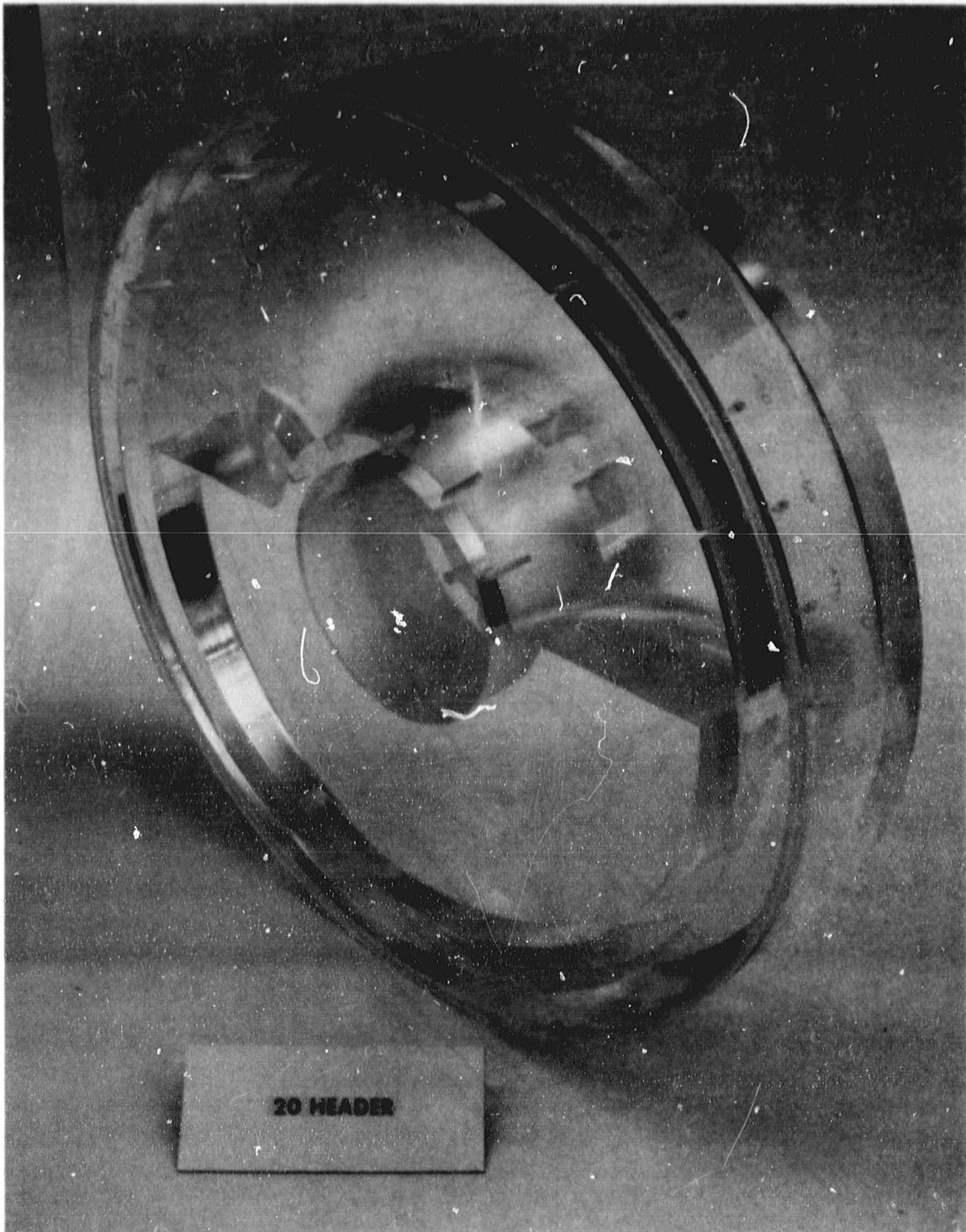


Figure 138. HP Rig Clear Acrylic Exhaust Housing.

4.5 Gearbox/Transmission

Single-shaft gas turbine engine optimization for automotive applications requires the use of a continuously variable speed transmission. In addition, the transmission must provide a high ratio speed reduction between the high speed turbine engine and the relatively low speed of the vehicle drive line.

The transmission system selected for the AGT101 consists of a high-speed variable single-stage differential planetary gearbox in conjunction with a modified four-speed automatic overdrive (AOD) transmission. This combination results in a nearly stepless, continuously variable speed transmission required for single-shaft gas turbine vehicle system optimization.

The planetary gearbox incorporates a differential in which power is split into two paths. Power is input at the planetary sun gear and extracted from the planetary carrier. In this planetary system, all elements rotate and the relative speeds are interdependent. One power path extends directly from the sun gear to the carrier; the second power path passes through the planetary ring gear to a variable stator torque converter (VSTC) that is used as a speed changing device. The torque converter variable output speed is connected to the carrier through a clutch that is open during vehicle idle operation and closed during normal driving modes. Speed ratio modulation across the VSTC results in a variable output speed of the planetary carrier, which in turn geared directly into the AOD transmission. Step ratio changes in the AOD are phased with off-setting speed ratio changes in the variable speed gearbox to produce a continuously variable drive line system.

The AGT101 drive system schematic is shown in Figure 139. Turbine power is introduced into the gearbox through a 22-tooth, 28-diametrical pitch (0.785 inch pitch diameter) sun gear normally operating over a range of 55,000 to 100,000 rpm. The sun gear drives three 112-tooth planets and a 248-tooth ring gear. Further speed reduction in the differential leg to the VSTC is obtained in a compound layshaft using 12-diametrical pitch gearing. This layshaft reduction is identified as the "X" ratio. A common drive shaft for all engine accessories is geared directly to the layshaft. The VSTC is driven by the layshaft through a 39-tooth idler and an 83-tooth VSTC drive gear. The 83-tooth VSTC drive gear also drives the main oil pump for the gearbox and transmission.

Power from the planetary carrier is transferred to the AOD input shaft through a helical gear set of 72 and 75 teeth identified as the "Z" ratio. An electrical starter is geared to the AOD input shaft through a 36-tooth idler gear.

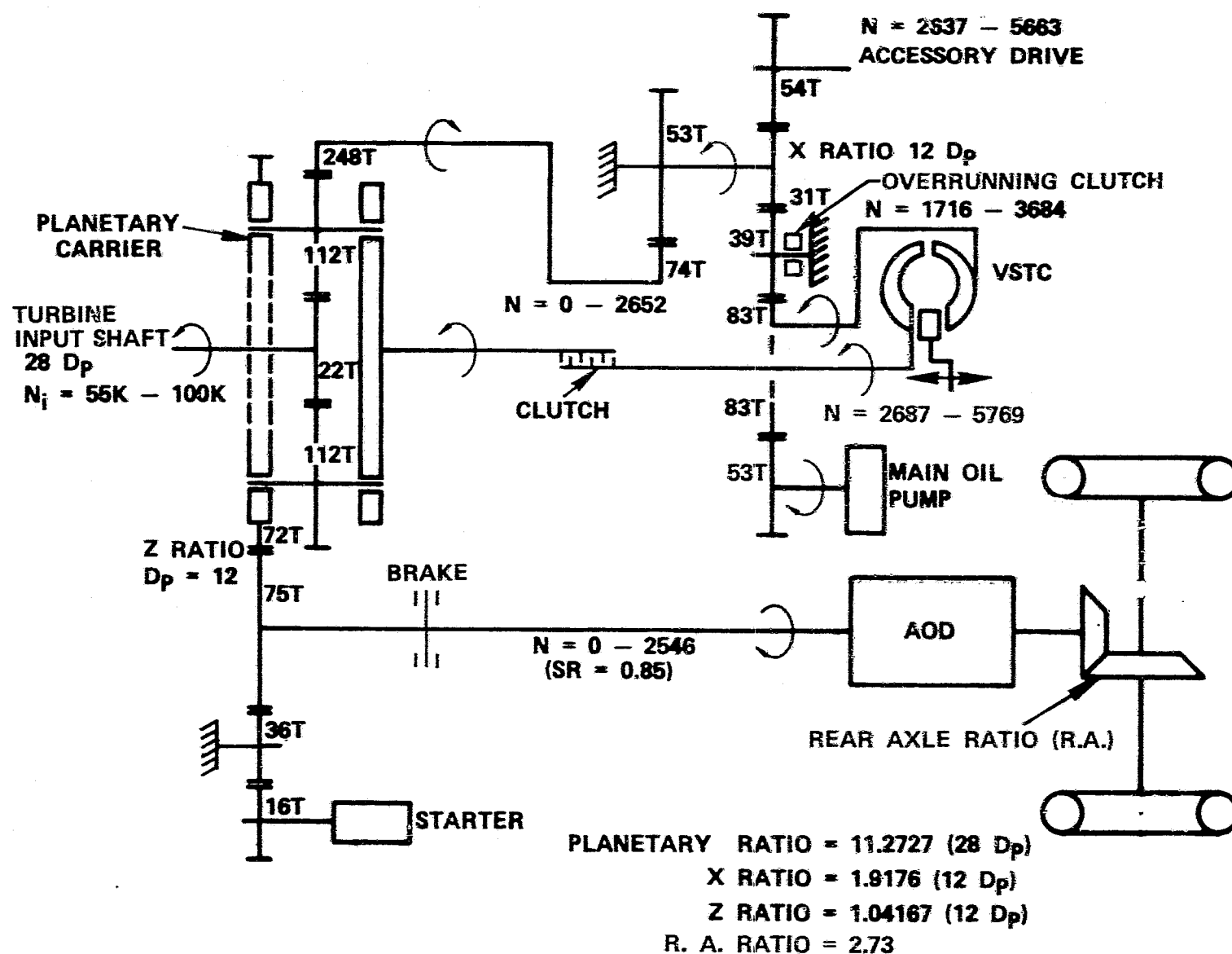


Figure 139. AGT101 Drive System.

The differential nature of the gearbox requires an overrunning clutch be added to the 39-tooth layshaft idler gear to prevent the accessory drive and VSTC from revolving during an engine start. Upon starter cut-out, engine power reverses torque through the layshaft, and the accessories and VSTC begin to revolve. However, the differential action is such that the speeds of these components can not be predicted unless the second differential leg to the AOD input shaft is controlled or stopped. An AOD input shaft brake has been incorporated to prevent the shaft from rotating while the transmission is in neutral. The brake function can be incorporated in the AOD when production warrants modification.

The AGT101 transmission system cross section is shown in Figure 140. The gearbox geartrain has been emphasized by solid black shading for clarification.

Due to the differential feature of the geartrain, the accessory drive and VSTC input speeds vary inversely with the carrier output speed as a function of the VSTC speed ratio. The VSTC input speed, accessory drive speed and output carrier speed relationships are shown in Figures 141 and 142 for 55,000 and 100,000 rpm turbine input speeds respectively. Other than starting the vehicle from a stop, the VSTC operates at speed ratios between 0.45 and 0.85 and the VSTC and accessory drives are limited to approximately 2 to 1 changes in speed over the normal gas turbine engine operating range. This feature permits selection of accessory speeds for optimum vehicle performance as well as VSTC operation in high efficiency areas.

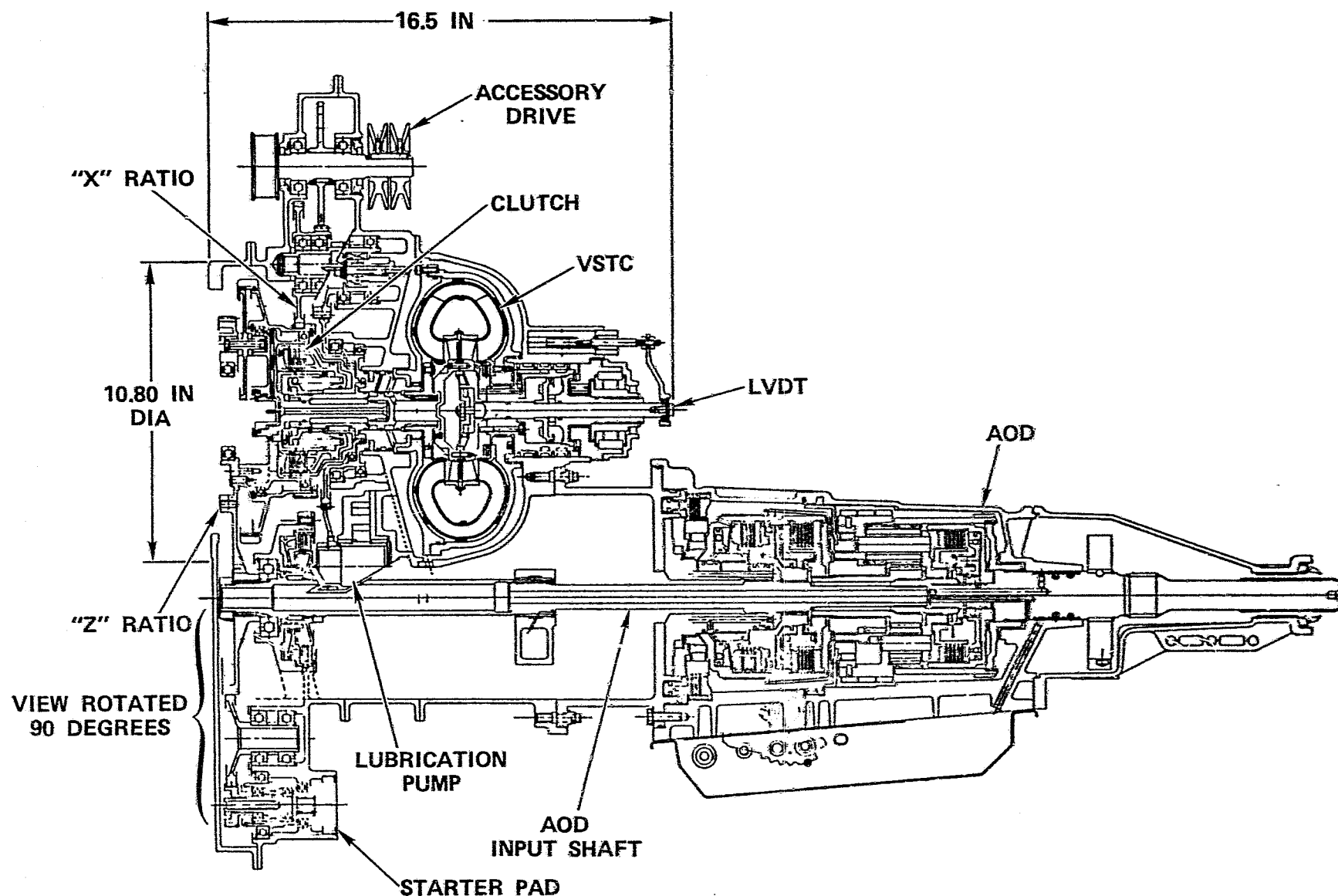
The geometric characteristics of each gear used in the gearbox are summarized in Tables 16 and 17. The stress data for each gear are summarized in Tables 18 and 19. In each case, the stress levels and other operating parameters are well within current production practice.

The bearings selected for the gearbox are listed in Table 20 with the speeds, loads, capacity and B_1 -fatigue life specified for each. The fatigue life has been determined on the basis of individual maximum loads and speeds of the respective bearing with the engine operating at maximum speed. In most cases the maximum speeds or loads are not concurrent so that the analysis is conservative.

Test rig design has been initiated and is based on the schematic shown in Figure 143.

4.5.1 Variable Stator Torque Converter (VSTC)

A 9.18-inch diameter VSTC of Ford design and manufacture was tested to generate a performance map covering the extended speed ranges, ratios, and stator blade angles required for the AGT101 application. The VSTC map is shown in Figure 144. Efficiency islands as



ORIGINAL PAGE IS
OF POOR QUALITY

Figure 140. AGT101 Transmission System.

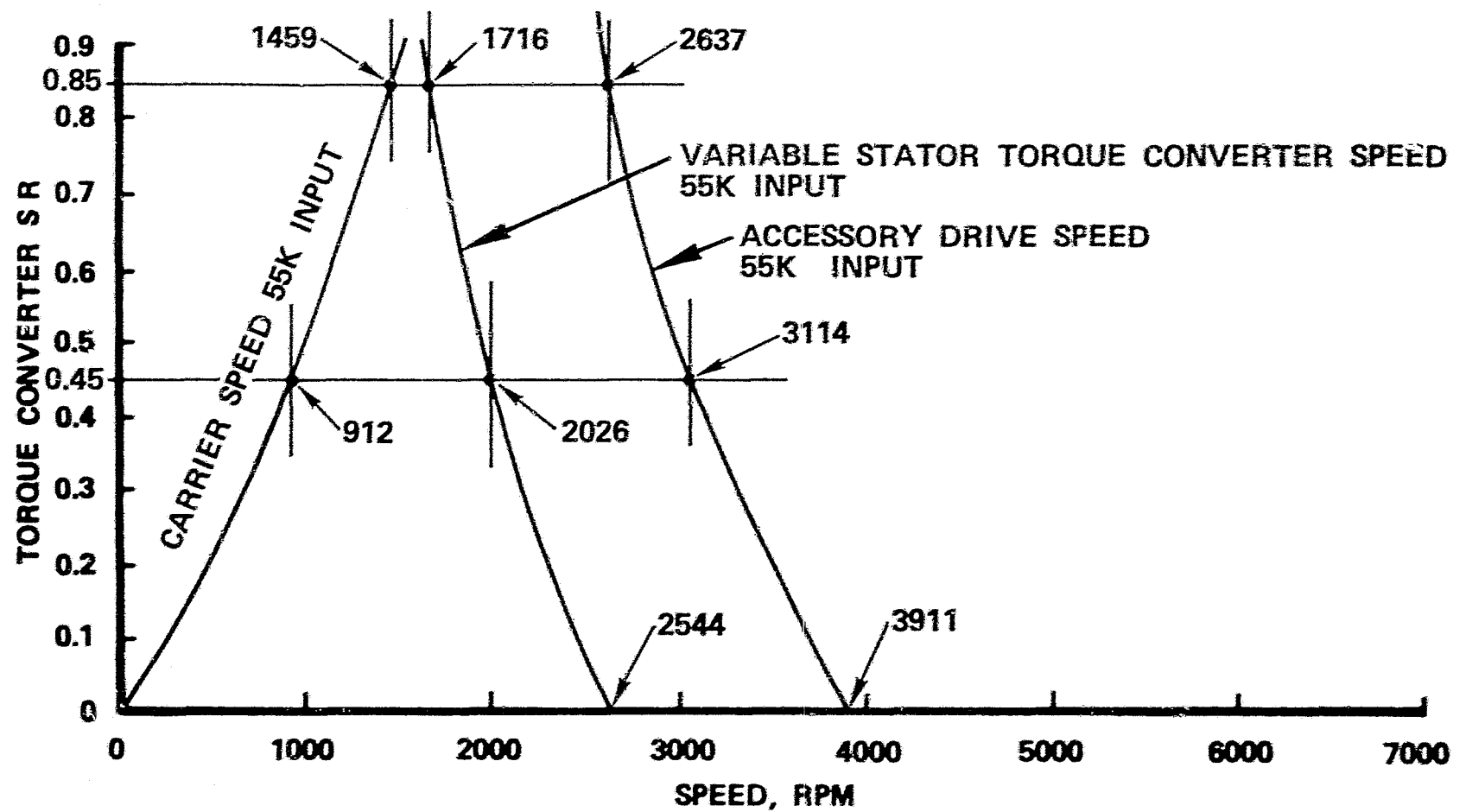


Figure 141. AGT101 Split Path Layshaft Gearbox Component Speeds.

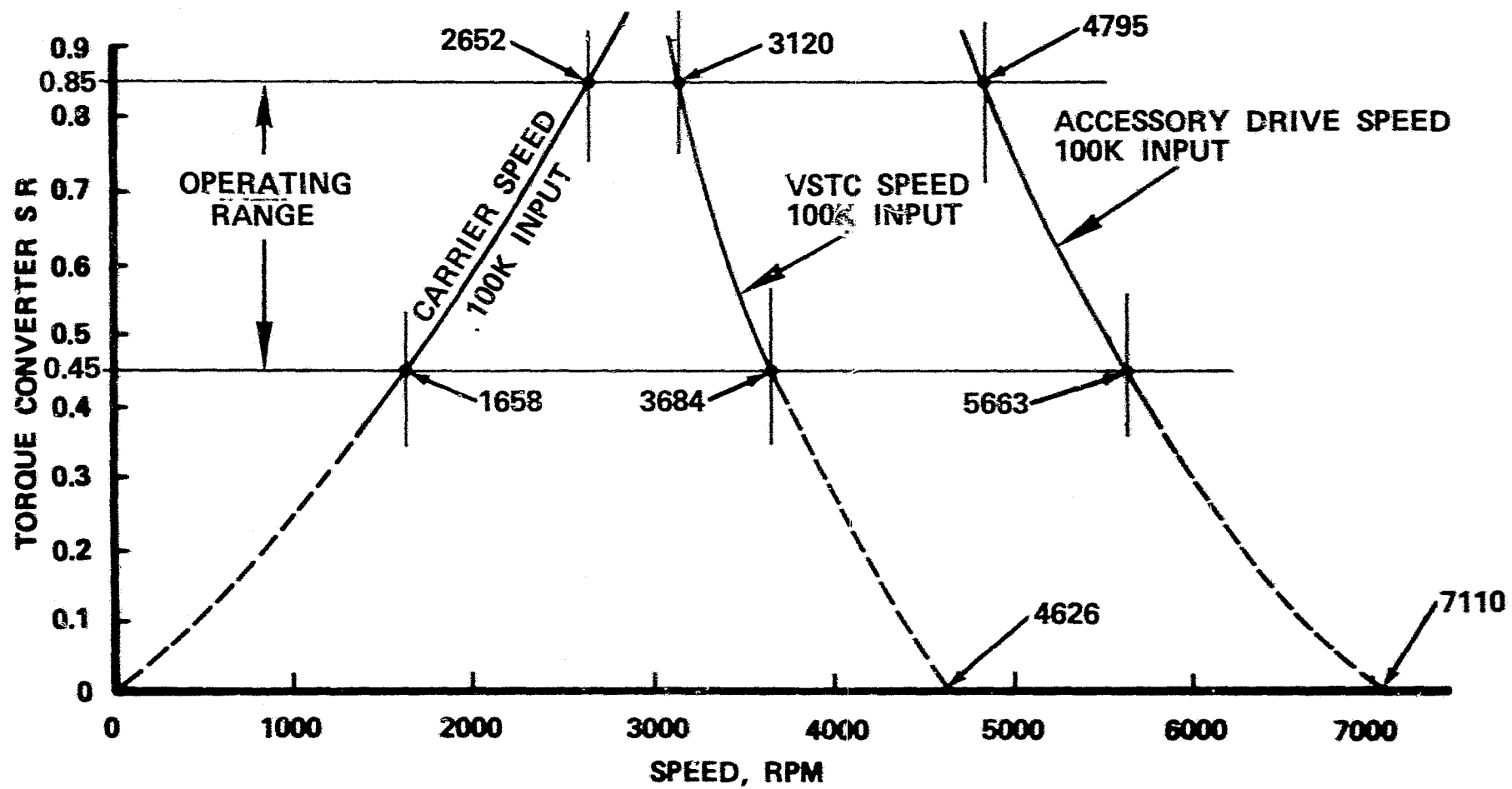


Figure 142. AGT101 Split Path Layshaft Gearbox Component Speeds.

TABLE 16. AGT101 GEAR DATA SUMMARY

GEAR	PART NO	MATERIAL	MIN HARDNESS ROCKWELL C		NO OF TEETH	NORM DIAMET PITCH	MAX TRANS OPER PRESS ANGLE DEG	HELIX OR SPIRAL ANGLE DEG	MIN FACE WIDTH INCH	MAX OUTSIDE OR MIN INSIDE DIA INCH	MIN ROOT DIA OR MAX ROOT DIA INTERNAL INCH	NOM CENTER DIST INCH	MIN CONTACT RATIO (PROFILE)	TRAN TIP WIDTH INCH	QUAL GRADE A G M A	FACE CONTACT RATIO
			CORE	CASE												
COMPOUND GEAR		4340		50	31	12	20.34		0.500	2.805	2.308	3.545	2.002	0.0272	9-10	
ACC GEAR		4340		50	54				0.700	4.719	4.222			0.0347		
Z RATIO		4340		50	72	12	27.6	26.34	0.650	6.858	6.439	6.832	1.141	0.0497	9-10	1
Z RATIO		4340		50	75				0.500	7.132	6.713			0.0497		
Z RATIO		4340		50	75	12	27.47	26.34	0.600	7.132	6.713	5.157	1.249	0.0498	9-10	0.576
IDLER		4340		50	36				0.350	3.527	3.103			0.0435		
IDLER		4340		50	36	12	28.77	26.34	0.350	3.527	3.103	2.438	1.085	0.0435	9-10	0.576
STARTER GEAR		4340		50	16				0.500	1.689	1.263			0.0317		

TABLE 17. AGT101 GEAR DATA SUMMARY

GEAR	PART NO	MATERIAL	MIN HARDNESS ROCKWELL C		NO OF TEETH	NORM DIAMET PITCH	MAX TRANS OPER PRESS ANGLE DEG	HELIX OR SPIRAL ANGLE DEG	MIN FACE WIDTH INCH	MAX OUTSIDE OR MIN INSIDE DIA INCH	MIN ROOT DIA EXTERNAL OR MAX ROOT DIA INTERNAL INCH	NOM CENTER DIST INCH	MIN CONTACT RATIO (PROFILE)	TRAN TIP WIDTH INCH	QUAL GRADE A G M A	FACE CONTACT RATIO
			CORE	CASE												
SUN		9310 AIR MELT	33	60	22	28	21.03		0.300	0.967	0.683	2.406	1.757	0.0200	11-12	
PLANET		8620	24	58	112				0.207	4.078	3.896			0.0264		
PLANET		8620	24	58	112	28	18.68		0.207	4.078	3.896	2.406	1.349	0.0264	11-12	
RING		4340		50	248				0.207	8.762	8.943			0.0293		
RING TAKEOFF		4340		50	74	12	20.54		0.335	6.336	5.917	5.300	1.438	0.0090	9-10	
COMPOUND GEAR		4340		50	53				0.335	4.583	4.164			0.0059		
COMPOUND GEAR		4340		50	31	12	20.26		0.500	2.805	2.308	2.919	2.000	0.0272	9-10	
IDLER		4340		50	39				0.535	3.470	2.974			0.0313		
IDLER		4340		50	39	12	20.31		0.535	3.470	2.974	5.008	2.002	0.0313	9-10	
TORQUE CONVERTER		4340		50	83				0.325	7.127	6.640			0.0426		
TORQUE CONVERTER		4340		50	83	12	20.34		0.325	7.127	6.640	5.6725	2.003	0.0426	9-10	
LUB PUMP		4340		50	53				0.100	4.634	4.151			0.0363		

TABLE 13. AGT101 GEAR STRESS SUMMARY

GEAR	NO OF TEETH	H P	RPM	TORQUE IN -LB	TANGEN TOOTH LOAD LB	TOOTH STRENGTH		TOOTH WEAR			PITCH LINE VELOCITY FPM MAX	SLIDING VELOCITY AT TIP TOOTH FPS MAX	SCORING MAXIMUM FLASH TEMPERATURE WITH 250° INLET OIL TEMPERATURE DEGREES F	0.06 COEFF OF FUNCTION MAXIMUM EFFICIENCY %
						BENDING STRESS PSI	COMBINED AGMA K FACTORS (7)	COMPRESSIVE STRESS		COMBINED AGMA C FACTORS (9)				
								AT P D	MAX					
COMPOUND GEAR AISI 4340	31	20	8451 (9634)*	149.148	115.214	6804 (35,949)	5.28	71,531	111,131 (124,750)	1.12	6,513	34.59	270.37	98.94
ACC GEAR AISI 4340	54		4851.7 (5530)*	259.806		14,174 (36,644)	2.58					37.05		
***Z RATIO AISI 4340	72	93	1601.3 (2588)	3660	1094.5	32,094 (43,158)	1.3448	112,965	112,965 (167,472)	1.432	4,528	8.08	272.7	99.62
***Z RATIO AISI 4340	75		1537.3 (2484)	3813		33,885 (43,213)	1.2755					7.90		
**Z RATIO AISI 4340	75	3.33	320	656.25	188.2	6,317 (34,342)	5.436	80,902	80,902 (219,355)	2.711				
**IDLER AISI 4340	36		666.6	315.0		11,689 (33,484)	2.86							
**IDLER AISI 4340	36	3.33	666.6	315.0	185.94	11,126 (33,482)	3.01	118,232	118,232 (209,671)	1.773				
**STARTER GEAR AISI 4340	16		1500.0	140		9,578 (43,389)	4.53							

(DESIGN ALLOWABLE STRESSES)

*MAXIMUM RPM FOR THIS GEAR, NOT THE SAME AS FULL VEHICLE SPEED

**THIS IS EQ. LIFE CONDITION, BASED ON START CURVE. IT DOES NOT REPRESENT THE FULL SPEED OR HIGH TORQUE POINT ON THE START CURVE

***DESIGNED FOR MAXIMUM TORQUE INPUT OF AOD, NOT FULL VEHICLE SPEED

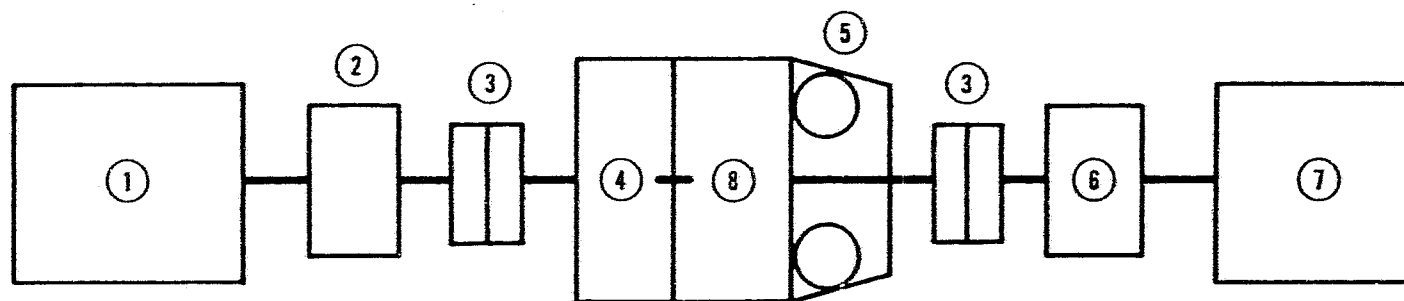
TABLE 19. AGT101 GEAR STRESS SUMMARY

GEAR	NO. OF TEETH	HP	RPM	MAX TORQUE IN LB	TANGENTIAL LOAD LB	TOOTH STRENGTH		TOOTH WEAR		PITCH LINE VELOCITY FPM MAX	SLIDING VELOCITY AT TIP FPM MAX	ROOMING MAXIMUM TEMPERATURE WITH 75% INLET OIL TEMPERATURE DIFFERENCE	0.88 COEFF OF FUNCTION MAXIMUM EFFICIENCY %
						BENDING STRESS PSI	COMBINED AGMA FACTOR (1)	COMPRESSIVE STRESS	COMBINED AGMA FACTOR (2)				
SUN AISI 8620	22	150.5	100,000	82,310	69.3	30801 (84,570)	1.778	141,873	148,800 (174,816)	1.188	20,887	91.08	99.17
PLANET. AISI 8620	112		10134.5	138,523		31,884 (38,813)	1.161						
PLANET AISI 8620	112	109.0	10134.5	138,523	70.8	31,711 (38,816)	1.161	31,718	48,440 (143,470)	3.381	19,870	9.07	99.88
RING AISI 4340	240		8053	826.8		26,129 (39,222)	1.800						
RING TAPERED AISI 4340	74	89.0	8053 (8900)*	826.8	208.4	30,358 (41,944)	1.358	115,804	116,488 (152,686)	1.311	31,137	33.11	98.44
COMPOUND AISI 4340	83		8451.4 (9834)*	863.8		41,106 (48,750)	1.102						
COMPOUND GEAR AISI 4340	31	80.0	8451.4 (9834)*	863.8	513.0	30,335 (40,740)	1.343	92,928	138,488 (152,758)	1.103	8315	39.40	98.83
IDLER AISI 4340	39		8717.7 (7858)*	838.12		25,580 (30,000)	1.204						
IDLER AISI 4340	30	89.0	8717.7 (7858)*	838.12	513.5	25,557 (30,000)	1.205	95,952	130,408 (184,848)	1.108	6515	40.47	99.81
TORQUE CONVERTER INPUT AISI 4340	83		3158.5 (13508)*	1777.3		38,000 (42,161)	1.189						
TORQUE CONVERTER INPUT AISI 4340	83	8.43	3158.5 (13508)*	178.4	17.0%1	2734 (37,181)	13.603	54,775 (71,007)	1.780	6515	29.80	263.37	99.34
LUBE PUMP GEAR AISI 4340	53		4044 (3634)*	83.0		9750 (16,620)	3.756						

*MAXIMUM RPM FOR THIS GEAR, NOT THE SAME AS PULL VEHICLE SPEED
(BASED ON ALLOWABLE STRESS)

TABLE 20. AGT101 SPLIT PATH LAYSHAFT GEARBOX BEARING SUMMARY

BEARING LOCATION	SIZE AND TYPE	MAX SPEED, RPM	DESIGN LOAD, LBS	CAPACITY, LBS	B ₁ FATIGUE LIFE, HRS
PLANETS	3/8 IN X 9/16 IN X 1/2 IN NEEDLE	19,134	110	891	627
RING GEAR	5 1/2 IN X 6 1/8 IN X 5/16 IN BALL	6,053	25	580	14,860
	5 IN X 5 3/4 IN X 3/8 IN BALL	6,053	295	1080	108
PLANET CARRIER	9/16 IN X 3/4 IN X 3/8 IN NEEDLE	2,588	INDETERMINATE	1340	>20,000
	3/4 IN X 1 IN X 3/8 IN NEEDLE	2,588	INDETERMINATE	688	>20,000
COMPOUND IDLER	25 MM X 52 MM X 15 MM BALL	8,451	234	2630	1,890
	25 MM X 52 MM X 15 MM BALL	8,451	384	2630	428
54T IDLER	25 MM X 52 MM X 15 MM BALL (2)	4,852	61	2630	>20,000
39T IDLER	25 MM X 52 MM X 15 MM BALL	6,718	672	2630	100
	25 MM X 52 MM X 15 MM BALL	6,718	348	2630	723
T C OUTPUT	105 MM X 130 MM X 13 MM ROLLER	3,157	800	9200	12,100
	4 IN X 4 3/4 IN X 3/8 IN BALL	3,157	254	860	138
T C INTERSHAFT	3 IN X 3 1/2 IN X 1/4 IN BALL	3,157	INDETERMINATE	400	>20,000
STARTER IDLER	25 MM X 52 MM X 15 MM BALL	5,556	524	2630	128,000 STARTS
	25 MM X 52 MM X 15 MM BALL	(667 DES)	325	2630	536,000 STARTS
STARTER CLUTCH	40 MM X 62 MM X 12 MM BALL	12,500	392	2520	119,000 STARTS
	25 MM X 42 MM X 9 MM BALL	(1500 DES)	183	1460	228,000 STARTS
	15 MM X 32 MM X 9 MM BALL		INDETERMINATE	965	>100,000 STARTS



- ① PTI CONTROLS 30 TO 40 SHP VARIABLE SPEED ELECTRIC MOTOR, 400 TO 4375 RPM
- ② LEBOW TORQUE SHAFT, MODEL 1226, 6000 RPM RATED, 25,000 IN -LB MAXIMUM TORQUE
- ③ SIER-BATH COUPLING
- ④ SLAVE GEARBOX, 26:1 SPEED-UP RATIO, 55K TO 100K RPM SPEED CAPABILITY
- ⑤ FORD VARIABLE STATOR TORQUE CONVERTER (VSTC)
- ⑥ LABORATORY FORCE RING CONTAINING STRAIN GAGES
- ⑦ VICKERS MODEL 3915 HYDRAULIC LOAD RATED AT 355 HP, 1.519 CIPR AT 3000 PSIG
- ⑧ DIFFERENTIAL GEARBOX WITH OPERATIONAL VSTC

Figure 143. Differential Gearbox and VSTC Test Rig.

ORIGINAL PAGE IS
OF POOR QUALITY

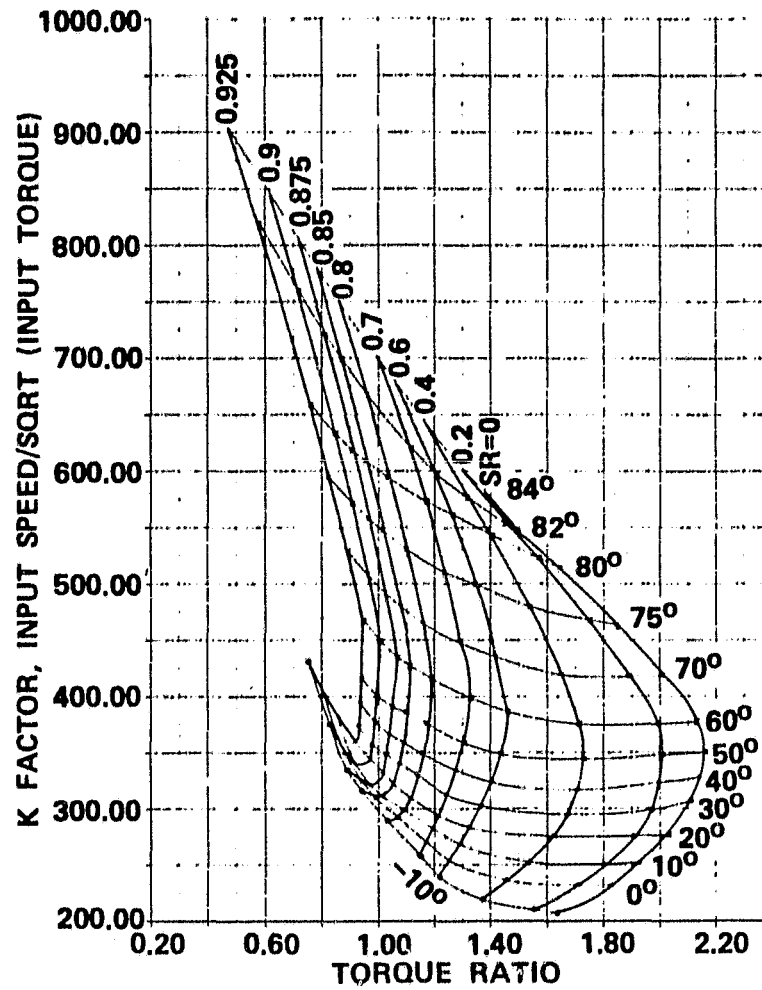


Figure 144. VSTC Test Results.

**ORIGINAL PAGE IS
OF POOR QUALITY**

high as 95 percent have been identified and the gearbox differential ratios were selected to operate the VSTC in the most efficient areas over the CFDC.

The VSTC layout was completed with emphasis on optimizing the stator blade crank angle position to provide the maximum possible lever arm throughout the blade operating angle. The design is a unitized assembly for plug-in to the AGT101 gearbox. Stator cranks were increased in thickness from 0.125 to 0.188 inch, and will be made of hardened alloy steel, as opposed to the annealed low carbon steel used in the prototype design.

The overrunning clutch design for the VSTC stator support is complete. This clutch design will give the converter an idle K factor of 16,000 to 24,000, thus reducing idle fuel losses.

4.5.2 Transmission

The transmission to be used in the AGT vehicle will be the Ford Automatic Overdrive Transmission (AOD).

The transmission will use the same oil flow path as the present AOD (i.e., from pump through the converter to the cooler and then lube). The VSTC will bring oil in from the transmission, through the converter and back to the cooler. Cooler return will be to both transmission and engine lube. VSTC stator piston actuation will have transmission line pressure of 60 to 100 psig and the transmission line pressure also will be available for neutral clutch actuation.

4.6 Structures

Thermal and stress analyses were performed on the engine major structural components, including steady-state and transient operation. Figures 145 through 147 show the associated static pressure distribution and thermal models for maximum power and idle conditions, respectively. Figure 148 depicts the "worst case start" transient used for the ceramic structures. Although this start transient is more severe than the normal engine operational mode, it provides a conservative analysis of the components and was used to isolate preliminary design deficiencies. During this start cycle, the turbine inlet temperature (TIT) increases to 2500°F in 4 seconds and engine speed to 75,000 rpm in 10 seconds. Temperature and stresses were calculated at several different times during the transient to determine peak magnitudes as a function of time. Figure 149 identifies the engine structural components.

4.6.1 Metallic Structural Analysis

The major metallic structures analyzed, as shown in Figure 149, are the compressor outer housing, compressor backshroud, and exhaust housing. Materials for these components are Meehanite GMN-60, cast iron 120-90-02, and Meehanite GM-60, respectively. Thicknesses were selected based on casting technologies. The following paragraphs describe results of these analyses.

4.6.1.1 Compressor Outer Housing

The compressor outer housing is subjected to internal pressurization and axisymmetric blow-off loads acting over the lower half of the exhaust housing/compressor outer housing bolt flange, as shown in Figure 150. Maximum power pressure forces were used for this analysis. Fourier series loads were used to obtain the axisymmetric loading profiles.

During the structural deflection analysis, external ribs (Figure 151) were added to reduce outer housing movement and maintain acceptable regenerator pocket dimensional changes (Figure 152).

4.6.1.2 Compressor Backshroud

The compressor backshroud housing was analyzed at maximum power conditions to determine foil bearing surface deflections. The backshroud is restrained from axial movement at the outer bolt circle (see Figure 149) and was free to radially deflect. As shown in Figure 153 deflection at the foil bearing surface is approximately 0.003 inch, which is considered acceptable since most operation is at idle/cruise condition. No stress or thermal problems are anticipated.

PRESSURES SHOWN ARE PSIA

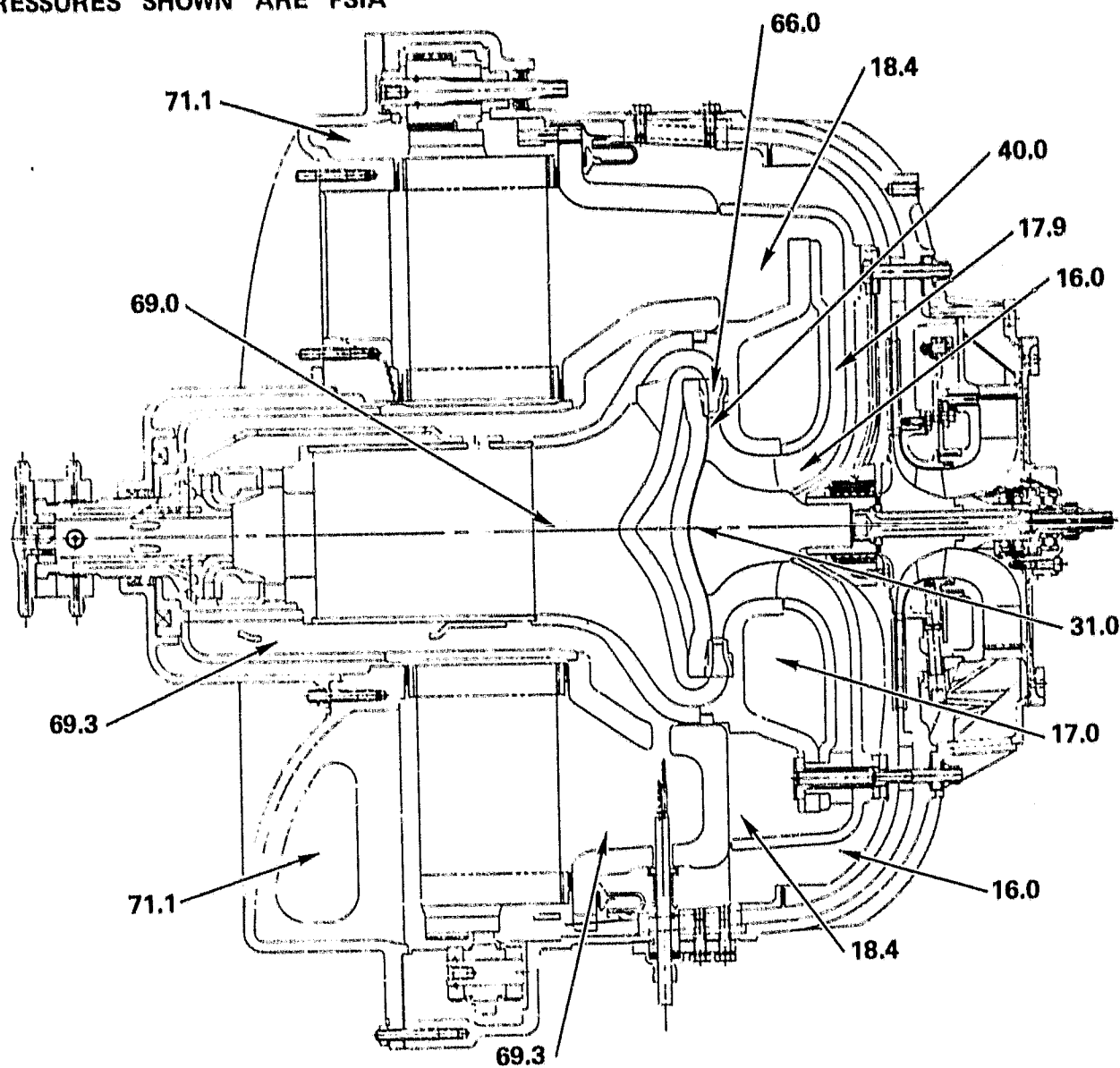


Figure 145. Static Pressure Distribution.

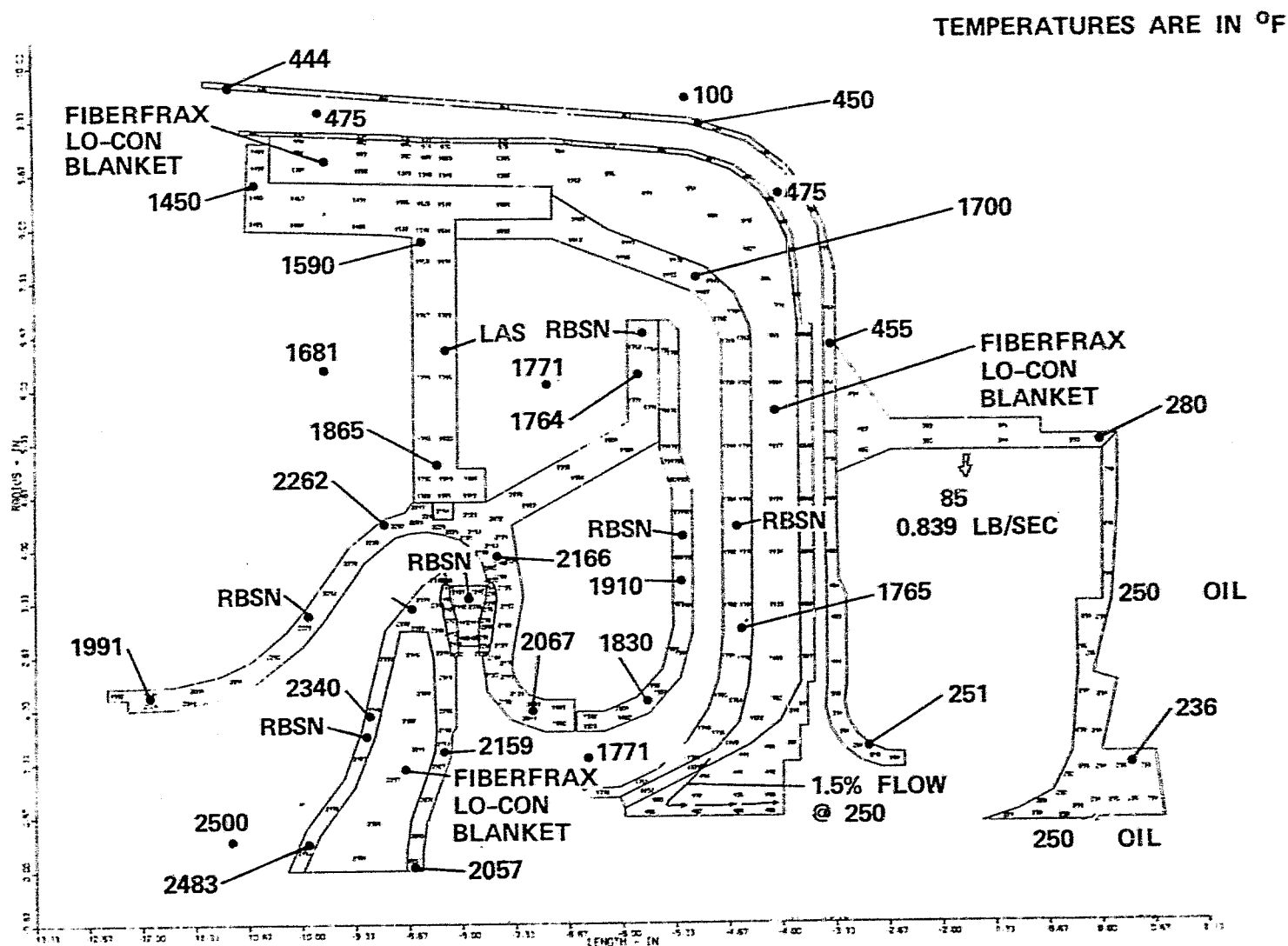


Figure 146. Static Structure Temperatures Maximum Power Condition.

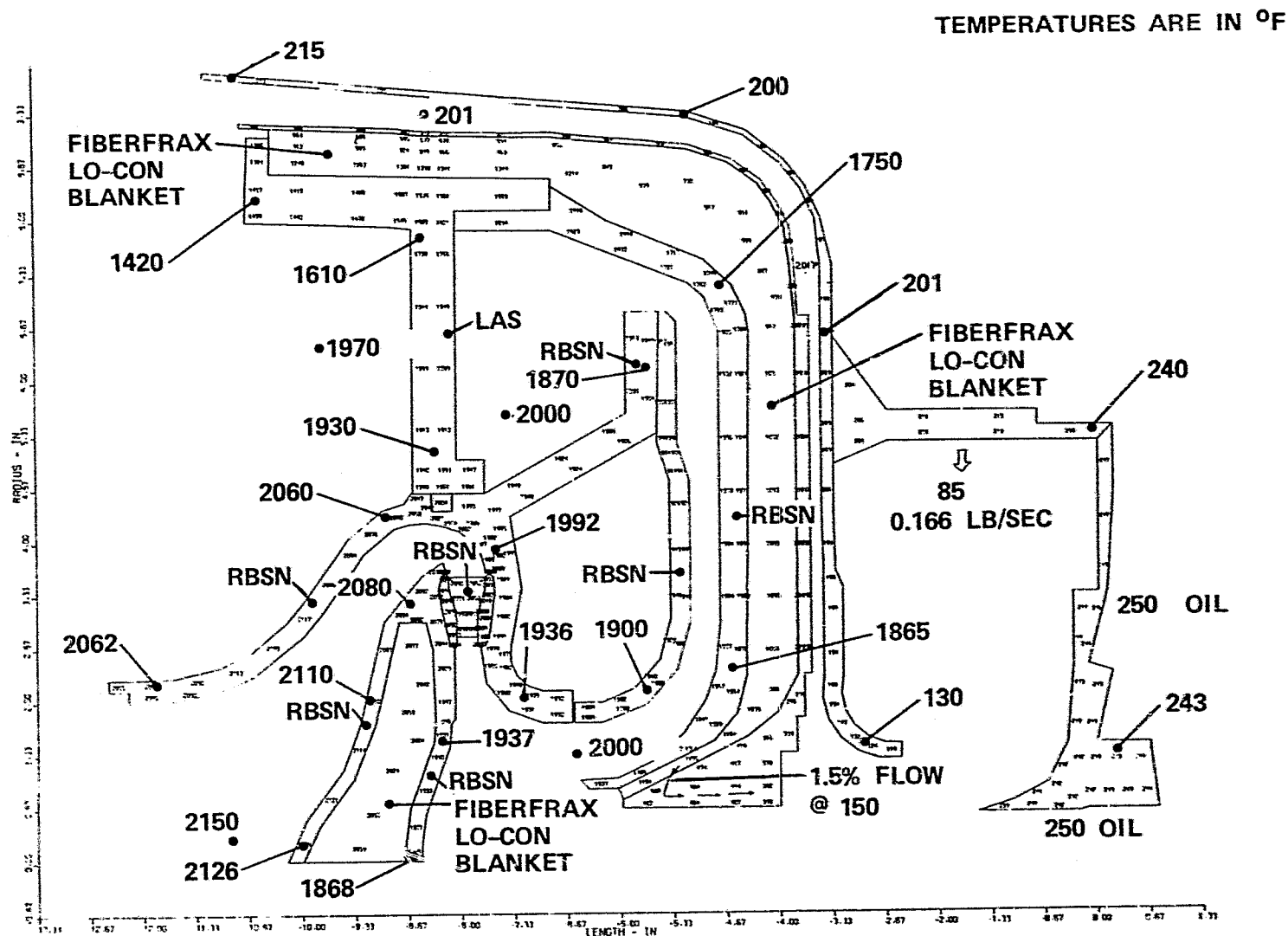
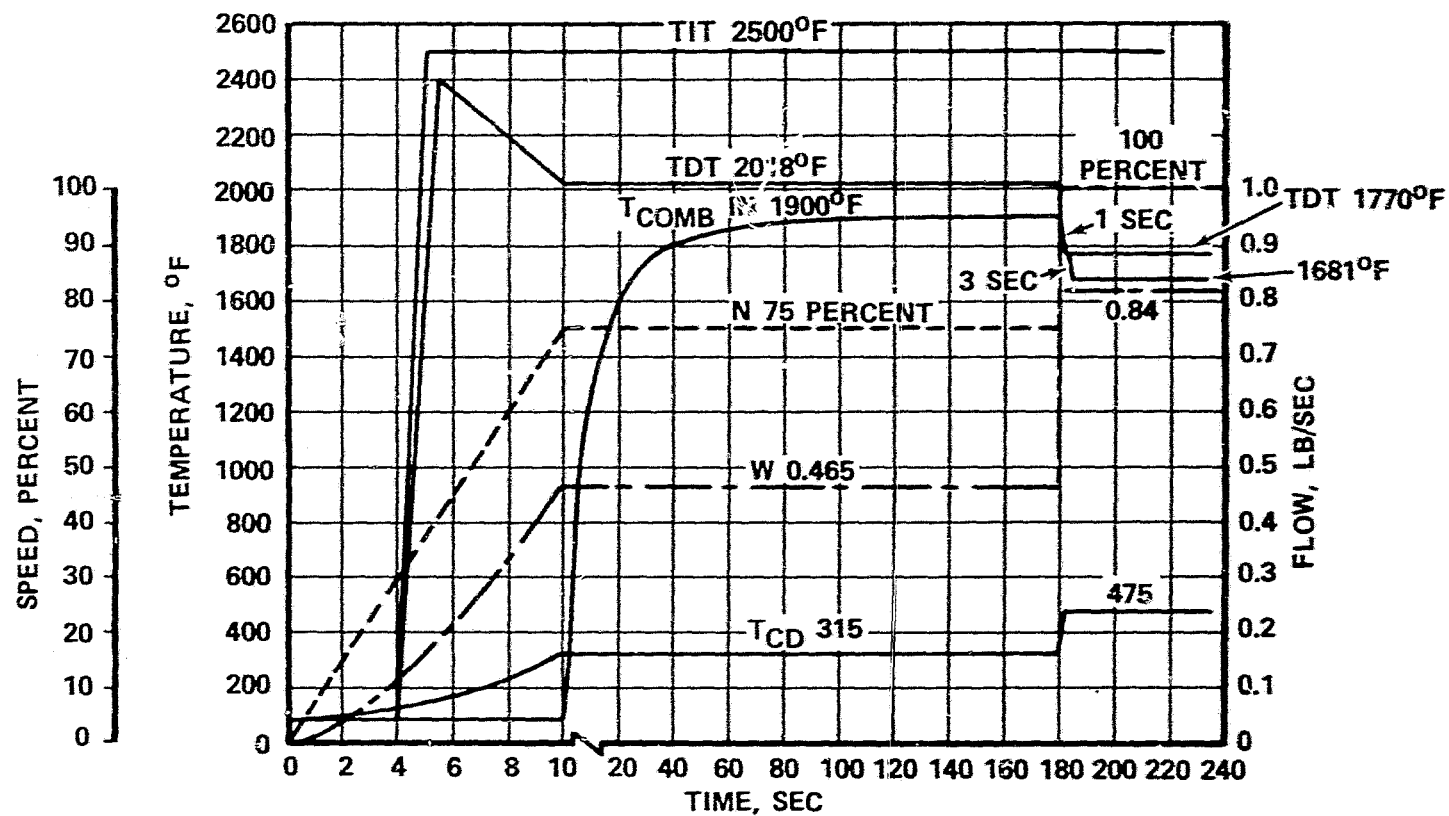


Figure 147. Static Structure Temperatures Idle Power Condition.

ORIGINAL PAGE IS
OF POOR QUALITY



TIT = TURBINE INLET TEMPERATURE
 TDT = TURBINE DISCHARGE TEMPERATURE
 T_{CD} = COMPRESSOR DISCHARGE TEMPERATURE

Figure 148. Worst Case Start Cycle.

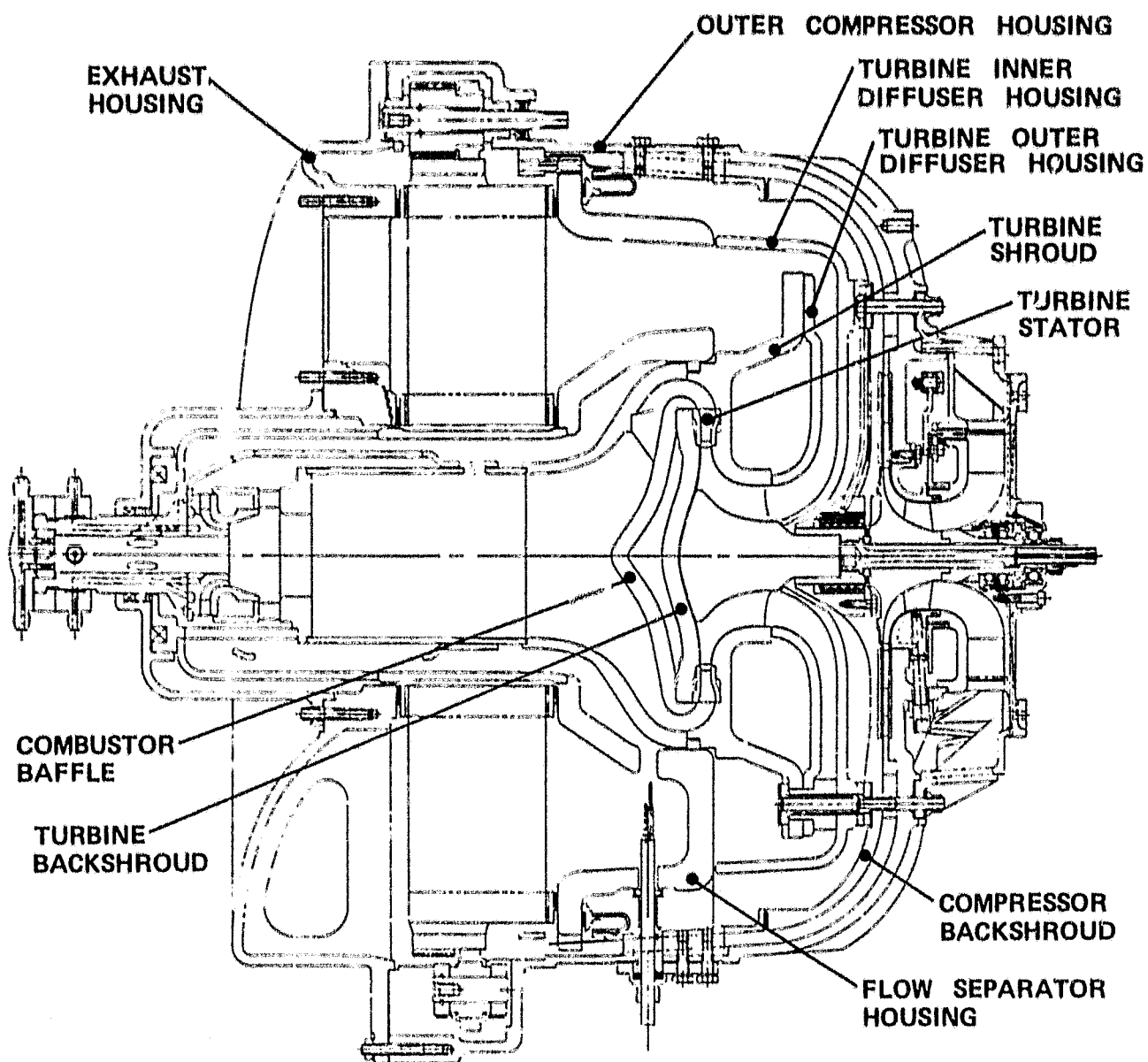


Figure 149. Power Section - Mod II.

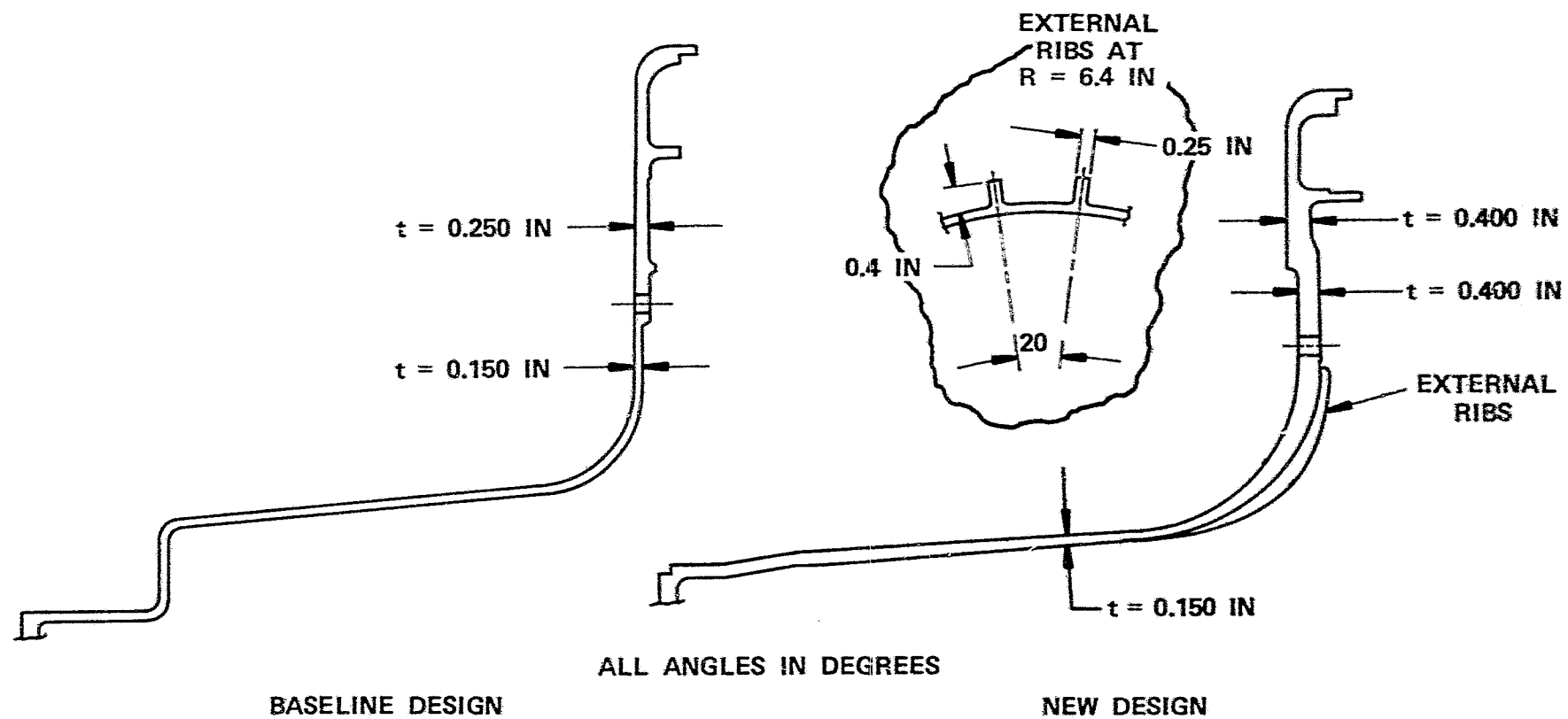


Figure 150. Design Configurations - Compressor Housing.

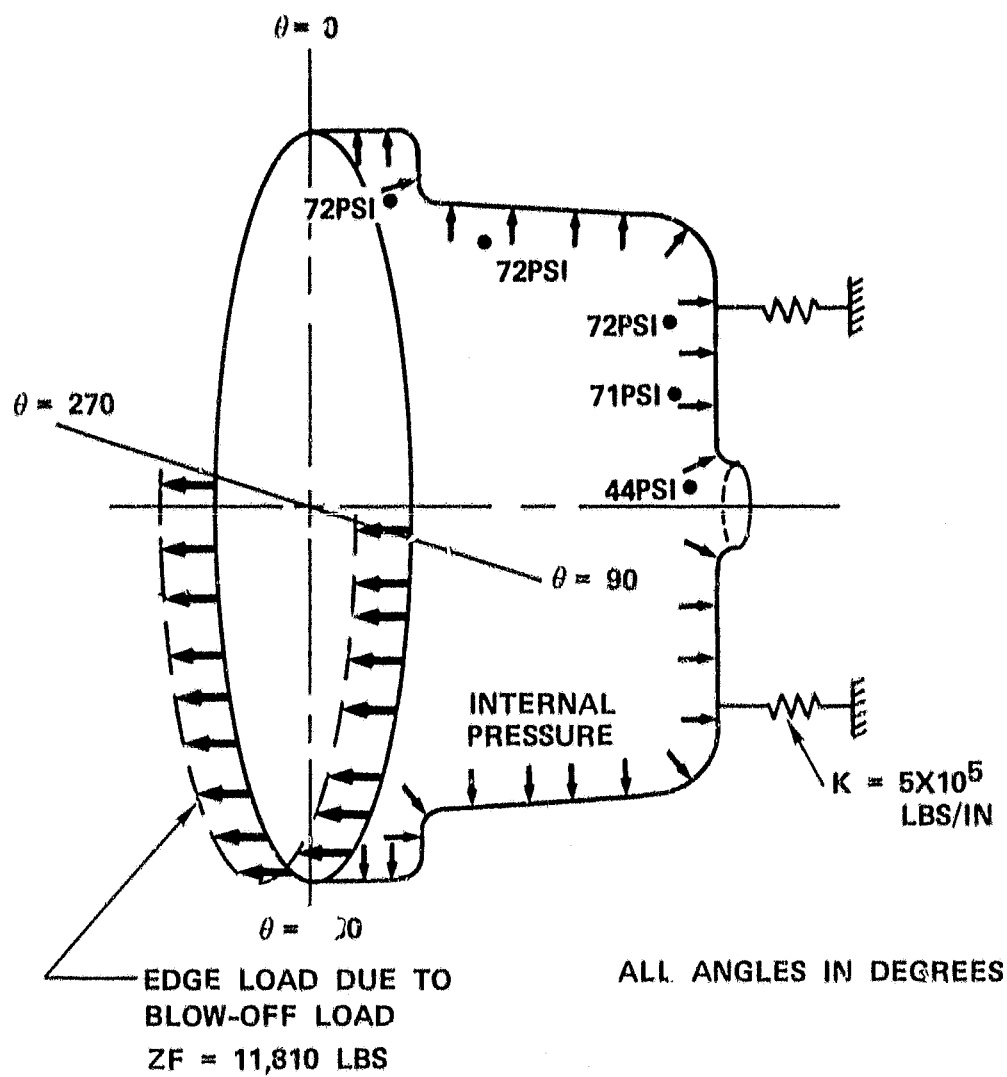


Figure 151. Outer Housing Loading.

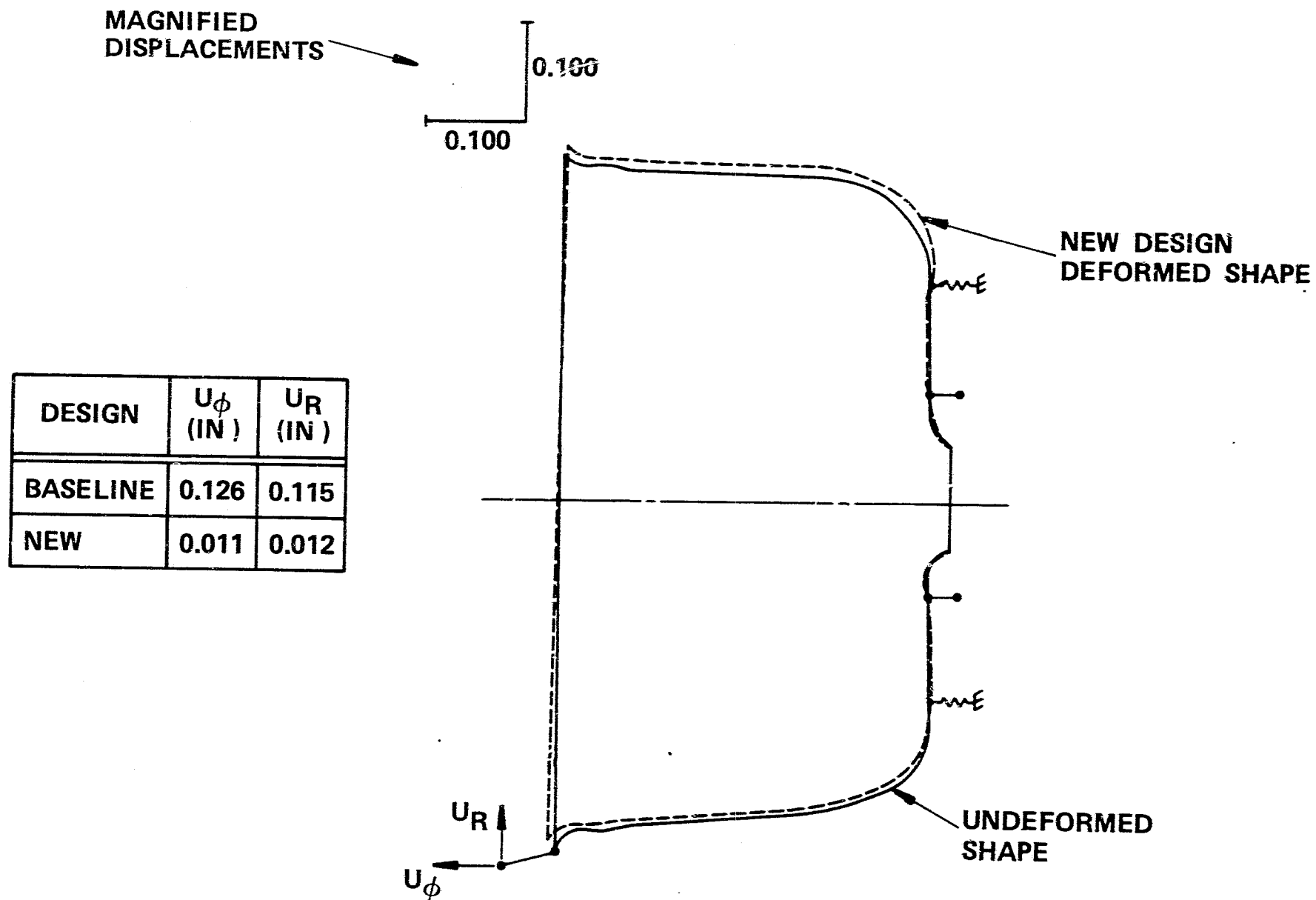


Figure 152. Compressor Housing Deflections.

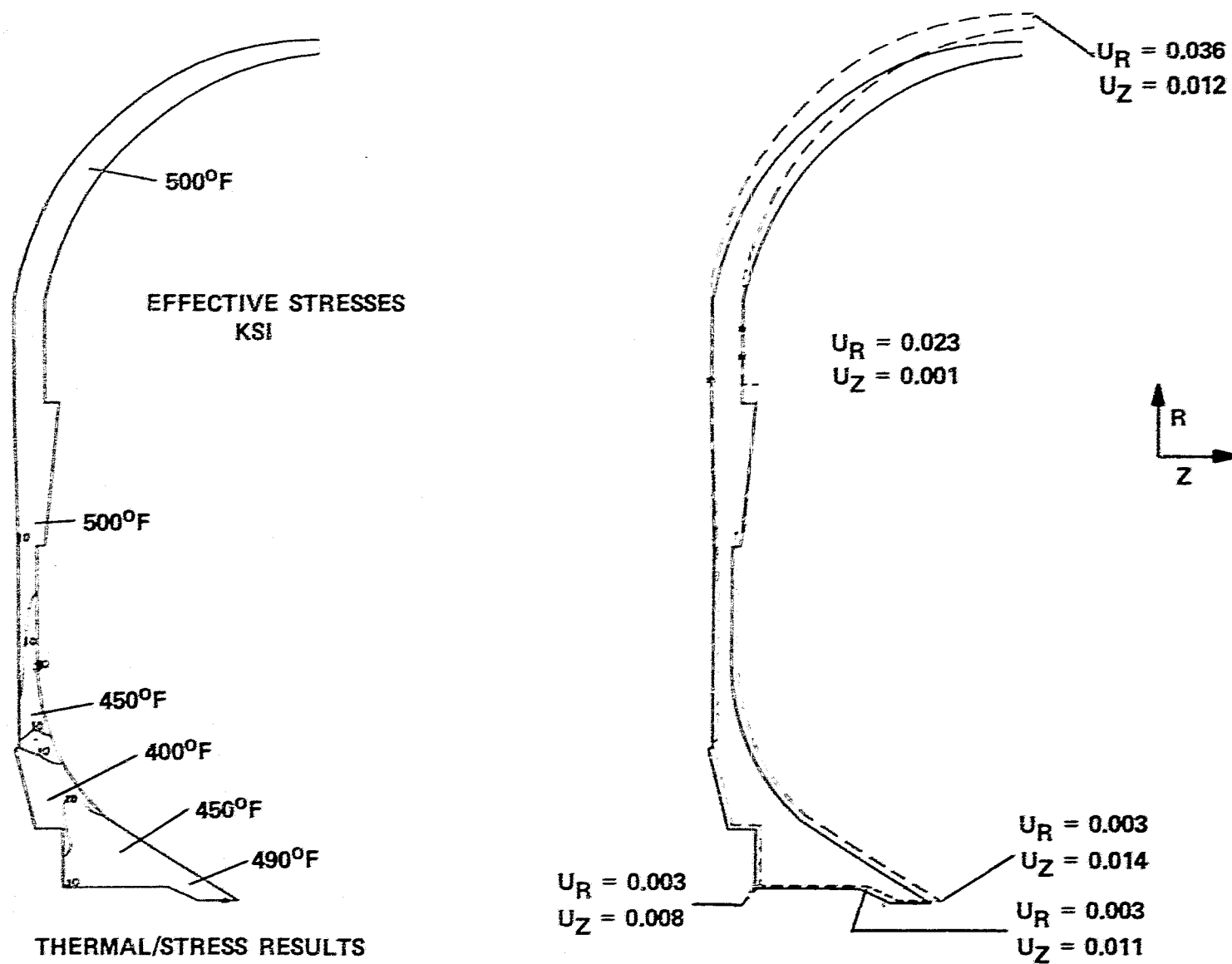


Figure 153. Compressor Backshroud Thermal/Stress Analysis.

4.6.1.3 Exhaust Housing

As discussed in Sections 3.1 and 4.4, herein, regenerator pocket dimensional control has been optimized. This optimization includes the compressor outer housing deflection analysis, discussed above, flow separator housing support and the exhaust housing. Figure 154 presents the exhaust housing 3-D finite element model. Utilizing high pressure flow control devices, (i.e., ribs, as effective stiffeners for deflection control), the exhaust housing deflections are minimized and therefore are only a small contributing factor to regenerator pocket growth. Figure 155 summarizes the exhaust housing deflections. No thermal or stress problems are anticipated.

4.6.2 Ceramic Structures Analysis

Seven major ceramic structural components have been analyzed: turbine inner diffuser housing, turbine outer diffuser housing, turbine shroud, turbine backshroud, combustor baffle, flow separator housing and turbine stator (see Figure 149). Stresses calculated and reported herein are for RBSN material that will be used for all components except the flow separator housing which will be fabricated from LAS. Work currently is in progress to calculate stresses for these same components, except the flow separator housing, using sintered α SiC material properties.

4.6.2.1 Turbine Inner Diffuser Housing

The element grid used for both heat transfer and stress analysis, including steady-state maximum power heat transfer boundary conditions for the turbine inner diffuser housing, is shown in Figure 156.

The peak maximum principal stress location and magnitude as a function of time during the worst case start transient condition is shown in Figure 157. Stresses shown are thermally and mechanically induced. The peak stress is dominated by the thermal stresses with very little contribution from the pressure differential across the component.

4.6.2.2 Turbine Outer Diffuser Housing and Shroud

The turbine outer diffuser housing and shroud are coupled in the element grid shown in Figure 158. Also included are the heat transfer boundary conditions, varied appropriately as a function of time.

The peak maximum principal stress occurs during the "worst case start" transient and is predominantly a thermally induced stress with very little contribution from mechanical loading. The stress distribution at 85 seconds into the start, and the location and magnitude of the peak stress as a function of time are shown in Figure 159.

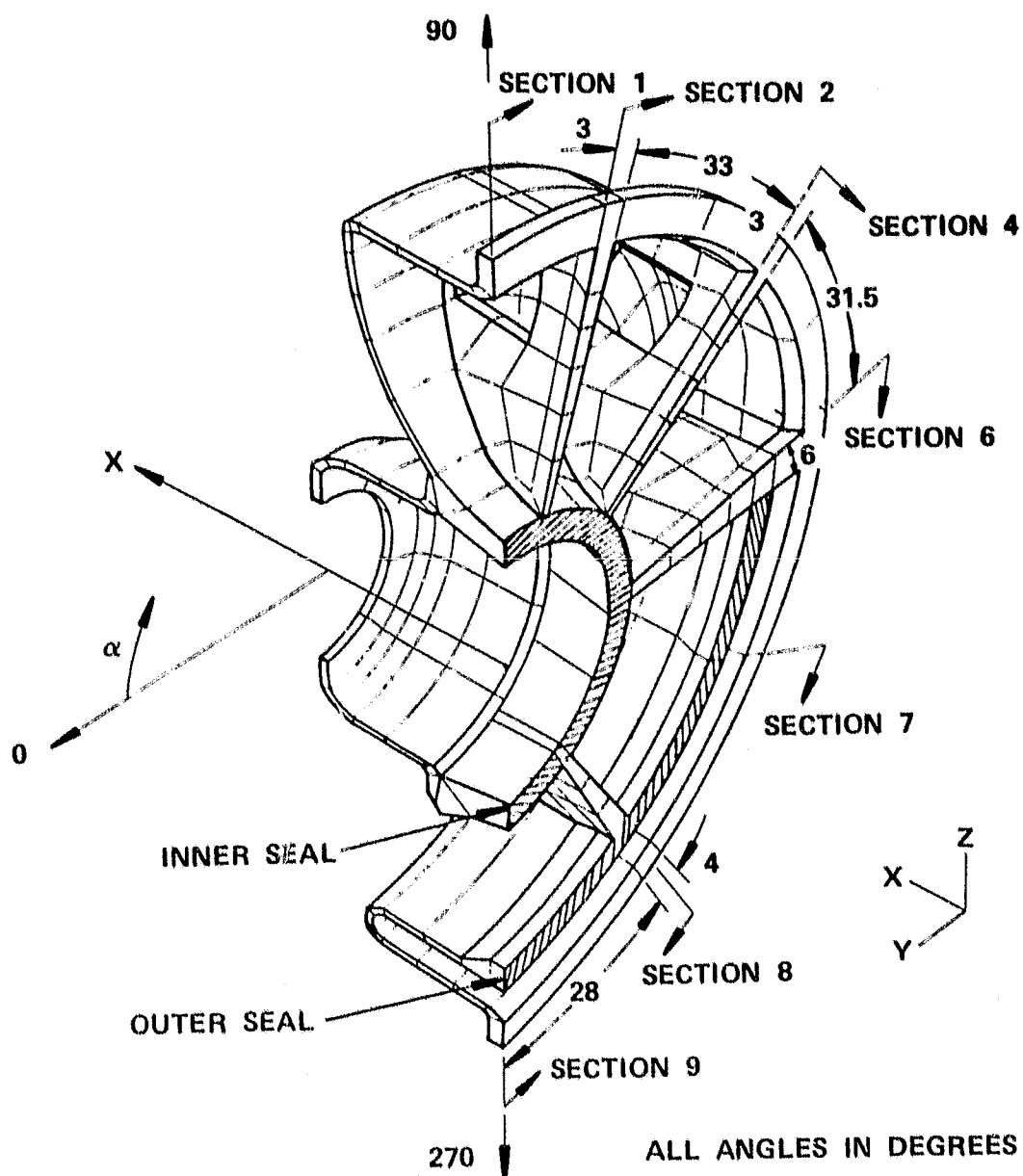


Figure 154. Exhaust Housing - 3-D Finite Element Model.

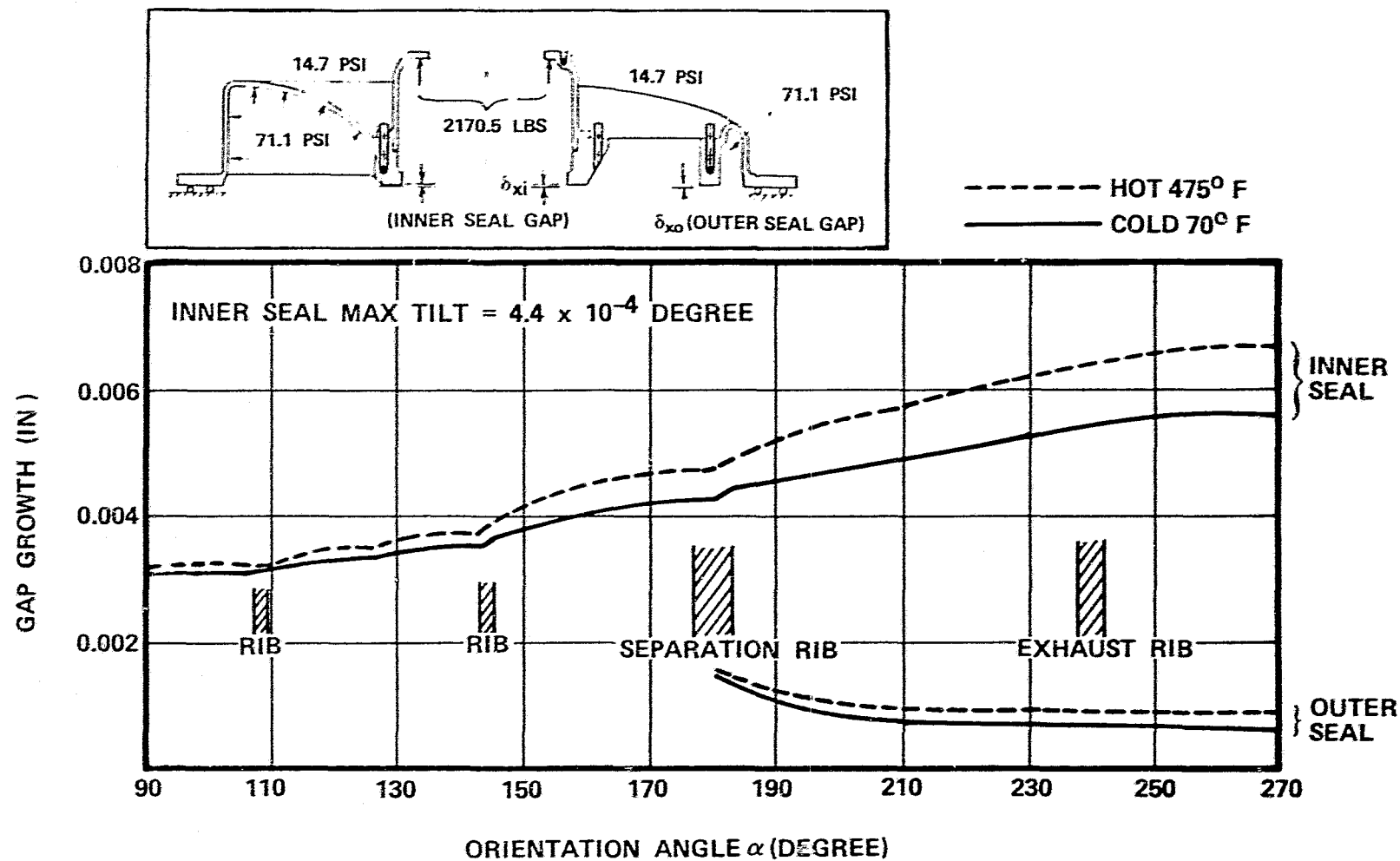


Figure 155. Exhaust Housing Regenerator Header Seal Gap Growth.

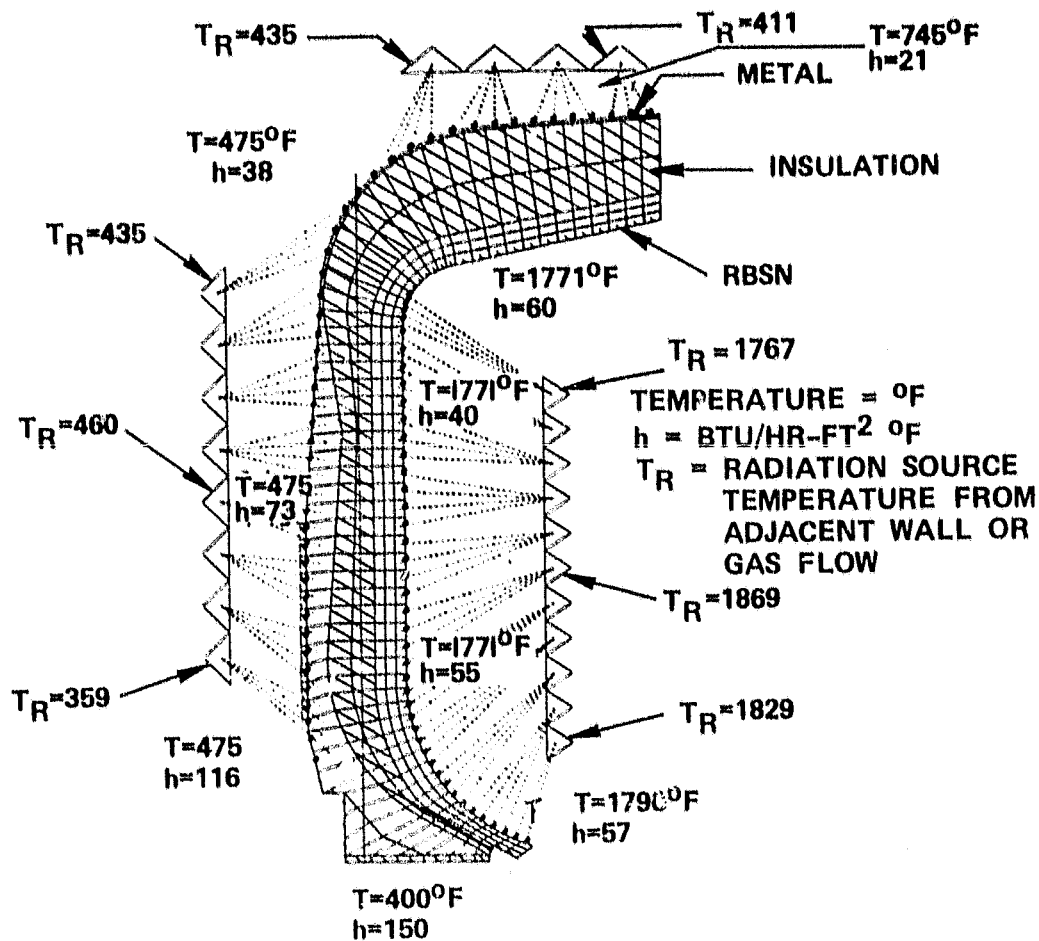


Figure 156. Inner Turbine Diffuser Housing Analysis Grid and Maximum Power Boundary Conditions.

MATERIAL: RBSN

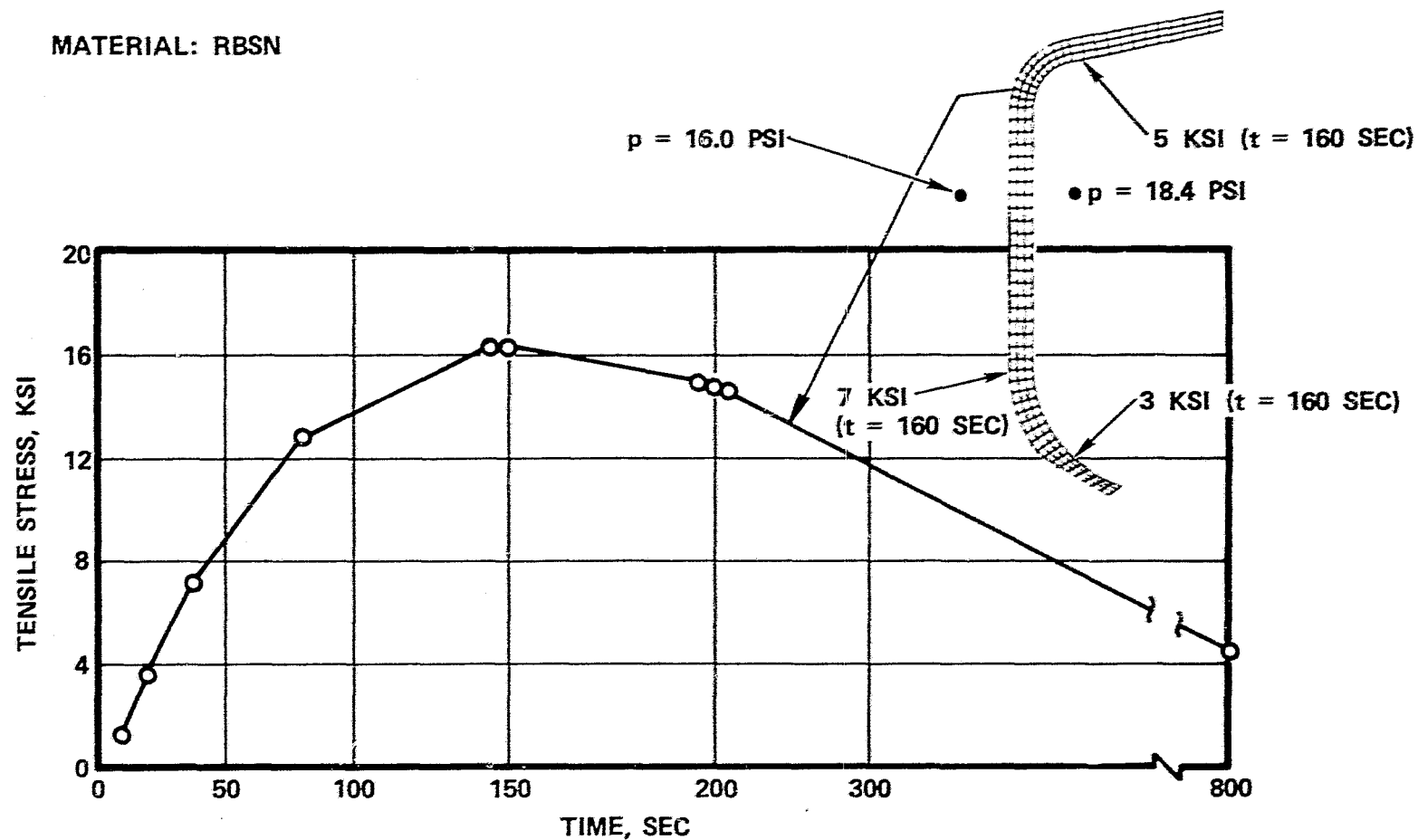


Figure 157. Inner Turbine Diffuser-Maximum Thermal and Mechanical Principal Stresses During Worst Case Start.

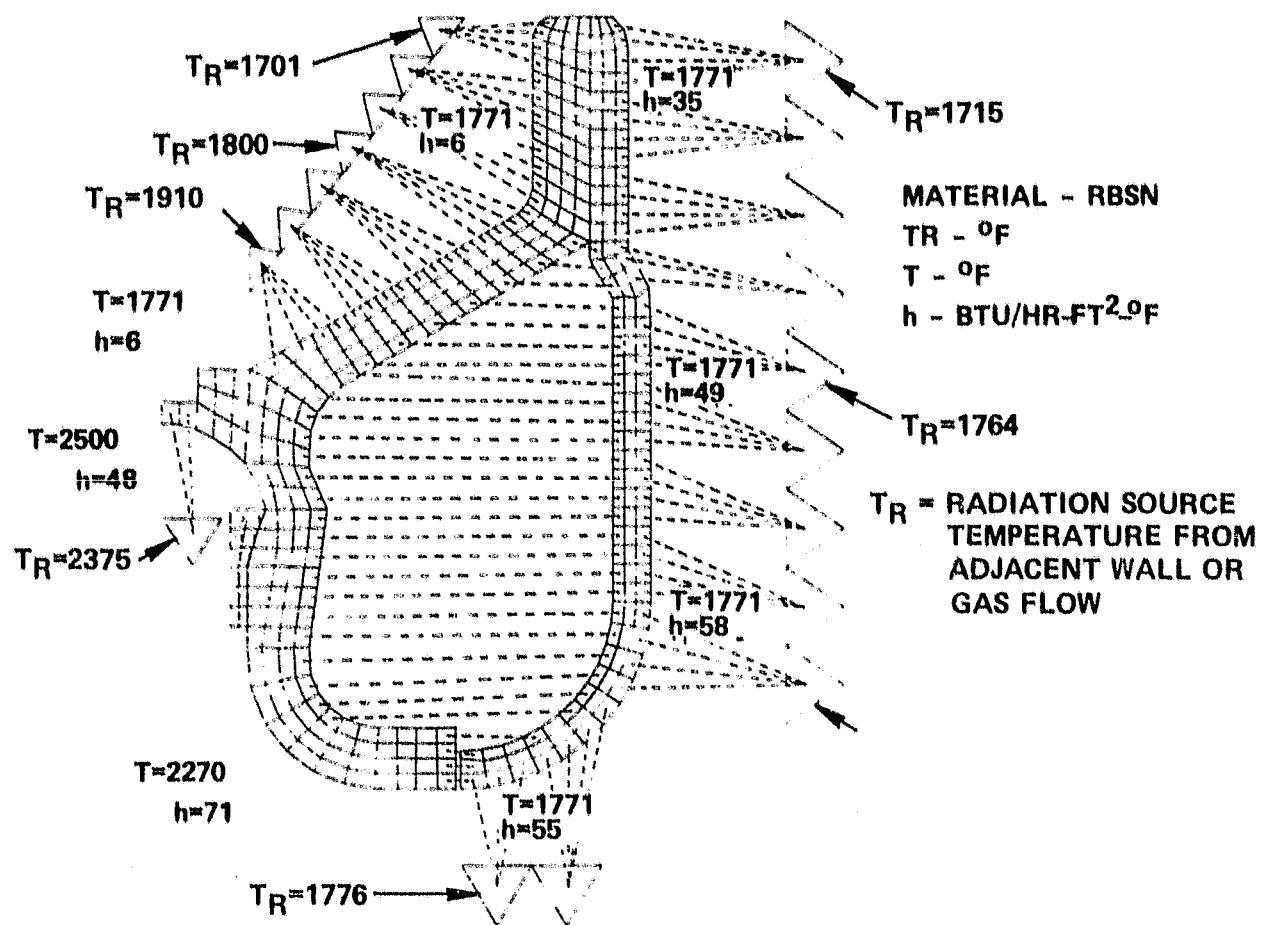


Figure 158. Turbine Shroud and Outer Diffuser Housing Grid With Maximum Power Boundary Conditions.

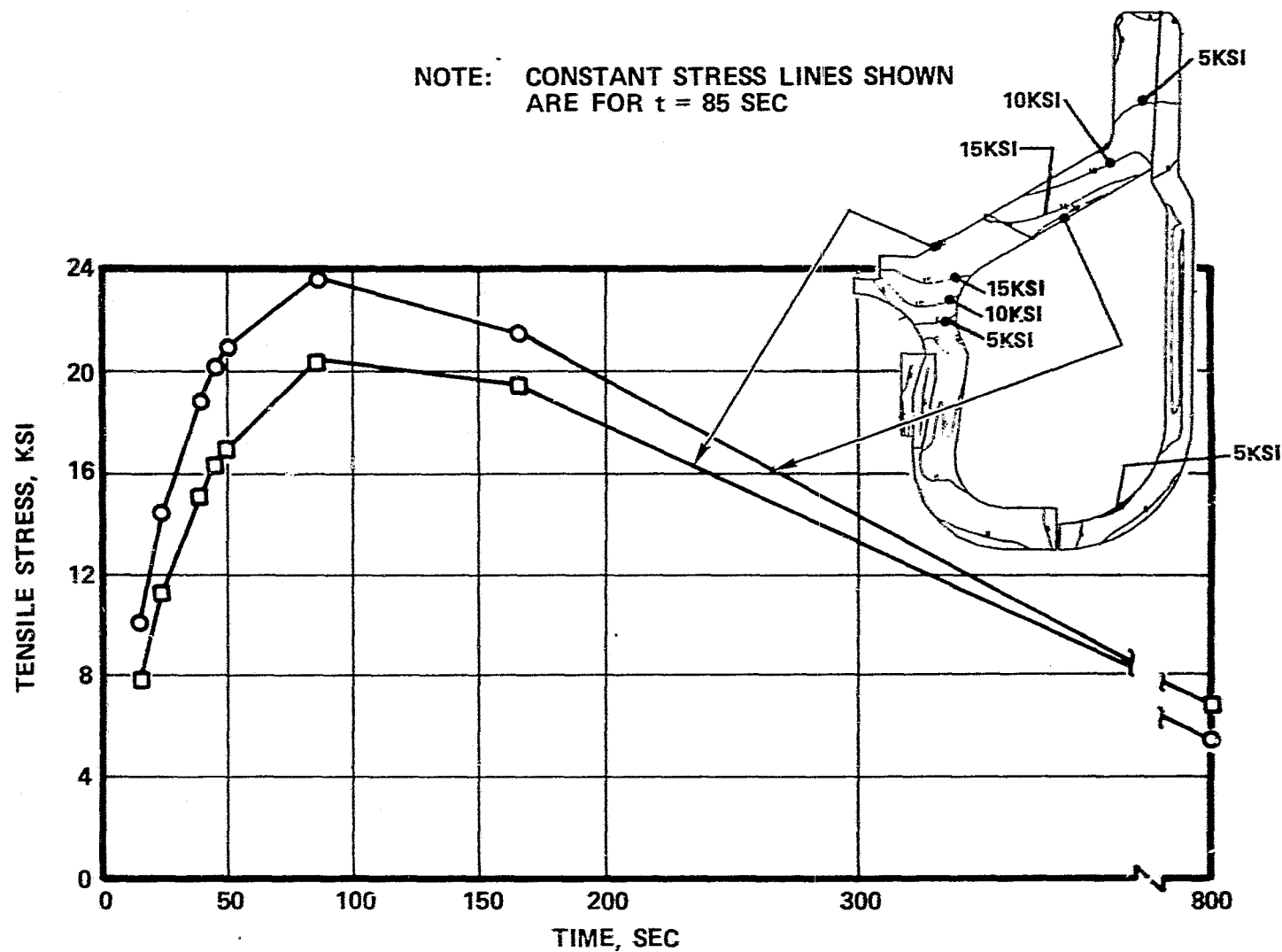


Figure 159. Turbine Shroud and Outer Diffuser-Maximum Thermal and Mechanical Principal Stresses for Worst Case Start.

4.6.2.3 Turbine Backshroud and Combustor Baffle

The turbine backshroud and combustor baffle were considered together in the combined model shown in Figure 160, along with the heat transfer boundary conditions associated with the maximum power operating condition. This particular model was used to evaluate the effect of a thick (0.40 inch) versus thin (0.26 inch) wall configuration with respect to thermally induced stresses, particularly during the transient operating condition.

The thermally induced stresses calculated for the two configurations are shown in Figure 161. Note that the trend is to have somewhat higher stresses with a thick wall design; however, the stress levels are well within the strength capabilities of the RBSN material. Additionally the peak stresses shown occur at the same location and at the same operating condition for both designs and are equal in magnitude.

Therefore, comparative analysis results indicate that either wall thickness provides a safe design. The thick wall design has been chosen for the final design because it provides a simpler interface between the baffle, backshroud, and stator segments.

4.6.2.4 Flow Separator Housing

A 3-D thermal and stress analysis of the flow separator housing evaluated maximum stresses during steady-state, worst-case start-up and shutdown conditions. Two conditions of OD insulation were considered; one with perfect insulation (i.e., no heat transfer at the outer boundary) and the second which assumed a 0.65-inch thick layer of Fiberfrax ceramic insulation between the OD and compressor discharge flow. Two configurations of OD were investigated; the baseline design (old) which has a flat outer surface and the current design (new) which incorporates a stiffening ring or flange on the OD. Figure 162 depicts the applicable heat transfer boundary conditions.

Maximum thermal stresses were found to be relatively low primarily due to the low thermal expansion and elastic modulus of the lithium-aluminum-silicate material and the large thermal mass of the component. Peak thermal stresses of 1.4 and 1.8 ksi occurred during the start-up transient for the insulation exposed to compressor discharge and perfectly insulated cases, respectively. The addition of pressure loading increased the maximum principal stress to 3.4 ksi during start-up for the old configuration and 2.7 ksi for the new configuration. The addition of a stiffening ring to the OD results in a significant reduction of peak stress level. Figures 163 and 164 show the locations of the peak stresses, and a tabulation of stresses for various operating conditions.

TEMPERATURE = °F

h = BTU/HR. FT². °F

T_R = RADIATION SOURCE
TEMPERATURE FROM
ADJACENT WALL OR
GAS FLOW

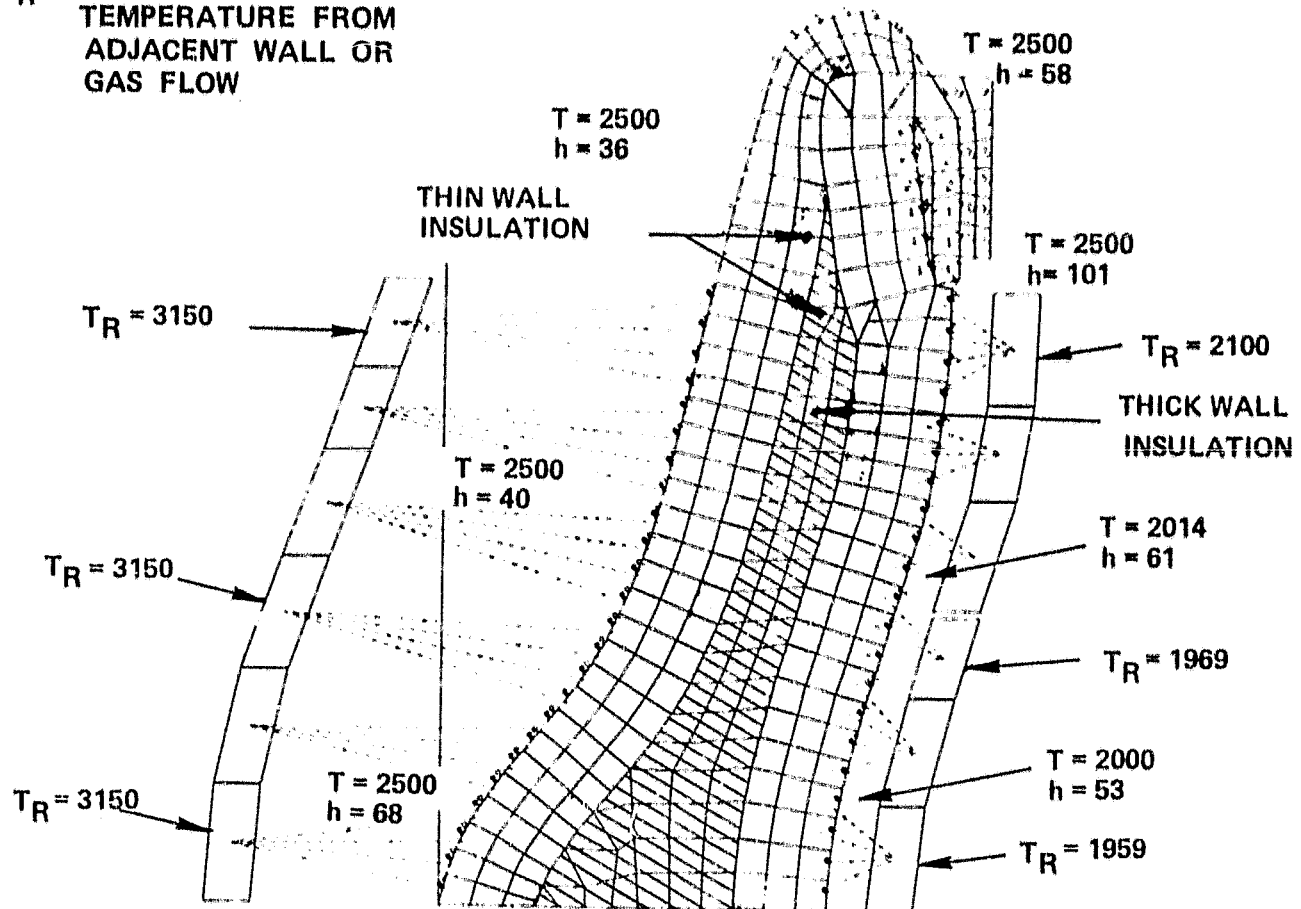


Figure 160. Turbine Backshroud and Combustor Baffle Stress and Heat Transfer Model.

MATERIAL - RBSN

STRESS - PSI

THICK = 0.40 WALL THICKNESS

THIN = 0.26 WALL THICKNESS

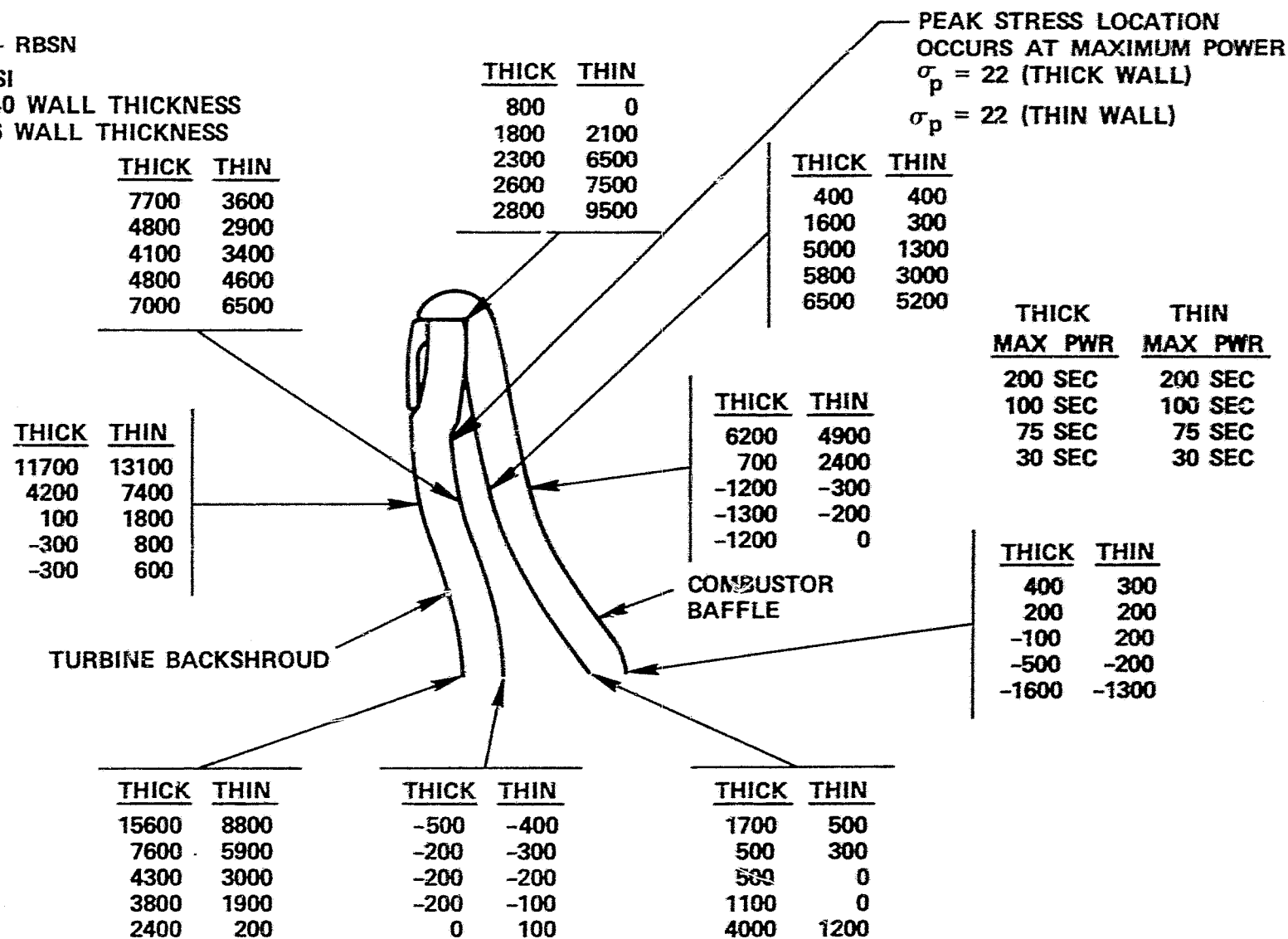


Figure 161. Thermally Induced Stresses for Turbine Backshroud and Combustor Baffle.

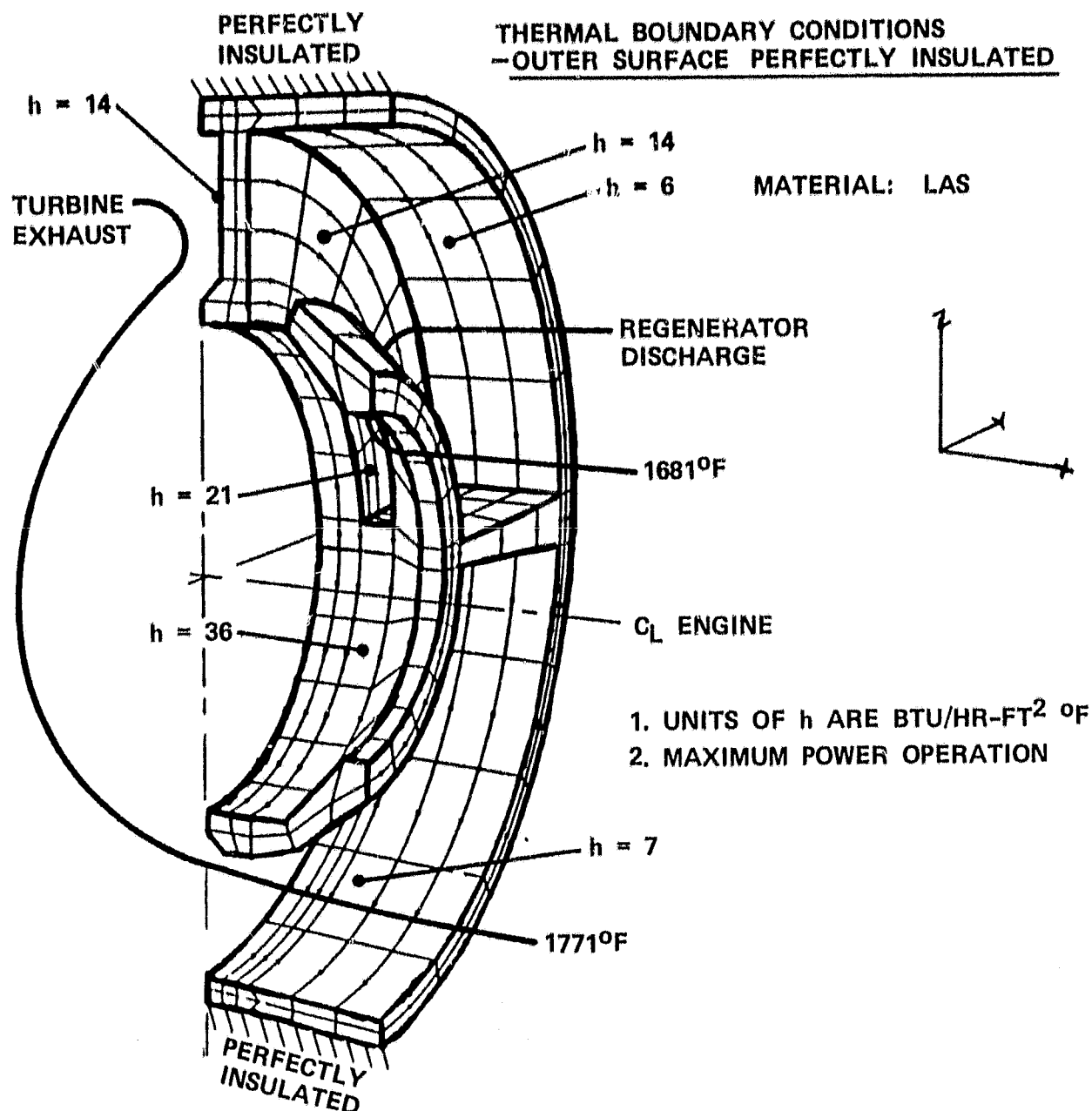


Figure 162. Flow Separator Housing Finite Element Model and Thermal Boundary Conditions - Outer Surface Perfectly Insulated.

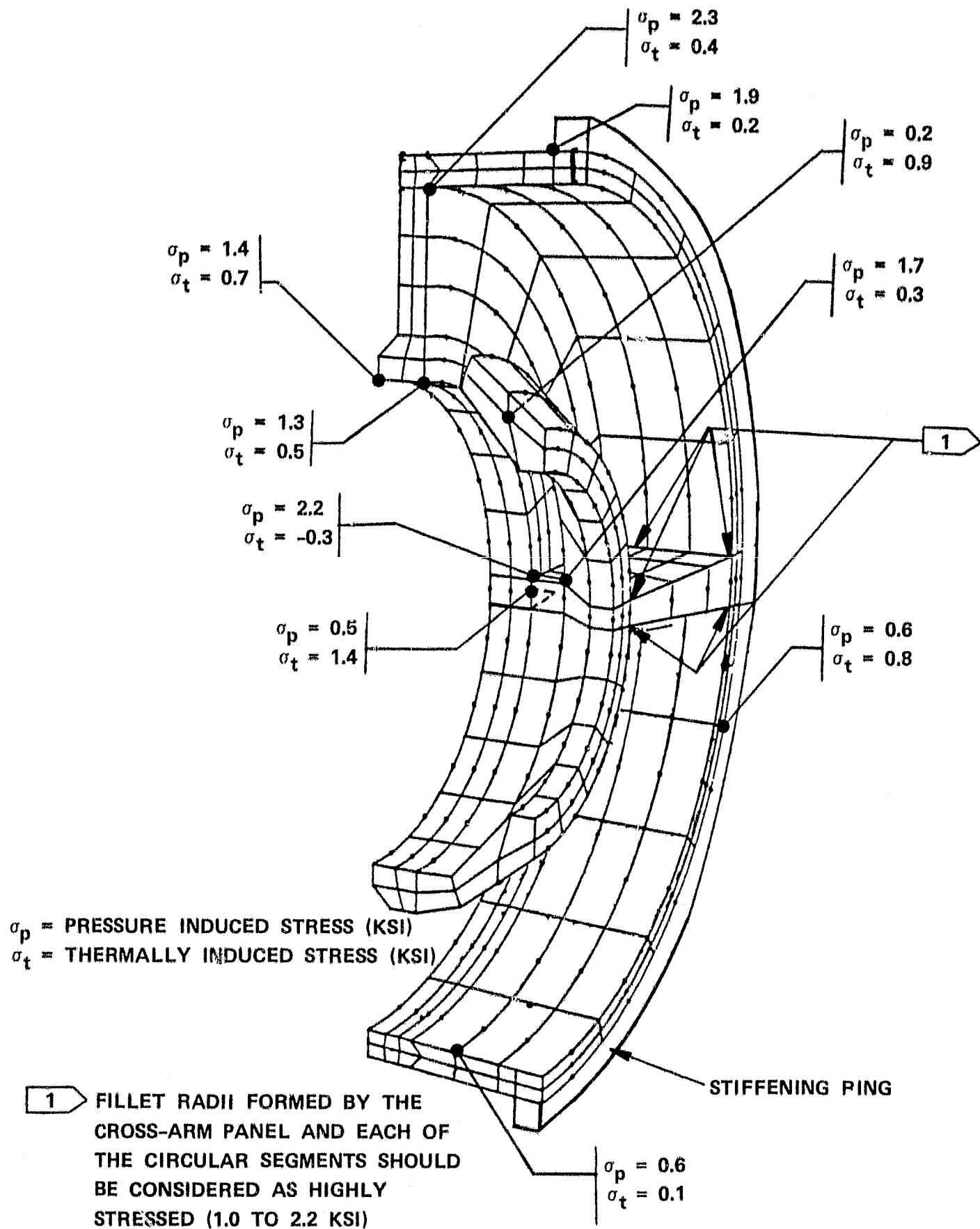


Figure 163. AGT101 Flow Separator Housing Peak Stress Locations and Magnitudes.

IDENT	WITH PERFECT O D INSULATION									O D FIBER FRAX INSULATION EXPOSED TO T _{CD}	
	STEADY STATE PRESS ONLY		STEADY STATE TEMP & PRESS		START, 300 SEC PRESS & TEMP		START, 300 SEC TEMP ONLY	START, 978 SEC TEMP ONLY	STOP, 521 SEC TEMP ONLY	START, 240 SEC TEMP ONLY	STOP, 40 SEC TEMP ONLY
	NEW	OLD	NEW	OLD	NEW	OLD					
1	2.3	2.9	2.3	2.9	2.7	3.4	0.7	1.3	0.6	0.8	0.5
2	2.2	2.2	2.2	2.2	2.2	2.2	1.1	1.4	0.5	0.9	0.8
3	0.3	0.3	0.4	0.4	0.7	0.7	0.2	0.8	0.6	0.6	0.5
4	1.7	1.7	1.7	1.7	2.4	2.4	0.9	0.4	0.2	1.8	1.3
5	1.6	1.6	1.6	1.6	1.0	1.0	1.1	1.4	0.5	1.0	1.4

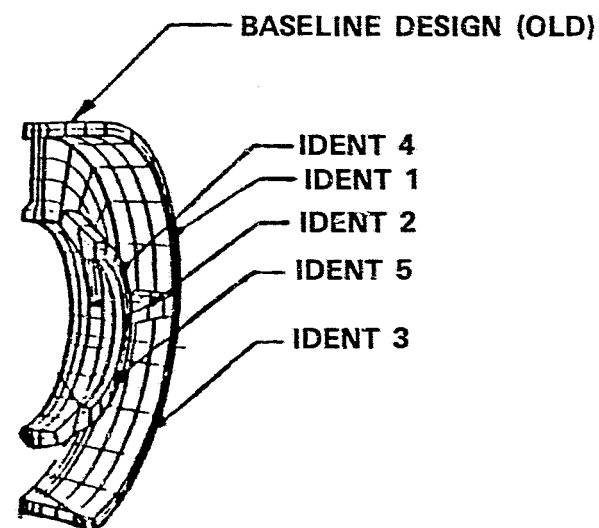
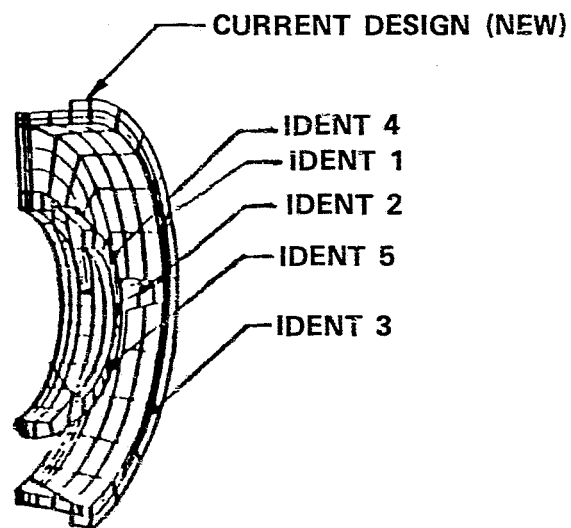


Figure 164. Flow Separator Housing Maximum Principal or Effective Stresses (KSI).

4.6.2.5 Turbine Stator

The turbine stator was analyzed in detail using a combination of structural analyses programs. Figure 165 and 166 show the 3-D finite element model used in this analysis. The material is RBSN. The thermal model grid was compatible with the stress model and the requirements for obtaining good transient temperatures. The model was designed to have small elements in regions of high stress and rapid temperature change. The effects of contact resistance, enclosed cavities and radiation were included.

Figures 167 and 168 show the transient temperatures of the turbine inlet gas during a normal start and worst case shutdown. The highest thermal gradients occur approximately 10 seconds after start. Stresses were evaluated at points of maximum thermal gradient.

Stress results show the maximum principal tensile stress occurs near the center of the trailing edge. For normal start condition, this maximum stress is 23 ksi for RBSN material. Analysis is underway for SiC material and an integral design using RBSN material.

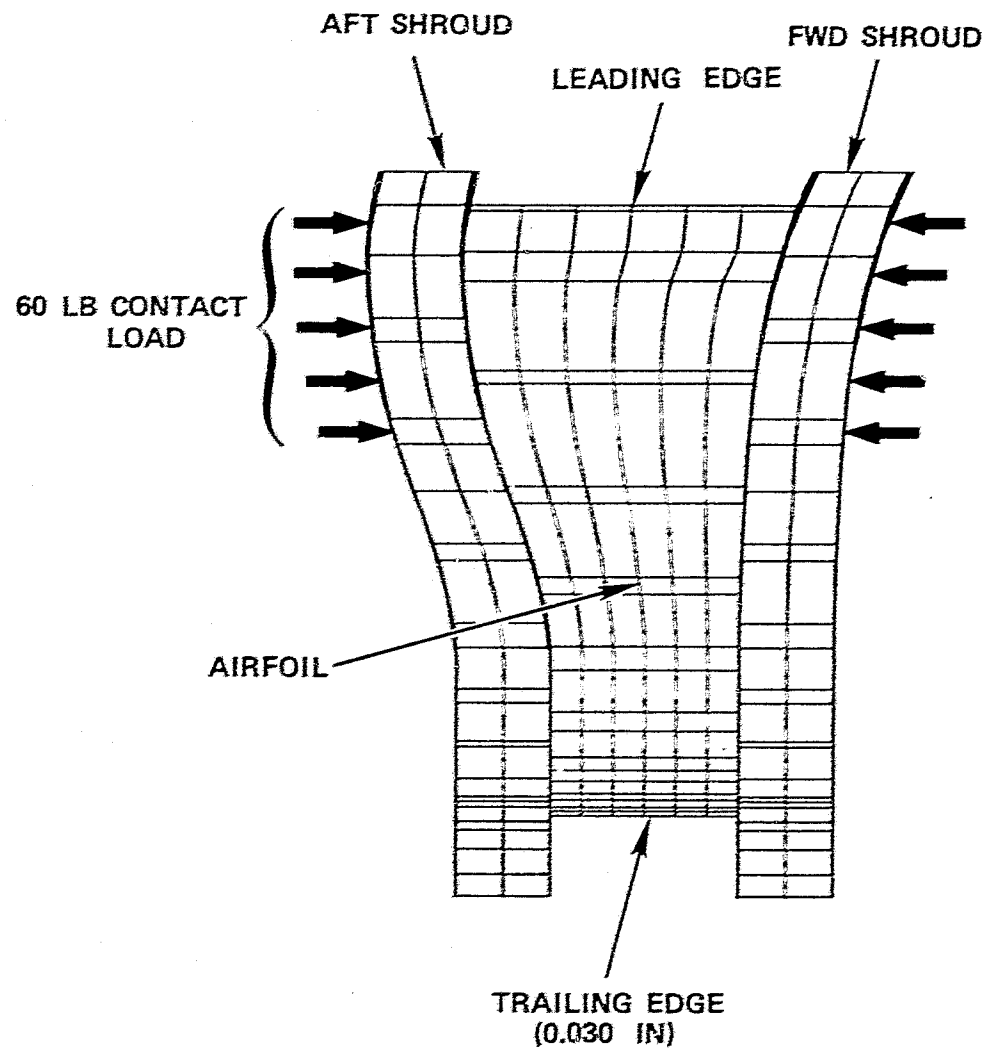
A risk assessment for the ceramic stator was performed using the finite element stress results. The RBSN material parameters used in this evaluation were a characteristic strength of 42.8 ksi and a Weibull slope of 8. The results are summarized on Table 21.

4.6.2.6 Ceramic Structures Summary

The current design configuration has been shown satisfactory for RBSN material during both maximum power and "worst case start" transient operating conditions. Currently sintered α SiC is being evaluated for these same conditions. Future plans also call for an investigation of thermal stresses during a shutdown transient condition.

The maximum principal stresses in the structural components are summarized below:

	Stress (ksi)	Operating Condition
o Combustor Baffle		
Thin Wall	9.5	Worst start at 30 seconds
Thick Wall	6.5	Worst start at 30 seconds



TOTAL NODES: 2163

TOTAL ELEMENT: 548

MATERIAL: RBSN

TYPE OF ELEMENT: ISOPARA-
METRIC SOLID ELEMENT

Figure 165. Stator 3-D Finite Element Model.

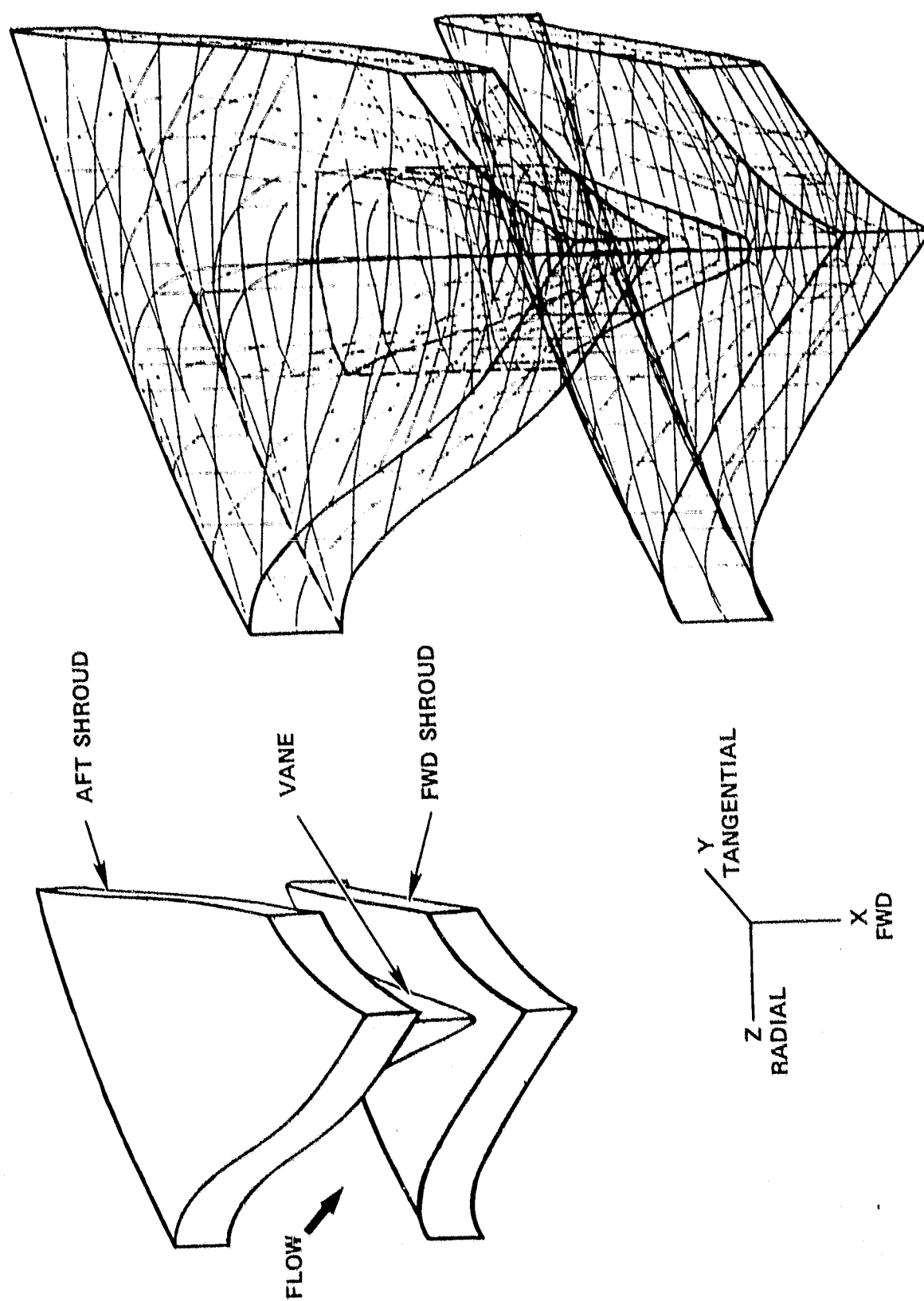


Figure 166. Segmented Stator - 3D Finite Element Model.

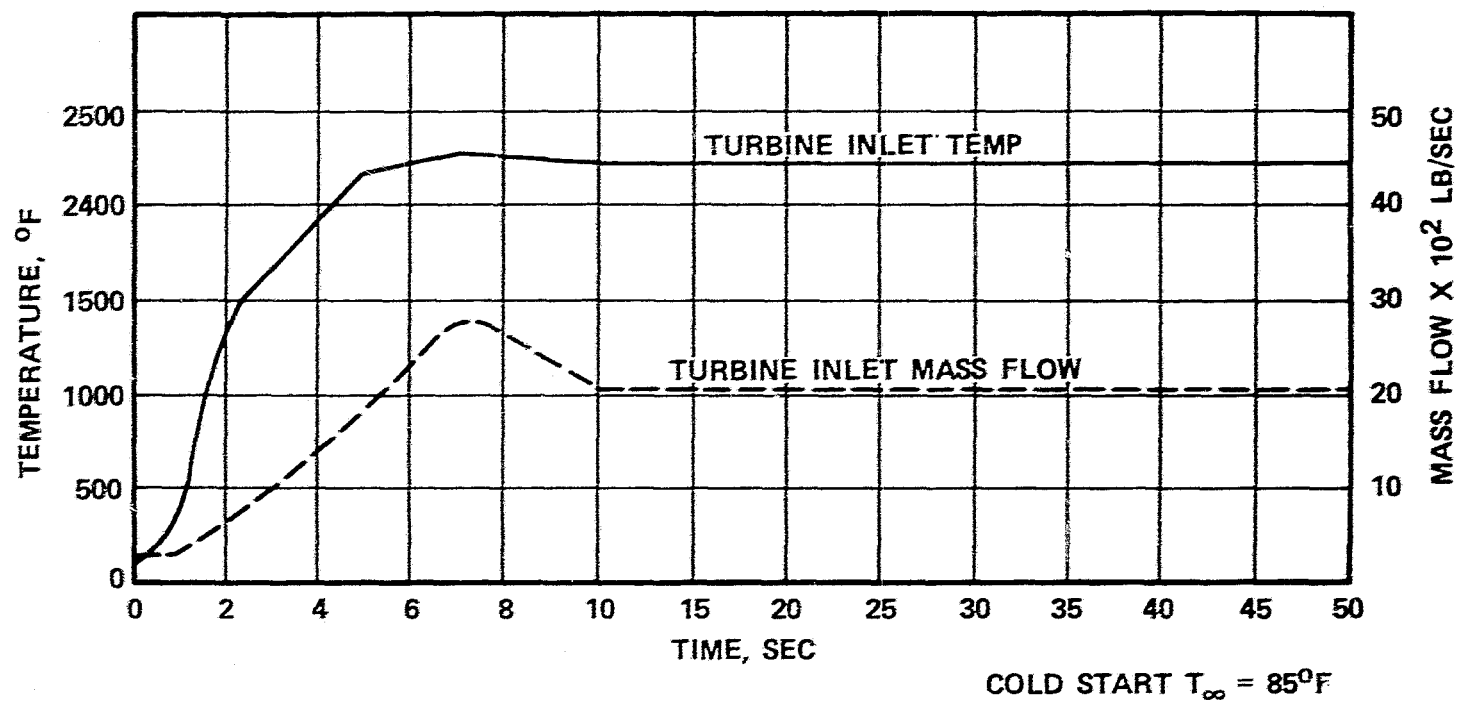


Figure 167. Ceramic Turbine Transient Inlet Conditions.

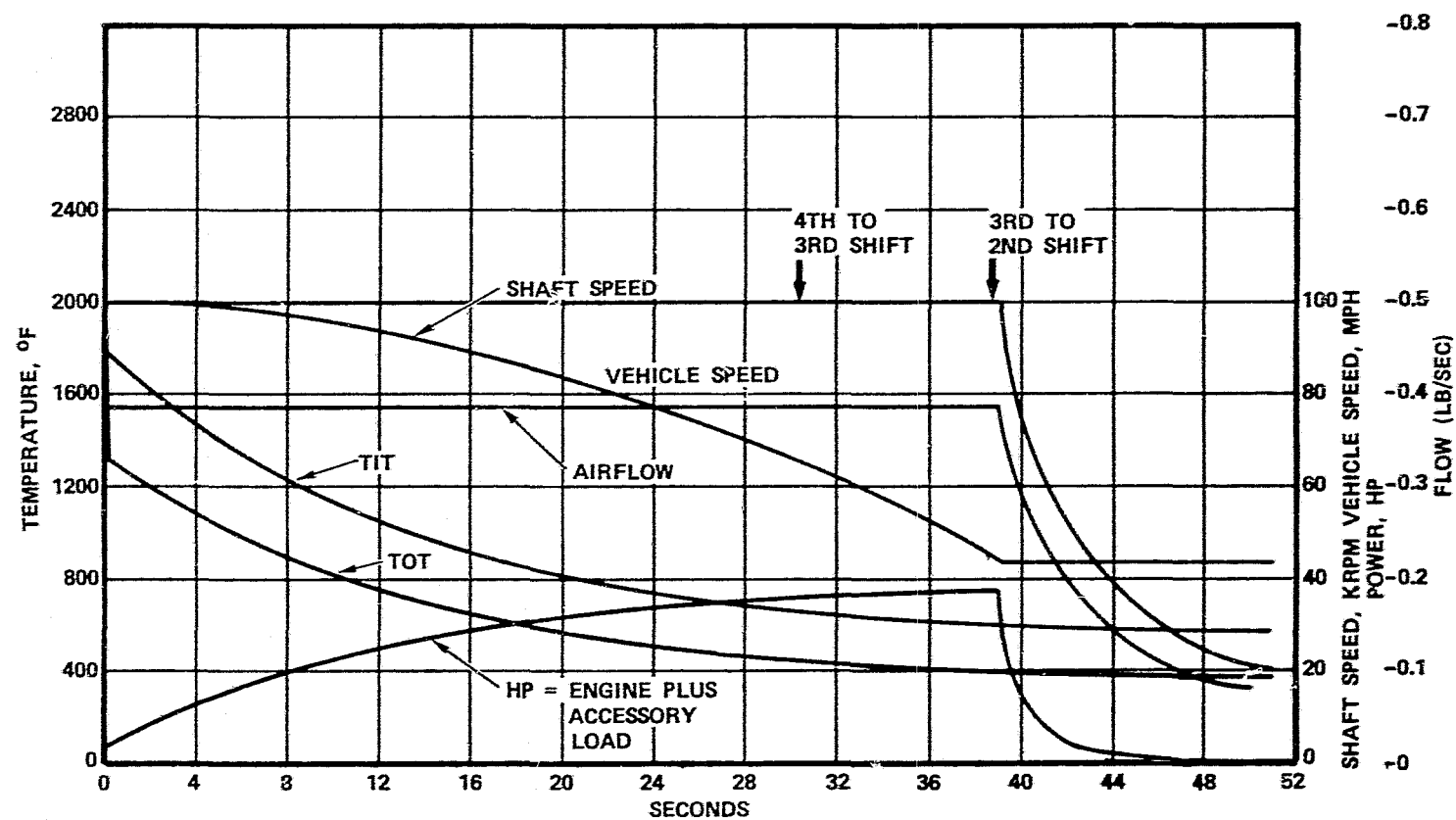


Figure 168. Worst Case Shutdown Cycle.

TABLE 21. AGT CERAMIC STATOR THERMAL STRESS ANALYSIS

AGT Ceramic Stator Structural Summary

Cycle Conditions	Stress (ksi)			CPS Vane per Vane Segment
	FWD Shroud	AFT Shroud	Vane	
Steady State	2.0	3.9	3.5	100.0000
Normal Start	11.0	11.6	23.3	99.9998
Worst Start	15.2	15.3	35.4	99.9948
Worst Shutdown	7.9	5.7	7.9	100.0000

CPS = Cumulative Probability of Success

	Stress (ksi)	Operating Condition
o Turbine Backshroud		
Thin Wall	22.0	Maximum power
Thick Wall	22.0	Maximum power
o Turbine Shroud	23.8	Worst start at 85 seconds
o Turbine Outer Diffuser Housing	10.4	Worst start at 85 seconds
o Turbine Inner Diffuser Housing	16.3	Worst start at 152 seconds
o Flow Separator Housing	2.7	Worst start at 300 seconds
o Turbine Stator	35.4	Worst start at 10 seconds

4.7 Ceramic Component Development

This section discusses ceramic material and component development and evaluation at AiResearch Phoenix and at the subcontractors.

4.7.1 Ceramic Material Evaluation

4.7.1.1 Evaluation Test Plan

Baseline specimens of each candidate material are being evaluated at AiResearch Phoenix to obtain data for design support, establish a basic understanding of strength/microstructure relationships and to identify sensitivity to time, temperature and environmental effects. Table 22 lists tests being conducted on baseline specimens. Results of these tests and associated fractography analysis will identify materials that have acceptable probability of survival for each component or if additional material improvement is required. The quantitative test output will provide direction to the amount and nature of improvements required.

Most of the tests in Table 22 are being conducted on specimens 2-inches long with 0.25 x 0.125 inch cross sections. All strength tests at AiResearch Phoenix are being conducted in quarter point bonding with an outer span of 1.5 inch and an inner span of 0.75 inch at a crosshead speed of 0.02 inch/minute. A steel fixture was used for the room temperature measurements and a hot-pressed silicon carbide fixture was used for the high temperature tests. The latter were conducted in air using a fast response C-M Rapid Temp furnace with a hold time of 5 to 10 minutes. Weibull analysis of the data is conducted with a computer program using a least squares fit with median ranking

$$\frac{i - 0.3}{N + 0.4} \text{ of the data.}$$

As testing of specimens progresses, test procedures and facilities will be presented in more detail along with the specific data.

4.7.1.2 ACC Baseline Materials

Samples of three silicon nitride materials, RBN 104 (slip cast RBSN), RBN 126 (injection molded RBSN) and SNN 522 (injection molded silicon nitride sintered with 8-percent Y_2O_3 and 4-percent Al_2O_3) have been received from ACC for material characterization. No samples of ACC SNN 502 slip cast sintered Si_3N_4 have been received for evaluation. Characterization studies include room temperature and elevated temperature 4 point flexure of as-received materials; room temperature 4 point flexure strength evaluations of transverse ground longitudinally ground and/or heat treated bars; stress rupture testing in static and gas fired environments; oxidation exposures; and SEM, EDX and X-ray diffraction analyses.

TABLE 22. BASELINE MATERIAL EVALUATION

TEST	EVALUATION
Flexure Strength Room Temperature 3 Elevated Temperatures Transverse Machined Longitudinal Machined	Characteristic Strength Weibull Modulus Fractography Microstructure X-ray Diffraction
Oxidation/Corrosion Gradient Furnace Static Oxidation Cyclic in NASA/AiResearch Phoenix Rig	Residual Strength Fractography EDX
Stress Rupture Static Air Gas Fired	Stress/Temperature versus Life Residual Strength Fractography EDX
Contact Stress/Interface Compatibility	Residual Strength, Coefficient of Friction, Fractography, Computer modeling
Post Fabrication Treatment Oxidation Annealing Coatings Infiltration (RBSN only)	Strength, oxidation resistance, Stress Rupture, Fractography, Microstructure, X-ray diffraction

Where transverse and longitudinal machined surfaces were evaluated, all test surfaces were prepared by grinding with 320 grit diamond wheels.

Characterization of the ACC materials is not complete; however, a summary of current results is presented in the following paragraphs.

4.7.1.2.1 RBN 104

RBN 104, a 2.8 g/cc slip cast reaction bonded Si_3N_4 , is the primary ACC material candidate for static structural components excluding the turbine stator. Test bars of this material were machined from green slip-cast plates then nitrided. Slips were prepared from air-classified Si powder with a 3-percent Fe_2O_3 nitriding aid. Unless otherwise stated, all test bars were evaluated in the as-nitrided condition to simulate most component surfaces. Test bars 2 x 0.250 x 0.125 inches were used for all evaluations.

Results of flexure testing bars with as-nitrided and as-machined surfaces at 72, 2200 and 2500°F are presented in Figure 169. Material strength distributions are presented in the Weibull plots of Figure 170 for the as-nitrided materials. As illustrated in Figure 171, strength is slightly higher at 2200 and 2500°F than at 72°F. A similar result has been reported by Carruthers et al.⁽⁵⁾ and by others with RBSN materials and is attributed partially to surface flaw blunting by oxide formation.

Examination of longitudinally ground and as-nitrided test bar fracture surfaces revealed surface and subsurface low density agglomerates and porosity as the primary fracture sites. These are typified in Figures 171 and 172. Figure 172b also illustrates the formation of an Si bead at a low density site after a 2500°F fracture. Figure 172a illustrates the microstructure of the RBN 104 material and shows the free silicon content of the structure. Occasionally, large laminar low density regions, possibly a result of cracks in the Si billet prior to nitriding, were the source of low strength fractures. This type material flaw is responsible for the low flexure strength (17 ksi) bar tested at room temperature, and the bi-modal strength distribution of Figure 170a.

Results for machining and oxidizing treatments on RBN 104 test bars are summarized in Figure 169 and 173. As shown in Figure 171, surface damage resulting from machining in the longitudinal direction has no significant effect on material strength. However, results show that machining in the transverse direction (perpendicular to the principle stress direction) reduces the characteristic strength by approximately 65 percent. Results shown in Figure 173, also show that 2-hour heat treatments at 1650 and 2460°F, performed subsequent to the transverse grinding operation, partially or fully restore the material strength.

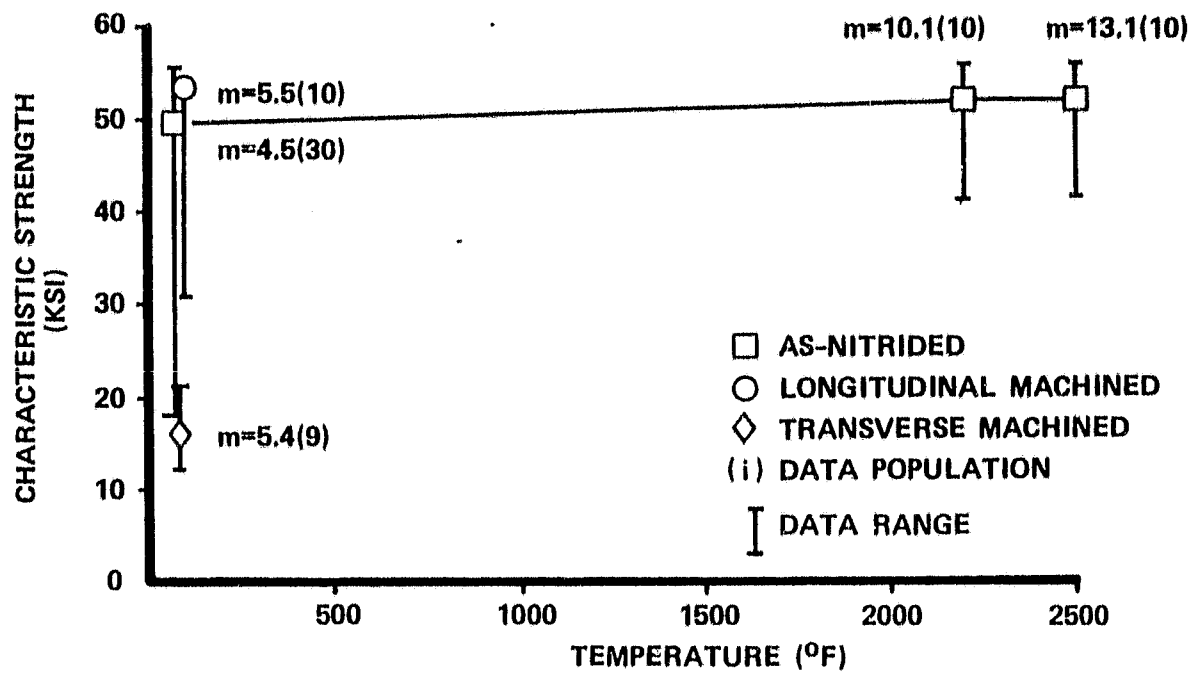


Figure 169. Baseline Strength ACC RBN 101 Slip Cast RBSN.

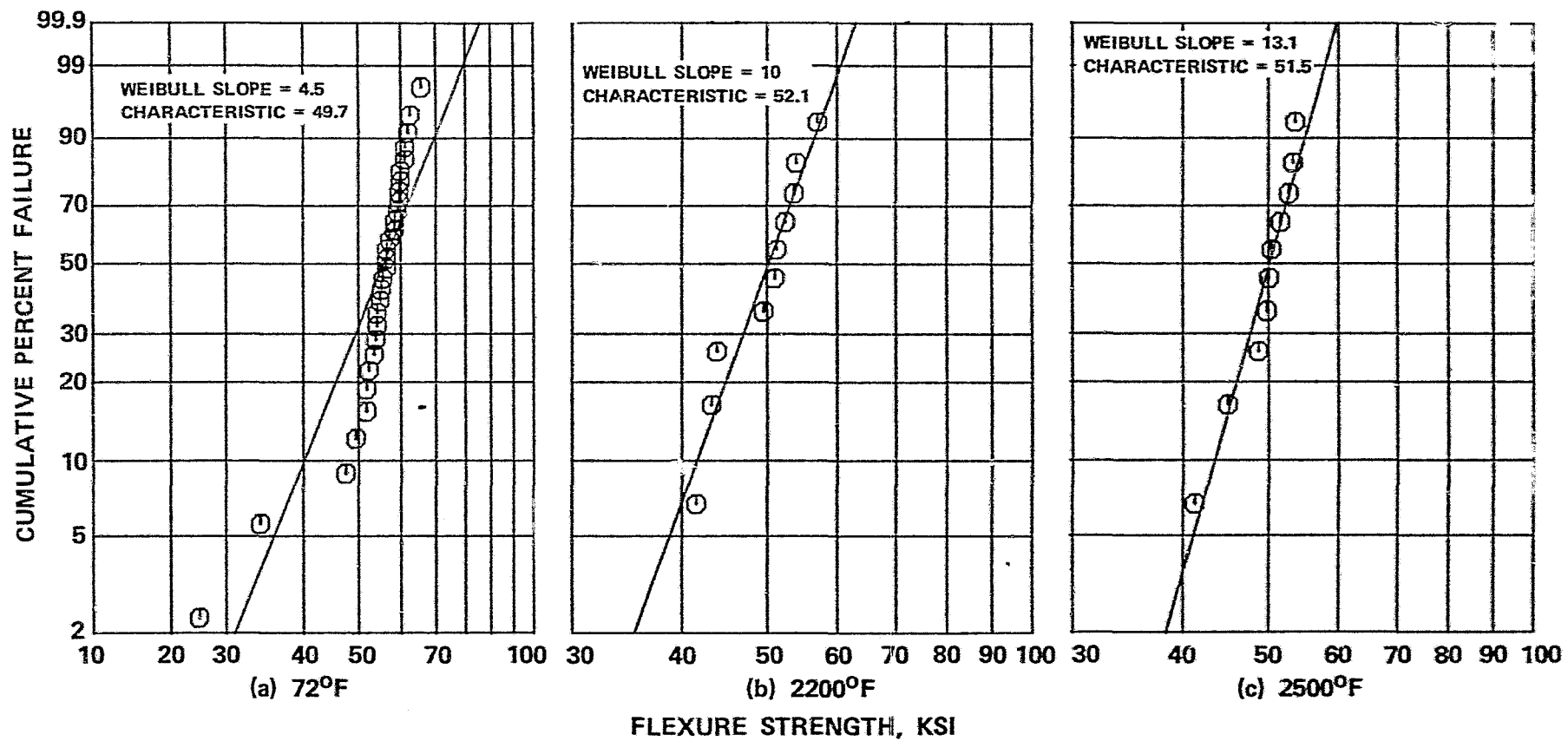
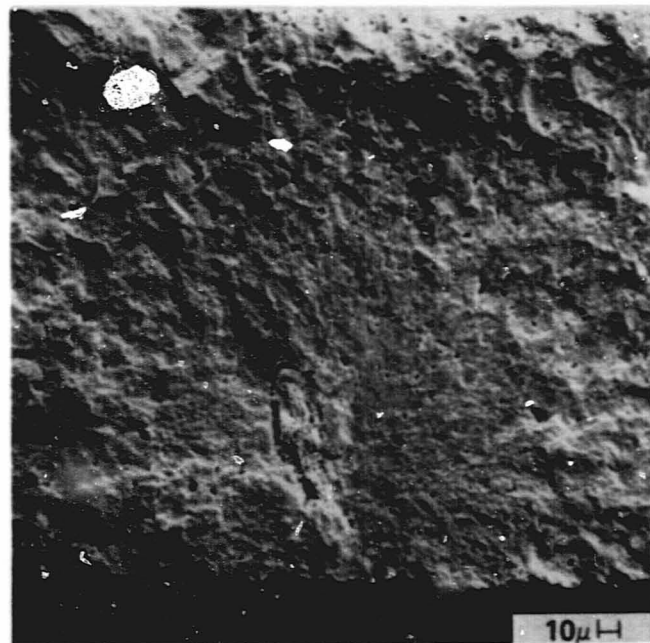
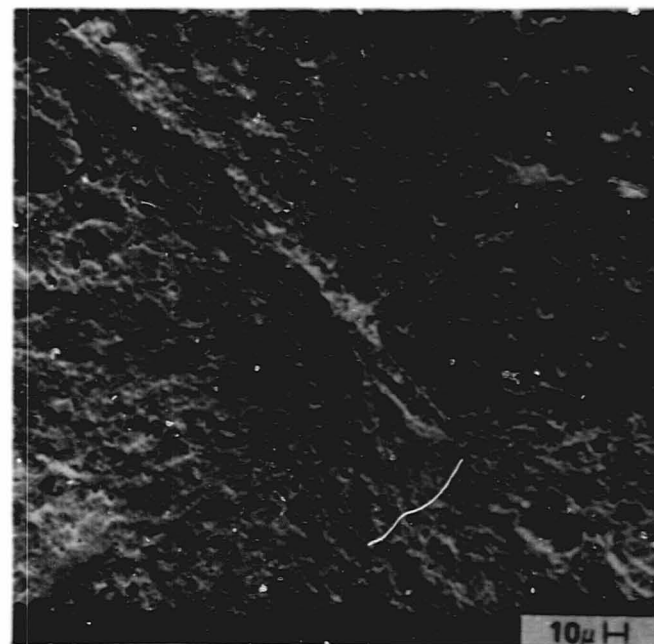


Figure 170. Two Parameter Weibull Plots for As-Nitrided RBN 104.



SPECIMEN 7450
43.5 KSI MOR AT 80°F
POROUS REGION

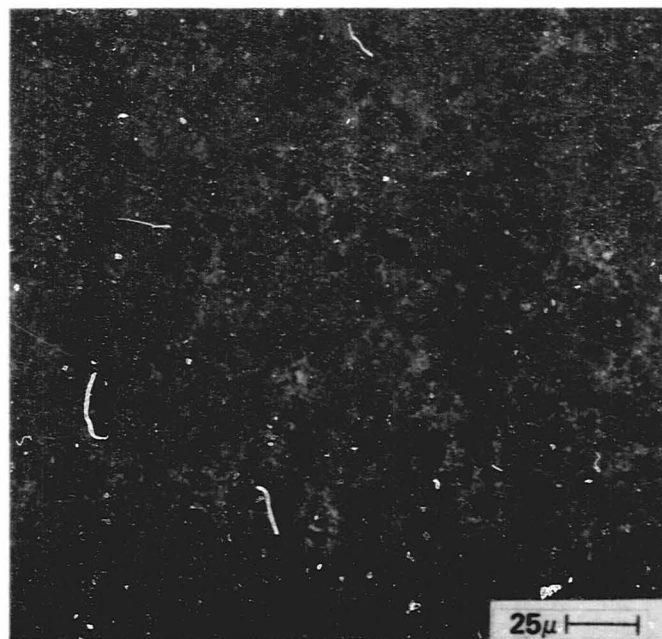


SPECIMEN 7448
51.0 KSI MOR AT 2200°F
LINEAR LOW DENSITY REGION

ORIGINAL PAGE
BLACK AND WHITE PHOTOGRAPH

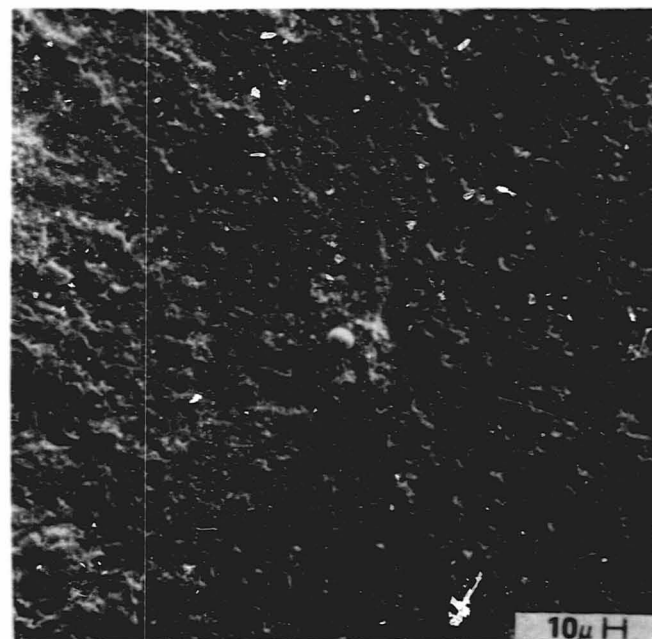
Figure 171. Typical Fracture Origins for ACC RBN 104 RBSN.

MP-73297



SPECIMEN 7508
MICROSTRUCTURE AT APPROXIMATELY
400x MAGNIFICATION

(A)



SPECIMEN 7484
44.9 KSI MOR AT 2500°F
LOW DENSITY REGION WITH METALLIC (Si) BEAD

(B)

ORIGINAL PAGE
BLACK AND WHITE PHOTOGRAPH

Figure 172. RBN 104 Microstructure and 2500°F Fracture Origin.

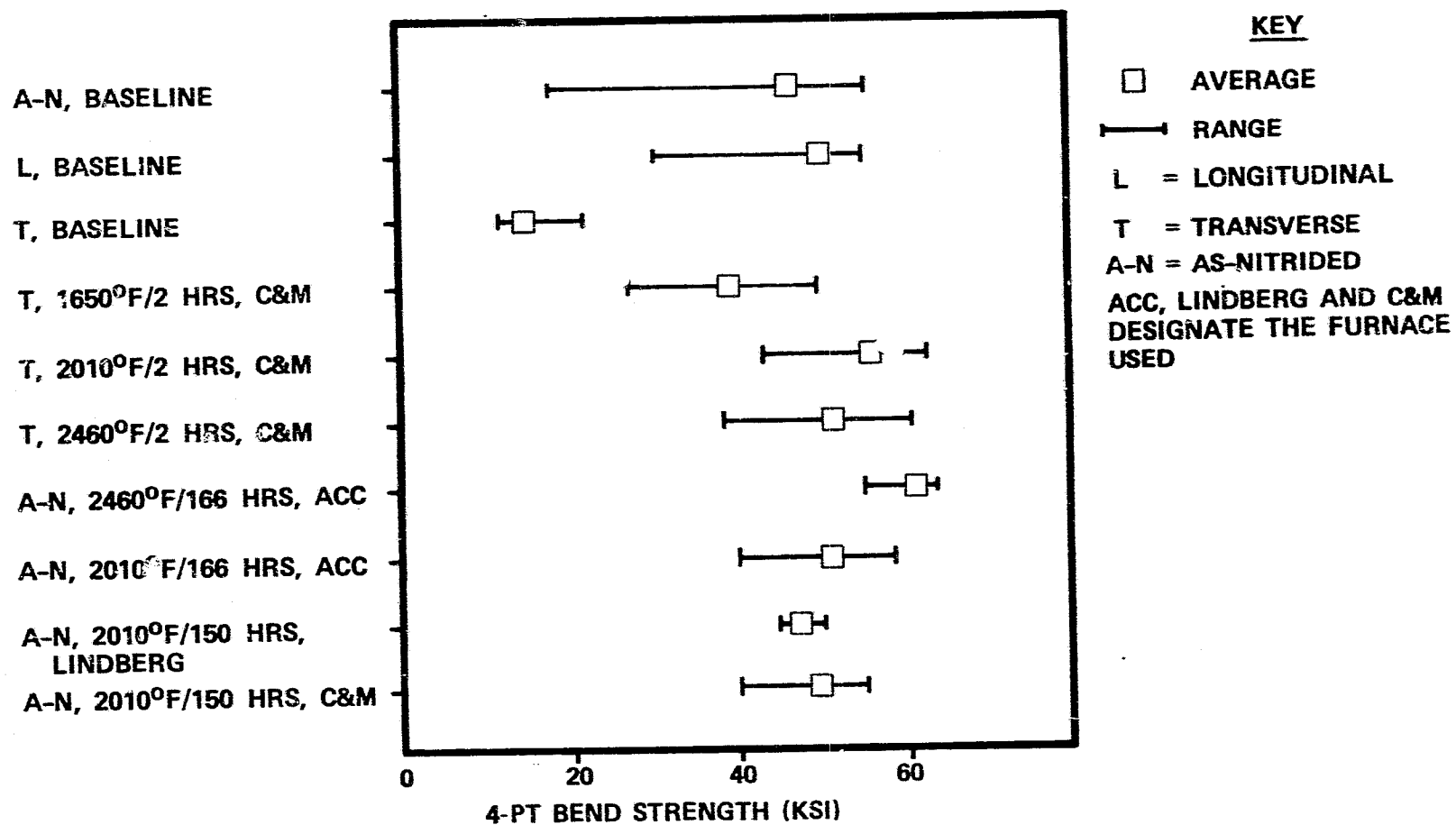


Figure 173. ACC RBN 104 Surface Machining and Oxidation Exposure Results.

Oxidation exposure results also indicate that heat treatments performed on as-nitrided RBN 104 at 2010 and 2460°F for up to 166 hours have a strength-enhancing effect. This strength improvement is particularly evident from the ACC furnace exposure of 166 hours at 2460°F. Weight gains during all exposures were less than 0.2 percent.

Stress rupture testing of RBN 104 test bars is currently being performed. Initially eight test bars will be tested simultaneously in a gas-fired atmosphere at 2500°F for 300 hours. Bars will be loaded in bending at 16 ksi for the initial 150 hours, and survivors will be loaded to 20 ksi for the remaining 150 hours.

4.7.1.2.2 RBN 126

RBN 126, injection-molded reaction-bonded Si_3N_4 , is the primary ACC material candidate for the turbine stator vanes. Test bars of this material were tested in the as-injection-molded and nitrided condition.

Results of flexural testing RBN 126 at 72, 2200 and 2500°F are presented in Figure 174. Material strength distributions are presented in the Weibull plots of Figure 175. A comparison between the RBN 104 (Figure 169) and RBN 126 (Figure 174) shows RBN 104 to be stronger at 72 and 2500°F. At 2200°F the materials showed equal strengths. Fractography of the RBN 126 surfaces revealed that fractures initiated from low density agglomerates and pores, as well as from several surface debris sites. The lower strengths obtained for RBN 126 compared to RBN 104 may be attributed to the surface debris and the larger size low density agglomerates observed in the material. The surface debris is typified in Figure 176. EDX analyses of the debris revealed traces of Al, Na and Ca contaminants. Surface debris is thought to be a result of die cavity contamination and/or extruding products produced during the nitriding process. No analysis of the starting powder was performed.

4.7.1.2.3 X-Ray Diffraction of RBN 126 and RBN 104

As-nitrided samples of RBN 126 and RBN 104 were analyzed using X-ray diffraction techniques. Results are presented in Figure 177. These results primarily indicate α and β - Si_3N_4 structure with smaller amounts of Si. Results also were analyzed using quantitative techniques described by Mencik and Short⁽⁴⁾ to determine the α to β ratios of the two materials. These ratios were determined to be 2.7 for RBN 126 and 5.2 for RBN 104. The RBN 126 analysis also indicates a higher content of Si than the RBN 104.

4.7.1.2.4 SNN 522

SNN 522, injection molded sintered silicon nitride, is the primary ACC material candidate for the turbine rotor. Test bars of this material were tested in the as-injection-molded and sintered condition, and in the transverse or longitudinal ground state. Although

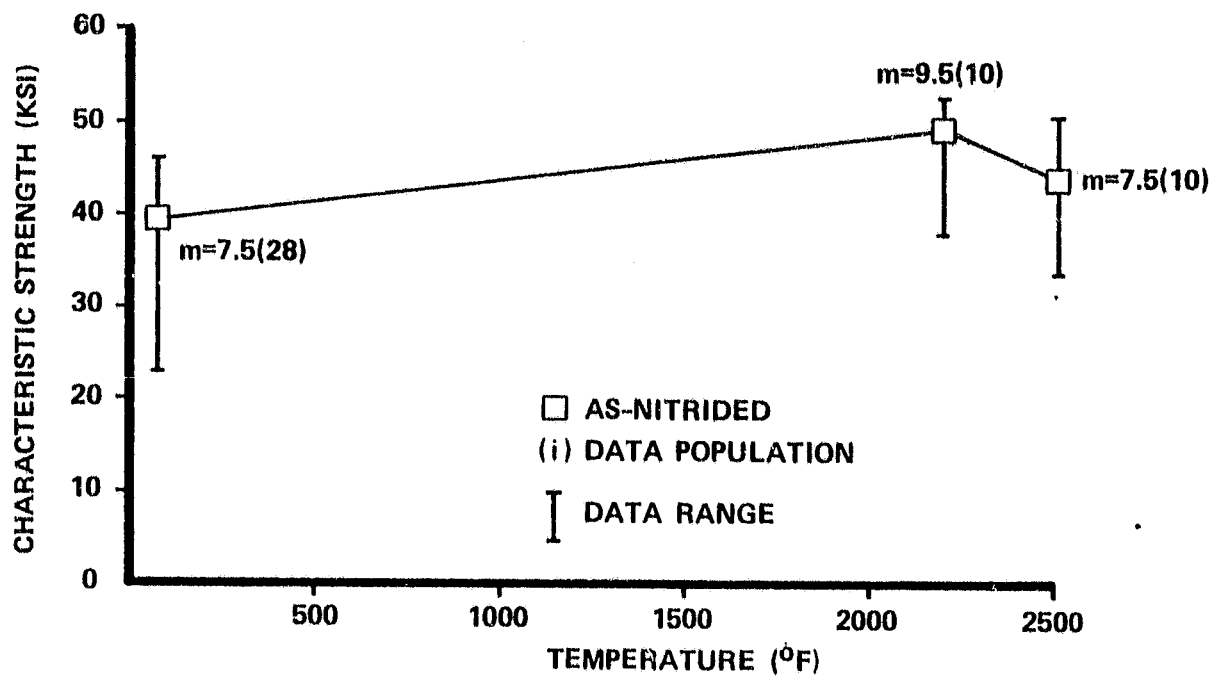


Figure 174. Baseline Strength ACC RBN 126 Injection Molded RBSN.

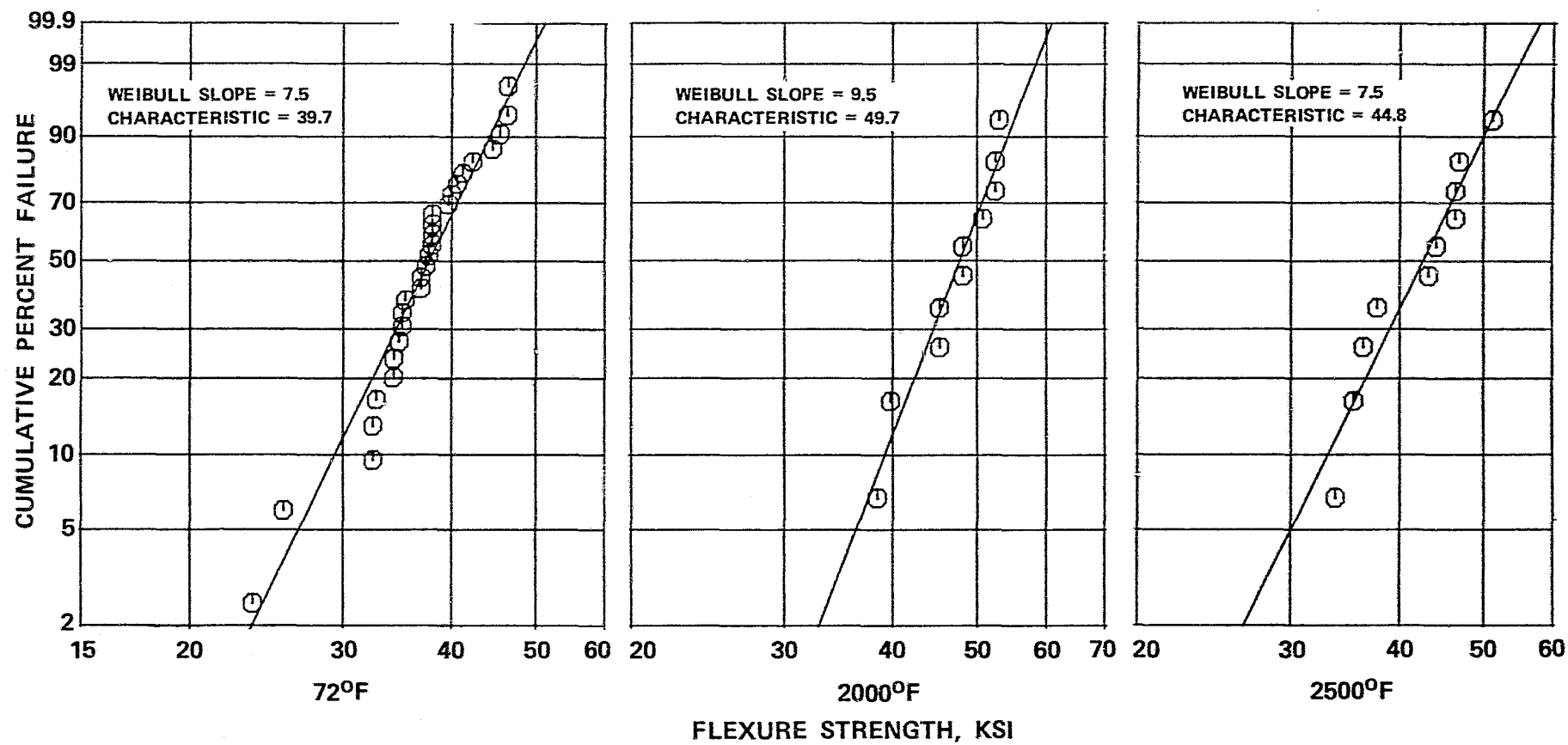


Figure 175. Two Parameter Weibull Plots for As-Nitrided ACC RBN 126.

ORIGINAL PAGE IS
OF POOR QUALITY

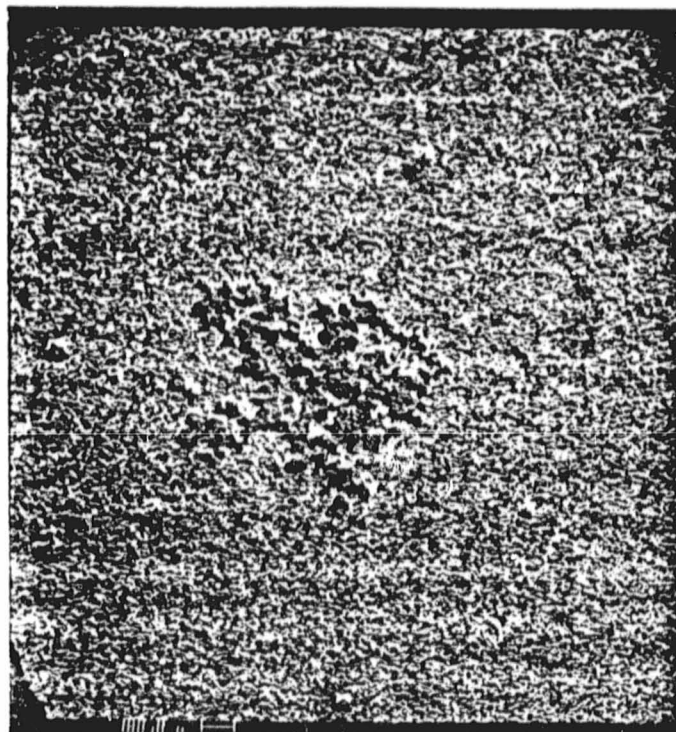


Figure 176. 40x Photo of Surface Debris on RBN 126,
Specimen Number 7372.

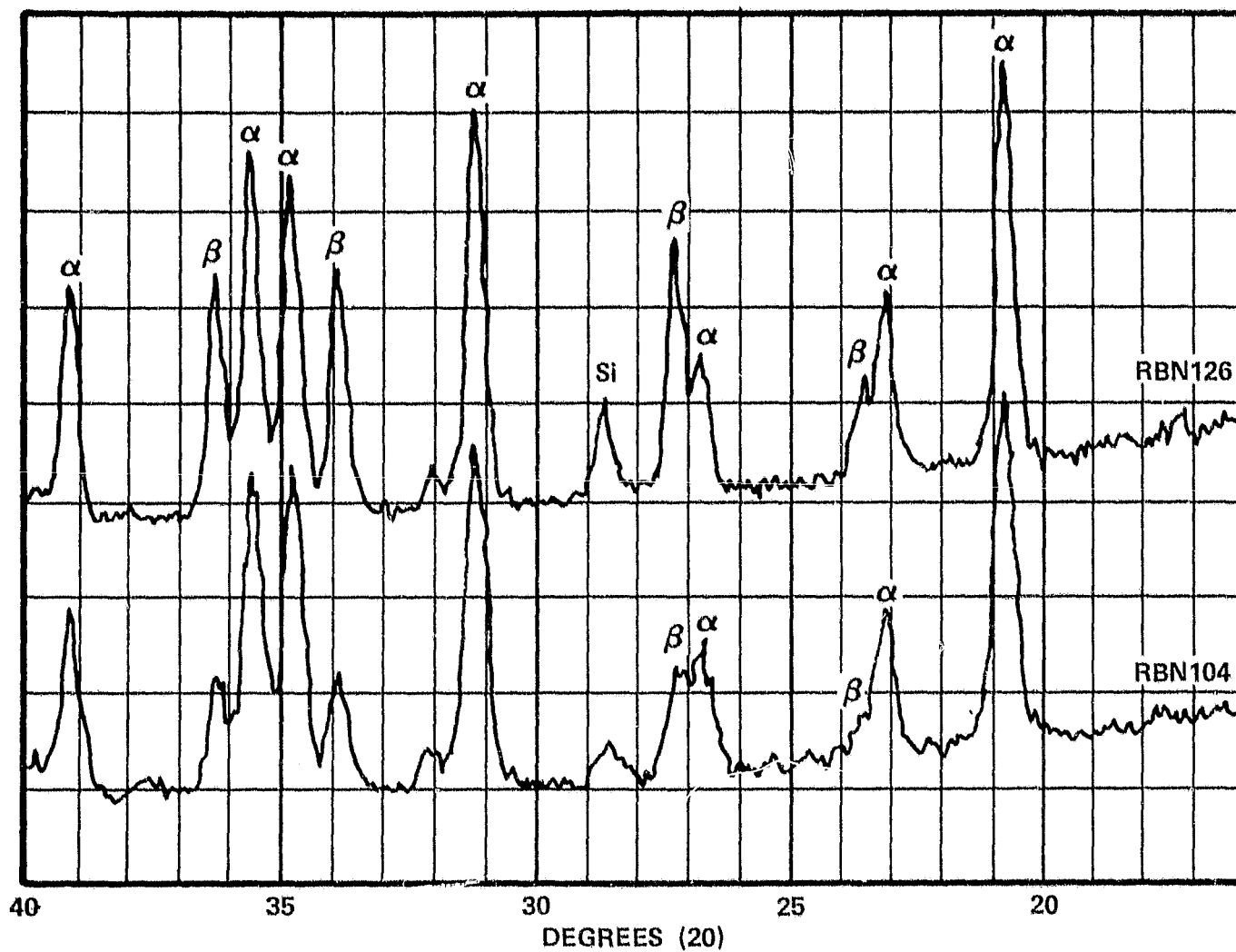


Figure 177. X-Ray Diffraction Results for As-Nitrided RBN 104 and RBN 126.

test bars of SNN 522 are injection molded in 2 x 0.250 x 0.125 inch cavities, shrinkage during sintering results in test bars with approximately 0.214 x 0.108 inch cross sections. All SNN 522 bars tested were of these dimensions.

Results of flexure testing as-sintered and as-machined test bars are summarized in Figure 178. Material strength distributions are presented in the Weibull plots of Figure 179 and 180 for the as-sintered materials. These figures illustrate a decrease in flexure strength with increasing temperature, but no decrease in strength as a result of surface grinding.

Fractography performed on SNN 522 bars tested from room temperature up to 2200°F indicates that these bars typically fractured at near-surface sites of porosity or at iron-based inclusions as illustrated in Figures 181 and 182. The porosity sites were of three general types: tubular, spherical and irregular shapes, and ranged in size from 20 to 200 microns. Iron-based inclusions as large as 100 microns also were observed. EDX analyses of these inclusions indicated the presence of Cr. The source of these iron-chrome inclusions is not known, although abrasion of the metal cylinder and plunger during the injection molding process is a possible source. All test bars fractured at 2500°F and exhibited slow crack growth, as shown in Figure 182b.

X-ray diffraction analyses of as-sintered and 2200°F flexure-tested SNN 522 primarily indicate β - Si_3N_4 before and after the brief elevated temperature exposure. An unidentified peak at 32.7 degrees ($d = 2.74$) is visible in both analyses, as shown in Figure 183. Material exposed to 2200°F also showed traces of SiO_2 as shown in Figure 183.

Polished-section and EDX analyses (Figure 184) also reveal the presence of Fe, Ca, Ti, Ni, Mo, and Sn contaminants in the sintered materials. The source of these contaminants is being pursued through SEM, EDX, and X-ray diffraction analyses of all powders used during the processing of SNN 522.

Stress rupture testing of SNN 522 has been initiated in static furnace conditions at 2000°F. Stress levels of 35 through 50 ksi initially are being evaluated. Although results are incomplete, a summary of current results is presented below:

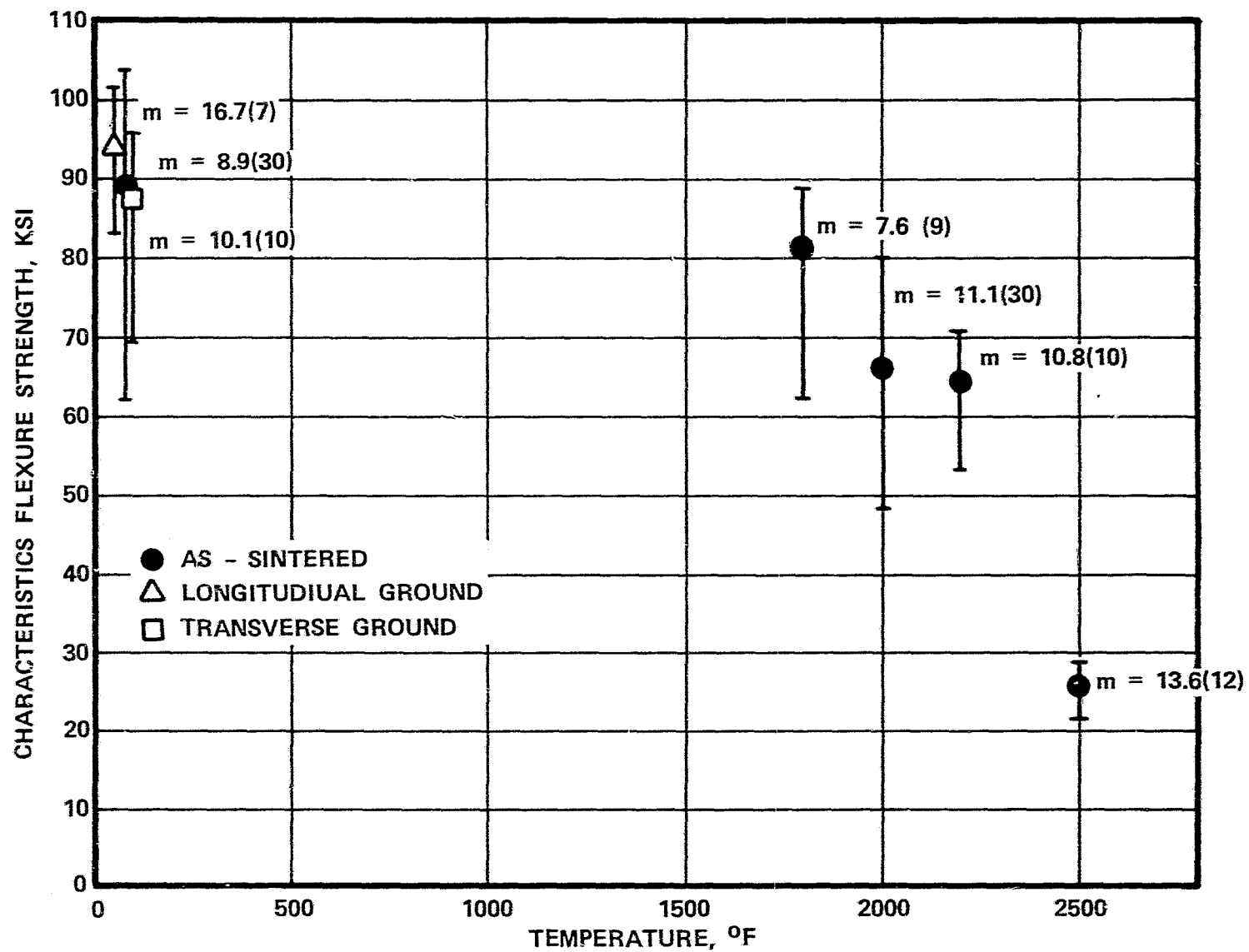


Figure 179. Four Point Flexure Strength Summary for ACC SNN 522.

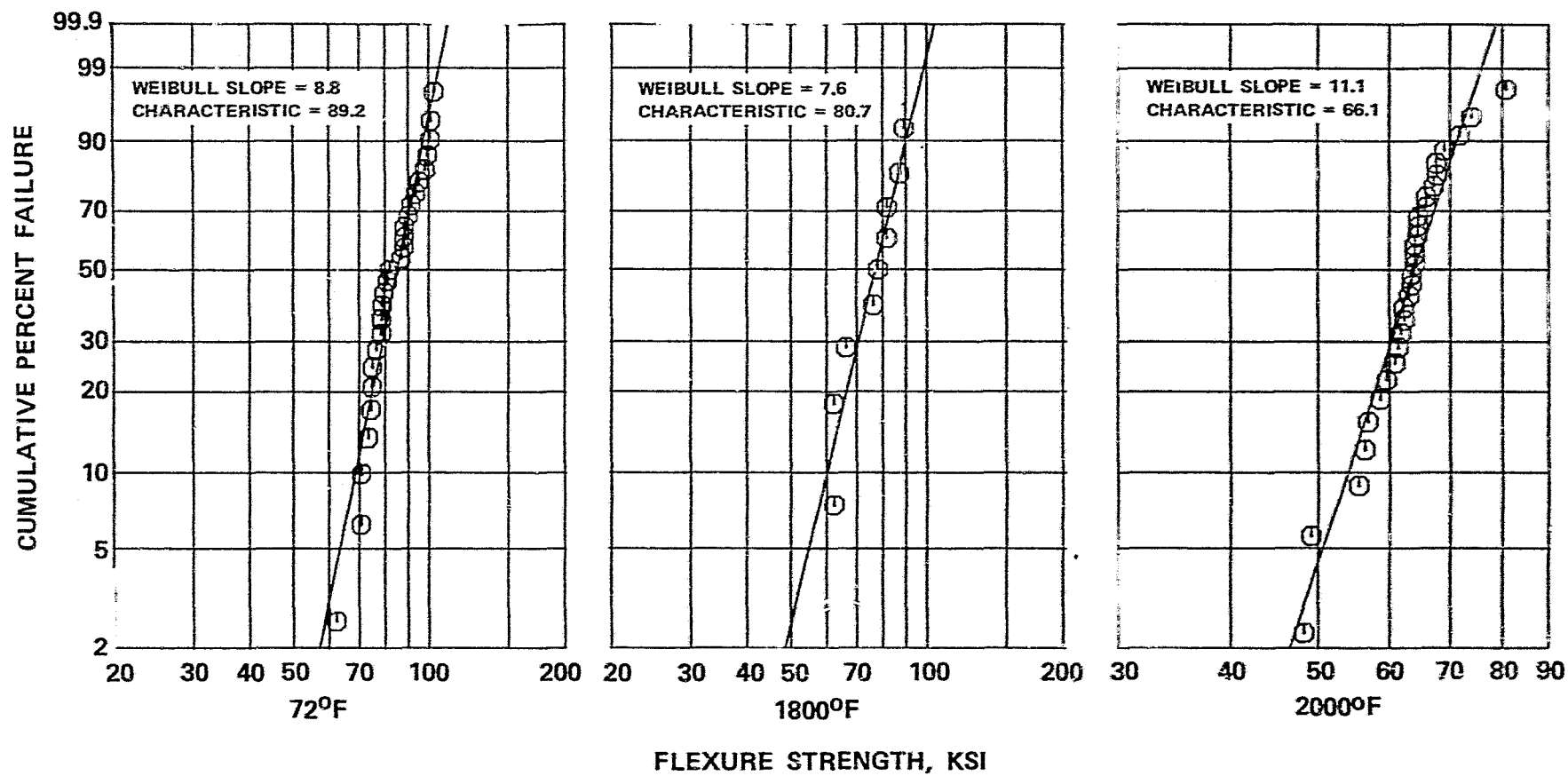


Figure 179. Two Parameter Weibull Plots for As-Sintered SNN 522.

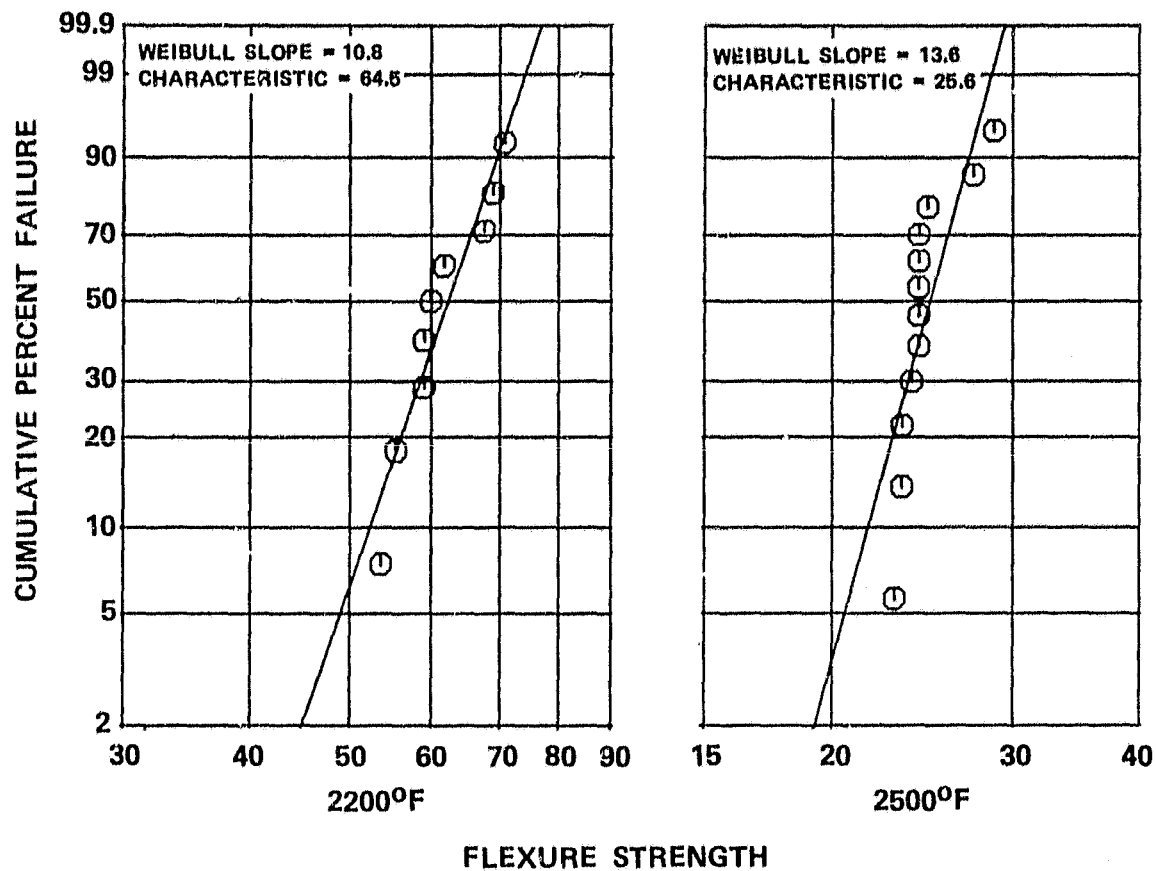
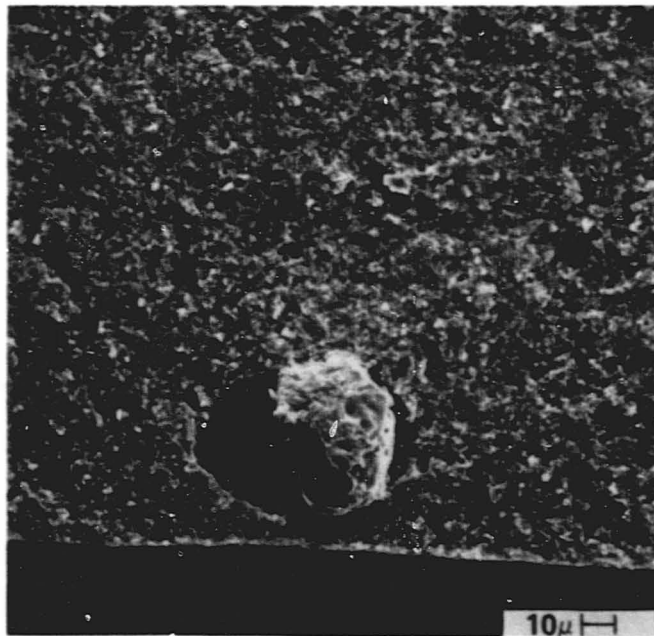
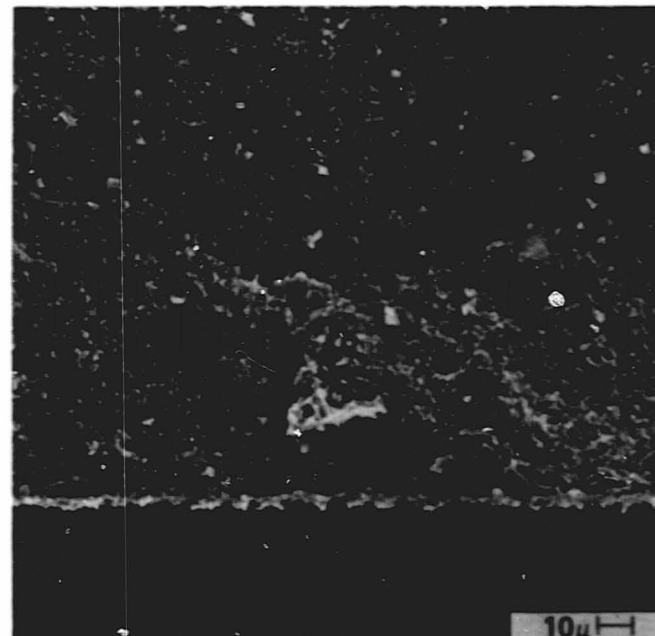


Figure 180. Two Parameter Weibull Plots for As-Sintered SNW 522.



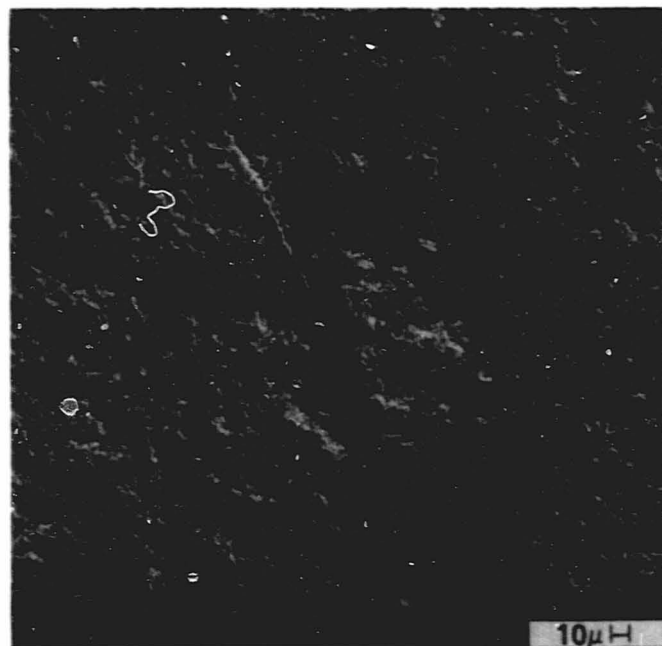
SPECIMEN 8203
76.6 KSI MOR AT 80°F
IRON-BASED INCLUSION WITH PORE



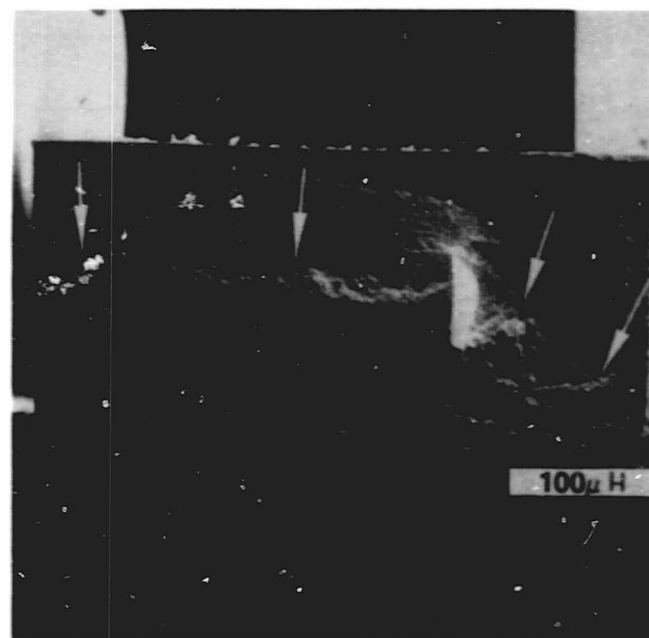
SPECIMEN 8195
74.8 KSI MOR AT 80°F
IRREGULAR PORE

ORIGINAL PAGE
BLACK AND WHITE PHOTOGRAPH

Figure 181. Typical Fracture Origins for ACC SNN 522
Sintered Si_3N_4 .



SPECIMEN 8171
67.6 KSI MOR AT 2200°F
LINEAR OR TUBULAR VOID



SPECIMEN 8238
24.8 KSI MOR AT 2500°F
SLOW CRACK GROWTH

ORIGINAL PAGE
BLACK AND WHITE PHOTOGRAPH

Figure 182. Typical Fracture Origins for ACC SNN 522
Sintered Si_3N_4 .

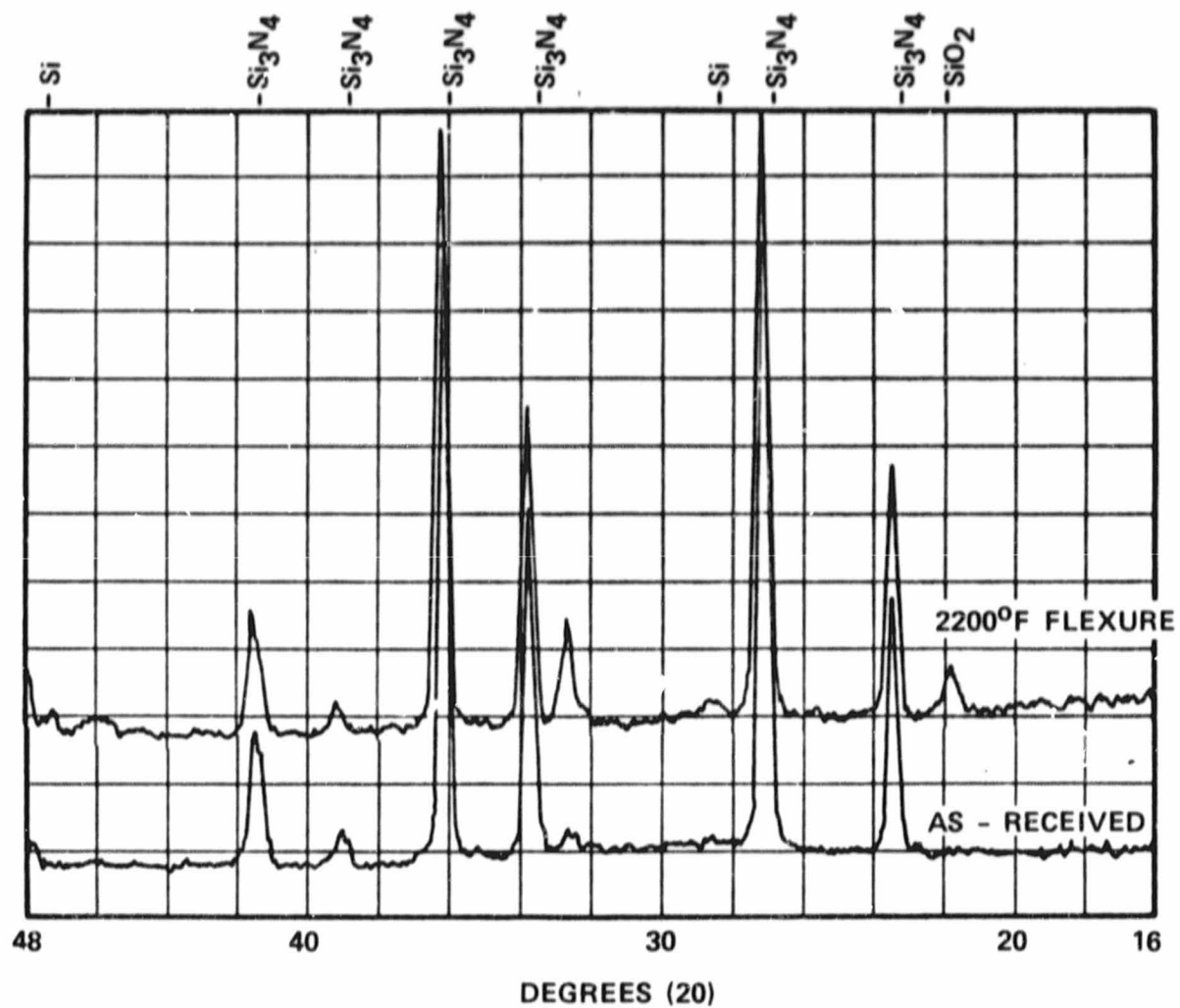
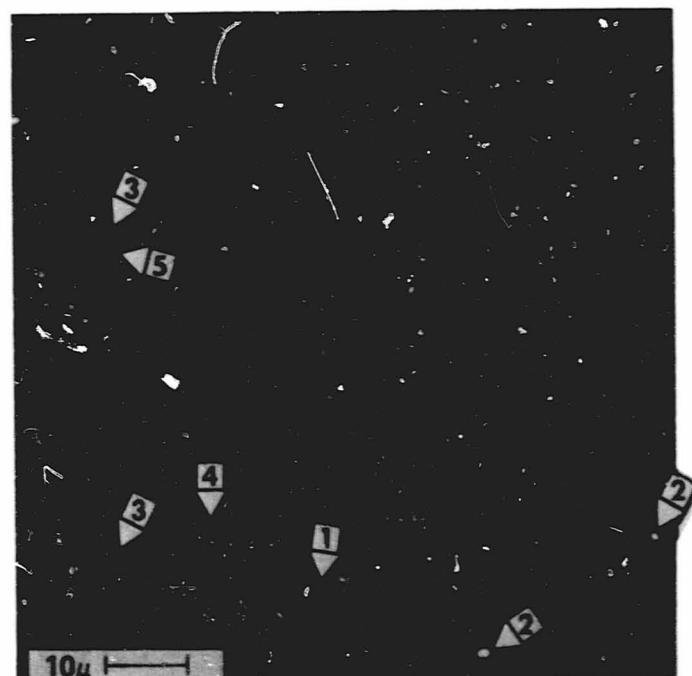


Figure 183. X-Ray Defraction Results for as Sintered SNN 522.



<u>AREA</u>	<u>EDX RESULTS</u>
1	Al, Si, Fe, Ca, Ti, Ni
2	Si, Al, Y, Mo, Fe, Cr
3	Si, Al, Sn, Fe
4	Si, Al
5	Si, Al, Ca

ORIGINAL PAGE
BLACK AND WHITE PHOTOGRAPH

Figure 184. EDX Analysis of ACC SNN 522 Microstructure.

<u>Specimen S/N</u>	<u>Approximate Stress (ksi)</u>	<u>Results</u>
7949	35	Discontinued after 325 hours, no failure
8233	45	Discontinued after 325 hours, no failure
8012	50	Fractured at metallic inclusion at 4 minutes
8072	50	In progress, over 220 hours accumulated
8112	50	In progress, over 230 hours accumulated

4.7.1.3 Carborundum Baseline Materials

4.7.1.3.1 Strength

The nine static components being fabricated by Carborundum from sintered α -SiC (SASC) are presented in Table 23 along with the current fabrication approach for each item. Due to difficulties in processing thick injection-molded shapes, the rotor will be fabricated by bonding an injection-molded outer shell to a core fabricated by another process such as isopressing. A large number of flexural bars have been tested to determine the baseline strength properties of the component fabrication materials. In addition, cold-pressed test bars have been utilized for a variety of tests to establish the general behavior of SASC.

Figures 185 through 187 show the Weibull plots for the as-received materials and the data are summarized in Table 24. All flexural tests were conducted on 0.125 x 0.25 x 2 inch test bars using 4-point loading with a 1.5-inch outer span, a 0.75-inch inner span and a crosshead speed of 0.02 in/min.

The initial group of cold-pressed test bars had exaggerated grain growth due to improper sintering conditions. As indicated in Table 24, the second group of cold pressed test bars (Cold-Pressed II) appears to have improved properties at room temperature. The elevated temperature tests for the cold-pressed material indicate no change in characteristic strength but the Weibull modulus is significantly higher. An examination of the data indicates that, at the extremes, the high temperature test bars were neither as strong nor as weak as the bars tested at room temperature. For example, the low temperature strength of the original cold-pressed material ranged from 36.3 to 61.1 ksi. This indicates that the flaw population was modified as a result of high temperature exposure. A reduction in the severity of machining flaws by oxidation treatment is commonly observed in silicon-based ceramics and is discussed below for SASC. This mechanism may be responsible for the improvement in low strength values. In the high

TABLE 23. SINTERED SILICON CARBIDE COMPONENTS
AND FABRICATION APPROACH

Fabrication Approach	Component
Injection Molded SASC	Stator Segments
	Turbine Shroud
Slip Cast SASC	Transition Duct
	Combustor Baffle
	Inner Diffuser
	Outer Diffuser
Isopress/Green Machine SASC	Turbine Backshroud
	Regenerator Shield
	Duct Spacer

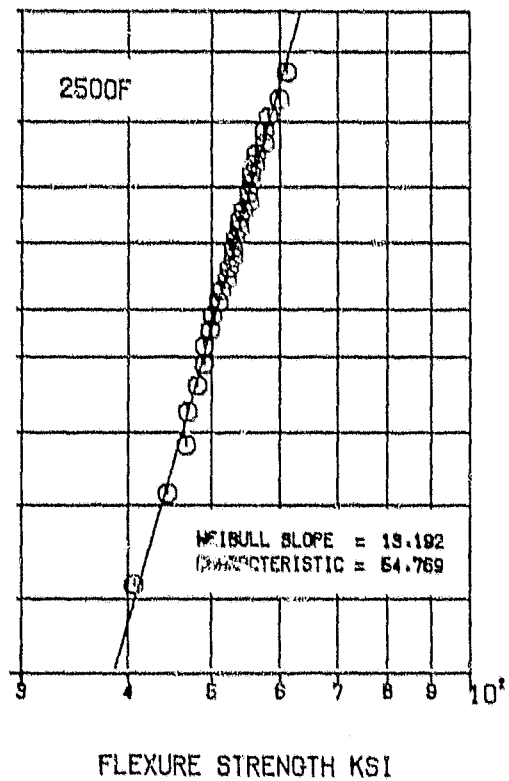
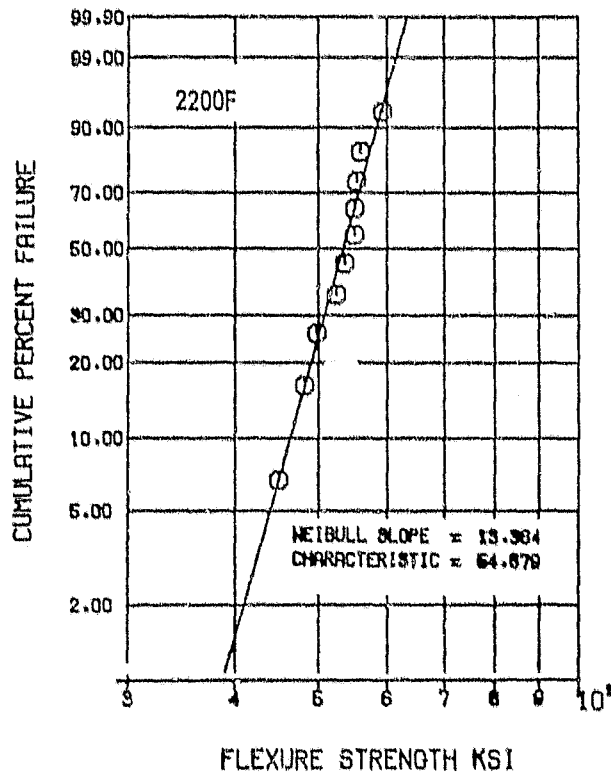
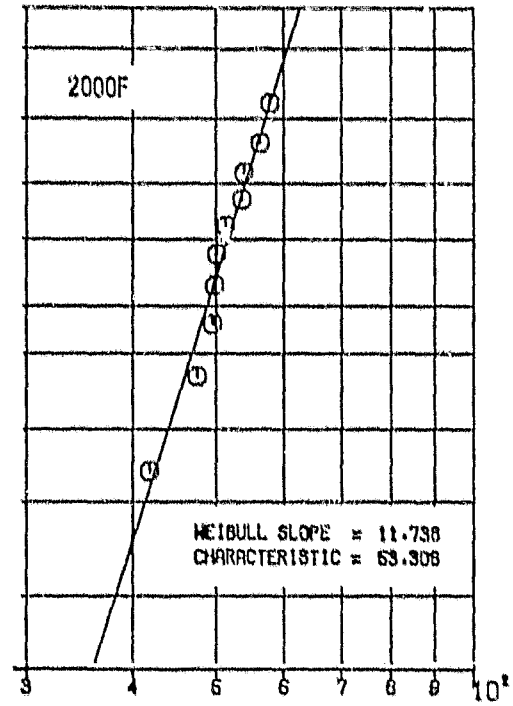
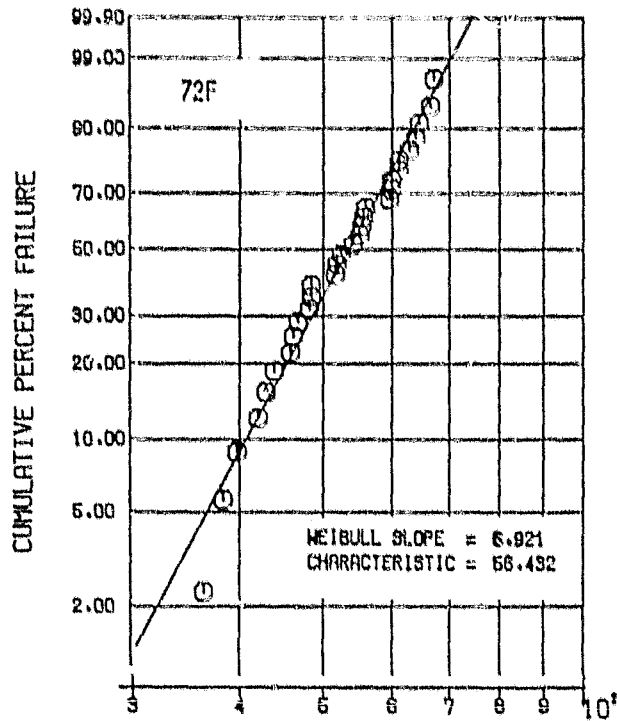
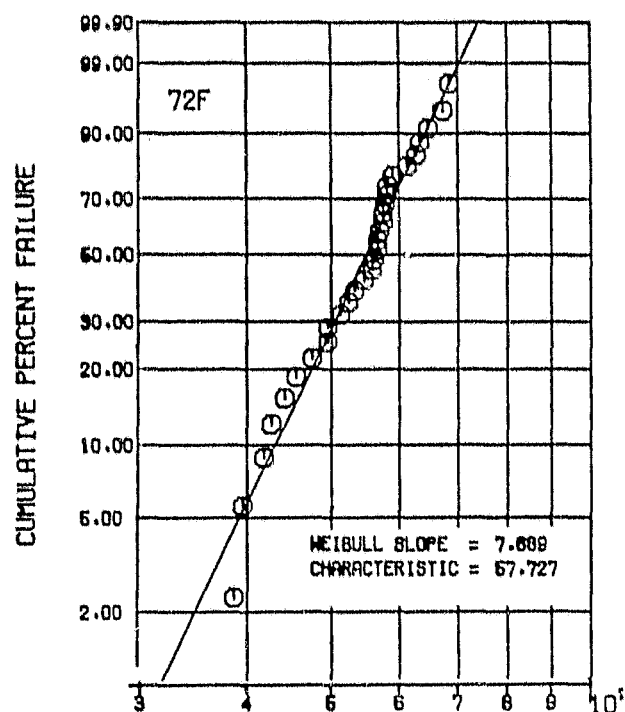
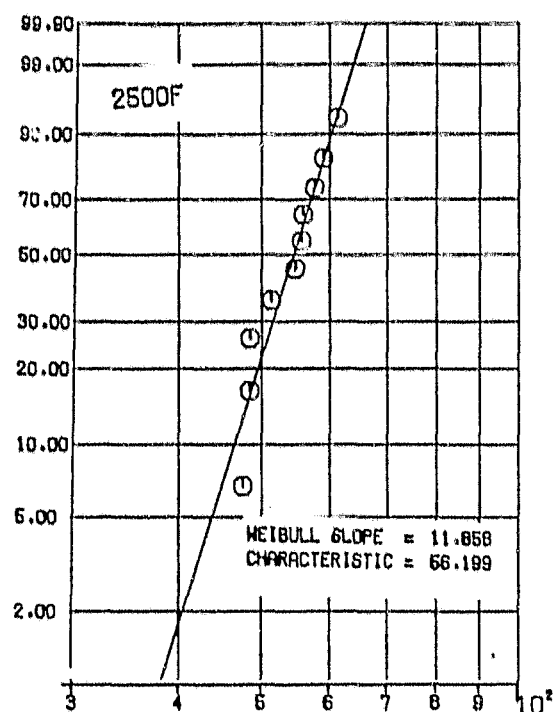


Figure 185. Weibull Plots for Cold-Pressed SASC at Various Temperatures.

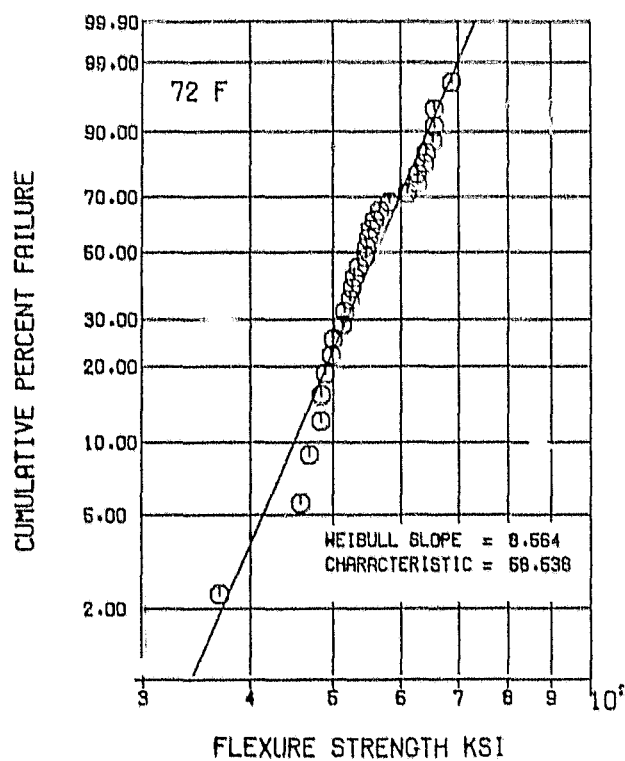


FLEXURE STRENGTH KSI



FLEXURE STRENGTH KSI

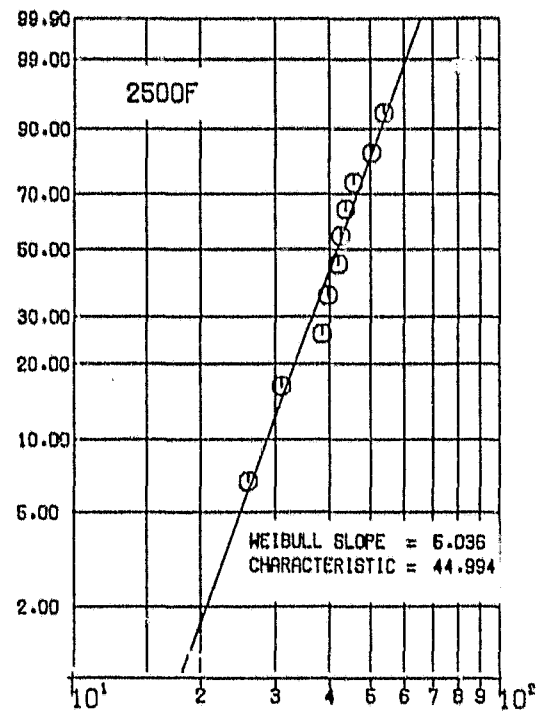
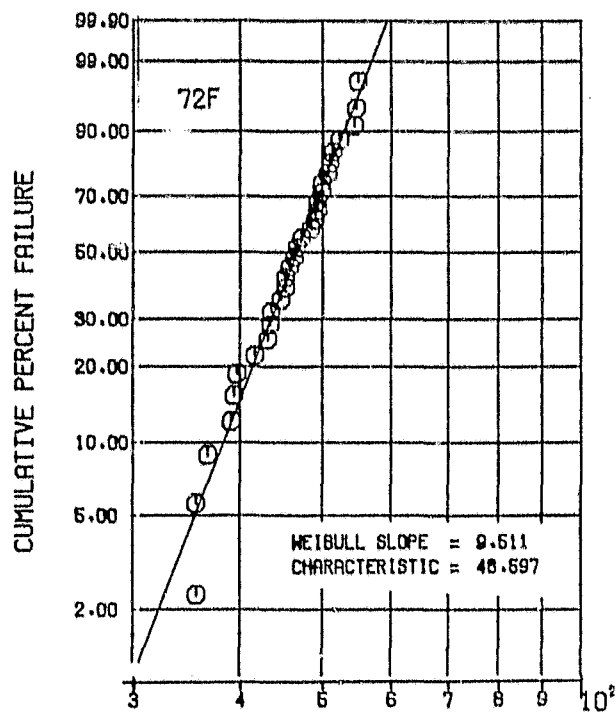
(A) ISOPRESSED MATERIAL



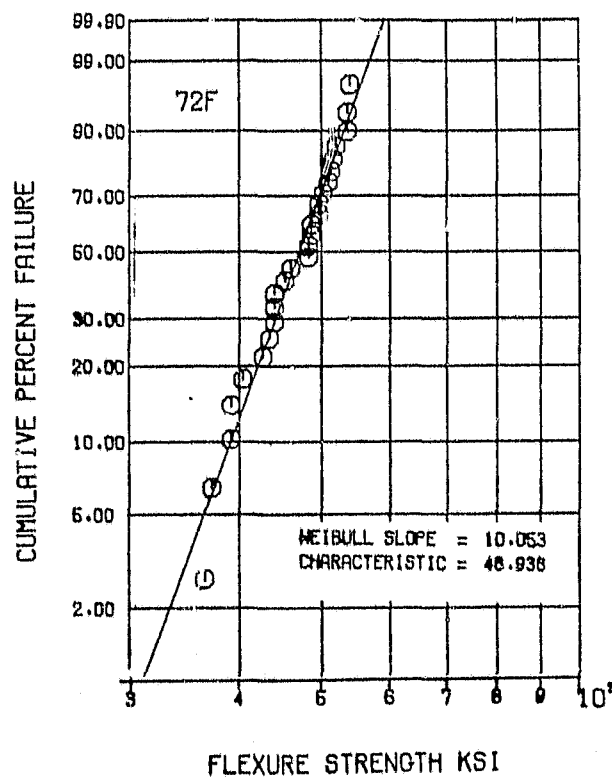
FLEXURE STRENGTH KSI

(B) FINE GRAIN COLD-PRESSED MATERIAL

Figure 186. Weibull Plots for SASC.



(A) AS-FIRED



(A) AS-FIRED
(B) MACHINED

(B) MACHINED

Figure 187. Weibull Plots for Injection Molded SASC.

TABLE 24. WEIBULL PARAMETERS OBTAINED FROM FLEXURAL TESTS ON AS-RECEIVED SASC

Material (population)	Temperature (°F)	Characteristic Strength (ksi)	M-Value
Cold-pressed I* (30)	72	56.4	6.9
Cold-pressed I* (10)	2000	53.3	11.7
Cold-pressed I* (10)	2200	54.9	13.4
Cold-pressed I* (30)	2500	54.8	13.2
Cold-pressed II** (30)	72	58.5	8.6
Isopressed (30)	72	57.7	7.7
Isopressed (10)	2500	56.2	11.6
Injection-molded ⁺⁺ (30)	72	48.6	9.5
Injection-molded ⁺ (26)	72	48.9	10.1
Injection-molded ^o (10)	2500	45.0	5.0

*Material exhibiting coarse grain growth

**Fine-grained material

⁺⁺As-Fired surface

⁺Surface machined in longitudinal direction with 320 grit diamond

^oAs-fired, surface pitted and inferior to usual injection molded
α SiC

strength range, the oxidation of surface pits and voids may decrease strength. Residual stress in the as-received bars also would affect the strength but inert gas annealing treatments performed by Carborundum (See Appendix III) did not indicate the presence of any residual stress.

The characteristics of the isopressed material were similar to the cold-pressed material. The injection-molded test bars had a lower initial strength which was the same for both as-fired and machined surfaces. The low strength correlated with a higher density of surface pits and voids. Opposite sides of these test bars were visually different, one side containing a much higher density of pits. This side inadvertently was placed as the tensile side in the 2500°F tests and is responsible for the decreased strength observed. From these results and the fractography discussed below, it is apparent that this group of injection-molded SASC is not representative of good quality material. Slip-cast test bars have not yet been received for testing.

4.7.1.3.2 Fractography

In general, the predominate flaws in SASC are small voids. In the cold-pressed material having exaggerated grain growth, some failures were associated with large grains but fractures did not appear to be due to the large grain.

Figure 188 shows two examples of fracture origins in cold-pressed SASC. In one case, fractures originated from a linear pore inside a large grain while in another case failure initiated at a pore intersecting the surface and adjacent to a large grain. In the fine grain cold-pressed material, fractures initiated primarily at voids intersecting the machined surface as shown in Figure 189.

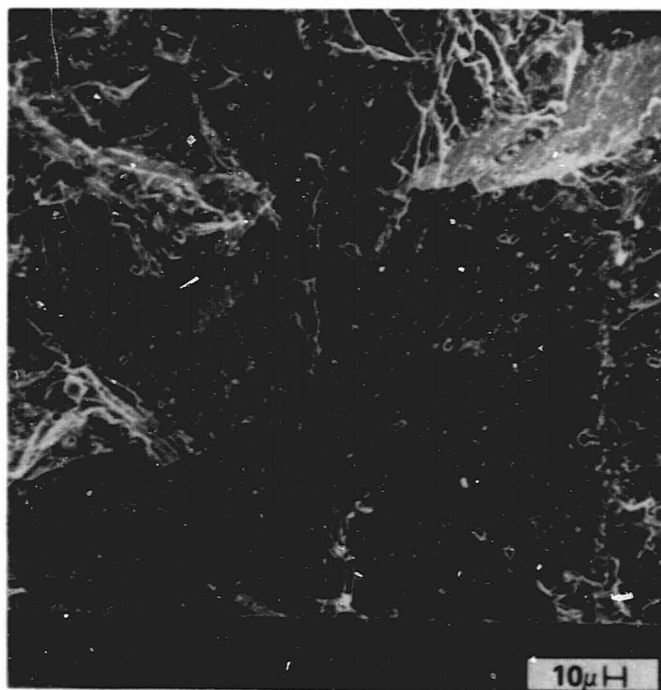
Typical fracture origins for isopressed SASC are shown in Figure 190. In this particular case, the voids are slightly subsurface. In the isopressed test bar group there also were several examples of surface-initiated failures with no apparent processing related origins. Figure 191 shows two examples of these less typical origins most likely due to machining damage.

As indicated above, the injection-molded material was substandard and had relatively large internal voids as well as pits on the as-fired surface. Figure 192 shows examples of both a large internal void and a void intersecting the machined surface. Figure 193 shows a surface pit on an as-fired surface acting as a flaw initiation site.

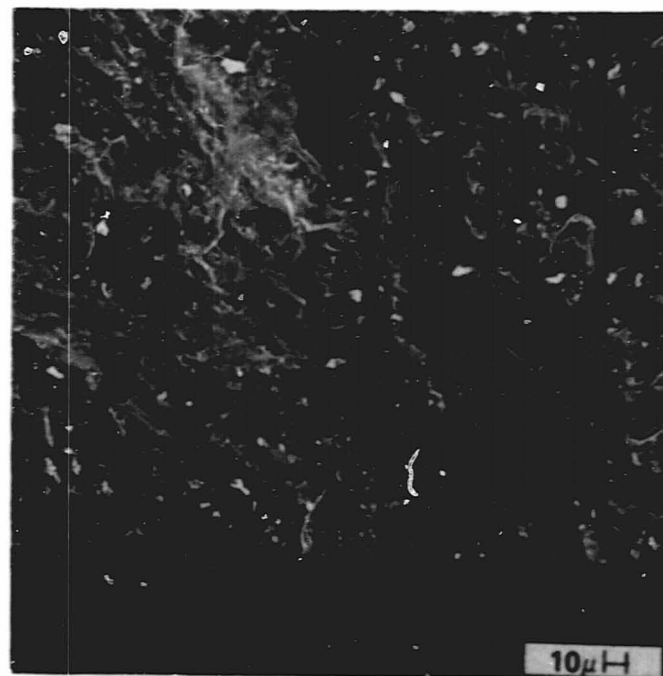
4.7.1.3.3 Oxidation Exposure

In previous programs involving Si_3N_4 as well as other materials (7,8), it has been demonstrated that transverse grinding (i.e., grinding in a direction normal to the applied tensile stress) results

MP-73294



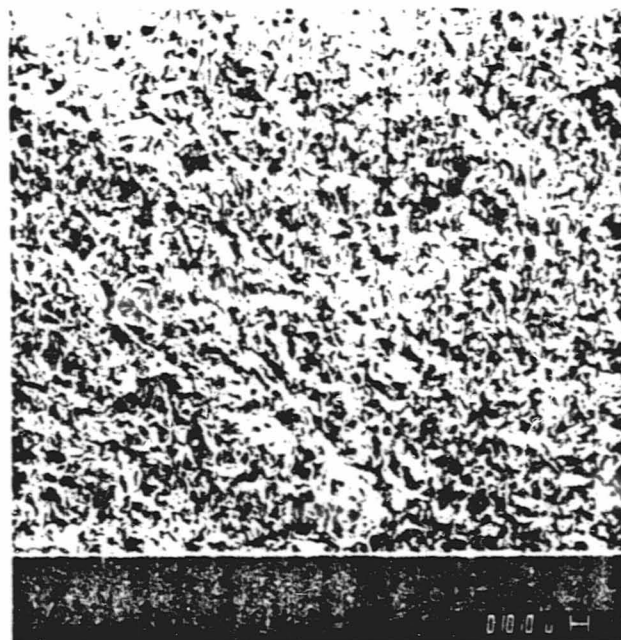
SPECIMEN 7021
59.9 KSI MOR AT 80°F
ORIGIN AT LINEAR PORE IN LARGE GRAIN



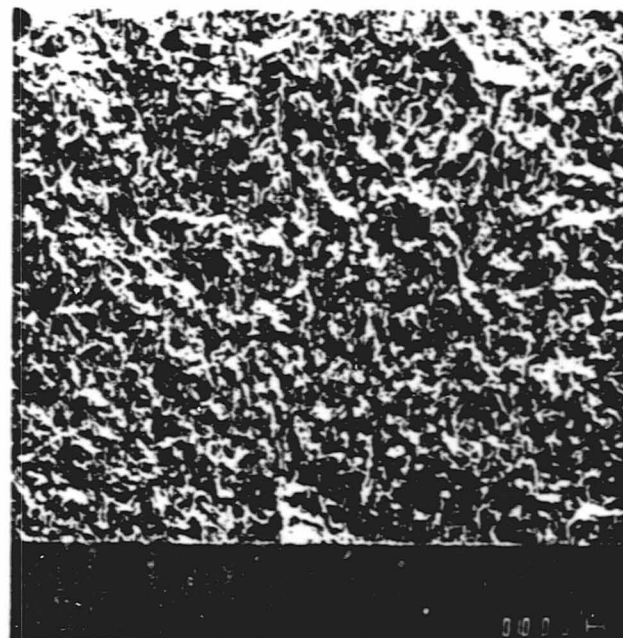
SPECIMEN 7080
55.0 KSI MOR AT 80°F
ORIGIN AT PORE NEXT TO LARGE GRAIN

ORIGINAL PAGE
BLACK AND WHITE PHOTOGRAPH

Figure 188. Typical Fracture Origins for Cold-Pressed SASC.



SPECIMEN 8408
58.2 KSI MOR AT 72°F

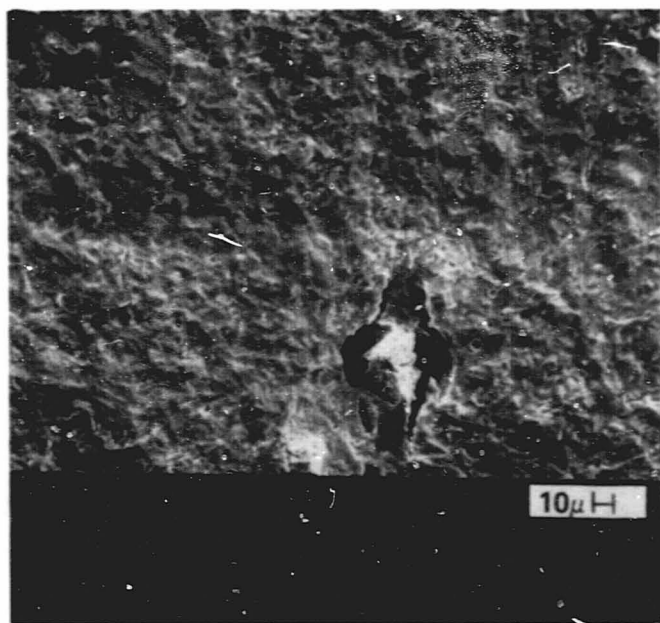


SPECIMEN 8398
65.4 KSI MOR AT 72°F

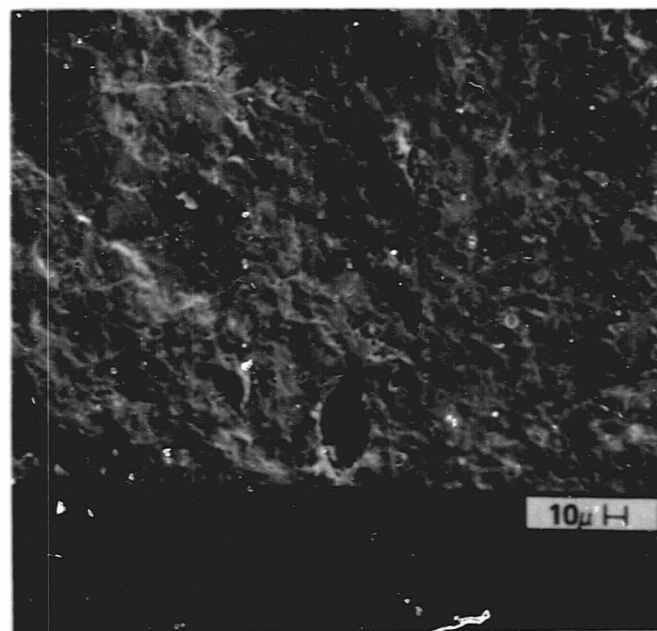
ORIGINAL PAGE
BLACK AND WHITE PHOTOGRAPH

Figure 189. Typical Fracture Origins for Fine Grain Cold-Pressed SASC - Voids Intersecting Machined Surfaces.

MP-73295



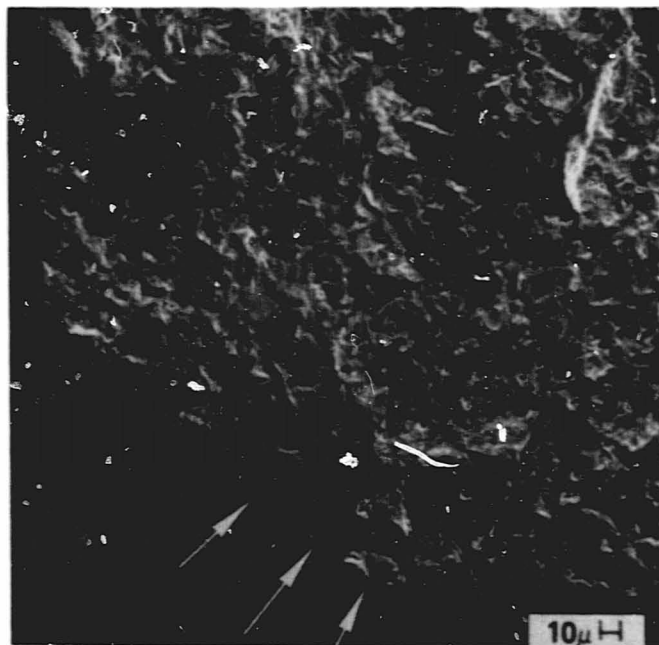
SPECIMEN 7842
47.5 KSI MOR AT 80°F



SPECIMEN 7811
55.9 KSI MOR AT 2500°F

ORIGINAL PAGE
BLACK AND WHITE PHOTOGRAPH

Figure 190. Typical Fracture Origins for Isopressed SASC
Sub-Surface Voids.



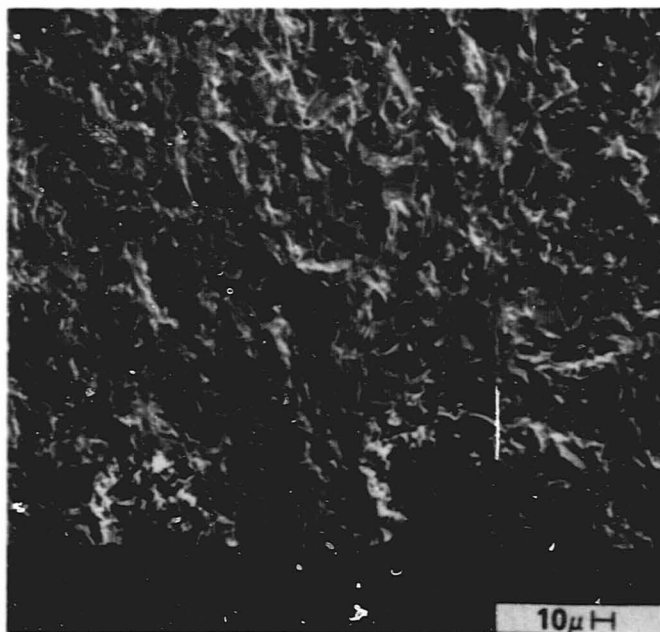
SPECIMEN 7802
53.3 KSI MOR AT 80°F



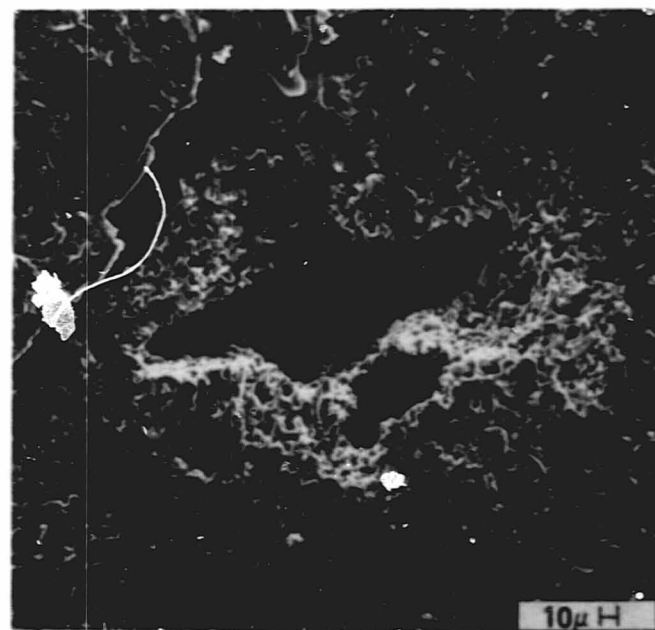
SPECIMEN 7813
54.7 KSI MOR AT 2500°F

ORIGINAL PAGE
BLACK AND WHITE PHOTOGRAPH

Figure 191. Less-Typical Fracture Origins for Isopressed SASC.



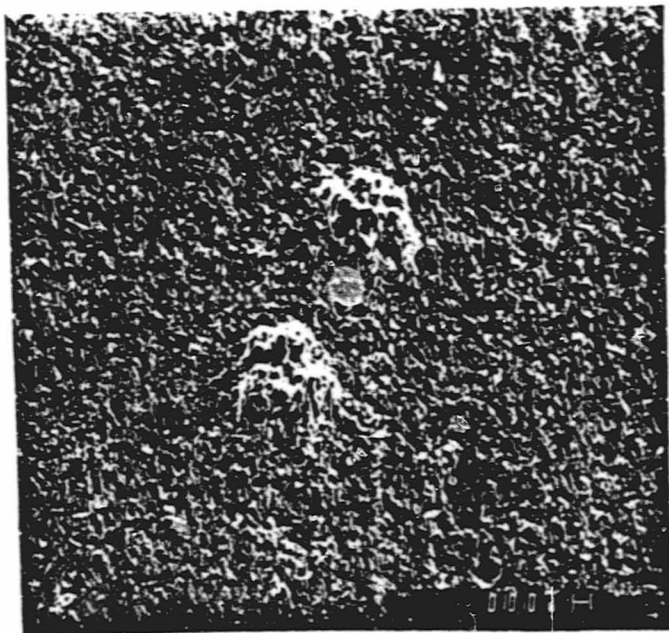
SPECIMEN 7789
48.7 KSI MOR AT 80°F



SPECIMEN 7730
42.0 KSI MOR AT 2500°F

ORIGINAL PAGE
BLACK AND WHITE PHOTOGRAPH

Figure 192. Typical Fracture Origins for Injection Molded SASC.



SPECIMEN 7718

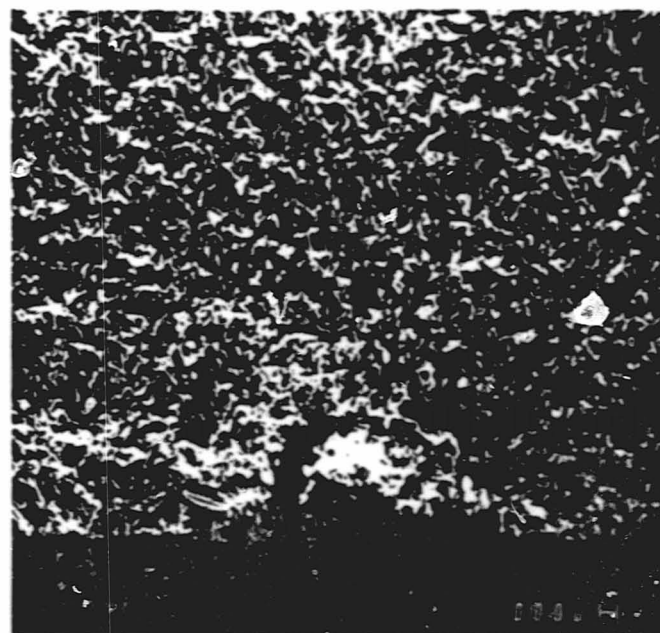
SPECIMEN 7719
45.8 KSI MOR AT 72°FORIGINAL PAGE
BLACK AND WHITE PHOTOGRAPH

Figure 193. Pits on As-Fired Surface of Injection Moulded SASC.

in a large decrease in strength. This occurs because the deepest flaw associated with grinding is parallel to the direction of grinding and thus becomes the critical flaw during flexural testing.⁽⁷⁾ It also has been found^(7,10) that oxidation treatments can blunt machining flaws resulting in a strength increase.

Cold-pressed test bars were utilized for similar studies on SASC. These specimens were remachined at AiResearch Phoenix using 320 grit diamond grinding wheels. After measuring the typical strength properties of the ground bars, the effect of oxidation treatments were determined. The results are shown in Table 25 and Figure 194. The major points are that transverse grinding decreases the strength by 40 to 45 percent but that the baseline strength can be recovered by oxidation treatments. It also is apparent that oxidation tends to increase the Weibull modulus without a decrease in strength. These results indicate the need to give all components an optimum oxidation treatment, not only to increase the Weibull modulus but also to compensate for the fact that component stresses are multiaxial and stresses transverse to the grinding direction cannot be eliminated.

4.7.1.4 Ceramic Interface Evaluation

Studies under the DARPA/NAVY/AiResearch Phoenix Ceramic Engine Demonstration Program show that chipping and cracking of static components, which ultimately led to engine failure, were due to a contact stress mechanism at interfaces. This mechanism was identified in the DARPA program⁽¹¹⁾ and a parallel ONR program⁽¹²⁾ as localized high tensile stress due to biaxial loading resulting from a combination of axial aerodynamic loading and radial thermal expansion relative movement.

Based on the DARPA and ONR program studies, contact stress appears to be one of the most critical considerations of static-structure component design and material evaluation. In summary, these studies show that for high contact loads a large strength reduction resulted with bare surfaces in contact, moderate strength reduction resulted with high temperature lubricants present, and little or no strength reduction resulted with a suitable metal compliant layer between the surfaces. Additional studies are required to further evaluate high and low contact loads, lubricants, and compliant layers and/or coatings. The test apparatus developed in the DARPA program (shown in Figure 195) for interface evaluation is being used to evaluate the materials and estimated contact conditions of AGT components.

The contact rig consists essentially of a furnace, a pneumatic cylinder and leveraged load train for applying a normal force and an Instron test machine for applying relative motion (which produces a tangential force). Perhaps the best way to describe the function and flexibility of the contact rig is to describe the sequence conducting a test. The sequence is as follows:

TABLE 25. EFFECT OF OXIDATION ON WEIBULL PARAMETERS OF COARSE GRAINED COLD-PRESSED SASC HAVING DIFFERENT GRINDING TREATMENTS

Condition (population)	Characteristic Strength (ksi)	m-Value
A, as-received (30)	56.4	6.9
A, 2200°F/20 hrs (10)	60.2	8.5
A, 2500°F/4 hrs (10)	61.7	12.2
L, longitudinal grind (10)	56.9	14.4
L, 2200°F/20 hrs (10)	56.2	14.2
T, transverse grind (10)	32.3	12.9
T, 2200°F/20 hrs (10)	57.3	10.7
T, 2200°F/2 hrs (10)	61.1	12.7
A, as-received* (30)	58.5	8.6
L, longitudinal grind* (10)	59.3	10.2
T, transverse grind* (10)	31.8	7.7

*Fine grain material

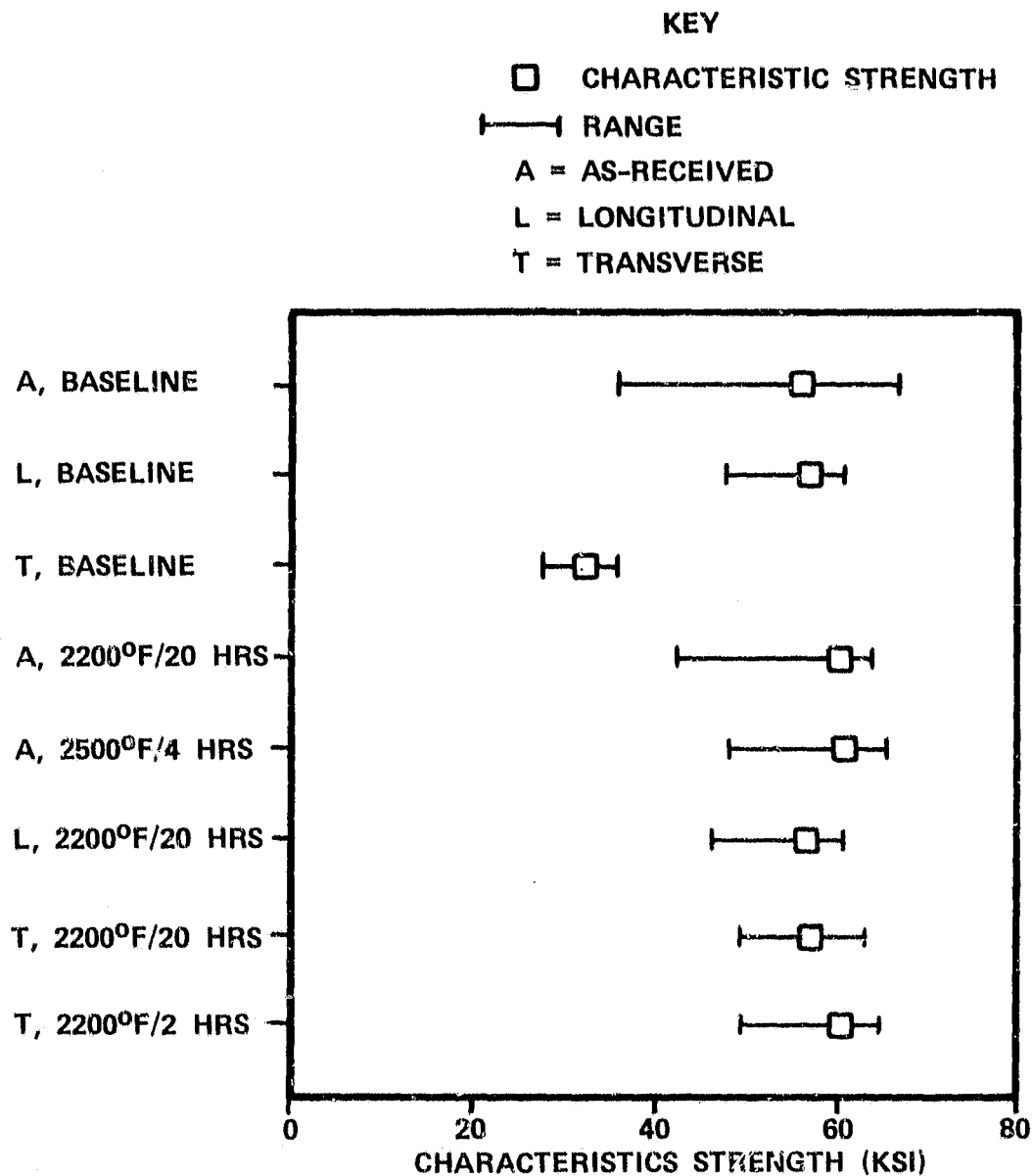


Figure 194. Oxidation Exposure Results for SASC.

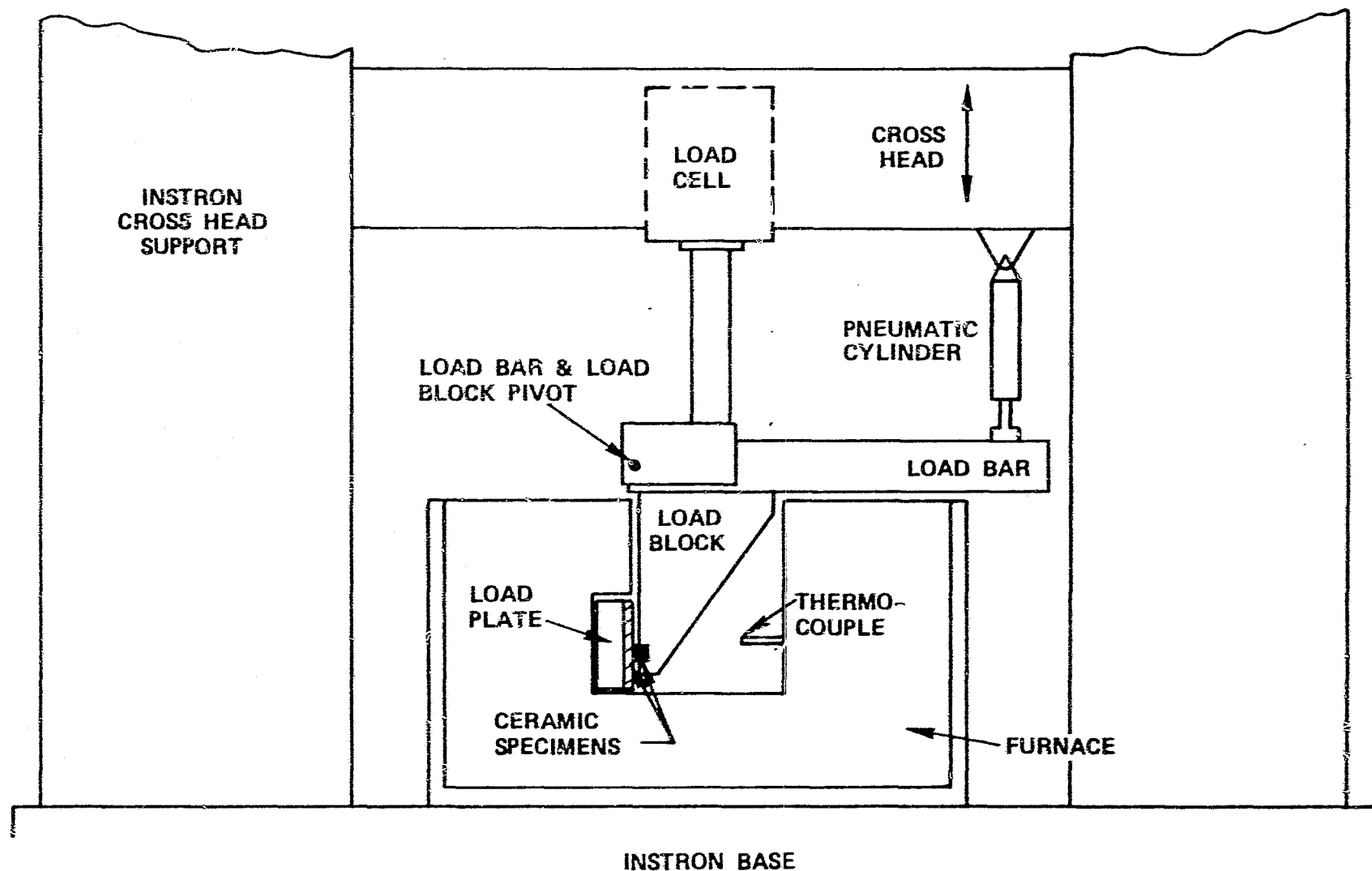


Figure 195. Interface Test Apparatus.

- o Step 1 - Specimen Positioning - The ceramic test bars are inserted into notches in the load plate and load block such that the long axes are perpendicular to each other. Both specimens are crowned on one surface and flat on the opposite surface. By selectively pairing the surfaces to be in contact, point loading, line loading or area loading can be achieved. Further test variation can be achieved by placing a compliant layer material on a lubricant between the two test bars. The specimen fixturing is made of hot pressed SiC.
- o Step 2 - Application of Normal Force - The pneumatic cylinder is pressurized to provide the desired normal force at the specimen interface. The cylinder has previously been calibrated by replacing the specimen and load plate with a load cell.
- o Step 3 - Heat to Test Temperature - The furnace is turned on and specimens are heated to the selected test temperature and soaked for the selected soak time. During this heating, the Instron is set to maintain zero tangential force by automatically re-positioning the crosshead to account for thermal expansion of the fixturing.
- o Step 4 - Application of Tangential Force - The load block and its ceramic specimen (referred to as the moving specimen) are moved relative to the load plate and the ceramic specimen (referred to as the stationary specimen) by translating the Instron crosshead at a controlled speed (usually 0.02 inch per minute). The tangential force as a function of interface movement distance is plotted on the Instron chart recorder. From this data, the static and dynamic coefficients of friction are calculated. The test can be conducted with a single pass or can be cyclic.
- o Step 5 - Flexure Strength Measurement - The stationary test bar is removed from the load plate and strength tested in 4-point bending with the original contact surface in tension to determine if the contact conditions result in strength degradation.
- o Step 6 - Fractography - The contact area is compared with adjacent areas and the fracture surface is compared with baseline test bars which have not been exposed to the contact conditions. These observations are correlated with friction and property data and with stress analysis in an effort to understand the mechanisms of contact damage.

Initial tests to determine the sensitivity of the AGT candidate materials to contact loading with simultaneous relative movement have been initiated. Data for RBN 104 slip-cast reaction-bonded Si_3N_4 at

low contact loads are shown in Figure 196. These results indicate that substantial strength loss occurs with bare surface in contact, but that no loss occurs when compliant layers and/or lubricants are present. Similar results were obtained for the Carborundum sintered α -SiC Figure 197, although the degree of strength reduction is substantially less than for RBSN.

Testing will continue to determine whether results similar to those obtained during the DARPA studies occur at higher contact loads.

Prior contact studies indicate that friction increases as temperature increases in the 1600 to 2200°F range. In addition, the difference between static and dynamic friction for a given material also increases, suggesting that at least part of the cause of higher friction at high temperature is associated with the contact surfaces sticking or binding. To further study this and attempt to develop a solution, plasma spray oxide ceramic coatings were applied to both α -SiC and RBN-104. Initial results are summarized in Figure 197. Although very few data points are available, the following trends are apparent:

- o The coatings were successfully applied to the sintered α -SiC without damaging the α -SiC
- o Adherence was excellent for the mullite but moderate to poor for the Cr_2O_3 and Al_2O_3
- o The RBN-104 was damaged by thermal shock during coating; no further strength reduction occurred due to contact exposure
- o Coated α -SiC showed no decrease in strength due either to room temperature or 2000°F contact testing
- o All coated specimens had lower coefficient of friction than bare specimens
- o Increasing the load from 10 to 30 pounds did not change the coefficient of friction and did not result in any visual damage

4.7.2 Subcontractor Ceramic Development

4.7.2.1 Ford Motor Company

The Ford semi-annual report is included as Appendix I.

4.7.2.2 AiResearch Casting Company (ACC)

The ACC semi-annual report is included as Appendix II.

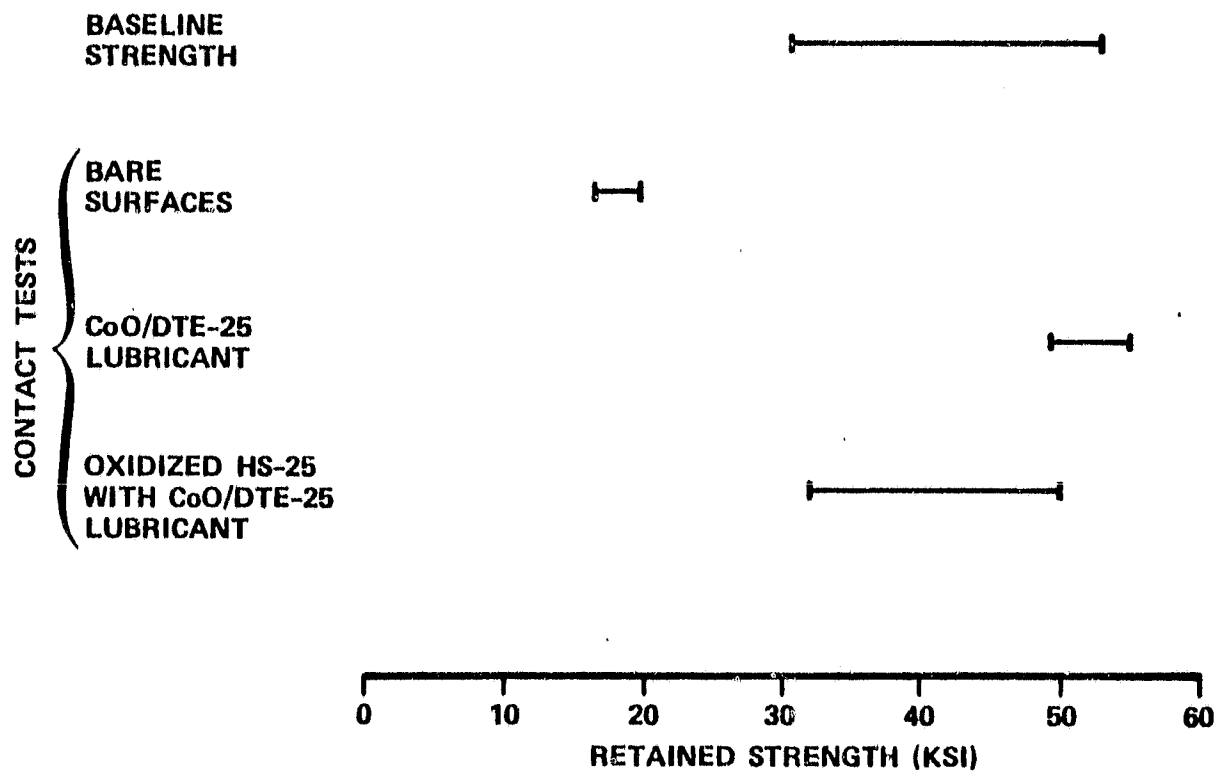
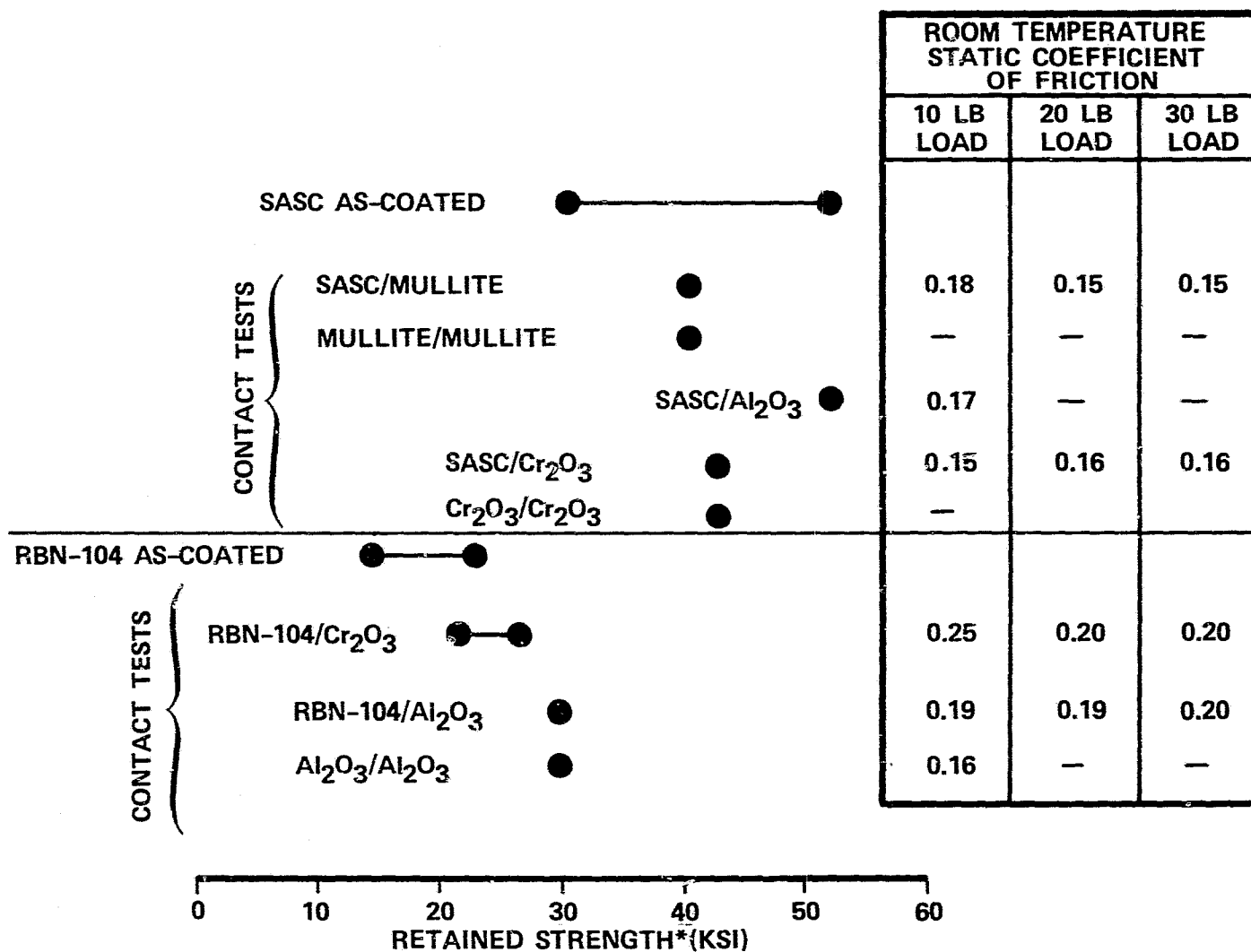


Figure 196. Initial Contact Results for RBN 104, 2000°F/ 0.5 Hour Hold.



*FOR CONTACT TESTS CONDUCTED AT 10 LB LOAD, LINE CONTACT,
1/4 INCH RADIUS, 2000°F/0.5 HR HOLD

Figure 197. Initial Contact Results With Plasma Spray Coatings.

4.7.2.3 The Carborundum Company

The Carborundum semi-annual reports for common and unique tasks are included as Appendices III and IV, respectively.

4.7.2.4 Pure Carbon Company

The Pure Carbon Company semi-annual report is included as Appendix V.

4.8 Foil Gas Bearing

Design requirements for the AGT101 gas foil bearing encompass large extremes in speed, load, and temperatures. The bearing must be capable of thousands of start-stop cycles without excessive wear and sustained operation at speeds between 50,000 and 100,000 rpm for at least 4000 hours. Bearing temperature extremes for start-stop and sustained operation extend from -20 to 1050°F.

The bearing is a hydrodynamic design requiring no external air supply for operation. Consequently, the bearing must generate a gas film at as low a speed as possible to minimize starting power and foil wear during the start-stop cycle. This film generation speed also must be compatible with a stable gas film over operating speeds, loads, and temperatures.

Normal bearing operating loads range from 3 to 4.5 pounds for the Mod II and Mod I AGT101 engines, respectively. Gyroscopic bearing loads resulting from a skidding or spinning vehicle must be sustained as well as short duration 6-g shock loads.

These stringent bearing requirements necessitate a foil bearing development program to establish and confirm proper bearing operation prior to actual engine operation. Two foil bearing test rigs have been designed to satisfy the development plan.

One test rig is a single test bearing rig shown in Figure 198. The purpose of this test rig is to screen potential bearing designs for stability, load capacity, and power loss. This rig incorporates a turbine driven 1.35-inch diameter shaft supported on two slave foil journal bearings and one bidirectional thrust slave bearing. The single test bearing is located between the two slave journals and is capable of being selectively loaded. The test bearing carrier is hydrostatically mounted on a spherical seat that permits self-alignment of the test bearing under all loads and also permits the reactive torque of the test bearing to be accurately measured to within ± 0.001 in-lb.

The single foil bearing test rig has been fabricated and currently is being used in the development program. Two preliminary bearing configurations have been evaluated at speeds up to 110,000 rpm and 13-pounds sustained load. Bearing power loss as a function of load and speed for the two configurations is shown in Figures 199 and 200. The maximum start/stop torques and hydrostatic lift-off speeds for loads up to 10 pounds have been established for the bearings. These data are presented in Tables 26 and 27. Testing to establish optimum foil bearing parameters for preformed radius, backing spring stiffness, sway space, foil thickness, and foil length is continuing.

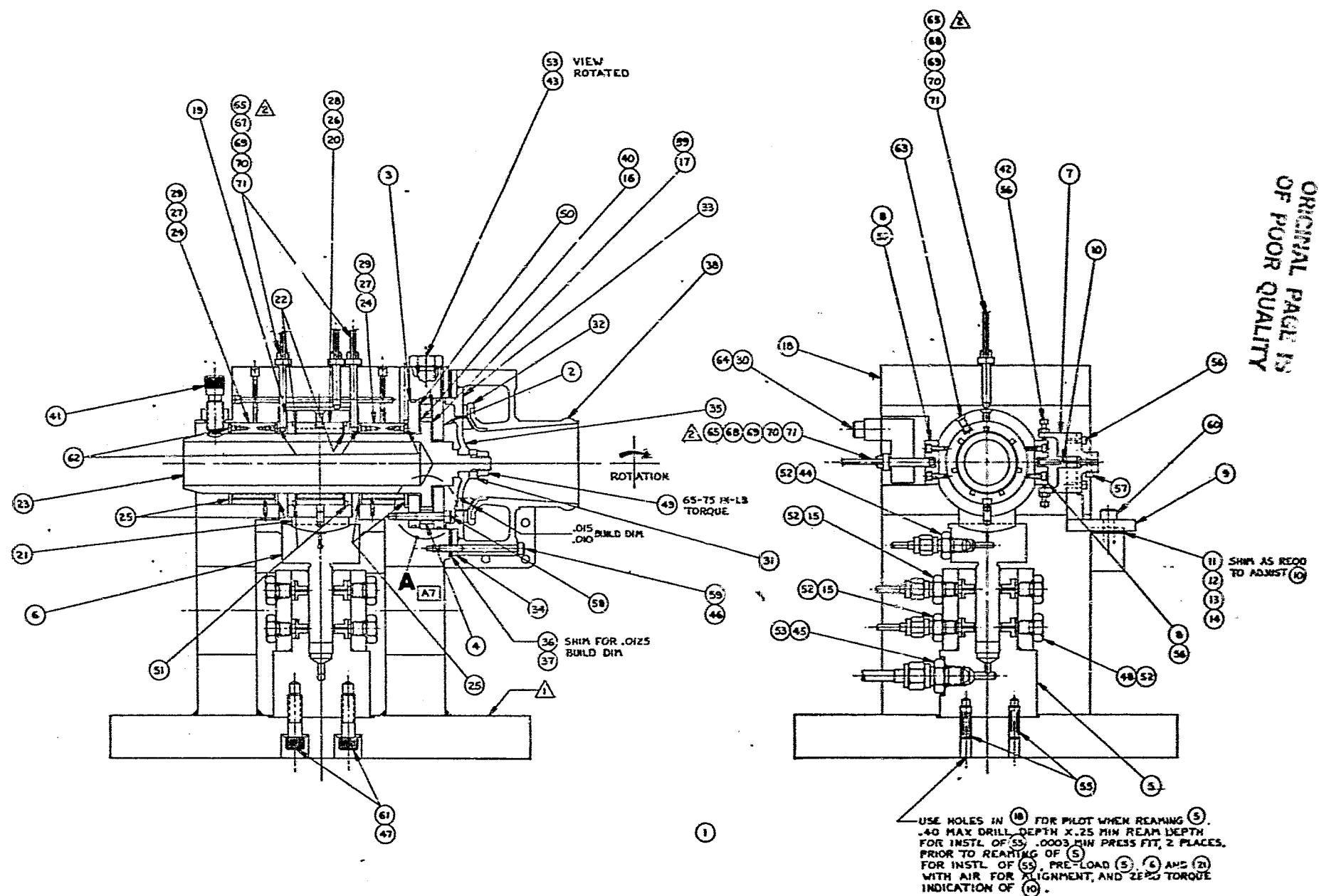


Figure 198. Single-Foil Bearing Test Rig.

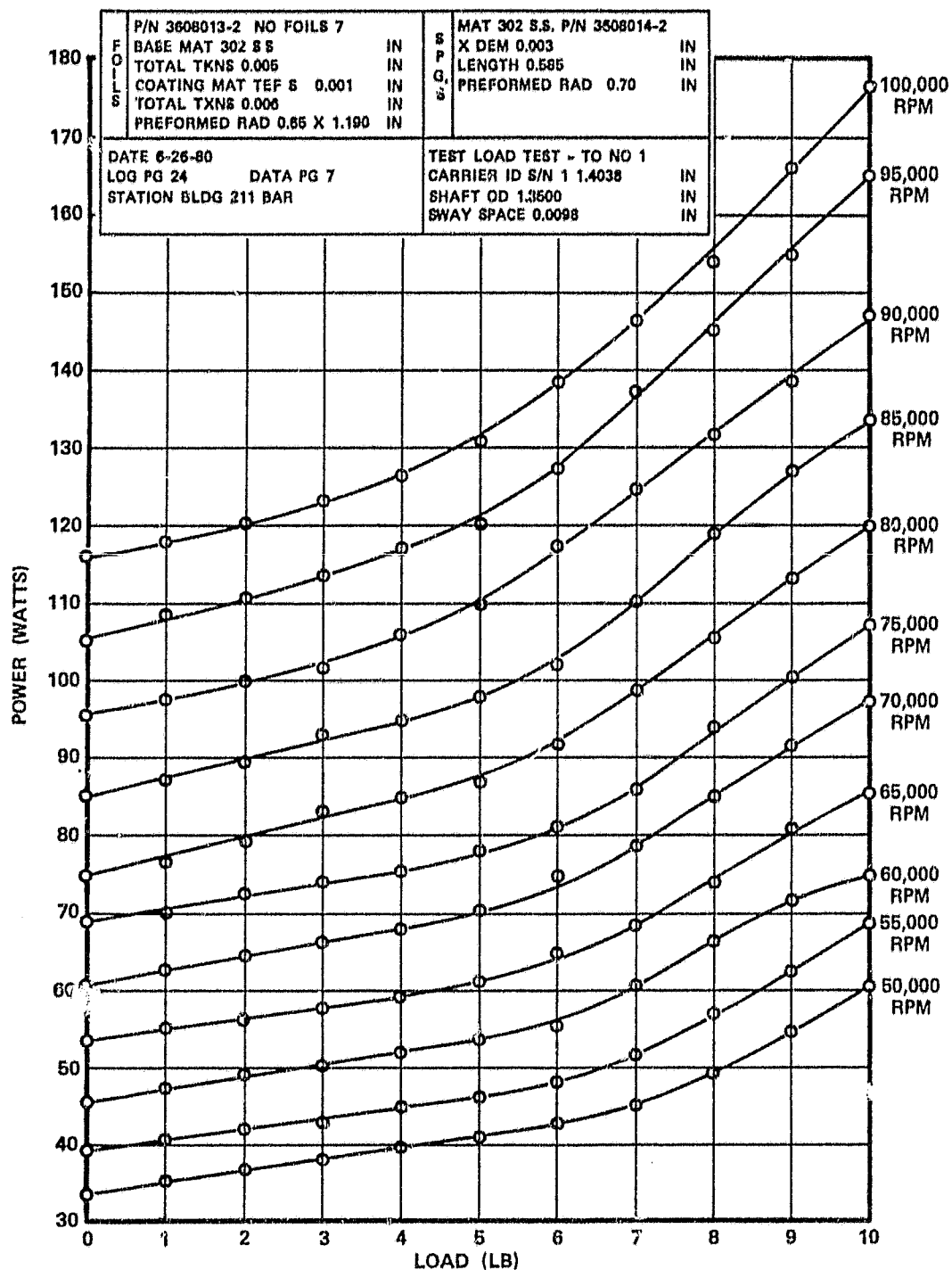


Figure 199. Plot of Power Loss Vs. Load for AGT101 Foil Bearing Test.

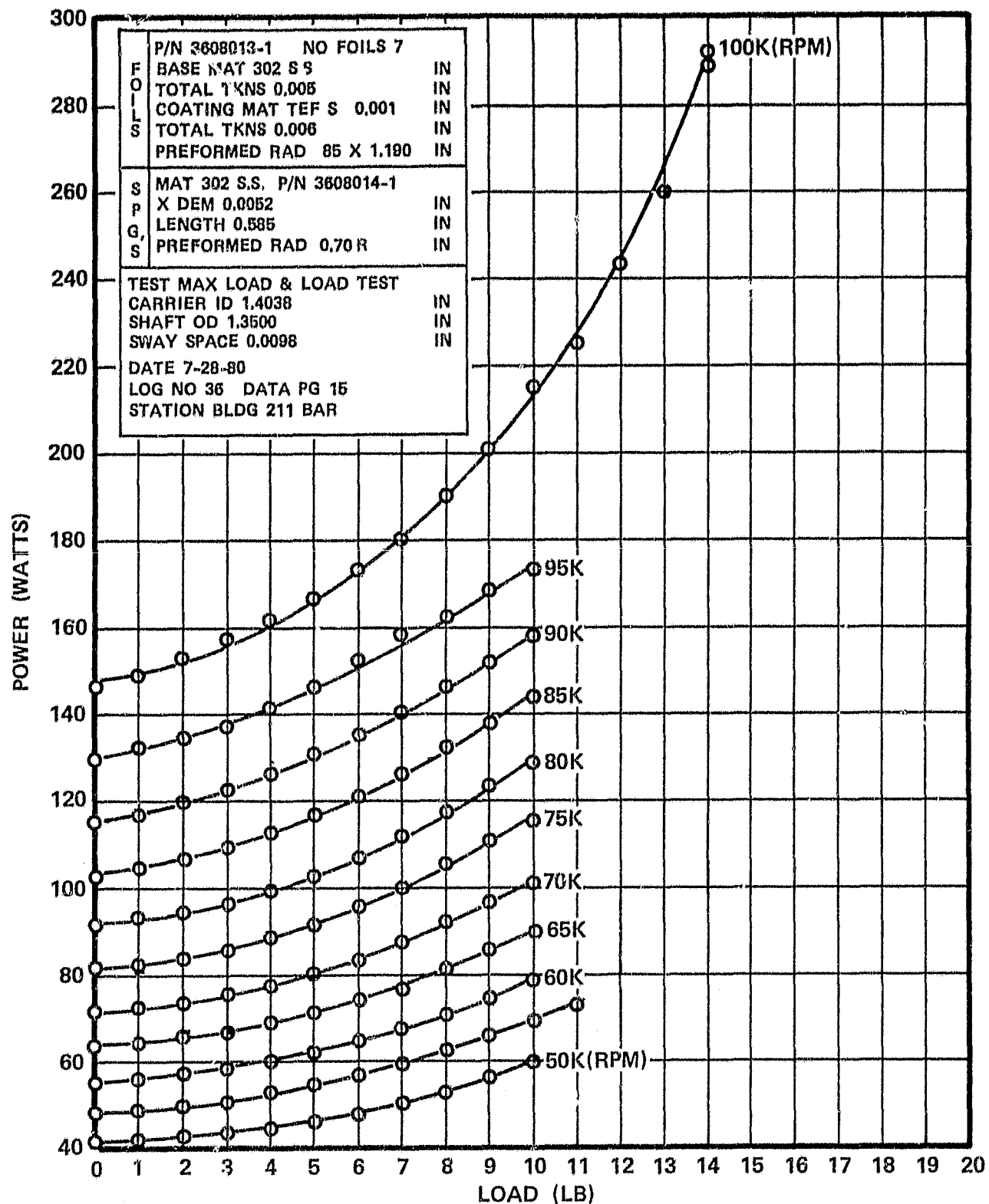


Figure 200. Plot of Power Loss Vs Load for AGT101 Foil Bearing Test.

TABLE 26. START/STOP CHARACTERISTICS, FOIL BEARING
CONFIGURATION NO. 1, 0.003-INCH BACKING
SPRING

Load (Lbs)	Maximum Start Torque (in-lb)	Maximum Stop Torque (in-lb)	Hydrodynamic Speed (rpm)
0	2.24	2.10	6,250
1	2.45	2.20	6,300
2	2.70	2.45	7,250
3	3.00	2.62	7,900
4	3.50	3.10	9,700
5	3.55	3.35	10,250
6	3.60	3.40	11,550
7	3.62	3.40	13,625
8	3.62	3.40	13,250
9	3.70	3.40	14,750
10	3.68	3.35	16,500

TABLE 27. START/STOP CHARACTERISTICS, FOIL BEARING
CONFIGURATION NO. 2, 0.005-INCH BACKING
SPRING

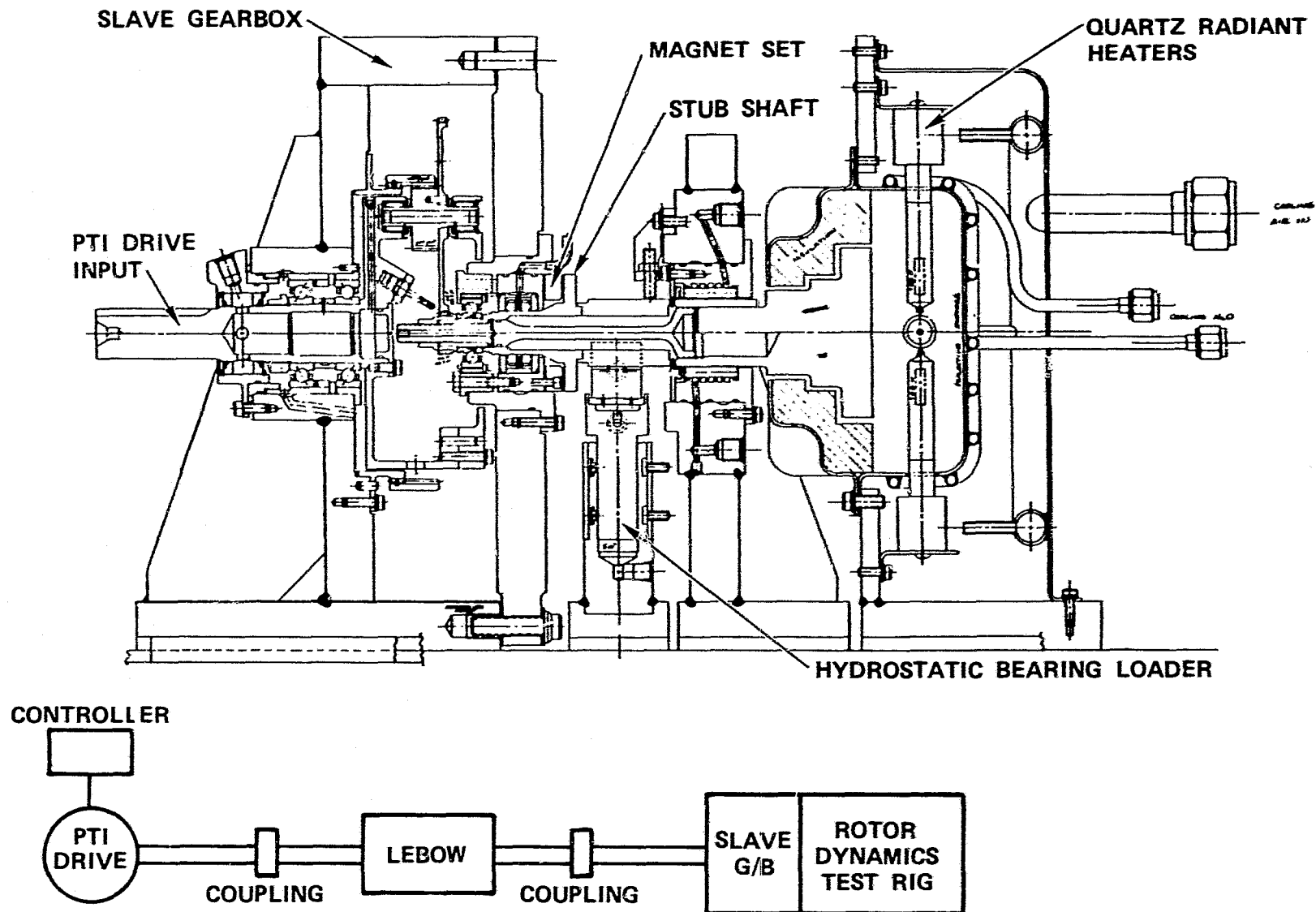
Load (lb)	Maximum Start Torque (in-lb)	Maximum Stop Torque (in-lb)	Hydrodynamic Speed (rpm)
0	3.85	3.75	8,950
1	3.90	3.70	8,000
2	3.88	3.84	8,625
3	3.79	3.64	9,250
4	3.71	3.49	9,875
5	3.66	3.40	11,000
6	3.54	3.36	11,525
7	3.51	3.28	12,225
8	3.46	3.25	13,750
9	3.39	3.24	Indeterminant
10	3.39	3.18	20,725

C-4

Foil coating screening tests currently are being conducted on an existing R&D test rig and results are not yet available.

The second test rig to be used in the development of the foil bearing is shown in Figure 201. This rig is a variation of the Rotor Dynamic Test Rig with modifications to allow radial loading of the complete dummy AGT101 rotating group and to simulate thermal gradients to the foil gas bearing. This dynamic foil bearing test rig will permit stability and load capacity tests for the bearing under predicted thermal environmental conditions. Development of the foil bearing cooling system also will be conducted on this rig.

The rig design has been completed and components are being fabricated.



ORIGINAL PAGE IS
OF POOR QUALITY

Figure 201. Dynamic Foil Bearing Test Rig.

4.9 Bearings and Seals

The AGT101 high speed rotating group pinion bearing and floating ring seals are shown in Figure 202. The pinion bearing is a 15 mm 202 series ball bearing designed to carry a maximum predicted radial load of 41 pounds and a thrust load of approximately 300 pounds at 100,000-rpm. Bearing loads and speeds vary considerably over the 100,000 mile CFDC design goal; however 58 percent of the required 3900-hour bearing life operation will be at speeds of 56,000 rpm, radial loads 9.5 pounds and thrust loads of approximately 70 pounds. The remaining 42 percent of the required CFDC life would cover transient operation at speeds up to 85,000 rpm radial loads and thrust loads to approximately 240 pounds. The 100,000-rpm speeds and 300-pound thrust loads would occur only during wide-open throttle (WOT) acceleration to vehicle speeds above 60 mph.

The bearing was designed to meet the following conditions:

Design Conditions

Speed:	55,000 to 100,000 rpm
Radial loads:	9.5 to 41 pounds
Thrust loads:	70 to 300 pounds
Life:	CFDC 3900 hours - variable speed and load 100 hours at 100,000 rpm and 300 pounds
Lubricant:	Automotive transmission fluid (ATF)
Lubricant Temperature:	100 to 300°F

Bearing component details are summarized in Table 28.

Bearings for the AGT101 development program are being fabricated by:

- o Split Ball Bearing Company
- o Fag Bearing Inc
- o Barden Corporation

4.9.1 Gearbox Bearings

The bearings for the AGT101 gearbox are discussed under the gearbox section of this report.

ORIGINAL PAGE IS
OF POOR QUALITY

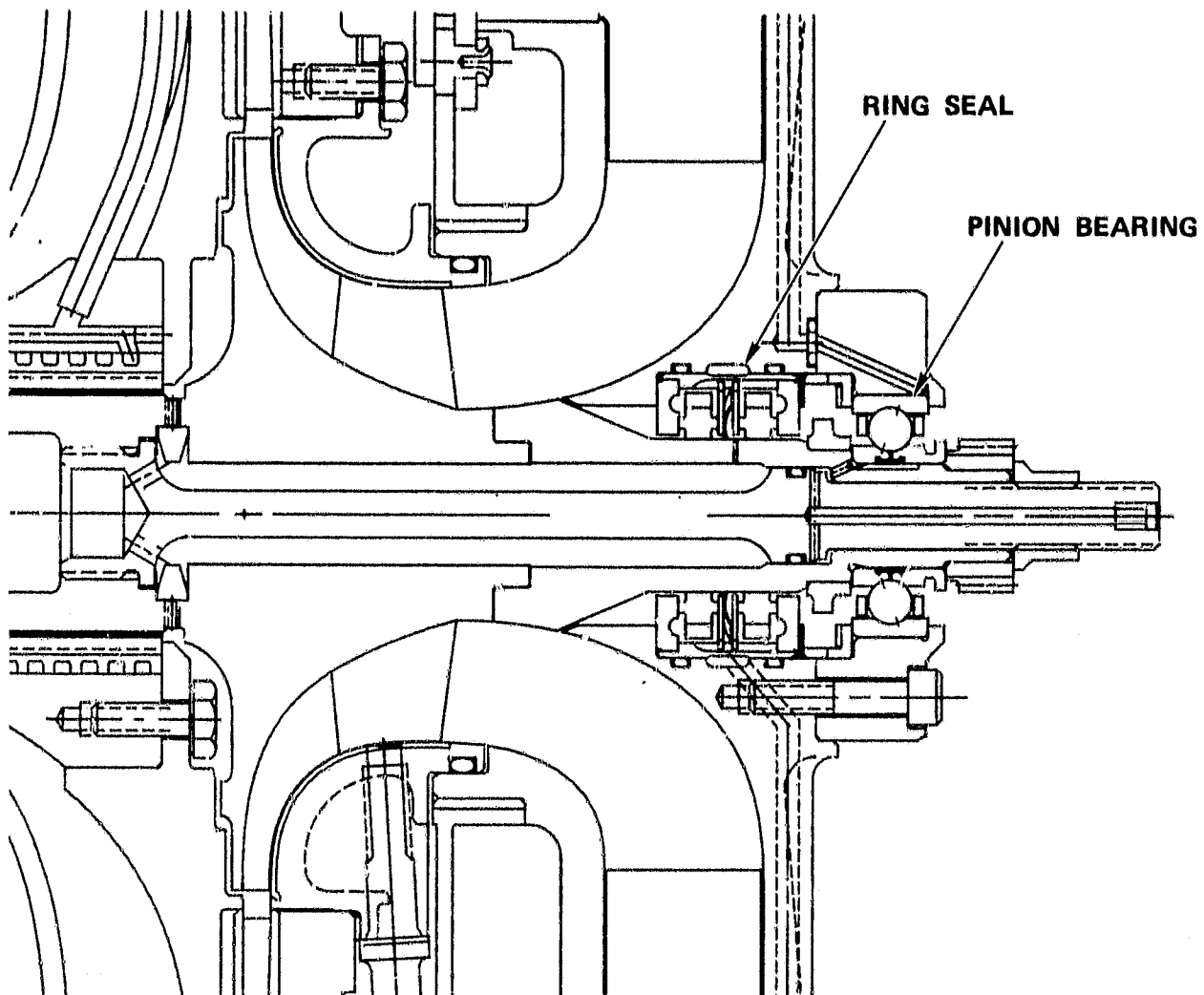


Figure 202. High Speed Pinion Bearing and Rotor Ring Seals.

TABLE 28. PINION BEARING COMPONENT DETAIL

Bearing Description-ball, Split-Inner-Ring, 202; Grade ABEC 5

<u>Inner Ring</u>	<u>Outer Ring</u>
Material - SAE 52100 STL-R _c 58-64	Material - SAE 52100 STL-R _c 58-64
Bore - 0.5904-0.5906 (15 mm)	OD - 1.3778-1.3780 (35 mm)
Width - 0.525-0.535	Width - 0.4281-0.4331 (11 mm)
Race Depth - 24 min % Ball/Roller Dia	Race Depth - 16 min % Ball/Roller Dia
Race Curvature - 51.6-52.4% Ball/Roller Dia	Race Curvature - 50.6-51.4% Ball/Roller Dia
Separator Pilot Land	Separator Pilot Land
To Groove Runout - TIR	To Groove Runout - 0.0005 TIR
<u>Separator</u>	<u>Rolling Elements</u>
Material - SAE 4340 STL-R _c 34-38	Material - SAE 52100 STL-R _c 58-64
Silver Plated 0.0005-0.0015	Elements per Row-10
Thick per AMS 2410	Element Dia-1/4 Inch
Construction - Machined	Element Length
Assembly - One-Piece	
Pilot Surface - Outer Ring Lands	
Pilot Clearance - 0.010-0.016	
Assembled Bearing Characteristics	
Total Axial Clearance of	
0.0078 Max Under 1 lb Gage Load	

4.9.2 High Speed Ring Seals

The high speed ring seals for the AGT101 are shown in Figure 202. These seals are a double floating carbon ring design as shown in Figure 203 and are designed with provisions for buffer air between the carbon elements.

Development of the high speed ring seal for the AGT will be accomplished on two test rigs. The rig to be used in preliminary screening of seal materials and seal leakage tests is shown in Figure 204. The rig consists of a high speed turbine driven shaft mounted on foil gas bearings. The test seal is mounted at the end of the shaft with provisions to introduce and measure buffer air between the carbon rings. Leakage flow through the rings also can be measured. Instrumentation to measure shaft runout and temperature has been included.

This test rig has been designed and currently is being fabricated.

Additional development of the ring seal will be accomplished on the Rotor Dynamics Test Rig as described in Section 4.0 of this report. The seal development on the Rotor Dynamics Test Rig will permit seal evaluation under actual rotor conditions prior to incorporation in an operating engine.

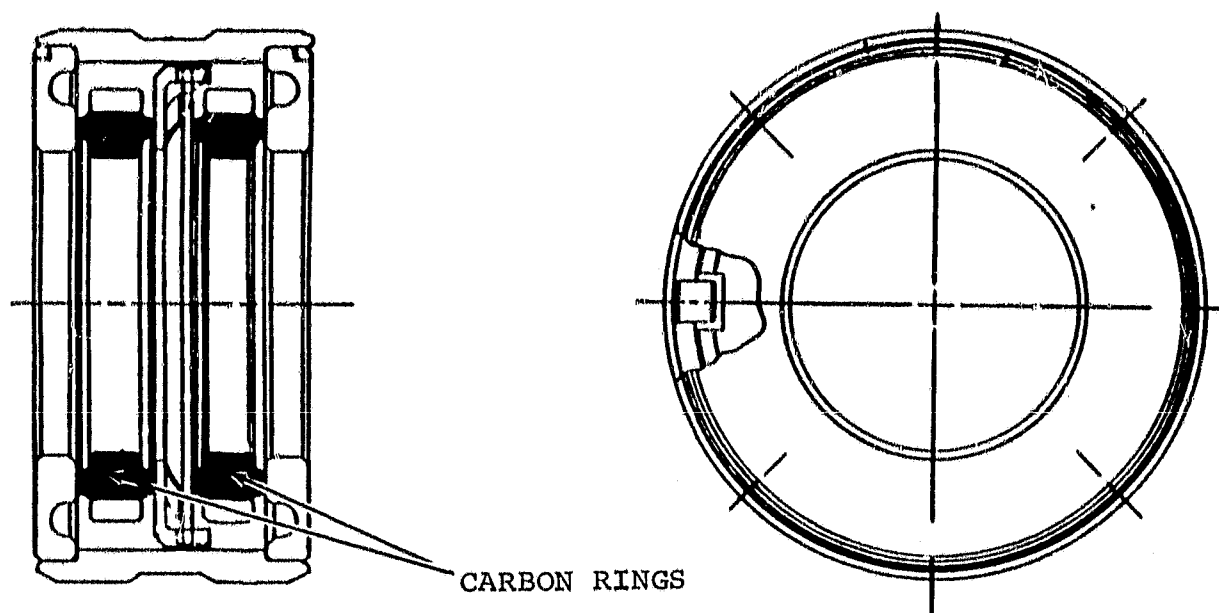


Figure 203. High Speed Ring Seals, P/N 3826200.

ORIGINAL PAGE IS
OF POOR QUALITY

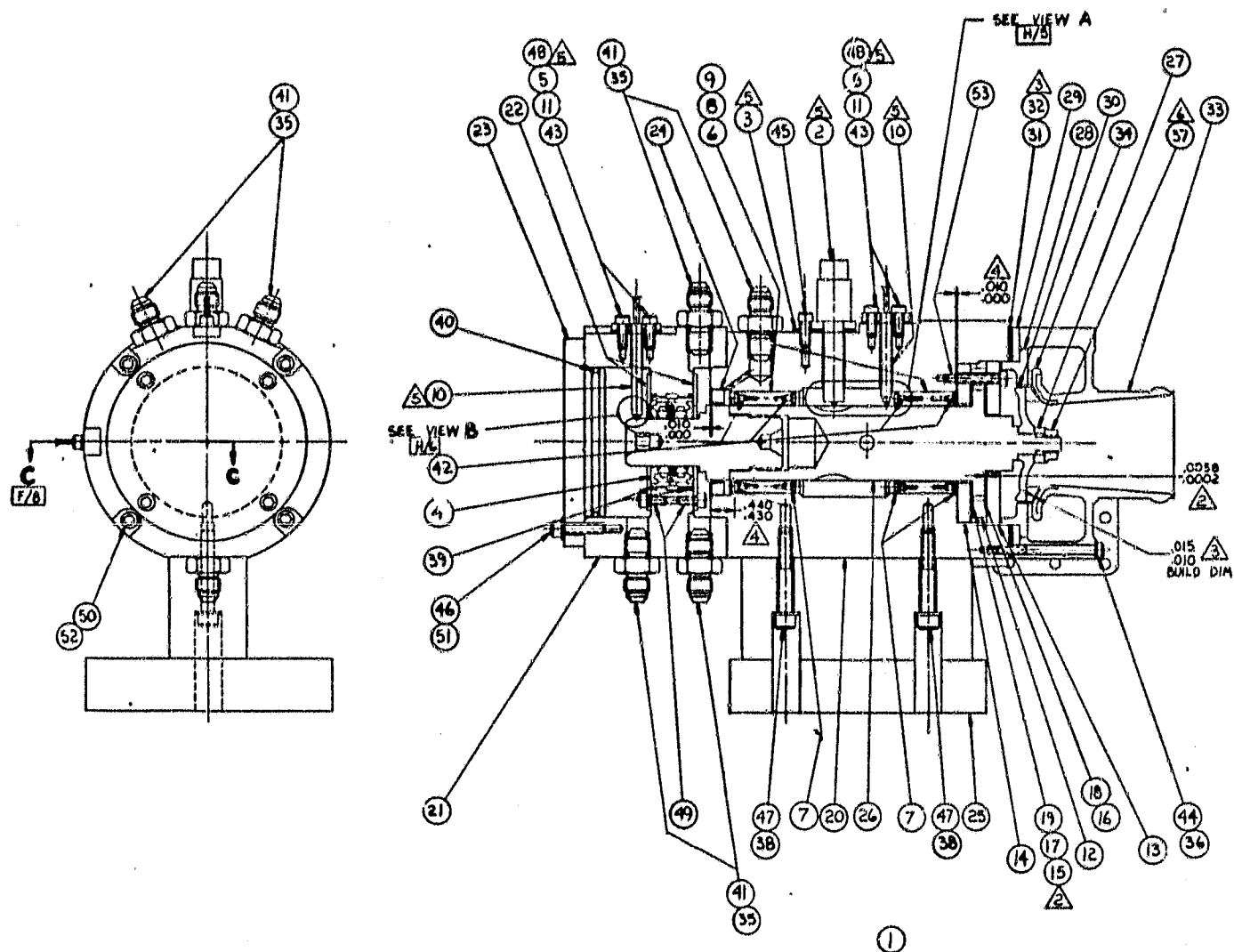


Figure 204. Seal Test Rig, P/N 3608316.

4.10 Rotor Dynamics Development

The following paragraphs summarize the AGT Rotor Dynamics Development Task progress over the past 6 months and planned activity through 1980. The purpose of this task is to establish a stable engine rotor system comprised of a high-speed pinion gear, ball bearing, ring seals, foil gas bearings, aerodynamic components and interfaces, tie-bolt, and ceramic turbine attachment.

4.10.1 Development Approach

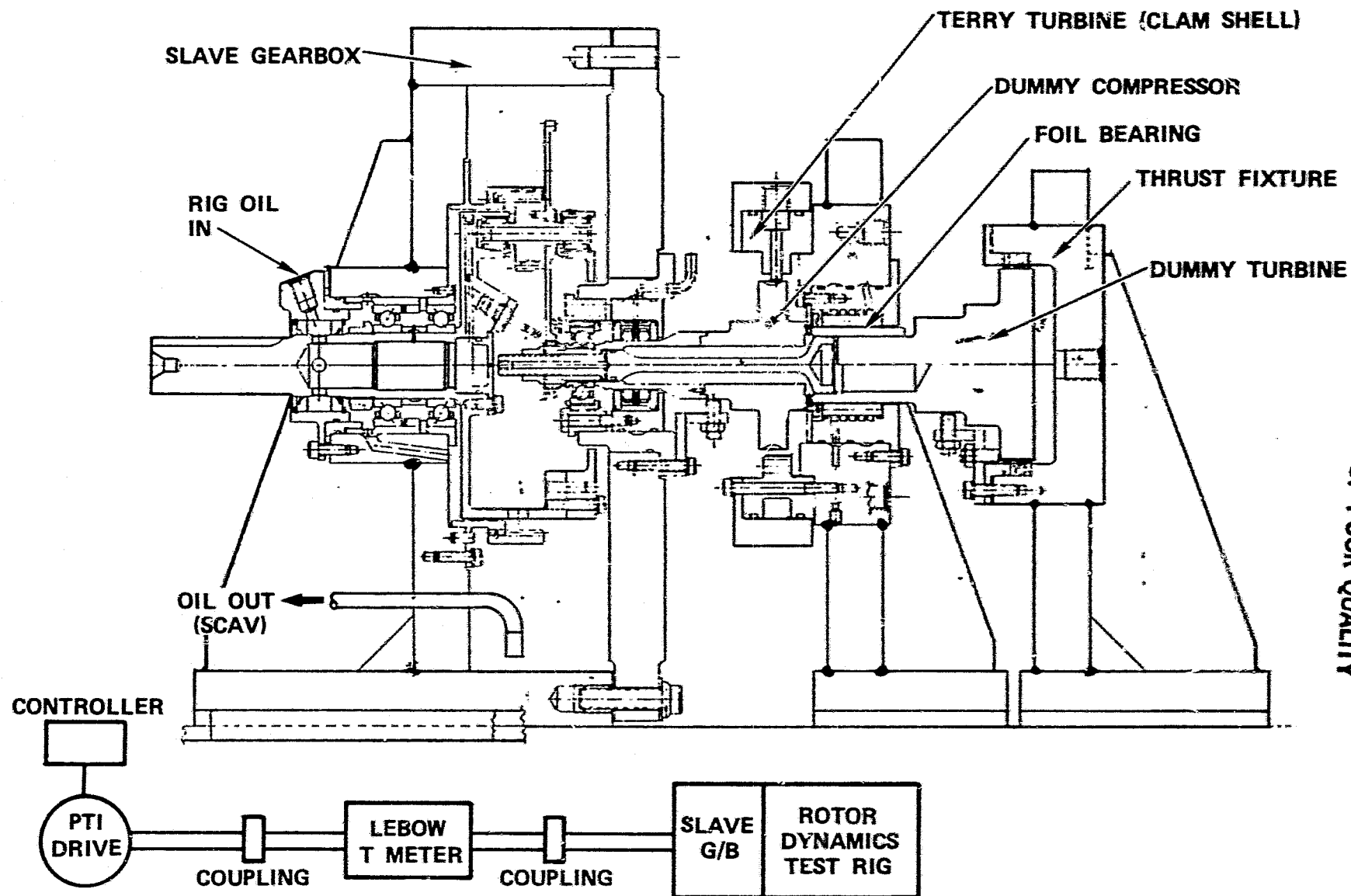
The rotor dynamics development task will be conducted utilizing the rotor dynamics test rig shown in Figure 205. A dummy AGT rotor system will be driven by a 40-hp PTI variable speed motor and a speed step-up gearbox designed to simulate the AGT gearbox first mesh and planetary carrier speeds. A "Terry" turbine has been incorporated in the dummy compressor and will be used to load and drive the geartrain as required to simulate normal engine operation and engine braking modes. This development approach will allow power transmission in either direction across the planet/sun gear mesh.

Axial thrust on the rotor is controlled by regulating the air pressure chamber surrounding the large end of the dummy turbine. The system has been designed to supply axial loads up to 300 pounds with 32 psi air.

The dummy compressor and turbine wheels were designed to simulate the mass and inertia properties of the engine impeller and metal turbine wheels. An optional version of the dummy turbine design using an aluminum hub with a shrink fit attachment to a metal sleeve will be used to simulate the ceramic turbine.

For simulation of the foil bearing thermal environment a second development approach is achieved by converting the rotor dynamics test rig into the hot foil bearing test rig shown in Figure 206. To produce the desired hot foil bearing configuration, the following modifications will be necessary:

- o The dummy compressor wheel will be moved forward and a ring magnet used to supply 30 to 40 pounds of axial thrust to the ball bearing
- o A hydrostatic bearing loader will be used, where the dummy compressor was located, to provide rotor side load
- o An IN718 dummy turbine will be used to represent the dual alloy AGT turbine
- o A 2219 aluminum dummy turbine will be used to represent the AGT ceramic turbine during initial testing



ORIGINAL PAGE IS
OF POOR QUALITY

Figure 205. Rotor Dynamics Test Rig.

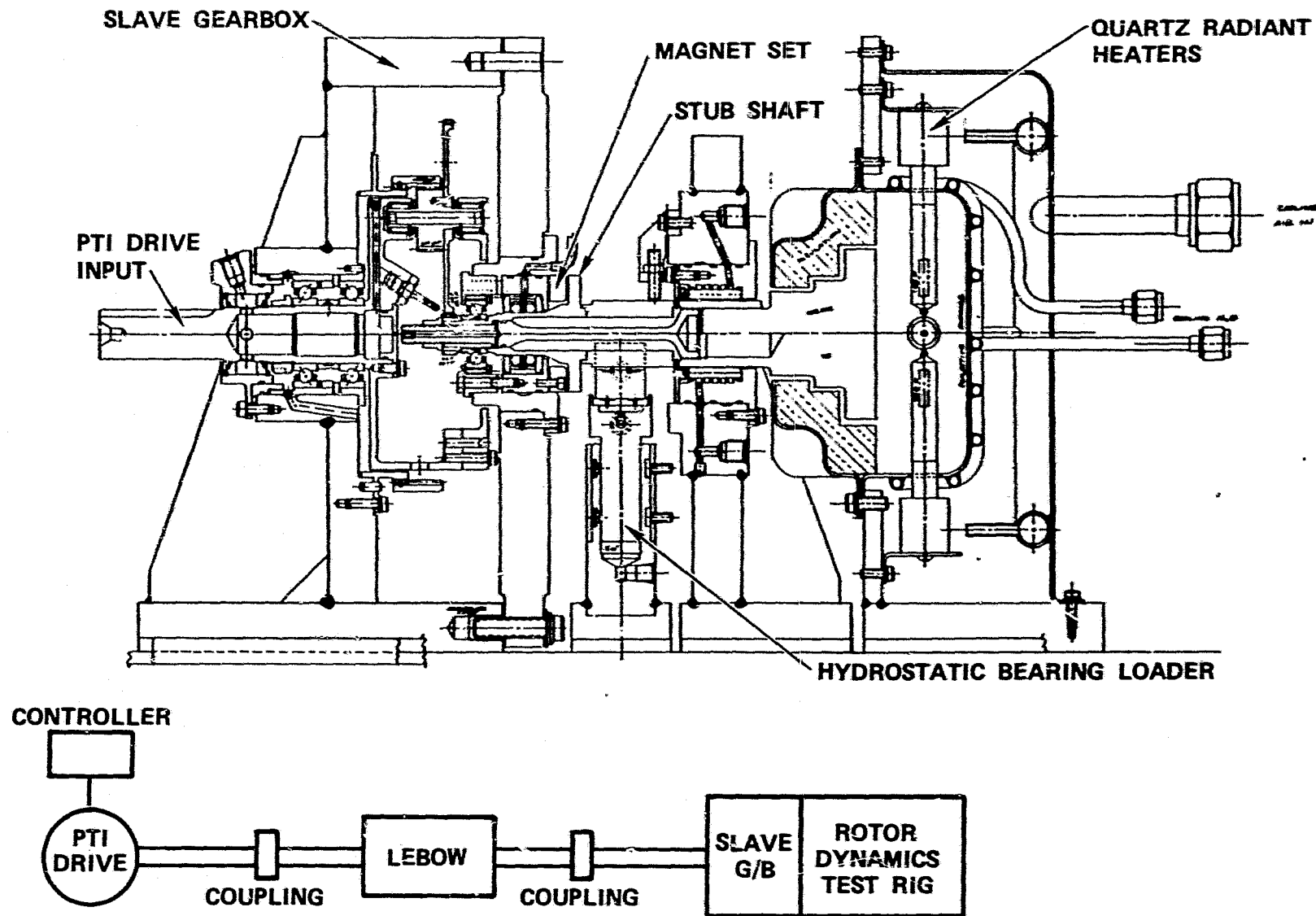


Figure 206. Hot Test Foil Bearing Test Rig.

- o Metallic and ceramic dummy turbines will be used for hot testing. The turbines will be heated by radiant heaters
- o An insulated enclosure will be required around the turbine wheel to obtain a temperature environment at the ceramic-metal attachment representative of engine conditions

4.10.2 Test Objectives

A design review was held for the purpose of evaluating hardware designs and test objectives for the rotor dynamics test rig. As a result of that meeting, the following test objectives were established:

- o Rotor response amplitude over the full engine operating speed range
- o Influence assessment of the planet gearset on rotor response amplitudes
- o Foil bearing operating characteristics evaluation in the rotor environment under 1-g loads in a room temperature environment
- o Balance sensitivity assessment of the rotor bearing system
- o Provide a test vehicle for evaluating the ceramic-metal turbine attachment design in the rotor, environment prior to committing to an engine test

The hot foil bearing test rig will have the following test objectives:

- o Evaluate foil bearing load capacity in the rotor environment
- o Evaluate foil bearing tolerance to high temperature operation
- o Gain insight into foil bearing cooling requirements

Oil bearing cooling will be achieved via the liquid cooling passages in the support structure and/or by forcing cooling air axially through the bearing.

4.10.3 Rig Test Parameter Ranges

The following is an operating range summary of the various test rig configurations:

- o Speed 0 to 100,000 rpm
- o Gear Load 20 to 40 hp
- o Oil Temperature 70 to 250°F
- o Oil Pressure 50 psi nominal
- o Foil Bearing Journal Temperature Range 1100°F maximum
- o Thrust Load 300 pounds maximum
- o Foil Bearing Side Load 18 pounds (6-g load)

4.10.4 Instrumentation

The following is an instrumentation requirement list for the rotor dynamics version of the rig:

- o Speed
- o Torque
- o Oil supply pressure
- o Oil inlet temperature
- o Forward sump temperature
- o Shaft excursions radially at the oil slinger dummy compressor, dummy turbine and axially at the dummy turbine. Two probes at 90 degrees will be used at each of the above locations
- o Shaft temperature adjacent to the foil bearing
- o Thrust piston pressure

The following instrumentation changes will be required for the hot foil bearing rig:

- o Hydrostatic loader pressure
- o Delete shaft excursion measurements at the dummy turbine
- o Foil temperature
- o Foil bearing coolant temperature

4.10.5 Test Schedule

The rotor dynamics and hot foil bearing test rigs presently are in the hardware procurement stage for all component parts and installation fixturing.

4.10.6 Conclusion

The AGT101 program will pursue testing of a rotor dynamics test rig configuration designed to simulate the actual engine environment. Critical rotor speeds are absent throughout the continuous operating speed range of 55,000 to 100,000 rpm, but two critical speeds will be encountered in the acceleration transient. These nominally are rigid body modes and can be routinely encountered without excessive bearing loads or vibration amplitude due to the dissipative influence present in the bearings. A third critical, which is primarily a bending mode, is well above the maximum operating speed.

4.11 Controls and Accessories

The AGT controls and accessories effort is comprised of five major areas of activity:

- o Systems analysis and integration
- o Fuel control system
- o Electrical accessories
- o Electronic control
- o Accessories

Systems analysis and integration primarily is an analytical effort involved with the design, analysis, and transient modeling of the control system. In addition to the controls, the transient modeling activity also includes representations of the engine and vehicle as a part of the fully integrated system. The transient model is an important and necessary analytical tool providing insight into performance and interaction of the controls and accessories, and the engine/vehicle system.

Systems analysis and integration activities also entail the integration of all elements of the controls and accessories hardware into a complete and fully operational system. The other areas of activity discussed herein, involve the analysis, design, and development of the various specified elements of the controls and accessories hardware. A simplified schematic overview of the AGT control system is shown in Figure 207.

4.11.1 Performance System Analysis

4.11.1.1 Model Description

The computer model is an analytical tool for designing control logic and evaluating various vehicle/powertrain transients. As a transient model, it includes dynamic simulation of the various sensors and actuators as well as inertias of the powertrain components. A simplified system block diagram is shown in Figure 208, with the major control elements enclosed in dashed lines.

4.11.1.1.1 Powertrain

Simulation of the powertrain may be described using the block diagram, starting with the engine map. Engine torque, airflow, turbine exit temperature, and compressor exit temperature are calculated from engine speed, IGV position, and turbine inlet temperature. Of the torque generated by the engine, a portion goes to accelerate the

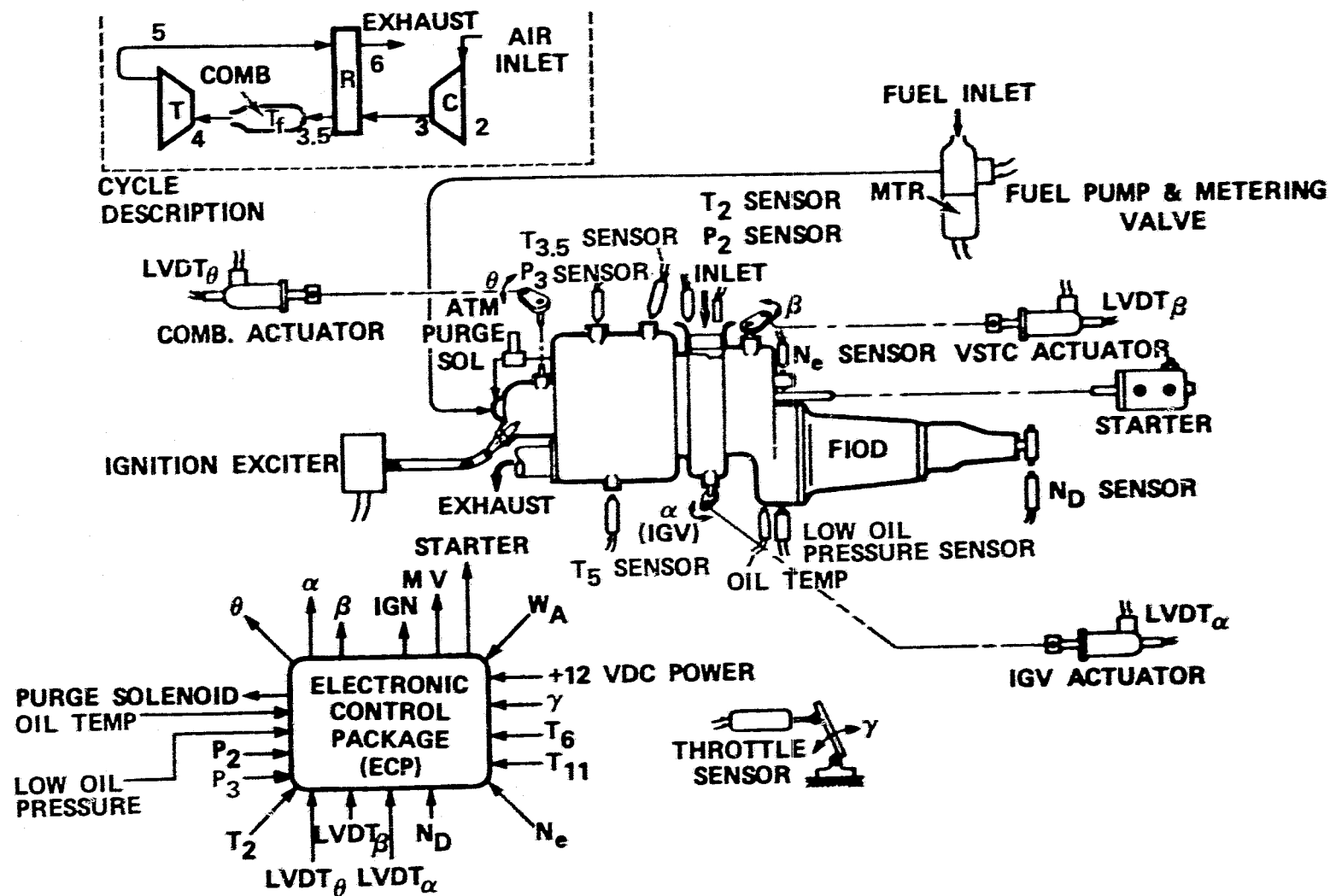


Figure 207. AGT Control System Schematic.

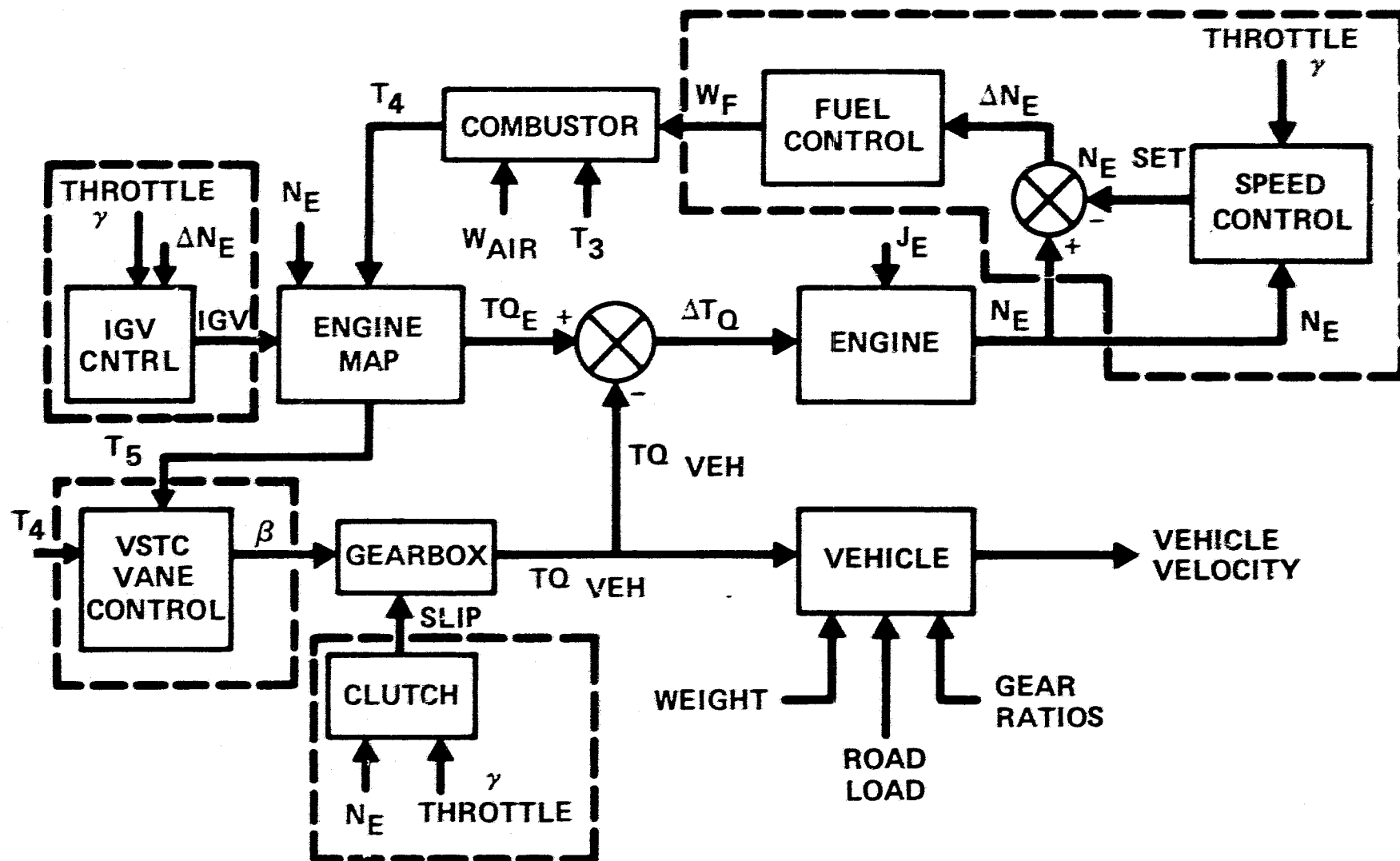


Figure 208. Transient Computer Model Block Diagram.

engine and the remainder goes to the wheels. The torque split between the engine and vehicle is controlled by the position of the variable stator in the torque converter (located in the gearbox). Engine speed is calculated based on the unbalanced torque on the engine rotor, and rotor inertia. Torque to the rear wheels is determined from the various gear ratios and powertrain efficiencies. This torque then is employed to obtain vehicle velocity considering grade, aerodynamic drag, and rolling friction.

Air temperature entering the combustor (exiting the regenerator) is calculated, assuming steady state operation, based on airflow rate through the regenerator, compressor discharge temperature (T_3), and turbine exhaust temperature (T_5). For transient operation, the combustor inlet temperature is calculated by applying a first order lag to the previously determined steady state value. Turbine inlet temperature (T_4) then is obtained using an empirical model of the combustor. Inputs to this model are combustor inlet air temperature, air flow rate, and fuel flow rate. Fuel flow rate (W_f) and IGV position are set by the controls and described below.

4.11.1.1.2 Controls

Basically, the only powertrain control exerted by the driver is the throttle. This directly affects commanded engine speed and IGV position. All other controls are automatic. The major controls are described below.

IGV Control - At steady state, IGV position is exclusively a function of throttle position, as stated above. However, during transient operation, the position is biased by engine speed error (i.e., commanded minus actual speed).

VSTC Vane Position (β) Control - Torque converter vanes are controlled by engine temperature, either turbine inlet temperature (T_4) or turbine exhaust temperature (T_5), depending on which is highest with respect to the set point. As engine temperature rises, the vanes start to close, effecting a decoupling between the engine and vehicle; this tends to unload the engine.

The torque converter vanes also are controlled integrally to keep engine temperature up to the set point during steady state operation for maximum efficiency.

Fuel Metering Control - The commanded engine speed is set by throttle position. To avoid abrupt changes in fuel flow during a transient, the governor speed setting gradually moves toward the commanded speed at a rate that is a function of speed error (i.e., commanded minus actual speed). The rate at which the governor moves is biased by ambient pressure to provide good driveability at altitudes. At steady state, actual engine speed is

equal to commanded speed, and the governor speed setting is sufficiently above actual speed to provide the required fuel flow.

If the engine temperature exceeds the overtemperature limit, fuel is reduced via a proportional control. This control is effective when the VSTC vanes reach the closed limit.

4.11.1.2 Typical Acceleration Transient

Figure 209 shows various calculated vehicle parameters as a function of time for a typical 0 to 50 mph transient. At 0.1 seconds throttle position is increased from 0 degrees (idle) to 60 degrees (maximum). As velocity approaches 50 mph, a simulated driver gradually adjusts throttle setting to a steady state setting.

During the initial portion of the transient, a rapid increase in fuel flow causes high engine temperatures. During this initial period, VSTC vane angle is at the closed limit and fuel is limited by the overtemperature control. Because the VSTC vanes are fully closed, engine power is split in favor of the engine. Thus, engine speed quickly rises while vehicle velocity lags.

As engine speed rises temperature falls, allowing the VSTC vanes to start opening, allowing more power to go to the vehicle. Therefore, vehicle acceleration increases at about 2 seconds.

Up to 9 seconds, the throttle is at maximum setting, which causes the IGVs to fully open, for maximum power.

With the present transmission shift logic, shifts occur when the VSTC vanes reach a maximum open (maximum coupling) position. The shifts are noted on the Figure 209 plot.

4.11.1.3 Summary

The basic computer model including powertrain simulation and associated controls, now is complete and available for use as an analytical tool for further control development. Gains for the basic control have been defined to provide stable operation. This control logic, developed with the model, has been implemented in the AGT wiring diagram (Figure 210).

It is anticipated that the model will be a valuable tool in future development of a number of control components. This will require considerable refinement both in the control and powertrain simulation logic.

ORIGINAL PAGE IS
OF POOR QUALITY

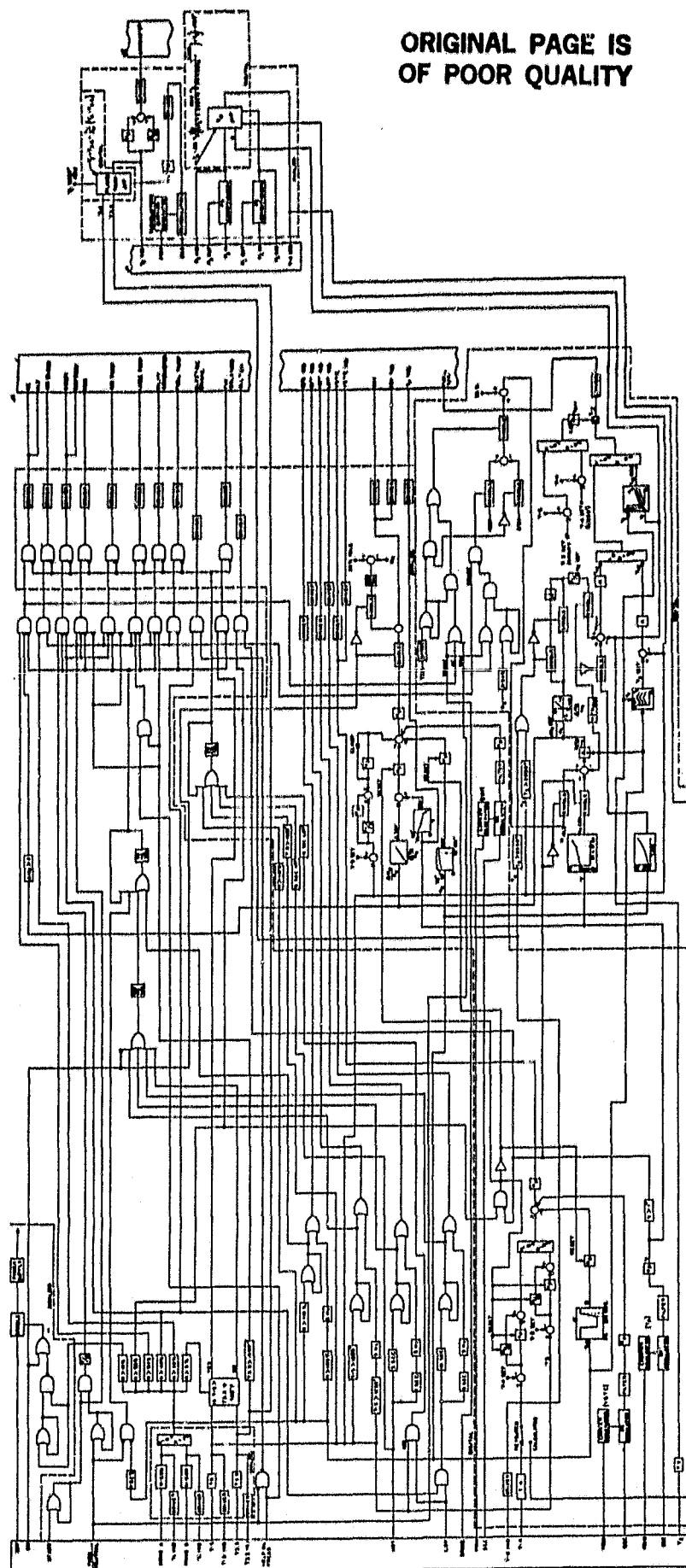


Figure 210. AGT101 Wiring Diagram (Logic).

4.11.2 Fuel System

The fuel delivery system for the AGT must operate over a broad range of fuel pressures and delivery rates. As a result of these constraints, specifically the ability to meter fuel at rates as low as one pound per hour, most of the more conventional gas turbine fuel systems were eliminated from consideration. After careful review of various approaches, two primary concepts were selected for further investigation. (1) These concepts are based on a variable admission, three piston pump as shown in Figure 211 and (2) Bosch automotive fuel injectors depicted in Figure 212.

4.11.2.1 Piston Pump

Initial testing of the variable admission pump demonstrated excessive leakage, resulting in higher minimum flows than desired (see Figure 213). Two changes were made to improve low flow capability and linearity; accurately held metering edges and a close valve clearance of 0.00015 inch diametral. Test results for this configuration, Figure 214, show the significant improvement in low flow control.

The automotive fuel injector system (Figure 212) is being considered as an alternative to the piston pump concept. Testing of the injector system revealed some problems with linearity of the output fuel flow. Based on recommendation of Bosch, an injector from the 1980 Lincoln was tried. The pulse effect of fuel pressure was evaluated and determined to be on the order of 25 percent of the signal. This is felt to be unacceptable and would require evaluation of pulsators to provide a more constant pressure, in the event that the fuel injector concept were implemented.

4.11.3 Electrical Accessories

Drawings are complete for the thermocouple probes used for T_4 , $T_{3.5}$ and T_5 . Thermocouple design consists of an enclosed lead, reduced-tip Platinell II probes. Each thermocouple assembly consists of two staggered junctions connected in parallel and averaged internally. The output leads are chromel-alumel connected in parallel with a right and left probe assembly to obtain a circumferential average included with the short radial average. The mounting configuration is a nut and ferrule design to allow variable immersion during the development effort. A unique sealing technique will be incorporated to minimize leakage.

The hydraulic system low oil pressure (LOP) switch incorporates a "shunt disc" actuating element. A resistive element temperature sensor is specified to monitor high oil temperature and ambient air temperature.

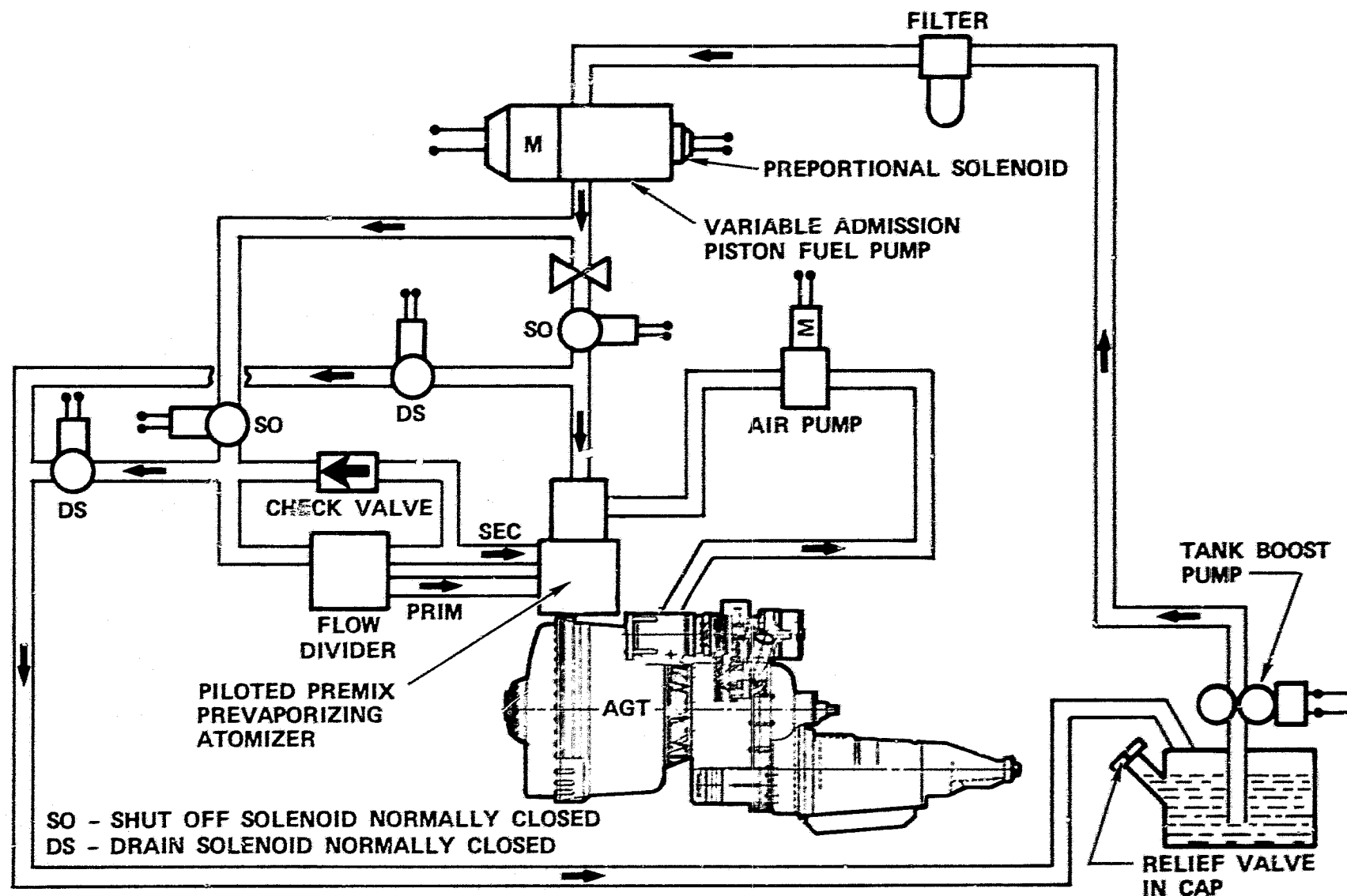


Figure 211. AGT101 Fuel Management System.

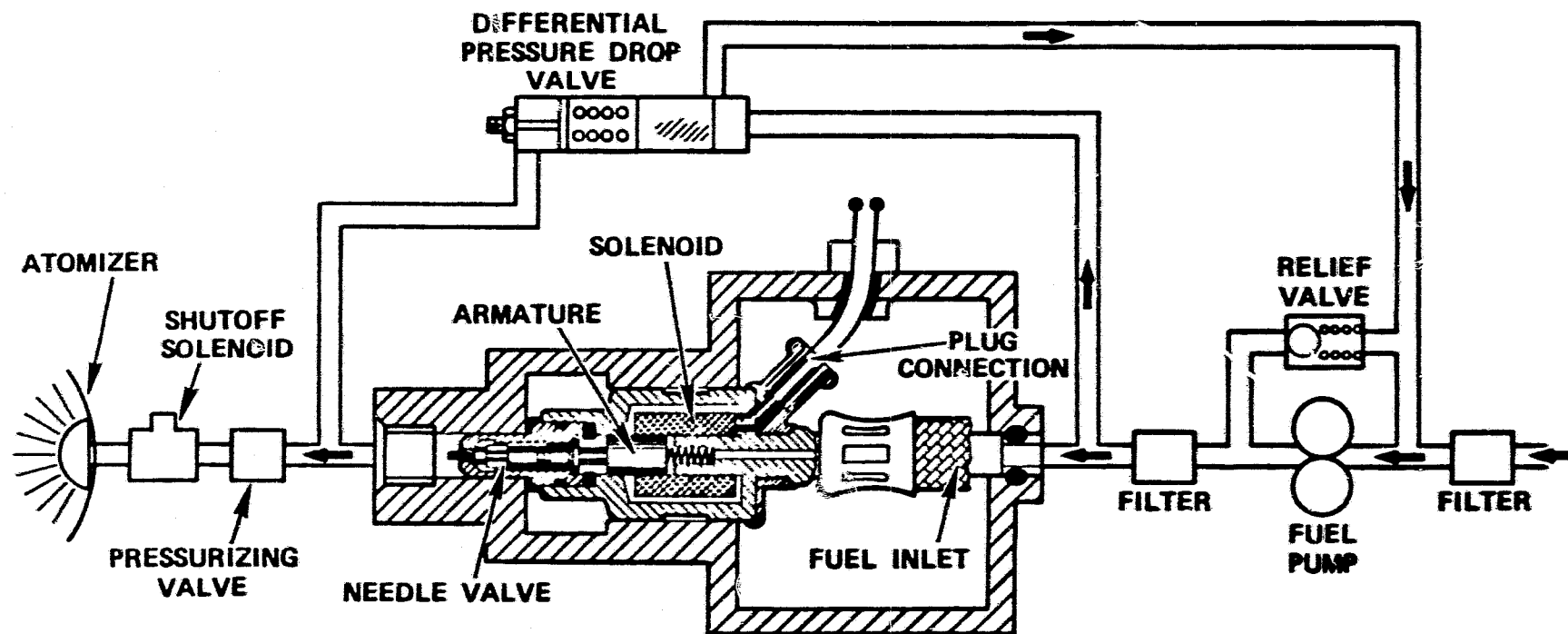


Figure 212. Automotive Based Injector Fuel Delivery System.

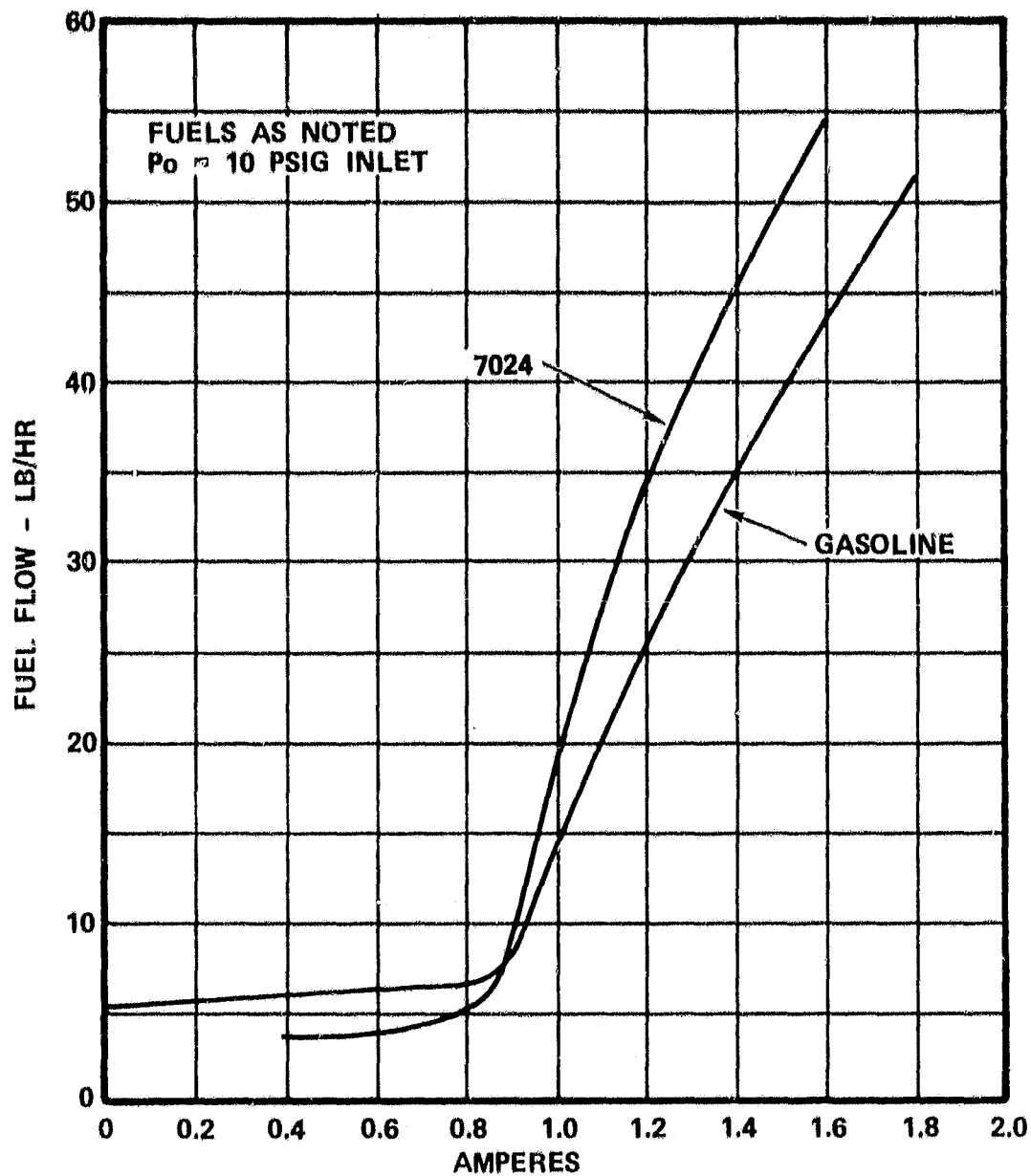


Figure 213. 3-Piston Pump, Variable Admission.

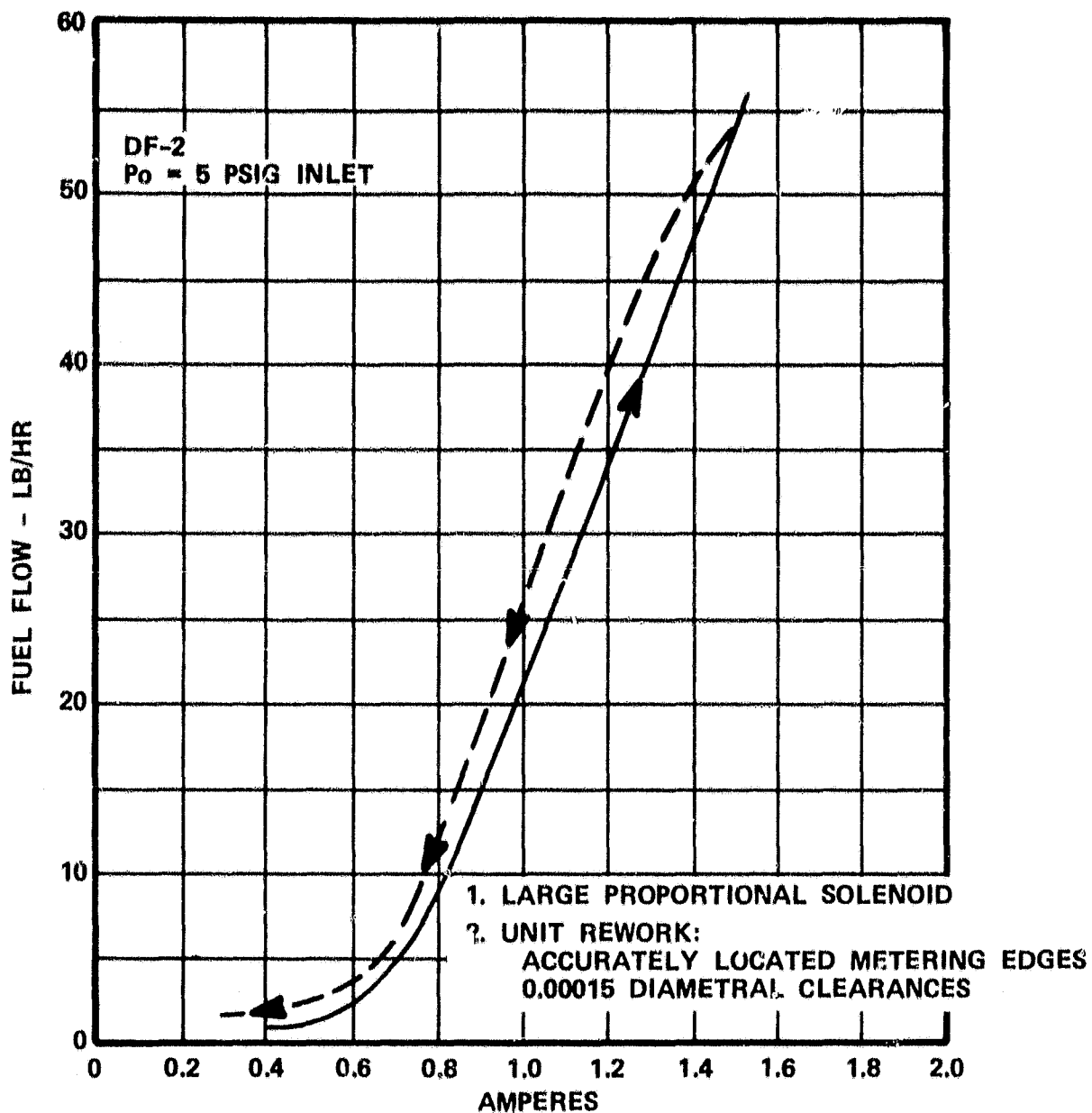


Figure 214. 3-Piston FPD Pump With Variable Admission.

VSTC position sensor LVDT has been selected and the mounting approach established. Development release rough draft drawings are in design for formal drawing activity. As shown in Figure 215, the actuating rod from the VSTC is supported on an antifriction ball bearing on the rotating input shaft. The lever is fixed at the LVDT connecting link via an anti-rotational constraint and is allowed to travel in an axial direction only with respect to the LVDT core.

Engine speed sensing currently is under further evaluation to establish alternate sensor locations. The transducer type will be the eddy current killed oscillator (ECKO) type using a miniature 0.070 inch diameter probe tip supplied by Bently Nevada Corp. Preliminary bench tests were successfully completed using AiResearch Phoenix design excitation and signal conditioning electronics. After evaluation of the alternate sensor locations and mounting constraints, a high speed test rig will be fabricated to further evaluate and finalize the mechanical and electrical design of the ECKO transducer system.

A 3-way solenoid design, for the hydraulically actuated gearbox clutch and brake assemblies has been established. The design consists of existing solenoid subassemblies to be integrated into a low-volume, low-weight package. The actuators are a direct-acting ball and seat configuration using a low current draw (1.5 amperes maximum) continuous operating coil.

Connectors selected for development use are readily available, in-house, MIL-C-5015 threaded connectors with 16-gauge contacts. The ECU and the APU harness will have two connectors with 48 and 36 contacts for a total of 84 terminations. The 48- and 36-contact connectors are common with all boom cables and interface connectors in the test cells. The APU harness wiring will utilize standard 18-gauge stranded wiring throughout.

Provisions have been made on the pilot combustor to accept a high tension igniter plug to be used with either a high energy or low energy high tension ignition system, or alternately accept a low tension plug for use with a low energy system. The final ignition system and minimum energy requirements will be evaluated during engine development.

Efforts are continuing in the evaluation and selection of a viable battery and charging system compatible with automotive requirements.

4.11.4 Electronic Control Unit (ECU)

Four hybrid (analog/digital) ECUs are being designed and fabricated for use in the early engine development program.

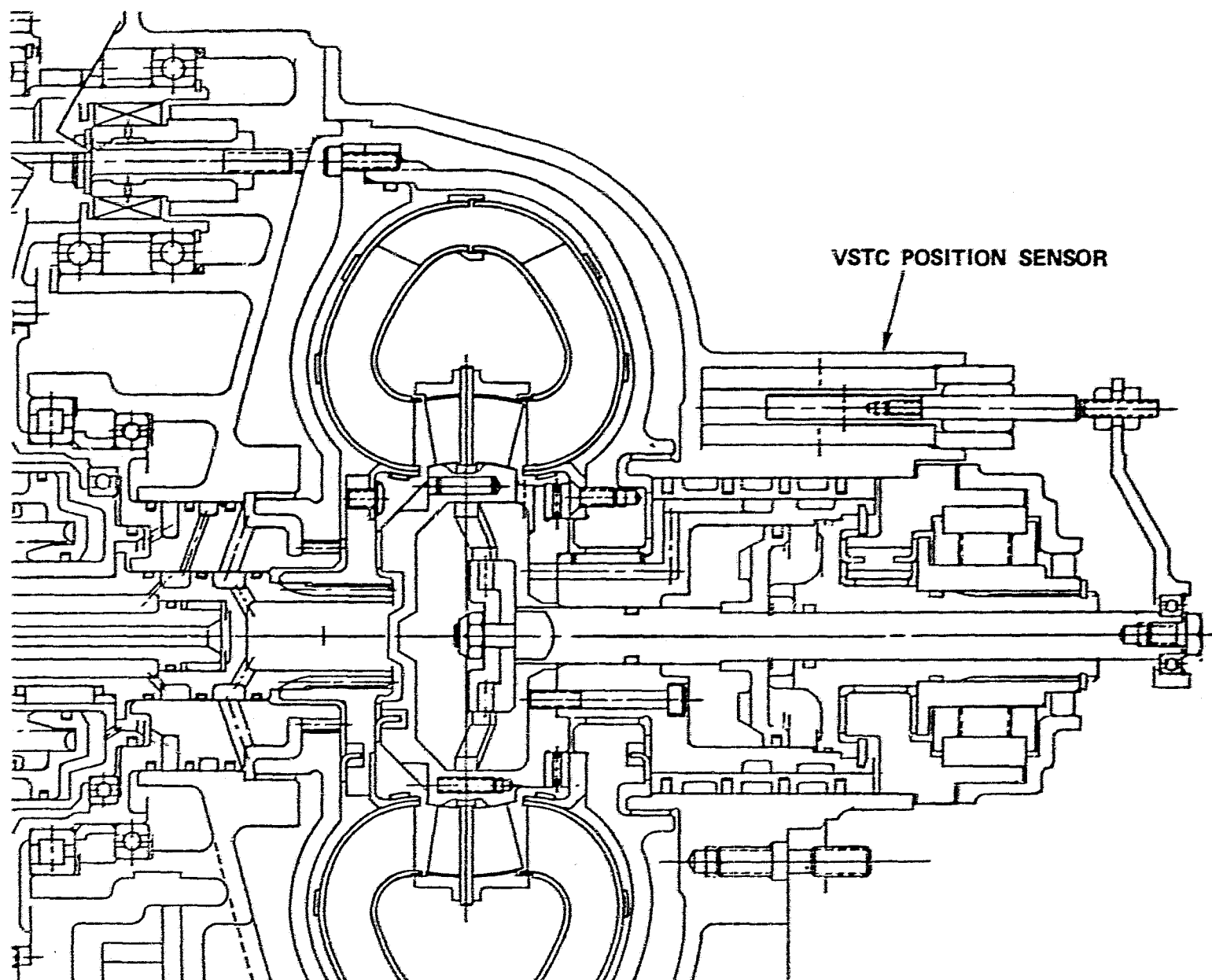


Figure 215. Variable Stator Torque Converter, Actuator, and LVDT Position Sensor.

The digital hardware design, based on use of the Intel 8086 microprocessor, has been completed and all parts have been ordered. Software development has been outlined and preliminary timing estimates for the temperature calculation loops have been performed.

The present control configuration includes 10 analog and 2 digital control boards. Design and fabrication of the control is approximately 50 percent complete. Design of an ECU tester is 90 percent complete.

4.11.5 Mechanical Accessories

Engine accessory performance data were analyzed and various components were selected. Initial accessory array layouts were made, however, final determination will not be accomplished until the engine/vehicle configuration is finalized.

The transient analysis required for actuator sizing was completed for the VSTC and VIGV.

The VIGV and variable geometry combustor actuators were ordered. Components have been selected for the VSTC actuator.

The performance requirements of the hydraulic and lubrication circuit have been determined and the circuit design was completed (see Figure 216).

Most hydraulic circuit components are incorporated into a hydraulic module. The module and miscellaneous component designs were started.

Analysis and sizing of the gearbox clutch and brake assemblies were completed.

[illegible]

319

PRECEDING PAGE BLANK NOT FILMED

APPENDIX I

FORD MOTOR COMPANY

Advanced Gas Turbine (AGT) Powertrain Program
First Semi-Annual Technical
Progress Report

Task 2.3 - Ceramic Rotor - Ford

Introduction

The development of monolithic rotors in pressureless sintered Si_3N_4 was selected as the primary approach for this program. Two approaches were proposed: a primary approach on sintered reaction bonded Si_3N_4 and a back-up approach on the more conventional sintering of Si_3N_4 powder. There are a number of advantages to the SRBSN approach as compared to sintered Si_3N_4 :

- o The starting material, primarily silicon, is readily available
- o RBSN fabrication technology, slip casting and injection molding, is highly developed
- o The high green densities of RBSN (72 to 85 percent) result in sintering shrinkages of only 5 to 10 percent

With either approach, prior to producing a complete turbine rotor, various developmental tasks must first be successfully completed. These tasks include a material development effort combined with a fabrication development effort leading to the production of a simulated turbine rotor. This bladeless rotor must then be successfully spin tested before work on the actual rotor begins; allowing for iterative material and/or fabrication development on a relatively simple shape which can then be evaluated in a manner representative of the final application. During this development-testing loop, experience can be gained which increases the probability of successfully producing a fully bladed monolithic turbine rotor of good quality and having requisite properties.

Sintered Reaction Bonded Si_3N_4

As the principal approach, a fabrication method was selected which consisted of the sintering to near full density of reaction bonded silicon nitride shapes; the method involves adding the sintering aid to silicon particles, followed by shaping and nitridation. The resultant Si_3N_4 article can then be pressureless sintered to form a high density sintered Si_3N_4 (SRBSN) component.

Prior to this program, it was demonstrated that the SRBSN approach can be used to fabricate complex shaped turbine components(1). An example of this technology, a turbine stator, is presented in Figure 217.

The fabrication method chosen for the monolithic turbine rotor is a Ford-patented fugitive wax slip casting technique(2,3). This

ORIGINAL PAGE
BLACK AND WHITE PHOTOGRAPH

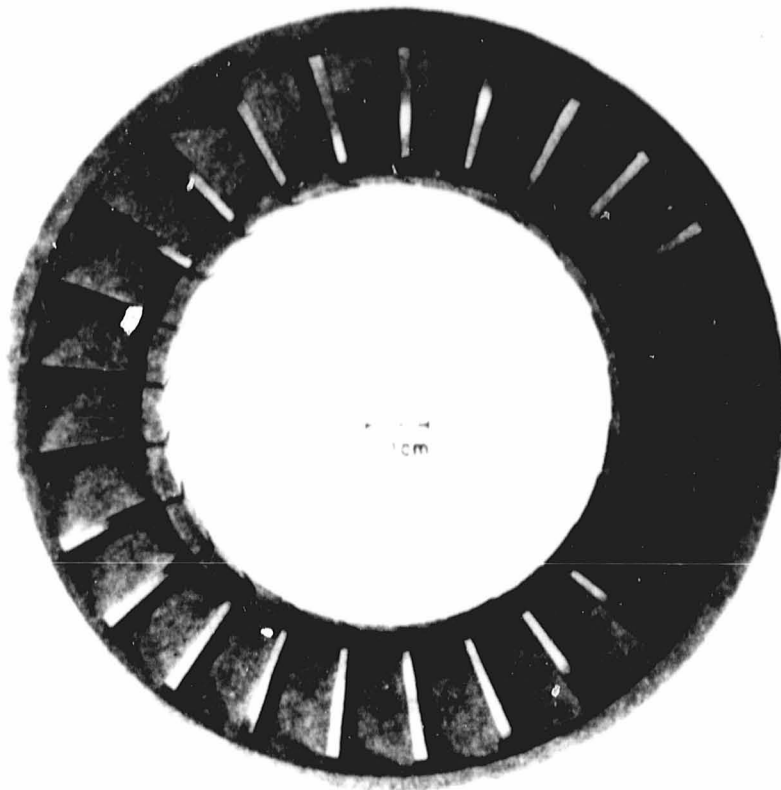


Figure 217. Sintered Reaction Bonded Turbine Stator
(98 Percent T.D.).

process has been used to successfully fabricate a number of complex ceramic turbine components.

Initial SRBSN material selection is the $\text{Si}_3\text{N}_4\text{-Y}_2\text{O}_3$ system. A potentially severe oxidization problem has been observed in this system at low temperatures (600 to 1000°C) (4,5). However, this problem has recently been found to be due to contamination by W, WC or carbon (6,7). If these impurities are absent, the $\text{Si}_3\text{N}_4\text{-Y}_2\text{O}_3$ system becomes very attractive (8,9). This system has inherently good high temperature strength properties, with only minimal loss in strength to over 1200°C. It has excellent creep resistance. It also has been demonstrated that this system can be pressureless sintered to high densities. The following sections will discuss material and process development on the SRBSN approach during this reporting period.

Slip Development

The slip development effort consisted of determining the effect of a number of slip variables (pH, viscosity, specific gravity, particle size and particle size distribution) on the casting time and, more importantly, the green density of the casting. All the slips used in this study were in the Si-8 percent $\text{Y}_2\text{O}_3\text{-H}_2\text{O}$ system varying the water content to change the slip's specific gravity. The castings were made in a 1 1/4" x 1 1/4" x 6 in plaster mold. The wet weights of the castings were used as an indication of the green density, and consequently the nitrided density. Figure 218 shows how the nitrided density of a casting varies with its wet weight.

Slips were produced using two different particle size distributions of silicon (Figure 219). The 253 distribution is coarser and broader than the 245 distribution.

The slips were allowed to mix for a period exceeding seven days to insure chemical stability (3,10).

The results of the slip casting experiment can be summarized as follows:

- o Viscosity of a slip can be controlled by the pH of the slip. Increasing pH results in decreasing slip viscosity at each specific gravity level which was evaluated (Figure 220)
- o The higher the viscosity, the lower the casting time (higher casting rate) (Figure 221)
- o For a given slip viscosity, the higher the specific gravity, the higher the green density (wet weight) (Figure 222)
- o The higher the viscosity, the lower the cast density

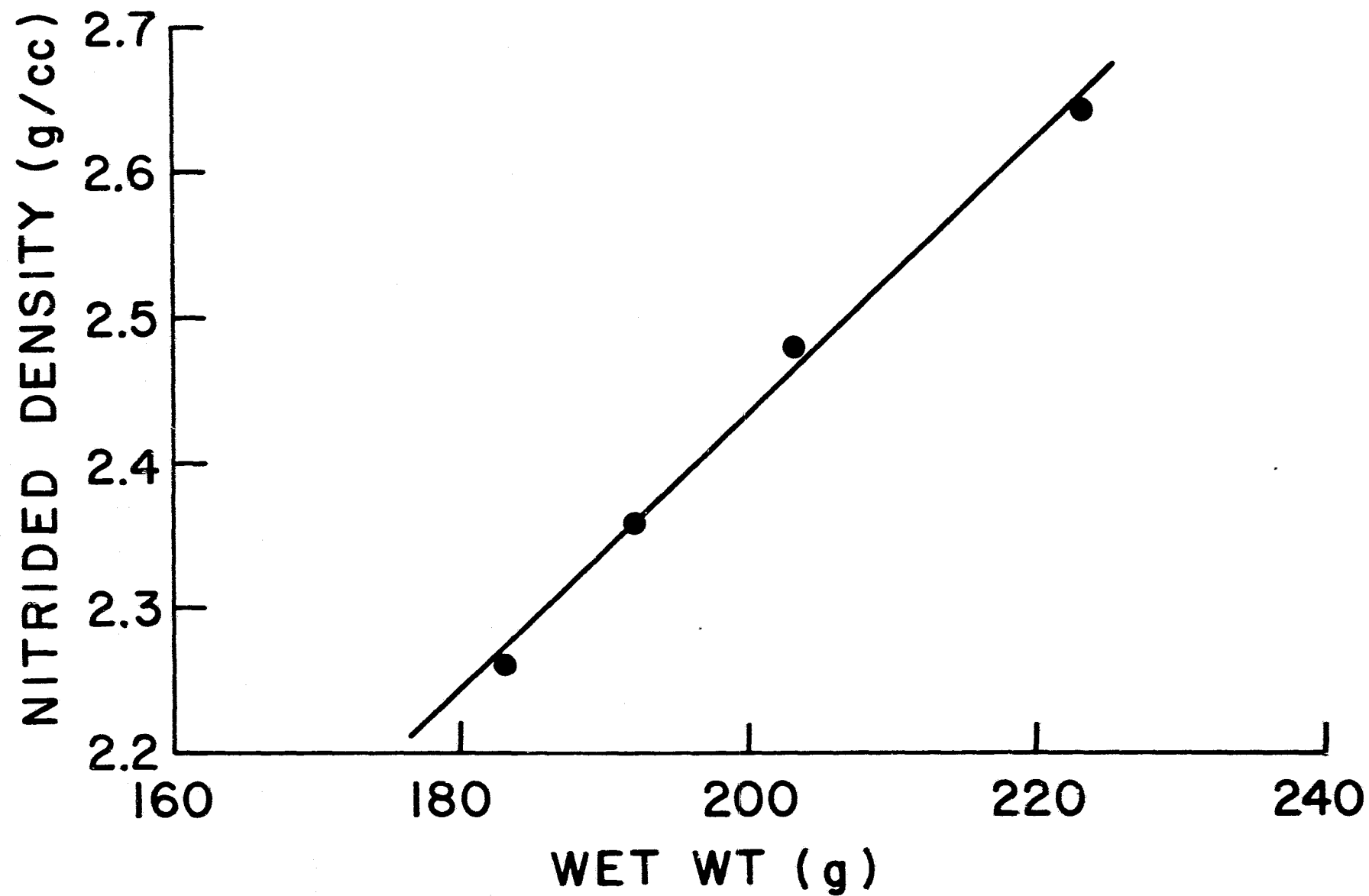


Figure 218. Wet Weight Vs Nitrided Density of a Cast Test Sample, Composition 8 Percent Y_2O_3 - 92% Silicon

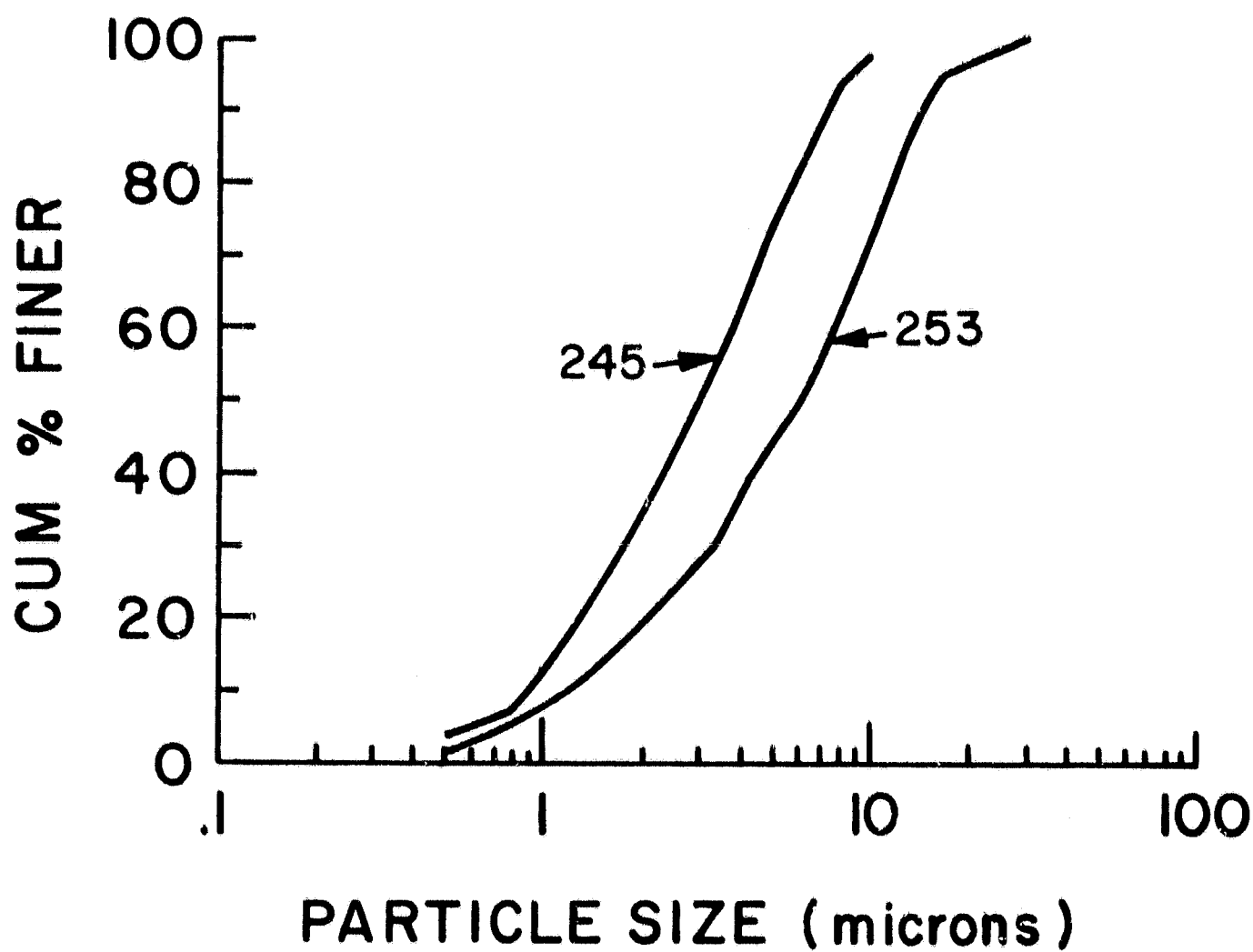


Figure 219. Silicon Particle Size Distribution Used to Make Slips 245 and 253.

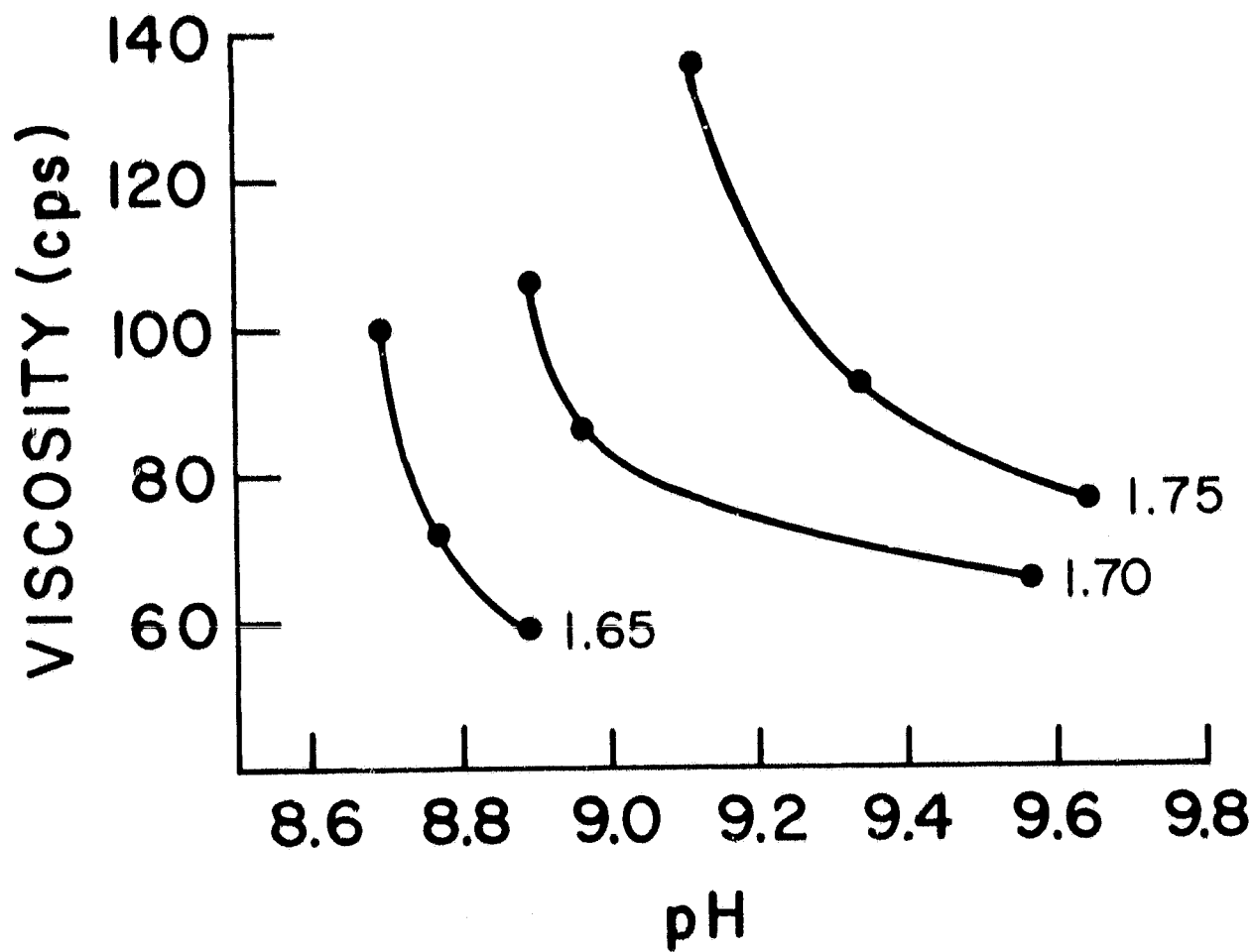


Figure 220. Viscosity as a Function of pH and Specific Gravity for Slip 253.

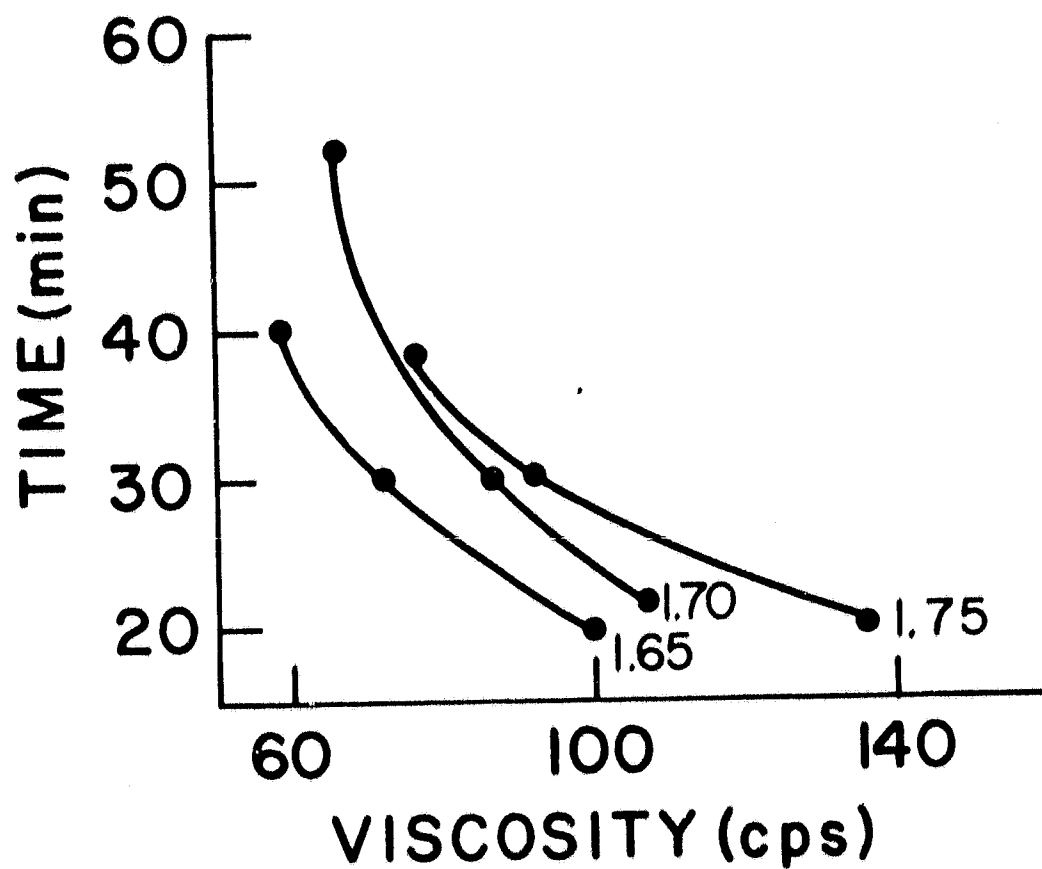


Figure 221. Casting Time of Test Samples 1 x 1 x 6 Inches Long as a Function of Viscosity and Specific Gravity

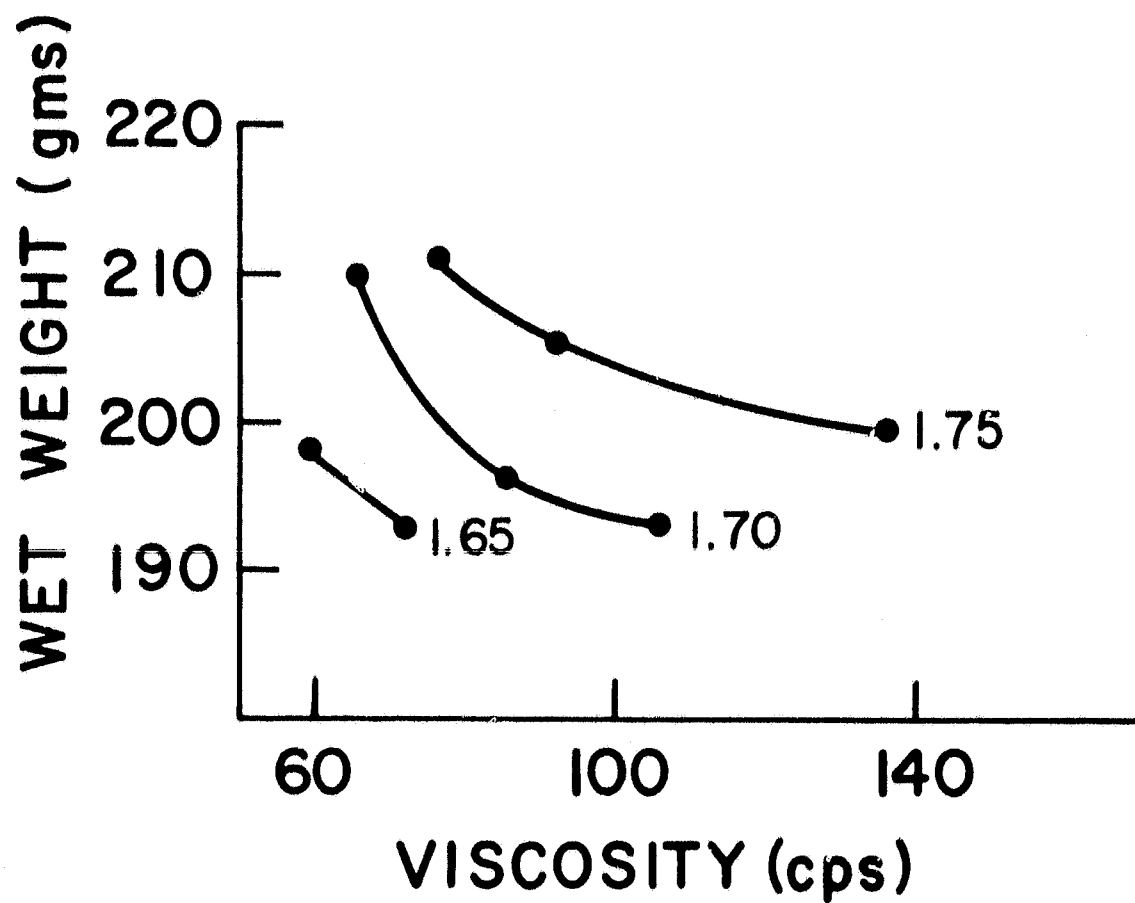


Figure 222. Wet Weight of Test Samples 1 x 1 x 6 Inches Long as a Function of Viscosity and Specific Gravity for Slip 253.

These generalized results were found to be independent of particle size or particle size distributions. It is expected that the size and shape of the particle size distribution will have some effect on the green density of the castings. From particle packing considerations, the material with the broadest particle size distribution curve should result in the highest density casting. This was shown to be true at least for the low specific gravity (1.65 g/cc) (Figure 223). However at the higher specific gravity (1.70 g/cc), no difference in wet weights were observed.

The work performed thus far has shown that slips in the Si-8% Y₂O₃ system do behave in a predictable and reproducible manner.

Slip Cast Fabrication Development

Concurrent with the slip development effort was a slip cast fabrication development program to produce the simulated rotor. The patented method⁽²⁾ which is to be used to produce this component is a modified fugitive wax slip casting technique. This technique is expected to be adapted to the fabrication of fully bladed rotors in the future. This technique, as applied to this component, is shown pictorially in Figures 224 and 225. The process begins with the fabrication of a positive model of the desired part (Figure 224A), from which the wax molds will be made (Figure 224B). In this case, the positive model of the top portion of the simulated rotor was machined from aluminum. The wax mold is made from a water insoluble/organic solvent soluble wax, and is formed by the repeated dipping of the metal model into liquid wax. The bottom portion of the simulated rotor is cast directly in a plaster mold (Figure 225C). The casting assembly is shown in Figure 225D. The wax mold (top portion of simulated rotor) is set in the machined formed plaster mold (bottom portion of simulated rotor) and filled with slip. The plaster draws the water out of the slip, resulting in a unidirectional casting starting from the bottom. Casting times of 2 to 6 hours are typically required (depending on slip parameters) to cast the part. After the casting has solidified, the wax mold is removed by dissolving in an appropriate solvent. Figure 225E shows a green casting.

After controlled drying at room temperature, the parts are nitrided. A completed "as nitrided" simulated rotor is shown in Figure 225F.

Initially many problems were encountered during casting; the two most severe were cracking of the castings and bubbles forming on the part surface during the casting operation.

Development is underway to achieve density control such that castings can be fully nitrided (refer to nitriding section). Castings with reproducible density have been made, but this density is slightly higher than desired for complete nitridation. Work in the next period

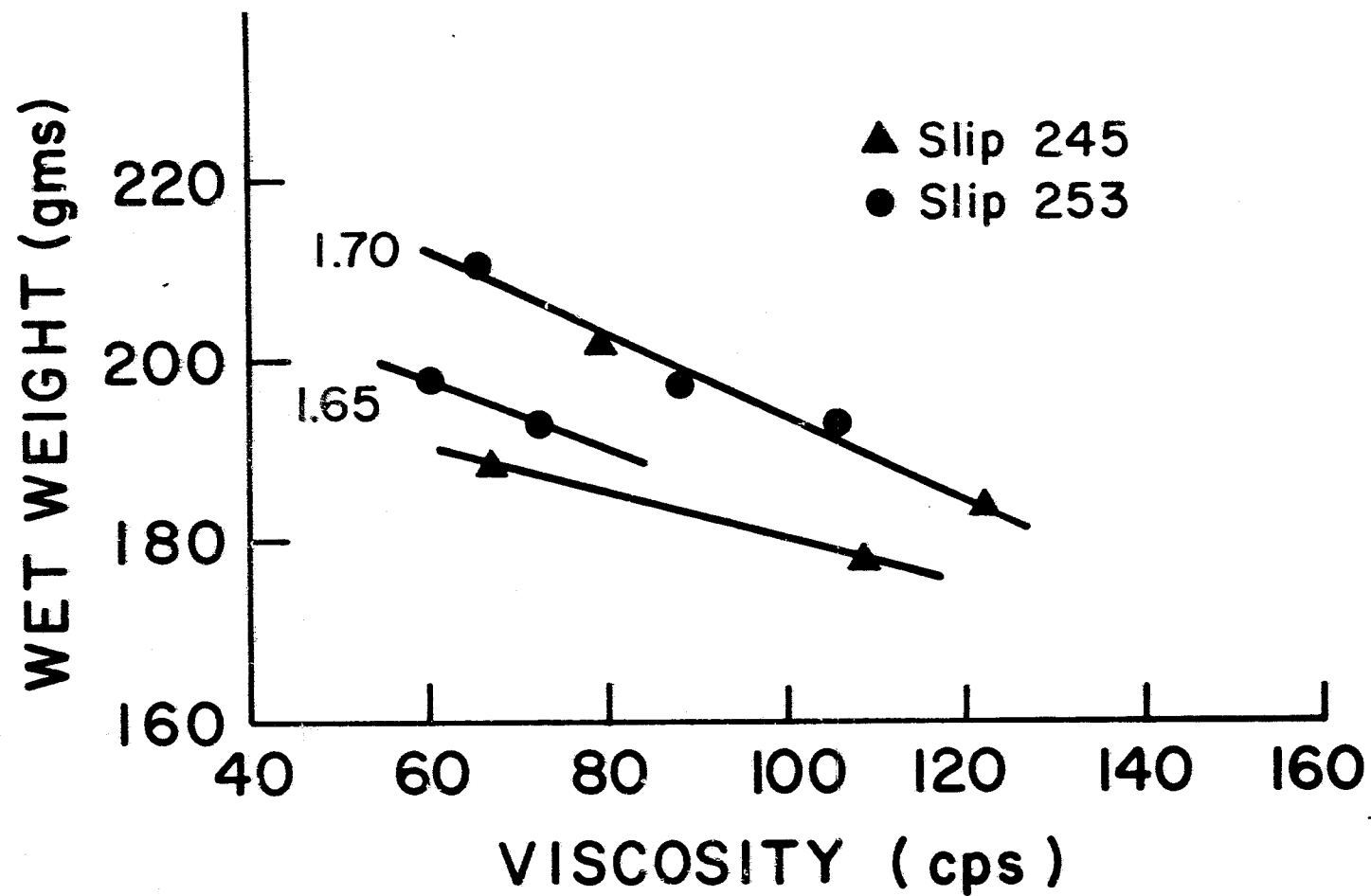
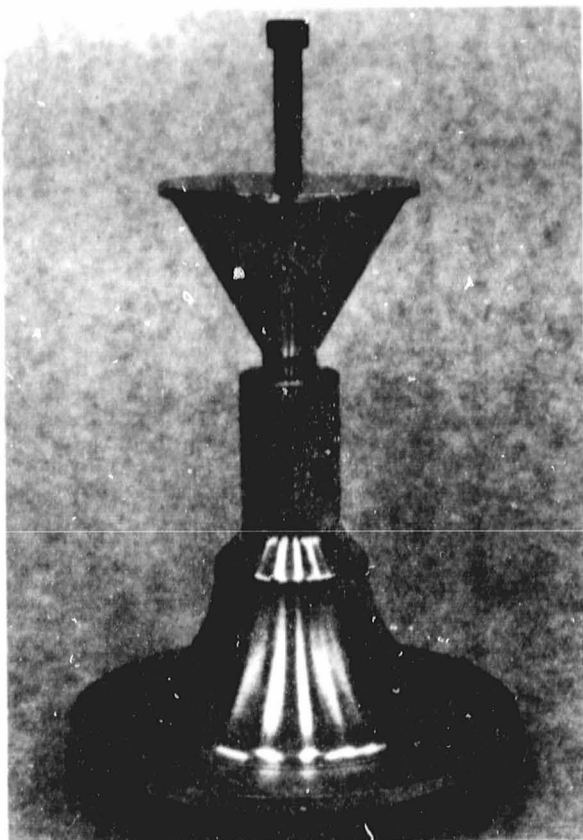


Figure 223. Wet Weight of Test Samples 1 x 1 x 6 Inches Long as a Function of Viscosity and Specific Gravity for Slips 245 and 153.

ORIGINAL PAGE
BLACK AND WHITE PHOTOGRAPH



A. METAL MASTER PATTERN
FOR A PORTION OF THE
ROTOR



B. WAX MOLD CAST AROUND
METAL PATTERN

Figure 224. Modified Fugitive Wax Mold Slip Casting Process
for the Simulated Rotor.



C. PLASTER MOLD FOR CASTING THE
REMAINING PORTION OF THE ROTOR

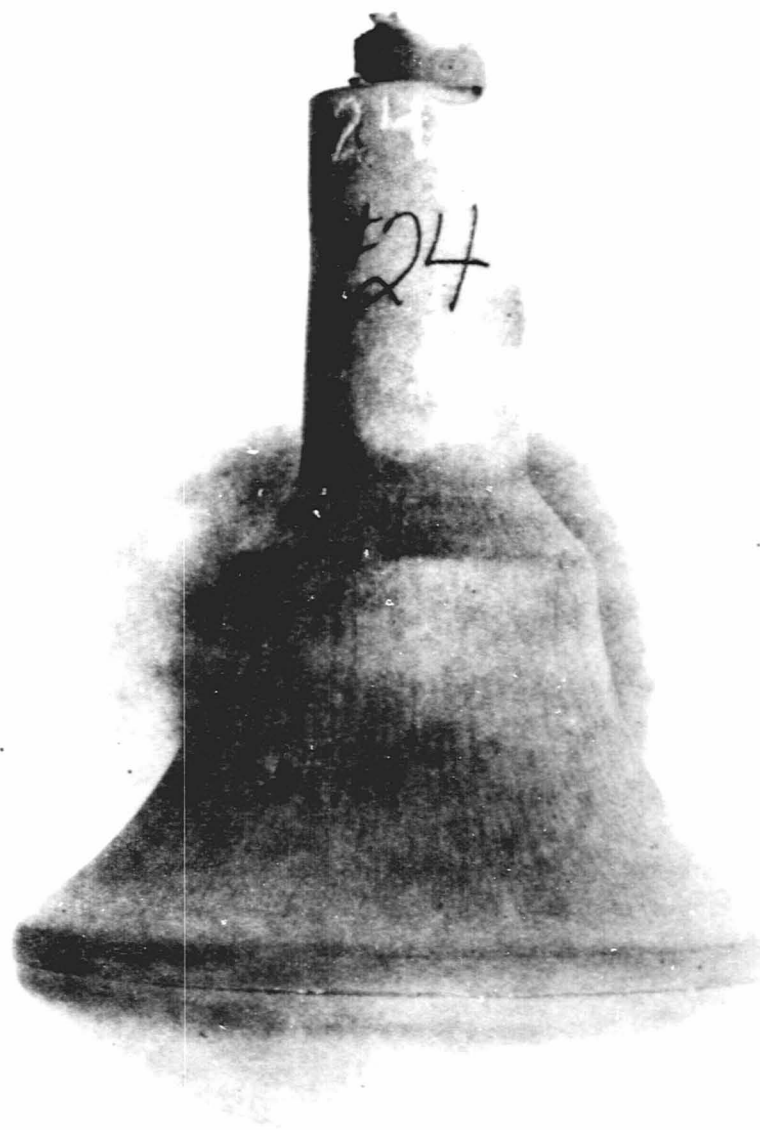


D. WAX MOLD MOUNTED
ON PLASTER MOLD

Figure 225. Modified Fugitive Wax Mold Slip Casting Process
for the Simulated Rotor.



E. AS-CAST SIMULATED
ROTOR



F. AS-CAST NITRIDED
SIMULATED ROTOR

ORIGINAL PAGE IS
OF POOR QUALITY

Figure 225. Modified Fugitive Wax Mold Slip Casting Process
for the Simulated Rotor.

also will be aimed at eliminating internal casting flaws of the type shown in the bottom portion of rotor No. 26 (Figure 230B).

Nitriding Development

Previous programs (11,12,13) have examined the nitriding of silicon in great detail with a number of unique methods being developed such as the nitrogen demand nitriding cycle and the use of mixed gas nitriding atmospheres. Most of this work has, however, been performed using relatively thin cross-section (1/2 inch) silicon compacts. The simulated rotor, however, has a maximum section thickness of 3.6 inches and required nitrogen penetration of 1.2 inches from all surfaces to completely nitride the center section. The direction of nitriding development has been to examine the effect of known nitriding techniques on the nitriding behavior of simulated rotors. The major variable is the density of the rotor. It has been assumed that if the rotor density is systematically decreased, a density level will be reached which allows for complete nitridation.

Two cycles were employed for the nitriding studies. The cycle descriptions are given in Table 29. The principal difference between these cycles is the cycle time, the time-temperature profile (Figure 226) and the nitriding rate.

A number of simulated rotors of various densities have been nitrided using these two cycles. The significant data are summarized in Table 30 with the results itemized as follows:

- o For a given density and nitriding cycle, an Argon sintered rotor will not nitride as well as one that has not been Argon sintered. (Compare rotor 5 with 6 and 17).
- o If the density is low enough, Argon sintered rotors will completely nitride (rotor 12).
- o For constant density and processing, the full demand cycle will nitride rotors more completely (compare rotor 20 with 6 and 26 with 17).
- o Rotors with densities of 2.35 g/cc can be completely nitrided with the full demand cycle (rotor 26)

Various other observations can be made about the overall quality of the rotors produced thus far. Various rotors have had large cracks extending well into the interior. The material appears to nitride due in part to nitrogen diffusion along these cracks (example - rotor No. 5).

Various other rotors appear to have smaller cracks throughout the interior, such as cracks in rotors, 12 and 20, axial or radial cracks

TABLE 29. NITRIDING CYCLE DESCRIPTION

	Modified Demand (Ref 13)	Full Demand (Ref 13, 14)
Furnace Hood	45000 g	45000 g
Backfill Gas	4% H ₂ /N ₂	4% H ₂ /N ₂
Nitriding Gas	2% He/N ₂	2% He/N ₂
Time-Temperature Input Program	Figure 226	Figure 226
Time-Temperature Profile	Figure 227	Figure 227
Cycle Time	170 hours	174 hours
Nitriding Rate	9.9 2/hr	17.2 2/hr
Atmosphere at the End	4% H ₂ 20-25% He/N ₂	4% H ₂ /20-25% He/N ₂

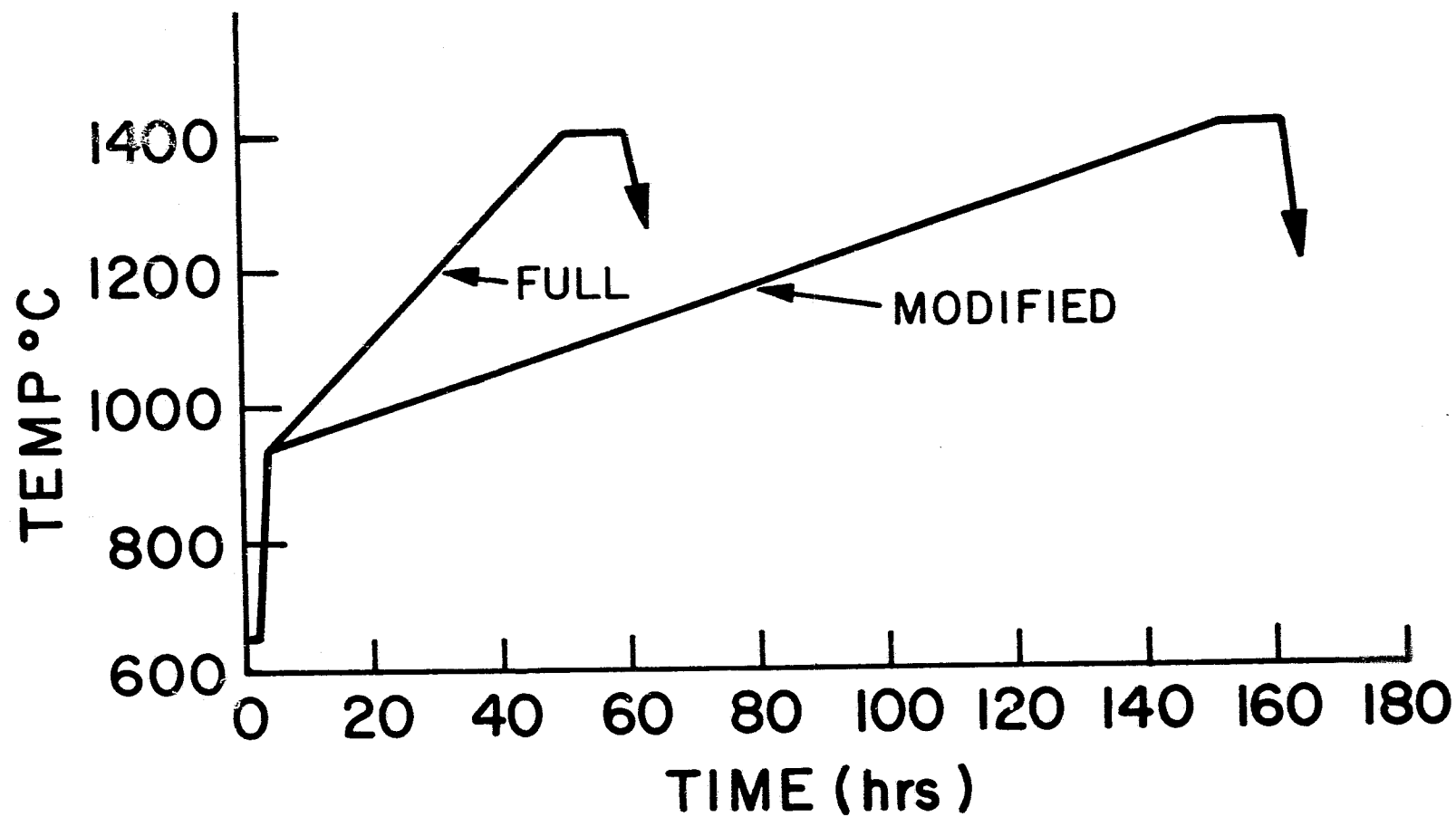


Figure 226. Time-Temperature Input Program for the Full and Modified Nitrogen Demand Cycles.

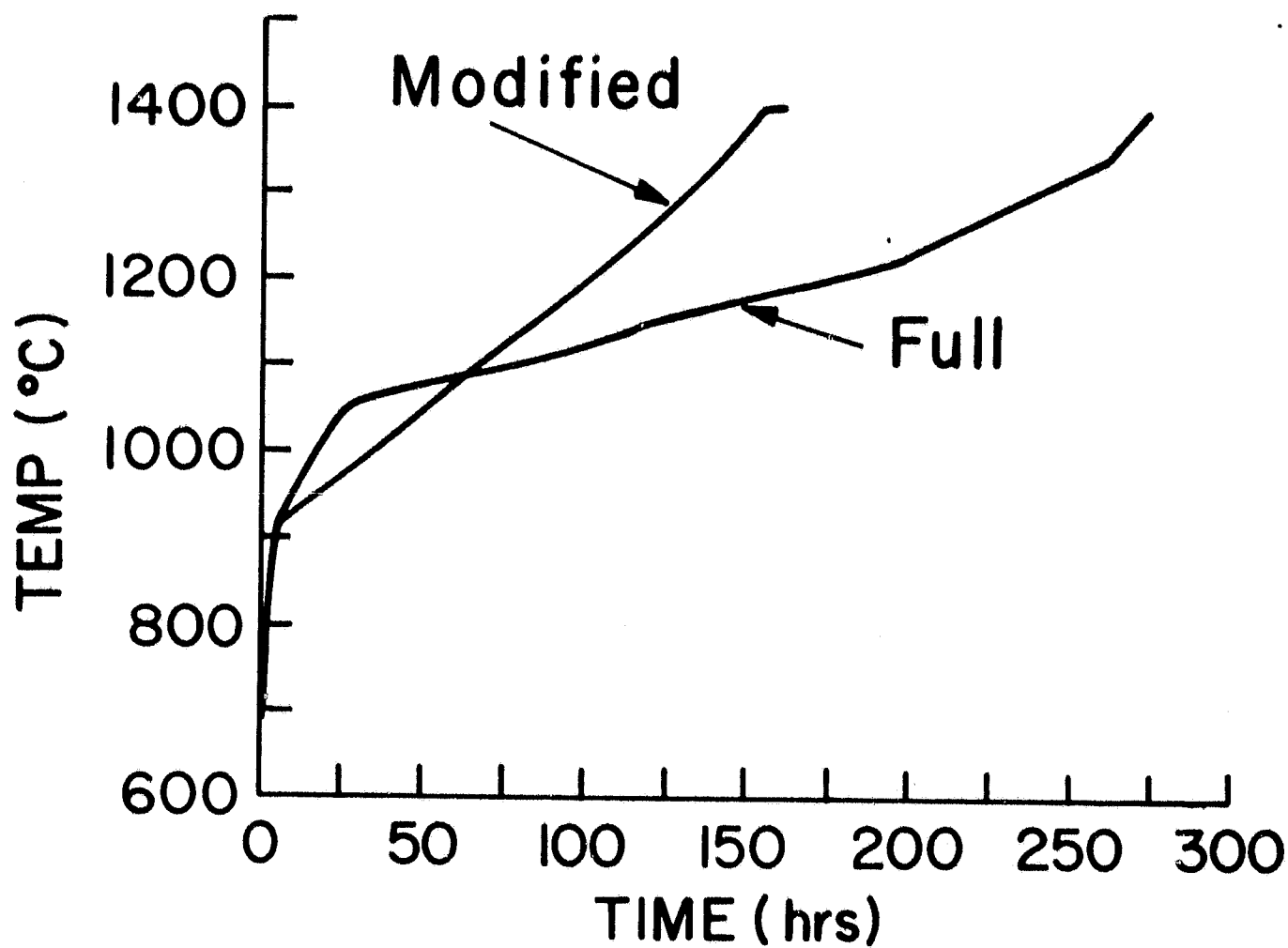


Figure 227. Actual Time-Temperature Profiles for the Modified and Full Nitrogen Demand Cycles.

TABLE 30. SUMMARY OF NITRIDING DATA FOR SIMULATED ROTORS

Rotor No	Cycle Type	Nitrided Density	Composition	Argon Sintered	Nitriding Rating	Pertinent Figure
5	Modified Demand	2.35g/cc	8% Y_2O_3	Yes	Poor	Figure 228
6	Modified Demand	2.41g/cc	8% Y_2O_3	No	Fair	Figure 228
12	Modified Demand	2.16g/cc	8% Y_2O_3	Yes	Good	Figure 229
17	Modified Demand	2.33g/cc	8% Y_2O_3	No	Fair, good	Figure 229
20	Full Demand	2.43g/cc	8% Y_2O_3	No	Fair, good	Figure 230
26	Full Demand	2.35g/cc	8% Y_2O_3	No	Good	Figure 230

ORIGINAL PAGE
BLACK AND WHITE PHOTOGRAPH

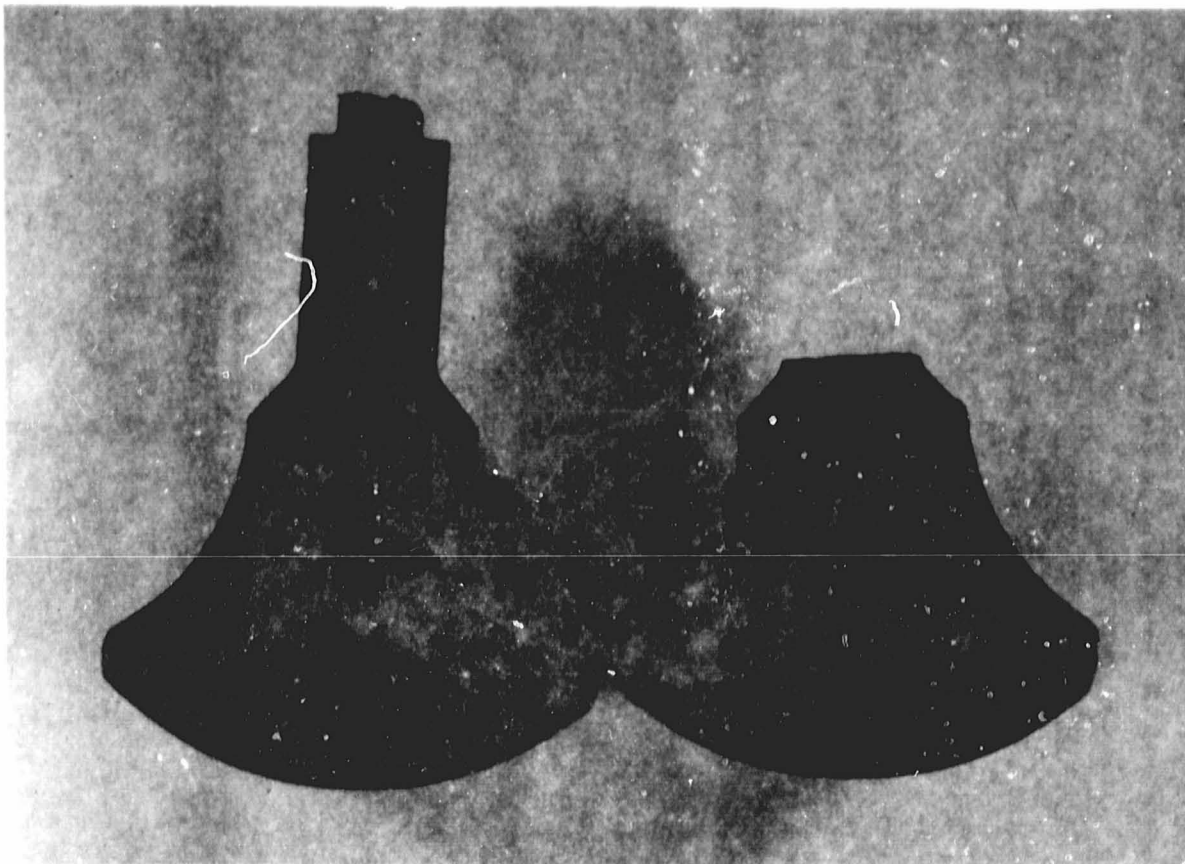


Figure 228. Sectioned Simulated Rotors Numbers 5 and 6.

ORIGINAL PAGE
BLACK AND WHITE PHOTOGRAPH

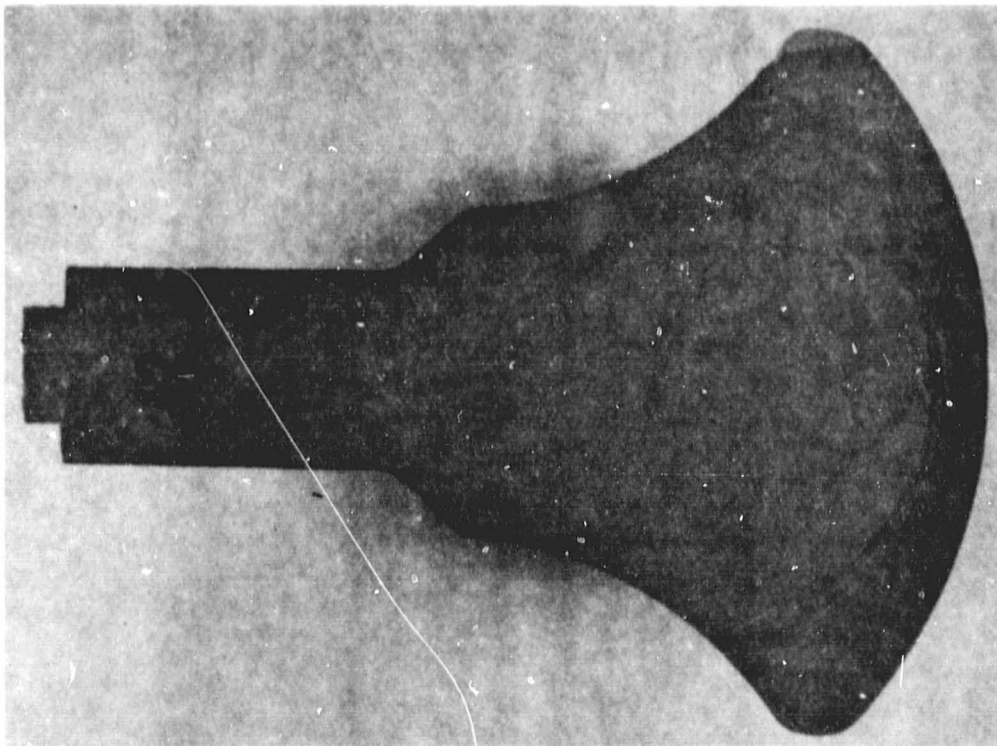
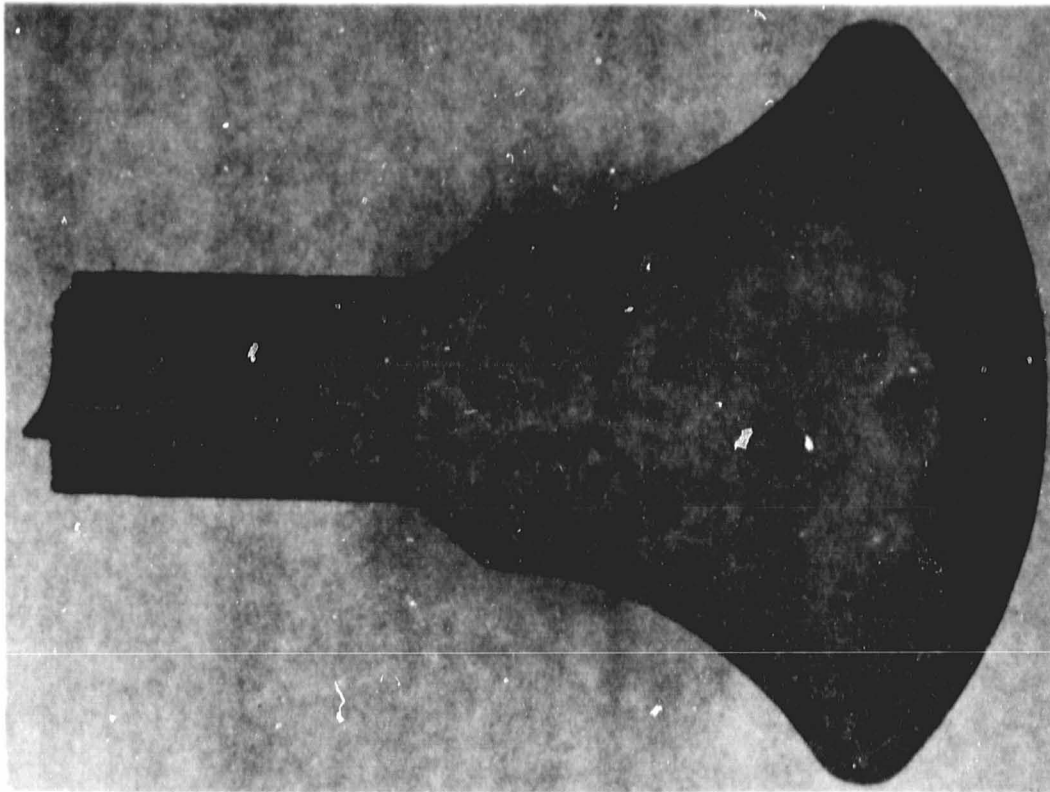
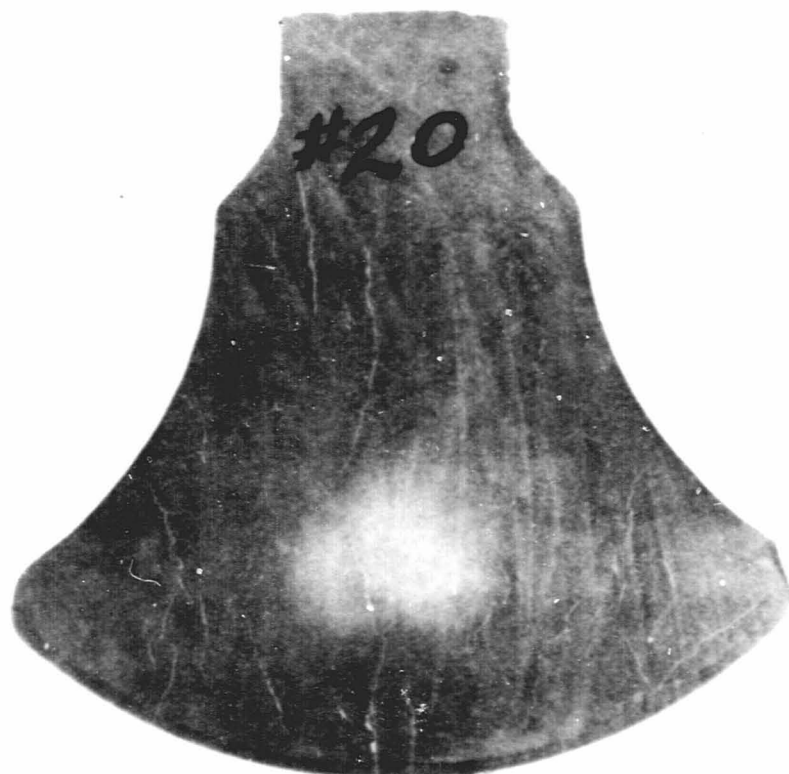
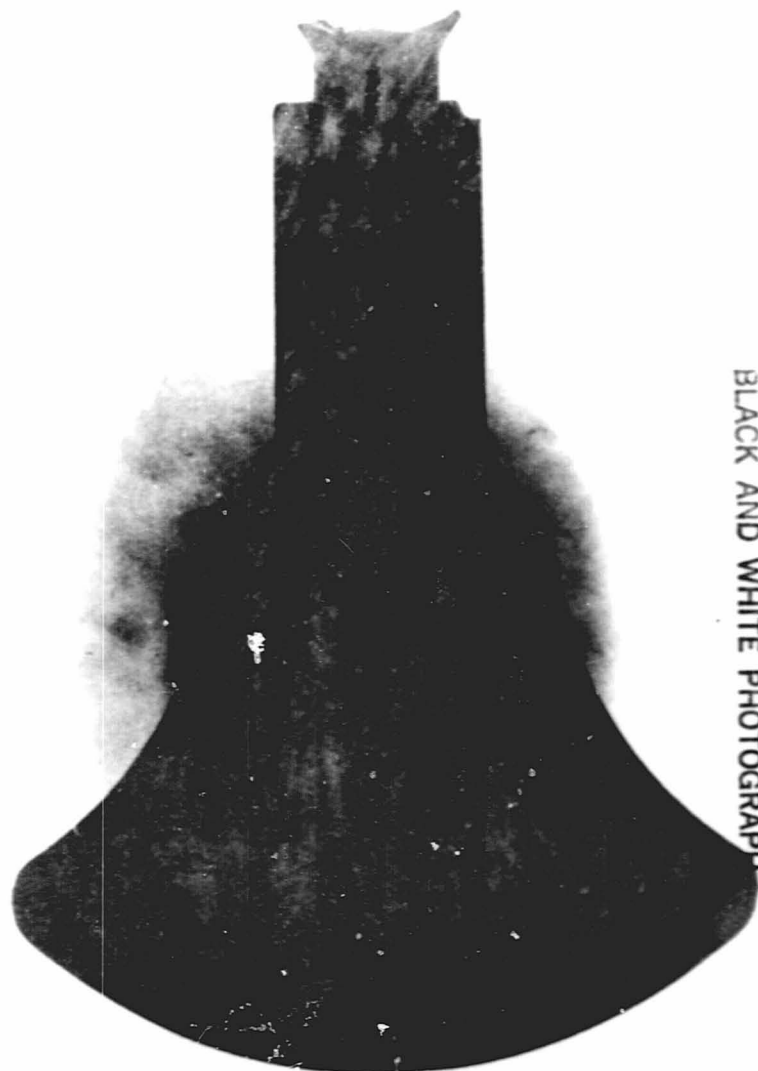


Figure 229. Sectioned Simulated Rotors Numbers 12 and 17.



A.



B.

ORIGINAL PAGE
BLACK AND WHITE PHOTOGRAPH

Figure 230. Sectioned Simulated Rotors Numbers 20 and 26.

in rotor 12 and 26. Rotor 12 and 26 also have pronounced radial casting planes across the interior. These problems will be attacked during the next reporting period.

The rotors which were not completely nitrided had regions of dark material in their interior (example Rotors 5 and 6). Micrographs of these dark regions show a large amount of unreacted silicon and porosity relative to a "normal" region (Figure 231A and B). Rotors also exhibit a "lighter gray" region in the center of the interior (example Rotor 20). These regions were examined and were found to be completely nitrided, but contain high porosity (Figure 231C and D).

Work performed thus far has shown that simulated rotors with a density of 2.35 g/cc can be completely nitrided. Rotors of this density will continue to be produced. In addition, work in the next report period will evaluate the effect of a nitriding aid (Fe_2O_3) on the nitriding behavior of rotors of various densities.

Sintering

The sintering approach taken during this reporting period was the sintering of reaction bonded Si_3N_4 (SRBSN) under a nitrogen overpressure (1,14,15). The work during this period is an extension of these previous studies.

As explained in the introduction, the primary advantage of the SRBSN approach is low sintering shrinkages. This amount of shrinkage is always dependent on the density of the "green" compact (in this case, the nitrided density of the compact). Figure 232 shows the shrinkage curve for the 8 percent Y_2O_3 -SRBSN system as a function of the nitrided density. Simulated rotors have been shown to be completely nitrided at a maximum density of 2.35 g/cc. Consequently, the expected shrinkage of these components should be 10 percent. The amount of shrinkage would change slightly with composition, because of changes in the theoretical density for the different Y_2O_3 - Si_3N_4 compositions as shown in Figure 233.

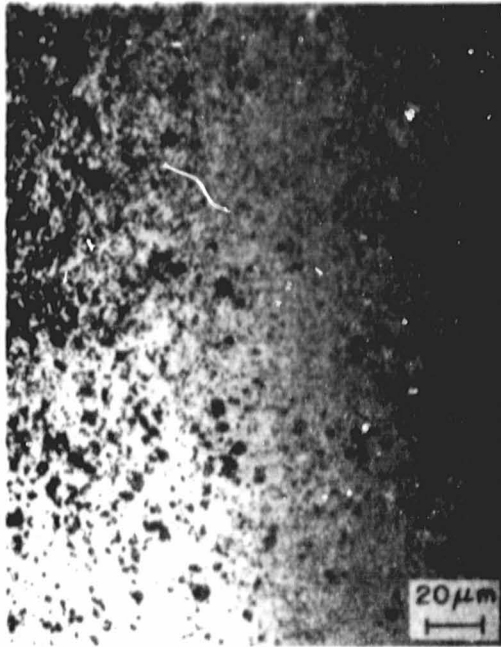
The initial sintering runs were made using an 8 percent $\text{Y}_2\text{O}_3/\text{Si}_3\text{N}_4$ composition with a nitrogen overpressure in the furnace of 20 atmospheres. The temperature range of the runs was 1875 to 2000°C. The principal variable in these runs was the nitrided density of the test coupons.

The results from these 20 atmosphere runs are illustrated in Figure 234.

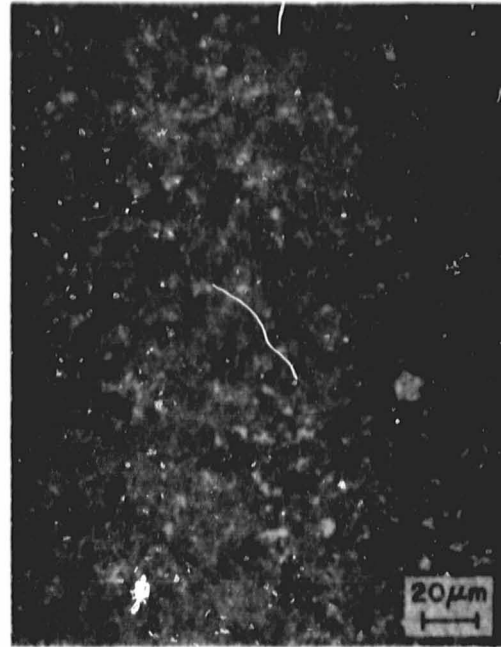
A number of observations can be made:

- o The green density of a compact affects the sintered density. For example, a compact with a low nitrided density will have

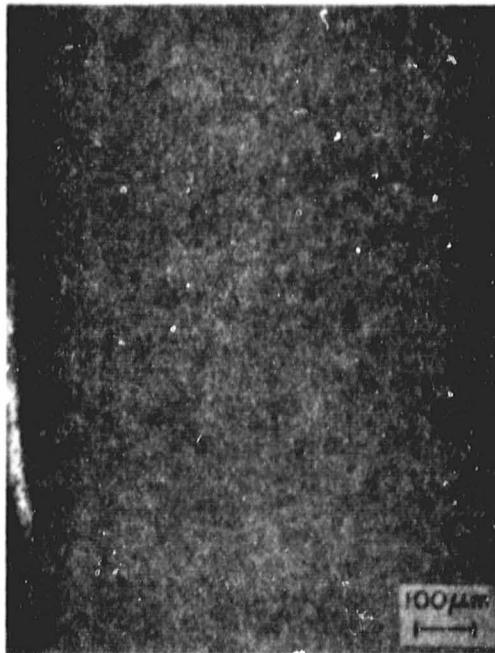
ORIGINAL PAGE
BLACK AND WHITE PHOTOGRAPH



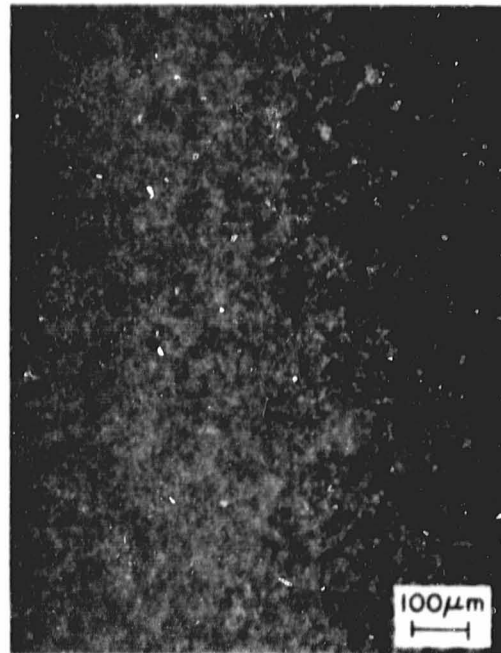
A. Nitrided Region of
Rotor Number 5



B. Incompletely Nitrided
Region (Dark Colored
Center Portion) of
Rotor Number 5



C. Nitrided Region of
Rotor Number 20



D. Center Light
Colored Region
of Rotor Number
20 Showing
Increased Porosity

Figure 231. Microstructure of Simulated Rotors (Polished Sections, Reflected Light).

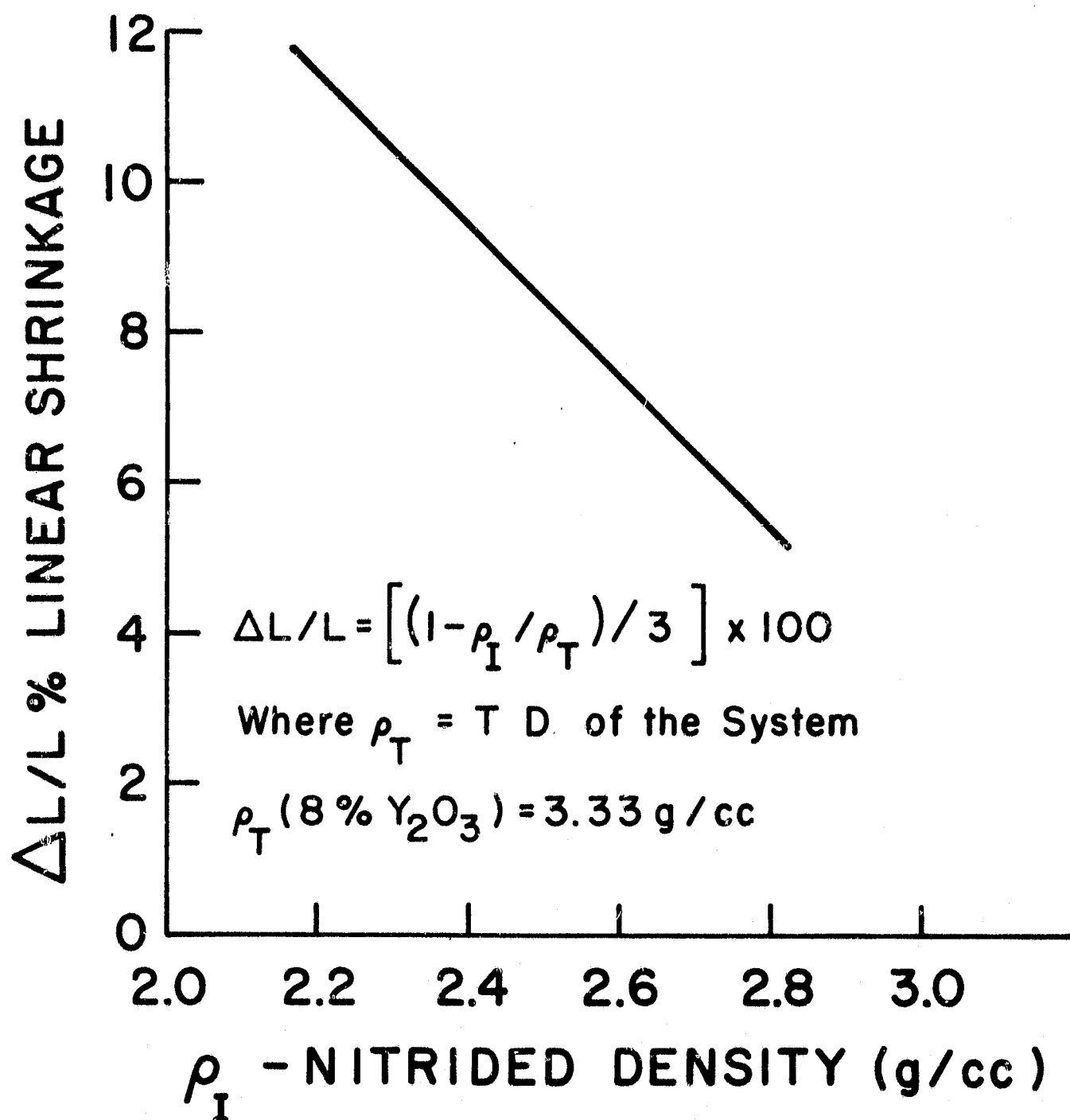


Figure 232. Linear Shrinkage of Sintered Reaction Bonded Silicon Nitride (8% Y_2O_3) as a Function of Nitrided Density.

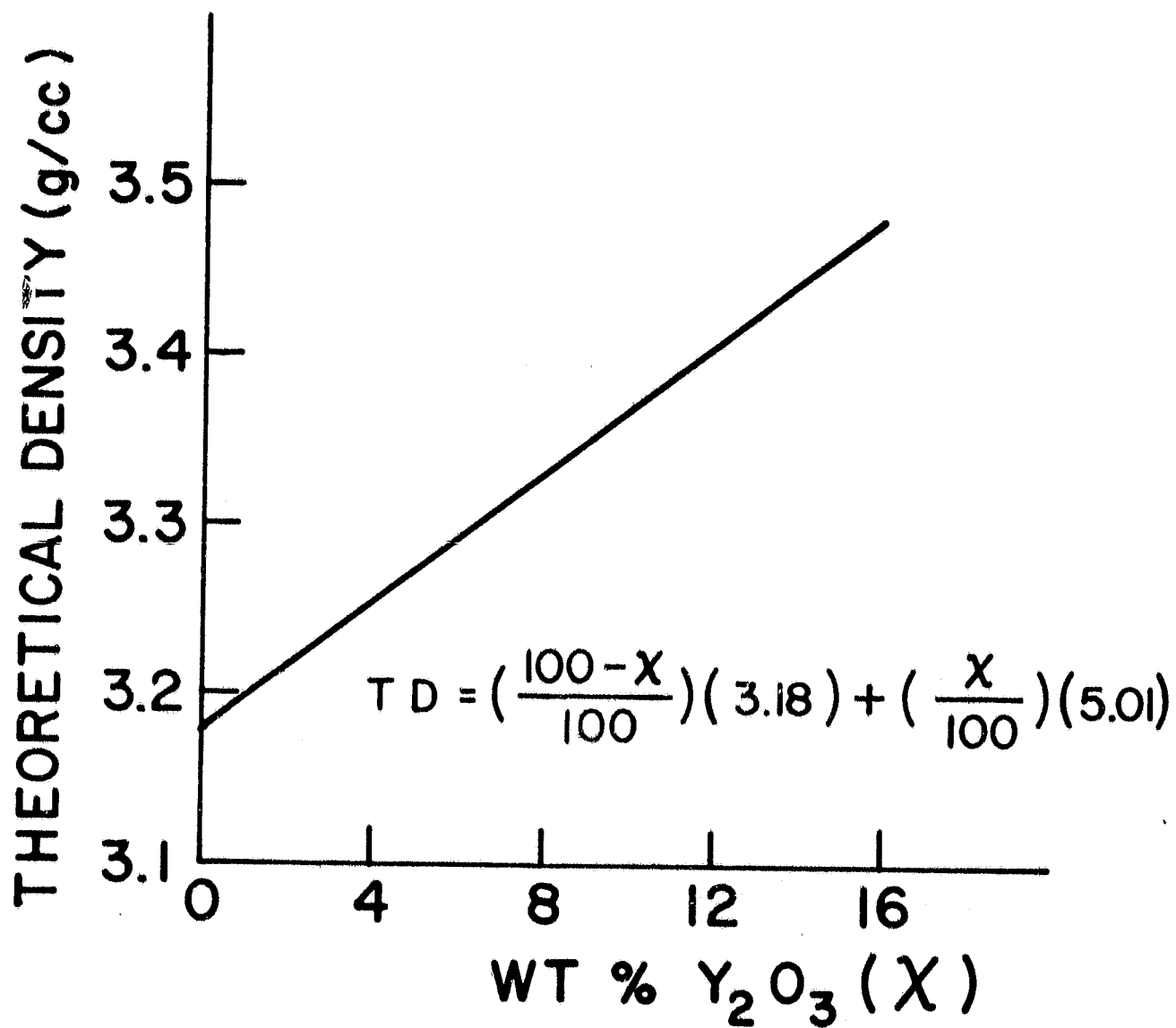


Figure 233. Calculated Theoretical Density of $Y_2O_3-Si_3N_4$.

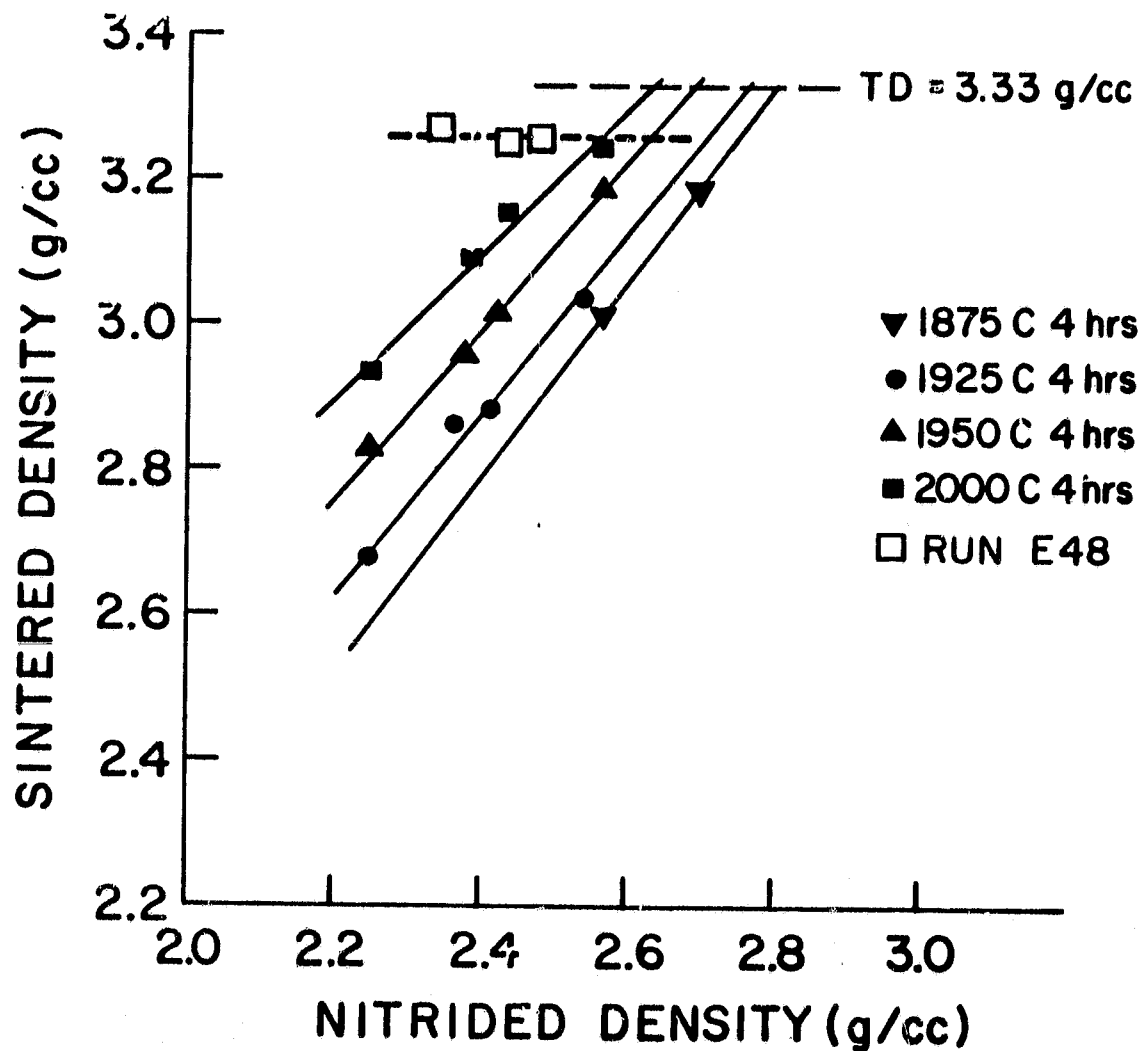


Figure 234. Sintered Density of Sintered Reaction Bonded Silicon Nitride, (8% Y_2O_3) as a Function of Nitrided Density, Sintering Temperature, and Sintering Pressure.

a lower sintered density than one with a higher nitrided density

- o This "nitrided density effect" appears to become slightly less severe with increasing temperature
- o The higher the sintering temperature, the higher the sintered density, for any given nitrided density
- o For compacts with nitrided densities of 2.3 to 2.4 g/cc (the density range anticipated for simulated rotors), the maximum sintered density which could be expected is 3.0 to 3.1 g/cc (90% to 93% T.D.).

Experiments were conducted (at 20 atmosphere N₂) to examine the effect of increased sintering times. These results indicate minimal increases in density (Figure 235) when samples were sintered for 8 hours instead of 4 hours.

Additional sintering experiments were undertaken to attempt to increase sintered density, culminating with Run #48. The results of this run are shown in Figure 235. Densities of 3.27 g/cc were obtained, with these densities being independent of the starting density. This type of sintering cycle was the most successful to date.

Physical Property Evaluation

Figure 236 shows the average room temperature strength of the sintered materials (8% Y₂O₃) as a function of sintering temperature. The strength increases (along with density) as the sintering temperature is increased to 1875°C. As the temperature is further increased to 2000°C, the strength remains constant (515 MPa) even though the density continues to increase. This behavior is explained by the exaggerated grain growth which begins to occur at 1875°C(14).

The strength of the baseline 8% Y₂O₃ material at beginning of work on the AGT program is illustrated in Figure 237, showing a room temperature characteristic strength of 526 MPa with a Weibull modulus of 10.3. The strength of the 8% Y₂O₃ material sintered in Run E48 was the best obtained during this reporting period, resulting in a room temperature strength of 741 MPa with a Weibull modulus of 17.8 (Figure 238).

Sintered Si₃N₄

Al alternate and back-up approach for the manufacture of the ceramic turbine rotor and simulated rotor consists of the slip casting and sintering of Si₃N₄.

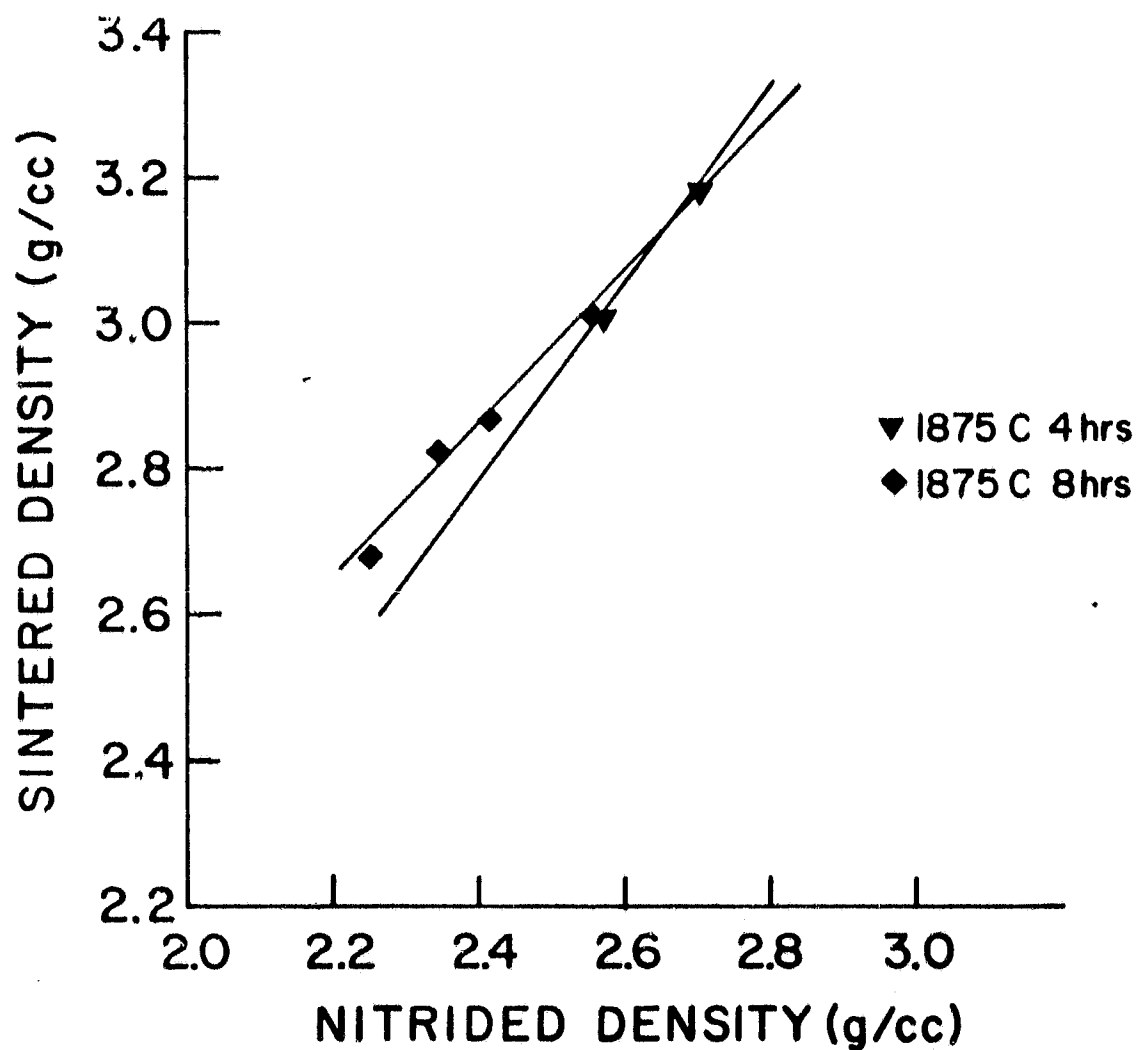


Figure 235. Sintered Density of Sintered Reaction Bonded Silicon Nitride (8% Y_2O_3) as a Function of Nitrided Density, Sintering Temperature, and Sintering Time.

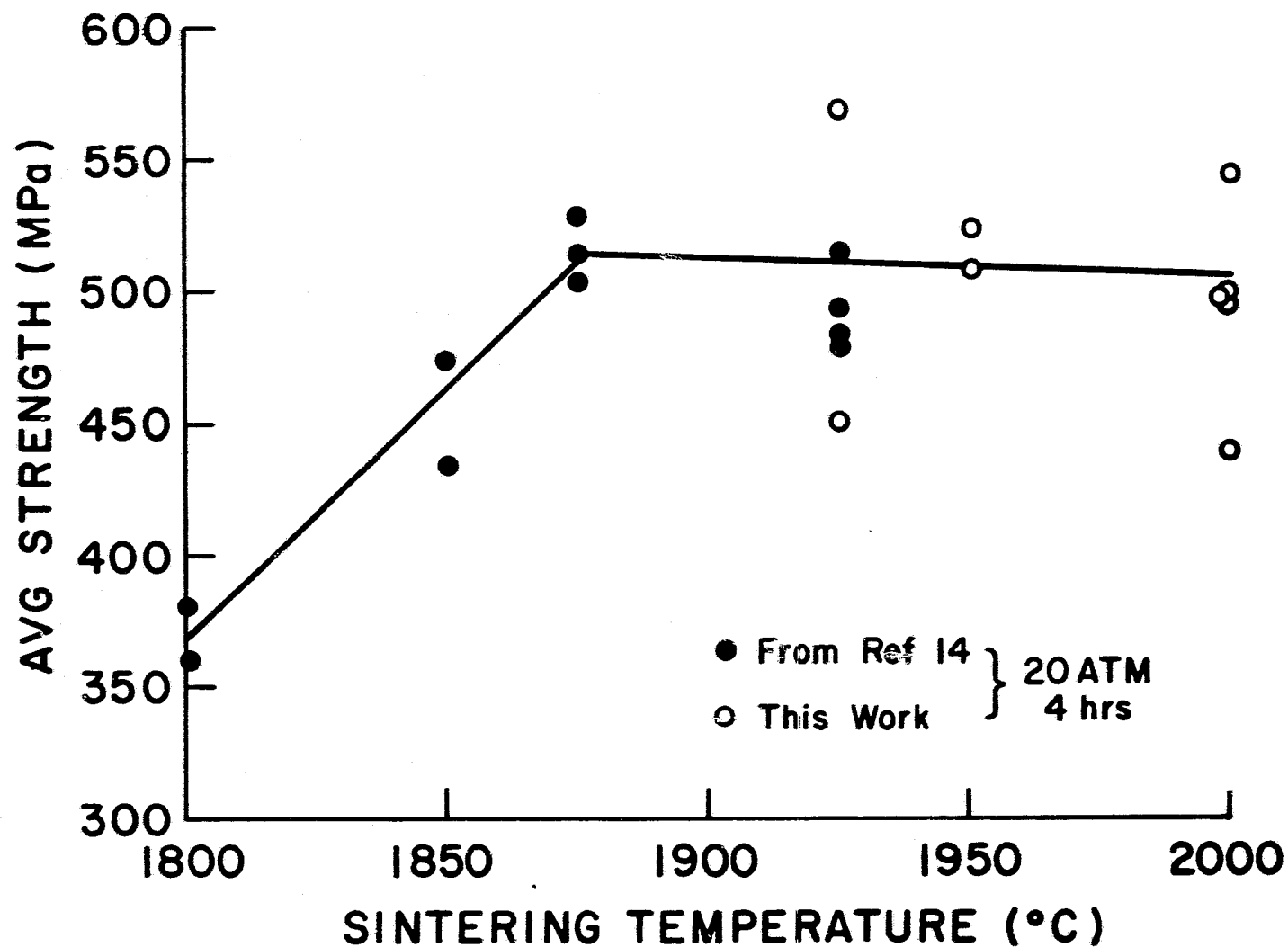


Figure 236. Average Strength of Sintered Reaction Bonded Silicon Nitride (7% Y_2O_3 as a Function of Sintering Temperature).

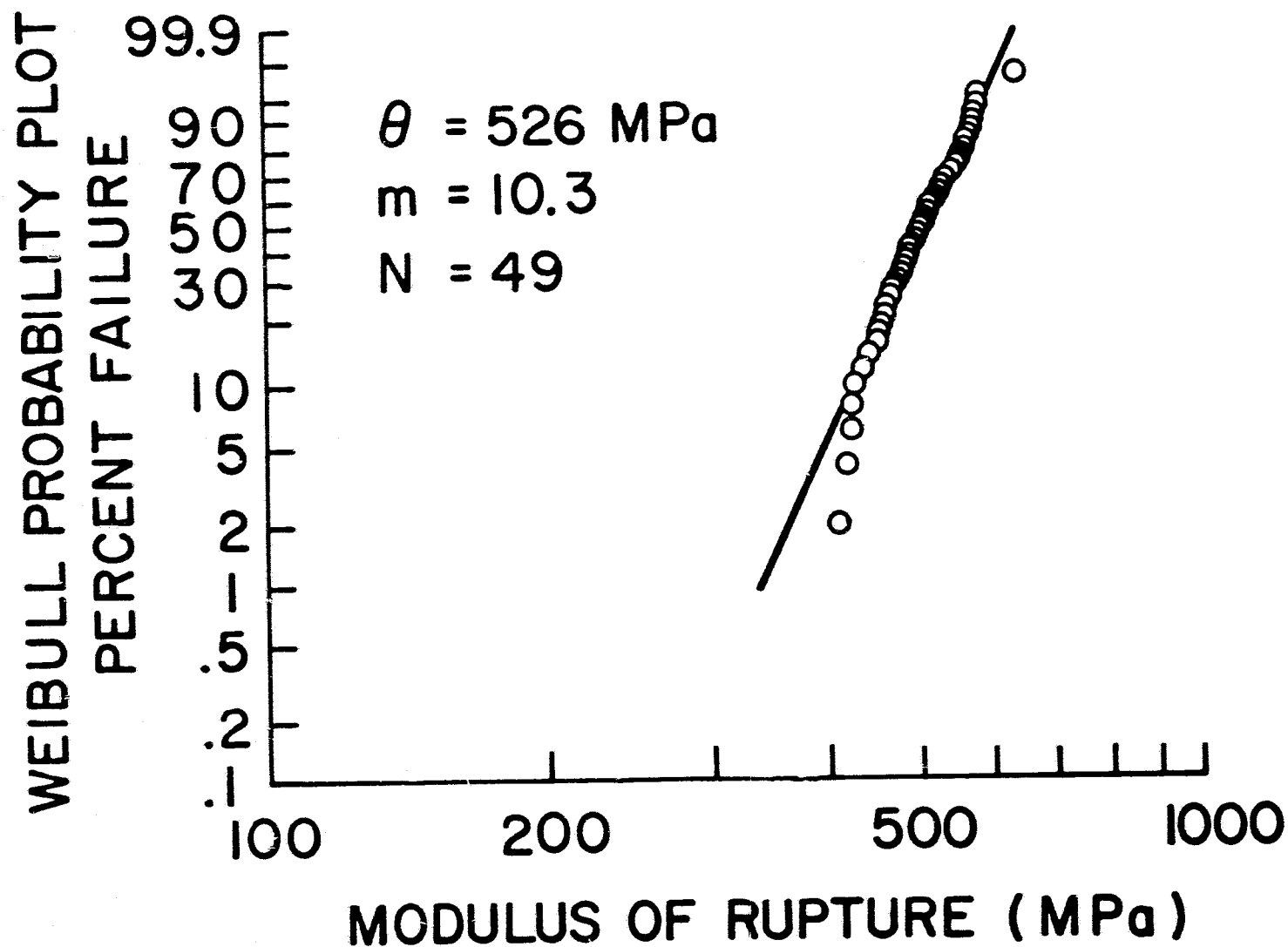


Figure 237. Weibull Probability Plot of the Strength of Sintered Reaction Bonded Silicon Nitride (8% Y_2O_3) at the Beginning of the Program.

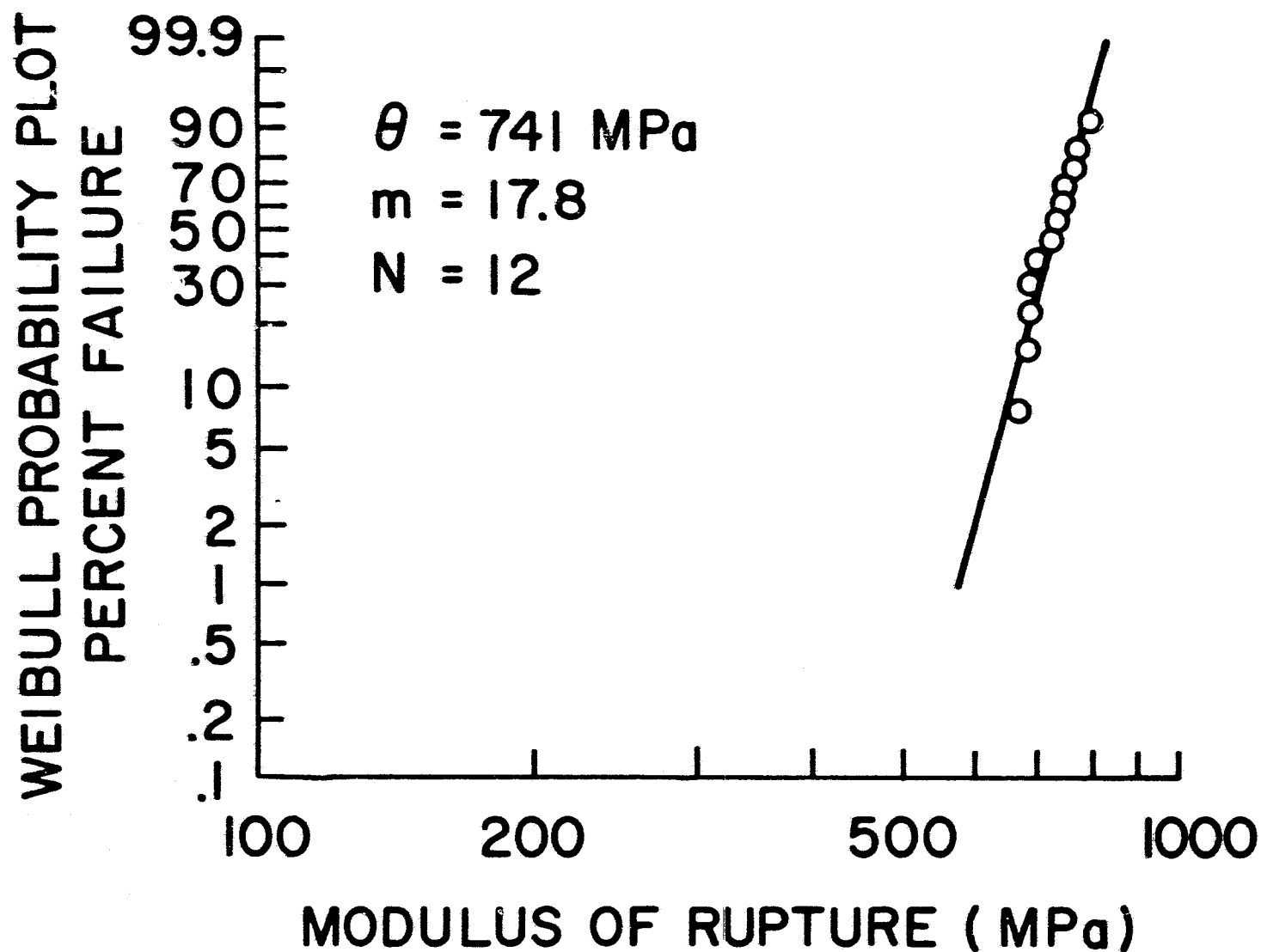


Figure 238. Weibull Probability Plot of the Strength of Sintered Reaction Bonded Silicon Nitride (8% Y_2O_3) Processed in Run E48.

Preliminary work was performed to investigate the feasibility of this approach. Slip casting and sintering experiments were performed using a variety of Si_3N_4 powders along with a variety of additives. Four types of Si_3N_4 powders were studied: Starck LC1 and LC10, AME CP85, and GTE502. Various mixtures of the LC1 and LC10 were also studied.

Yttrium Oxide (8 wt%) was the most common additive. However, 15 wt% Y_2O_3 also was employed as well as mixtures of 8% Y_2O_3 and 4% Al_2O_3 and 8% Al_2O_3 . In all cases the powders were used in their "As Received" conditions, with the additive being mechanically mixed into the slip casting slurry.

Aqueous slips were made from these powders, with the solid content of the slips being between 76 and 75 wt. %. The slips were cast into plaster molds. The green densities varied between 1.5 and 2 g/cc depending on the powder and the casting conditions. The most common green densities were in the 1.75 - 1.80 g/cc range.

These castings were then sintered along with the SRBSN samples (same conditions and same runs). In every case the Si_3N_4 samples had a significantly lower sintered density than the SRBSN samples. The sintered densities ranged from 2 to 2.3 g/cc, seemingly independent of sintering conditions, powder type or additive composition. One sample, however, achieved a sintered density of 2.87 g/cc in Run E48. This sample was made using LC-1 powder with 10% Y_2O_3 and 4% Al_2O_3 .

The suspected reason for these poor sintering results is the low as-cast densities. As pointed out by Mann (15), a threshold green density exists in this system in order for the system to undergo sintering. He states that this threshold density must be greater than 2 g/cc. In no cases were our cast densities above this threshold, consequently sintering to high density should not have been expected.

Future Plans

During the next reporting period, work in all of the preceding areas will continue. The slip development and sintering work will be expanded to investigate the effect of Y_2O_3 concentration on sintering and strength. The characterization effort also will be expanded to evaluate the high temperature strength, oxidation behavior and microstructure of the various sintered materials. Sintering of simulate rotors will begin, with the expected completion of 5 simulated rotors by the end of 1980. Test bars of this rotor material also will be delivered along with the rotors.

Task 2.3 - Mechanical Testing

Cold spin testing of sample sintered silicon nitride simulated rotors will utilize a previously developed bonding technique to connect the rotor to a metal spin arbor. Since the technique was developed for 2.55 g/cc RBSN and the sintered rotors will be much denser, a reduced size pull test specimen of HPSN was fabricated to determine if the bond joint integrity was affected by the density of the ceramic. Figure 239 shows the double ended pull test specimen before testing. This assembly successfully supported 125 pounds up to a temperature of 324°F. Calculations relating the differential thermal strain in this test to the centrifugally induced differential strain encountered during cold spin testing indicated speeds in excess of 130,000 rpm should be achieved with this joining technology.

In order to check out the bonding and removal of rotors following cold spin testing, a section of hot pressed silicon nitride having the dimension of the mounting region of the simulated rotor was bonded to a full size metal spin arbor as shown in Figure 240. This assembly was successfully cold spun to 130,000 rpm without incident. Inspection of the bond point showed it to be intact. Subsequently the parts were disassembled successfully.

An available low quality simulated rotor which had been processed through the reaction sintered stage only was bonded to a metal spin arbor (Figure 241). Visual and dimensional inspection indicated a good bond had been achieved. This assembly will be balanced and cold spun to destruction to checkout the balancing and spinning procedures of a full size component.

ORIGINAL PAGE
BLACK AND WHITE PHOTOGRAPH

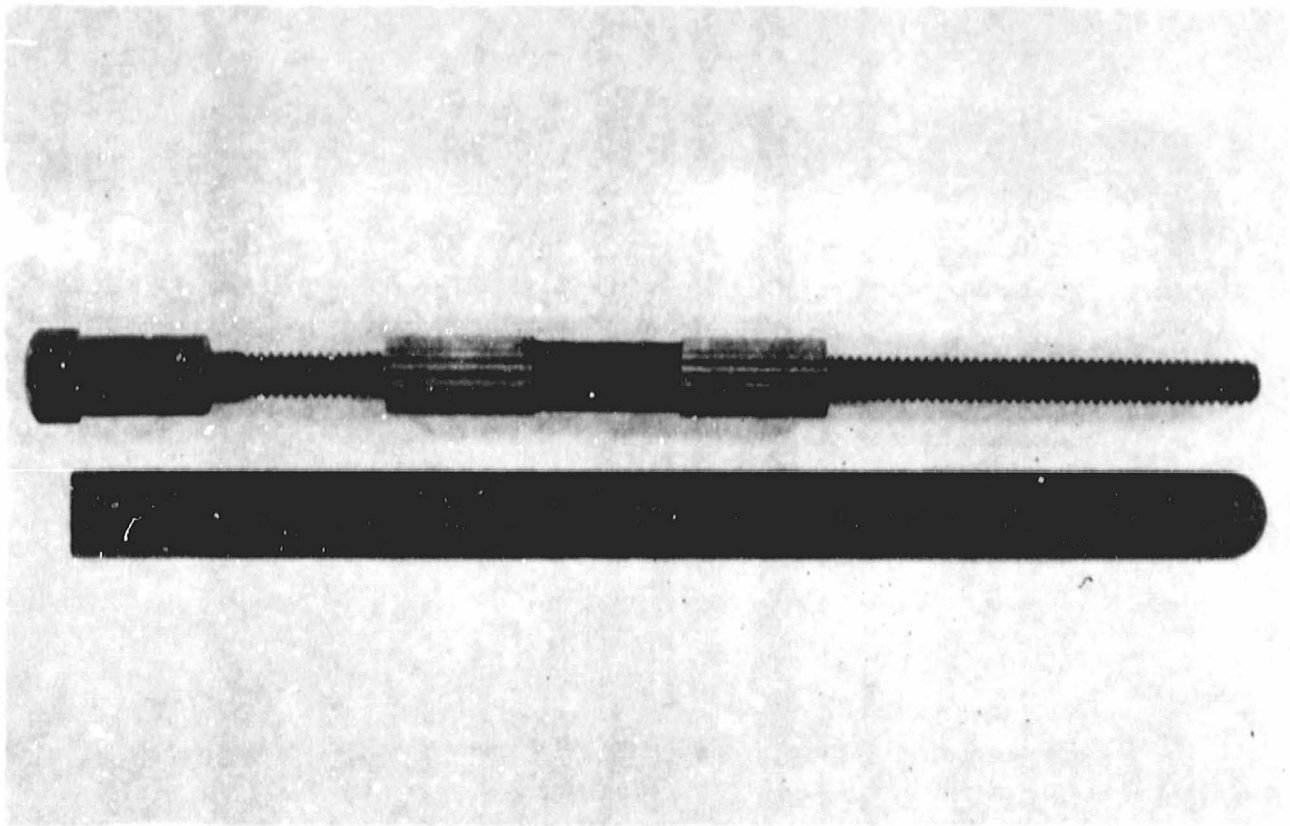


Figure 239. Double Ended Bond Joint Pull Test Specimen.

ORIGINAL PAGE
BLACK AND WHITE PHOTOGRAPH

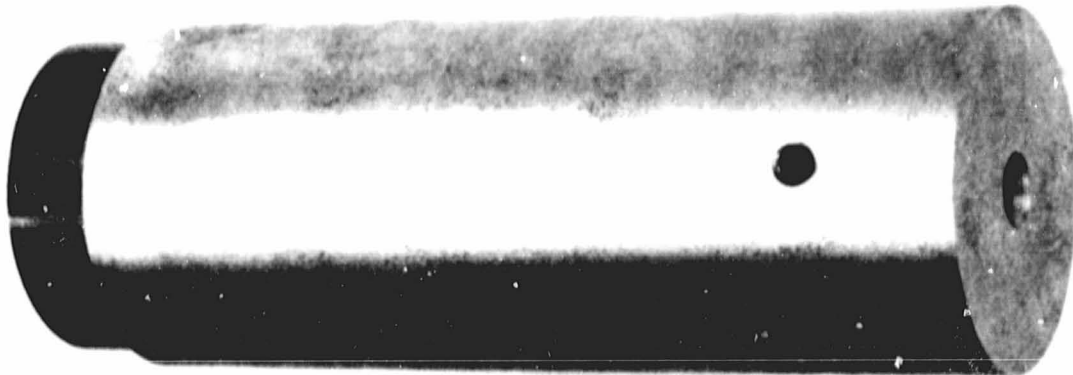


Figure 240. Hot Pressed Silicon Nitride Stub Bonded to Metal Spin Arbor.

ORIGINAL PAGE
BLACK AND WHITE PHOTOGRAPH

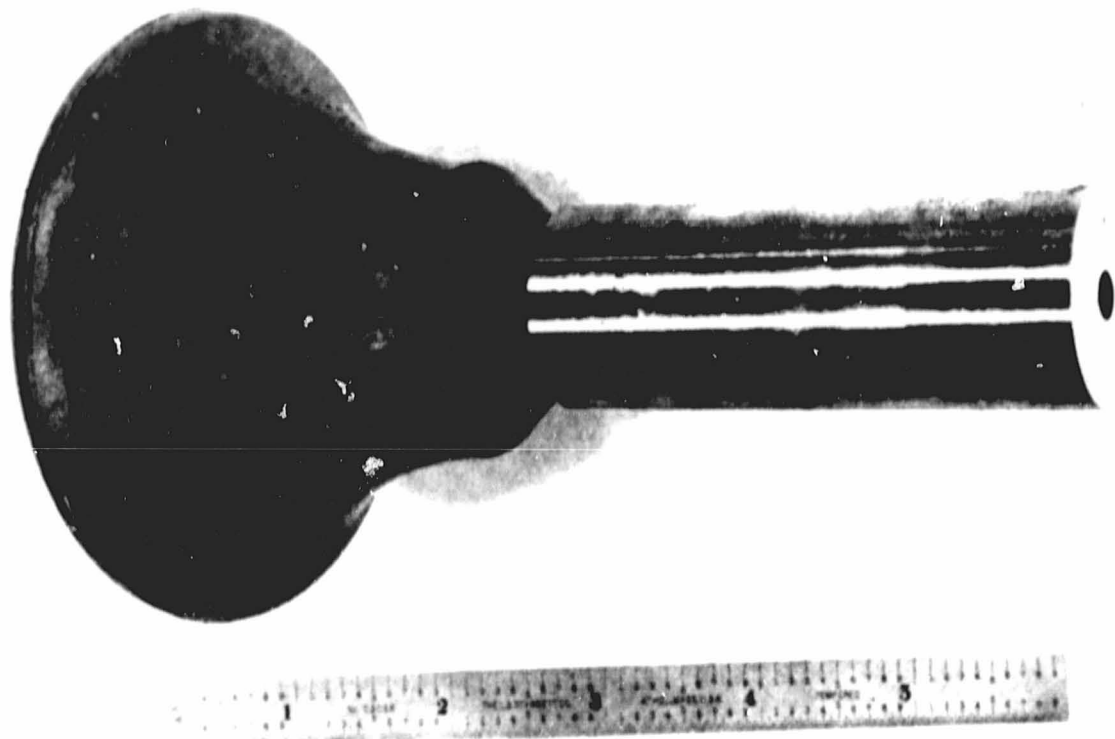


Figure 241. Reaction Bonded Silicon Nitride Simulated Rotor Bonded to Metal Spin Arbor.

Task 27 - Stator

Introduction

Injection molding of a one-piece ceramic stator was selected as the fabrication approach for AGT101 stators, based upon several years of material and process development and component evaluation of axial turbine monolithic ceramic stators. Reaction bonded silicon nitride (RESN) of 2.7 g/cc density (85% TD) was selected as the initial material, although injection molded material of a higher density(1, 13) may be substituted later in the program.

Work during the first year of the program is divided in two activities.

- o Analytical study of mold cavity filling
- o Molding process development

Progress in each of these activities will be discussed in turn.

Analytical Study of Mold Cavity Filling

A program to apply mathematical modeling of the injection molding process as applied to the AGT101 stator design was initiated at Cornell University. The overall objectives of this program were (1) to determine if specific problems existed in the stator geometry which would produce molding problems (knot lines in particular) prior to tooling fabrication, preventing expensive and time consuming tooling rework, and (2) to reduce experimental time in the determination of molding parameters.

The work by Cornell University was planned in three stages as follows:

- o Calculation of non-isothermal static cavity filling of a single blade with an appropriate geometric representation
- o Calculation of non-isothermal dynamic cavity filling with advancing melt front
- o Calculation of the processing and thermal bonding conditions on flow behavior during cavity filling

The finite element grid in the X-Y plane is shown in Figure 242. It contains uniform mesh increments across the variable thickness in the Z direction. As in subsequent models, material enters the cavity along AB and leaves along CDEF. Results obtained with this model agreed with predictions for velocity variation, temperature gradients, and pressure gradients. A foundation for further modeling was thus established.

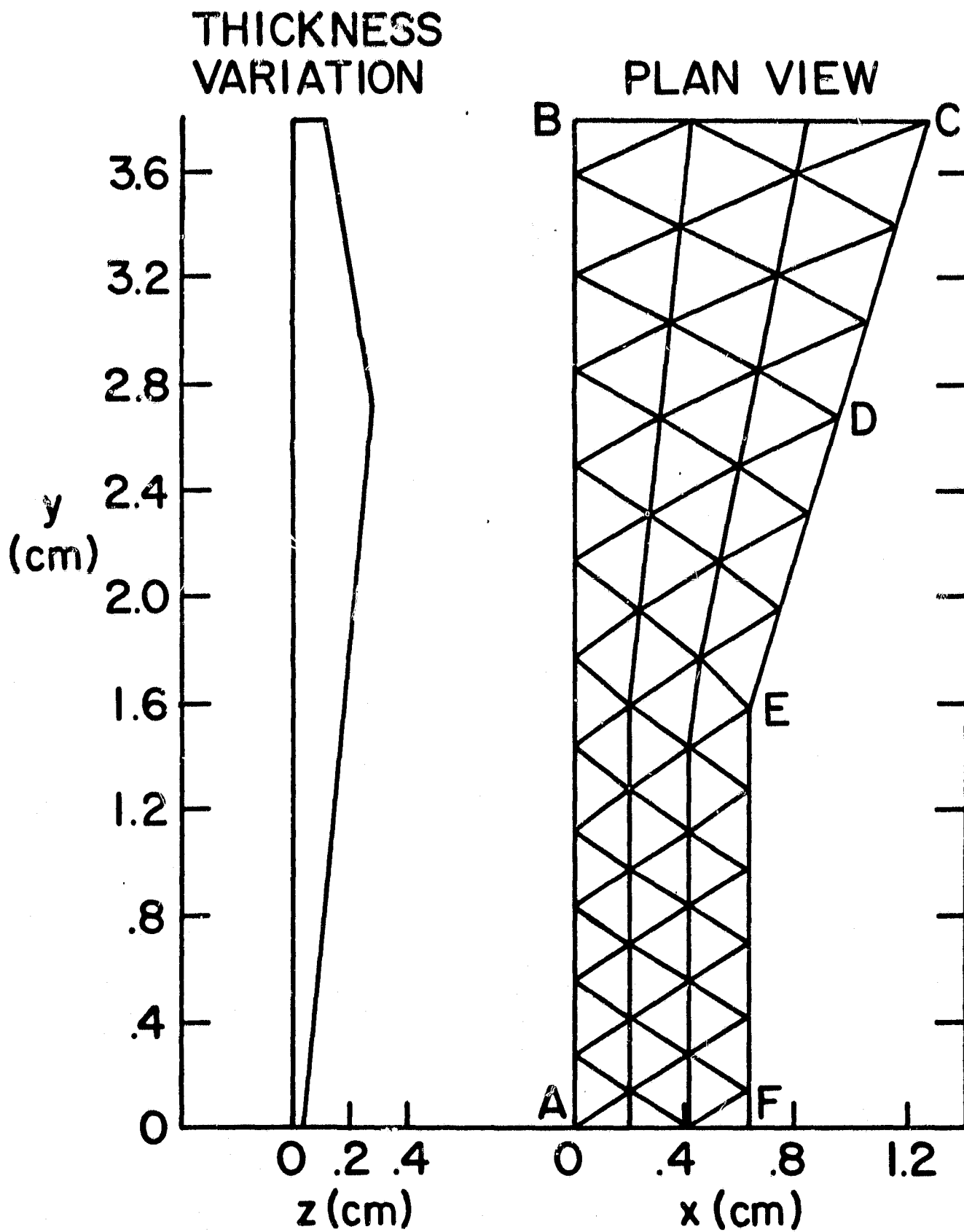


Figure 242. Finite Element Grid of Stator Vane Model.

Parameters of temperature, time, and flow rate were assumed to be those that have been used to mold the axial integral stator (i.e., $T_0 = 383^\circ\text{K}$; $t_{\text{fill}} = 0.35 \text{ sec.}$; $Q = 3 \text{ cc/sec.}$). Viscosity at 383°K had been investigated on various rheological instruments prior to this work. The material exhibited thixotropic and Bingham behavior. Thermal properties were determined by a commercial laboratory. Values used in work to date have been taken as:

$$k = 2 \times 10^5 \text{ erg/sec cm } ^\circ\text{K}; C_p = 9.2 \times 10^6 \text{ erg/gm } ^\circ\text{K}; \rho = 1.89 \text{ gm/cc}$$

Cornell has undertaken a study of stator material rheological properties at various temperatures using knurled cylinders as well as smooth ones in a rotary viscometer, which has been found to be most suitable for this material. This information will add to the confidence level of process variable options available to achieve a desirable material flow pattern in the model.

Dynamic cavity fill analysis is sufficiently complex that an isothermal program was needed before undertaking a non-isothermal one. Figure 243 shows the isothermal finite element representation of the melt-front location at $t = 0.28, 0.38, 0.48, \text{ and } 0.58 \text{ second}$. This analysis strongly suggests that when the right boundary (CDEF in Figure 242) is not impermeable but, rather, attached to another cavity (the opposite sidewall) that material will tend to flow into the cavity rather than turning its flow direction towards the inner sections of the blade. In this case the blade will be filled at a later time and at a reduced pressure, with the thin-sectioned portions of the blade tending to be filled from the left rather than from above or the right.

To address the question of whether back flow from the shroud to the blade may result in a knit line, an analytical program is under development which treats the flow in two separate planes, corresponding to the blade and the segmented sidewall. The finite element grids for blade and segmented shroud planes are shown in Figures 244A and B, respectively. Mathematical coupling between the two domains is effected by requiring that the pressures along BC be the same in both planes and that the volumetric flow rate across BC in Figure 244A be equal to the flow emanating from BC in Figure 244B. The direction of flow across BC is left to the calculation, thus allowing for possible back flow and knit line generation.

As a part of this study Cornell has fabricated a mold which simulates the stator vane in order to verify analytical results through injection molding experiments on an available injection molding machine.

Molding Process Development

To achieve the highest quality components possible, precise and rapid control of process temperatures, pressures, and times are necessary. The injection molder control system that is being developed,

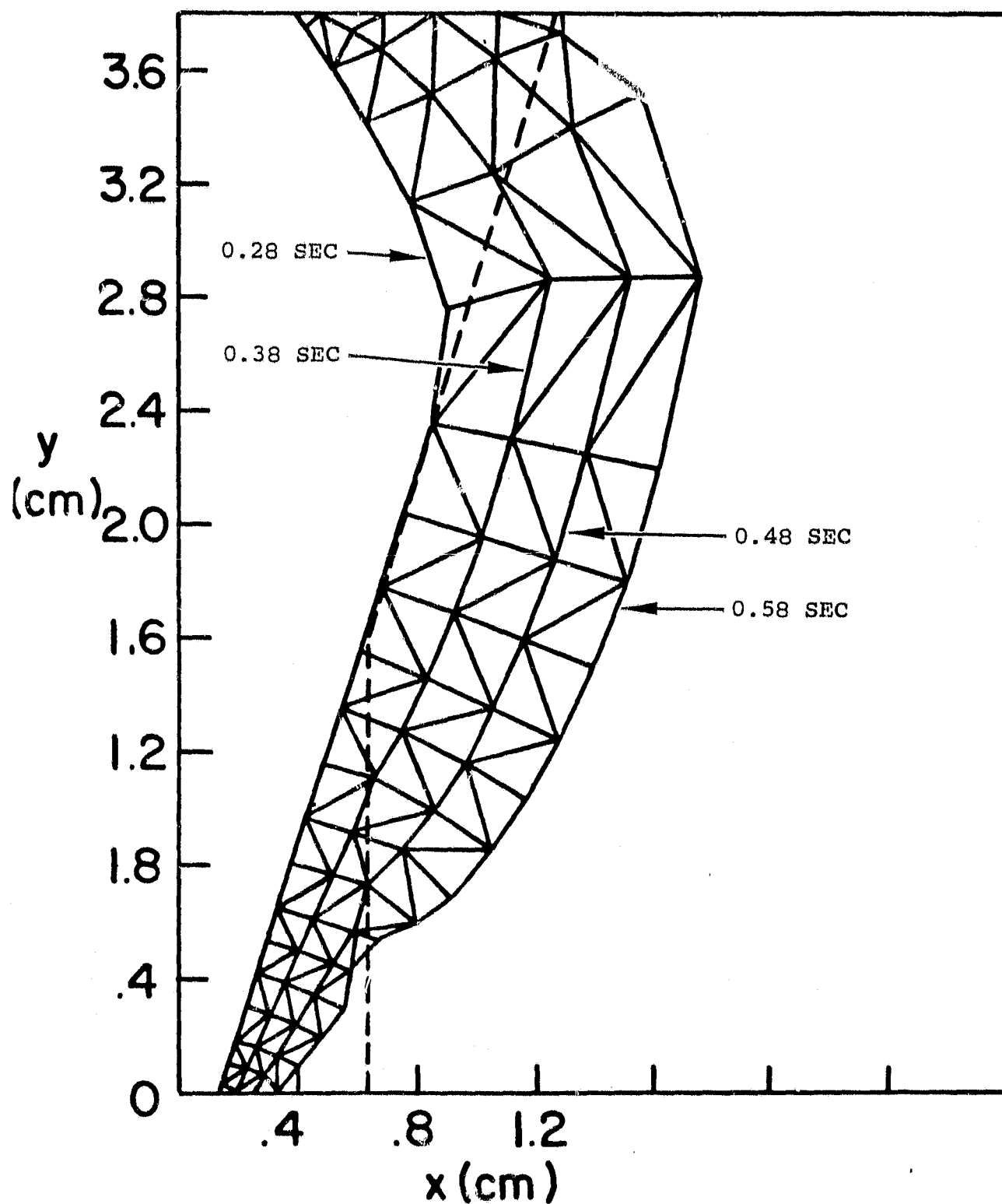
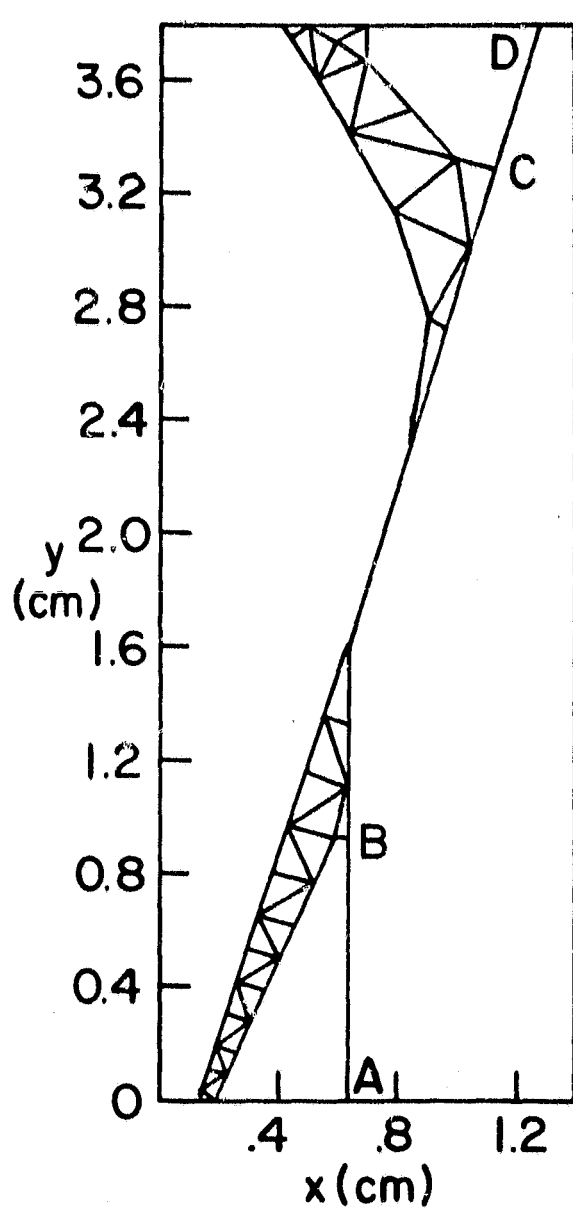
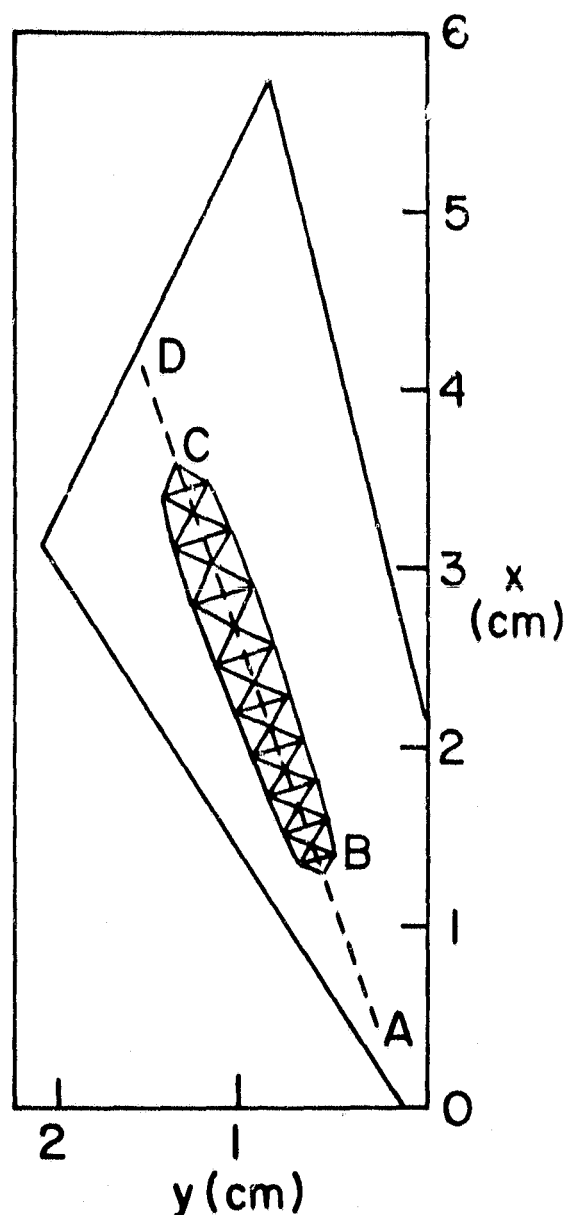


Figure 243. Finite Element Grid Showing Advancing Material Flow Front (Left to Right) at Times of 0.28, 0.38, 0.48 and 0.58 Seconds.



A. View of Blade Finite Element Added Between Times of 0.28 and 0.38 Seconds



B. End View of Interaction of Blade with Segmented End Wall With Finite Element Corresponding to Volume Passing Areas ABCD Between Times of 0.28 and 0.38 Seconds

Figure 244. View of Finite Element Grids and Segmented Shroud Planes.

incorporates a microprocessor. In its final configuration, the system will control a 160 ton Tempcratt vertical injection molding machine. This molder will be used to mold AGT101 stators and test specimens.

The program will be loaded into the microcomputer system. Pertinent data will be displayed for the operator via a CRT terminal. The operator can "start", or "hold" the automatic injection process from this terminal.

The system will be designed to monitor and/or control the process temperatures at up to eight different zones. During machine set-up, the zone temperatures will be displayed and updated on the CRT terminal so that the operator will know when to initiate the injection cycle. During the molding cycle, up to eight different zone temperatures will be recorded at the peak injection pressure. After the molding cycle is completed, the component will be removed from the mold, and the operator will input the results of his visual examination. A complete data sheet then will be automatically printed. This sheet will contain a part number as well as all pertinent data. In its final configuration, the magnetic tape will be used primarily for data storage.

A process monitor panel allows the operator to monitor the injection molding process. In addition to showing the current status of the injection molding process, several "run time" options can be selected. The process also can be put on "hold" or switched to "manual" once the injection process has been started, which would allow the operator to complete the process manually. When the control system is completely developed, these data tapes will receive further processing, as shown in Figure 245, through the use of a computer system (Hewlett-Packard 9845).

During this reporting period development of the stator software for the microprocessor machine control and data acquisition system was started. Temperatures and pressures will be recorded on magnetic tape for data storage and future analysis.

ORIGINAL PAGE IS
OF POOR QUALITY

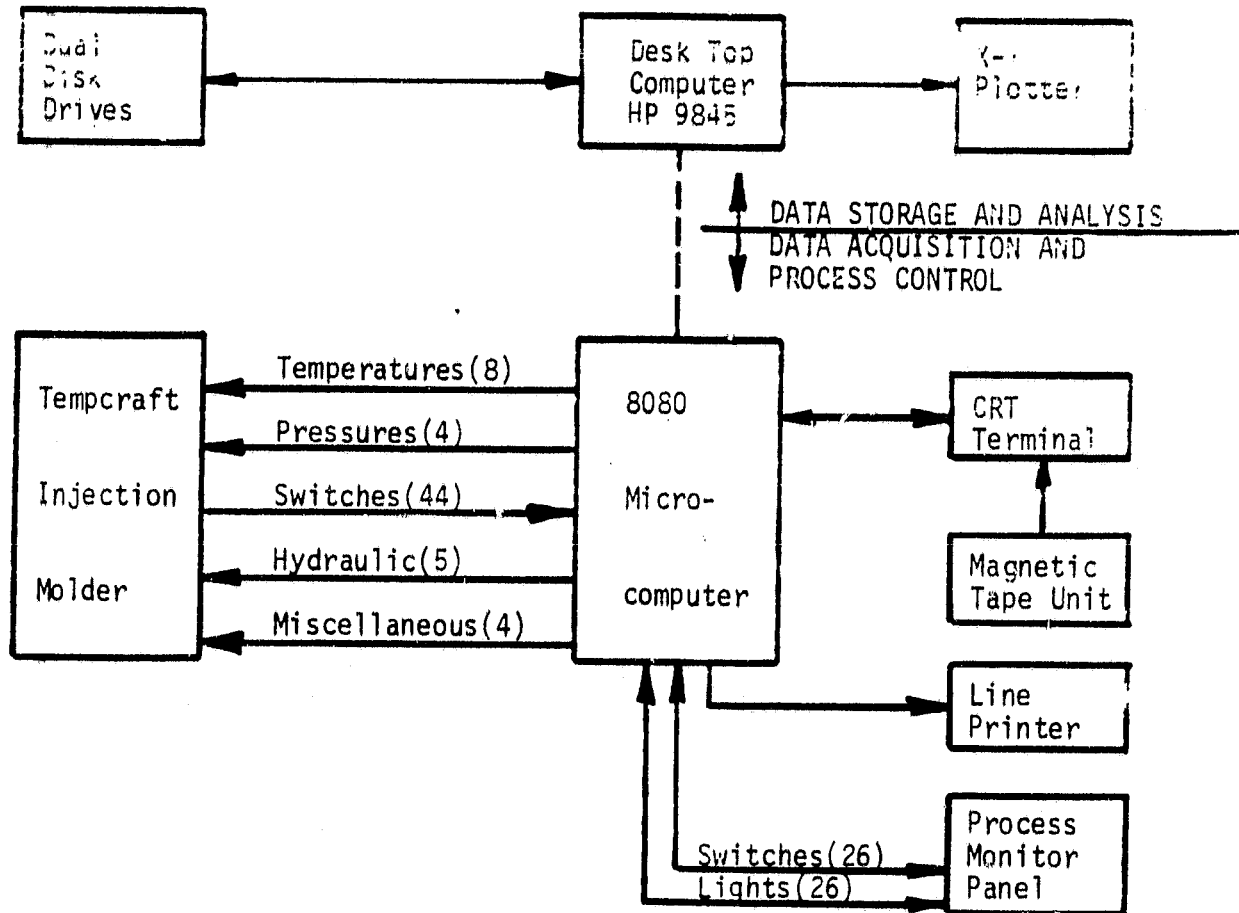


Figure 245. Block Diagram of Injection Molding Control and Data System.

Task 2.7 - Flow Separator Housing

Introduction

The flow separator housing, Figure 246 is a ceramic component that provides a gas flow path from and to the heat exchanger, acts as a support structure for hot flow path components, and provides a sealing surface for the rotating heat exchanger.

The material selected for this component is a low thermal expansion lithium aluminum silicate (LAS) ceramic. Specifically, the component will be made by Corning Glass Works in their Code 9458 LAS. The process for making the flow separator housing consists of slip casting an aqueous suspension of crushed glass into the desired shape using Plaster of Paris molds. The component then is removed from the mold, dried to remove residual water, sintered, and critical surfaces are diamond machined.

Physical Properties of 9458 LAS

Physical property data on Code 9458 material is shown in Table 31 and Figures 247, 248, and 249.

The bulk density of 9458 LAS measured approximately 2.3 g/cc. The apparent or open porosity is zero, for all practical purposes. The material is estimated to be about 92 percent of theoretical density.

The thermal expansion of 9458 shown in Figure 247 is characteristic of beta spodumene type ceramics. The material has a negative expansion from room temperature to approximately 300°C followed by a much sharper positive expansion up to 900°C.

The flexural strength data in Figure 247 shows a slight decrease in strength over the range from room temperature to 500°C. Above 500°C the strength increases somewhat indicating the possibility of microcrack healing.

Thermal conductivity, based on measurements of specific heat and thermal diffusivity, has been averaged using two different techniques and is shown in Figure 249. Unlike most ceramics, there is an increase in conductivity with temperature.

Design Modifications

A full scale model of the flow separator housing, shown in Figure 246, was fabricated using foam plastic material. This model proved useful during discussion of design iterations. The model also served as a guide for the development and fabrication of a more permanent wood model at Corning Glass Works. This wood model in turn will be used to fabricate patterns for the plastic tooling.

ORIGINAL PAGE
BLACK AND WHITE PHOTOGRAPH

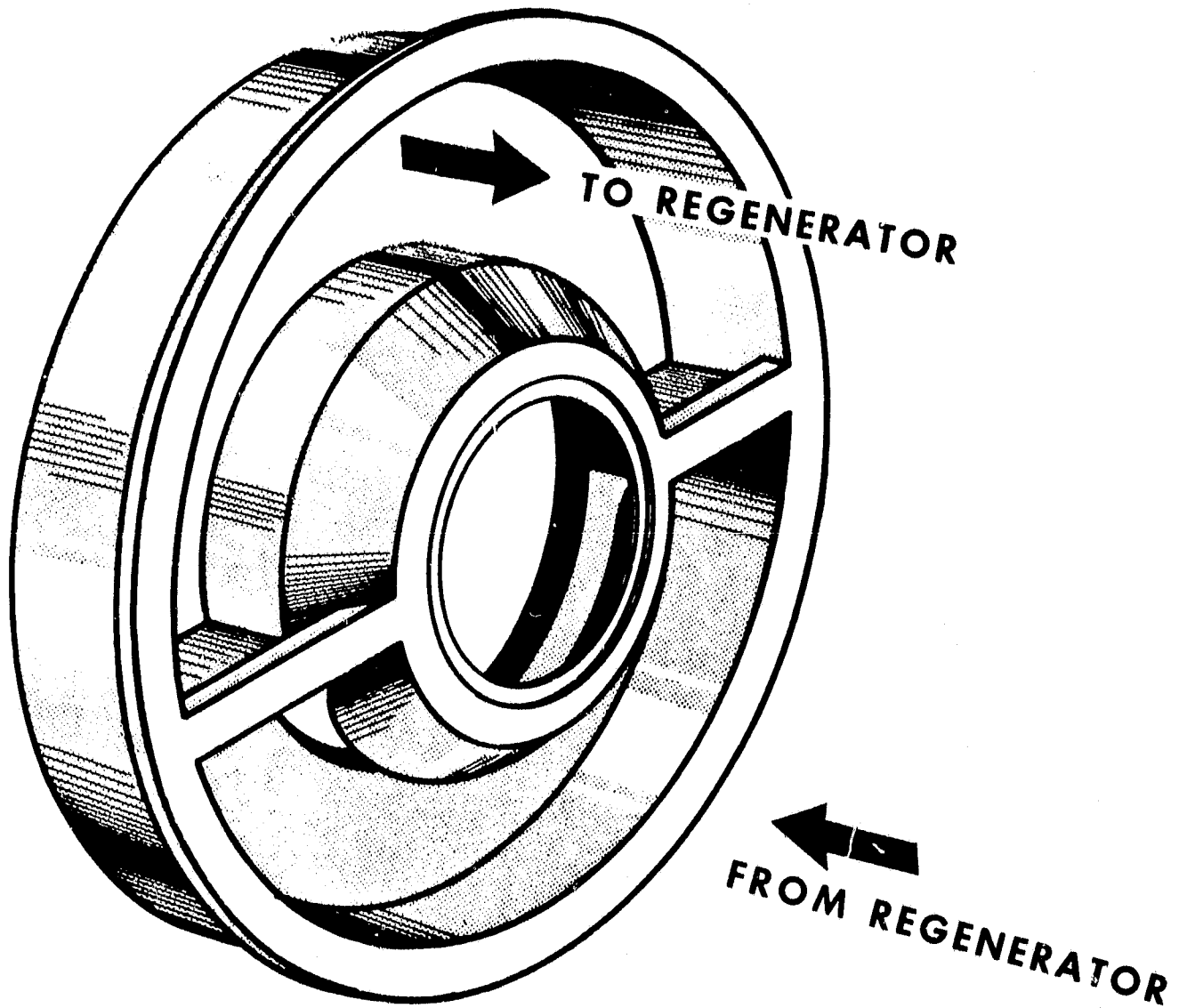


Figure 246. Sketch of Flow Separator Housing.

TABLE 31. PHYSICAL PROPERTIES OF CORNING 9458 LAS

Bulk Density	2.3 g/cc
Apparent Porosity	Zero
Thermal Instability - Linear (500 hrs at 1800°F)	±100 ppm max

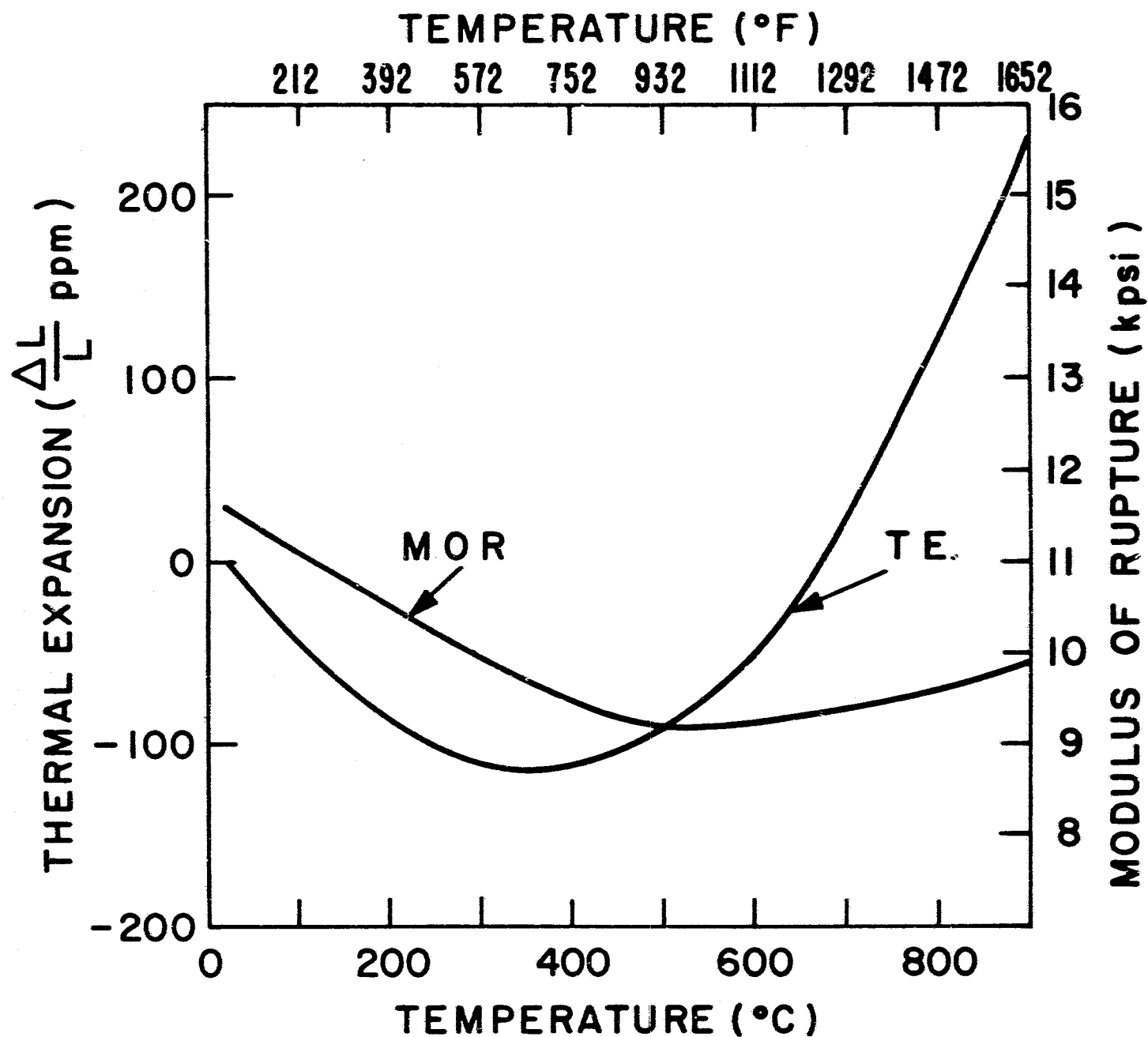


Figure 247. Strength and Thermal Expansion of Corning Code 9458 Lithium Aluminum Silicate.

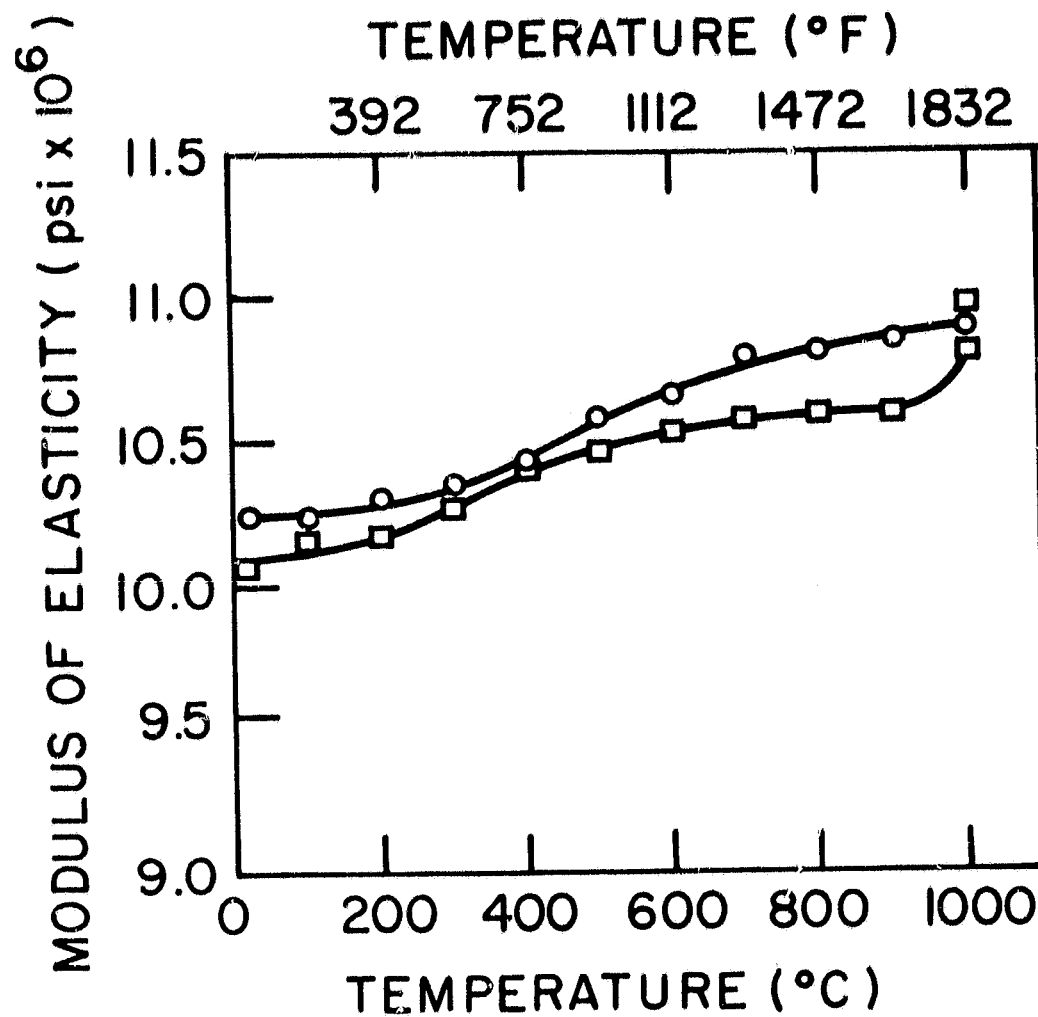


Figure 248. Modulus of Elasticity of Corning Code 9458 Lithium Aluminum Silicate.

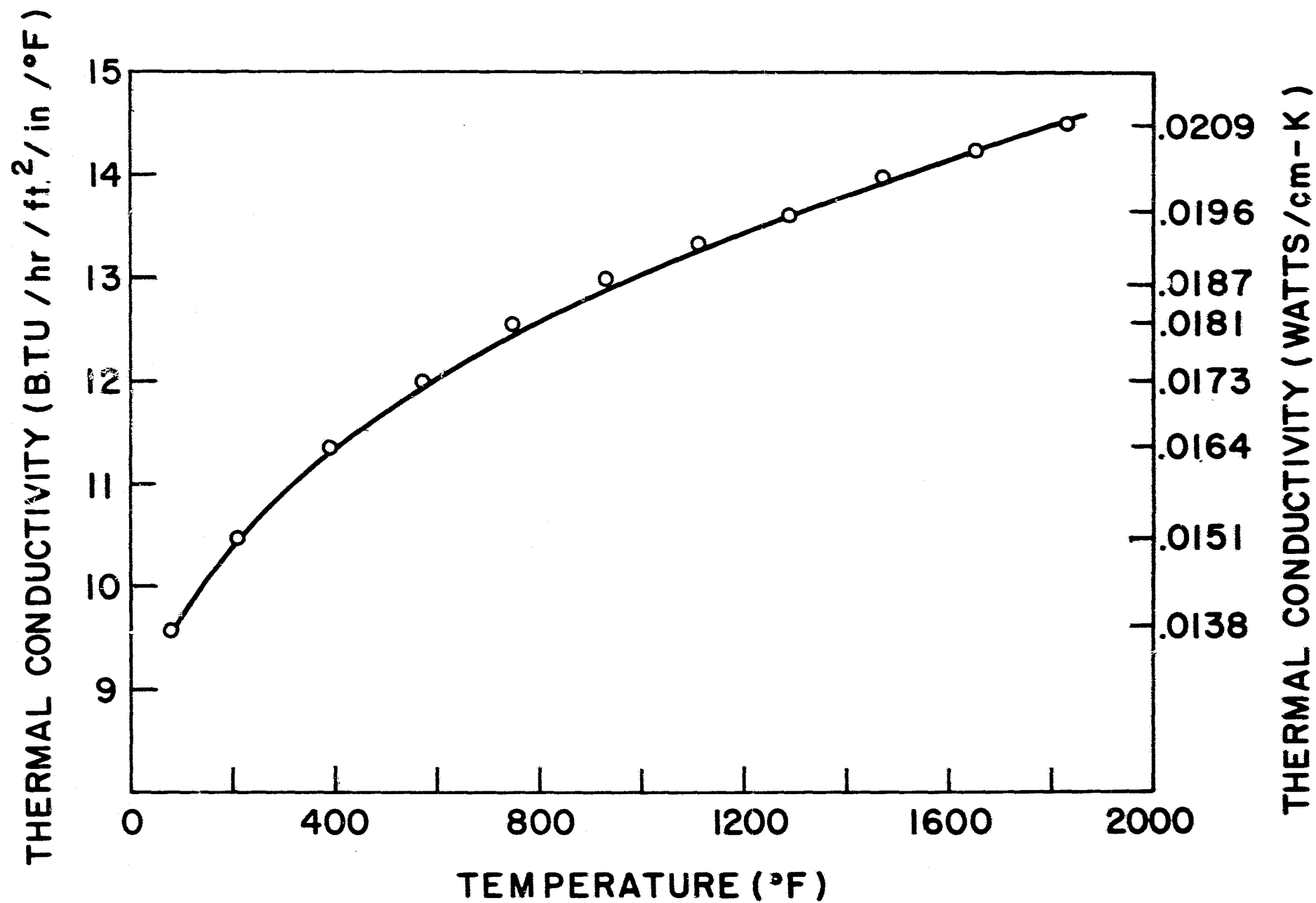


Figure 249. Thermal Conductivity of Corning Code 9458 Lithium Aluminum Silicate.

A number of design iterations in the flow separator housing were made to facilitate fabrication and minimize mechanical and thermal operational stresses. The latest stress analysis of the current design, as conducted by AiResearch Phoenix, revealed that maximum combined stresses (mechanical and thermal) have been reduced from 3.4 kpsi to 2.7 kpsi. Detailed drawings of the design are now available and fabrication development will begin shortly.

REFERENCES

1. J.A. Mangels, G.J. Tennenhouse, "Densification of Reaction Bonded Silicon Nitride," accepted for publication by the American Ceramic Society.
2. A. Ezis, J.M. Nicholson, "Method of Manufacturing a Slip Cast Article," U.S. Patent No. 4,067,943.
3. A. Ezis, J.T. Neil, "Slip Casting of Silicon Based Ceramics," Bull. Amer. Ceram. Soc. Vol. 58, No. P, p. 883.
4. F.F. Lange, S.C. Singhal, R.C. Kuznicki, "Phase Relations and Stability Studies in the Si_3N_4 - SiO_2 - Y_2O_3 Pseudoternary System," J. Amer. Ceram. Soc. Vol. 60, No. 5-6, 1977, p. 249.
5. W.D. Carruthers, K.W. Benn, "3500-Hour Durability Testing of Commercial Ceramic Materials," NASA Contract DEN3-27, 3rd Quarterly Progress Report, 1978.
6. H. Knoch, G.E. Gazza, "Carbon Impurity Effect on the Thermal Degradation of a Si_3N_4 - Y_2O_3 Ceramic," AMMRC TR 79-27, 1979.
7. S.R. Schuon, "Effect of W and WC on the Densification and Oxidation of Sintered Si_3N_4 +8 Y_2O_3 ," Bull. Amer. Ceram. Soc. Vol. 59, No. 3, (1980), p. 356.
8. G.O. Weaver, J.W. Lucek, "Optimization of Hot-Pressed Si_3N_4 - Y_2O_3 materials," Bull. Amer. Ceram. Soc., Vol. 57, No. 12, (1978) p. 1131.
9. J.T. Smith, C.L. Quackenbush, "Phase Effects in Si_3N_4 Containing Y_2O_3 or CeO_2 : I, Strength; II, Oxidation," Bull. Amer. Ceram. Soc. Vol. 59, No. 5, (1980), p. 529.
10. A. Ezis, "The Fabrication and Properties of Slip Cast Silicon Nitride," Ceramics for High Performance Applications, J.J. Burke, A.E. Gorum and R.N. Katz Editors, Metals and Ceramics Information Center, Columbus, Ohio, p. 207.
11. J.A. Mangels, "Development of Injection Molded Reaction Bonded Si_3N_4 ," Ceramics for High Performance Applications II, J.J. Burke, E.N. Leno, R.N. Katz, Metals and Ceramics Information Center, Columbus, Ohio, p. 113.
12. J.A. Mangels, "The Effect of Rate Controlled Nitriding and Nitriding Atmospheres on the Formation of Reaction Bonded Si_3N_4 ," submitted to American Ceramic Society, 1980.

13. J.A. Mangels, "Development of Moldable, High Density Reaction Bonded Si_3N_4 ," NASA Contract DEN3-20, Quarterly Reports 4 to 8, 1979 and 1980.
14. J.A. Mangels, G.J. Tennenhouse, "Sintering Behavior, Microstructure Development and Properties of Yttria-Doped Reaction Bonded Silicon Nitride," Bull. Amer. Ceram. Soc., Vol 59, No. 3 (1980) p 356.
15. D.L. Mann, "Injection Molding of Sinterable Silicon-Base Non-Oxide Ceramics," AFML-TR-78-200, (1978).

PRECEDING PAGE BLANK NOT FILMED

APPENDIX II

AIRESEARCH CASTING COMPANY (ACC)

**ADVANCED GAS TURBINE (AGT) POWERTRAIN PROGRAM
FIRST SEMI-ANNUAL TECHNICAL
PROGRESS REPORT**

1.0 INTRODUCTION

ACC is conducting efforts in both rotor and static component fabrication development for the AGT101 Program. Rotor efforts are directed toward fabrication of both injection molded and slip cast rotors of both sintered silicon nitride and sintered RBSN. Several injection molding approaches using different injection equipment and injection approaches are being evaluated. Injection molding studies have indicated a problem of an air entrapment during injection. Efforts to eliminate this entrapment have dominated the injection molding studies.

For slip cast rotors, several variations of casting, drying and sintering have been made. Primary problems encountered have been cracks occurring during drying and sintering cycles.

Static component development is directed toward fabrication of reaction-bonded Si_3N_4 static hardware. Efforts have been directed toward coordinating. AiResearch Phoenix design goals with ACC fabrication capabilities, and demonstrating fabrication capabilities of complex shapes.

Baseline test bars of all materials anticipated for use in the AGT101 also were prepared and provided to AiResearch Phoenix.

A more detailed discussion of the ACC development efforts is presented in the following paragraphs.

2.0 ROTOR MATERIALS AND FABRICATION DEVELOPMENT

2.1 Baseline Materials

All of the 300 baseline SNN522, injection molded sintered Si_3N_4 test bars have been shipped to AiResearch Phoenix for evaluation. Five additional test bars were selected at random and subjected to room temperature four point bend tests. The results are shown in Table 32.

TABLE 32. ROOM TEMPERATURE FOUR POINT BEND TEST RESULTS

Specimen No	Sintered Density	MOR (ksi)
1	3.07 gm/cc	75.5
2	3.17 gm/cc	91.4
4	3.27 gm/cc	84.0
5	3.17 gm/cc	80.9
7	3.17 gm/cc	88.7

Average MOR: 84.1 ksi; Standard Deviation: 6.3 ksi

Ten additional SNN522 test bars which were injection molded from another batch were selected for room temperature and 2200°F bend tests. The average of the five bars broken at room temperature was 87.5 ksi. Standard deviation was 2.2 and Weibull modulus was 29.7. Figure 250 shows the Weibull plot. The average of the five bars broken at 2200°F was 63.9 ksi. Standard deviation was 4.7 and Weibull modulus was 10.9. Figure 251 shows the Weibull plot. Eleven SNN522 test bars were submitted to IITRI for room temperature evaluation approximately one year ago. The values obtained on these bars plus those described above for room temperature results were used to obtain a 16 point Weibull modulus. The results, as shown in Figure 252, reveal an average MOR value of 83.1 ksi, 5.3 ksi standard deviation and a Weibull modulus of 15.9. No slip cast SNN502 test bars have been fabricated successfully for evaluation by AiResearch Phoenix.

2.2 Injection Molded Rotors

Tempcraft injection molder was received, installed and put into operation. In order to certify the operation and mold fill capabilities of the Tempcraft unit, a batch of silicon powder with binder was injected into the simulated rotor tool. Although flow lines were observable on the surface, the material appeared to completely fill the mold. This rotor also was successfully used to evaluate the binder extraction cycle. Through weight calculations, it appeared that all of the binder was removed. The rotor is in the present nitriding run.

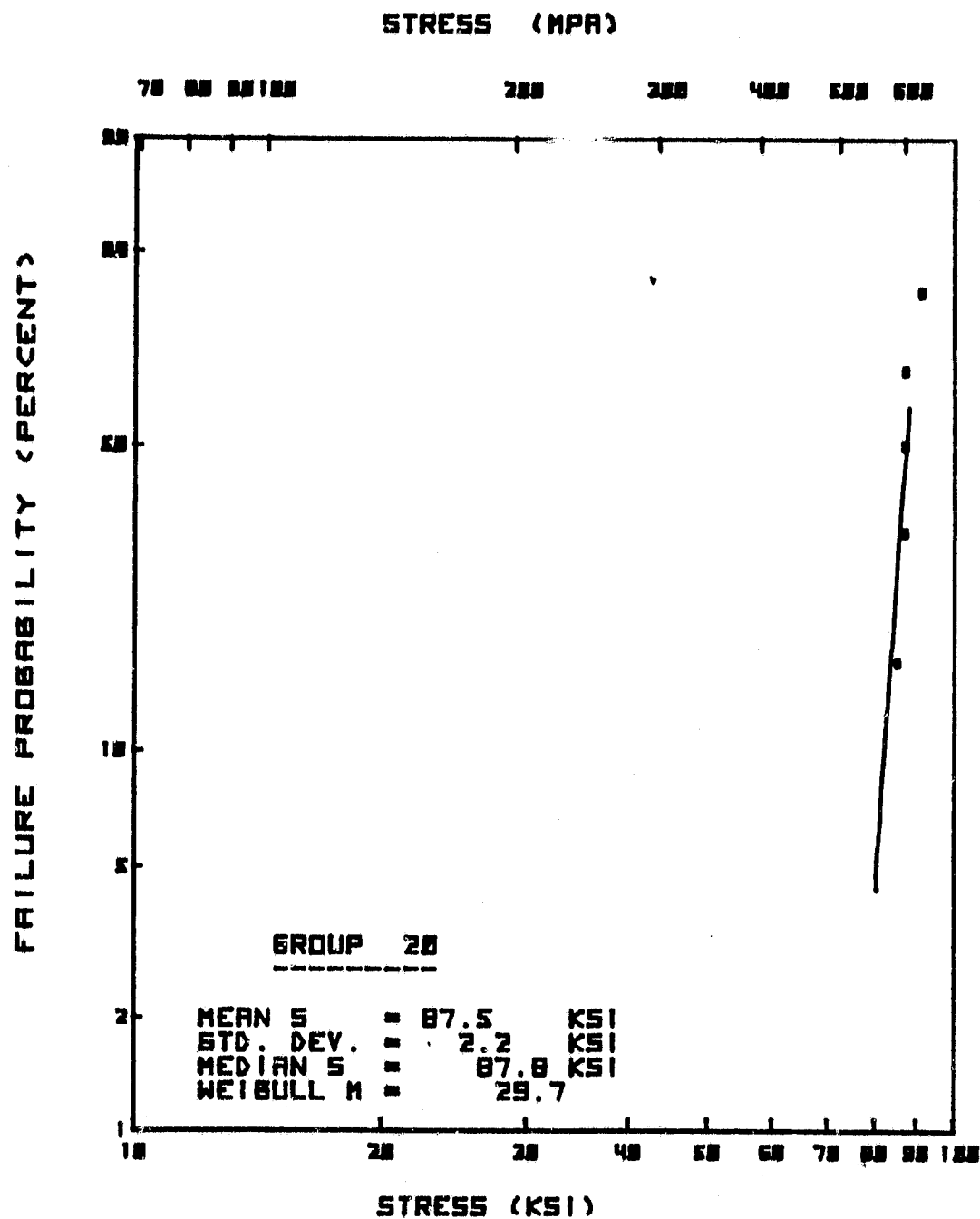


Figure 250. SNN522 Baseline Injection Molded Si_3N_4 Room Temperature MOR.

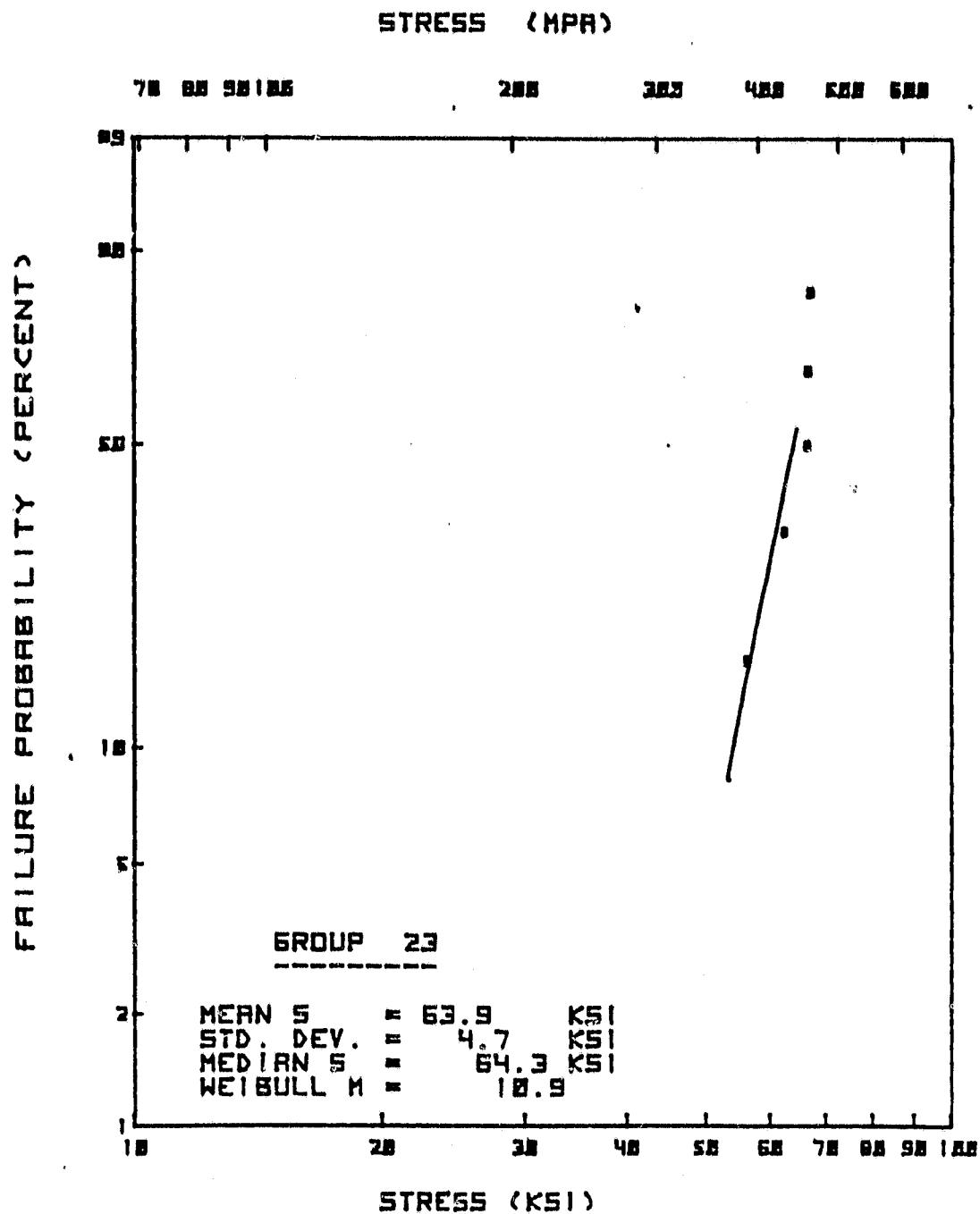


Figure 251. SNN522 Baseline Injection Molded Si_3N_4 2200°F MOR.

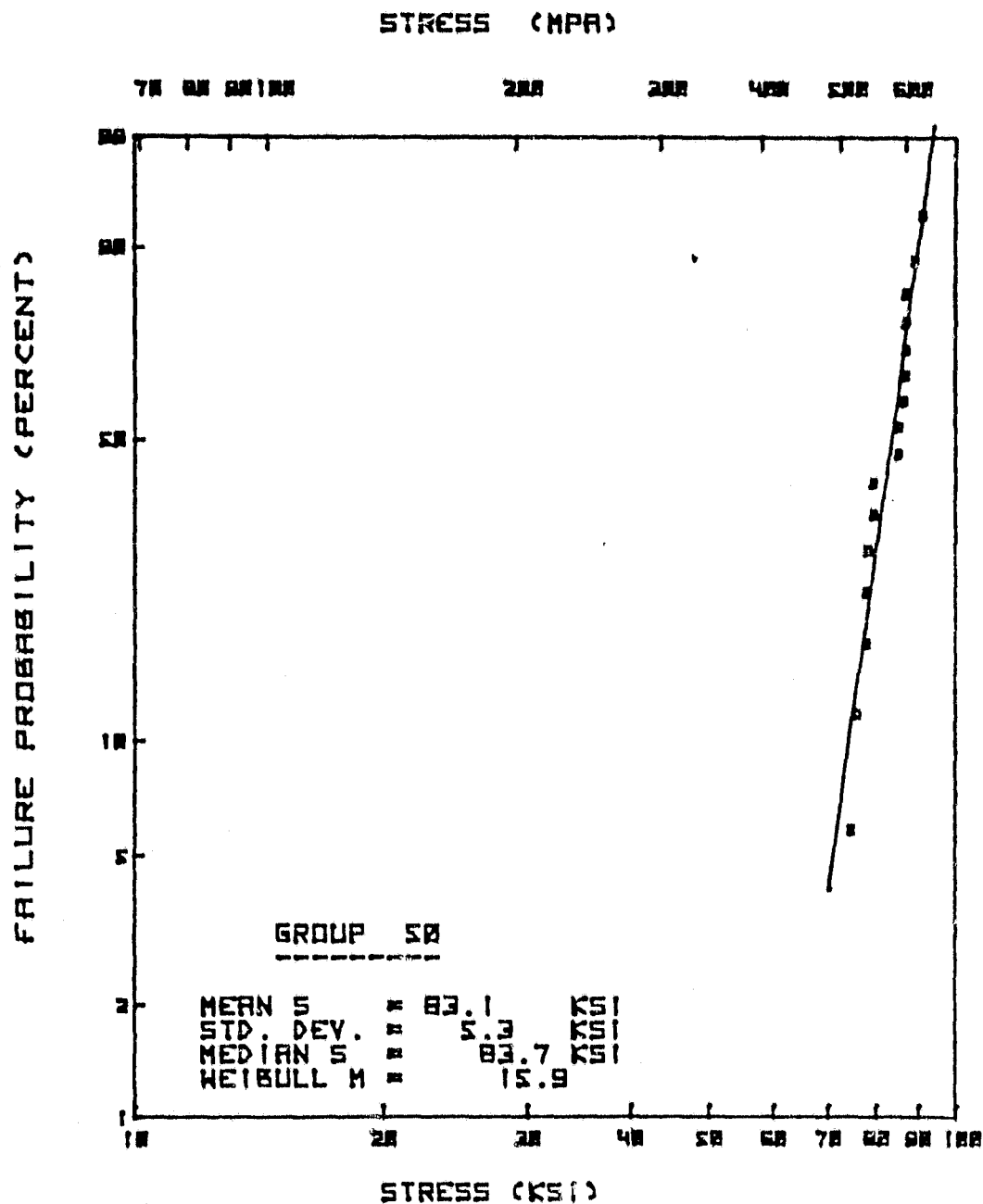


Figure 252. SNN522 Baseline Injection Molded Si_3N_4 Room Temperature MOR - Five Bars From Group 20 (Figure 1) and Eleven Bars from IITRI Evaluation.

A large number of silicon nitride simulated rotors were injected to evaluate the wide variety of molder adjustments. These include variations in injection pressure, tool clamp pressure, flow control, barrels and nozzle temperature, injection and cooling time. In spite of the wide choice of parameter variations, a problem of air entrapment within the rotor was not alleviated.

It was decided to modify the simulated rotor tool configuration. Originally, the base portion of the tool was made in two halves in order to permit future simulated vanes at the vertical parting lines. However, it was found that the tool could not be clamped with sufficient pressure to resist flashing. This caused release of injection pressure resulting in poor surface and incomplete mold fill. A new one piece base section was built which eliminated the flashing problem and improved surface cosmetics but did not eliminate air entrapment.

In the original tool design the ingate was in the shaft end. It was felt that the swirling action created by having the injected material enter the shaft first and then the backface could entrap air. The tool was again modified so that the ingate was reversed to permit material entry into the backface first and ultimately into the shaft end. This modification reduced the amount of air entrapment but did not completely eliminate it. The next tool modification designed to solve the problem of entrapped air was to provide the capability to evacuate the cavity prior to injection. It was found that the vacuum had to be turned off simultaneously with material injection or the material would flow into the vacuum system requiring extensive clean-up. However, even with the ability to evacuate the mold cavity, air within the injection molder barrel with the injection batch enters the mold with the batch material when injected.

In an alternate approach, channels were machined into the top and bottom sections of the tool to permit the flow of controlled temperature water capable of heating and/or cooling each section. Several rotors were injected with variations in tool temperatures. To a greater or lesser extent, all contained voids. Where rotors were injected that exhibited significant reduction of entrapped air, tool temperature was maintained while other injection parameters were varied such as injection speed, injection pressure, barrel and nozzle temperatures, injection and cooling time. None of these efforts were completely successful.

It was felt that possibly the direction of material injection from top to bottom was creating an improper flow thus causing poor mold fill. The tool was again modified to permit material injection from the bottom of the tool. This was accomplished by adding removable plates to one side and the bottom into which runners were machined. The tool was inverted so that injection was still into the backface of the rotor. Injected material flow is down the side of the

tool between the tool and added plate, across the bottom and up into the cavity. Several attempts to inject a rotor by varying setting parameters described above were also unsuccessful.

In order to determine the actual flow path, the ceramic was thoroughly cleaned out of the molder and replaced with clear polystyrene. After two attempts to cast a plastic rotor shape, it could be seen that instead of flowing into the cavity in a solid wave front pushing the air in front to be voided at the top, the material entered the cavity flowing up the walls leaving a void in the center. As the material continues to flow, it ultimately seals off at the shaft leaving the trapped air void within the part.

Therefore, it appeared that another form of warm molding, such as transfer molding, would be required for a successfully injected rotor. The original two-piece rotor tool is being modified to permit its use on the extruder which will serve as a transfer molder. Heater bands will be attached to the mold to control temperature and the entire assembly will be encased in a steel jacket and attached to the extruder.

2.3 Slip Casting

Slip rheology improvement with respect to the casting characteristics of SNN series slips were performed. It was felt that increasing the solids content could eliminate observed surface cracking by reducing the excessively long casting time required with previous slip compositions. Various deflocculents were evaluated until a slip composed of 78 weight percent solids content was produced with good casting characteristics. Several test plates were cast and dried without observable surface defects.

Five baseline SNN502 (slip cast) test bars were formed and sintered. The room temperature results are shown in Table 33.

TABLE 33.

Specimen No.	Sintered Density	MOR (Ksi)
2	3.23	64.9
3	3.23	64.5
8	3.23	64.5
9	3.23	62.4
10	3.18	59.5

Average MOR value: 63.2 ksi, standard deviation 2.3 ksi. The Weibull plot is shown in Figure 253.

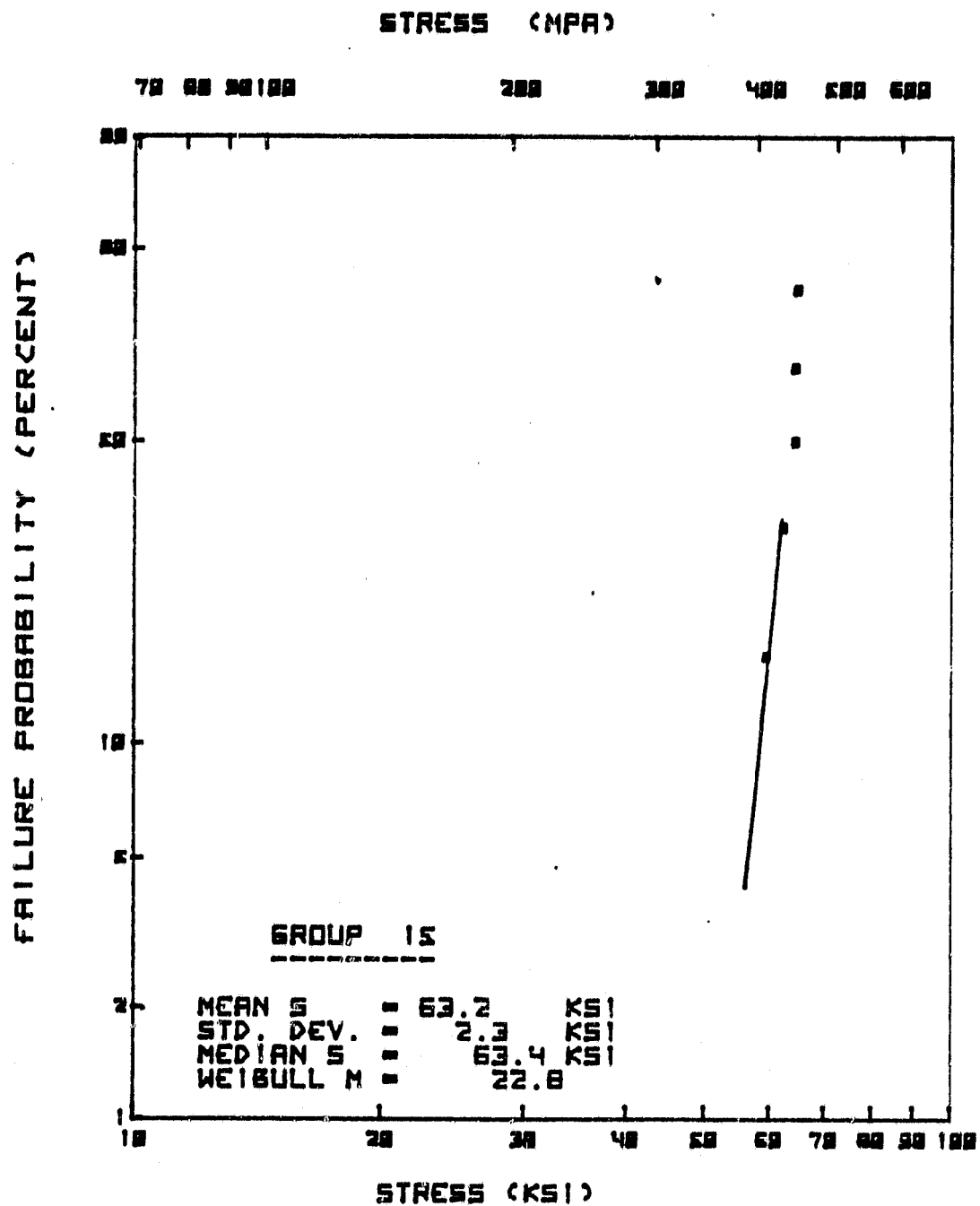


FIGURE 253.

Five additional test bars were cast in conjunction with a simulated rotor. One bar was broken prior to sintering. The remaining test specimens were sintered along with the rotor. These test results are shown in Table 34 and the Weibull plot can be seen in Figure 254.

TABLE 34.

Specimen No.	Sintered Density	MOR (Ksi)
1	3.20	67.5
2	3.23	86.0
3	3.23	78.2
4	3.22	77.2

Average MOR value: 77.2 ksi, standard deviation 7.6 ksi.

The rotor that was cast and sintered with the test specimens noted in Table 34 cracked in the hub area.

Several additional rotors were cast without observable surface defects. One of these was placed in a sintering run but cracked extensively during the cycle. A second rotor was embedded in loose silicon nitride powder in an effort to provide a more even heat distribution during heat-up. This rotor also cracked but not as extensively as the first one which indicated that slower heat-up rates would be advantageous.

The original casting technique for fabricating slip cast rotors involved a plaster mold for the backface shape with a two piece metal mold for the hub and shaft portion as illustrated in Figure 255. Slip was poured into the shaft end. It was decided to increase the plaster-slip contact in order to accelerate casting time. This was accomplished by forming a two-piece plaster mold for the hub and shaft shape and a domed backface shaped in wax. The casting direction was inverted so that slip was then poured into the "dome" end (see Figure 255).

This variation in mold position and plaster contact resulted in several successful castings of simulated rotor shapess. These were sliced in half longitudinally and showed complete fill. One of the castings was sintered to a 2.98 gm/cc density. This part was placed back in a subsequent sintering run resulting in a density of 3.1 gm/lcc indicating that longer time at sintering temperature is necessary to optimize sintered density.

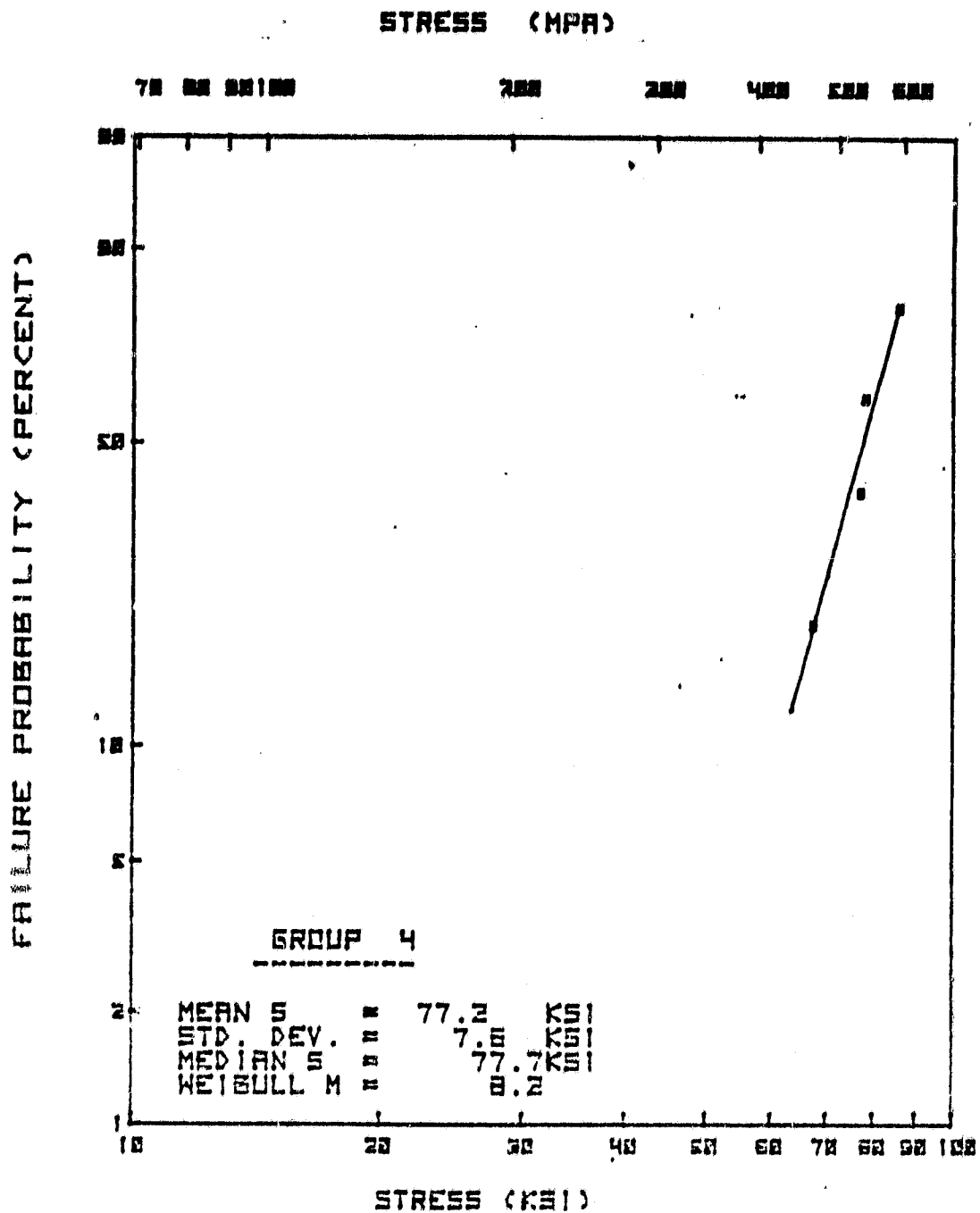
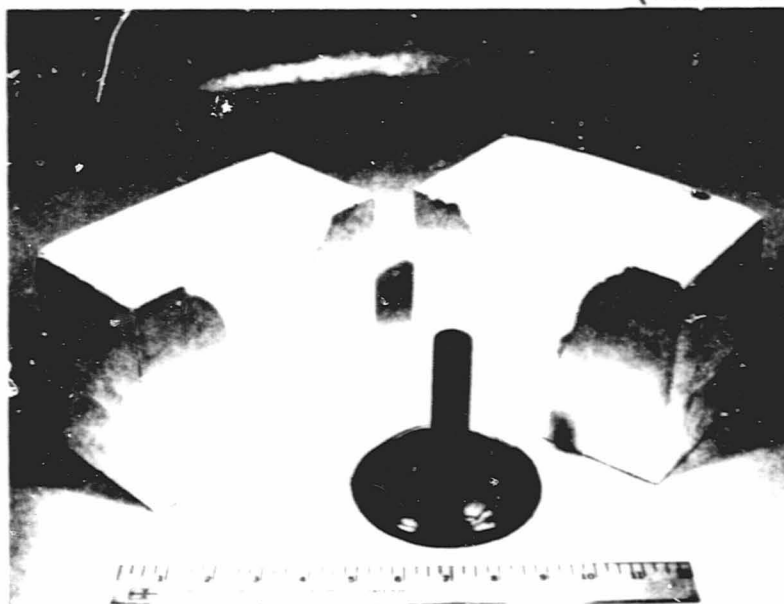
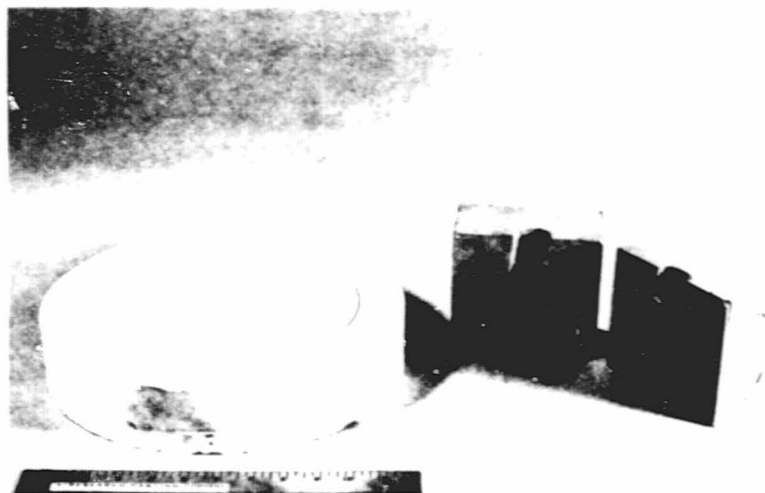


Figure 254. SNN502 Baseline Slip Cast Test Bars - Room Temperature MOR.

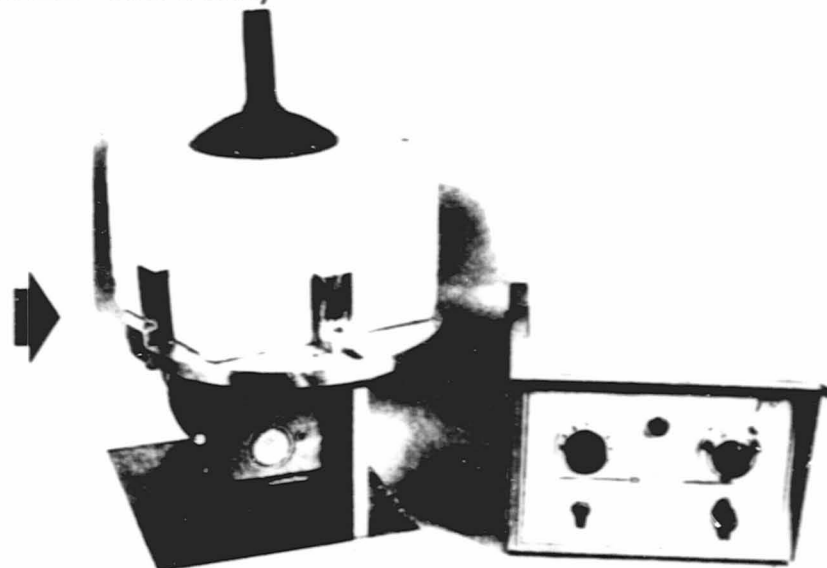
(SIMULATED ROTOR)



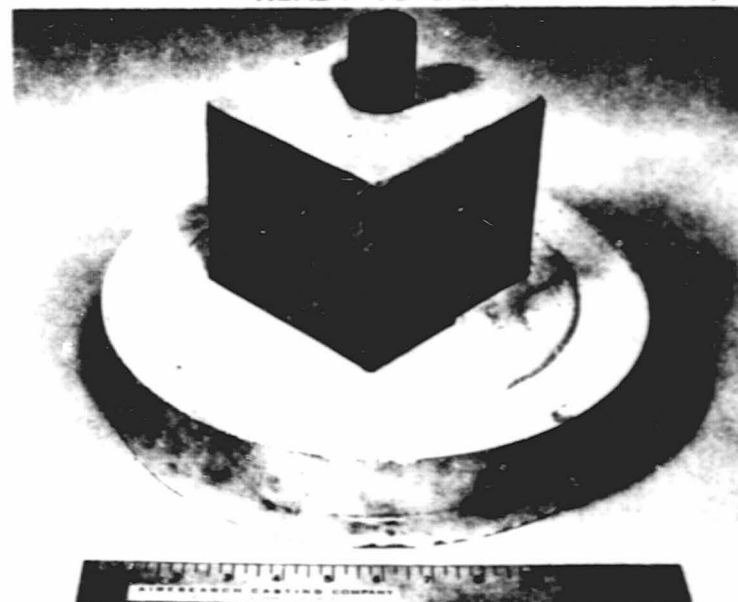
PLASTER FORM, WAX BACKFACE AND SPRUE



PLASTER BACKFACE, RUBBER OR METAL MOLD



READY TO CAST



READY TO CAST

Figure 255. Variations in Casting Techniques.

The present mode of cycle control for the sintering run is manual which provides very little latitude for cycle time variations and virtually no capability for potentially optimized longer cycles. Automating the Inductotherm power supply will permit the needed cycle time latitude deemed to be necessary. Automated cyclic controls have been procured and one expected to be operational in September 1980.

Four additional SNN502 slip cast rotors were fabricated during this report period. One cracked upon removal from the mold. A second rotor cracked after air drying. The third and fourth appeared to be crack-free. One of these was placed in a drying oven and the temperature was slowly increased until the chamber temperature was at 170°F and the skin temperature of the rotor was 100°F. At this temperature cracking could be observed and the test was discontinued. The fourth rotor will be dried in a humidity controlled oven where, at the start of the cycle, the humidity will be high as the temperature is gradually increased and the humidity is gradually decreased. This cycle is typical of drying classical clay-ware and may also be appropriate for this system.

Other slip improvement experiments involved calcining the GTE-SN502 "as-received" powder, pulverizing the agglomerates and screening the resulting powder. Slip was prepared and a 3 inch x 3 inch x 1/4 inch plate was cast along with a 1/2 inch diameter x 1/4 inch disc. Both were sintered without cracking. The plate density is 3.17 gm/cc and that of the disc; 3.20 gm/cc. Additional experimentation in both systems is in progress.

2.4 Alternate Materials

Sinterable silicon nitride powder systems other than GTE-SN502 material was also evaluated.

A small sample of Lucas SYALON 342/32 powder was received and prepared into an injection mold batch. Efforts to inject this material into a stator vane tool were unsuccessful in that the material would not fill the cavity and exhibited excessive shrinkage.

A small quantity of lubricant was added to the batch which improved the mold fill. These vanes were sintered and X-rayed. The X-Rays revealed internal flaws such as voids and density variations. Inasmuch as the Lucas SYALON material is considered to be a viable candidate for the rotor, the efforts to inject stator vanes was discontinued and attempts to fabricate rotors were initiated.

After several simulated rotors were injected and sectioned for examination, it was decided to alter the direction of material entering the mold. Originally the sprue was located at the shaft end but it was found that the powder/binder chilled out before complete mold fill could be realized. The sprue was plugged and a new sprue was drilled

into the opposite end where the material would enter the larger mass area first. Although this configuration has not eliminated the incomplete mold fill, homogeneity is expected to improve with the ability to control mold temperature. However, the limited quantity of remaining powder forced the abandonment of rotor fabrication for the present. The remaining SYALON material has been injected into test bars. One-half of these were shipped to Lucas for sintering and the remaining half will be sintered at ACC in a standard sintering run. Lucas will return the bars after sintering for evaluation simultaneously with ACC sintered bars to evaluate the efficiency of each sintering cycle and equipment.

A small sample of sinterable alpha silicon nitride powder from Toshiba (Japan) also was procured. Several small batches of varied Si_3N_4 : Y_2O_3 : Al_2O_3 ratios were prepared and cold pressed into discs and sintered. The material looks promising in one composition which sintered to 3.27 gm/cc density. A larger batch of this composition was prepared for injection molding. Test bars were molded but were of very poor quality. X-Ray radiography revealed material lamination and internal flaws. Flexural strength tests could be conducted on only three bars at room temperature and three bars at 2200°F. The average value of the room temperature bars was 47.7 ksi with a standard deviation of 8.7 ksi. The average value of the bars broken at 2200°F was 67.4 ksi with a standard deviation of 4.6 ksi.

Low shrinkage, high density (SRN series) material compositions were experimentally evaluated. Two compositions containing different nitriding aid chemistries were injection molded into test bars. Group 1 bars were sintered after nitriding with the density increasing from 2.7 to 3.1 gm/cc and the room temperature MOR increasing from 32 to 40 ksi. Group 2 test bars increased from 2.7 to 3.05 gm/cc and room temperature MOR increased from 35 to 59 ksi.

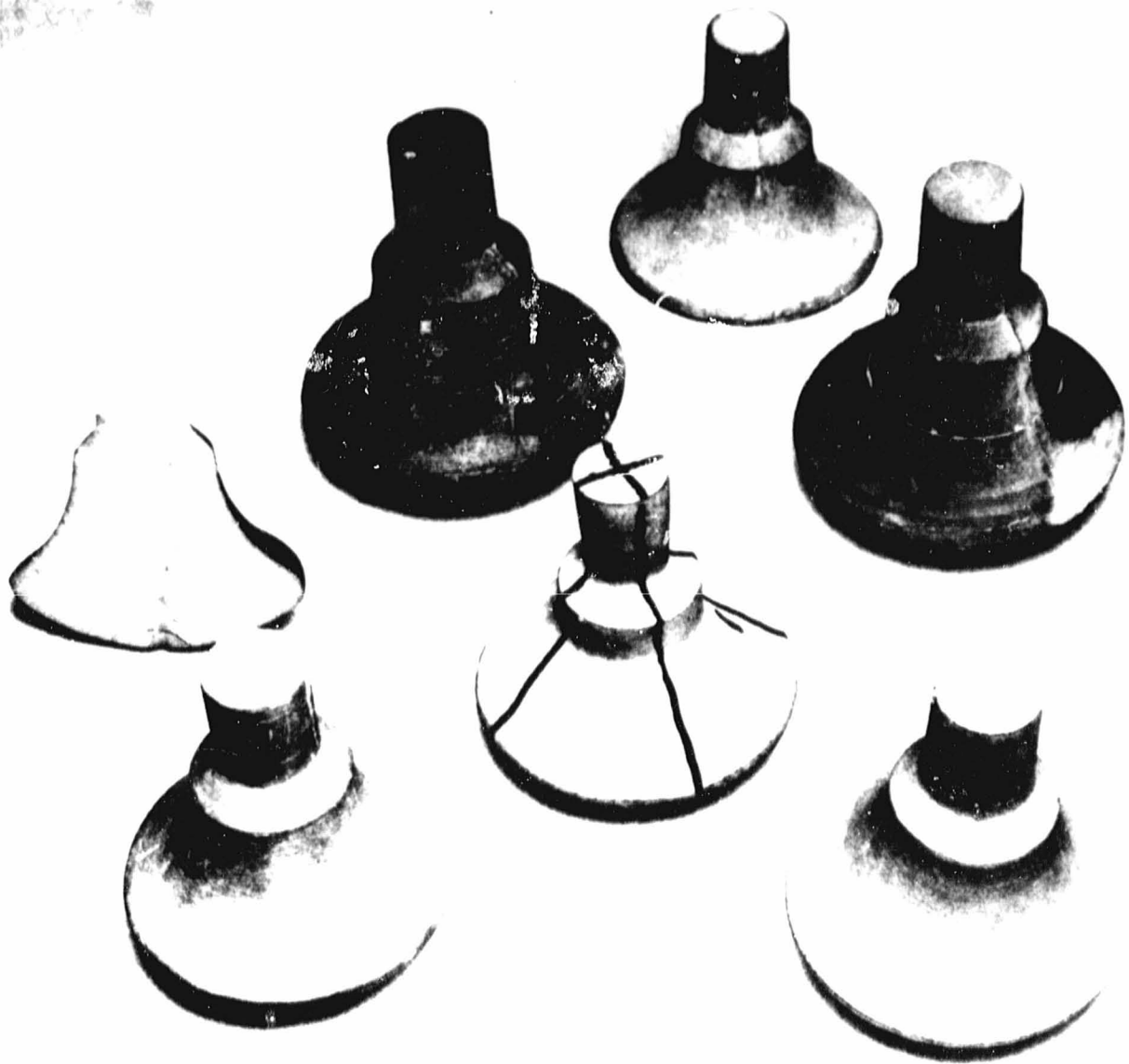
Several SRN series rotors were slip cast along with test bars. However, the green density was high and the weight gains during nitriding were low indicating substantial amounts of unreacted silicon.

An SRN802, slip cast rotor with lower solids content than previously cast rotors in this materials system was cast and is in the present nitriding run. Results will be reported in the next report period.

A summary of several cast simulated rotors is illustrated in Figure 256.

C-5

ORIGINAL PAGE
BLACK AND WHITE PHOTOGRAPH



SNN AND SRN SERIES SIMULATED ROTORS

SPA 6386-114

Figure 256. AGT Rotor Development.

3.0 CERAMIC STRUCTURES

3.1 Materials and Process Development

RBN104 baseline slip was cast into plates which were machined into test bars at AiResearch Phoenix. These were nitrided and the required 300 test specimens were shipped to AiResearch Phoenix for evaluation.

RBN126 baseline injection molded test bars were also nitrided and shipped to AiResearch Phoenix for evaluation. The shipments of RBN104 and RBN126 completes the required number of baseline RBN series test specimens for the primary and back-up fabrication processes.

Experiments aimed toward density control of silicon slips prepared with various fractions of air classified powder were performed. Limits exist between pH and green density such that the controllable range of green density by pH adjustment alone appears to be between 1.65 and 1.75 gm/cc.

Another experiment aimed toward slip improvement involved wet milling in an effort to disperse agglomerates. A slip batch was prepared and permitted to age until outgassing had apparently ended. One half of the slip batch was remilled for two hours after which both batches were cast into plates and, subsequently machined into test bars and nitrided in the same run. Table 35 shows the comparative results of the experiment.

TABLE 35. WET MILLED VERSUS BASELINE RBN104

	Wet Milled	Baseline
Green Density	1.74	1.71
Nitrided Density	2.72	2.77
Percent Weight Gain	59.1	60.5
Characteristic Strength Ksi		
Weibull Slope		

Judging by the improvement in Weibull slope, wet milling appears to be advantageous. Continued experimental work will be conducted for more definitive evaluation.

Another materials improvement evaluation involved post nitriding heat treatment of flash oxidation.

Flash oxidation of RBN104 test bars was conducted to determine the potential improvement in oxidation resistance of reaction bonded silicon nitride. Figure 257 shows the results recorded as an average of 10 test bars for each oxidation treatment and each subsequent post-oxidation exposure. In addition to the 900°C/50 hour exposure shown, each group was also subjected 900°C/150 hour exposure. An identical flash oxidation experiment was conducted on baseline RBN126 (injection molded) test bars. Table 36 presents a comparison between slip cast and injection molded test specimens at identical heat treatments.

In order to determine the actual degree of oxidation, five test bars were inserted in the oxidation furnace and the temperature was raised to 1100°C and held for 2 hours. Four place weight measurements were taken before and after and the percent weight gain was calculated. Four of these bars were again placed in the furnace at 1100°C and held for 166 hours. Weights were again taken and percent change in weight both from unoxidized bars and 2 hour oxidized bars were calculated. The identical experiment was performed on five other test bars at 1350°C. After the 1100° and 1350°, 166 hour exposure, the test specimens had very low weight gains. At 1100°C the gain was 0.138 percent and at 1350°C the gain was 0.100 percent.

Other material and processing parameter variations that have been conducted during this period include nitriding capability of thick sections, nitriding aid chemistries associated with different levels and combinations of nitriding aid and the effect of particle size blending of powders. Also the effect of a 4 percent helium addition to the normal H₂-N₂ nitriding atmosphere. Test plates of RBN104 material were cast in thicknesses ranging from 1/4 inch to 1-3/4 inches to evaluate the nitriding capability of the standard cycle. These plates have been nitrided and are presently being evaluated for the presence of unreacted silicon. Plates cast to determine the effect of nitriding aid changes included baseline 3 percent Fe₂O₃, 1-1/2 percent Fe₂O₃, and 1-1/2 percent Fe₂O₃ Cr₂O₃. Plates that were cast to evaluate the effect of particle size blending included slips prepared from 1-10µm, 1-20µm and 2-20µm fractions.

Both the nitriding aid and the particle size fraction test specimens were machined into test bars. One half of each of these groups were nitrided in a standard nitriding cycle and the remaining half was nitrided in cycle containing a 4-percent helium atmosphere addition. The data on each of these studies are presently being evaluated.

B. Fabrication Development

Turbine Baffle

As part of the feasibility study, the simulated baffle with integral struts was successfully cast and nitrided. The unit was delivered to AiResearch Phoenix for evaluation. Figure 258 shows the simulated shape.

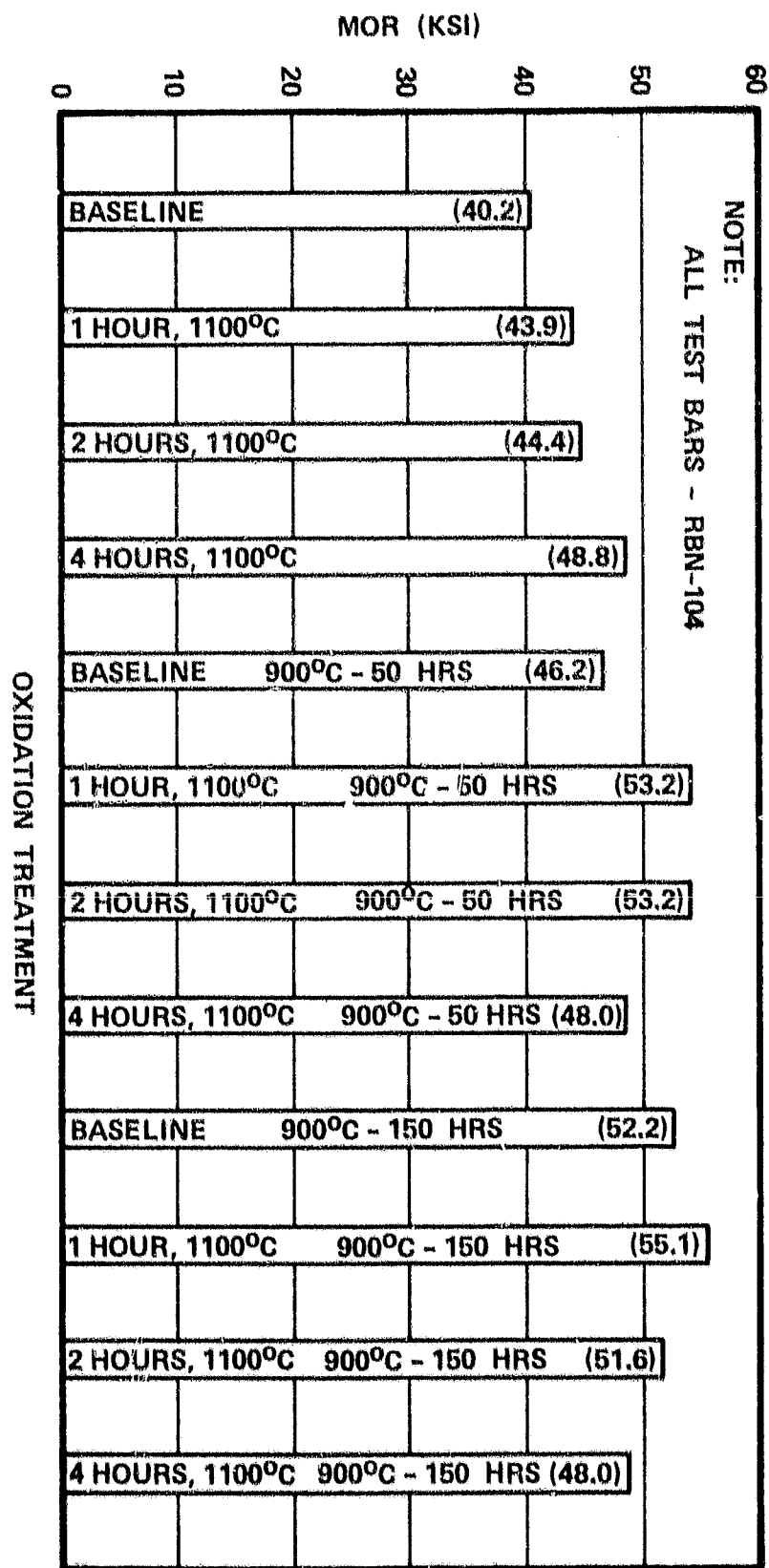


Figure 257. Results of Flash Oxidation Treatment and Post Oxidation Exposure at Elevated Temperature.

TABLE 36.

Oxidation Exposure	Slip Cast			Injection Molded		
	MOR (ksi)	S/D (ksi)	M	MOR (ksi)	S/D (ksi)	M
Baseline-No exposure	40.2	5.2	7.5	33.4	3.3	9.3
1100°C/1 hour	43.9	5.9	7.0	33.2	4.3	7.1
1100°C/2 hours	44.4	11.2	3.8	35.0	6.8	4.7
1100°C/4 hours	48.8	4.1	11.4	36.9	4.2	8.1
No flash-900°C/50 hours	46.2	5.9	7.4	36.1	5.8	5.4
1100°C/1 hour-900°C/50 hours	53.2	5.5	8.6	38.1	5.3	6.4
1100°C/2 hours-900°C/50 hours	48.0	6.2	7.2	39.4	3.0	12.1
1100°C/4 hours-900°C/50 hours	48.0	9.4	4.9	39.5	3.3	11.3
No flash-900°C/150 hours	50.7	8.4	5.9	36.6	2.9	12.1
1100°C/1 hour-900°C/150 hours	55.1	5.0	10.3	38.5	4.9	7.3
1100°C/2 hours-900°C/150 hours	51.6	6.4	7.8	40.4	4.2	8.8
1100°C/4 hours-900°C/150 hours	48.0	7.8	5.8	41.5	4.1	9.6

ORIGINAL PAGE
BLACK AND WHITE PHOTOGRAPH



Figure 258. Simulated Turbine Baffle With Integral Struts.

Turbine Inner Diffuser Housing

The simulated turbine inner diffuser was successfully cast and nitrided (Figure 259). This also was shipped to AiResearch Phoenix for evaluation.

Both the simulated baffle and simulated inner diffuser had nitrided weight gains of 59 percent.

A meeting was held at AiResearch Phoenix on April 8, 1980 to discuss each of the MOD A component prints. As a result of the meeting several changes were effected and prints have been revised accordingly. Final tooling design prints for the components of ACC responsibility will soon be ready to submit to tooling vendors for quotation and delivery dates. Tooling orders are expected to be placed shortly.

ORIGINAL PAGE
BLACK AND WHITE PHOTOGRAPH



Figure 259. Simulated Turbine Inner Diffuser Housing.

APPENDIX III

CARBORUNDUM COMPANY ADVANCED GAS
TURBINE (AGT) POWERTRAIN PROGRAM FIRST
SEMI-ANNUAL TECHNICAL PROGRESS REPORT,
COMMON WORK

1.0 INTRODUCTION

This Semi-Annual Progress Report of the AGT Program Common Work summarizes the technical activities between October 1979 and June 1980. The objective of the Common Work is to provide baseline technology for fabrication of both AiResearch and DDA AGT components. The work plan consists of five tasks:

- o Rotor Fabrication
- o Nondestructive Evaluation
- o Mechanical Properties
- o Physical Properties
- o Machining Studies

2.0 ROTOR FABRICATION

2.1 Injection Molding

Because of the present limitations in baking thick sections of injection molded SiC, an alternative approach is to injection mold segments, process them separately and then join them by appropriate means. A rotor tool from an earlier Chrysler program was modified to evaluate this approach. The tool modification consisted of fabricating a series of inserts which when placed into the existing tool cavity, allowed a shell, an inner core, and a bottom plate to be formed separately. The segments could then be used for bonding studies. Leaving out the inserts still allowed solid rotor hubs to be molded.

Molding, baking, and sintering of rotor segments made with the modified tool were achieved with a minimum of visual defects. These segments were used for joining development studies by hot pressing.

Baking of large solid rotors could not be accomplished by using an extended baking cycle, plasma bake or vacuum bake approaches. It is recommended that some efforts be undertaken under the unique AGT programs where mold tool design is better.

Successful joining of rotor segments was achieved by hot pressing using an extrudable silicon carbide mix at the interface. Consistently high densities (>3.13 g/cc) for the final assembly were obtained. Grain growth across the joint interface was also observed by optical microscopy. In test bars, base material or joint material failure occurred in many instances rather than joint failure.

2.2 Alternate Fabrication Methods

Significant progress was made in the thixotropic casting of reaction bonded silicon carbide rotors. Using a mix with an optimized carbon content resulted in crack-free casting and curing, and complete siliconization.

A shaft attachment to a thixocast reaction bonded silicon carbide rotor using a thixocast reaction bonded silicon carbide mix was successfully demonstrated. Visual examination revealed the bonding to be excellent.

As an initial effort, 125 injection molded test bars of α -SiC were fabricated, inspected, and divided into 5 groups of 25 bars. Twenty-five (25) bars were retained as a control to evaluate strength. Twenty-five (25) bars each were shipped to:

- San Fernando Laboratories
- Materials Technology Corporation
- Deposits and Composites, Inc.
- Refractory Composites, Inc.

Five (5) bars will be used to establish coating conditions and twenty (20) bars will be coated by each for Carborundum evaluation.

The first phase of the HIP'ing program will evaluate densification of partially sintered silicon carbide with various densities and hence decreasing amounts of open porosity. Hipping will be conducted at NASA. Microstructural analysis of bars of α -SiC hipped earlier at NASA indicated ksi pore shrinkage at 1950°C but not at lower temperatures.

3.0 NONDESTRUCTIVE EVALUATION

The seeding and fabrication of large (125-250 μ m) and intermediate (50-125 μ m) size void disks of α -SiC of all thicknesses have been completed. The fabrication of disks with large (125-250 μ m) carbon inclusions was completed. NDE will follow for these specimens. The fabrication of disks with B₄C inclusions is in progress.

An evaluation of Knoop flaws on as-fired SiC specimens has been completed by Prof. R. L. Thomas of Wayne State University using the SPAM technique. Although the SPAM traces show good resolution and reproducibility and display the characteristic defect features of these surfaces, the intrinsic defects on the SiC surface made characterization of the Knoop indentations very difficult.

An evaluation of Knoop flawed SiC disks also was completed by Sonoscan, Incorporated using the SLAM technique. Although all of the Knoop flaws were detected by SLAM it was difficult to distinguish them from the background on as-fired surfaces.

4.0 MECHANICAL PROPERTIES

The baseline properties data for alpha silicon carbide manufactured by different processing techniques have been evaluated and the results are given in Tables 37 and 38.

In all cases, the specimen cross section was $1/8 \times 1/4$ inch and a total of 30 specimens were tested per each baseline data.

It should be noted that the strength data obtained for injection molded specimens were obtained for as-furnaced surface condition. For the case of cold pressed and slip cast material, the surfaces were machined by using 180 grit diamond wheel. The test bars were annealed for 2 hours in argon atmosphere prior to flexural test. Fractography still is to be conducted.

TABLE 37. STRENGTH DATA FOR INJECTION MOLDED ALPHA SiC

4-Point Bend; 1.5 In Outer Span; 0.5 In Inner Span

Material		Average Strength (10 ³ psi)	Standard Deviation (10 ³ psi)	Weibull Modulus (m)	Charact. Strength (10 ³ psi)	Low Strength (10 ³ psi)	High Strength (10 ³ psi)
77°F Data	As-Received	54.49	13.07	4.98	64.70	37.26	83.41
	Annealed	61.52	11.05	5.76	66.19	40.56	78.62
2192°F Data	Annealed	57.46	10.31	5.97	61.85	35.28	76.92

TABLE 38. ROOM TEMPERATURE STRENGTH DATA FOR COLD PRESSED AND SLIP CAST ALPHA SiC

4-Point Bend; 1.5 In Outer Span; 0.5 In Inner Span

Material		Average Strength (10 ³ psi)	Standard Deviation (10 ³ psi)	Weibull Modulus (m)	Charact. Strength (10 ³ psi)	Low Strength (10 ³ psi)	High Strength (10 ³ psi)
Cold Pressed		48.05	6.25	8.42	50.78	36.24	59.62
Slip Cast		54.46	11.39	4.84	59.40	29.22	72.79

PRECEDING PAGE BLANK NOT FILMED

APPENDIX IV

CARBORUNDUM COMPANY ADVANCED GAS
TURBINE (AGT) POWERTRAIN PROGRAM FIRST
SEMI-ANNUAL TECHNICAL PROGRESS REPORT,
UNIQUE WORK

ORIGINAL PAGE IS
OF POOR QUALITY

1. INTRODUCTION

This report summarizes the first 6 months work carried out by the Carborundum Company for AiResearch Phoenix on the Advanced Gas Turbine Powertrain System Development Program authorized under NASA Contract DEN3-167 and sponsored by the Department of Energy (DOE).

As a major subcontractor to the program, Carborundum is required to develop silicon carbide components for the hot flow path of the AGT engine. Overall design of the engine is the responsibility of AiResearch Phoenix. However, several joint meetings were held in which Carborundum provided inputs on the capability of various fabrication methods to meet the component geometries and dimensional tolerances required. As a result, several iterations were required before finalization of component design.

The current development program separates rotor development from static structures development. Thus far, injection molding, slip casting, and green machining have been selected for fabrication of silicon carbide components for the program. Wherever possible, components were provided with a secondary fabrication method in the event that problems arise with the primary approach.

In principle, the best fabrication approach for the rotor would be injection molding. This technology has been successfully demonstrated to produce complex shapes economically with a high degree of precision on small items such as turbine blades, stator vanes, small rotors and the like where maximum cross-sections not exceeding 1 inch are encountered. However, the AiResearch Phoenix rotor designed for the AGT engine challenges the current state-of-the-art because of its size, which exceeds 3 inches in diameter at the base of the hub. In this thickness, the bake-out of organic binders becomes increasingly difficult and even when very slow temperature increases over long periods of time are used, cracked parts frequently result. Although it is anticipated that technology developments will advanced sufficiently so that thick molded sections can be devehicilized efficiently by the end of the program. This assumption provides high risk for the alpha silicon carbide rotor fabrication approach. Therefore, alternative approaches based on currently available technology were selected to provide turbine rotors for the early part of the program. These include a variety of ceramic-to-ceramic bonding methods which are applied to the assembly of smaller components. The Carborundum rotor development program emphasized these approaches during the first 6 months of the project.

2. ROTOR DEVELOPMENT

The AiResearch Phoenix approach to rotor development encourages the evaluation of multiple process variations at the start of the program. The number will be narrowed down at milestone points. Further, in order to demonstrate that the material properties and fabrication approaches are adequate prior to procuring complex tooling, it was stipulated that initial efforts be directed toward producing and evaluating a non-bladed rotor which simulates the bladed rotor in mass and shape. The simulated rotor design is shown in Figure 260. Based on future needs to produce a complex bladed rotor, Carborundum selected the injection molding process to produce the part. An injection molding tool was designed with removable cores to produce two shell configurations as well as a solid hub. The shells represent thicknesses within the processing limits of current technology while the solid hub provides development opportunities for thick section binder removal and subsequent sintering studies.

2.1 Molding Development

Molding activities for the rotor program were carried out on a Reed 250 TG machine equipped with a GE PM 2000 solid state control incorporating microprocessors for repeatable set-ups via digital inputs. In addition, auxiliary microprocessors by SCI were installed for cycle repeatability and fine control adjustment.

Important molding variables which were investigated include: melt temperature, mold temperature, injection velocity, and peak cavity pressure. Pressure was measured using a transducer type sensor positioned behind a dummy ejector pin within the cavity.

Several hundred pounds of molding compound were prepared for use exclusively in rotor molding development.

2.1.1 First Generation Rotor Shell

The tooling for the first generation simulated rotor shell was installed on the 250T Reed Reciprocating Screw Injection Molding Machine at G-W* alpha silicon carbide test molding facility. Prior to molding, the ejector mechanism was reworked to provide freer sliding action.

Preliminary molding was carried out to assess functional design and to verify dimensional accuracy of the tool.

*G-W Plastic

ORIGINAL PAGE IS
OF POOR QUALITY

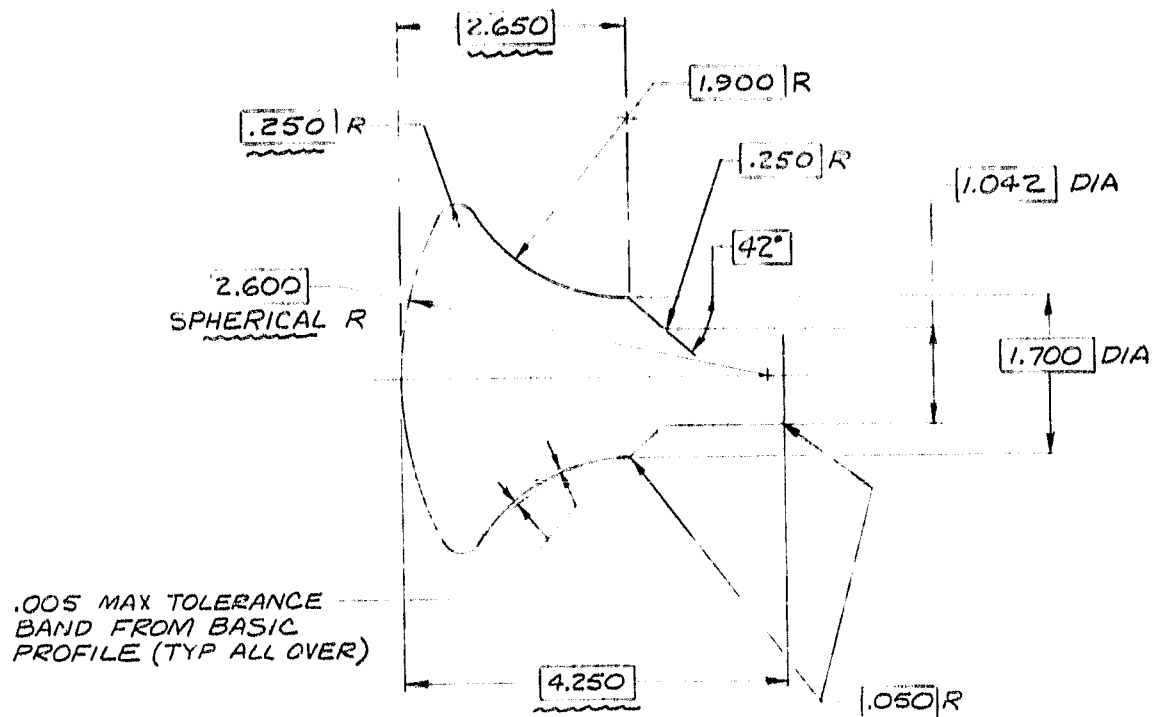


Figure 260. Spin Test Rotor.

Figures 261 and 262 show the back and front sides of the tool mounted on the press platens. The projecting core was designed to seat on four sections of the sprue bushing thereby allowing the cavity to fill through four equally spaced gates. A molded rotor shell with sprue attached is shown prior to ejection in Figure 263.

All of the rotor shells showed visible flow line indications concentrated at the lower section of the inner rim. A cross section of the molded rotor shell is shown in Figure 264 and the arrows indicate the region where the flow lines are predominant. Attempts were made to correct this problem by enlarging the gates to allow maximum pressure transmission for a longer period of time. Subsequent molding trials with the enlarged gates produced no noticeable improvements.

A summary of molding conditions is shown in Table 39. Since changes in molding conditions produced only subtle changes in the product, a decision was made to modify the core to produce a filling pattern consistently from thick to thin sections.

2.1.2 Second Generation Rotor Shell

Since the enlarged gates did not produce significant improvements in minimizing flow lines on the original shell, the core was changed to provide a thinner wall in the problem area. This was accomplished by shrink fitting a conical ring over the existing core. The ring insert can be reconfigured and is removable should the original wall be desired in the future.

Molding was carried out and conditions determined to produce acceptable parts. As with the original configuration, the range of molding conditions investigated produced marginal changes in the product. A summary of molding conditions is found in Table 40. The overall result of the core modification, however, was a minimization of flow lines. The flow lines appeared much smaller and closer to the edge of the inner rim. At the present time, the consequences of flow lines in this region of the rotor is not known since joining techniques may be effective in filling and healing whatever linear indications are present. Figure 265 shows a cross section of the molded shell.

Thus far, both configurations are being evaluated in further processing steps.

2.1.3 Solid Simulated Rotor

During this period, a modest effort was made to produce the solid simulated rotor configuration. This was accomplished when the original core was removed for modification.

ORIGINAL PAGE
BLACK AND WHITE PHOTOGRAPH

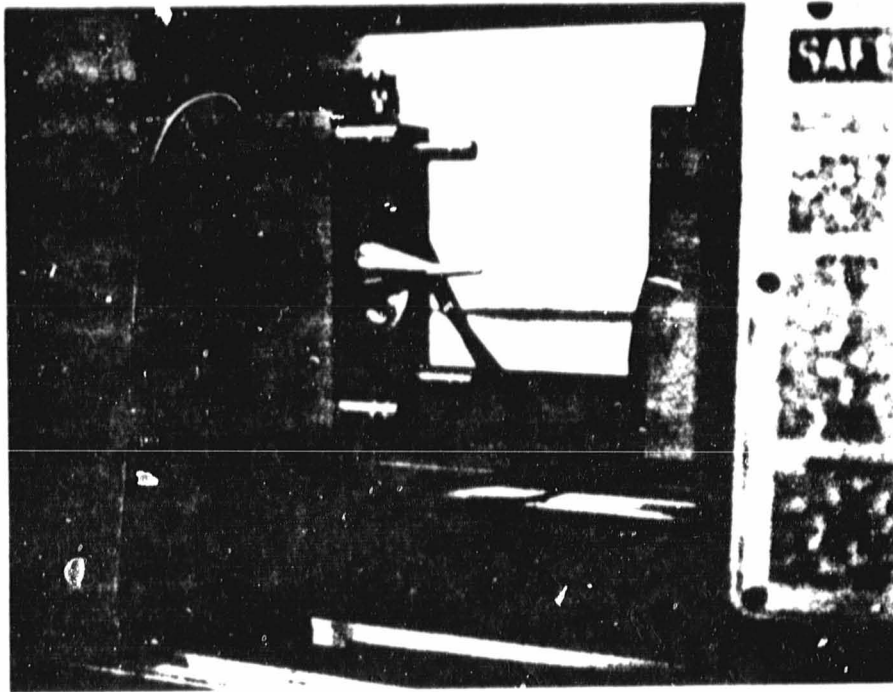


Figure 261. Backside of Simulated Rotor Shell Tool.

ORIGINAL PAGE
BLACK AND WHITE PHOTOGRAPH

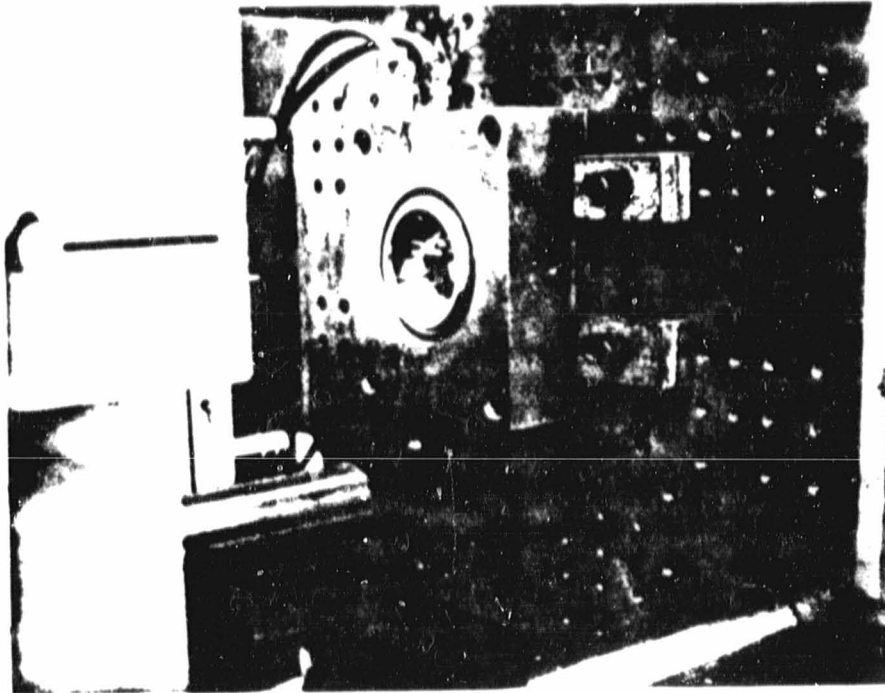


Figure 262. Front Side of Simulated Rotor Shell Tool.

ORIGINAL PAGE
BLACK AND WHITE PHOTOGRAPH

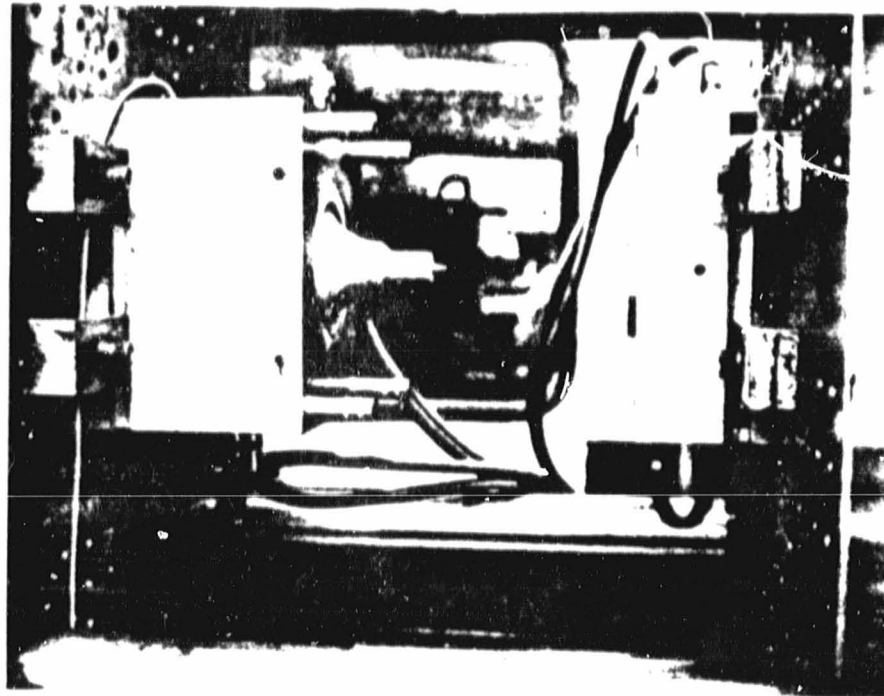


Figure 263. Molded Rotor Shell Prior to Ejection.

ORIGINAL PAGE
BLACK AND WHITE PHOTOGRAPH

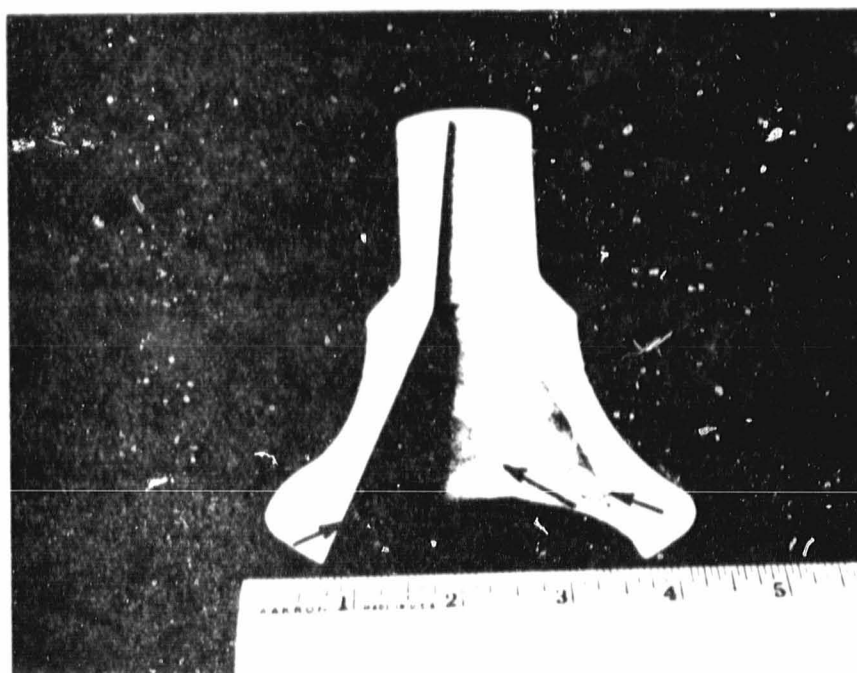


Figure 264. Cross-Sectional View of First Generation Rotor Shell as Molded.

TABLE 39. MOLDING SUMMARY FIRST GENERATION SHELLS

Part No	Temperature (°F)	Pressure (psi)	Velocity*	Mold Temperature (°F)	Comments
1	310	NA	Constant M	100	Short Shot
2	310	NA	Constant M	100	4 Gates
3	310	NA	Constant M	100	4 Gates
4	310	NA	Constant M	100	1 Gate
5	310	NA	Constant M	120 - 80	1 Gate
6	310	NA	Constant M	120 - 80	1 Gate
7	310	NA	Constant M	125	4 Gates
8	310	NA	Constant M	125	1 Gate
9	310	1700	Constant M	125	1 Gate
10	310	1700	Constant M	125	1 Gate
11	310	1700	Constant M	125	1 Gate
12	310	1700	Variable S-F	125	1 Gate
13	310	1700	Variable S-F	125	1 Gate
14	310	1700	Variable S-F	125	1 Gate
15	310	1700	Variable S-F	125	1 Gate
16	310	1700	Variable S-F	125	1 Gate
17	310	1700	Variable S-F	125	1 Gate
18	310	1700	Variable S-F	125	1 Gate
19	310	1700	Variable S-F	125	1 Gate
20	310	1700	Constant F	125	4 Gates
21	310	1700	Constant F	125	1 Gate
22	310	1000	Constant F	125	1 Gate
23	310	1000	Constant F	125	4 Gates
24	310	1700	Constant F	125	4 Gates
25	320	1400	Variable S-F	80	4 Gates Enlarged
26	350	1400	Variable S-F	100	4 Gates Enlarged
27	350	1400	Variable S-F	100	4 Gates Enlarged
28	300	1400	Constant F	100	4 Gates Enlarged
29	300	1400	Constant F	100	4 Gates Enlarged
30	300	1400	Constant F	100	4 Gates Enlarged
31	310	1450	Constant F	100	4 Gates Enlarged
32	310	1400	Variable S-F	120	4 Gates Enlarged
33	310	1400	Variable S-F	120	4 Gates Enlarged
34	310	1400	Variable S-F	120	4 Gates Enlarged
35	310	1400	Variable S-F	120	4 Gates Enlarged
36	310	1400	Variable S-F	120	4 Gates Enlarged
37	310	1400	Variable S-F	120	4 Gates Enlarged
38	310	1400	Variable F-S	120	4 Gates Enlarged
39	310	1400	Variable F-S	120	4 Gates Enlarged

* M = Medium
 S-F = Slow Initial - Fast Final
 F = Fast
 F-S = Fast Initial - Slow Final

TABLE 40. MOLDING SUMMARY SECOND GENERATION SHELLS

Part No	Temperature (°F)	Pressure (psi)	Velocity	Mold Temperature (°F)	Comments
30-1	350	1400	Constant M	100	4 Gates Enlarged
31-2	350	1400	Constant S	100	4 Gates Enlarged
32-3	350	1400	Constant S	100	4 Gates Enlarged
33-4	330	1400	Variable S-F	100	4 Gates Enlarged
34-5	330	1400	Variable S-F	100	4 Gates Enlarged
35-6	330	1400	Variable S-F	100	4 Gates Enlarged
36-7	330	1400	Variable F-S	100	4 Gates Enlarged
37-8	330	1400	Variable F-S	100	4 Gates Enlarged
38-9	330	1400	Variable F-S	100	4 Gates Enlarged
45-10	300	1400	Constant F	100	4 Gates Enlarged
46-11	310	1400	Constant M	120	4 Gates Enlarged

ORIGINAL PAGE
BLACK AND WHITE PHOTOGRAPH

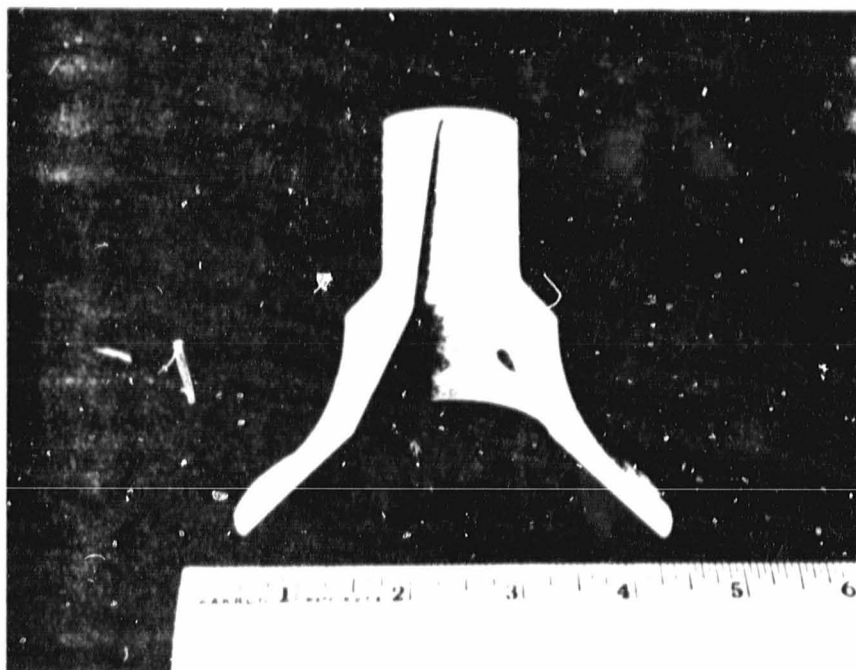


Figure 265. Cross-Sectional View of Second Generation
Rotor Shell as Molded.

Initially, the thickness of the part posed problems during molding due to shrinkage on cooling and air entrapment during filling. By changing molding conditions, shrinkage could be accommodated and porosity due to air entrapment could be reduced but not completely eliminated. Progress in porosity reduction is shown in Figure 266. It is expected that porosity could be completely eliminated by further work on molding and/or tooling modifications. This activity is planned for the next reporting period.

Conditions used to produce four solid configurations for further processing are listed in Table 41.

2.2 Baking Development

Binder removal is one of the most critical steps in the production of sintered alpha silicon carbide shapes. Although other techniques were considered, thermal degradation of the binder was selected since a great deal of prior experience existed with this method.

In order to be successful in the removal of organics from an injection molded silicon carbide body, heat must be applied slowly at a gradually increasing rate to produce micropassages which allows the decomposition products from the binder to escape from the body without causing any cracks. An inert environment is required to prevent oxidation of the SiC at the peak temperatures used. A uniform temperature distribution is needed in the ovens to remove the binder without introducing cracks throughout the part. The overall length of cycle and rate of temperature rise is dependent on part size and cross sectional thickness.

Cam controlled ovens with percentage on-off timers were used for binder bake-out of the injection molded simulated rotor shapes.

All of the processed parts from the second generation design were baked out crack-free and suitable for sintering; whereas only 6 out of 34 from the first generation design were crack-free. Much of the cracking on the latter was slight and they could be processed further to produce sintered shells for subsequent joining work.

To date, four solid configurations have been baked using two different temperature histories. A group of two were baked using a standard cycle normal for large parts. Both items were severely cracked and could not be processed further. Another group of two were baked out using one-half the rate of temperature rise as the standard cycle. The overall cycle, therefore, was lengthened by a factor of 2. Both pieces were cracked where the shaft is attached to the shoulder of the rotor. The hub, on the other hand, which is the thickest part of the rotor, remained intact.

ORIGINAL PAGE
BLACK AND WHITE PHOTOGRAPH

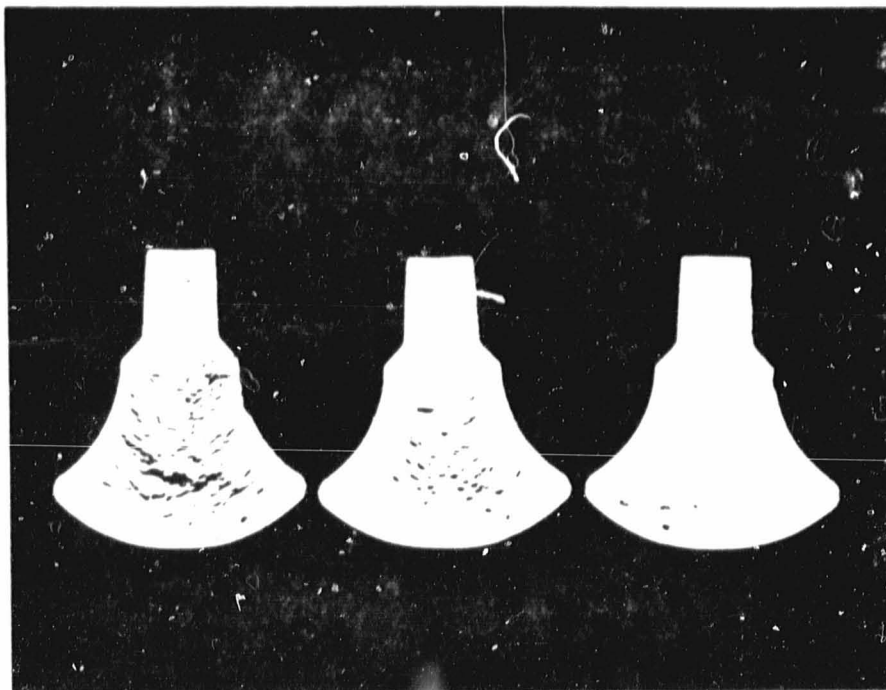


Figure 266. Cross-Section of Solid Simulated Rotor
Porosity Reduction Effort.

TABLE 41. MOLDING SUMMARY SOLID SIMULATED ROTOR

Part No	Temperature (°F)	Pressure (psi)	Velocity	Mold Temperature (°F)	Comments
26-1	330	1400	Variable S-F	80	4 Gates Enlarged
27-2	340	1400	Variable S-F	80	4 Gates Enlarged
39-3	330	1400	Constant F	100	4 Gates Enlarged
40-4	330	1400	Constant F	100	4 Gates Enlarged

Based on this development, additional work will be done in process optimization during molding and baking for this configuration.

2.3 Sintering

The availability of both continuous and batch-type furnaces for the densification step of alpha silicon carbide provided an opportunity to evaluate both systems for the program.

A continuous tube furnace was used to sinter 10 first generation rotor shells. All contained minor cracks from the baking step. Thus far, mixed results were obtained on density measurements for items sintered under identical conditions. The reason is not clear at the present time. Attempts are underway to determine differences in prior history which could account for this. Another group of 10 first generation shells were sintered in the batch furnace. Good densities were obtained in all pieces.

To date, 11 second generation rotor shells have been sintered in the batch furnace. All have good densities and 5 appear crack-free. All are useable for development of joining techniques. Density measurements are listed in Table 42.

2.4 Joining Development

The goal of the joining program is to produce a solid simulated rotor having properties equal to or better than the monolithic shape. Preliminary work with pseudo rotor shapes in the Common Work Program has indicated that a hot pressing technique which bonds a presintered shell to a presintered core should be successful. The joining work for the unique AiResearch rotor is just getting underway, and the first experiments carried out during the period emphasized this approach.

The hot pressing arrangement is shown schematically in Figure 267. The technique utilizes additional SiC as an extrudable mix at the shell/core interface. The core is fabricated from isopressed, green machined, and sintered alpha SiC.

Two hot pressing attempts were made during this period using a conical segment and the first generation shell. The first attempt produced a low density interface due to oversized stops during the hot pressing procedure. The stops prevent full pressure transmission to the core thereby resulting in low density. A second attempt was made and was unsuccessful due to rupturing of the mold housing during pressing. Stronger mold stock was ordered and will be used to fabricate future molds.

TABLE 42. DENSITY OF SINTERED SHELLS

Part. No	Rotor Configuration	Sintering Furnace*	Density (g/cc)
5	1st	T	2.98
15	1st	T	3.04
19	1st	T	3.02
22	1st	T	2.99
24	1st	T	3.08
28	1st	T	3.10
29	1st	T	3.11
30	1st	T	3.11
34	1st	T	3.14
36	1st	T	3.12
37	1st	T	3.14
30-1	2nd	B	3.14
32-3	2nd	B	3.15
33-4	2nd	B	3.15
34-5	2nd	B	3.15
35-6	2nd	B	3.15
37-8	2nd	B	3.14
38-9	2nd	B	3.15
45-10	2nd	B	3.15

* T = Continuous Tube Furnace

B = Batch Furnace

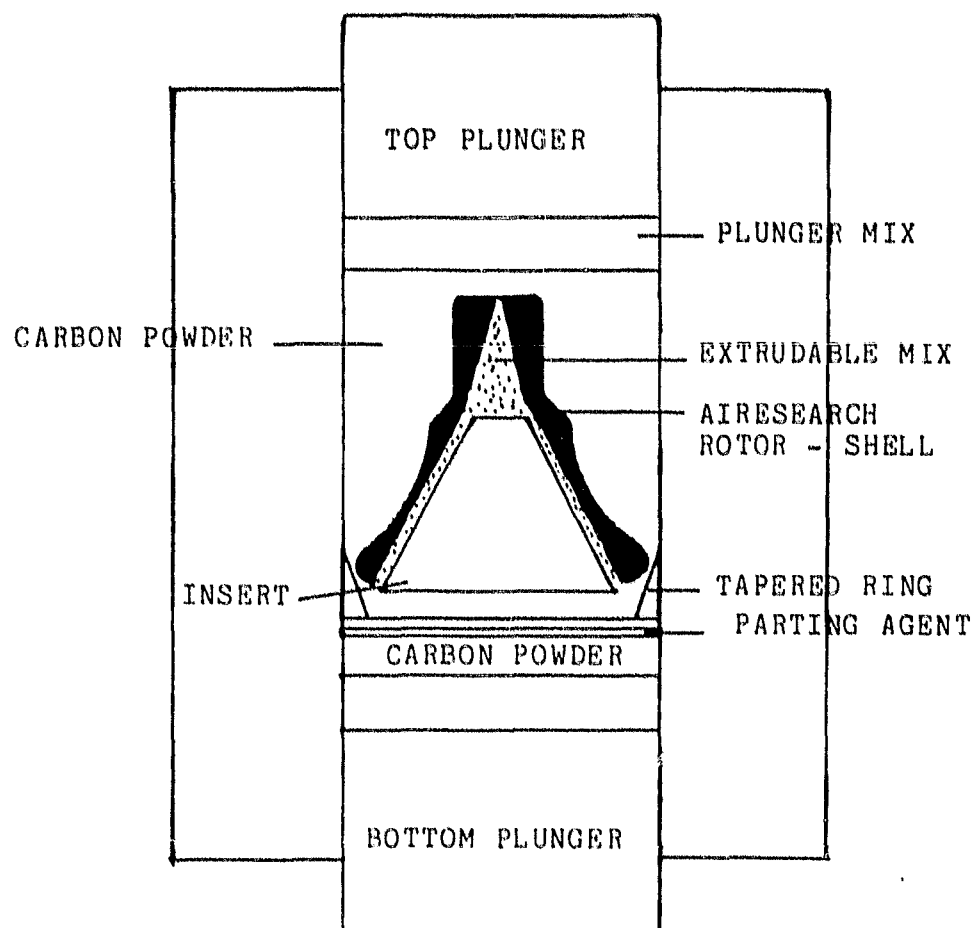


Figure 267. Schematic of Pressing Arrangement.

3. STATIC STRUCTURES

Several joint meetings were held with AiResearch Phoenix design personnel and Carborundum process engineers in order to finalize component design and to ascertain that fabricability to the necessary tolerances was attainable.

3.1 Turbine Stator

Both segmented and integral designs were initially considered for the stator section of the engine. For aerodynamic efficiency, the airfoil shape contains both convex and concave contours. In order to fabricate a functional tool to produce the integral stator, concessions on the airfoil contours would have been required. Aerodynamically, these concessions were undesirable and not allowed at this time. Therefore, Carborundum recommended and is pursuing the segmented approach which will produce the preferred airfoil shape. A single cavity tool has been designed and ordered. Delivery is expected during the last quarter of FY 80.

3.2 Turbine Shroud

The finalized turbine shroud design presents a challenge to current sintered SiC fabricating technology. The slip casting approach, originally considered for this component, produces a constant wall thickness. If this method were to be used, a great deal of diamond grinding would be required to produce the final geometry. Carborundum suggested and is pursuing the injection molding approach which is capable of net shape fabrication. Technologically, it should be feasible; however, there is some risk involved inasmuch as a part of this size has not yet been fabricated using the injection molding process. The tool has been ordered. The slip casting process with final grinding will be used as a backup in the event that insurmountable problems surface in the injection molding process.

3.3 Spacer, Duct

Carborundum suggested and is pursuing the green machining of isopressed stock prior to sintering for this component.

Isopressed rods were produced and green machined to shape during this period. Sintering will be carried out during the next period.

3.4 Shield, Regenerator

Carborundum suggested and is pursuing the green machining of isopressed tubes prior to sintering for this component. The tubes have been formed. Machining is on hold pending a minor design change.

3.5 Backshroud, Turbine

Carborundum suggested and is pursuing the green machining of isopressed billets prior to sintering for this component. Tooling to produce the correct size billet for machining has been ordered.

3.6 Combustor, Baffle

Since only one surface of the part is critical to the hot gas flow path, slip casting was suggested as the primary method of fabrication. Because of the need for spacers in 3 places on the gas path side of the component, 3 depressions will be produced on the opposite wall corresponding to the spacer locations. These were judged as noncritical to the performance of the part. The model to produce the casting mold has been ordered.

3.7 Diffuser, Inner

Changes were made in the original concept to accommodate the slip casting process. Carborundum is pursuing this approach for fabrication. The model to produce the slip casting molds has been ordered.

3.8 Transition Duct

Two designs for this part have been received for consideration. The aerodynamically preferred design shows variable wall thickness which would be difficult to produce.

The preferred design in terms of fabricability shows a constant wall thickness and was selected by Carborundum to produce via the slip casting process. The model to fabricate molds has been ordered.

3.9 Diffuser, Outer

Changes were made in the design to provide constant wall thickness to accommodate the slip casting process. The model has been ordered to produce the mold for casting.

APPENDIX V

PURE CARBON CO
ADVANCED GAS TURBINE (AGT) POWERTRAIN PROGRAM

FIRST-SEMI-ANNUAL TECHNICAL
PROGRESS REPORT

PURE CARBON COMPANY
AGT POWERTRAIN PROGRAM
FIRST SEMI-ANNUAL TECHNICAL
PROGRESS REPORT

Pure Carbon Co., acting as British Nuclear Fuel Ltd (BNFL) U.S. distributor, will provide simulated rotors and test bars of Refel, reaction-sintered SiC for AGT101 evaluation. Reaction-sintered SiC products are fabricated by a process in which a porous SiC/carbon body is exposed to silicon at elevated temperatures and the carbon is converted to bonding SiC. No material shrinkage occurs during the conversion process. "Green" materials to be reaction sintered may be formed by a variety of routes, e.g., slip casting, injection molding, extrusion, isopressing and warm molding, and the green body may be machined before firing. Requirements of binder removal prior to firing and silicon penetration during firing, however, impose thick section limitations on component geometries. These limitations are determined experimentally, although penetration up to one inch has been demonstrated.

Based on these known limitations, BNFL will perform a study to demonstrate binder bake-out and carbon conversion in the thick rotor sections prior to the initiation of a rotor fabrication development program. For expediency, this study is being performed using isopressed and green machined simulated rotors. Once binder removal and Si conversion have been demonstrated, slip casting or injection molding fabrication approaches will be pursued. Successfully reacted simulated rotors will be sent to AiResearch Phoenix for evaluation.

Five simulated rotors have been isopressed and currently are being machined. Binder removal and firing are scheduled to begin by September 1980.

Pure Carbon/BNFL also will provide test bars of slip cast Refel to AiResearch Phoenix for material characterization. Test bar materials have been fired, but will require machining by Pure Carbon prior to delivery. Delivery is scheduled for October 1980.

The following list provides definitions of acronyms as used in this document.

ACC	- AiResearch Casting Company
AGT	- Advanced Gas Turbine
AOD	- Automatic Overdrive Transmission
APU	- Auxiliary Power Unit
AS	- Aluminum Silicate
BNFL	- British Nuclear Fuels Ltd
CBO	- Carborundum
CFDC	- Combined Federal Driving Cycle
CPS	- Cumulative Probability of Success
DARPA	- Defense Advanced Research Project Agency
DOE	- Department of Energy
DS	- Directionally Solidified
EDX	- Energy Dispersive X-Ray Analysis
EPA	- Environmental Protection Agency
HIP	- Hot Isostatic Pressing
HP	- High Pressure Side, Air Side
LAS	- Lithium Aluminum Silicate
LP	- Low Pressure Side, Gas Side
MAS	- Magnesium Aluminum Silicate
Mod I	- Evolutionary Version of RPD - Metallic Engine
Mod II	- Evolutionary Version of RPD - Ceramic Engine
MOR	- Modulus of Rupture
ONR	- Office of Naval Research

PM	- Powder Metal
PM/PV	- Premixed Prevaporizing
RBSN	- Reaction Bonded Silicon Nitride
RPD	- Reference Powertrain Design
SASC	- Sintered Alpha Silicon Carbide
SEM	- Scanning Electron Microscopy
SI	- Spark Ignition
SiC	- Silicon Carbide
Si ₃ N ₄	- Silicon Nitride
SLAM	- Scanning Laser-Acoustic Microscopy
SPAM	- Scanning Photo-Acoustic Microscopy
SRBSN	- Sintered Reaction Bonded Silicon Nitride
SSN	- Sintered Silicon Nitride
TE	- Trailing Edge
TIT	- Turbine Inlet Temperature
VIGV	- Variable Inlet Guide Vane
VSTC	- Variable Stator Torque Converter
WOT	- Wide Open Throttle (Maximum Power)

REFERENCES

1. Conceptual Design Study of Improved Automotive Gas Turbine Powertrain--Final Report, NASA CR-159580, May 1979.
2. Advanced Gas Turbine (AGT) Powertrain System Initial Development Progress Report, NASA CR-165130, August 1980.
3. A Rapid Approximate Method for Determining Velocity Distribution on Impeller Blades of Centrifugal Compressors, Stanitz, J.D. and Prian, V.D., NACA TN 2421.
4. Aerodynamic Design of Axial Flow Compressors, Johnson, I.A., et al, NASA SP 36, 1965.
5. Carruthers, W.D., D.W. Richerson and K.W. Benn, 3500 Hour Durability Testing of Commercial Ceramic Materials, Interim Report NASA CR-159785, July 1980.
6. Menzik, Z. and M.A. Short. Quantitative Phase Analysis of Synthetic Si_3N_4 by X-Ray Diffraction: An Improved Procedure, Ford Motor Co. Scientific--Research Staff Technical Report No. SR-72-98.
7. Richerson, D.W., J.J. Schuldies, T.M. Yonushonis and K.M. Johansen, in Ceramics for High Performance Applications II (J.J. Burke, E.N. Leno and R.N. Katz, eds.) Brook Hill Publishing Co., Chestnut Hill, Mass., 1978
8. Rice, R.W. and J.J. Mecholsky,, in The Science of Ceramic Machinery and Surface Finishing II, (B.J. Hockey and R.W. Rice, eds.), NBS Special Publication 562, 1979, pp. 351-378.
9. Rice, R.W., S. Freiman, J.J. Mecholsky, R. Ruh and Y. Harada, in Ceramics for High Performance Applications II (J.J. Burke, E. N. Leno and R.N. Katz, eds), Brook Hill Publishing Co., Chestnut Hill, Mass, 1978.
10. Richerson, D.W., T.M. Yonuhonis and C.Q. Weaver, in Ceramic Gas Turbine Demonstration Engine Program Review (J.W. Fairbanks and R.W. Rice, eds.), MCIC Report MCIC-78-36, March, 1978, pp 193-217.
11. Ceramic Gas Turbine Engine Demonstration Program, Interim Report No. 17, May, 1980, pp. 4-1 to 4-49, prepared under Contract N00024-76-C-5352.
12. Finger, D.G., Contact Stress Analysis of Ceramic-Metal Interfaces, Final Report, Contract N00014-78-C-0547, September, 1979.